Thermal Bremsstrahlung probing nuclear multifragmentation in nucleus-nucleus collisions around the Fermi energy

D. d'Enterria

GANIL T 00 03

UNIVERSITÉ DE CAEN/BASSE-NORMANDIE

THÈSE

en cotutelle avec

UNIVERSITAT AUTÒNOMA DE BARCELONA

présentée

par

David G. D'ENTERRIA

pour obtenir

le GRADE de DOCTEUR EN SCIENCES DE L'UNIVERSITÉ DE CAEN
Spécialité : Constituants élémentaires

sujet :

Bremsstrahlung thermique comme sonde de la multifragmentation nucléaire dans les collisions noyau-noyau aux énergies de Fermi

soutenue le 5 Mai 2000 devant le jury suivant :

Monsieur	Jörg	AICHELIN	
Monsieur	José	DIAZ	rapporteur
Monsieur	Francisco	FERNANDEZ	directeur
Monsieur	Jean-François	LECOLLEY	
Monsieur	Herbert	LOEHNER	rapporteur
Monsieur	Yves	SCHUTZ	directeur

UNIVERSITAT AUTÒNOMA DE BARCELONA

TESI DOCTORAL

en cotutela amb la

**UNIVERSITÉ DE CAEN/
BASSE-NORMANDIE**

presentada

per

David G. D'ENTERRIA

per obtenir

**el grau de Doctor en Ciències Físiques
per la Universitat Autònoma de Barcelona**

**i el grau de "Docteur en Sciences"
(especialitat: "Constituents elementals")
per la Université de Caen/Basse-Normandie**

títol:

"Thermal Bremsstrahlung probing nuclear multifragmentation in nucleus-nucleus collisions around the Fermi energy"

Març de 2000

GANIL T 00 03

UNIVERSITÉ DE CAEN/BASSE-NORMANDIE

THÈSE

en cotutelle avec

UNIVERSITAT AUTÒNOMA DE BARCELONA

présentée

par

David G. D'ENTERRIA

pour obtenir

le GRADE de DOCTEUR EN SCIENCES DE L'UNIVERSITÉ DE CAEN
Spécialité : Constituants élémentaires

sujet :

Bremsstrahlung thermique comme sonde de la multifragmentation nucléaire dans les collisions noyau-noyau aux énergies de Fermi

soutenue le 5 Mai 2000 devant le jury suivant :

Monsieur	Jörg	AICHELIN	
Monsieur	José	DIAZ	rapporteur
Monsieur	Francisco	FERNANDEZ	directeur
Monsieur	Jean-François	LECOLLEY	
Monsieur	Herbert	LOEHNER	rapporteur
Monsieur	Yves	SCHUTZ	directeur

El sotasignant, Dr. Francisco Fernández, catedràtic del Departament de Física de la Universitat Autònoma de Barcelona,

CERTIFICA

que la tesi doctoral **“Thermal Bremsstrahlung probing nuclear multifragmentation in nucleus-nucleus collisions around the Fermi energy”** en cotutela entre la Universitat Autònoma de Barcelona i la “Université de Caen/Basse-Normandie”, - realitzada sota la meva direcció i del Dr. Yves Schutz, investigador de l’“Institut National de Physique Nucléaire et de Particules”-, pel Sr. David Garcia-d’Enterria i Adan, llicenciat amb grau en Ciències Físiques, reuneix les condicions requerides per a ser defensada davant el tribunal que es designi a tal efecte.

I perquè així consti, signem a 13 de març de 2000

Dr. Francisco Fernández Dr. Yves Schutz

Résumé

Cette thèse aborde l'étude des propriétés thermodynamiques de la matière nucléaire portée à températures et densités où l'on s'attend à observer la transition de phase liquide-gaz nucléaire. Les photons durs ($E_\gamma > 30$ MeV) émis dans des collisions noyau-noyau sont utilisés comme sonde expérimentale. La production des photons et particules chargées dans quatre réactions d'ions lourds différentes (^{36}Ar+^{197}Au, ^{107}Ag, ^{58}Ni, ^{12}C à 60*A* MeV) a été mesurée de façon exclusive et inclusive en couplant le spectromètre de photons TAPS avec deux autres détecteurs de particules légères et de fragments de masse intermédiaire couvrant quasiment la totalité de l'angle solide.

Nos résultats confirment l'origine dominante des photons durs comme étant due au rayonnement de freinage émis dans les collisions proton-neutron (*pn*γ) de première chance (hors équilibre). Nous établissons aussi de façon définitive l'existence d'une composante de radiation thermique dans le spectre photon mesuré dans les sytèmes lourds, et attribuons son origine au rayonnement de freinage émis dans les collisions *pn* de deuxième-chance. Nous exploitons cette observation pour i) démontrer que la matière nucléaire atteint un équilibre thermique lors de la réaction, ii) valider un nouveau thermomètre basé sur les photons du rayonnement de freinage, iii) déduire les propriétés thermodynamiques de la matière nucléaire chaude (en particulier, pour établir la "courbe calorique") et iv) évaluer les échelles de temps du processus de fragmentation nucléaire.

Abstract

The thermodynamical properties of nuclear matter at moderate temperatures and densities, in the vicinity of the predicted nuclear liquid-gas phase transition, are studied using as experimental probe the hard-photons ($E_\gamma > 30$ MeV) emitted in nucleus-nucleus collisions. Photon and charged-particle production in four different heavy-ion reactions (^{36}Ar+^{197}Au, ^{107}Ag, ^{58}Ni, ^{12}C at 60*A* MeV) is measured exclusively and inclusively coupling the TAPS photon spectrometer with two charged-particle and intermediate-mass-fragment detectors covering nearly 4π.

We confirm that bremsstrahlung emission in first-chance (off-equilibrium) proton-neutron collisions (*pn*γ) is the dominant origin of hard photons. We also firmly establish the existence of a thermal radiation component emitted in second-chance proton-neutron collisions. This thermal bremsstrahlung emission takes place in semi-central and central nucleus-nucleus reactions involving heavy targets. We exploit this observation i) to demonstrate that thermal equilibrium is reached during the reaction, ii) to establish a new thermometer of nuclear matter based on bremsstrahlung photons, iii) to derive the thermodynamical properties of the excited nuclear sources and, in particular, to establish a "caloric curve" (temperature versus excitation energy) and iv) to assess the time-scales of the nuclear break-up process.

Acknowledgments

This joint-supervisor PhD thesis in experimental nuclear physics is the result of the work performed between roughly January 1997 and Mars 2000 at 4 different laboratories: GANIL in Caen, KVI in Groningen, Subatech in Nantes, and Grup de Física de les Radiacions in Barcelona, and therefore it has involved the valuable participation and engagement of many different people. Nonetheless, this work could have never been accomplished without the coherent contributions of three people: Ginés Martínez, Yves Schutz and Francisco Fernández. Ginés has not only been the proposal leader of the experiment which constitutes the subject of this thesis and a precious source of knowledge, physical insight and discussion, but he has also become a good friend during these years of close work. I am permanently in debt with Paco and Yves because, apart from taking in charge the direction of this thesis and counting on their permanent confidence and support, they have opened to me the doors of the physics research world accepting me as a full member of the "Grup de Física de les Radiacions" and of the GANIL/Subatech "TAPS/Groupe Photons" respectively.

I am also specially grateful to the following colleagues and friends with whom I have been more directly working (and enjoying myself) the last years: Laurent Aphecetche (for introducing me to the world of code management, and for developing the core of the main TAPS analysis programmes used in this work), Hugues Delagrange (for a careful reading of this manuscript and for his multiple advices), Rosario Turrisi (for one-year-and-a-half of friendly and healthy office "cohabitation" at GANIL), María-Jesús Mora (for her useful collaboration in a few of the less motivating TAPS and Dwarf-Ball calibration procedures), and Raquel Ortega. I am also thankful to Marc-Jan van Goethem and Marieke Hoefman for their worthful collaboration during the experimental setup and run periods at KVI (as well as Nadia, Vladimir and Reint), and during the first steps of the data analysis.

I want specially to thank Herbert Loehner and Jose Díaz not only for having accepted to report this thesis, but also because they were a source of instruction during my stay at KVI. All the rest of the members of the jury: Jörg Aichelin, Enrique Fernández, David Jou and Jean François Lecolley are also greatly acknowledged.

I want to express my gratitude to Daniel Guerreau and Hans Gutbrod, directors of the GANIL and Subatech laboratories, for providing the necessary means which have permitted the successful completion of this thesis.

A particular word of acknowledgement for Regina Nebauer (for making available her latest version of QMD) and Pol-Bernard Gossiaux (for his help during the very last hours

of the redaction process). Last but not least, I also want to acknowledge the whole set of people (not already mentioned) with whom I have shared a pleasant day-to-day life during the last years: the members of the Grup de Física de les Radiacions (Pere, Lluís, Joan, Khalil, Moad, Tayeb, together with Carme, Carles, Joan-Albert and Fermi), as well as the (ex-)“thésards” at GANIL (Anne, María-José, Olivier, Fred, Jean-Michel, Karim, Lynda, Anne-Sophie, ...) and at Subatech (Fabrice G., Fabrice R., François, Hajo, Javier, Tanguy, Laurent C. ...).
Mercès a tots ! / Merci à tous !

Naoned/Nantes, le 20 Mai 2000

Als meus pares i germà.
A la Marta.

If from things we take away the void
All things are then condensed, and out of all
One body made, which has no power to dart
Swiftly from out itself not anything -
As throws the fire its light and warmth around
Giving thee proof its parts are not compact.

De rerum natura. Lucretius, circa 95-55 BC.

Contents

Outline of the thesis **v**

1 Fundamental properties of nuclear matter **1**
1.1 The equation of state of nuclear matter . . . 2
1.2 The phase diagram of nuclear matter . . . 4
1.3 The atomic nucleus . . . 7
1.4 The nuclear force . . . 8

2 Heavy-ion physics **11**
2.1 Characteristics of HI reactions . . . 12
2.1.1 The bombarding energy . . . 13
2.1.2 The impact parameter . . . 16
2.1.3 The projectile-target combination . . . 16
2.2 HI reactions in the intermediate-energy region . . . 17
2.2.1 The nuclear liquid-gas phase transition . . . 17
2.2.2 Experimental approaches . . . 20
2.2.3 Theoretical approaches . . . 21
2.3 Phase-space evolution of the nucleus-nucleus collision . . . 23
2.4 Nuclear multifragmentation and the liquid-gas phase transition . . . 26

3 Photon production in nucleus-nucleus collisions at intermediate energies **35**
3.1 Sources of photons in HI collisions around the Fermi energy . . . 36
3.2 Hard-photon production in HI collisions around the Fermi energy . . . 41
3.2.1 Experimental systematics . . . 41
3.2.2 Theoretical models . . . 47
3.3 New experimental results of hard-photon production: Thermal hard-photons 49
3.4 Goals of the experiment. Motivation of the thesis . . . 53

4 Experimental setup **57**
4.1 Detector overview . . . 58
4.2 AGOR accelerator . . . 59
4.3 Argon beam . . . 60
4.4 Carbon-Fiber reaction chamber . . . 60
4.5 Targets . . . 65
4.6 TAPS electromagnetic calorimeter . . . 68
4.6.1 Main characteristics . . . 68

4.6.2 BaF_2 crystals . . . 69
4.6.3 Charged-Particle Vetoes . . . 70
4.6.4 Photon identification . . . 71
4.6.5 TAPS front-end electronics . . . 72
4.7 Dwarf-Ball charged-particle multidetector . . . 75
4.7.1 Main characteristics . . . 75
4.7.2 BC400-CsI(Tl) phoswiches . . . 77
4.7.3 Particle identification capabilities . . . 79
4.7.4 Dwarf-Ball electronics and pre-trigger logics . . . 79
4.8 Forward Wall charged-particle multidetector . . . 84
4.8.1 Main characteristics . . . 84
4.8.2 NE102A-NE115 phoswiches . . . 85
4.8.3 Particle identification capabilities . . . 85
4.8.4 Forward Wall electronics . . . 87
4.9 Data-acquisition system and trigger logics . . . 89
4.9.1 Data acquisition system . . . 89
Data stream handling . . . 90
On-line analysis . . . 92
Parameter control . . . 92
Taping . . . 92
4.9.2 Trigger logics . . . 93
Triggers definition . . . 94
Trigger logics generation . . . 94
Final total data volume . . . 97

5 Data analysis and detector calibration 99
5.1 Data analysis and simulation software packages . . . 101
5.2 TAPS Energy calibration . . . 102
5.3 TAPS Time calibration . . . 104
5.3.1 Single detector time calibration . . . 104
5.3.2 *TOF* drift correction . . . 106
5.3.3 Walk and cross-talk correction . . . 106
5.4 Photon reconstruction: cluster analysis . . . 106
5.4.1 Single-detector particle identification (*PSA* vs. *TOF*) . . . 108
5.4.2 Clustering routine . . . 108
Cluster Energy . . . 111
Cluster position . . . 113
5.5 Dwarf-Ball analysis . . . 114
5.5.1 DB light-charged particle isotopic identification . . . 114
5.5.2 DB IMF identification . . . 116
5.6 Forward Wall analysis . . . 118
5.6.1 FW LCP/IMF separation . . . 118

6 Inclusive experimental results **121**
6.1 Hard-photon energy spectra . . . 122
6.1.1 Raw photon spectrum . . . 122
6.1.2 Detector response function . . . 124
6.1.3 Cosmic-rays background . . . 125
6.1.4 Photons from neutral pion decay . . . 125
6.1.5 Corrected inclusive photon spectra . . . 128
6.1.6 Direct and thermal slopes and intensities . . . 139
6.2 Hard-photon angular distributions. Source velocity analysis . . . 142
6.2.1 "Direct" and "thermal" hard-photon angular distributions . . . 142
6.2.2 Total hard-photon ($E_\gamma > 30$ MeV) angular distributions . . . 147
6.3 Inclusive charged-particle and fragment distributions . . . 153
6.3.1 Inclusive charged-particle multiplicities . . . 153
6.3.2 Inclusive LCP and IMF multiplicities . . . 157
6.4 Inclusive cross-sections and multiplicities . . . 160
6.4.1 Cross-sections formulae . . . 160
6.4.2 Charged-particle detection efficiencies . . . 161
6.4.3 Hard-photon detection efficiency . . . 162
6.4.4 Total reaction cross-sections . . . 164
6.4.5 Hard-photon production cross-sections and multiplicities . . . 166

7 Exclusive experimental results **173**
7.1 Event selection . . . 174
7.2 Exclusive photon spectra . . . 178
7.2.1 Central reactions . . . 179
7.2.2 Peripheral reactions . . . 181
7.2.3 Multifragmentation reactions . . . 181
7.3 Impact-parameter dependence of the photon yield . . . 184
7.4 Summary of the experimental results and preliminary interpretation . . . 188
7.4.1 GDR photons . . . 189
7.4.2 Coherent nucleus-nucleus bremsstrahlung . . . 191
7.4.3 Cooperative cluster bremsstrahlung . . . 192
7.4.4 Proton-proton ($pp\gamma$) bremsstrahlung . . . 193
7.4.5 Bremsstrahlung from second-chance NN collisions. Preequilibrium or thermal ? . . . 193

8 Model comparison **197**
8.1 Boltzmann-Uehling-Uhlenbeck (BUU) model . . . 198
8.1.1 Description of the model . . . 198
8.1.2 Collision dynamics in the ^{36}Ar+^{197}Au, ^{107}Ag, ^{58}Ni, ^{12}C at 60A MeV reactions . . . 200
8.1.3 Bremsstrahlung production within BUU . . . 210
8.2 Quantum Molecular Model (QMD) . . . 218
8.2.1 Description of the model . . . 218
8.2.2 Collision dynamics in the ^{36}Ar+^{197}Au, ^{107}Ag, ^{58}Ni, ^{12}C at 60A MeV reactions . . . 219

8.2.3 Bremsstrahlung production within QMD 229

9 Derivation of thermodynamical properties 235
9.1 Thermal bremsstrahlung model 236
9.1.1 Description of the thermal model 236
9.2 Extraction of a nuclear temperature 240
9.3 Thermal hard-photons: a new thermometer of nuclear matter 243
9.4 Derivation of the nuclear "caloric curve" 246

Conclusions and outlook 251

Conclusions (català) 257

Conclusions (français) 263

Appendix 1: Scintillators 269
.1 Scintillation mechanism 270
.2 Crystal scintillators 271
.3 Plastic scintillators 273
.4 Charged-particle detection with 4π arrays in nuclear physics 274
.4.1 Two-component inorganic scintillators 274
.4.2 Phoswiches 276

Appendix 2: Nuclear Bremsstrahlung 279
.1 Classical $NN\gamma$ Bremsstrahlung cross-section 281
.2 Covariant $NN\gamma$ Bremsstrahlung cross-section 283

Appendix 3: The nuclear Equation-of-State 287
.1 EoS of cold nuclear matter 288
.2 EoS of moderately hot and compressed nuclear matter 289
.3 EoS of hot nuclear matter 293

Appendix 4: Heavy-ion kinematics formulae 295

Appendix 5: Dwarf-Ball electronics and pre-trigger logics 299

Outline of the thesis

It is commonly believed that nuclear matter undergoes a *liquid-gas phase transition* at subnuclear densities and moderate temperatures. In the early 80's it was suggested that such a phase transition might be probed in heavy-ion reactions at bombarding energies between 20*A* MeV and 100*A* MeV (i.e. around the *Fermi energy*, defined as the average kinetic energy of the nucleons inside the nucleus) by observing the disintegration of the colliding nuclei into many fragments of different sizes, a phenomenon commonly known as *multifragmentation*.

The present thesis reports on an investigation of the (thermo)dynamical state of nuclear systems produced in nucleus-nucleus collisions at intermediate bombarding energies and excited to the vicinity of the predicted liquid-gas phase transition. *Bremsstrahlung photons* ($E_\gamma > 30$ MeV), emitted in individual nucleon-nucleon collisions, are used as experimental probes of the phase-space evolution of the reaction as well as of the thermodynamical properties of the produced hot systems. In particular, I address the importance of thermal bremsstrahlung emission which signs second-chance proton-neutron collisions within a thermalized nuclear source.

The first three chapters of this thesis are devoted to an introductory description of the basic features of nuclear matter, heavy-ion physics and hard-photon production in nucleus-nucleus collisions at intermediate-energies. The fourth chapter describes the experimental setup used to detect and identify the different reaction products: hard-photons, and nuclear charged particles and fragments. Data analysis and detector calibration procedures are explained in chapter 5. Chapter 6 and 7 present the inclusive and exclusive experimental results, respectively, as well as their preliminary interpretation. A comparison of the obtained data with two different microscopical transport approaches and the derivation of thermodynamical properties of the hot produced systems by means of a thermal model are carried out in chapters 8 and 9 respectively. Finally, the conclusions and outlook of this work are summarized. Appendices 1 - 5 give respectively an overview of the principles of scintillation detectors, of the elementary process of photon Bremsstrahlung in nucleon-nucleon collisions, of the EoS of nuclear matter, of some basic heavy-ion kinematics formulae used in this work, as well as a detailed electronics and logics scheme of one of the charged-particle multidetectors.

Chapter 1

Fundamental properties of nuclear matter

Summary

1.1 The equation of state of nuclear matter 2
1.2 The phase diagram of nuclear matter 4
1.3 The atomic nucleus 7
1.4 The nuclear force 8

1.1 The equation of state of nuclear matter

One of the most exciting challenges in modern experimental and theoretical nuclear physics consists in understanding the behaviour of nuclear matter under extreme conditions of density and temperature. Nuclear matter is an idealized extrapolation of the atomic nucleus to infinite size (i.e. without surface or other finite-size effects) at the known saturation density of the nucleus ρ_0, without Coulomb interaction and with equal proton and neutron densities (i.e. zero isospin). In its ground state, nuclear matter can be hence described as a many-body system with constant density ρ_0, constituted of protons and neutrons at zero temperature and pressure, interacting through the long range part of the strong interaction. The quantitative description of such a many-body strongly interacting system when it is far away from the saturation state relies on the knowledge of the nuclear equation of state (EoS). The EoS of nuclear matter defines the dependence of the pressure $P = P(T,\rho)$ or, alternatively, of the energy per nucleon $\varepsilon = E/A = \varepsilon(T,\rho)$ (the so-called "caloric EoS") on two (macro)canonical variables: the temperature T and the density ρ (see fig. 1.1 and Appendix 3).

In the present day, the empirical information on the nuclear EoS in the ε vs. ρ plane is only known with certainty at the ground state point at T = 0 and $\rho = \rho_0$ [Sura93]:

- From electron-nucleus scattering measurements and from the interpretation of the nuclear binding energies, the value of the saturation density and the nuclear binding energy per nucleon ε at T = 0 are [Myer76, Beth71]:

$$\begin{aligned} \rho_0 &= (0.16 \pm 0.01)\ \mathrm{fm}^{-3} \\ \varepsilon(\rho=\rho_0) &= (-16.0 \pm 0.5)A\ \mathrm{MeV} \end{aligned}$$

- The ground state equilibrium condition, i.e. the condition that the energy ε is minimum at $\rho = \rho_0$, requires the derivative at this point to be zero, $(d\varepsilon/d\rho|_{\rho=\rho_0} = 0)$. Or, in terms of the equation-of-state, the pressure must be zero at ground-state:

$$P = \rho^2 \left(\frac{\partial \varepsilon}{\partial \rho}\right)_{\rho=\rho_0} = 0 \tag{1.1}$$

- The second derivative (the curvature) of ε at $\rho = \rho_0$, characterizes the compressibility of nuclear matter. The bulk incompressibility modulus κ_∞ of nuclear matter is defined as the second derivative of the energy at the minimum with respect to the density:

$$\kappa_\infty \equiv 9 \left(\frac{\partial P}{\partial \rho}\right)_{\rho=\rho_0} = 9\rho^2 \left(\frac{\partial^2 \varepsilon}{\partial \rho^2}\right)_{\rho=\rho_0} \tag{1.2}$$

  According to measurements of the giant monopole vibrations in spherical nuclei [Blai95], κ_∞ lies[1] between 180 MeV [Blai80] and 300 MeV [Shar88].

The nuclear EoS provides a way to describe the bulk properties of a nuclear many-body system in thermodynamical equilibrium, governed at the microscopic level by the

[1] The most recently reported value is κ_∞ = 231 ± 5 MeV [Youn99].

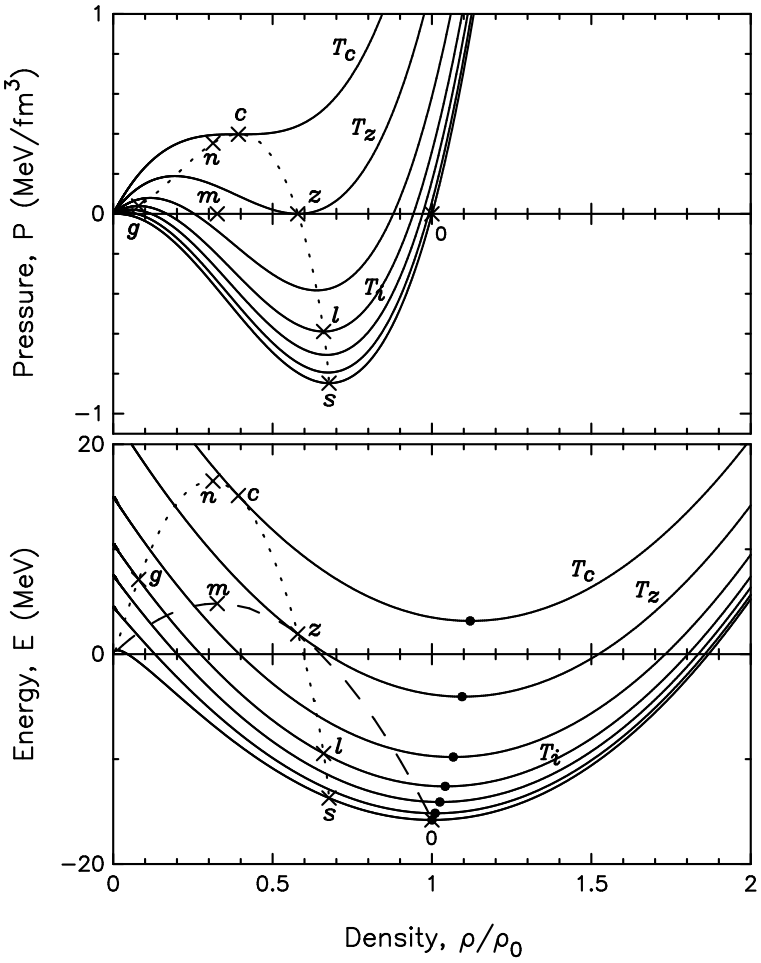

Figure 1.1: *Nuclear equation-of-state around the ground-state (or saturation) point [Lee97]. "Thermodynamical" EoS $P = P(T,\rho)$ (upper figure) and "caloric" EoS $\mathcal{E} = \mathcal{E}(T,\rho)$ (lower figure) of nuclear matter for different isothermal curves (from bottom to top): T_i (MeV) = 0, 3, 5, 7, 10, 15.16 (= T_z at which the minimum pressure is zero), and 20.95 (= T_c, the critical temperature); obtained with a nuclear mean-field interaction of the form $U = U(\rho)$. The saturation point 0 corresponds to P = 0 (otherwise the system would expand or contract) or $\mathcal{E}$ = -16 MeV, T = 0 MeV and ρ_0 = 0.16 fm^{-3}. The critical point c in this model is at T_c = 20.95 MeV, $\rho_c = 0.39\rho_0$ = 0.062 fm^{-3} and P = 0.4 MeV fm^{-3}. The dotted points delimit the mechanically unstable low-density "spinodal" region where $dP/d\rho\,|_T < 0$ (i.e. the region where the incompressibility $\mathcal{K}_\infty$ becomes negative). In the lower figure, the dashed line corresponds to the zero pressure, and the solid circles to the points of minimum energy for each temperature T. (See Section 2.2.1 for the details of this plot.)*

two-body nucleon-nucleon (*NN*) interaction. The *NN* potential exhibits a short-range repulsive part and a long-range attractive part (fig. 1.2) akin to the Lennard-Jones interaction between molecules in a macroscopic Van der Waals real fluid (fig. 1.3). This similarity suggests that nuclear matter could exist in gaseous states as well as liquid states. As a matter of fact, it is commonly believed that nuclear matter experiences different phase transitions (see next Section) [Cser86, Stoe86].

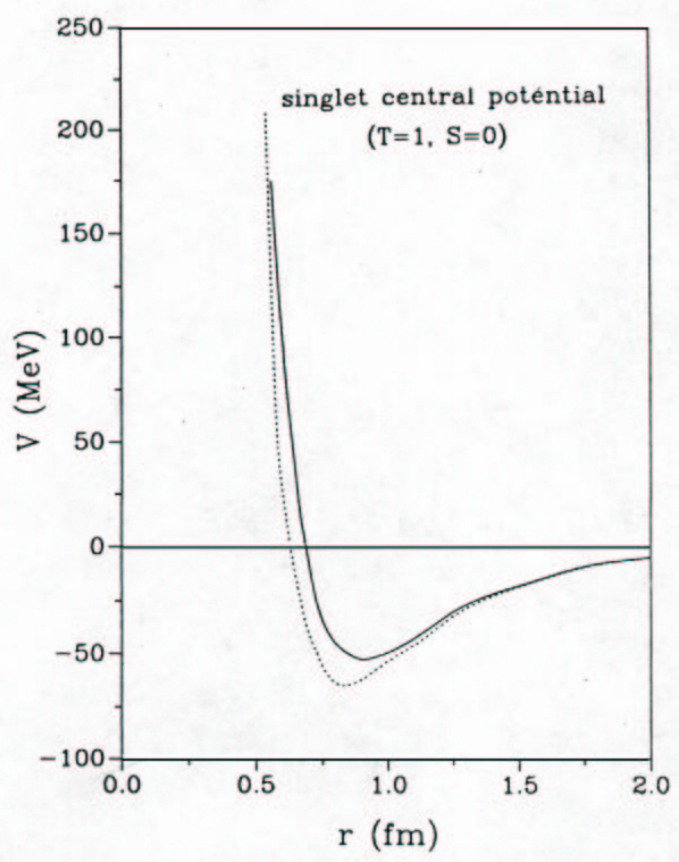

Figure 1.2: *Basic central nucleon-nucleon potential (for spin S = 0 and isospin T = 1). From [Mach94].*

1.2 The phase diagram of nuclear matter

Several phase transitions have been conjectured in the ε vs. ρ phase diagram of infinite nuclear matter (fig. 1.4). At $T = 0$, nuclear matter is in the form of a Fermi liquid. For densities below half the saturation value ($\rho = 0.25\rho_0$ - $0.4\rho_0$) a liquid-gas transition (from the nuclear liquid to a gas of individual nucleons) has been predicted to occur (for a recent review see e.g. [Poch97]) around a moderate critical temperature: $T_c \approx 16$ MeV for infinite nuclear matter [Lamb78, Jaqa83], and T_c = 8 - 10 MeV for finite (and charged) nuclei [Siem83, Bond85]. For increasing temperatures ($T \approx 20$ - 100 MeV), the nucleon gas transforms into a gas of *excited* hadrons. For very high temperatures ($T_c = 150 \pm$

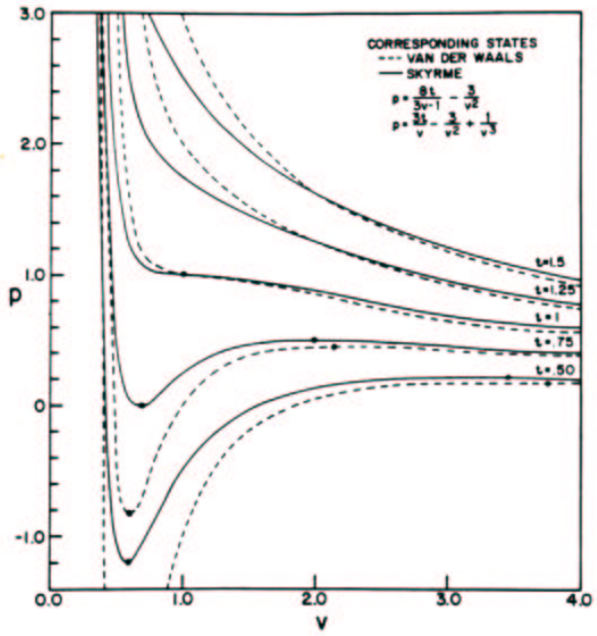

Figure 1.3: *Comparison between the EoS, $P = P(T,V)$, of a Van der Waals gas and the EoS of nuclear matter (described by a density-dependent Skyrme mean-field potential) [Jaqa83, Bert88].*

20 MeV) and/or high densities ($\rho \approx 10\rho_0$), lattice QCD calculations (see e.g. [DeTa95]) predict the existence of two phase transitions: i) the color-deconfinement transition, and ii) the restoration of chiral symmetry. At these high temperatures, hadronic matter is in the state of a plasma of deconfined quarks and gluons [Mcle86] and the chiral symmetry of the QCD Lagrangian might probably be restored. This new state of matter is believed to have existed during a few tens of microseconds after the Big Bang. In addition, other more "exotic" phase transitions have been proposed at rather low temperatures and relatively high densities such as a color superconducting phase [Raja99], or pion and kaon condensation [Heis99]. In all cases, apart from confirming their existence, the order[2] (first or second) of the expected phase transitions is one of the major issues.

Studying the behaviour of nuclear matter far from its saturation point is motivated not only by nuclear physics but also for the understanding of astrophysics and cosmology phenomena. Indeed, the EoS of nuclear matter (and specially its density-dependence more than its dependence on T) is a fundamental ingredient to describe the dynamics of stellar collapse and supernovae explosion [Latt00], as well as for the formation and structure of neutron stars [Glend88, Glend92, Latt00, Heis99] or more complex systems such as "strange stars" [Li99] or "binary mergers" (neutron stars and black holes) [Latt00].

[2] In general, for infinite systems (i.e. in the thermodynamical limit), if the first derivative of the thermostatistical potential adapted to the physical situation under study is discontinuous, the phase transition is "first-order" (e.g. the common liquid-gas transition of water at constant pressure); conversely when the *second derivative* is diverging the phase transition is said to be of "second-order" (or "continuous") [Chom00].

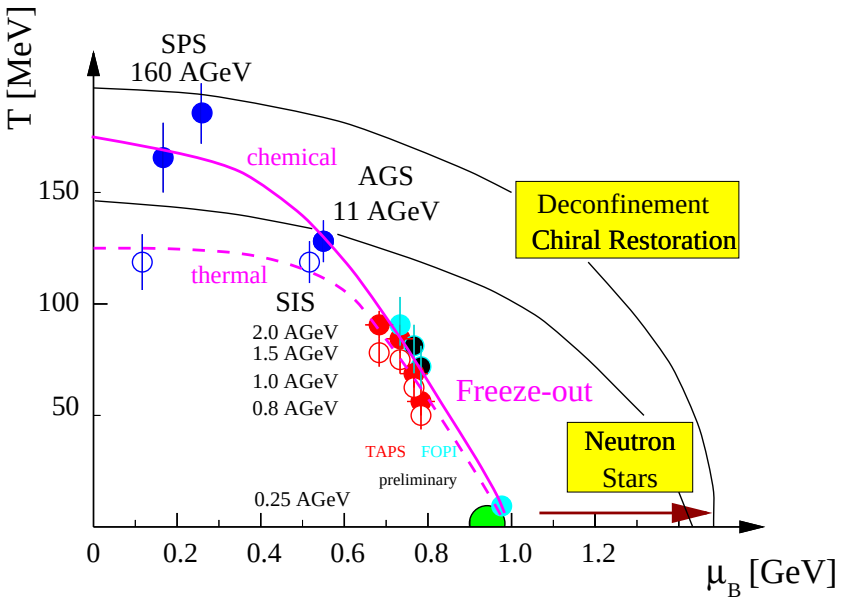

Figure 1.4: *Phase diagram of nuclear matter in the temperature versus baryochemical potential (T, μ_B) plane [Aver98], where μ_B has been derived from yield ratios of particles produced in nucleus-nucleus collisions at different incident energies. The solid (dashed) curve through the data points represents the predicted curve of chemical (thermal) freeze-out.*

Similarly, a detailed knowledge of the quark-hadron phase transition is basic for the study of the dynamics of the early universe (deconfined nuclear matter) and, e.g., the Big-Bang nucleosynthesis (hadronized nuclear matter) [Reev91, Borg00].

Experimentally, the systematic study of the properties of nuclear matter at values of temperature and pressure far away from the ground-state can be performed in the laboratory only by making collide "chunks" of nuclear matter (atomic nuclei) with a finite number of constituents. During the collision the nuclei interact strongly, and part of the incident kinetic energy is dissipated into internal (thermal) and compressional degrees of freedom, leading to the formation of an ephemeral system of hot and dense nuclear matter. As it expands and cools, the system may thus dynamically traverse the various phase transitions. When the reaction time is long enough to reach thermal equilibrium[3] and when the number of interacting particles is not too small, it is reasonable to reduce the description of the system in terms of thermodynamical variables (density, temperature, pressure) allowing the study of the nuclear matter properties with the help of an EoS. The choice of the relative kinetic energy, the impact parameter and the (relative) mass (size) of the colliding nuclei defines the degree to which nuclear matter can be heated and compressed and, thus, allows to select the domain of the phase diagram one wishes to explore. The availability of accelerators capable of delivering beams with a large variety of kinetic energies and masses permits thus to cover a broad domain of densities and temperatures.

[3] Recently also a generalized Gibbs equation for nuclear matter *out* of equilibrium [Bida98] within the formalism of extended irreversible thermodynamics [Jou98] has been proposed.

Experiments aiming at such studies during the last 20 years have exploited the heavy-ion beams available at several facilities: GANIL (Caen), KVI (Groningen), SARA (Grenoble), RIKEN (Tokio), NSCL (Michigan State University), TAMU (Texas), UNILAC and SIS (GSI, Darmstadt) for the intermediate bombarding energies from 20*A* MeV to 100*A* MeV; SIS (GSI), SATURNE[4] (Saclay), BEVALAC[3] (LBL, Berkeley), and JINR (Dubna) for relativistic projectile energies around a few *A* GeV; and AGS (BNL, Brookhaven), SPS (CERN), RHIC (BNL) and LHC[5] (CERN) for ultrarelativistic incident energies above 10*A* GeV.

1.3 The atomic nucleus

The atomic nuclei usually employed in heavy-ion reactions are considered as finite-size (R = 1.2 - 7.5 fm, i.e. V = 10 - 1800 fm^3) quantal many-body systems constituted from[6] A = 4 (for the ^{4}He nucleus) up to[7] $A \approx 250$ strongly interacting fermions, -the nucleons-, of two types (Z protons and N neutrons). The fundamental properties of the nucleus can be summarized as [Povh95]:

1. The ground state of the nucleus has a roughly constant (central) density of ρ_0 = 0.16 fm^{-3} (equivalent to an energy density $\approx$ 0.15 GeV/fm^{-3}). The density of nuclei saturates at $\rho = \rho_0$, i.e. increasing the number of nucleons does not modify this value, which is an evidence for the finite range of the nuclear force. This also implies that the nuclear radius R varies approximately as $R = r_0 A^{1/3}$, with $r_0 \approx 1.2$ fm. The (charge) density distribution of nuclei (with $A > 10$) corresponds to that of a sphere with a diffuse surface. It can be described to a good approximation by a Woods-Saxon (Fermi distribution) function: $\rho(r) = \rho_0/[1 + e^{(r-c)/a}]$, with c = $1.07\,A^{1/3}$ fm and a = 0.54 fm; the surface thickness, defined as the layer over which the charge density drops from $0.9\rho_0$ to $0.1\rho_0$, amounting to $d = 2a \ln 9 \approx 2.4$ fm.

2. The binding energy per nucleon inside a nucleus remains roughly constant at around 8*A* MeV. This value can be understood, through the semi-empirical Weizsäcker mass formula, as the net result of the combination of one *attractive* and three *repulsive* contributions[8]: the nuclear binding energy (the volume or bulk term in the Weizsäcker formula) which amounts to $\approx$ -16*A* MeV; the Coulomb force between protons (1*A* - 4.5*A* MeV, being approximately proportional to $Z^2/A^{1/3}$), the surface *tension* (6*A* - 3*A* MeV, with a $A^{2/3}$ dependence), and the isospin asymmetry arising from the increasing number of neutrons in heavier stable nuclei (which goes as $(N-Z)^2/4A$).

[4] Shut-down to date.

[5] Operational in near-future.

[6] The liquid-drop description is meaningless for the lightest clusters. So, as far as ^{2}H, ^{3}H, ^{3}He have no excited states, they together with nucleons are usually considered as "elementary" particles in heavy-ion physics.

[7] Actually, A = 209 for the heaviest *stable* nucleus (^{209}Bi), $A \approx 250$ for the *unstable* actinide nuclei, and $A \approx 300$ for newly created *super-heavy* short-living elements.

[8] Additionally, a fifth contribution has to be added due to the coupling of protons and neutrons in pairs. This pairing energy can be written phenomenologically as $\pm 11.2/A^{1/2}$ MeV, with the negative (positive) sign for even-even (odd-odd) nuclei.

The aforementioned properties of the atomic nucleus in its ground state lead to consider it as a degenerate quantum Fermi fluid (a liquid in the sense that the particle interaction energy is of the order of their kinetic energy) at zero temperature and zero pressure. In this simple Fermi model, also called *independent-particle* picture, the nucleus can be described as a system of quasi-free particles obeying Fermi-Dirac statistics, interacting only weakly with each other and, to first approximation, moving inside a single-particle central potential (the "mean field") of depth $V_0 \approx -46$ MeV arising from its interaction with all the other nucleons. As spin 1/2 quantum particles the nucleons inside a nucleus naturally obey Pauli exclusion principle. At zero temperature the lowest states will thus all be occupied up to a maximal momentum (the Fermi momentum) connected to the density through the relation: $k_F = (3\pi^2\rho/2)^{1/3} \approx 1.36$ fm^{-1} (i.e. $p_F \approx 270$ MeV/c) which is equivalent to a kinetic energy of $K_F = \sqrt{p_F^2 + m_N^2} - m_N \approx 38A$ MeV. The difference $V_0 - K_F \approx -8A$ MeV gives roughly the ground state binding energy. Nucleons, thus, move inside the nucleus as fast as 30% of the speed of light ($\beta \approx 0.3c$) with an internucleonic mean distance of about 2 fm.

1.4 The nuclear force

The nuclear force holding together nucleons inside a nucleus is a residual ("molecular"-like) interaction of the color force mediated by the fundamental exchange of gluons between the constituent quarks of the nucleons. The nuclear force arises, thus, from very strong and highly non-linear interactions at the quark level. These residual *soft* strong processes are not readily calculable by perturbative means within the Quantum Chromo-Dynamics (QCD) theory, -the nonabelian gauge theory of coloured quarks and gluons based on the $SU(3)_c$ group of three colors-, due to the large strength of the QCD coupling constant at low energies (or large distances). At low-energies, however, the nucleon can be approximately considered as a three-quark core surrounded by a pionic cloud, and the description of a nucleus can be done, as long as one restricts oneself to distances larger than roughly 1 fm, not in terms of partonic degrees of freedom but in terms of nucleons as the fundamental constituents interacting through the exchange of virtual mesons (see for example [Myhr88] and [Mach94]). This One-Boson-Exchange (OBE) picture yields an effective Yukawa-like [Yuka35] finite-range force, $U(r) = (e^{-m_\pi r})/r$, between the nucleons in agreement with free NN scattering data at low energy ($K_{lab} < 300$ MeV).
The effective nucleon-nucleon interaction is usually divided into three regions depending on the distance r between the centers of the two nucleons: a long-range ($r > 2$ fm) and an intermediate-range (1 fm $< r <$ 2 fm) attractive regions (interpreted by the exchange of a single pion and two pions respectively), and a short-range ($r < 1$ fm) repulsive region (interpreted as the result of the exchange of heavier mesons), the radius of the repulsive core being ≈ 0.6 fm. In the nuclear medium, the attractive part causes nucleons to be bound in the nucleus, whereas the repulsive core leads to the finite size (saturation) of the nucleus. The short-range correlations give rise to a smearing of the Fermi surface and enhance high momentum components of the wave function. The different exchange terms not only account for the central part of the NN potential but also show up in the angular momentum structure of the potential as a spin-orbit (responsible of the shell structure in the nucleus), tensor (accounting for 5% - 10% of the strength of the nuclear force) and

an isospin dependence, as well as a minor spin-spin component. Fig. 1.2 shows the basic form of the *central* nuclear potential (spin and isospin dependence are not shown). The effective free *NN* interaction can be theoretically derived within such an OBE-model based on the exchange of mesons, either within a dispersion-relation theory that relates πN and $\pi\pi$ scattering to the *NN* potential, (the parametrized Paris potential [Laco80] that substituted the older Reid-soft purely phenomenological parametrization [Reid68]), or within a quantum-field formalism (e.g. the Bonn potential [Mach87]).

Deriving, however, the effective nuclear potential from the free *NN* potential for a many-body system such as a finite nucleus is a very difficult (and not yet fully successful) task (see e.g. the relativistic Hartree-Fock [Horo83] or the Dirac-Brueckner [Malf88, TerH87] approaches). Nonetheless, it has been, since long, well established that the effective interaction between two nucleons in a nucleus depends upon the density of the surrounding medium [Beth71]. This density dependence ensures that nuclear matter saturates rather than collapses. The net *NN attraction* in the medium thus weakens as ρ increases. In an usual approach one, hence, invokes the local density approximation (LDA) and defines a nuclear mean-field, resulting from the superposition of the long-range or *soft* interactions of all nucleons, either as function of nuclear density alone $U = U(\rho)$ (phenomenological local Skyrme or Zamick parametrization [Skyr59, Zami73]), or as a function, in addition, of a momentum-dependent interaction $U = U(\rho, \vec{p})$ (e.g. non-local Gogny parametrization [Gogn75]) or, in a covariant framework, using the expression given by the $\sigma - \rho$ Walecka relativistic mean-field model [Wale74, Sero86]. As it is shown in Appendix 3, different forms of the density-dependent nuclear mean field potential $U(\rho)$ lead to different EoS.

Chapter 2

Heavy-ion physics

Summary

2.1 Characteristics of HI reactions 12
2.1.1 The bombarding energy 13
2.1.2 The impact parameter 16
2.1.3 The projectile-target combination 16
2.2 HI reactions in the intermediate-energy region 17
2.2.1 The nuclear liquid-gas phase transition 17
2.2.2 Experimental approaches 20
2.2.3 Theoretical approaches 21
2.3 Phase-space evolution of the nucleus-nucleus collision 23
2.4 Nuclear multifragmentation and the liquid-gas phase transition . . 26

Heavy-ion physics is a 20-years-old research field which employs the collisions of nuclei accelerated at different incident energies to form, by complete or incomplete fusion, nuclear matter at various conditions of density and temperature. Typical geometrical nuclear reaction cross-sections, defined as πb^2 where b is the impact parameter of the reaction, are of the order 1 - 7 barn depending on the size of the colliding ions. When a nucleus-nucleus collision takes place, the initial relative kinetic energy is dissipated into internal degrees of freedom (randomized energy: heat) as well as into collective degrees of freedom (rotation and deformation at low energies, compression followed by expansion at higher energies) leading to the destruction of the nuclear-matter ground-state, and producing hot and/or dense nuclei. With increasing bombarding energies, part of the energy is used in the excitation of nucleonic resonances and to the production of new particles, such as hard-photons or light mesons, not present (or only virtually present) in the entrance-channel. Up to the present day, heavy-ion (HI) physics has used the collision of projectile ions, accelerated with cyclotrons and synchrotons, against fixed target nuclei at rest in the laboratory. However new heavy-ion colliders are about to start their way in the (very) near future (RHIC in June 2000 and LHC in 2005).

2.1 Characteristics of HI reactions

In heavy-ion collisions, the systems of interest, hot and/or compressed nuclei prepared through the reaction, are however transient states of very short lifetimes and small sizes. The typical time scale[1] of the interaction phase is about $\tau_{int} = 2\,(R_p + R_t)/v_p$, where $R_{p,t}$ are the radius of projectile and target respectively and v_p the velocity of the projectile. In the intermediate-energy regime for example, $v_p = \sqrt{2K_{lab}(A\,\mathrm{MeV})/m_N} \approx 0.2$ - $0.4\,c$ and $\tau_{int} \approx 50$ - 100 fm/c. Typical interaction volumes, corresponding to the subset of participant nucleons, are of the order of a few hundreds of fm^3. In general, the relevant space-time reaction-volume of nuclear matter is, thus, of the order $V = c\,\tau_{int} \approx R^4 \approx A^{4/3}\,\mathrm{fm}^4$. These small volumes render difficult the description of the system in terms of thermodynamical quantities and require a detailed knowledge of the dynamical evolution of the system.

When dealing with hot and dense nuclear matter produced in heavy-ion reactions, three basic initial conditions have to be considered: the *incident kinetic energy per nucleon* (K_{lab}), the *impact parameter* (b) and the (relative) *size of projectile and target*. Those three entrance-channel properties completely determine the reaction mechanism. The first one, K_{lab}, determines the relative wavelength of the system and the mean free path of the nucleons during the collision and, thus, the relevant elementary physical processes dominant at each scale. The second one, b, is directly connected with the degree of violence of the collision and with the attainable volume of the interaction region and, thus, to the degree of excitation energy per nucleon $\varepsilon^\star$ deposited in the system. The last one, the size of the colliding nuclei, defines the total number of nucleons present in the system and, ultimately, the maximum compression the system can undergo (for light systems, $A_{tot} < 100$, one expects density-related effects to play a minor role).

[1] 1 fm/c = $10^{-15}\,[m]\,/\,3\cdot 10^{8}\,[m/s] = 3.3\cdot 10^{-24}$ s, is the convenient time unit adopted in nucleus-nucleus reactions.

2.1.1 The bombarding energy

According to the bombarding energy per nucleon of the heavy-ion projectile , K_{lab}, (commonly measured in AMeV $\equiv$ MeV/nucleon units) one can define four different regimes related to different behaviours of nuclear matter which open to the exploration different regions of the density-temperature (T, ρ) plane of figure 1.4. The limits of these domains are mainly determined by the different elementary physical processes prevailing at each level:

1. **Low-energy regime** ($K_{lab} < 20A$ MeV, leading to maximum excitation energies[2] $\varepsilon^{\star}_{max} \approx 3A$ MeV in the nucleus-nucleus center-of-mass). In this regime, the bombarding energies are of the same order as the Coulomb barrier of the colliding nuclei ($V_C = e^2 Z_1 Z_2 / R_{int}$ = 0.75A - 8.0A MeV, for Z_1, Z_2 = 4 - 92) and the maximum attainable excitation energies $\varepsilon^{\star}$ are below the average binding energy of the nucleons in the nucleus ($\sim 8A$ MeV). The wavelength associated to a projectile nucleon ($\lambda = \hbar/p$ = 197 [MeV fm c^{-1}]/136 [MeV c^{-1}] $\approx$ 1.5 fm for an incident nucleon with K_{lab} = 10A MeV, for example) is larger than the average distance between the nucleons in the target ($r_0 = (9\pi)^{1/3}/2k_F \approx$ 1.12 fm). Consequently, the interaction is mainly of collective nature and can be described by invoking the real part of the nucleus-nucleus "optical potential" (the "mean-field"), direct nucleon-nucleon collisions being severely hindered by Pauli principle. Dynamical (preequilibrium) emission of individual nucleons remains marginal, and the reaction mechanisms are essentially governed by the long range part of the nuclear force, the so-called *one-body dissipation* due to the mean field. The projectile excites the collective degrees of freedom of the target and the incident available energy is converted into (low) excitation energies, $\varepsilon^{\star} \approx 2A$ MeV, and angular momentum without destroying the nucleus.

   The resulting phenomenology [Schr84] is complete fusion for the most central collisions, and binary dissipative (also called "deep inelastic" reactions, following multi-nucleon transfers between the colliding nuclei) and quasi-elastic reactions for increasingly peripheral collisions. Since no compression effects are present ($\rho \approx \rho_0$), the expansion of the excited system is negligible and $\varepsilon^{\star}$ is purely thermal, i.e. $\varepsilon^{\star} = \varepsilon^{\star}(T) = aT^2$ according to the Fermi gas relation applicable in this low excitation-energy domain (see Appendix 3). The subsequent decay mechanisms of the moderately excited nuclear fragments proceed sequentially through neutron and light-charged-particle (LCP, with Z = 1, 2) evaporation from the nuclear surface (emission of heavier species is very unlikely due to higher barriers) and binary fission (for the heavier partners where deformation, the shape degree of freedom, and not excitation dominates the instability). Both are slow statistical processes: $t >$ 300 fm/c for particle evaporation and $t \geq$ 1000 fm/c for fission. Finally, statistical gamma emission sets in for excitation energies below the particle emission threshold (e.g. below $B_n \approx$ 8 MeV for neutron emission). Due to the large times between consecutive emissions, global equilibration is a good approximation and the

[2] In heavy-ion collisions the total energy available in the nucleus-nucleus CM (for non-relativistic energies) amounts to: $K_{AA}[AMeV] = \mu/A_{tot} \cdot K_{lab}[AMeV]$, where μ is the reduced mass of the system. The *maximum* excitation energy which can be attained amounts, thus, to $\varepsilon^{\star}_{max} \approx K_{AA}$.

use of a statistical compound nucleus theory (Weisskopf model [Weis37, Lyn83]) is justified. Typical ground-state effects like shell and pairing effects can still be present.

2. **Intermediate-energy regime** ($20A$ MeV $< K_{lab} < 100A$ MeV leading to $\varepsilon^{\star}_{max} \approx 3A$ - $20A$ MeV). In this energy domain, the projectile energy K_{lab} is comparable to the Fermi kinetic energy of the nucleons inside the nucleus[3], $K_F \approx 38A$ MeV, and one is sensible to both the long-wavelength attraction of the nuclear mean field and to the short-range repulsion due to hard *NN* collisions. This is thus a transition domain between the low-energy deep-inelastic and the participant-spectator scenarios prevailing at low and high energies respectively. The incident relative energy is redistributed into thermal and compressional degrees of freedom as a result of the mean field effects (*one-body dissipation*) and individual nucleon-nucleon elastic collisions, $NN \rightarrow NN$ (*two-body dissipation*). The latter are inhibited as a consequence of the Pauli exclusion principle (around 90% of the *NN* collisions are Pauli-blocked at $50A$ MeV according to molecular dynamics models [Aich91]). Excitation energies up to a significant fraction and even above the nuclear binding energy ($8A$ MeV) and densities of about $1.5\rho_0$ can be attained. For central collisions with incident energies above $30A$ MeV (equivalent to $\varepsilon^{\star}_{max} \gtrsim 5A$ MeV), the compressional excitation energy can account for about 1/3 of the available center-of-mass energy [Poch97]. This compressional energy is subsequently released as a collective radial flow of nucleons. Both thermal pressure and compressional expansion can dilute the nuclear systems to subnuclear densities ($\rho \approx 1/4\rho_0$). Experimental measurements and theoretical calculations (either microscopic or statistical ones) have concurrently established the gross features of the reaction mechanisms[4] which, following increasing impact parameter, are [Dura97, Tama97]:

   - **Peripheral reactions**: Dominance of the binary character of the collisions with the production of two primary nuclear fragments: an excited forward-moving quasi-projectile (QP) and an excited slowly-moving quasi-target (QT). This memory of the entrance channel is an indication of the still dominant mean-field effects in the evolution of the collision, although the pre-equilibrium emission of particles starts to appear. The slightly excited ($\varepsilon^{\star} \lesssim 4A$ MeV) primary fragments decay mainly by sequential emission processes (evaporation and/or fission) in a similar way as established at lower energies (see former paragraph).
   - **Semi-central reactions**: Primary binary dissipative collisions still dominate following the formation of an incomplete-fused system with the occurrence of a neck-like structure between the excited QP and QT. The preequilibrium emission of light-particles, due to *NN* collisions taking place during the early stages of the reaction and/or to non-equilibrium particles emitted by the composite system before thermalization, gains in importance. The three primary excited fragments: QP, QT and neck-like fragment, with excitation energies

[3] This is the reason why these bombarding energies are usually referred to as the "Fermi energy" domain.

[4] This has been a rapidly evolving field in the last 5 years when an important amount of new data from 4π multidetectors has become available.

$4A$ MeV $< \varepsilon^{\star} <$ $9A$ MeV, decay mainly by *"multifragmentation"*, i.e. by multiple (at least 3 fragments) and fast emission of the so-called *Intermediate Mass Fragments* (IMFs) with $3 \leq Z \approx 20$ (see Section 2.4).

- **Very-central collisions** (corresponding only to about 1% of the reaction cross-section i.e. a few tens of millibarns): The formation of a quasi-fused single nuclear system with $\varepsilon^{\star}$ close or even larger than the nuclear binding energy of $8A$ MeV, which subsequently decays as a whole by multifragmentation, has been observed [Mari95, Mari97]. Pre-equilibrium emission becomes less important. Vaporization, i.e. the completely disassembly of the system into LCPs (Z = 1, 2), sets in for excitation energies greater than $9A$ MeV.

3. **Relativistic regime** ($100A$ MeV $< K_{lab} <$ $10A$ GeV leading to T = 20 MeV - 100 MeV [Stoe86, Sto86, Peil94, Cser95]). In this energy range (with lower limit just below the pion rest mass $m_{\pi} \approx 138$ MeV), the projectile energy is not only transformed into thermal energy (temperatures between 20 to 100 MeV are attained) and compression effects (ρ reaches 2 - $3\rho_0$), but also into baryonic excitations of the participant nucleons [Stoe86, Gutb89]. With increasing bombarding energy the kinematically possible post-scattering states of the nucleons are less occupied (e.g. only around 20% of NN collisions are Pauli-blocked at $1A$ GeV according to molecular dynamics models [Aich91]), and binary NN scattering now dominates. Since Pauli blocking plays a minor role due to the larger available phase space, the dynamics is dominated by hadronic intranuclear cascades. Above the free pion production threshold ($K_{lab}^{NN \to NN\pi} \approx 290$(A) MeV) nuclear matter is no more basically nucleonic but also other hadronic degrees of freedom have to be taken into account with a significant production of nucleon resonances ($\Delta(1232)$ isobars, $N^{\star}(1440)$ and $N^{\star}(1535)$) and mesons (π, η) stemming from inelastic NN channels ($NN \to N\Delta$, $N\Delta \to NN$, $N\Delta \to N\Delta$, $\Delta\Delta \to \Delta\Delta$ and $NN \to NN\pi$). At an incident energy of $2A$ GeV more than 30% of the nucleons are excited to resonant states [Aver94], and the term "resonance matter" has been suggested for this state of nuclear matter [Meta93, Mose93].

   The reaction mechanism is governed mainly by geometrical aspects leading to the so-called "participant-spectator" scenario. In the interaction zone the relative motion of target nucleons versus projectile ones is slowed down due to the energy loss, in binary nucleon collisions, from longitudinal to transverse degrees of freedom, and to π-Δ production. This participant region develops a shock compression (the relative velocity of the colliding nuclei clearly exceeds the nuclear velocity of sound $v_s = (\kappa_{\infty}/9m_N)^{1/2} \approx 0.2c$) due to stopping and thermalization producing a high energy density zone called the "fireball". The compression energy generated is released in an important production of *ordered* collective movement (*flow*) [Jeon94]. Those parts of the colliding nuclei which do not belong to the overlap region between projectile and target, the *spectators*, stream apart freely with lower excitation energies. The study of *projectile spectators* produced in relativistic heavy-ion collisions, with $\varepsilon^{\star}$'s comparable to those encountered in hot nuclei produced in central reactions at the intermediate-energy region, constitutes also a relevant research field in heavy-ion physics and multifragmentation studies (see e.g. [Poch97, Schw99, Muel99, Traut99]).

4. **Ultrarelativistic regime** ($K_{lab} > 10A$ GeV, leading to T above 100 MeV). At these high-energies the partonic structure of the nucleons in the colliding nuclei comes into play (see e.g. [Wong96, Mcle86, Cser95]). Experimental results of fixed target collisions in the range K_{lab} = 10A GeV - 200A GeV performed in the last 5 years already indicate the attainment of a partonic phase during the collision [Hein00]. New high-energy heavy-ion experiments programmed at RHIC and LHC colliders aim at producing energy densities high enough to form a plasma of free quarks and gluons. At this very high energies, and according to the commonly accepted Bjørken picture [Wong96], the Lorentz-contracted projectile and target pass through each other after a time of $\approx$ 1 fm/c leaving behind a hot ($T > 100$ MeV) fireball of gluons, quarks and antiquarks at mid-rapidity (essentially baryon-free) produced in soft parton-parton collisions. Energy densities one order of magnitude larger ($\approx$ 1 GeV fm^{-3}) than the energy density of nuclear matter in equilibrium will be reached. Albeit in a small region of space and during a short duration of time (the hadronization time is estimated to be around 5 - 10 fm/c), neighbouring individual hadrons could merge into one big hadron "bag" inside which quarks and gluons would move freely forming the so-called Quark Gluon Plasma.

2.1.2 The impact parameter

Concerning the second entrance-channel property which determines the relevant reaction mechanisms, the impact parameter b, it is straightforward to see from geometrical considerations, $\sigma_R = \pi b^2$, that the size of the dense nuclear matter zone produced in the collision and ultimately the attained excitation energy, strongly depends on the impact parameter of the reaction. It is thus essential to sort out the collisions according to their centrality. The impact parameter, which characterizes the initial state, is not however directly measurable and it is thus necessary to find an experimental observable strongly correlated with it. The simplest observable one can think of, and therefore the most universally used, is the total multiplicity of detected (charged) particles, M_{cp}, as confirmed by all theoretical models predictions [Cava90]. Other observables employed [Fran97] are the neutron multiplicity M_n [Gali94, Schr92], the hard-photon multiplicity M_γ [Ries92], the total produced transverse energy $E_\perp$ [Luka97], the Fox&Wolfram second-order moment [Fox78], and the so-called *flow angle* [Cugn83, Salo97].

2.1.3 The projectile-target combination

Finally, regarding the reaction mechanisms in nucleus-nucleus collisions, the (relative) size of the projectile-target combination, defines, on the one side, the maximum available number of nucleons to form the excited system and, thus, the"closer" we are to the (infinite) nuclear matter limit (excited heavy systems are closer to the independent-particle picture of bulk nuclear matter than small few-body ones). On the other side, it determines also the importance of compressional effects in the collision dynamics: the bigger the colliding nuclei are, the more significant the density-related effects may be during the collision. That is the reason why, complementary to heavy-ion reactions, the preparation of hot nuclei has also been done in GeV hadron- or light-ion- induced reactions, in which

basically only the thermal aspects of the disassembly process (no compression effects) need to be taken into account (see e.g. [Cugn87, Gold96, Kwia98, Jahn99, Lefo99]).

2.2 HI reactions in the intermediate-energy region

The main physical motivation behind the study of nucleus-nucleus collisions in the "Fermi" region of bombarding energies, $20A$ MeV $< K_{lab} < 100A$ MeV, is the possibility of "preparing" pieces of nuclear matter with excitation energies in the range $4A$ MeV $\lesssim \varepsilon^{\star} \lesssim 20A$ MeV, i.e. excitation energies around the binding energy of a nucleon inside the nucleus. Nuclear systems produced in such reactions are heated and compressed so that during their subsequent decompression and cooling they may follow a path that enters into the low-density region of the phase diagram (fig. 2.1). At densities $\rho < \rho_0$, the behaviour of the system is governed by the balance between long-range attractive and short-range repulsive nuclear forces on one side, with the long-range Coulomb force on the other side. Thus, in analogy with the classical Van der Waals gas where an interplay between long-range attractive and short-range repulsive forces leads to a phase transition, it has been suggested [Bert83, Bert83b, Siem83, Lope84] that a similar liquid-vapor phase transition would also take place in the expanding nuclear systems formed in heavy-ion collisions.

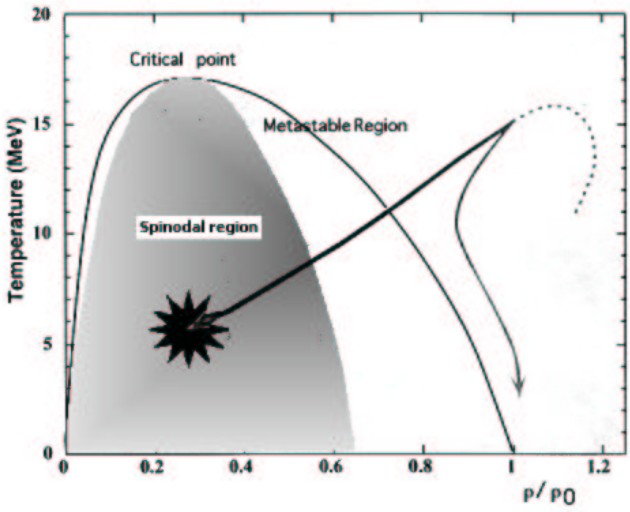

Figure 2.1: *The low density part of the phase diagram of nuclear matter and the critical region of the liquid-gas phase transition. The trajectories depicted in the figure correspond to the possible paths followed by a nuclear system produced in a central heavy-ion reaction.*

2.2.1 The nuclear liquid-gas phase transition

The behaviour of "nuclear matter" during a heavy-ion collision can be followed in the $\varepsilon = \varepsilon(s,\rho)$ plane obtained for a Skyrme equation-of-state $U = U(\rho)$ (fig. 2.2). Initially

the reaction carries the system from the ground state to some point with higher internal energy: the interpenetrating nuclei create a system with a certain density $\rho > \rho_0$ and entropy per nucleon $s_i > 0$ (e.g. point A). From this excited position with positive pressure[5] the system will then expand along an isentrope[6] until a metastable point of equal internal energy is reached on the left (point B). For very high initial energies (e.g. for excitation energies above $\varepsilon^\star = 20A$ MeV, leading to entropies above the critical point at $s = 2.7$ marked with an open circle in fig. 2.2), the pressure will remain positive for all densities (see also fig. 1.1), and one may describe the process as an instantaneous vaporization (the gas phase lying above the critical point and the liquid phase below). At low energies, the region of the left side of the isentrope has a negative pressure and the expansion will be slowed down and eventually stopped when the kinetic energy of the expansion has been converted back into internal energy. The system, due to the restoring effect of the nuclear mean-field, oscillates back and forth along decreasing isentropes through the coexistence phase. This is a metastable region where the "liquid" system (identified as a heavy fragment with $\rho \approx \rho_0$) cools progressively due to "gas" (light-particle and cluster) evaporation and other dissipative effects (like collective oscillations) which bring it down to the stable ground state.

A third possibility appears if one takes into account the fact that nuclear matter is dynamically unstable in the region where κ_∞ is negative (or, stated equivalently, in the region where the sound velocity, $v_s \propto \sqrt{\kappa_\infty}$, becomes imaginary). This dynamically unstable region can be determined via the so-called isentropic "spinodal" curve defined by the condition $\kappa_\infty \propto \partial P/\partial\rho \mid_s \leq 0$. The region of the $\varepsilon = \varepsilon(s,\rho)$ plane in which this occurs is shown in fig. 2.2 (and also in figs. 1.1 and 2.1 in the P-ρ, ε-ρ and T-ρ planes respectively). If the initial values of the entropy and density are high enough to expand the system into this mechanically unstable region (i.e., for example, to reach the point C in fig. 2.2), the original homogeneous metastable liquid will experience a "spinodal decomposition" [Siem83]: density fluctuations will be no more damped but exponentially amplified leading to a "fragmentation" phase[7] composed of "liquid" droplets of different sizes and "gas" (individual nucleons and light clusters). On the left of the spinodal line, nuclear matter will spontaneously form into droplets (whose most favourable sizes [Heis88] are those whose wavelength corresponds to the maximum growth rate); whereas on the right the mean field dynamics will basically preserve the homogeneous (liquid) phase. The basic conclusion of such reasoning [Siem83] is that the experimentally observed multiple production of intermediate-mass-fragments in *multifragmentation* reactions is intimately related with the entrance into the spinodal region and that "fragmentation" therefore arises due to density instabilities in the central part of the excited blob of nuclear matter (see Section 2.4).

[5] Since $P = \rho^2 (\partial\varepsilon/\partial\rho)_s$, nuclear matter is in equilibrium if it is at an energy minimum of an isentrope ($s = const$), otherwise the pressure is non zero and the system will expand or contract.

[6] The assumption that the volume change takes place at constant entropy is realistic since there is little dissipation associated with the expansion process, and the initial value of the entropy corresponds to the maximum value attained at the end of the highest compression phase.

[7] In fig. 2.2, the system jumps at point C from the initial metastable isentropic curve s_i, representing the uniform phase, to the proper thermodynamically stable (mixed phase) isentrope s_f that crosses the spinodal line at the same point as the s_i curve.

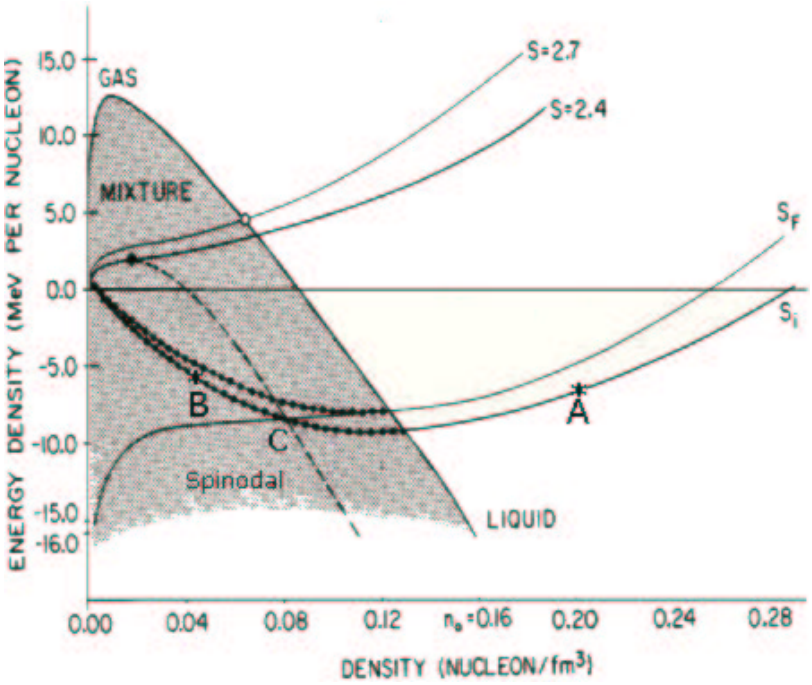

Figure 2.2: *Isentropes in the* (ε, ρ) *plane corresponding to the critical point (open circle,* $s = 2.7$*) and the end point of the spinodal (full circle,* $s = 2.4$*). Also shown inside the mixture zone (shadow) are the spinodal (dashed line), and the Maxwell construction of the final entropy per nucleon curve s, as well as the unstable isentropes* s_i *and* s_f *(dotted lines). [According to this model, in the small gap between* $s = 2.4$ *and* $s = 2.7$ *the system experiences neither fragmentation nor instantaneous vaporization but goes from one phase to another in a continuous manner]. Adapted from [Lope84].*

The fact that excited nuclei produced in dissipative nuclear collisions are finite-size systems in which surface, Coulomb and isospin effects play a major role does not change much this interpretation. Indeed, although the inclusion of these effects lowers substantially the considered (critical) values of the energy (or entropy) per nucleon, the modification of the trajectories of the expanding matter down to the region of the instability thresholds is quite small, and the basic scenario described for infinite nuclear matter remains basically unaltered. The existence itself of the spinodal-like phase transition, or of an observable signaling the passage through the critical region, as well as its possible connection with the process of multifragmentation is however still a subject of intense debate (see Section 9.4).

2.2.2 Experimental approaches

In the domain of intermediate excitation energies, nuclear collisions are governed by complicated many-body processes leading to the production of hot nuclei which deexcite emitting in all directions different nuclear species in a large range of masses A, charges Z and kinetic energies K: light-charged-particles, LCP, with $Z \leq 2$ (i.e. the three isotopes of hydrogen and the two isotopes of helium: $p, d, t,$ ^{3}He and α), neutrons, nuclear fragments ($Z \geq 3$), as well as newly created particles (hard-photons, light mesons) not originally present in the system. A detection as complete as possible of all reaction products is an experimental goal which is duly, but in general only partially, reached by using detectors covering most of the available phase space. On the experimental side, hence, the major efforts in the last years have been focused in the design and construction of (almost) 4π multidetectors (Dwarf-Ball [Stra90], Miniball [Souz90], Multitics [Iori93], Indra [Pout95], Isis [Kwia95]) for the recording of kinematically complete events and the measurement of double and even triple differential cross sections for most of the reaction products. The experimental observables that experimentalists have at hand to try to unravel the complex reaction mechanisms and extract the relevant (thermo)dynamical properties of the dense and excited nuclear matter formed during the reaction, can be schematically grouped in four categories:

- **Thermal** variables: Excitation energies $\varepsilon^\star$ are evaluated using *nuclear calorimetry* methods [Dura97], either by energy balance through the complete determination of A, Z and K of the decay products [Cuss93], using neutron multiplicities [Gali94], or, indirectly, by measuring the relative velocity of the quasitarget and quasiprojectile fragments. Nuclear temperatures are determined with *nuclear thermometry* methods [Bene94, Dura97] either using the slopes of the kinetic energy spectra of the produced particles (*kinetic* temperatures) [Wada89, Baue95], the double-isotope yield ratios (*double-ratio* temperatures) [Albe85] and/or from the discrete excited state population ratios of selected nuclides (*excited state* temperatures) [Poch85, Bene94]. Correlating these two variables in a $\varepsilon^\star$ versus T plot, one determines the so-called nuclear "caloric curve" [Poch95].

- **Compressional** variables: The measurement of the sidewards collective flow of particles and the associated radial expansion energy has been studied to obtain in-

formation on the density-dependent part of the EoS (see e.g. [Stoe86] or, more recently, [Neba99b, Ming99]).

- **Space-time** variables: Information on the dynamical evolution (*nuclear chronometry*) of the reaction process can be obtained by looking at (subthreshold) particle production mechanisms [Cass90, Mose91] and by studying two-particle correlation functions with intensity-interferometry techniques: γ-γ [Marq97] and hadron-hadron [Aich94] using the Koonin-Pratt [Gong91] formalism, or fragment-fragment using *n*-body Coulomb-trajectory simulations [Glas94].

- **Phase transition** variables: Critical parameters and critical point exponents in different power-law experimental distributions [Gilk94, Pan98, Dors99], and discontinuities in the nuclear "heat capacity" [DAgo99] have been proposed as possible signatures of a liquid-gas nuclear phase transition as predicted by the Fisher's droplet model in the vicinity of the critical point [Fish67].

2.2.3 Theoretical approaches

On the theoretical side, the description of the many-body problem appearing in heavy-ion reactions at these bombarding energies has lead to the development of different models which can be globally grouped in two categories, **macroscopical** (**statistical**) or **microscopical** approaches:

- On the one side, the **statistical models**, such as the sequential decay models at low excitation energies (e.g. GEMINI [Char88] or SIMON [Dura92]) based on the Weisskopf theory [Weis37, Haus52] for compound nucleus formation and subsequent deexcitation; or the MMMC[8] [Gros97], SMM[9] [Bond95, Botv95], and EES[10] [Frie90] models in the intermediate-energy region; are all based on the assumption that the produced nuclear system at the end of the purely dynamical stage of the collision process (see next Section) reaches (local) thermodynamical equilibrium (i.e. thermal and, likely, also chemical equilibrium). The underlying approach of those models is the replacement of the original complex collection of strongly interacting nucleons and fragments by a new ensemble of particles in thermal equilibrium, shifting the complicated dynamics to the density of states. The main idea of this approach is that at high excitation energy a very large number of degrees of freedom is involved in the process and the probabilities of different decay channels are mainly determined by statistical weights (i.e. to the number of microscopic states leading to a certain final state) rather than by the detailed dynamics of the process. The question turns to calculating statistical weights of various break-up channels (the possible final states of the decaying system) under given constraints on the total energy, mass number and charge contained in the break-up volume $V_b = A_0/\rho_b$. The models basically differ in the use of different statistical ensembles (microcanonical,

[8] Microcanonical Metropolis Monte Carlo
[9] Statistical Multifragmentation Model
[10] Expanding Emitting Source

canonical or macrocanonical), in the way of describing the individual fragments and in the calculation procedures[11].

- On the other side, the **semi-classical microscopic model** calculations try to follow the dynamical evolution of the interacting nucleons from the first instants of the reaction and are based on suitable approximations of the time dependent many-body Schrödinger equation for the *n*-particle wave function, $\Psi(\vec{r}_1,...,\vec{r}_n;t)$, or stated equivalently in the quantum statistical picture, of the Von-Neumann equation for the time evolution of the *n*-particle density matrix Φ_n which in configuration space is defined as [Bona94]:

$$\Phi_n = \Phi_n(\vec{r}_1,...,\vec{r}_n,\vec{r}_{1'},...,\vec{r}_{n'};t) = \Psi(\vec{r}_1,...,\vec{r}_n;t)\Psi^\star(\vec{r}_{1'},...,\vec{r}_{n'};t) \tag{2.1}$$

The quantum Liouville equation (or Von Neumann equation) reads:

$$i\hbar\frac{d\Phi_n}{dt} = [H,\Phi_n], \tag{2.2}$$

where H is the *n*-body Hamiltonian and the brackets represent the usual commutator operation. Since this equation is not readily solvable, several approximations have been proposed[12] in the $\hbar \to 0$ limit. The microscopic models can be subdivided into two classes. Those which reduce the problem to the time evolution of the *one*-body (nucleon) density matrix $\Phi_1(\vec{r}_1,\vec{r}_{1'};t)$ and those which are based on *n*-body molecular dynamics:

1. **Boltzmann Equation** models: The crucial ingredient of these semiclassical transport models is the description of the system through the nucleon phase-space function $f(\vec{r},\vec{p},t)$, which is nothing but the Wigner transform[13] of the one-body density matrix $\Phi_1(\vec{r}_1,\vec{r}_{1'};t)$:

$$f(\vec{r}_1,\vec{p}_1;t) = \frac{1}{(2\pi\hbar)^3}\int d^3r\, e^{i\vec{p}_1\vec{R}_1/\hbar}\,\Phi_1(\vec{r}_1+\vec{R}_1/2,\vec{r}_1-\vec{R}_1/2;t) \tag{2.3}$$

The time development of $f(\vec{r},\vec{p},t) \equiv f$ is determined also by "Wigner transforming" both sides of equation (2.2), which finally yields the Boltzmann kinetic equation containing the time-dependent (nuclear) mean-field force $\vec{F}(\vec{r},\vec{p},t) = \partial U(\vec{r},t)/\partial\vec{r}$ and a 2-body *NN* Pauli-blocked collision term I_{coll} (for details see Section 8.1):

$$\frac{\partial f}{\partial t} + \frac{\vec{p}}{m}\frac{\partial f}{\partial \vec{r}} + \vec{F}\frac{\partial f}{\partial \vec{p}} = I_{coll}[f] \tag{2.4}$$

[11] Closely-related to these approaches, lattice gas models for nuclear matter have also been developed (see e.g. [Camp97, Pan98b, Mull99, Borg99]) to study not specifically the situation encountered in heavy-ion reactions but the more general liquid-gas phase transition of excited nuclear systems.

[12] Actually, it has been demonstrated that all the different microscopical models used so far may be derived formally from a proper truncation of the quantum statistical BBGKY (for Bogoliubov, Born, Green, Kirkwook, and Yvon) hierarchy for the *n*-body density matrix (see e.g. [Li93, Bona94]).

[13] The use of the Wigner transform, defined in general as a Fourier transform of the *n*-particle density matrix, is a typical procedure in all these microscopical models since it allows to formulate the complicated quantum statistical system in a language very close to classical transport theory, providing an intuitive understanding of the time evolution of the reaction [Aich91].

At low incident energies, the two-body correlation function I_{coll} can be safely neglected (i.e. the r.h.s. of eq. (2.4) is basically zero) and the resulting Vlasov equation or its quantal version, the time-dependent Hartree-Fock (TDHF) mean-field [Nege82], are suitable approximations. At intermediate energies the collision-less limit does not hold anymore and one has to solve equation (2.4). For that purpose, several semiclassical phase-space simulations have been proposed: BUU[14]/VUU[15] [Stoe86, Bert88, Cass90], BNV[16] [Bona94] and Landau-Vlasov [Greg87]. These different versions basically differ in the numerical realization employed for solving the transport equation (the particular implementation of the *test-particle* method) or in the particular nuclear mean-field parametrization $U(\vec{r},\vec{p},t)$ used (Skyrme, Skyrme+momentum-dependent force, Gogny force ...). More details are given in Section 8.1.1.

2. **Molecular Dynamics** approach: The "Quantum" Molecular Dynamics Model QMD [Aich91, Li93] (and their different realizations [Hart98]) goes beyond the pure one-body description outlined above. Retaining the correlations among nucleons, it tries to describe also the process of fragment formation. It is a true *n*-body theory which simulates the time evolution of a heavy-ion reaction, - the *n*-body wave function of the system being written as the direct product of *n* nucleons represented by coherent gaussian states -, on an event-by-event basis by means of a generalized variational principle (more details can be found in Section 8.2.1).

Several extensions of these transport models have also been developed to further include e.g. stochastic fluctuations in the collision term (Boltzmann-Langevin approaches [Abe96, Ayik90, Rand90, Burg91, Sura92, Chom94]), non-local collision terms [Malf92, Dani96, Mora99], genuine quantum effects by proper antisymmetrization and diffusion of the wave packet (FMD [Feld00], AMD/AMD-V [Ono98]), and for relativistic energies, a fully covariant formalism (RBUU [Maru94], RQMD [Sorg89, Bass98]) or the off-shell propagation of nucleons (HSD [Cass99]).

2.3 Phase-space evolution of the nucleus-nucleus collision

Transport model calculations of the BUU or QMD type are useful to predict the phase-space evolution of a nucleus-nucleus collision at intermediate energies and to follow the space-time evolution of several significant reaction quantities (see e.g. [Goss97, Neba99a, Eude98]). The relevant time scales of the different stages of the reaction, measured in fm/c units, are mainly determined by looking at the evolution of the density and the number of *NN* collisions of the colliding system as a function of time (see fig. 2.3 for a typical Landau-Vlasov calculation).

These microscopical simulations outline a picture of a typical heavy-ion collision in the Fermi energy regime consisting of the following phases (fig. 2.3):

[14] Boltzmann-Uehling-Uhlenbeck
[15] Vlasov-Uehling-Uhlenbeck
[16] Boltzmann-Nordheim-Vlasov

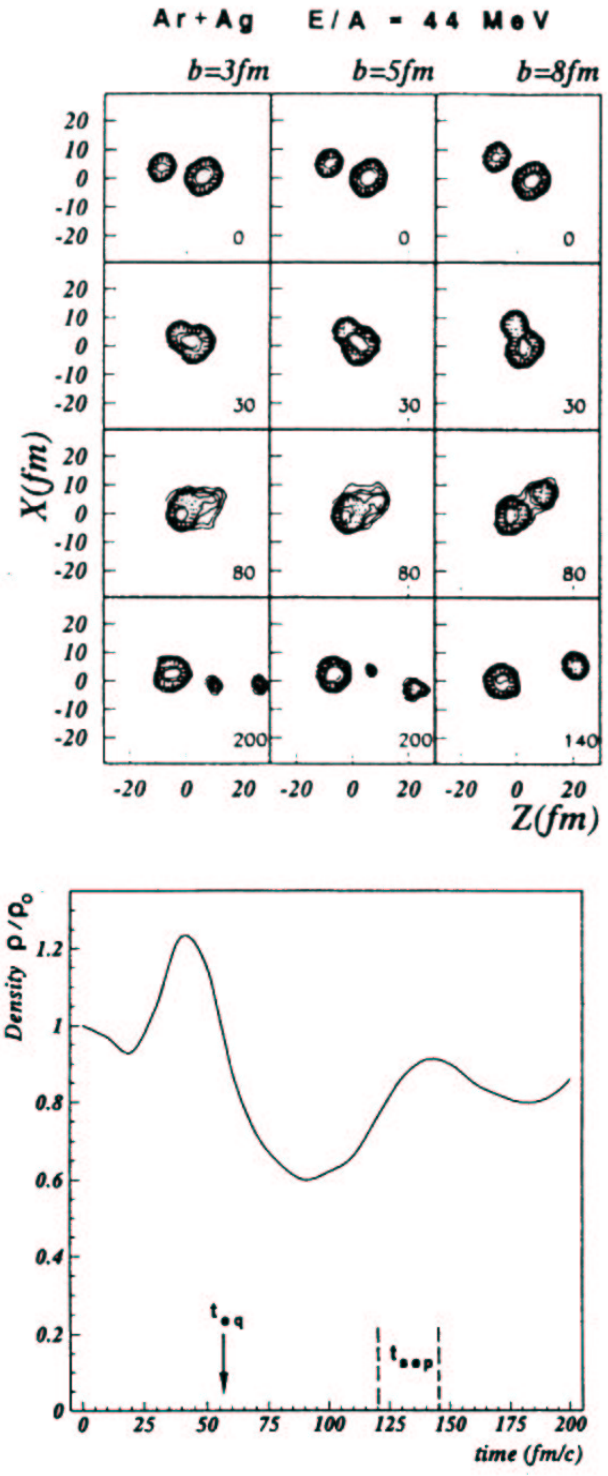

Figure 2.3: *Landau-Vlasov simulations [Hadd96]: Density profile in coordinate space for the Ar(44A MeV)+Ag reaction at different impact parameters (upper part). Time evolution of the normalized mean density for the same reaction (lower part).*

1. **Preequilibrium compression phase** ($0 < t \lesssim 40$ fm/c). At t = 0 fm/c the two nuclei start to overlap. An initial non-equilibrium phase develops during which collisions in the zone of the overlapping region of the colliding ions occur at the nucleonic level. At this level, only collisions between nucleons from the target and nucleons from the projectile can take place due to Pauli blocking. These energetic collisions have a highly anisotropic initial momentum distribution. Transverse momentum transfers occur between these *NN* collisions rising the "temperature" (interpreted as the resulting random motion of the nucleons) and generating much entropy in the interaction region. A certain amount of nucleon-nucleon collisions boost particles to unbound states far from the Fermi sea producing the dynamically prompt emission of preequilibrium energetic particles: LCPs and neutrons (also called "Fermi jets") as well as subthreshold particles (hard photons, pions, kaons). In momentum space, these particles are mainly located at midrapidity in the center of mass system[17]. The system, out of equilibrium, starts to compress. The density reaches its maximum value at t $\approx$ 30 fm/c, which roughly corresponds to the time of a pure geometrical *passage-through* of the *centers* of the colliding nuclei at these incident energies ($\tau_{int} = R_{int}/v_p$ = 10 fm/0.3c = 30 fm/c). The rate of *NN* collisions reaches its maximum value somewhat later during the first instants of the subsequent expansion stage.

2. **Expansion phase** ($40 \lesssim t \lesssim 100$ fm/c). After the compression stage, matter starts to flow under the influence of the pressure gradient generated by the repulsive core of the nuclear force. The nucleons start moving away from each other, the number of collisions diminishes quickly and the entropy changes very little. At t = 60 (80) fm/c for peripheral (central) collisions[18] the composite system recovers its normal density. This spatial *separation* time is considered usually as the end of the pure preequilibrium scenario.

   From that moment, and depending on the initial conditions (the impact parameter and the relative size of target and projectile), the original di-nuclear system gives birth to the excited nuclear system(s). For semi-peripheral and peripheral reactions, a primary quasi-projectile and quasi-target (and, possibly, a neck-like zone in between) are produced. For very central reactions a single source of "quasi-fusion" may be formed. The fate of such hot and (isentropically) expanding nuclear system(s) during the subsequent "disassembly" or "break-up" stage is the main subject of investigation.

3. **Fragmentation or Clusterization phase**.

   (a) On the one side, if the expansion (thermal plus collective) energy is large enough, at around t = 100 fm/c the density of the expanding and cooling nuclear system can be of the order of $1/3\rho_0$. At these low densities, the nuclear

[17] The accessible range of rapidities y for a given nucleus-nucleus interaction ranges from the maximum value corresponding to the limit of the incident particle elastically scattered at zero angle $y = y_p$, down to the minimum value corresponding to $y = -y_p$. Thus in the CM system, normalizing to the projectile rapidity: y/y_p = -1, 0, 1 correspond to target, CM and projectile rapidities, respectively.

[18] t $\approx$ 60 fm/c is roughly the time needed for the two incoming nuclei to *completely* traverse each other at these incident energies.

binding causes the close together hadrons (in space- and momentum- space) to aggregate into IMF and LCP in a "coalescence" process. As the expansion goes on, the global density of the system falls to a value where the constituents are no longer interacting strongly. This is the **freeze-out stage**.

(b) On the other side, if the internal pressure is not sufficiently high the system does not reach the "cracking point" within the spinodal region and after some expansion it reverses to compression. Several damped oscillations of this sort may occur while the system looses excitation by the subsequent slow final decay modes (evaporation, fission ...).

Fragments loose contact (no matter or energy exchanges occur) and their distribution becomes stable after t $\approx$ 250 fm/c [Puri96] i.e. primary chemical compositions (the different population of nuclear species) become fixed. From this point on, the produced fragments, move only under the action of their Coulomb trajectories.

4. **Final deexcitation**. The fragments at the output of the freeze-out phase still have a certain amount of excitation energy which is released by slow sequential processes like neutron and LCP evaporation or statistical gamma emission from unbound excited states (see Section 3.1). At the end of the decay chain ($t > 1000$ fm/c), any remaining excited massive residue may decay through fission; whereas the last low-lying bound states decay by statistical discrete gamma emission of several hundreds of keV to a few MeV.

What the detectors measure is the result of the evolution of all the produced fragments up to asymptotic times. In general, there is a general common agreement between models and experiments and between models themselves, in the interpretation of the first purely dynamical and pre-equilibrium stage (compression plus expansion phases) as it has been described here. There is also little doubt about the evolution of the moderately excited systems existing after freeze-out. However, different and even contradictory theoretical explanations (see next Section) have been proposed to describe the fragmentation phase starting at the end of the compression-expansion stage (t $\approx$ 100 fm/c) and finishing at about t $\approx$ 250 fm/c.

2.4 Nuclear multifragmentation and the liquid-gas phase transition

The multiple ($M_{IMF} \geq 3$) production of nuclear fragments with charges $3 \leq Z \leq 20$, usually called "intermediate-mass-fragments" (IMF), larger than the typical evaporated LCPs ($Z \leq 2$) but smaller than the evaporation residues or the fission products ($Z > 20$), has been experimentally observed to be an important reaction channel of heavy-ion collisions at intermediate-energies[19], i.e. for nuclear systems with excitation energies 4*A*

[19]This production of several nuclear fragments with charges $3 \leq Z \leq 20$ was actually observed for the first time in proton- and pion- induced reactions with heavy targets more than 40 years ago [Serb47, Frie54] and in heavy-ion reactions in the late seventies and first eighties: first in emulsion [Jako82] and plastic-nuclear-track-detectors studies (see e.g. references in [DEnte93, DEnte95]) and afterwards with electronic detectors [Viyo79, Egel81, Warw83].

MeV $\lesssim \varepsilon^{\star} \lesssim 9A$ MeV. This process has been called "nuclear multifragmentation" (see fig. 2.4) and understanding its origin is one of the central issues in intermediate-energy heavy-ion physics for the last 15 years. The interest in this study is triggered by the fact that it has been argued that it could be a signature of the existence of a nuclear liquid-gas phase transition. Three experimental features seem to characterize nuclear multifragmentation:

- Multifragmentation seems **not** to be a conventional **sequential** decay channel of excited nuclei. The IMF multiplicity and kinetic energy distributions are severely underpredicted by low-energy statistical models [Hube92, Llope95, Beau96] like e.g. GEMINI [Char88] which describe fragment formation by successive binary splittings from an equilibrated hot (rotating) nucleus and/or sequential evaporation from the nuclear surface.

- Multifragmentation is a **fast** decay channel of excited nuclei. The emission time of IMFs seems to be much faster than that of a conventional slow statistical decay like fission or evaporation for which $\tau_{emis} > 500$ fm/c [Dura95], or faster than the characteristic "Coulomb time" $\tau \approx 10^{-21} \approx 300$ fm/c of a system which disassembles inside its own Coulomb field [Shap94]. Indeed, the systematics of fragment emission times in heavy-ion reactions at intermediate-energies indicates that the estimated time between two fragment emissions is around 500 fm/c for a source with $\varepsilon^{\star} \approx 3A$ MeV and saturates at ≈ 100 fm/c for $\varepsilon^{\star} > 5A$ MeV [Tama97]. Similarly, in hadron- and light-ion- induced reactions on heavy nuclei, IMF emission times as fast as 50 - 100 fm/c have been recently reported [Beau99, Viol99, Oesc99].

- Multifragmentation sets in as the **dominant** exit channel between fission and evaporation[20], for $\varepsilon^{\star} \lesssim 4A$ MeV, and the total vaporization of the system into individual nucleons and light clusters, for $\varepsilon^{\star} \gtrsim 9A$ MeV [Bacr95, Rive96, Bord99]. The mean IMF multiplicity $\langle M_{IMF} \rangle$ increases monotonically with increasing excitation energies starting at $\varepsilon^{\star} \approx 3A$ MeV [Biza93] up to a maximum value at around $\varepsilon^{\star} \approx 9A$ MeV [Souz91]. For larger $\varepsilon^{\star}$, $\langle M_{IMF} \rangle$ decreases due to the increasing role of vaporization exit-channels.

The first and second characteristics indicate that IMF emission is a decay process significantly different than sequential fission which results from nuclear shape deformation at normal density induced by surface and Coulomb instabilities. At variance with this low-energy and slow[21] mechanism, fragmentation could result from a fast[22] breakup due to the passage of the excited system through a low-density *spinodal* region (see Section 2.2.1) after the initial compression phase. This kind of disassembly process is driven by mechanical (volume) instabilities due to the entrance of the system in the region where density fluctuations are no more damped but exponentially amplified. In this phase, liquid droplets (identified as intermediate-mass fragments) and gas (nucleons and light ions)

[20] Fission and evaporation still remain significant exit-channels for Gold-like nuclei heated up to $\varepsilon^{\star} \approx 4A$ MeV with antiproton projectiles [Pien00].

[21] Times of the order of $\tau = 10^{-21}$ - 10^{-20} s $\approx$ 300 - 3000 fm/c are necessary for shape deformation to develop.

[22] The system falls apart on a very short time scale ($t \approx 10^{-22}$ s $\approx$ 30 fm/c) [Beau99] in a process known as "bulk emission" when the spinodal boundary of the phase diagram is crossed.

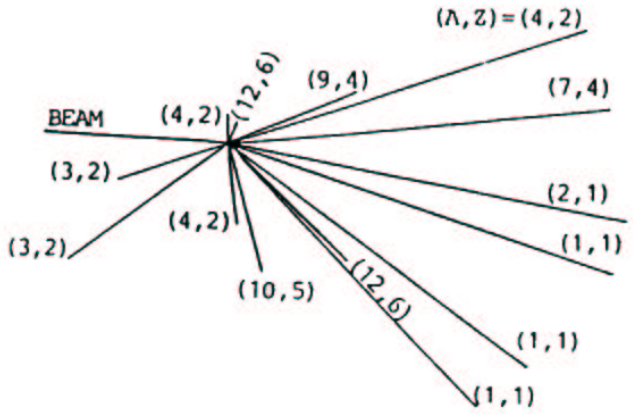

Figure 2.4: *Photography of a multifragmentation reaction as seen by nuclear emulsion experiments with heavy-ion beams at intermediate energies [Jako82].*

would coexist[23]. One pictures, thus, the fragmentation happening as a local redistribution of cooling and expanding matter that forms clusters of nuclei out of the previously homogeneous excited medium. During the clusterization, the homogeneous metastable liquid goes into a mixed phase composed of gas and liquid. Such a formation of clusters is an effect of the attractive nature of the nucleon-nucleon interaction and can be associated to the occurrence of a liquid-gas phase transition in a finite-size nuclear system.

This passage through a liquid-gas phase transition would explain also the third aforementioned characteristic of nuclear multifragmentation. For small excitation energies ($\varepsilon^\star \lesssim 3A$ MeV) the nuclear system is assimilable to an excited Fermi liquid (drop) which, in order to release its extra excitation energy, simply evaporates LCP and nucleons from its surface or, if heavy enough, it fissions. In the limit of very large $\varepsilon^\star$ ($\varepsilon^\star > 10A$ MeV), the system behaves essentially as a classical dilute Maxwell-Boltzmann gas of individual nucleons. Multifragmentation would "fill" the excitation-energy region between those two extremes (table 2.1 and fig. 2.5). The maximum of the IMF production would mark the borderline between the regime of residue formation and the regime of vaporization (or naively speaking between the "liquid"-like and the "gaseous"-like regime).

Additionally to the aforementioned experimental characteristics of multifragmentation, it has been also claimed [Poch95] that the "plateau" in the T vs. $\varepsilon^\star$ "caloric curve" (fig. 2.7) observed in certain experiments is reminiscent of the liquid-gas phase transition of water, a behaviour predicted by certain statistical models (fig. 2.6). This experimental result has triggered an intense discussion the last years (see Section 9.4).

We have seen that the excited source formation step in heavy-ion reactions at energies below 100A MeV is incomplete fusion of target and projectile nucleons [More97]: for example, an Au target picks up a variable amount of mass from an Ar projectile (the smaller partner, due to the different potential barriers mainly determined by their volume-to-surface ratio [Polt95], appears always to be the donor) resulting in a source of a given

[23] Alternatively, one can also identify the "liquid" phase with the heaviest remaining fragment (the heavy "residue" or "remnant") and the "gas" one with the lightest LCP and IMF reaction products.

Table 2.1: *Characteristics of the three experimentally observed dominant decay modes of excited nuclear systems produced in heavy-ion reactions. n are neutrons, LCPs light charged-particles (Z = 1, 2), IMF the fragments with Z = 3 - 20, and HFs heavy fragments with Z > 20.*

$\varepsilon^{\star}$ (A MeV)	Decay process	Reaction products	Number of reaction prods.	Decay mode probability	Thermodyn. state
$\lesssim 3$	evaporation, fission	*n*, LCPs, HFs	small	large	Fermi liquid
3 - 9	multi-fragmentation	*n*, LCPs, IMFs	at least 3 IMFs	small	Fermi liquid and Boltzmann gas
$\gtrsim 9$	vaporization	*n*, LCPs	many	very small	Boltzmann gas

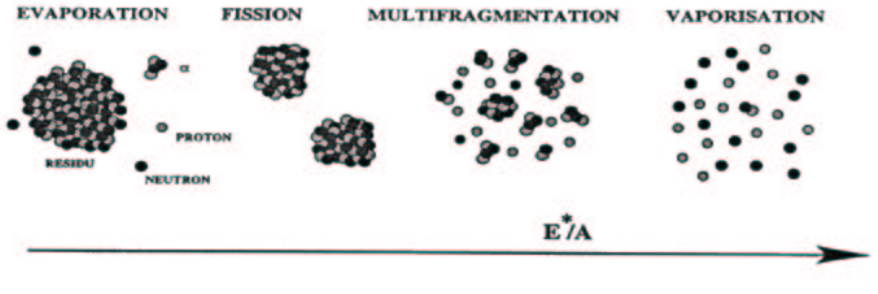

Figure 2.5: *Schematic view [Geno99] of the different decay-modes of an excited nuclear system produced in a heavy-ion collision for increasing excitation energies.*

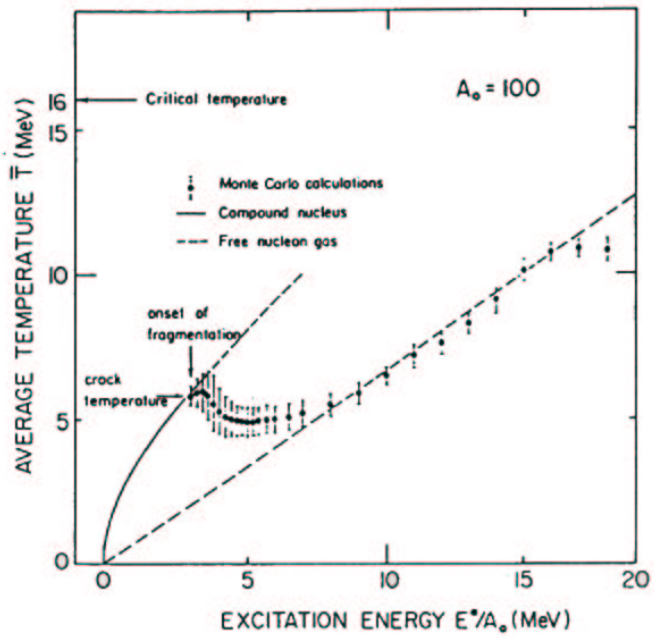

Figure 2.6: *Correlation excitation energy - temperature for a nucleus of mass A = 100 according to the Copenhagen statistical multifragmentation model [Bond85]. The dashed (solid) line illustrates the temperature of a free nucleon gas (of a Fermi liquid).*

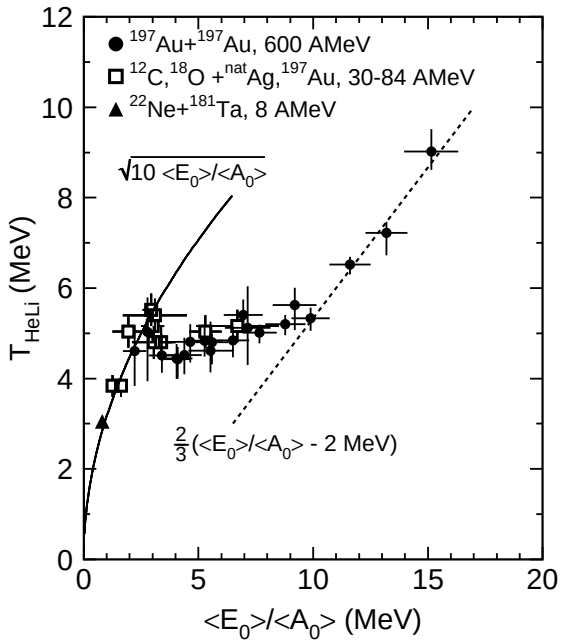

Figure 2.7: *Caloric curve of nuclei determined by the dependence of the so-called "isotope temperature" T_{HeLi} (see Section 9.3) on the excitation energy per nucleon $\mathfrak{E}^*$ [Poch95]. The solid curve corresponds to the Fermi liquid curve $\mathfrak{E}^* = T^2/10$, and the dotted one to the classical Boltzmann gas relation $\mathfrak{E}^* \propto 3/2\,T$.*

mass, momentum and excitation energy (apart from relatively small angular momentum[24] and Q-value[25] effects). The different decay modes of this source depend strongly on the excitation energy (thermal and compressional) deposited in the system (table 2.1). Increasing excitation energies are related with decreasing impact parameters, which at their turn are, from pure geometrical considerations ($\sigma_R = \pi b^2$), less probable. That is the reason why in intermediate-energy HI reactions most of nuclear reactions proceed via evaporation and fission, multifragmentation represents a less probable exit channel ($\lesssim$ 10%) and only a very few percent ($\lesssim$ 0.1%) of the total nuclear cross-section leads to total vaporization events (see e.g. [Bacr95, Rive96, Bord99]).

The underlying physical mechanism behind nuclear multifragmentation remains unclear and the debate is still controversial, mainly due to the fact that a few experimental results are in good agreement with the assumption that the fragments are emitted statistically from a thermalized system, whereas others can hardly be reconciled with this assumption (see below). Concerning the theoretical explanation of multifragmentation, several phenomenological models were first proposed explaining and/or reproducing only a few observables (for a review see [More93]). In the last years, they have been superseded by numerical models which predict results for several observables simultaneously (see Section 2.2.3). Presently, these models can be classified into two main categories: statistical and dynamical models. Their differences are based on the fundamental mechanism at the origin of fragmentation itself, on the time-scale of fragment production and on the assumptions of the state of the system at that time. On the one hand, statistical models claim that the first dynamical stage which leads to the source formation is decoupled from the subsequent statistical decay of the source. The decay phase occurs after thermodynamical equilibrium is reached and multifragmentation is mainly a thermally-(with a certain compressional component) driven process. Purely dynamical models, on the other hand, state that none of the relevant degrees of freedom equilibrate, and that fragment formation is a very early process triggered by the initial correlations among the nucleons of the colliding ions.

At the present moment, thus, only three models seem to be capable of explaining consistently several experimental observations concerning the multifragmentation process:

1. **Rapid Sequential Statistical** model. The Expanding-Emitting Source (EES) model [Frie88, Frie90] calculates the sequential (time-dependent) emission rates, within the statistical Weisskopf surface emission formalism, for a nucleus which expands following an initial thermal shock: the system initially cools by expansion and the emission of light particles. For sufficiently high initial excitation energies ($\varepsilon^\star > 5A$ MeV) the system will expand up to a density near $1/3\rho_0$ (T $\approx$ 5 MeV at this point) at which the free energy for producing a free particle is equal to the free energy for

[24]The average angular momenta produced in heavy-ion reactions at intermediate energies is of the order of $L \approx 50\hbar \approx 50 \cdot 0.2$ GeV fm. The rotational energy corrections to the total excitation energy are not large (however, the value of L can affect sizably the angular distributions of the reaction products [Yane96]): Assuming a spherical nucleus with A = 100 and moment of inertia $I = (2/5)AR^2 = 2/5\, r_0^2 A^{5/3}$, the rotational energy is only of the order: $\varepsilon^\star_{rot} = E^\star_{rot}/A \approx L^2/(2AI) \approx L^2/A^{8/3} = 10\,[\mathrm{GeV^2 fm^2}]/100^{8/3}\,[\mathrm{GeV\ fm^2}] \approx 0.4A$ MeV

[25]Large Q-values are normally considered for the very unlike "quasi-fusion" events for which the mass balance, $Q_{fus} = \Delta_{A_1} + \Delta_{A_2} - \Delta_{(A_1+A_2)}$, can constitute a sizeable source of extra energy deposited in the system.

producing a particle inside the volume. After this point is reached, surface emission stops and the model switches to volume emission favoring the rapid emission of IMFs. Such a (rather simple) model is capable of explaining several experimental observables and specially the multiplicity and kinetic energy distributions of LCP produced in coincidence with IMF [Boug99, Viol99].

2. **Simultaneous Statistical** multifragmentation models. The statistical multifragmentation models of the Berlin (MMMC) [Gros97] and Copenhagen (SMM) [Bond85] groups, assume that the produced nuclear system (or a subsystem of it) reaches thermodynamical equilibrium in the course of the reaction and maintains this equilibrium during the expansion phase until, at $t \approx 100$ fm/c, its density reaches a value between $1/2\rho_0$ - $1/10\rho_0$. Such an equilibrated and excited ($\varepsilon^\star \approx 5A$ MeV) expanding nucleus undergoes a simultaneous (also called "dynamical" in some works) clusterization at the freeze-out stage. Usually, the calculations start with a certain thermalized source at freeze-out with a given size (i.e. mass A_S and charge Z_S), (low) density and excitation energy $\varepsilon^\star$ (being basically thermal, but to which an extra collective compressional motion can be added accounting for a few *A*MeV). The probability of a certain final-state of the decaying system is then proportional to its statistical weight, i.e. to the number of microscopic states leading to this final state. These models predict very accurately the multiplicity and kinetic energy distributions of the IMF produced in very-central heavy-ion reactions for which a unique source can be isolated [Mari97, Boug97, Boug99]. *Caloric curves* ($\varepsilon^\star$ versus T plots) for nuclear matter which flatten in the excitation energy range 3 - 8 *A*MeV at temperatures near 5 to 6 MeV, and vaporization events above 9*A* MeV are also predicted.

3. Purely **Dynamical** models: Molecular dynamics approaches (like QMD [Goss95, Puri96, Goss97, Neba98, Neba99a] advocate a faster non-equilibrated process where fragments are pre-formed earlier in the reaction at densities higher than those present at the final break-up stage. The short time scales of the order of 50 fm/c after which the asymptotic fragments can be identified suggested by these studies, do not leave room for equilibration of the thermal and kinetic degrees of freedom. Fragmentation is triggered by the initial correlations among the nucleons of the projectile and target. The observed collective motion, and in general the kinetic energies of the produced fragments, are not produced by an expansion of the fragmenting system up to subnuclear densities, but have their origin in the original Fermi motion of the nucleons [Neba98, Neba99a]. Experiment-model comparisons for peripheral and mid-central collisions present a good agreement simultaneously for several observables (multiplicities and kinetic energy distributions for IMFs and heavy-fragments) [Tire98, Neba99a].

These statistical and dynamical theoretical models, based on rather different (and even contradictory) assumptions, predict very similar results for several key experimental observables. Probably, the resulting exit channels produced in multifragmentation reactions include both statistical and dynamical effects. To disentangle between the different proposed scenarios leading to multifragmentation processes one thus needs a detailed understanding of the collision dynamics looking for signals associated with each particular

phase (preequilibrium, fragmentation and final deexcitation). As we shall see in the next chapter, photons emerge undisturbed from these different phases of the nucleus-nucleus reaction and, hence, constitute precious tools to investigate the dynamics of heavy-ion reactions and, eventually, to obtain unique information on the time-scale of the fragmentation process and on the thermodynamical state of the fragmenting nuclear systems.

Chapter 3

Photon production in nucleus-nucleus collisions at intermediate energies

Summary

3.1 Sources of photons in HI collisions around the Fermi energy 36
3.2 Hard-photon production in HI collisions around the Fermi energy . 41
3.2.1 Experimental systematics 41
3.2.2 Theoretical models 47
3.3 New experimental results of hard-photon production: Thermal hard-photons 49
3.4 Goals of the experiment. Motivation of the thesis 53

As we have seen in previous sections, a quantitative understanding of the detailed dynamics of nucleus-nucleus collisions at intermediate bombarding energies is a basic prerequisite before one can study the nuclear EoS at subnuclear densities with or without a liquid-gas phase transition. Indeed, the knowledge of the time evolution of the reaction is necessary to disentangle the signals which are expected in the preequilibrium or in the late deexcitation phases from the signals connected to the fragment formation stage (possibly related to a phase transition). One thus has to exploit probes that are sensitive to specific periods of the reaction evolution and to specific phase-space regions. This is the primary motivation for the investigation of elementary particle production in heavy-ion collisions [Cass90, Mose91].

The creation of elementary particles such as photons, mesons or dileptons, not present in the initial state of the nucleus as real particles, has attracted much interest in intermediate-energy and relativistic heavy-ion physics since they are precise probes of the phase-space evolution of the reaction. Although they have very small production cross-sections, such energetic particles convey valuable information about the stages of the reaction in which they are created. Among them, photons are very clean probes since, due to their weak electromagnetic coupling to hadrons, they have a small probability of interacting with the surrounding nuclear matter and, thus, carry undisturbed information of the stage of the reaction in which they are emitted. Photons possess two additional interesting advantages. From a theoretical point of view the coupling of photons to other particles is in principle calculable. Experimentally, since photons move with $\beta = c$ they can be easily identified by time-of-flight techniques among a large background of slower hadronic particles.

3.1 Sources of photons in HI collisions around the Fermi energy

Electromagnetic radiation is emitted cumulatively throughout the evolution of the nucleus-nucleus interaction, supplying direct information, in principle, from all stages of the reaction process. Since photons of significantly different energies have different origins, they can be used to trace unambiguously the space-time evolution of the system. This is in contrast to nucleons or nuclear fragments which can be emitted from both the participant and/or the spectator part of the colliding nuclei and which suffer from final-state (nuclear and Coulomb) interactions. A typical inclusive[1] photon spectrum (fig. 3.1) emitted in nucleus-nucleus collisions at Fermi energies and measured with the TAPS photon spectrometer [Schu97, Gudi99], exhibits several contributions indicating different production mechanisms:

1. **Statistical gammas**. The region below $E_\gamma \approx 8$ - 10 MeV (i.e. energies below the particle separation energy $B_{n,p} \approx 8$ MeV) corresponds to the gamma rays emitted through statistical decay (after particle evaporation) of the low-excitation ($\varepsilon^\star \lesssim 2A$ MeV) reaction products which are present at the later stages ($t \gtrsim 500$ fm/c) of the nuclear reaction. Its exponential decreasing shape reflects the exponential increase of the nuclear level densities in their daughter nuclei as a function of their excitation

[1] An inclusive reaction means, in general, $A + B \rightarrow \gamma + X$

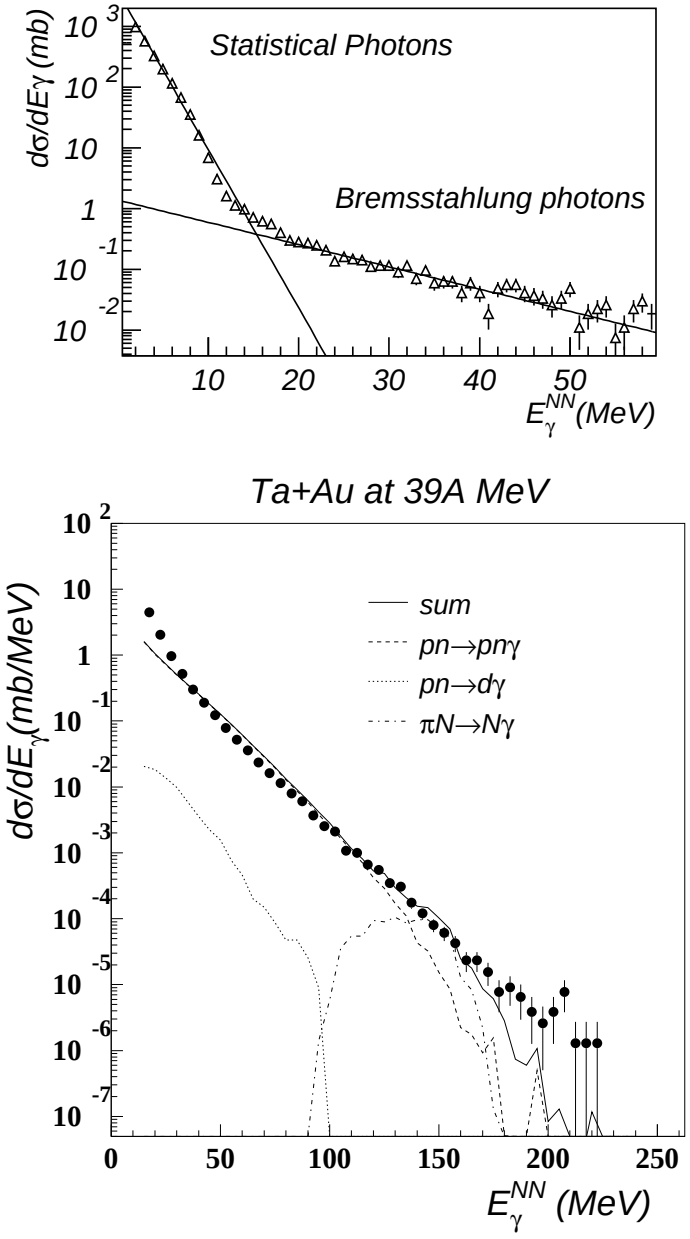

Figure 3.1: *Typical photon spectra, in the NN center-of-mass, emitted in a heavy-ion reaction at intermediate energies and measured with the TAPS photon spectrometer: in the low-energy (E_γ < 50 MeV) region (upper figure, [Schu97]), and in the region 20 MeV < E_γ < 200 MeV (lower figure, [Gudi99]). The different elementary contributions according to a "Dubna Cascade Model" calculation are identified on the bottom figure (the closed circles represent the experimental photon spectrum after cosmic-ray background subtraction).*

energy according to the simplified form of the Fermi gas level density (the so-called "Bethe formula" [Beth37]), $\rho(\varepsilon^\star) \approx e^{2\sqrt{a\varepsilon^\star}}$, with $a \approx A/13 - A/8$ being the level density parameter (see Appendix 3).

2. **GDR photons**. At energies ranging from 10 to 25 MeV the spectrum of nuclear excitations is dominated by giant resonances[2], strong collective oscillations of all the nucleons in a nucleus. In the experimental spectrum this is observed as an excess (a *bump*) of photons, on top of a exponentially decreasing function, coming from the gamma-ray decay of the Giant Dipole Resonances (GDR) built on the moderately hot nuclei ($\varepsilon^\star \lesssim 4A$ MeV) present at the beginning of the final deexcitation stage of the reaction. The GDR is an isovector electric (neutron and proton interpenetrating *fluids* oscillating in opposite phase) resonance mode of the nucleus which, microscopically, in the shell model, corresponds to a collective one-particle one-hole excitation [Snov86, Gaar92]. Since excitation energies of Giant Resonances are usually well above the nucleon binding energies, they mainly decay by neutron and proton evaporation and, in heavy nuclei, by fission. The electromagnetic channel is also open and GDR have a sizeable gamma-decay branch of the order of 10^{-3}.

   The GDR strength is usually characterized by a Lorentzian (also called a Cauchy or Breit-Wigner distribution) shaped distribution with three parameters: its centroid energy E_{GDR}, width Γ_{GDR}, and the so-called "Thomas-Reiche-Kuhn Sum Rule" strength S_{TRKSR} expressed as a percentage accounting for the degree of collectivity of the nucleons participating in the excitation. The centroid energy of the GDR varies roughly between 14 MeV (for the heaviest nuclei) to 22 MeV (for the lightest ones) and, for the excited-states, it is found to depend on the mass number [Gaar92] approximately as[3]:

$$E_{GDR} = 18A^{-1/3} + 25A^{-1/6} \tag{3.1}$$

   For increasing excitation energies the GDR width spreads roughly as $\Gamma = 4.8\,(1 + 1.6\varepsilon^\star)$ [Brac89] saturating around $\Gamma \approx 12$ MeV [Brac89, Hofm94] already for $\varepsilon^\star > 1A$ MeV, and its yield gets progressively quenched [Gaar92] (which can be expressed as: $S^*_{TRKSR} < 100\%$). Gamma rays from GDR decay can be emitted at all steps during the decay chain of the moderately hot and equilibrated nucleus, and therefore the measured gamma spectrum is not a direct reflection of the gamma emission from the nucleus at its initial temperature, but rather an average over all temperatures from the initial temperature down to zero (one assumes a GDR equilibration time around 300 - 400 fm/c). Statistical calculations, taking into account the entire decay sequence, can be carried out using the standard statistical decay code CASCADE [Puel77].

3. **Hard-photons**. Above $E_\gamma \approx 25$ MeV, the photon spectrum falls off exponentially over several orders of magnitude. This spectrum is completely dominated by the

[2] These nuclear excitations are called "giant" due to its collective origin in contrast with other transitions to discrete levels.

[3] The GDR of typical *cold* nuclei e.g. in the mass A = 110 region have a centroid energy $E_0^{g.s.}$ = 16 MeV, $\Gamma^{g.s.}$ = 4 - 5 MeV and sum-rule strength $S^{g.s.}_{TRKSR} \approx 100\%$. The GDR's built in an *excited-state* of the same nuclei have: E^*_0 = 15 MeV, Γ^* = 9 - 13 MeV and sum-rule strength $S^*_{TRKSR} \approx 50\%$ - 100%.

so-called "hard photons", created mainly by the incoherent superposition of bremsstrahlung radiation emitted in (chaotic) first-chance proton-neutron (*pn*) elastic collisions inside the overlapping region of projectile and target during the first stages of the reaction ($t \lesssim 50$ fm/c) [Cass90, Nife89, Nife90]. Photons with such energies are produced, at the bombarding energy under consideration, below the free $NN\gamma$ threshold energy in the laboratory ($K_{thr}^{NN\gamma} \approx 0.5 K_{lab}$, see footnote on next page). The extra energy needed for their emission is provided by the coupling of the intrinsic Fermi motion of the colliding nucleons ($p_F \approx 270$ MeV/c) to the beam momentum per nucleon $p_{lab} = \sqrt{2K_{lab}Am_N + K_{lab}^2}$. Typical hard-photon production cross-sections are of the order of a few millibarns. The characteristics of these photons, which constitute the subject of this thesis, are reviewed in more detail in the next section.

Above $E_\gamma \approx 50$ MeV, there is also a small contribution of photons coming from the electromagnetic decay of subthreshold neutral pions: $\pi^0 \rightarrow \gamma\gamma$ (BR = 99.8%, $\tau = 8.4 \cdot 10^{-17}$ s) produced in inelastic $NN \rightarrow NN\pi$ collisions[4]. Typical π^0 production cross-sections are of the order of several microbarns around 60*A* MeV, rapidly increasing with higher bombarding energies.

4. **Very hard photons**. Photons are observed at energies even higher than the so-called *kinematical limit* for bremsstrahlung[5]

$$E_\gamma^{max}(s) = \frac{s_{max} - 2m_N^2}{2\sqrt{s_{max}}}, \tag{3.2}$$

where $s_{max} = 2\frac{[E_F(m_N+E_{lab}) + p_F\, p_{lab}]^2}{m_N\,(m_N+E_{lab})}$ (with $E_F = \sqrt{p_F^2 + m_N^2}$ and $E_{lab} = K_{lab} + m_N$ being the Fermi and the beam energy respectively) is the maximum CM energy available in a knock-out *NN* collision from the two opposing pole caps of the momentum spheres of the two colliding nuclei (i.e. for a *NN* collision in which the intrinsic momenta of the two nucleons are anti-parallel and equal to the Fermi momentum p_F = 270 MeV/c). Several effects seem to be responsible for this very-deep subthreshold photon production:

- *Secondary interactions* or two-step mechanisms such as the radiative capture of the produced pions ($\pi N \rightarrow N\gamma$) or the electromagnetic decay of the Δ resonance ($\Delta \rightarrow N\gamma$) [Gudi96], as well as processes involving off-shell nucleons ($NN^* \rightarrow NN\gamma$) [Cass99], can produce photons with energies above E_γ^{max}.
- Experimental evidences of *high-momentum tails* in the nucleon spectral function extending much beyond the Fermi surface at $p_F \approx 270$ MeV/c have been observed in (*e*,*e'*p) data in the ground state of nucleus [Bobel95] and in AA collisions [Migne99]. This high-momentum nucleon component (either due

[4] Pions can be produced either directly, $NN \rightarrow NN\pi$, or in two-steps involving an intermediate Δ or off-shell nucleon [Bert96]: $NN \rightarrow \Delta N$ or $NN \rightarrow NN^*$ and then $\Delta \rightarrow N\pi$, or $\Delta N \rightarrow NN\pi$, or $N^*N \rightarrow NN\pi$ [Gudi99].

[5] According to this formula, the maximum photon energy in a HI collision of 60*A* MeV bombarding energy is $E_\gamma^{max}(s)$ = 194 MeV.

to off-shell effects or to dynamical fluctuations) increases the value of the kinematical limit E_γ^{max} for bremsstrahlung emission given by formula (3.2).

- *Particle correlations* effects [Ho93, Wang94], either due to the cooperative action of (two-, three- or four- nucleon) cluster structures present in the ground-state nuclei or due to *three-body* (and likely higher-order) *collisions* during the high-density phase of the reaction [Bona94], may generate a prominent energy boost in the nucleon distribution in phase-space. Such additional elementary bremsstrahlung-photon production processes, e.g. involving deuteron-like correlated pairs ($pn \rightarrow d\gamma$) [Boze98] or α-particles [Wang94], have been taken into account in some models of hard-photon production.

It is also interesting to note that those different mechanisms are also visible, as reverse processes, in the total photo-absorption cross-section on nuclei (fig. 3.2) i.e. in the reaction $\gamma A \rightarrow X$. In fig. 3.2, statistical gamma rays below 10 MeV are observed as photoexcitation of the nucleus into bound states (below E_γ = 2 MeV) and into unbound individual states (2 MeV $< E_\gamma <$ 9 MeV) which can be well explained in terms of the nucleus shell model. In the region between roughly 10 and 25 MeV, a broad structure corresponding to the excitation of the collective mode of the Giant Dipole Resonance is observed. Above incident gamma energies of 30 MeV, the photoabsorption cross-section has a rather weak energy dependence. This is the quasi-deuteron region, where absorption occurs on correlated proton-neutron pairs ($\gamma d \rightarrow pn$), a process that corresponds by crossing symmetry, to the t-reverse $pn \rightarrow pn\gamma$ bremsstrahlung process. Finally, above the photo-pion threshold, the cross-section rises to a maximum in the Δ resonance region.

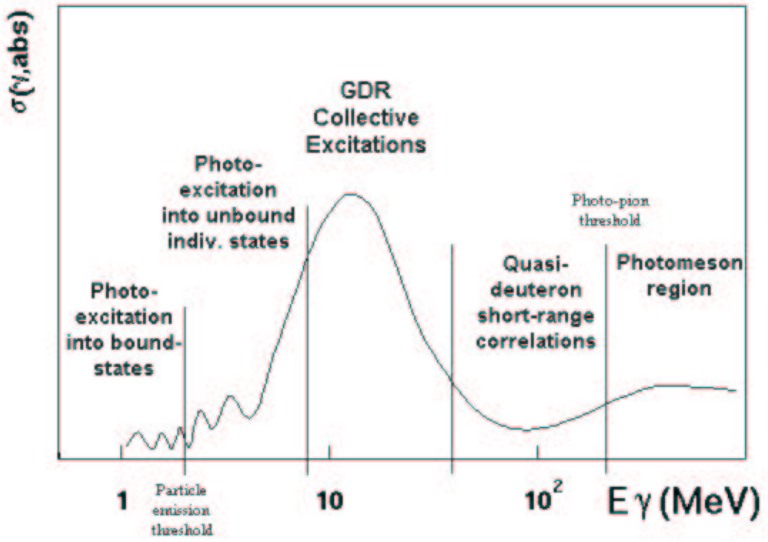

Figure 3.2: *Schematic representation of total photoabsorption cross-section on nuclei. Adapted from [Chri90].*

3.2 Hard-photon production in HI collisions around the Fermi energy

Hard-photons emitted in intermediate-energies heavy-ion reactions are conventionally defined as photons with energies above 30 MeV. These high-energy γ are produced below the free $NN\gamma$ threshold energy[6] and, thus, they are considered as subthreshold particles. In the past years, considerable experimental and theoretical efforts have been directed towards the understanding of this high-energy photon production in heavy-ion reactions at intermediate incident energies [Nife89, Cass90, Nife90].

3.2.1 Experimental systematics

The main characteristics of hard-photon ($E_\gamma > 30$ MeV) production in heavy-ion reactions at intermediate bombarding energies have been established experimentally since their first observation in 1984 [Gros84, Gros84b, Bear85, Gros85]. The experimental results (the so-called "systematics") collected up to 1992 can be reviewed in the reports of Nifenecker and Pinston [Nife89, Nife90], Cassing *et al.* [Cass90], and the thesis of van Pol [Polt95] and concern the energy spectra, the angular distributions and the cross-sections, as well as the impact-parameter dependence of these observables:

1. **Energy spectra**: The hard-photon energy spectrum in the *NN* center-of-mass follows an exponentially decreasing distribution (see fig. 3.1 in the $E_\gamma > 30$ MeV range) characterized by an inverse slope parameter E_0:

$$\frac{d\sigma}{dE_\gamma} = K e^{-E_\gamma/E_0} \tag{3.3}$$

   The slope E_0 of this exponential is independent of the size of the system and/or the target-projectile combination. E_0 shows only a linear dependence with the (Coulomb-corrected) beam energy per nucleon, $K_{Cc} = (K_{lab} - V_C)/A_p$, (fig. 3.3) according to [Polt95]:

$$E_0 = a\,(K_{Cc})^b \tag{3.4}$$

   with $a = 0.48 \pm 0.06$ and $b = 0.91 \pm 0.03$.

   The high value of the inverse slope (E_0 = 8 - 30 MeV for bombarding energies in the range K_{lab} = 20*A* - 100*A* MeV), and its dependence in the beam energy *per projectile nucleon* and not on the target-projectile combination nor on the total beam energy, is compatible with the composition of the beam velocity with the velocity of the nucleons' Fermi motion during the first instants of the collision. Indeed it has been seen that within a first-collision model for a heavy-ion collision (such as "Dubna Cascade Model" [Gudi99], or the "Nuclear Exchange transport model" [Vand98]),

[6] In a free $NN \to NN\gamma$ collision, the maximum photon energy applying equation (3.2) is $E_\gamma^{max} = K_{lab} m_N / \sqrt{2K_{lab}m_N + 4m_N} \approx K_{lab}/2$, i.e. to produce a photon with E_γ = 30 MeV one needs at least a nucleon with K_{lab} = 60 MeV incident energy.

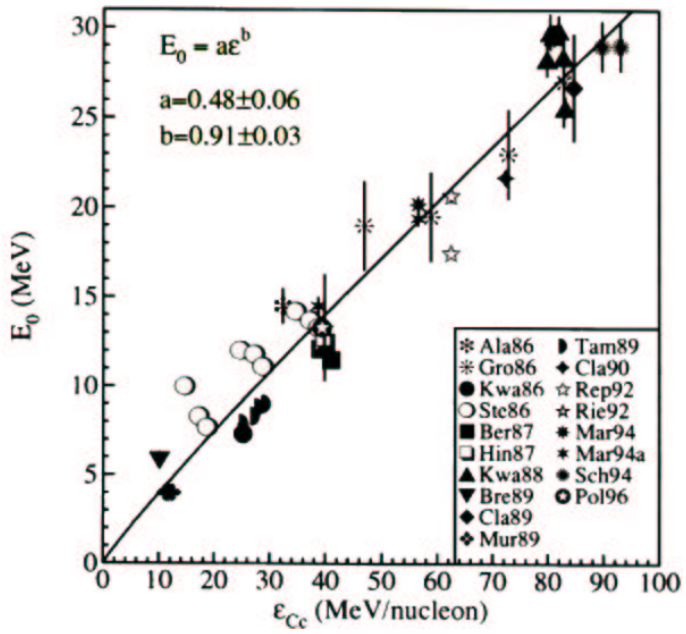

Figure 3.3: *Systematics of the experimentally measured hard-photon inverse slope parameter E_0 as a function of the Coulomb corrected bombarding energy per nucleon K_{Cc}. From [Polt95].*

the folding of the elementary bremsstrahlung $pn\gamma$ cross-section with the intrinsic momentum distribution of the colliding nucleons in a Pauli-blocked environment as encountered during a heavy-ion reaction, results in a basically exponential shape for the hard-photon spectrum.

2. **Angular distributions and photon source velocities**. As developed in Appendix 2, the *elementary* $pn \rightarrow pn\gamma$ double differential cross-section, $d\sigma/dE_\gamma d\Omega$, in the *NN* source frame results from the sum of an isotropic plus an anisotropic dipole ($\sin^2\theta_\gamma$) terms. The classical soft-photon approximation[7] reads:

$$\frac{d^2\sigma_{pn\rightarrow pn\gamma}}{dE_\gamma d\Omega_\gamma} = \frac{e^2}{4\pi}\frac{\sigma_{pn}}{4\pi^2}\frac{\beta^2}{E_\gamma}\left(\frac{2}{3}+\sin^2\theta_\gamma\right) \tag{3.5}$$

This observed dipolar component indicates that, in the free process, bremsstrahlung photons are emitted primarily in the direction perpendicular to the velocity of the scattered proton. The angular distribution of hard-photons emitted in heavy-ion reactions shows, however, a less enhanced anisotropic dipole component in comparison with this elementary differential cross-section. This is due to the smearing out of the bremsstrahlung in all directions caused by the random Fermi motion of the colliding nucleons. The double-differential cross-section for hard-photon production in nucleus-nucleus reactions has been thus usually parametrized, in the source frame, by the following phenomenological expression [Berth87] inspired in

[7] For a derivation of this formula see Appendix 2.

the elementary double differential $pn\gamma$ cross-section (3.5):

$$\frac{d\sigma}{dE_\gamma d\Omega} = K\left[1-\alpha+\alpha\sin^2\theta_\gamma^{cm}\right]e^{-E_\gamma^{cm}/E_0}, \tag{3.6}$$

where K is a normalization factor and α = 0.1 - 0.3 is the parameter of the dipole anisotropy.

Whereas the angular distributions have a (small) dipole component when viewed in the NN center-of-mass frame, they are forward-peaked in the laboratory frame. These asymmetric angular distributions, decreasing with the emission angle, are an indication that the photon source is moving forward in this frame. Denoting by β_S the source velocity and γ_S the related Lorentz factor, the Lorentz-boosted photon angular distribution in the laboratory frame[8] reads

$$\left(\frac{d\sigma}{dE_\gamma d\Omega}\right)_{lab} = \frac{K}{Z}\left[1-\alpha+\alpha\frac{\sin^2\theta_\gamma^{lab}}{Z^2}\right]e^{-ZE_\gamma^{cm}/E_0} \tag{3.7}$$

where $Z=\gamma_S(1-\beta_S\cos\theta_\gamma^{lab})$ is the Doppler factor.

The mean velocity β_S of the hard-γ source can be, thus, extracted fitting the formula (3.7) to the laboratory angular distribution (fig. 3.4).

3. **Cross-sections and multiplicities**: Hard-photon cross-sections are found to scale with the average number of NN collisions, $\langle N_{pn}\rangle$, in the overlapping volume between the two colliding ions following the simple relation [Nife85]:

$$\sigma_\gamma = \sigma_R M_\gamma = \sigma_R P_\gamma \langle N_{pn}\rangle_b \tag{3.8}$$

where σ_R is the total nuclear reaction cross-section, M_γ the photon multiplicity per nuclear reaction, and P_γ the photon emission probability per pn collision. Expression (3.8) simply factorizes the dependence of σ_γ on the energy and on the number of NN collisions through the parameters $M_\gamma = M_\gamma(P_\gamma, \langle N_{pn}\rangle_b)$ and $P_\gamma = P_\gamma(K_{lab})$. As experimentally observed, P_γ depends only on the (Coulomb-corrected) bombarding energy K_{lab}, through the E_0 parameter, according to [Polt95] (fig. 3.5):

$$P_\gamma = P_0\, e^{-30[\mathrm{MeV}]/E_0} \quad \text{with } P_0 = 6.3\cdot 10^{-4} \tag{3.9}$$

This general trend of the hard-photon emission probability per in-medium pn collision as a function of the (Coulomb-corrected) beam energy per nucleon in the laboratory system K_{Cc} is reminiscent of the K_{lab} dependence of the elementary $pn\gamma$ cross-section (see fig. 3 of Appendix 2). Of course the observed remarkable downwards shift of the threshold energy for hard-photon emission is due to the coupling of the nucleon Fermi motion inside the projectile and target with the relative motion of the colliding nuclei.

[8] We have make use of the following CM-LAB transformation formulas [Hage64] for the $pn\gamma$ process: $d\sigma/dE_\gamma^{lab}d\Omega_{lab} = (1/Z)\cdot d\sigma/dE_\gamma^{cm}d\Omega_{cm}$, $E_\gamma^{cm} = Z\cdot E_\gamma^{lab}$ and $\sin\theta_\gamma^{cm} = (1/Z)\cdot\sin\theta_\gamma^{lab}$, with $Z=\gamma_S(1-\beta_S\cos\theta_\gamma^{lab})$.

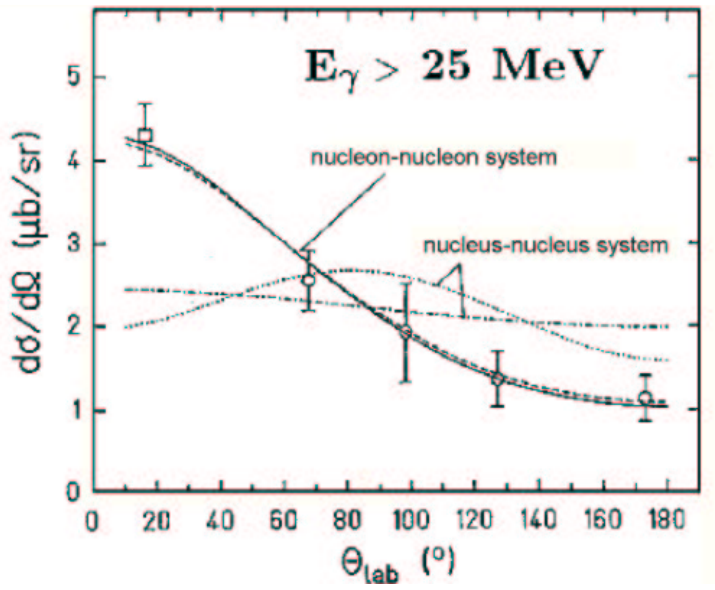

Figure 3.4: *Measured angular distribution of hard photons ($E_\gamma > 25$ MeV) in comparison to isotropic (dot-dashed) and dipole (dotted) radiation from the nucleus-nucleus system and to isotropic emission (dashed) from the nucleon-nucleon system. The solid line shows the best fit to the data with a source velocity of $\beta = 0.094 \pm 0.020$. From [Cass90].*

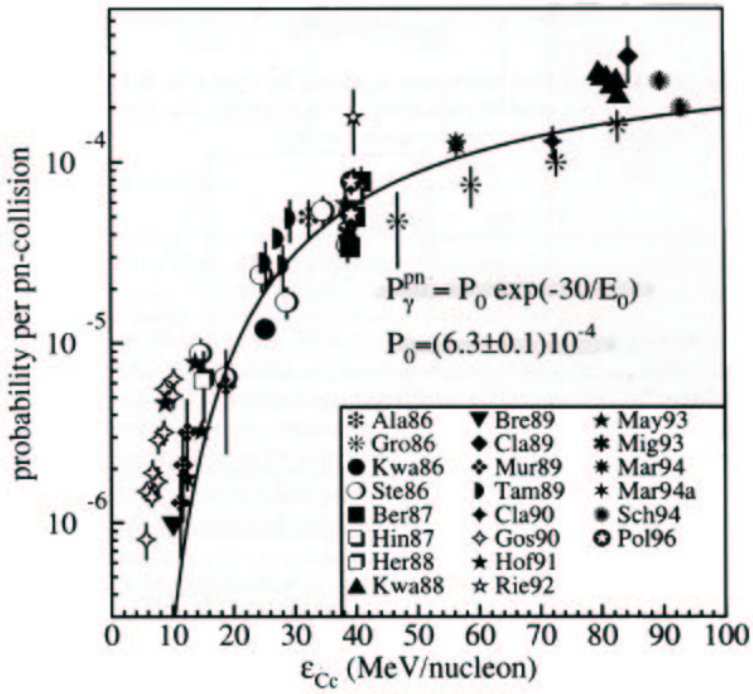

Figure 3.5: *Dependence of the bremsstrahlung photon production with respect to the (Coulomb-corrected) beam energy per nucleon measured for various systems. From [Polt95].*

The number of *pn* collisions averaged over impact parameter, $\langle N_{pn}\rangle_b$, can be calculated, in the framework of the "equal-participant" geometrical model [Nife85], as the number of *pn* pairs present in the region of (static) geometrical overlap between target and projectile nuclei:

$$\langle N_{pn}\rangle_b = A_{part}\cdot\left(\frac{Z_pN_t + Z_tN_p}{A_pA_t}\right) \tag{3.10}$$

$$\text{with} \quad A_{part} = A_p\cdot\frac{5A_t^{2/3} - A_p^{2/3}}{5(A_t^{1/3}+A_p^{1/3})^2} \tag{3.11}$$

The second factor in eq. (3.10) converts the number of nucleon participants, A_{part}, into the number of proton-neutron collisions, N_{pn}.

It has to be noted that the smallness of the hard-photon cross-sections compared with the nuclear reaction ones, $M_{\gamma(E_\gamma>30MeV)} = \sigma_\gamma/\sigma_R \approx 10^{-4} - 10^{-3}$, renders its detection an experimental challenge.

4. **Impact-parameter dependence**: The hard-photon multiplicity increases with the centrality of the reaction (saturating at the maximum nuclear overlap) due to the increased number of *pn* collisions for decreasing impact-parameter. The inverse slopes of the energy spectra become, thus, larger when going from peripheral to central collisions [Hing87, Lamp88, Kwat88, Sobo91, Ries92, Repo92, Mart94, Schu97] reflecting both the lower density (i.e. the smaller Fermi momenta) near the nuclear surface, in the case of peripheral collisions, and the modification of the intrinsic momenta of the participant nucleons during the compression phase, for the central ones [Mart94]. According to the equal-participant geometrical model, for a projectile nucleus (A_p, Z_p) bombarding a target nucleus (A_t, Z_t) at impact parameter b, one can extend expressions (3.10) and (3.11) to take into account the number of participant nucleons inside the overlapping zone between projectile and target for a given impact-parameter (fig. 3.6):

$$N_{pn}(b) = A_{part}(b)\cdot\left(\frac{Z_pN_t + Z_tN_p}{A_pA_t}\right) \tag{3.12}$$

where now A_{part} is assessed according to:

$$A_{part} = 5\frac{1}{4}A_p(2 - 3\cos\theta_p + \cos^3\theta_p) + \frac{1}{4}A_t(2 - 3\cos\theta_t + \cos^3\theta_t) \tag{3.13}$$

with $\cos\theta_{p,t} = \frac{b^2+R_{p,t}^2-R_{t,p}^2}{2bR_{p,t}^2}$ and $R_{p,t} = 1.15A_{p,t}^{1/3}$

Such a dependence of the number of *pn* collisions, N_{pn}, on the impact parameter, b, can be seen in fig. 3.7.

The bulk of experimental results collected in the "systematics" are consistent with the assumption that photons above 30 MeV mainly originate from the incoherent summation

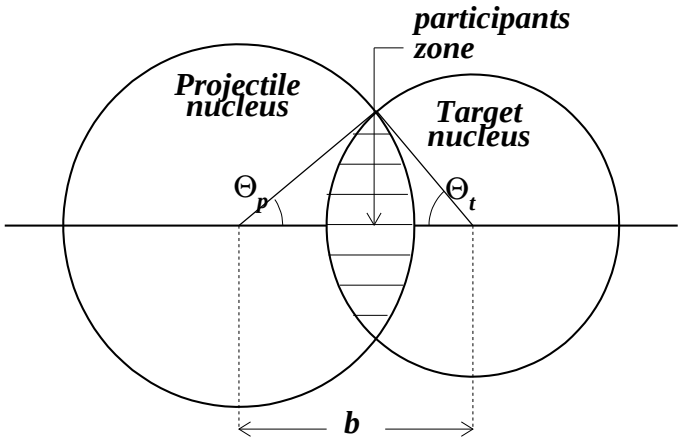

Figure 3.6: *Definitions of the geometrical parameters used in the "equal participant model". From [Schu97].*

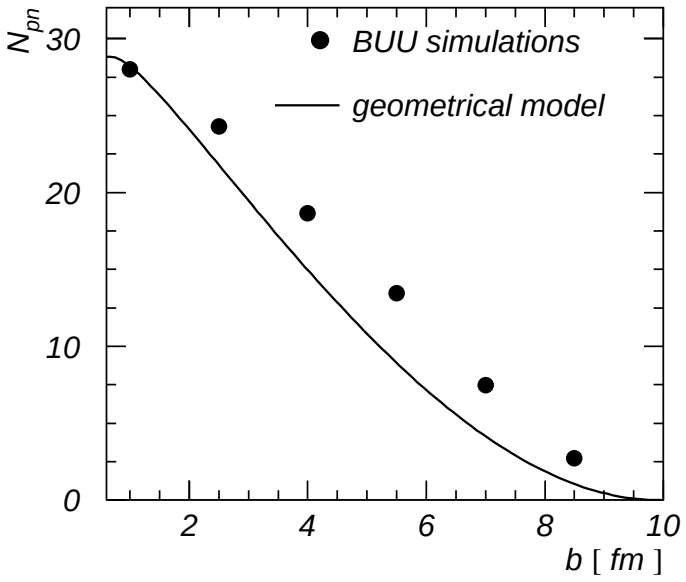

Figure 3.7: *Variation of the number of proton-neutron collisions, N_{pn}, with the impact parameter, b, calculated using eq. (3.12) for the system $^{86}Kr+^{58}Ni$. Dots represent the number of first chance pn collisions calculated with a BUU model. From [Schu97].*

of individual proton-neutron bremsstrahlung collisions produced in the first encounter between a nucleon from the projectile and a nucleon from the target within the participant overlapping zone of the colliding nuclei.

3.2.2 Theoretical models

Parallel to the experimental efforts, the determination of the exact origin of hard photons ($E_\gamma > 30$ MeV) produced in nucleus-nucleus collisions has been also the subject of an intensive theoretical study during the last 15 years. All proposed models for hard-photon production in heavy-ion reactions can be classified in two main groups:

1. **Incoherent $pn\gamma$ bremsstrahlung** models. Hard-photon production is assumed to arise from the incoherent summation of individual proton-neutron collisions ($pp\gamma$ bremsstrahlung has been experimentally [Koeh67, Edgi66] and theoretically [Nife85, Nife90] found out to be one order of magnitude inferior in this incident-energy regime). Under this assumption, two types of theoretical approaches have been proposed to explain Bremsstrahlung photon production: either dynamical or thermal models. Both types of approaches have to include necessarily the following two ingredients:

   - The **elementary** double differential $pn\gamma$ bremsstrahlung **cross-section** $d^2\sigma/dE_\gamma d\Omega_\gamma$. Since this cross-section is only very barely known experimentally, it has been estimated theoretically using several approaches (see Appendix 2): classical electrodynamics approximation (used e.g. in the works of refs. [Baue86, Bert88, Khoa91, Wang94]), detailed balance of the reverse deuteron photodisintegration $\gamma d \rightarrow pn$ process [Praka88, Herr88], modified classical approximations to take into account exchange currents [Pins89, Gan94, Russo94], and potential- [Naka89] or covariant- models calculations [Niit88, Biro87, Scha91].
   - The **nucleon phase-space distribution**: The phase-space distribution of the colliding nucleons has to contain typical quantal effects like the Fermi motion and the Pauli blocking. The evolution of this phase-space distribution is either governed by the reaction dynamics, in the case of dynamical models; or a realistic ansatz of the thermodynamical state of the system at the moment of hard-γ emission has to be assumed in the case of thermal models. On the one hand, in the pure dynamical description, the nucleon-nucleon collision history has been determined within a Boltzmann master equation approach [Rem86], BUU [Baue86, Cass90, Gan94], BNV [Russo94], QMD [Ohts90, Khoa91, Li92], Classical Molecular Dynamics (CMD) [Heue88], Nucleon-Exchange transport model [Rand88], or "Dubna Cascade Model" (DCM) [Gudi96, Gudi99]. Thermal models [Nife85, Stev86, Neuh87, Bona88, Alm95], on the other hand, have considered usually the formation of a expanding "fireball" of colliding nucleons with a certain Fermi distribution and temperature.

2. **Coherent or Collective Bremsstrahlung** models. In such approaches, the origin of hard-photons is assumed to be a coherent phenomenon involving *more than two* single colliding nucleons. As a matter of fact, such kind of bremsstrahlung is assumed

to play an important role in *few-body* systems [Baye85, Knol93, Baye92] like $\alpha + p$ or $\alpha + \alpha$ reactions[9]. In heavy-ion reactions two types of collective approaches have been proposed:

- **Coherent nucleus-nucleus** bremsstrahlung: Radiation is emitted collectively by the mutual deceleration of the colliding nuclei in the nuclear mean field [Vasa85, Vasa86, Stah87, Heue88, Koch90, Eich97].
- **Cooperative** bremsstrahlung of (virtual) **clusters** of nucleons within the colliding nuclei [Shya86, Wang94].

The theoretical interpretation, however, has not always been so clear-cut and a combination of a dynamical+thermal [Nife85] mechanism, a dynamical+cluster [Wang94] or a mixture of incoherent and coherent radiation [Stah87] contributions have also been proposed.

Nonetheless, according to the experimental results collected from 1985 to 1995, in first approximation the most successful theoretical models have been those which consider a pure first-chance incoherent nucleon-nucleon bremsstrahlung picture since such assumption is globally consistent with the characteristics of the experimental systematics. We will see, however, in the next Section that it has recently become increasingly clear that this scenario is too simple.

[9] Coherent bremsstrahlung has been actually recently observed in the radiation emitted in the $\alpha + p$ reaction at 50*A* MeV [Hoef99, Hoef00].

3.3 New experimental results of hard-photon production: Thermal hard-photons

The experimental hard-photon systematics detailed in Section 3.2 was mainly established from measurements using modest detection systems usually with a rather poor energy resolution and/or in a narrow energy range, as well as with a limited solid angle coverage. In the recent years, the development of a second-generation of precise electromagnetic calorimeters such as TAPS [Novo91] (or MEDEA [Mign92]), with large solid angle, high granularity and effective energy resolution, coupled to charged-particle multidetectors, has produced an important amount of inclusive and exclusive higher-quality and high-statistics data concerning photon production in several nuclear reactions at intermediate energies. These new measurements have allowed a more detailed analysis of the hard-photon energy spectrum in a wide energetic range, as well as the study of angular distributions, and two-photon intensity interference patterns for different projectile-target combinations. This studies have brought to light new aspects of hard photon production in heavy-ion reactions[10].

In particular, those detectors allowed for the first time:

- The exclusive measurement of hard-photon energy spectra in their widest range (30 MeV $< E_\gamma <$ 300 MeV) even above the "kinematical limit" given by equation (3.2).
- The use of the intensity (HBT) photon-photon interferometry technique to get information on the dynamical space-time extent of the emitting source.

These new possibilities lead to novel experimental observations in the 1992 TAPS campaign at GANIL for the systems ^{86}Kr+^{58}Ni at 60*A* MeV, ^{181}Ta+^{197}Au at 40*A* MeV and ^{208}Pb+^{197}Au at 30*A* MeV [Mart95, Marq95], and ^{36}Ar+^{197}Au at 95*A* MeV [Schu94], which deviated from the systematics known so far. The most interesting findings can be summarized as:

- The low-energy part of the hard-photon spectra showed a deviation from the pure exponential shape observed for the higher energy ($E_\gamma > 60$ MeV) photons produced in prompt bremsstrahlung *pn* collisions (fig. 3.8). An enhancement of low energy bremsstrahlung photons with a steeper slope was apparent in the region 30 MeV $< E_\gamma <$ 60 MeV for the systems ^{86}Kr+^{58}Ni at 60*A* MeV, ^{181}Ta+^{197}Au at 39.5*A* MeV and ^{208}Pb+^{197}Au at 29.5*A* MeV. Therefore, the whole hard-photon energy spectra could only be interpreted as the result of the sum of two exponential distributions with different slope parameters. The existence of a second exponential component with slope parameter smaller than the "conventional" *direct* component (due to first-chance *pn* collisions and following the systematics given by eq. (3.4)); was interpreted [Mart95] as an evidence for the existence of an additional emission of bremsstrahlung photons from secondary *NN* collisions in a later stage of the reaction where less energy is available.

[10] These new results can be found reviewed in the paper of Schutz *et al.* [Schu97].

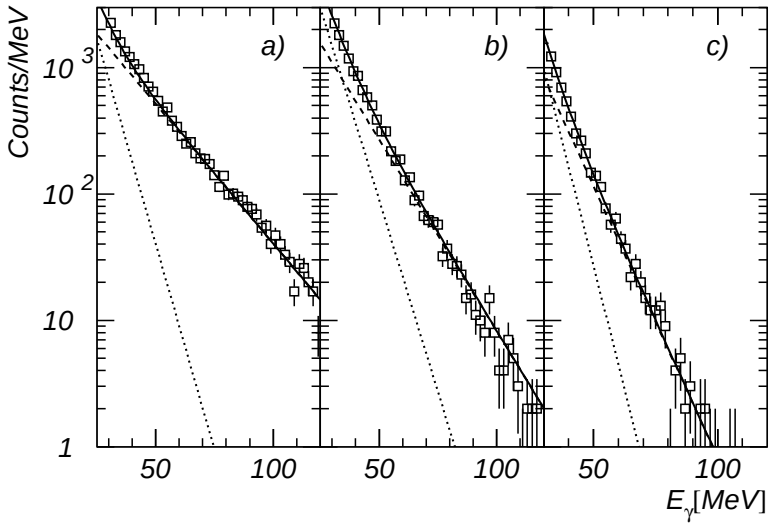

Figure 3.8: *Hard photon spectra for the systems a) $^{86}Kr+^{58}Ni$ at 60A MeV, b) $^{181}Ta+^{197}Au$ at 39.5A MeV, and c) $^{208}Pb+^{197}Au$ at 29.5A MeV measured in the TAPS campaign at GANIL in 1992. The deviation from the pure single exponential behaviour is apparent for all systems in the region of hard-photon energies $E_\gamma \approx$ 30 - 60 MeV. From [Schu97].*

The presence in the photon spectrum of two exponential distributions had been overlooked so far because of the experimental limitations which restricted the measurement of photon spectra only to a too narrow energy domain. There are only two exceptions where the photon spectrum had been measured up to rather high energies: E_γ = 120 MeV (^{14}N+^{208}Pb at 40*A* MeV) [Stev86] (fig. 3.9) and E_γ = 160 MeV (^{14}N+^{107}Ag at 35*A* MeV) [Luke93] (fig. 3.10). In both measurements, the two exponential components are clearly visible. In the first experiment, data were compared to calculations considering *pn* bremsstrahlung from a thermal source. These calculations correctly reproduced the low energy part of the spectrum but underpredicted the high energy part. In the second experiment, an extended version of the nucleon-exchange transport model [Rand88] was used. It reproduced the high-energy part of the photon spectrum but failed to reproduce the low-energy enhancement. The excess production was then tentatively attributed to GDR photons.

- A reduction of the velocity of the hard-photons source β_S was observed for the ^{36}Ar+^{197}Au system at 95*A* MeV with respect to the value predicted for an emission from the nucleon-nucleon CM frame (i.e. $\beta_S < \beta_{NN}$), except for very peripheral reactions. The much lighter ^{36}Ar+^{12}C system studied in parallel showed, however, a β_S value fully consistent with the picture of hard photon production in first-chance *pn* collisions ($\beta_S \approx \beta_{NN}$). This system-size and impact-parameter dependence of β_S was explained by the contribution of a second generation of photons in a later stage of the collision where a stopping and thermalization process was present leading to a lowering of the *average* velocity of the source of photons [Schu94].

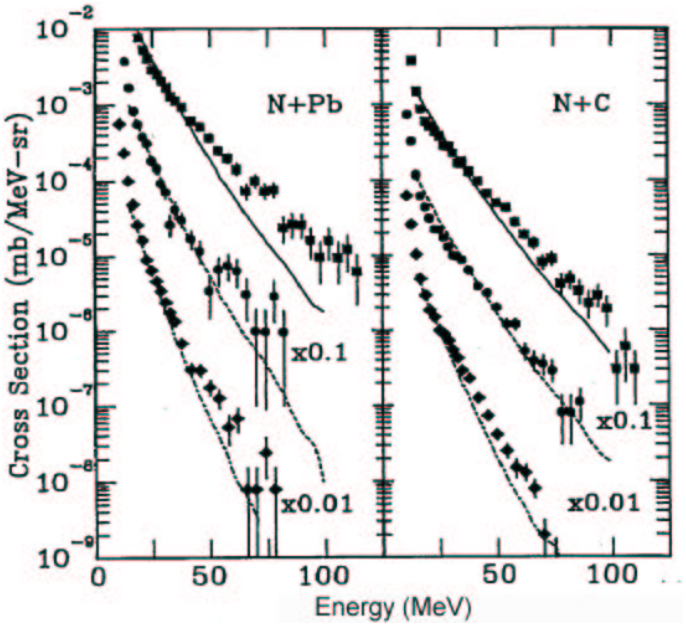

Figure 3.9: *Inclusive hard photon spectrum measured at θ = 90° for the systems $^{14}N+^{208}Pb$ and $^{14}N+^{12}C$ at beam energies of 40A (squares), 30A (circle), and 20A (diamond) MeV [Stev86]. Theoretical curves are those of a thermal bremsstrahlung model.*

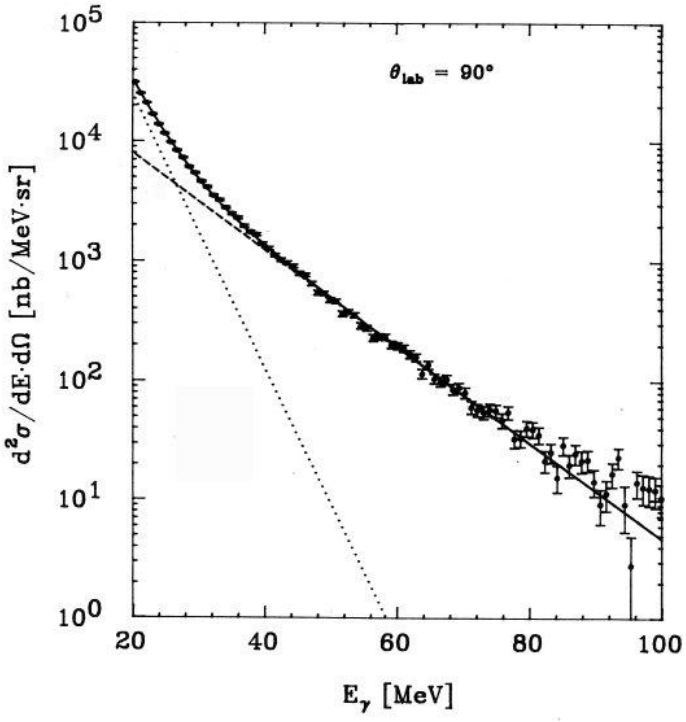

Figure 3.10: *Inclusive hard photon spectrum measured at θ = 90° for the system $^{14}N+^{108}Ag$ [Luke93]. The solid line is the result of a fit to two exponentials. The dashed and the dotted lines are the components of the fit.*

- A depletion of the two-photon correlation function $C_{12}(Q_{inv})$ with respect to the predictions of hard photon emission from a single source was also measured for the systems ^{86}Kr+^{58}Ni at 60*A* MeV and ^{181}Ta+^{197}Au at 39.5*A* MeV. The intensity interferometry technique (HBT analysis) of the photon-photon correlation function was found to be compatible with the existence of two different hard photon sources. Indeed, the measured shape of $C_{12}(Q_{inv})$ for the two systems (fig. 3.11) was best explained assuming the existence of two distinct sources for hard photon production separated in space and time [Marq95, Marq97].

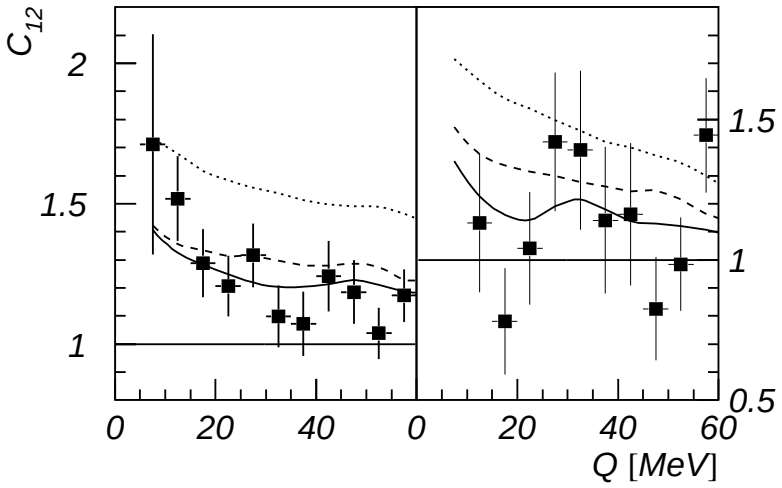

Figure 3.11: *Experimental γ-γ correlation function, $C_{12}(Q_{inv})$, for ^{86}Kr+^{58}Ni at 60A MeV (right side) and for ^{181}Ta+^{197}Au at 39.5A MeV (left side) compared to calculations based on Monte Carlo sampling for one source (dotted line), two sources (dashed line) and two sources of which one is fragmented (solid line). From [Schu97].*

3.4 Goals of the experiment. Motivation of the thesis

Photons, either radiated or scattered, have remained one of the most effective probes of every kind of terrestrial or celestial matter over the ages. Photons produced in nucleus-nucleus interactions carry information about the conditions of the matter from which they were emitted mapping out the entire history of the reaction. Interestingly, photons of increasing energies are radiated at correspondingly earlier times. In heavy-ion collisions at intermediate bombarding energies, hard-photons with E_γ = 30 - 200 MeV have been conventionally interpreted solely as issuing from the bremsstrahlung scattering of the protons against neutrons within the first 50 fm/c of the reaction. Such prompt hard-photons thus provide interesting information about *two-body* (nucleon-nucleon) dissipation effects in the compressed and non-equilibrated initial phase of the reaction [Mart95, Marq95, Polt95, Pol96, Schu96, Schu97]. GDR-photons, with lower energies, $E_\gamma \approx$ 10 - 20 MeV, signal the onset of mean-field driven collective excitations of the nuclear fragments present at the final deexcitation phase of the reaction (t $\gtrsim$ 200 fm/c) and constitute also efficient probes of the *one-body* (mean-field) dissipation mechanisms prevailing at that time. It is well established that, the temporal region in between those two emissions (50 fm/c $\lesssim$ t $\lesssim$ 200 fm/c) corresponds to the time where the fragmentation of the excited nuclear systems produced during the first stages of the reaction takes place.

During the last 5 years, it has been experimentally demonstrated that the production of hard-photons exclusively in terms of pre-equilibrium nucleon-nucleon collisions needed to be reconsidered and that the existence of a bremsstrahlung emission component of thermal origin could not be completely ignored [Mart95, Marq95, Schu96, Schu97]. Indeed, it has been observed that for large nuclear systems, nuclear bremsstrahlung continues to be emitted beyond first-chance collisions. This second-chance bremsstrahlung production shows up, with a steeper slope, more intensely in the region E_γ = 30 - 60 MeV of the hard-photon spectra (fig. 3.12), suggesting an emission from later reaction times when the initial kinetic energy has been mostly redistributed over the intrinsic degrees of freedom but has not still been completely damped into more collective (oscillatory) degrees of freedom. Such hard-photons hence may become valuable probes of the instants where nuclear multifragmentation occurs. Indeed, since this second-chance incoherent bremsstrahlung component reflects the nucleon-nucleon interactions which take place within the hot participant nuclear systems produced during the reaction, they may provide a measure of the average number of collisions each nucleon suffers during the cooling-down phase. This unique feature of this second radiation component would therefore allow a quantitative approach to the question of the time-scale and thermalization of the participant nucleons, a prerequisite to elucidate the possible connection of multifragmentation to a liquid-gas phase transition of nuclear matter.

To confirm the existence of this second emission of bremsstrahlung photons and to try to extract additional information on the time-scale and on the thermodynamical state of the hot nuclear systems present at stages of the reaction where fragment formation is supposed to take place, two campaigns of the TAPS collaboration were carried out in 1997 and 1998 at the KVI and GANIL facilities. These experiments coupled for the first time a photon spectrometer with different charged-particle multidetectors for γ-particle coinci-

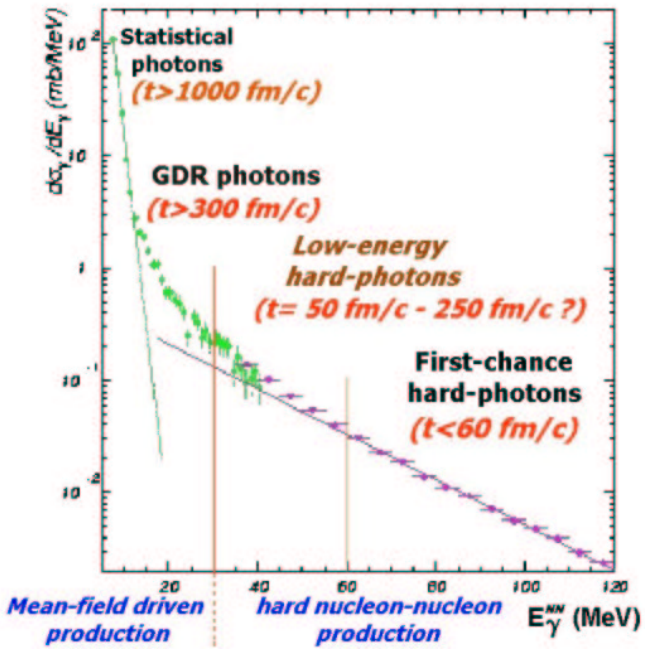

Figure 3.12: *Inclusive photon spectrum for the system $^{86}Kr+^{58}Ni$ at 60A MeV showing the direct and thermal bremsstrahlung regions as well as the low-energy statistical (GDR and discrete-state gamma decay) one. The approximative times of emission of these different types of photons are also indicated.*

dent detection over 4π. The heavy-ion reactions studied at KVI are ^{36}Ar+^{197}Au, ^{107}Ag, ^{58}Ni, ^{12}C at 60*A* MeV bombarding energy. The main goal of this thesis consists in the analysis and interpretation of the inclusive and exclusive data collected during this first KVI campaign. Such investigation of the collective properties of nuclear matter at temperatures and densities away from the saturation values using hard-photons as experimental probes, addresses the main following points:

- Is thermodynamical equilibrium attained ?
- If so, what is the temperature of the excited nuclear systems produced ?
- What is the density of the systems at freeze-out ?
- What is the time-scale of nuclear break-up ?
- Is multifragmentation a signal of the nuclear liquid-gas phase-transition due to the passage of the system through the low-density spinodal region ? or is it just a sequential slower process ?

Chapter 4

Experimental setup

Summary

4.1 Detector overview 58
4.2 AGOR accelerator 59
4.3 Argon beam 60
4.4 Carbon-Fiber reaction chamber 60
4.5 Targets 65
4.6 TAPS electromagnetic calorimeter 68
4.6.1 Main characteristics 68
4.6.2 BaF_2 crystals 69
4.6.3 Charged-Particle Vetoes 70
4.6.4 Photon identification 71
4.6.5 TAPS front-end electronics 72
4.7 Dwarf-Ball charged-particle multidetector 75
4.7.1 Main characteristics 75
4.7.2 BC400-CsI(Tl) phoswiches 77
4.7.3 Particle identification capabilities 79
4.7.4 Dwarf-Ball electronics and pre-trigger logics 79
4.8 Forward Wall charged-particle multidetector 84
4.8.1 Main characteristics 84
4.8.2 NE102A-NE115 phoswiches 85
4.8.3 Particle identification capabilities 85
4.8.4 Forward Wall electronics 87
4.9 Data-acquisition system and trigger logics 89
4.9.1 Data acquisition system 89
4.9.2 Trigger logics 93

The study of photons, produced in heavy-ion collisions at intermediate bombarding energies, over a wide spectral domain from low energy statistical gamma-rays ($E_\gamma \approx 10$ MeV) up to very energetic hard-photons ($E_\gamma^{max} \approx 200$ MeV), in coincidence with charged particles and nuclear fragments, requires the concurrent use of a photon spectrometer with a wide dynamic range in energy, together with a LCP and IMF detector system covering a large fraction of the available phase-space. Lead by such a consideration, we combined the Two Arm Photon Spectrometer (TAPS) with two charged-particle multidetectors. The first one, the Dwarf-Ball (DB) from Washington University at St Louis (USA), was dedicated to the detection of light-charged-particles (LCPs) and intermediate-mass-fragments (IMFs) emitted in the azimuthal hemisphere around the target. The second one, the Forward Wall (FW) from the KVI laboratory at Groningen (Netherlands), measured the LCPs and IMFs emitted in the forward direction. In this way we assembled a complete multidetector system consisting of as much as 540 individual detector-modules resulting in more than 2000 readout electronic channels. The response of those three detection systems to impinging nuclear particles depends on the scintillation properties of the different materials composing the detectors modules. These properties and materials are described in detail in Appendix 1.

The objective of the present experiment was the inclusive and exclusive study of four different nuclear reactions involving target nuclei of various masses and a unique ^{36}Ar beam at 60*A* MeV: ^{197}Au(^{36}Ar,γ)X, Ag(^{36}Ar,γ)X, Ni(^{36}Ar,γ)X, and C(^{36}Ar,γ)X. Only the first reaction, ^{36}Ar+^{197}Au, was measured exploiting the whole experimental setup (TAPS+DB+FW) with a limited beam intensity. A reduced setup (TAPS+FW) enabling higher counting-rates was used to measure the four reactions. The experiment was referenced by the KVI Programme Advisory Committee as *"PAC #R2: Thermal hard-photons"* and used 37 shifts (14 days) of beam-time during October and November 1997.

In the first part of this chapter the accelerator and the characteristics of the different reactions are outlined. In a second part, I will describe each subdetector system, their associated electronics and their particle identification properties. Finally, an overview of the data acquisition system and the trigger logics will be given in the third part of this chapter.

4.1 Detector overview

The overall detector layout of this experiment is shown in fig. 4.1, as designed within the GEANT-based simulation package KANE (see Section 5.1), and in the picture of fig. 4.2. The photon-detector system was the TAPS electromagnetic-spectrometer. It comprised 384 BaF_2 scintillation modules assembled in a six-block configuration (see fig. 4.1) and positioned around the target to cover a solid angle of about 15% of 4π. The detector was optimized for photon detection in the range 5 MeV $< E_\gamma <$ 300 MeV. Two phoswich multidetectors measured and offered the possibility of identifying isotopically the produced LCPs (p, d, t, ^{3}He, α) and IMFs ($3 \leq Z \lesssim 10$). The "Dwarf-Ball" [Stra90], comprising 64 BC400-CsI(Tl) phoswich telescopes positioned between polar angles $32^\circ < \theta < 168^\circ$ and the full azimuthal angle, covered a continuous solid angle close to 76% of 4π. The

"Forward Wall" hodoscope [Leeg92] consisted of 92 NE102A-NE115 $\Delta E - E$ phoswich detectors positioned in the forward direction to cover the angular range $2.5° < \theta < 21.5°$ and $2.5° < \phi < 21.5°$ with a geometrical acceptance close to 4% of 4π.

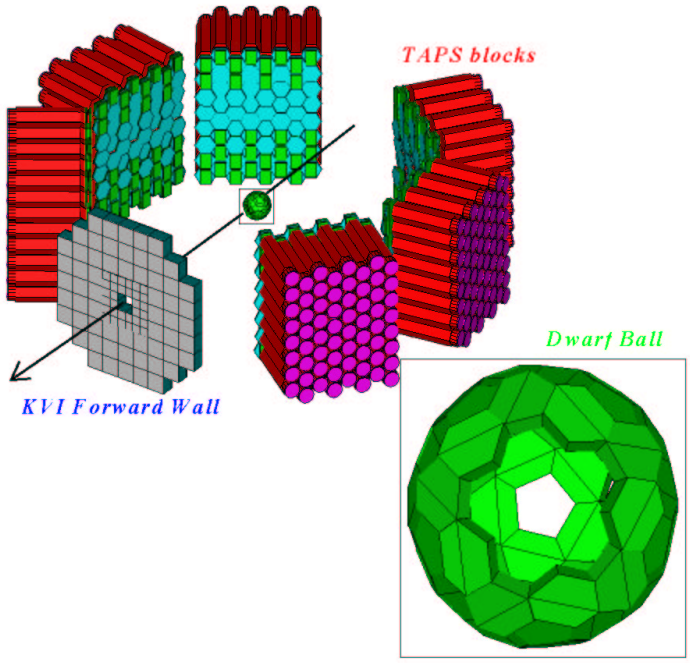

Figure 4.1: *Layout of TAPS, Dwarf-Ball and Forward Wall multidetectors as pictured by* GEANT. *The Ar beam enters the setup diagonally from the upper right part of the figure. The Carbon-fiber scattering chamber, in which the Dwarf-Ball is located and which matches the front part of the Forward Wall, is not shown.*

The overall detector system covered finally more than 80% of 4π for particle detection and 15% for photon.

4.2 AGOR accelerator

The experiment was carried out at the "Kernfysisch Vernsneller Instituut" (KVI) laboratory located at Groningen in The Netherlands. The beam was delivered by the French-Dutch AGOR[1] superconductor cyclotron. The detection system was set up inside cave A, at the end of the so-called *"p-line"* (fig. 4.3). Target and DB were installed inside a large Carbon-fiber scattering chamber [Hoef99]. The six TAPS blocks surrounded the chamber and the FW was positioned in place of the customary installed KVI's SALAD detector.

The AGOR cyclotron (fig. 4.4) has been constructed at Orsay, in a collaborative effort of the "Institut de Physique Nucléaire" IPN-Orsay and KVI laboratories. It was designed [Schreu98] as a compact, tripolar superconducting cyclotron (fig. 4.5) with bending limit K = 600 MeV, for the acceleration of proton, light and heavy ions. Protons and deuterons can be accelerated up to 200 MeV, light ions with charge-to-mass ratio Q/A = 0.5 up

[1] Accélérateur Groningen-Orsay

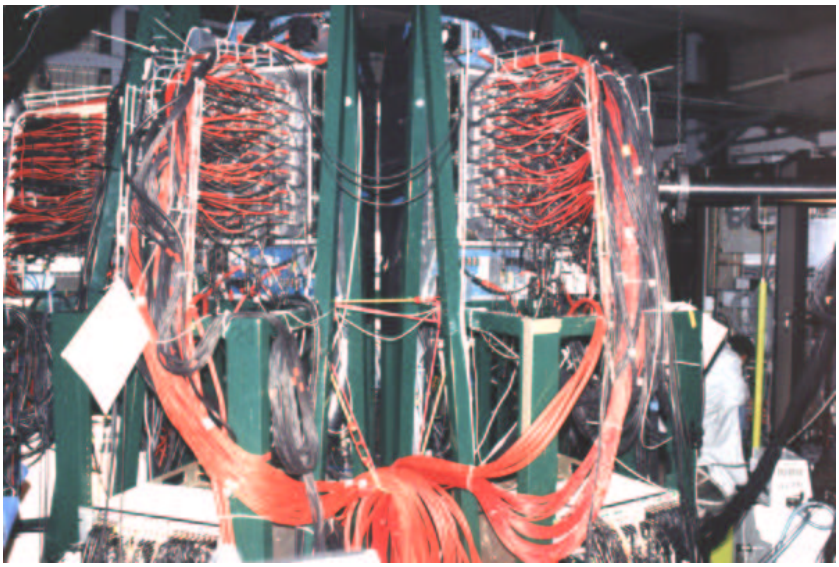

Figure 4.2: *Photography of the experimental setup. The beam pipe enters the setup from the right, and the backsides of 3 out of the 6 TAPS blocks are seen.*

to 100*A* MeV, and heavy-ions with lower Q/A, up to a maximum energy of 600 Q^2/A^2 (*A* MeV) (fig. 4.6). The first beam at KVI, a 200 MeV alpha beam, was successfully extracted on January 1996. The main parameters of the cyclotron are summarized in table 4.1.

4.3 Argon beam

The beam delivered for this experiment was a 60*A* MeV $^{36}Ar^{14+}$ beam extracted for the first time in October 97 right before the scheduled start of the experiment. This was the first AGOR beam with a total energy of more than 2 GeV. During the 14 days of running time the mean transmission of the beam through the cyclotron (from 250 to 910 mm radii) was 80%, with a 95% mean extraction efficiency and a 10% injection efficiency. Argon noble gas is, actually, one of the easiest elements to be accelerated in cyclotrons and our experiment was the first to use a heavy-ion ($Z > 2$) beam at KVI. The characteristics of the beam are summarized in table 4.2.

The different beam intensities used during the experiment, from a minimum 1.5 nA to a maximum 12.5 nA, were monitored instantaneously by measuring the current in a Faraday cup located at the end of the *p-line*, 5 meters away from the reaction chamber.

4.4 Carbon-Fiber reaction chamber

The Argon beam extracted from the cyclotron was conducted through the beam-pipe and focused on a spot located in cave A. The scattering chamber [Hoef99] made out of carbon-fiber, contained the target holder and the Dwarf-Ball multidetector system, both fixed to the chamber's top lid. Downstream the chamber a trumpet-shaped extension matched the

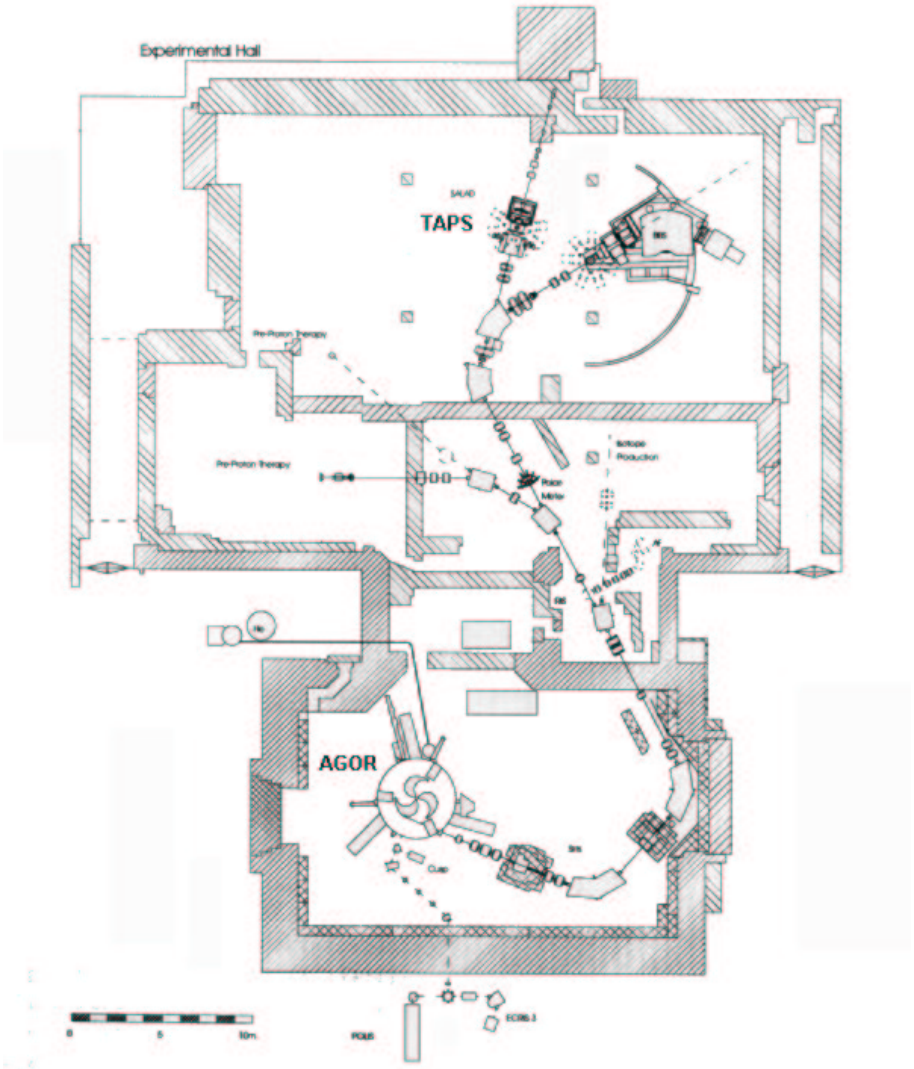

Figure 4.3: *Floor plan of the KVI facility at Groningen, The Netherlands.*

Figure 4.4: *Picture of AGOR cyclotron.*

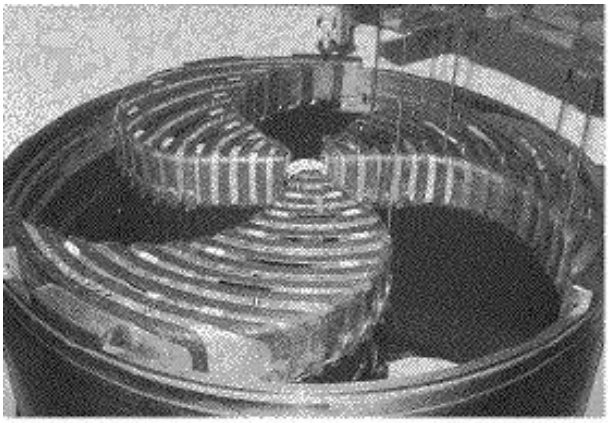

Figure 4.5: *Photography of AGOR spiral "Dees".*

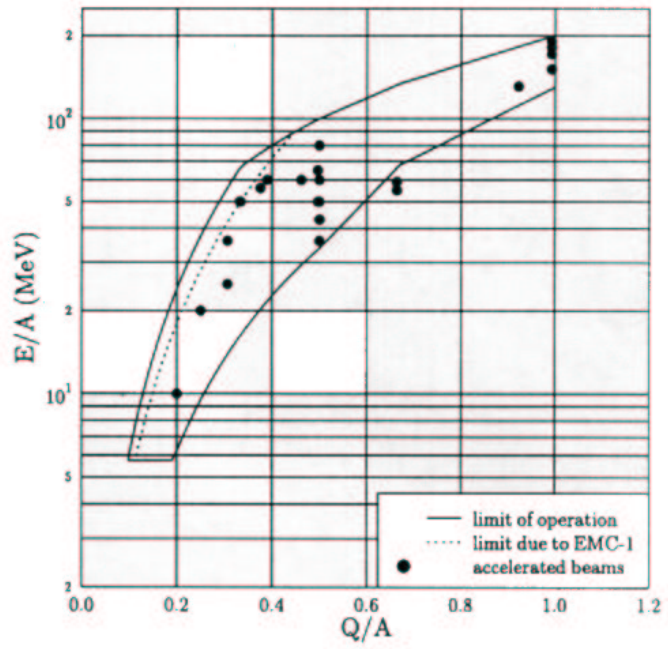

Figure 4.6: *Operating diagram (energy versus charge-to-mass ratio) for AGOR, indicated by the (red) solid lines. The (yellow) circles represent the beams which have been accelerated so far. Adapted from [KVI95b].*

Table 4.1: *AGOR cyclotron specifications.*

bending limit K_f	600 MeV
focusing limit K_b	200 MeV
pole diameter	1.88 m
number of sectors	3
spiral coefficient	R $<$ 0.30 m: no spiral R = 0.70 m: 18 mrad/cm R = 0.88 m: 43 mrad/cm
minimum hill gap	7 cm
maximum valley gap	168 cm
maximum current density	Coil 1: 4271 A/cm^2 Coil 2: 3270 A/cm^2
range of central magnetic field	1.70 - 4.01 T
number of trim coils	15
maximum current in trim coils	500 A
RF frequency range	24 - 62 MHz

Table 4.2: *Characteristics of the Argon beam used in the experiment.*

A_p	36
Z_p	18
Ion's charge state	+14
Energy (A MeV)	60
v_p(cm/ns)	10.3 (β = 0.36)
Cyclotron frequency RF	37.1 MHz (26.9 ns)
Intensity (nA)	$1.5 - 12.5$
Nuclei/s (Hz)	$0.7 \cdot 10^9$ - $5.6 \cdot 10^9$
Nuclei/bunch (12 part./nA)	$18 - 150$
Bunch width (mm)	$\approx$ 1 (FWHM)

opening angle of the Forward Wall front surface. Particles thus traveled in vacuum from the target to both particle detectors. The carbon chamber had a diameter of 70 cm and a height of 50 cm (fig. 4.7). It thus covered the azimuthal angles viewed by the TAPS blocks positioned at a distance of 30 cm from the chamber wall. The walls were 3.75 mm thick. Using a low Z material such as carbon reduced the electron-positron conversion probability of incident photons, which scales as Z^2, inside the walls of the scattering chamber[2]. During the experiment a vacuum of 10^{-4} mbar was reached within 3 - 4 hours, and the best measured vacuum was of the order of 10^{-5} mbar.

Figure 4.7: *Photographs of the Carbon-fiber scattering chamber used for TAPS experiments at KVI [Hoef99].*

[2]The pair production probability of a 10 (100) MeV photon traversing 4 mm of carbon is only of 0.4% (1.1%).

4.5 Targets

One of the main goals of the experiment was to compare the dependence of the hard-photon spectrum and yield on the size and excitation energy of the nuclear system(s) formed during the collision. For that purpose, four different isotopes: ^{197}Au, ^{107}Ag, ^{58}Ni and ^{12}C; spanning a wide range of nuclear masses, from 179 down to 12, and leading to maximum energies in the nucleus-nucleus CM in the range 7A MeV - 13A MeV (see Table 4.4), were used as targets. The selection of asymmetric projectile-target combinations allowed to distinguish between the velocities of the nucleus-nucleus and nucleon-nucleon center-of-mass in order to localize the photon source through Doppler-shift analysis (see section 6.2). The most intensively studied system was the heaviest ^{36}Ar+^{197}Au reaction, where the direct kinematics spreads the emission of the reaction products over the wide angular range covered by the Dwarf-Ball and the Forward Wall charged-particle multidetectors.

Since the hard-photon production rate is directly proportional to the number of nuclear interactions per pulse, $P_{int} = N_{reac}/RF$, it straightforwardly depends on the number of incident Ar projectiles, N_{inc}, and on the density of nuclei in the target, N_{at/cm^2}. We, thus, adjusted the beam intensity and the different target thickness so that the total accumulated hard-photon multiplicity remained statistically significant for all targets. These two parameters are related making use of the following expressions:

$$\sigma_R = \frac{N_{reac}}{N_{inc} \cdot N_{at/cm^2}} = \frac{P_{int}}{RF \cdot N_{inc} \cdot (N_{av}/A_t \cdot d_t)} \tag{4.1}$$

$$I_{beam} = Q/t = N_{inc} \cdot Q_p^+ \cdot Q_e \cdot RF \tag{4.2}$$

where σ_R is the total reaction cross-section for each projectile-target combination, N_{av} the Avogadro constant, A_t the target atomic number, d_t the target thickness (in mg/cm^2), RF the cyclotron radiofrequency (in s^{-1}) , Q_p^+ = 14 the Argon ion charge state, and Q_e the electron charge magnitude. From eqs. (4.1) and (4.2) we obtain:

$$P_{int} = \frac{I_{beam}}{Q_p^+ \cdot Q_e} \cdot \sigma_R \cdot (N_{av}/A_t) \cdot d_t \tag{4.3}$$

Hence, for a given nuclear reaction the combination (I_{beam}, d_t) determines uniquely the nuclear interaction rate P_{int}. Two experimental requirements constraint, however, this quantity and, thus, both the maximum possible beam intensity and target thickness. On the one side, the intensity must be limited to minimize the pileup probability (which is proportional to P_{int}^2) in the individual charged particle detectors. On the other side, target thicknesses must be kept of the order of a few mg/cm^2, i.e. to a few $\approx$ 0.01% nuclear interaction lengths, to prevent significant contamination of the experimental data by secondary reactions[3].
While the whole setup TAPS+DB+FW was in operation, the intensity was constrained

[3]Thinner targets have also a lower absorption of low-energy particles, and help to keep the e^+e^- conversion probability of produced photons inside the target at absolutely marginal values.

Table 4.3: *Characteristics of the different targets and total estimated counting rates for the different reactions for the selected target thickness - beam intensity combinations.*

Target	^{197}Au	^{197}Au	^{108}Ag	^{58}Ni	^{12}C
A_t	197	197	108	58	12
Z_t	79	79	47	28	6
Thickness (mg/cm^2)	1.0	7.5	7.0	6.6	18.0
Density (g/cm^3)	19.32	19.32	10.50	8.90	2.25
Aerial surface (10^{19} at./cm^2)	0.3	2.3	5.9	7.1	90.4
(Nuclear) int. length (g/cm^2)	190.0	190.0	163.0	130.0	86.3
Ar+X reaction cross-section (mb)	4600	4600	3850	3240	2240
Ar beam intensity (nAe)	3.0	12.5	8.0	8.0	1.5
Part./pulse [12 part./nA]	36	150	96	96	18
P_{int} (reac./pulse)	0.0005	0.0156	0.0142	0.0206	0.0355
Nuclear reaction rates (Hz)	$18.5{\cdot}10^3$	$580{\cdot}10^3$	$525{\cdot}10^3$	$760{\cdot}10^3$	$1.32{\cdot}10^6$

by the maximum allowed individual counting rate of 10^4 Hz imposed in the most forward Dwarf-Ball modules. This maximum number of detected particles per second corresponds to an interaction probability per beam pulse of $5{\cdot}10^{-4}$ which was achieved with an Ar-beam intensity of 3 nA and 1 mg/cm^2 thick Au target. In the absence of the DB multidetector, the intensity and/or the target thickness were increased to achieve a mean number of interactions per pulse almost two orders of magnitude larger ($P_{int} \approx 1.5\%$ - 3.5%). In that case, the limiting factor was not anymore the maximum counting rate allowed to avoid random coincidences in a single detector, but the maximum taping rate (2000 evts/s) of the data acquisition system (see section 4.9.1). In table 4.3 are listed several characteristics of the used targets and the calculated reaction rates.

The targets were mounted on a movable ladder attached to the chamber's top lid, and connected to a stepping motor remotely controlled. The target holder was equipped with 4 placements of surface 2×2 cm^2 and an empty frame. The empty frame was used to verify the alignment of the beam, to count the residual noise and to compare the values of the charges collected in the Faraday cup with and without target[4].

In table 4.4 the significant reaction properties for the four heavy-ion systems, computed with the formulas summarized in Appendix 4, are detailed[5].

[4] From this comparison, we deduced that the final Argon beam arriving at the Faraday cup after traversing the targets consisted of fully stripped Ar^{18+} ions and not the original Ar^{14+} beam.

[5] The beam kinetic energy K_{lab} = 60A MeV has been corrected to take into account the average energy loss of the Argon projectiles inside the different target thickness before undergoing a nuclear reaction with the target nuclei: $K_{lab}^{corr} = K_{lab} - \langle K_{loss} \rangle$. The values of these mean energy losses have been calculated with the relation given by [Hub90] and vary from $\langle K_{loss} \rangle$ = 0.78A MeV for the thickest C target to $\langle K_{loss} \rangle$ = 0.17A MeV for the Au target.

Table 4.4: *Properties of the reactions Ar+X (X = ^{197}Au, ^{107}Ag, ^{58}Ni, ^{12}C) at K_{lab}= 60A MeV, computed with the formulas listed in Appendix 4.*

Reaction	^{36}Ar+^{197}Au	^{36}Ar+^{108}Ag	^{36}Ar+^{58}Ni	^{36}Ar+^{12}C
σ_R (mb)	4600	3850	3240	2240
K_{lab}^{corr} (*A*MeV)	59.8	59.8	59.8	59.2
V_C (*A*MeV)	4.5	3.0	2.0	0.5
K_{Cc}^{lab} (*A*MeV)	55.3	56.8	57.8	58.7
K_{Cc}^{lab} (GeV)	1.99	2.05	2.08	2.11
K_{Cc}^{AA} (*A*MeV)	7.1	10.6	13.4	11.0
K_{Cc}^{AA} (GeV)	1.66	1.53	1.27	0.53
β_{beam}	0.35	0.355	0.36	0.36
β_{AA}	0.054	0.087	0.132	0.26
β_{NN}	0.175	0.178	0.18	0.18
A_{tot}	233	144	94	48
μ	30.4	27.0	22.2	9.0
R_{int} (fm)	12.6	11.4	10.3	8.5
θ_{gr}^{lab}	4.6	3.2	2.2	1.1
θ_{gr}^{cm}	5.3	4.0	3.0	1.9

4.6 TAPS electromagnetic calorimeter

4.6.1 Main characteristics

The Two-Arm-Photon-Spectrometer TAPS is a high granularity and large solid-angle electromagnetic calorimeter composed nowadays of more than 400 inorganic scintillating crystals. It was designed to detect photons and neutral mesons, -the latter being identified by the invariant-mass reconstructed from their 2 or 3 photon decay modes-, in a wide energy domain ranging from 1 MeV to 10 GeV. TAPS was built by a collaboration of five European laboratories and has been exploited at various facilities (SIS-GSI at Darmstadt, GANIL at Caen, MAMI at Mainz, SPS at CERN, and AGOR at KVI) to perform a broad research programme in heavy-ion and photonuclear physics (for a review of TAPS physics see e.g. [Stro96] and [TAPS97]), aiming at the study of various regions of the phase diagram for nuclear matter (fig. 1.4). The elementary module of TAPS is an hexagonal BaF_2-crystal equipped with a NE102A plastic scintillator veto positioned at its front side (fig. 4.8).

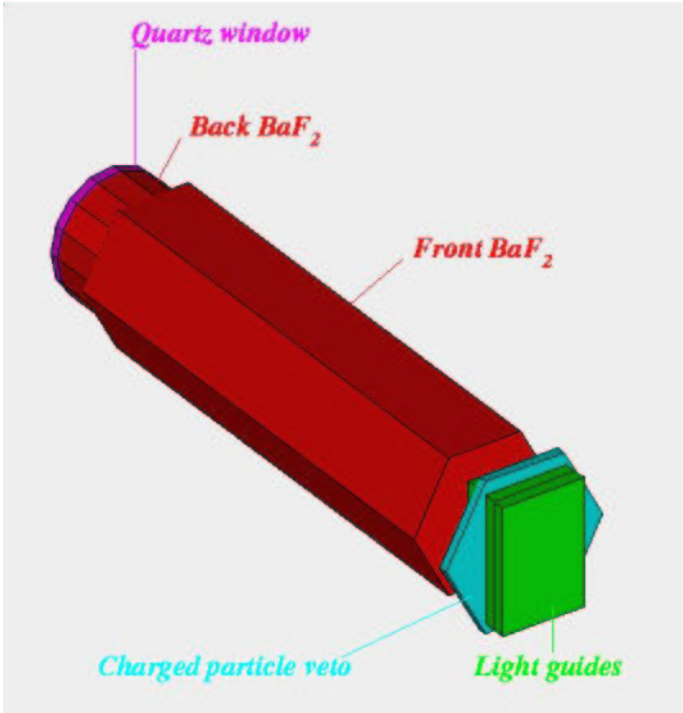

Figure 4.8: *Drawing of the basic detection element in TAPS: A hexagonal BaF_2 module with its associated CPV-detector.*

TAPS possesses the following outstanding properties:

1. A **good energy resolution** over a wide dynamic range is the main characteristics sought for any electromagnetic calorimeter. This is achieved for TAPS through the selection of BaF_2 crystal scintillators with appropriate dimensions. The longitudinal dimensions of the TAPS modules ensure an optimum absorption of the

electromagnetic shower generated by photons with energies in the interval from roughly 1 MeV up to ≈10 GeV. The achieved energy resolutions are of the order of $\Delta E/E = 2.17/[E(\mathrm{GeV})]^{1/4}$ %.

2. **Accurate impact position measurement** and, hence, precise determination of the direction of the photons, is required to determine, on the one hand, the invariant-masses of neutral mesons with high precision and, on the other hand, to allow a proper separation of overlapping electromagnetic showers. This is achieved through a high granularity of the spectrometer and with modules of transverse size of the order of one Molière radius (see Appendix 1). This fine segmentation ensures also a low probability for multiple hits in single modules.

3. An **excellent time resolution** is necessary to be able to separate photons from hadrons, and in particular neutrons, through time-of-flight (TOF) measurements. The fastest scintillation response, among all inorganic crystals, is obtained with the first scintillation component of BaF_2, yielding excellent time resolutions (< 200 ps).

4. Heavy-ion reactions lead to high hadron-multiplicities in the final state. Thus, a **proper charged-** versus **neutral- particle discrimination** is mandatory. Since BaF_2 crystals also respond to charged hadrons, an additional charged-particle veto (CPV) in front of every BaF_2 module permits such a discrimination on-line and adequately define a photon trigger. Moreover, CPV information turns out to be the only way to discriminate relativistic electrons from photons in off-line analysis.

5. **Modularity** is required to allow a flexible reconfiguration of the spectrometer as requested by the specific needs of different experiments or the constraints encountered at various facilities. TAPS individual modules have been arranged in several experimental configurations: from block setup dispositions as used in the present experiment or in earlier experiments at GSI [Novo91] and MAMI [Gabl94]; to a super-cluster setup as used at KVI (e.g. [Huis99]) and at CERN (e.g. [Agak98]).

4.6.2 BaF_2 crystals

The 384 BaF_2 crystals used in the present experiment constitute the central asset of the photon spectrometer. Their scintillation properties are thoroughly described in Appendix 1. They are 25 cm long which corresponds to 12 radiation lengths ($X_0[BaF_2]$ = 2.05 cm). This length ensures a significant absorption of the electromagnetic shower produced by the incident photons (96% for 100 MeV photons and 85% for 1 GeV photons) [Gabl94, Marq95b]. Each BaF_2 hexagonal module has an inscribed radius of 2.95 cm, corresponding to 85% of the Molière radius ($\rho_M[BaF_2]$ = 3.4 cm). The hexagonal shape maximizes the number of neighbours to each detector for an easy reconstruction of the shower. The rear end of the crystal is cylindrically shaped over a length of 2.5 cm to permit an optimal coupling to a Hamamatsu R2059-01 photomultiplier tube (PMT). These phototubes, covered with a μ-metal shield, are sensitive to the UV scintillation light emitted by the BaF_2 crystal.

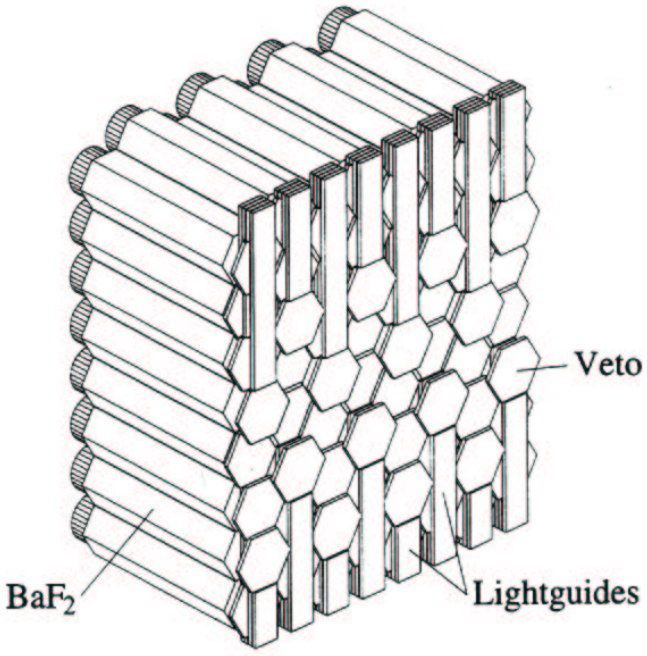

Figure 4.9: GEANT *representation of one TAPS block comprising 8×8 BaF_2 crystals with their respective NE102A veto detector.*

In the present experiment, we used the TAPS spectrometer in a configuration consisting of 6 blocks (such as the one shown in fig. 4.9), of 8×8 modules each, mounted in six towers placed symmetrically in the horizontal plane around the target (see fig 4.1). The polar angles with respect to the beamline direction and the distances from the target of each block are listed in table 4.5. Within this configuration about 15% of the solid angle is covered in a continuous range of polar angles spanned between 57° and 176° and between $-20°$ and $+20°$ in the azimuthal region. The high-voltage for each group of 64 modules was delivered by a single Lecroy 1440 HV system positioned next to each block. The high-voltage settings of the PMTs (in the range -1200 to -2000 V) were chosen to select for each individual TAPS module a dynamic range between 1 MeV and approximately 400 MeV (equivalent photon energy). This range is adapted to the energies of the photons produced at the 60*A* MeV bombarding energy in the considered reactions.

4.6.3 Charged-Particle Vetoes

The Charged-Particle Veto (CPV) system consists of 384 hexagonal, 5-mm thick NE102A polyvinyltoluene-based scintillator plastics (see Appendix 1). The diameter of the inscribed circle is of 6.5 cm. These scintillators are individually placed in front of each BaF_2 crystal in an one-to-one correspondence to associate each BaF_2 signal with a coincident veto signal. Their scintillation light is collected through perspex lightguides coupled to Philips XP2972 PMTs, the latter located at the top and bottom of each TAPS block. The thickness of the CPV, corresponding to 0.012 X_0 (X_0[NE102A] = 43 cm), were selected as a trade-off between low photon conversion ($< 2.5\%$) and sufficient en-

Table 4.5: *Positions of the 6 TAPS blocks for the KVI experiment. The distances and angles correspond to the center of the frontal side of each block.*

TAPS Block	Target-block distance [cm]	θ [^{o}]	ϕ[^{o}]
1	66	-76.5	0
2	66	-116.5	0
3	66	-156.5	0
4	66	156.5	0
5	66	116.5	0
6	66	76.5	0

ergy loss for charged particles (i.e. almost 100% efficiency) [Rasc92]. Fig 4.10 shows the typical dimensions of a CPV module. In fig. 4.9 the arrangement of up to 3 levels of CPV+lightguides for one TAPS block can be seen in front of the BaF_2 modules. The main goal of the CPV was to enrich collected data with neutral particles. The fast scintillating signal of the NE102A organic plastic is, for that purpose, incorporated in the trigger definition allowing for an on-line rejection of charged particles.

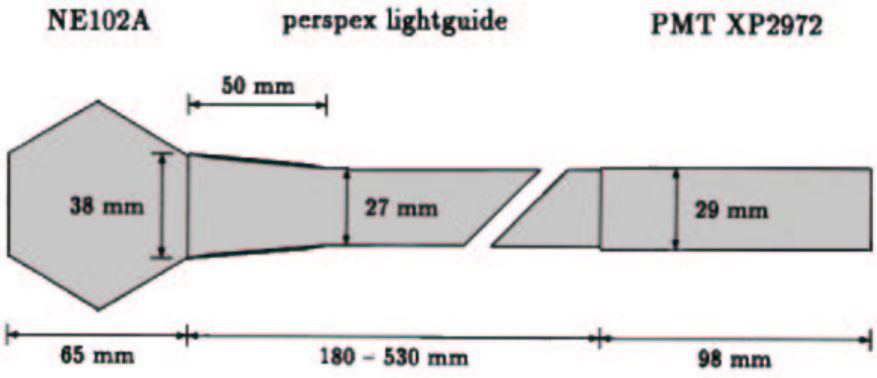

Figure 4.10: *Typical dimensions of a single NE102A CPV module. The lightguide lengths vary from 18 to 35 cm depending on the position of the CPV module in the block. From [Rasch97].*

4.6.4 Photon identification

The scintillation light of BaF_2 crystals consists of a fast (τ = 0.88 ns) and a slow (τ = 0.63 μs) component with very different underlying luminiscence mechanisms (see Appendix 1). The fast component is quenched with increasing energy loss dE/dx of traversing charged particles. Since charged hadrons have a higher ionization density than (lighter) electromagnetic particles, they induce a lower contribution of the fast scintillating signal to the total light output (fig. 4.11). The higher (lower) branch of this $E_n - E_w$ plot[6]

[6]In general, all throughout this thesis I will use the term(s) "narrow" ("wide") gate to refer to the integration of a "fast" ("slow") scintillation-light component, i.e. a component having a "short" ("long")

corresponds to the photon (hadron) signal. The pulse-shape factor defined as the ratio $PSA = E_n/E_w$ allows, thus, for a discrimination between hadronic and electromagnetic particles (PSA = 1 for photons, electrons and muons, PSA = 0.7 for protons and $PSA <$ 0.7 for heavier particles). Neutrons below 100 MeV, however, interact within the detector material predominantly via (n,γ)-reactions [Matu89] producing a high-energy photon signal. They can therefore only be distinguished from photons by time-of-flight measurement. Incident relativistic electrons (and positrons) are discriminated against γ's via CPV information.

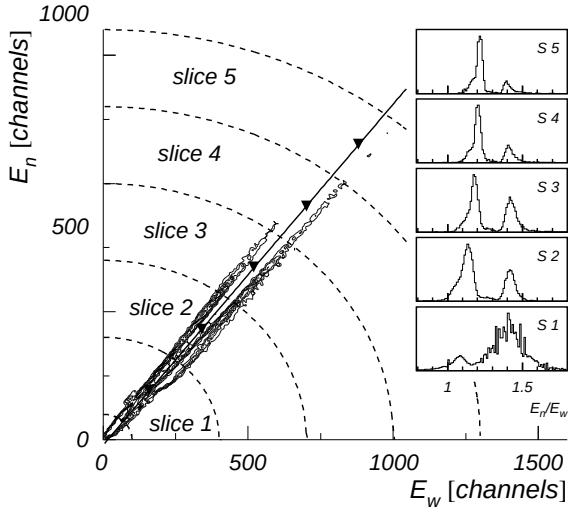

Figure 4.11: *E_n vs. E_w for a single BaF_2 crystal [Schu97]. The upper branch corresponds to the detection of photons and electrons (or high-energy neutrons) and the lower one to (low-energy) neutrons and LCP. The intrinsic properties of the two different scintillation components of the BaF_2 material allow to differentiate between electromagnetic-like (mainly photons) and hadronic-like (mainly protons) hits in the so-called "Pulse-Shape Analysis" (PSA) technique.*

The detailed procedure employed for photon identification with TAPS is developed in Section 5.4.

4.6.5 TAPS front-end electronics

In fig. 4.12 a sketch of the electronics per BaF_2-CPV detector module is shown. Most of the TAPS electronics is installed in standard CAMAC[7] crates located in the experimental hall or in the counting room. The different modules used are described in table

decay.

[7]CAMAC (Computer Automated Measurement and Control) is an IEEE standard modular system widely used in nuclear and particle physics for data acquisition and control. It contains 3 essential components [Leo92]: the "crate", with 23 "slots" where plug-in electronics modules of standard size are inserted, and the "dataway" or back-plane data bus for modules control and/or readout by the crate controller processor.

4.6. The recorded data per module have to be suitable for (ulterior) photon identification and cluster reconstruction. This is achieved in the off-line analysis, as mentioned in the former section, by Pulse-Shape-Analysis (*PSA*), as well as Time-Of-Flight (*TOF*) measurement and Charged-Particle-Vetoing (CPV). Those three techniques determine the basic elements of the TAPS electronics system.

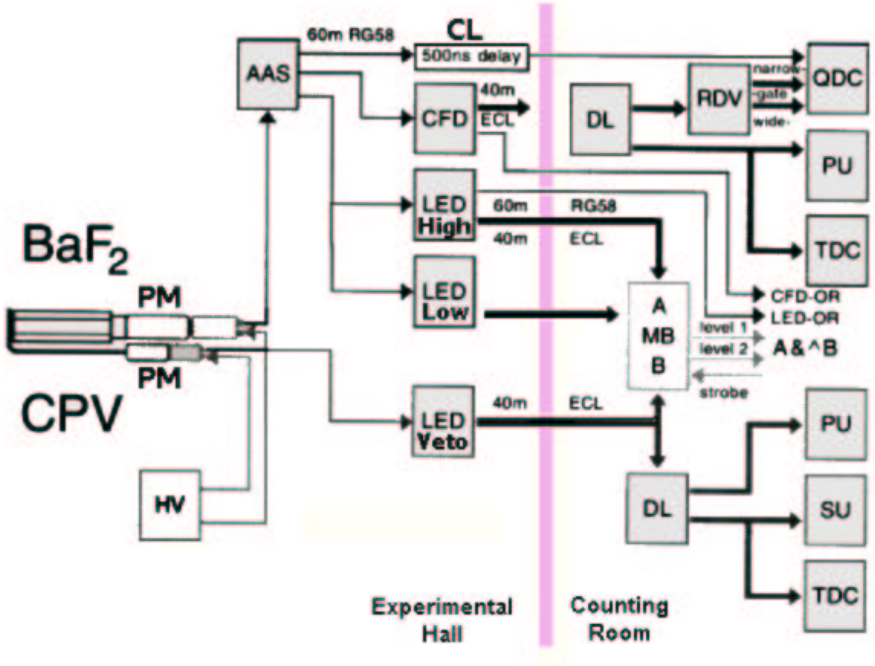

Figure 4.12: *Simplified TAPS electronics diagram per BaF_2-CPV module. The description of the different electronics modules is given in table 4.6.*

The analog signal delivered by each BaF_2 is first split by an Active Analog Splitter (AAS) placed at the bottom of each 8×8 block. The outputs of the AAS are employed for:

The energy signal: The original analog signal is delayed 500 ns by 50-Ω cable delay and is then fed into the Charge-to-Digital Converters (QDC) located in CAMAC crates in the counting room 50 m away from the experimental hall. If the event is accepted, the 12-bit QDC integrates the signal over two time intervals: 50 ns (narrow gate) and 2 μs (wide gate) to provide the charge corresponding to the two (fast and slow respectively) components of the BaF_2 scintillation light.

The timing branch: A Constant Fraction Discriminator (CFD) located, again, at the bottom part of the blocks to minimize the cable lengths and the deterioration of the timing performance, produces a fast logic pulse if the voltage of the PMT dynode signal surpasses a programmable threshold. In our case, the equivalent photon energy threshold was set to 5 MeV, well above the noise level of the photomultipliers. This logic signal provides, after a 500 ns logic delay, three outputs for:

- The stop signal of the Time-to-Digital Converters (TDC) which have been started by a *"common start"* obtained from a coincidence between the acquisition master trigger and the RF signal.
- The validation signal for the generation, via the RDV *"gate and delay generators"* modules, of the short and wide gates for the integration of the BaF_2 signal energy.
- The bit pattern (PU[8]) information, i.e. a register recording the firing detectors.

The trigger information: Two Leading Edge Discriminators (LED) with different thresholds (LED-low = 15 MeV and LED-high = 40 MeV equivalent photon energies respectively) issue a standard logical signal to be used as the corresponding LED-low and LED-high triggers for the selection of high-energy photons, if the PMT signal overpasses the programmable energy thresholds.

Finally, the CPV photomultiplier delivers a fast analog signal which is processed by a leading-edge discriminator (LED VETO set above noise, 500 keV) and sent to the Multiplicity box (MB) where they are combined with the corresponding BaF_2 detector module signals. Photon identification is mainly based on this veto signal processing. Such a setup allows to separate neutral from charged BaF_2 signals on a fast trigger level (see Section 4.9.2).

Table 4.6: *List of TAPS electronics modules used per BaF_2-CPV detector.*

Acronym	Type of module	Model ($\times$ number of channels)
AAS	Active Analog Splitter	Gießen ($\times$ 16)
CFD	Constant Fraction Discriminator	GANELEC FCC8 ($\times$ 8)
LED	Leading Edge Discriminator	GSI LE1600 ($\times$ 16)
QDC	Charge-to-Digital Converter	GANELEC 1612 F ($\times$ 8)
TDC	Time-to-Digital Converter	GANELEC 812 F ($\times$ 8)
MB	Multiplicity Box	ISN 4831 ($\times$ 64)
PU	Pattern Unit	LeCroy 4448 ($\times$ 48)
DC	Cable Delay (500 ns)	Gießen ($\times$ 64)
RDV	Gate and Delay Generator	GANELEC 8/16 A ($\times$ 8)
DL	Logic Delay	GSI DL1610 ($\times$ 16)
SU	Scalers Unit	GSI SC4800

More details on the typical electronics chain of a TAPS setup can be found elsewhere [Martt94, Marqt94]

[8] Pattern Unit.

4.7 Dwarf-Ball charged-particle multidetector

4.7.1 Main characteristics

The "Dwarf-Ball" (DB) [Stra90] is a quasi-4π charged-particle multidetector consisting of an array of up to 71 closely packed BC400-CsI(Tl) phoswiches. They form a hollow sphere with an inner radius of 41.5 mm and cover a maximum angular range between 24° and 168°. It was built at the Washington University of Saint Louis (USA) and designed to detect light charged particles (LCP, Z≤2) and intermediate-mass fragments (IMF, $3 \leq Z \lesssim 20$) emitted in multi-fragmenting exit channels of heavy-ion reactions. More specifically, the Dwarf-Ball meets the following criteria:

1. **Large solid angle** (≈ 4π sr) coverage to study multi-fragment disintegrations of excited nuclear systems. In the configuration used in this experiment the device covers the angular range $\theta_{lab} = 32^\circ - 168^\circ$ and the full φ, corresponding to 76% of the solid angle (see fig. 4.13).

2. **High granularity** to handle large multiplicity events. The 64 hexagonal and pentagonal phoswich detectors used in the present experiment are clustered at a mean distance of 4.15 cm from the target in a polar coordinate geometry.

3. **Isotopic identification** for LCP (H and He isotopes). The two scintillating light components of CsI(Tl), which vary with particle type, are exploited to achieve p, d, t, ^{3}He, and α separation (see Section 5.5.1).

4. **Charged-particle identification** for the produced nuclear fragments. The combination of CsI(Tl) with the thin scintillator plastic in the phoswich arrangement, permits, in our specific case, the identification of the IMFs up to Z ≈ 10 by means of pulse-shape techniques (see Section 5.5.2).

5. **Low energy thresholds** (≈ $1A - 2A$ MeV) and good energy resolution (however, this last capability was not exploited in the present experiment for which only LCP and IMF identification and separation, was sufficient).

6. **Modular design**; compact and portable. This portability allowed to easily pack and transport the DB between its home laboratory in the USA to the KVI and to the GANIL laboratories for the two consecutive TAPS experimental campaigns of 1997 and 1998.

7. The **small thickness** of the individual Dwarf-Ball modules[9] constituted an additional advantage of the device for our particular experimental requirements. Indeed, the produced photons traversing the Dwarf-Ball material have a low pair-conversion probability in comparison with other (thicker) existent 4π LCP and IMF multidetector arrays. This characteristic constituted a basic prerequisite for any detector of this kind to be coupled with TAPS.

[9] The maximum single detector thickness is $d \approx 70$ mm including absorber, phoswich material, light-guide and PMT.

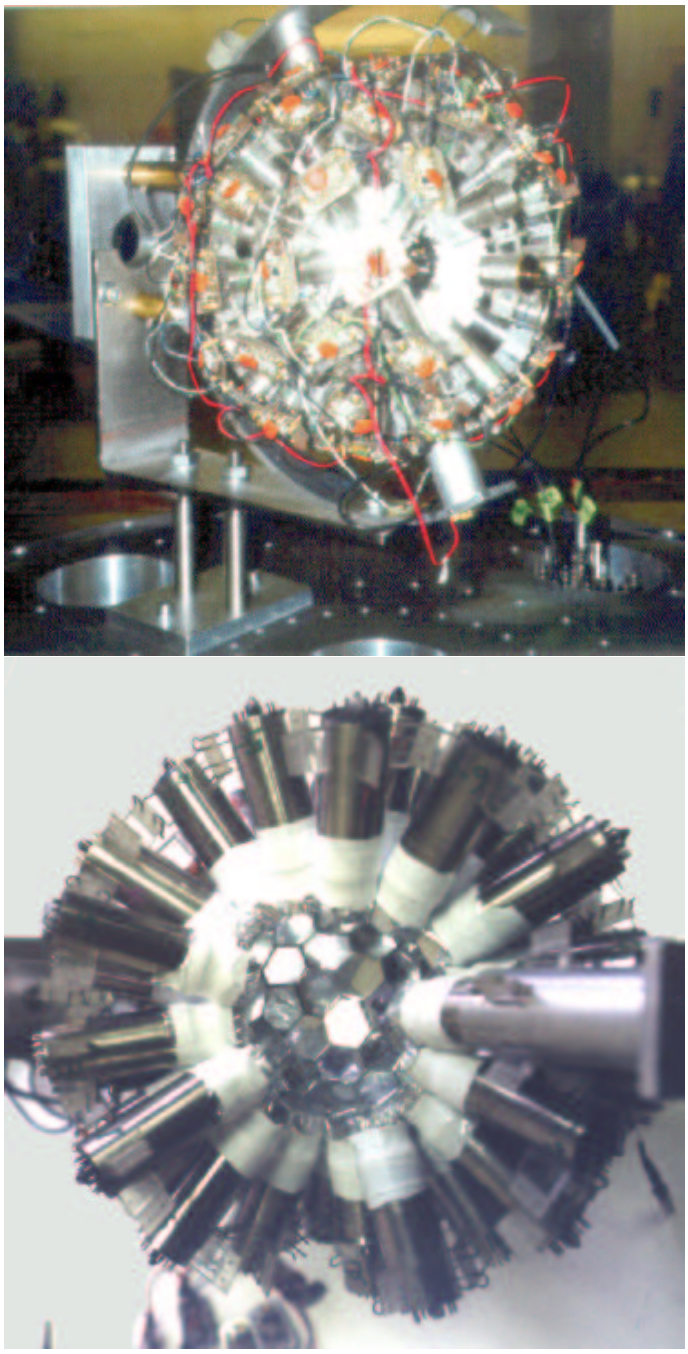

Figure 4.13: *Photographs of the Dwarf-Ball: a) The DB placed on the top lid of the carbon scattering chamber. b) Open view of the DB. Most of the detectors of one hemisphere, and all signal cables and PMT voltage dividers, have been removed to allow for a view of the device. The white Teflon tape wraps each phoswich and lightguide.*

4.7.2 BC400-CsI(Tl) phoswiches

The basic detection element of the DB is obtained by coupling a thin and fast (τ = 3 ns) organic plastic scintillator (Bicron BC400 or BC446) for ΔE measurement, together with a CsI(Tl) inorganic crystal scintillator for E measurement. They are readout in phoswich mode by a single photomultiplier (for details see the Appendix 1). The individual CsI(Tl) crystals are 4 - 8 mm thick (depending on the angle, the thicker in the most forward direction) prisms of hexagonal or pentagonal shape with the thin (10 - 40 μm, depending also on the angle) ΔE plastic scintillator adhered to its front side. 8-mm Lucite lightguides, matching the backside of the CsI(Tl) crystals, guide the scintillation light to a small ($\approx$ 50 mm) Hamamatsu R1666 six-stage PMT. These PMT have a typical gain of 10^5 and are connected in groups of 16 to a common LeCroy HV power supply delivering the required high-voltages between -800 and -1000 V (a gain selected in order to observe the punchthrough point of the α particles, see Section 5.5.1). The detectors are protected against δ atomic electrons stripped from the target, by Ta or Au absorber foils covering their front side. These foils had thicknesses between 2.8 and 4.9 mg/cm^2 for the most forward and backward modules respectively. A photograph and a cross-sectional view of a hexagonal element are given in fig. 4.14.

The polar angle θ, the azimuthal angle ϕ, and the thicknesses of each individual plastic-CsI(Tl) detector used in this experience, are given in table 4.7.

Table 4.7: *Dwarf-Ball telescope positions and thicknesses of their CsI(Tl) and plastic scintillators.*

# Detector	θ [°]	ϕ [°]	E (mg/cm^2)	ΔE (mg/cm^2)
1	41.59	230.02	8.08	4.08
2	41.59	302.02	8.38	4.07
3	41.59	14.02	8.20	4.06
4	41.59	86.02	8.33	4.05
5	41.59	158.02	8.20	4.03
6	49.51	191.73	8.13	3.98
7	49.51	263.73	8.20	3.97
8	49.51	335.73	8.28	3.95
9	49.52	47.73	8.41	3.93
10	49.51	119.73	8.33	3.92
11	63.43	216.00	4.34	3.89
12	63.43	288.00	4.39	3.87
13	63.43	0.00	4.37	3.86
14	63.43	72.00	4.31	3.84
15	63.43	144.00	4.34	3.81
16	67.93	242.39	4.04	3.80
17	67.93	314.39	4.32	3.79
18	67.93	26.39	4.24	3.76
19	67.93	98.39	4.34	3.76
20	67.93	170.39	4.27	3.73
21	77.52	194.74	4.06	3.72
22	77.52	266.74	4.42	3.68

Table 4.7: (continuation)

# Detector	θ [°]	ϕ [°]	E (mg/cm^2)	ΔE (mg/cm^2)
23	77.52	338.74	4.27	3.65
24	77.52	50.74	4.32	3.65
25	77.52	122.74	4.22	3.62
26	87.30	221.39	4.37	3.50
27	87.30	293.39	4.12	3.50
28	87.30	5.39	4.34	3.50
29	87.30	77.39	4.??	3.50
30	87.30	149.39	4.??	3.50
31	92.70	246.61	4.37	3.50
32	92.70	318.61	4.34	3.49
33	92.70	30.61	4.27	3.49
–	92.70	102.61	–	
34	92.70	174.61	4.32	3.42
35	102.48	201.26	4.27	3.39
36	102.48	273.26	4.06	3.38
37	102.48	345.26	4.34	3.37
38	102.48	57.26	4.24	3.34
39	102.48	129.26	4.??	3.32
40	112.07	225.61	4.32	3.30
41	112.07	297.61	4.29	3.30
42	112.07	9.61	4.32	3.26
43	112.07	81.61	4.12	3.23
44	112.07	153.61	4.24	3.21
45	116.57	180.00	3.96	3.18
46	116.57	252.00	4.22	3.17
47	116.57	324.00	4.32	3.13
48	116.57	36.00	4.34	3.12
49	116.57	108.00	4.06	3.11
50	130.49	204.27	4.24	3.04
51	130.49	276.27	4.17	3.04
52	130.49	348.27	4.22	3.04
53	130.49	60.27	4.29	3.02
54	130.49	132.27	4.34	3.00
55	138.41	237.98	3.99	2.98
56	138.41	309.98	4.37	2.97
57	138.41	21.98	4.32	2.95
58	138.41	93.98	4.28	2.94
59	138.41	165.98	4.32	2.92
60	155.58	202.89	4.32	2.83
61	155.58	274.89	4.37	2.83
62	155.58	346.89	4.34	2.83
63	155.58	58.89	4.24	2.80

Table 4.7: (continuation)

# Detector	θ [°]	ϕ [°]	E (mg/cm^2)	ΔE (mg/cm^2)
64	155.58	130.89	4.34	2.11

4.7.3 Particle identification capabilities

The CsI(Tl) is a scintillator material that presents the particularity of emitting light with two different ("slow" and "tail") time constants (τ_{sl} = 0.4 - 0.7 μs and τ_{ta} = 7.0 μs) that correspond to different scintillation mechanisms (see Appendix 1). The CsI(Tl) light output can be, thus, expressed in the following manner:

$$I_{CsI(Tl)} = I_{sl}e^{(-t/\tau_{sl})} + I_{ta}e^{(-t/\tau_{ta})} \tag{4.4}$$

I_{sl} and I_{ta} intensities depend on the energy and nature of the particle. Their ratio is, thus, sensitive to the mass and charge of the traversing particle. Using this property, one can achieve isotopic separation of the hydrogen (p, d, t) and helium (^{3}He, α) isotopes [Alar85], through CsI(Tl)$_{tail}$ versus CsI(Tl)$_{slow}$ bidimensional plots (fig. 4.15).

Apart from LCP identification obtained solely exploiting the pulse-shape properties of CsI(Tl), since the DB modules consist of 2 stages (fast plastic plus CsI(Tl)) phoswich telescopes, one can in principle construct two additional $\Delta E - E$ matrices for IMF identification:

- E_f from plastic scintillator vs. E_{sl} from CsI(Tl).
- E_f from plastic scintillator vs. E_{ta} from CsI(Tl).

In the present experiment only the E_f vs. E_{sl} array (see fig. 5.11) has been used.

4.7.4 Dwarf-Ball electronics and pre-trigger logics

As described in the previous section, the particle identification with the DB relies on pulse shape discrimination, i.e. on proper charge integration of the electronic signals over three different time intervals (given by the *"fast"*, *"slow"* and *"tail"* gates). These timing characteristics furnish the basic defining criteria for the design of the DB electronics (fig. 4.16). Table 4.8 gives a description of the individual electronics modules used in the DB setup. All the electronics modules fit in four NIM[10] bins (for the first elements of the chain) and in one CAMAC crate (for the FERA[11] analog-to-digital converters). These crates were all in a rack located in the experimental hall two meters away from the scattering chamber.

[10] NIM (Nuclear Instrument Module) is the earliest (and simplest) standard modular system used in nuclear and particle physics electronics. It consists of a "bin" with slots to accept 12 modules for digital and/or analog instruments. At variance with CAMAC back-plane data-bus, the NIM bus is just for power supply purposes, therefore no parameter readout can be performed.

[11] FERA (Fast Encoding and Readout ADC) is a high-speed (conversion time $\approx$ 5 μs) charge integrating analog-to-digital converter with 16 independent ADCs enabled by a common gate of 50 - 500 ns.

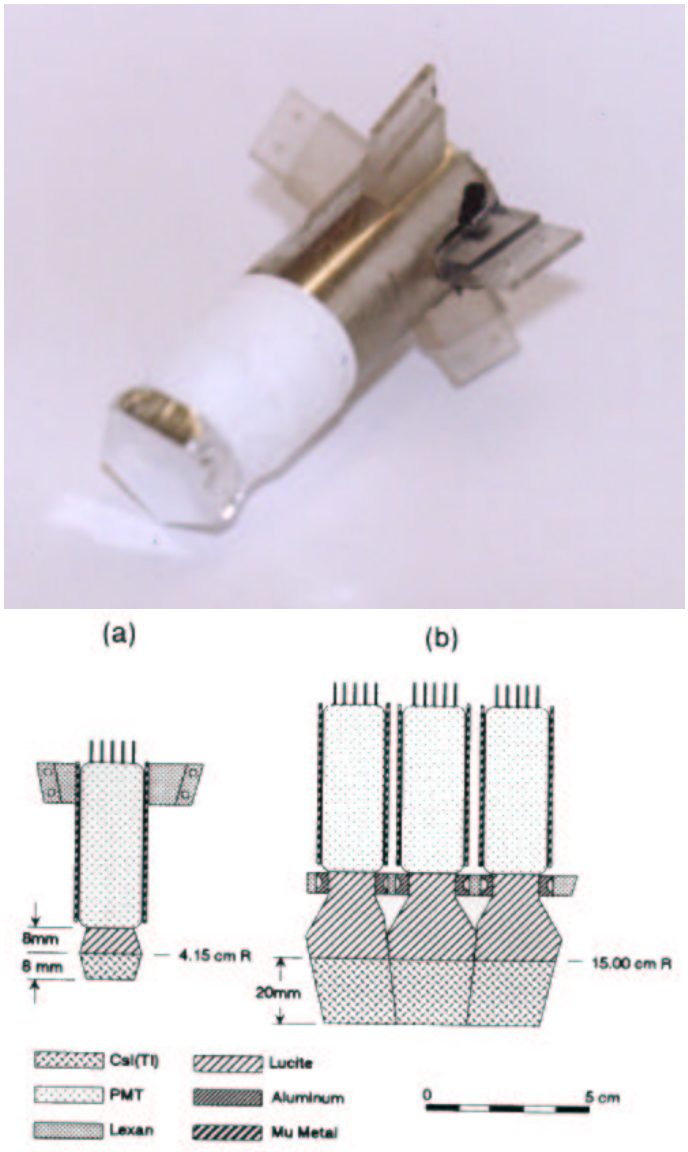

Figure 4.14: *Photograph (upper part) and cross-sectional view (left module in the lower part) of a hexagonal element of the Dwarf-Ball. The white Teflon tape covers the plastic-CsI(Tl) phoswiches and the Lucite light guide. The Ta/Au foils cover the front side of each detector.*

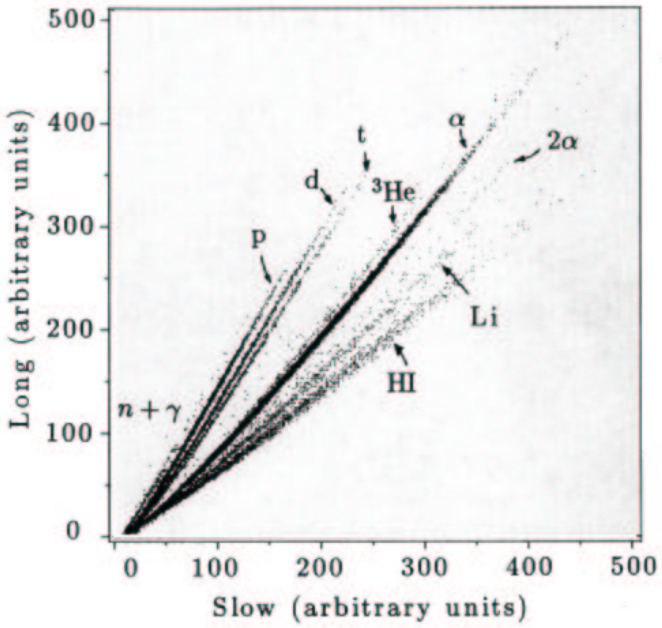

Figure 4.15: *Example of a typical array used for light-charged-particle identification in the DB: Isotopic identification of LCP using the CsI(Tl) "tail" (also called "long") versus "slow" energies 2D-plots [Stra90].*

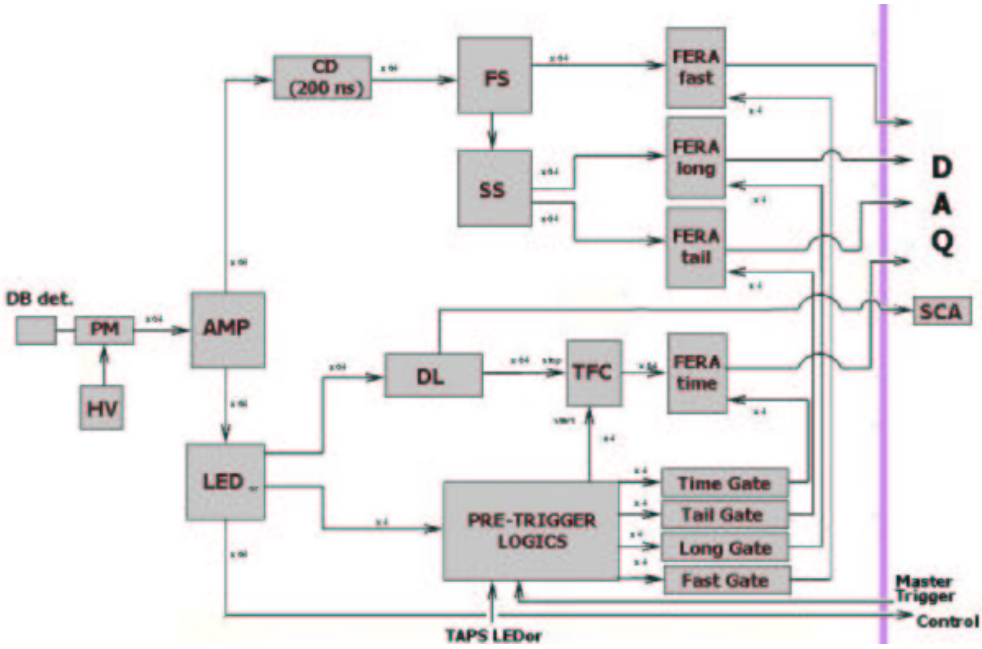

Figure 4.16: *Schematic diagram of the Dwarf-Ball electronics. The description of the different electronics modules is given in table 4.8. A more detailed scheme of the whole DB electronics and pre-trigger logics can be found in Appendix 5.*

The anode signal delivered by the PMT of each firing DB module is first amplified by fast, variable gain ($\times 2$ - $\times 40$) amplifiers placed (together with the trigger logics and gate-generation modules) in one of the aforementioned five NIM crates. One of the two amplifier outputs (the *"time branch"*) is used to generate the trigger logics and the integration gates, and to monitor each individual detector. The other output (the *"energy branch"*) as linear signals are digitized by the different analog-to-digital converters (Lecroy FERA 4300 ADC modules) placed in the CAMAC crate.

The time-branch: The signal from the time branch feeds first a leading-edge discriminator (LED) to eliminate the background noise. The threshold of each discriminator is selectable through a multiplexer bus and a PC located in the control room. This LED delivers three types of output:

1. Individual channel logic signals (differential ECL[12] pulses) retarded by up to 210 ns in an ECL delay module. They provide the **stop signals** for each detector in a time-to-FERA (TFC) converter module. This TFC module provides negative amplitude current pulses to the time FERA ADCs, the length of which depend on the time difference between the start and stop signals.
2. The logic OR of each group of 16 detectors is used to create the **three time gates** for the energy signal integration (*"fast"*, *"slow"* and *"tail"*) and the **start signal of the TFC**. In addition it generates the Dwarf-Ball **triggers** (DBor, DB Multiplicity 1 and 2) which are used in the DB pre-trigger system and in the general trigger box outside the cave (see below).
3. A **logic signal** of each individual detector for **on-line monitoring** purposes. This monitoring is performed with a dedicated PC in the control room.

As a matter of fact, to minimize the acquisition dead-time (see Section 4.9.1), four different pre-triggers are already built in the experimental cave without the need to go through the main trigger box: TAPSor, DB Multiplicity 1 and 2, and DBor (with a "hardware" scale-down factor of 10). If a particular DB event is in coincidence with one of these four trigger conditions, and the DB system is not busy treating an earlier event, the generation of the four integration gates (*"time"* at t = 100 ns, *"fast"* at t = 170 ns, *"slow"* at t = 500 ns and *"tail"* at t = 1700 ns; each one with its own width) proceeds by default (after some t = 75 ns from the reference start of the LED discrimination time). Likewise, at t = 3600 ns a *"fast clear"* signal is also automatically produced and sent to the FERA driver. This *"clear"* signal erases all the integrated signals in the corresponding ADCs unless there exists a coincidence with the *"master trigger"* signal coming from the central TAPS+DB+FW trigger system. In this case the *"clear"* signal is inhibited and the FERA driver sends all the information to the acquisition through its data bus. The implementation of this pre-trigger allows a faster response of the DB within the whole experimental setup.

The energy-branch: This second amplifier output is first delayed by 200 ns through RG-58 cable-delay to wait for the gate generation and it is then (fast) split into two equal signals with half the original amplitude:

[12] ECL (Emitter Coupled Logic) is a type of fast logic signals.

Table 4.8: *List of the basic Dwarf-Ball electronics modules used in the experiment (W.U. stands for "Washington University" custom-made modules).*

Item	Description (# of channels)	# of modules
NIM Standard:		
AMP	W.U. Fast Amplifier (×6)	12
CD	Cable Delay (66 ns + 126 ns) RG-58 cable (×64)	1
FS	W.U. Fast Splitter 50-Ω passive AC-coupled (×16)	4
FS	W.U. Slow Splitter 2-way AC-coupled (×16)	4
LED	W.U. Discriminator LED (×4,6)	5
DL	Delay ECL	4
TFC	W.U. Time-to-FERA converter	4
SCA	GSI Scaler SC4800	1
Level Translators	ECL-NIM-ECL (Lecroy 4616)	3
Gate Generators	Octal (EG&G 8000), Quadral and Dual (Lecroy 222)	4
CAMAC Standard:		
FERA ADC	Lecroy 4300B ADC (×16)	16
FERA Driver	Lecroy 4301	1

1. One branch is used for integration of the **fast plastic ΔE component** in one of the 16 channel ADC FERA modules. The signal is integrated with a fast gate of 70 ns width, started at d = -20 ns before the signal leading edge.
2. The second group of 16 outputs is further (slow) split and attenuated (by factors 12 and 4) to provide respectively the **slow (E signal)** and the **tail components** of the CsI(Tl). The signal is, thus, integrated twice in separate FERA ADCs: over a *"slow"* interval of 400 ns width (gate started at a delay d = 300 ns), and over a *"tail"* interval of 1.7 μs width. This tail gate is opened with a 1.5 μs delay with respect to the fast one. Finally, this last splitter also provides an **inspection (analog) output**. This output, together with the logic test signal, will serve to control on-line the settings of the DB energy thresholds in the discriminator with the help of the monitoring PC.

A more detailed scheme of the whole Dwarf-Ball electronics, timing and pre-trigger logics can be found in Appendix 5.

4.8 Forward Wall charged-particle multidetector

4.8.1 Main characteristics

The "Forward Wall" (FW) is a charged-particle hodoscope built at KVI [Leeg92, Hoef94]. It consists of an array of 92 fast-slow plastic scintillators telescopes (NE102A-NE115), located 760 mm away from the target and covering the polar angular range between 2.5° and 21.0° (in θ and ϕ) around the beam direction (fig. 4.17). It has a total area of 536×536 mm^2 and covers about 4% of the solid angle. The 32 smallest phoswiches (32.5×32.5 mm^2) are positioned at the most forward angles, where the counting rates are the largest, in order to increase the FW granularity thus allowing for higher counting rates per solid angle and improving the position resolution. The remaining 60 larger modules (65×65 mm^2) are positioned at the periphery. The whole array is mounted inside a double-frame structure placed in an aluminum box (fig. 4.17) matching, on the front side, the scattering chamber to ensure the proper vacuum conditions needed for the hodoscope. In order to dissipate the heat generated by the PMT bases, the FW is cooled down to $-40°$ with a liquid alcohol flowing through a Cu pipe.

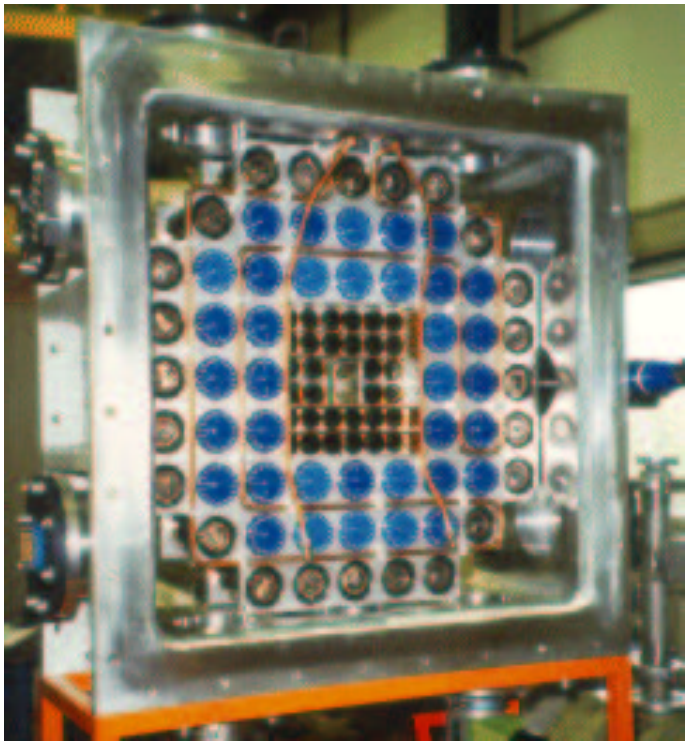

Figure 4.17: *Photograph of the backside of the Forward Wall multidetector. The two groups of small and large individual phoswiches can be seen surrounded by the aluminum box. The beam passes through the central hole.*

The design criteria of the Forward Wall were determined by its application as LCP/IMF multidetector system in the forward hemisphere of fixed-target nuclear reactions. In typical heavy-ion peripheral reactions the primary quasiprojectile fragment is often excited above the particle threshold and will subsequently decay into LCPs, neutrons and a quasi-

projectile fragment (QP). Due to kinematic focusing, these reaction products are emitted in the laboratory frame into a narrow cone. The Forward Wall was designed to detect these LCPs and light IMFs and to measure their energies at high count-rates (< 1 MHz). Fast organic plastics are used for ΔE measurement due to their excellent time response. The combination of $\Delta E - E$ plastics in phoswich mode was chosen for its pulse-shape capabilities to separate LCP and IMF, and because of their good radiation hardness against the high counting rates to which they are exposed.

4.8.2 NE102A-NE115 phoswiches

The basic constituents of the Forward Wall multidetector are phoswich detectors consisting of a 1-mm thick fast organic plastic NE102A (τ = 2.4 ns) for ΔE measurement, and 50-mm thick slow organic plastic NE115 (τ = 320 ns) for E measurement. They are heatpressed together [Kol86, Lid87] and readout by the same photomultiplier (glued to the backside of the phoswich with a two-component epoxy or a silicon glue). The small phoswiches are coupled to a 10-stage (type $XP2972$) photomultiplier and the larger ones to a 8-stage (type $XP2282B$) PMT[13] (see fig. 4.18). The bases for the large detectors are especially designed for high count-rates, with transistorized last stages. All the PMTs are powered by a common Lecroy HV power supply unit with voltages in the range -1100 V to -1900 V (aligned by selecting a certain channel range for the α punchthrough point). The most forward detectors are covered by a 100 μm thick Ni absorber to shield them against elastically scattered particles and atomic δ electrons. During the high-counting-rates runs, an additional thin aluminum mask was positioned in front of the first ring of inner detectors resulting in an energy threshold below which particles issuing from grazing (Rutherford) nucleus-nucleus scatterings are not detected [14].

4.8.3 Particle identification capabilities

Like in the case of the BC400-CsI(Tl) Dwarf-Ball phoswiches, the passage of a charged particle through the NE102A-NE115 detectors excites the molecular levels of the organic plastics and produces the emission of light characterized by a time constant specific to each material (see Appendix 1). This light is then collected by the common PMT located in the back side of the NE115. Since the time constants of both scintillators are very different (τ_f = 2.4 ns for the NE102A and τ_{sl} = 240 ns for the NE115) the integration of the same current signal done over two proper time intervals (usually called *"short"* and *"long"*, see footnote page 72) allows the distinction of both signals, from which the atomic number of the particles (and their energy) can be determined. Indeed, the first signal collected corresponds to the energy loss of the particle in the first stage of the telescope (ΔE), and the second one to the rest energy (E) in the second stage where the particle may stop or eventually punchthrough. We can exploit the characteristics of both signals to work in the so-called $\Delta E - E$ mode and build bi-dimensional representations like those of fig. 4.19, that permit a Z identification up to the charge of the projectile Z $\approx$ 18 (see Section 5.6.1).

[13] Actually, the detectors at the most outer ring use an older 12-stages photomultiplier (type 9814*B*).

[14] The grazing angles of elastically scattered projectiles for the reactions studied here are between 4.6 ° and 1.1° angles (see Table 4.4).

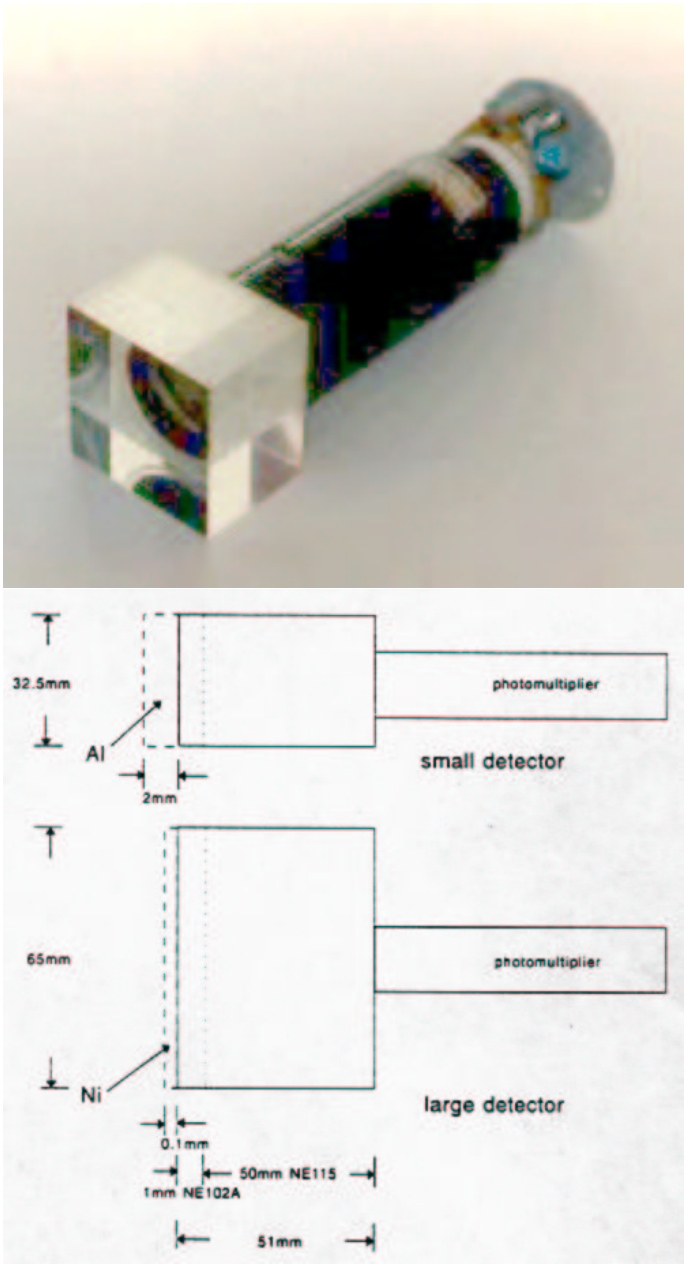

Figure 4.18: *Photograph (upper part) and cross-sectional view (lower part) of a small (and large) FW phoswich module.*

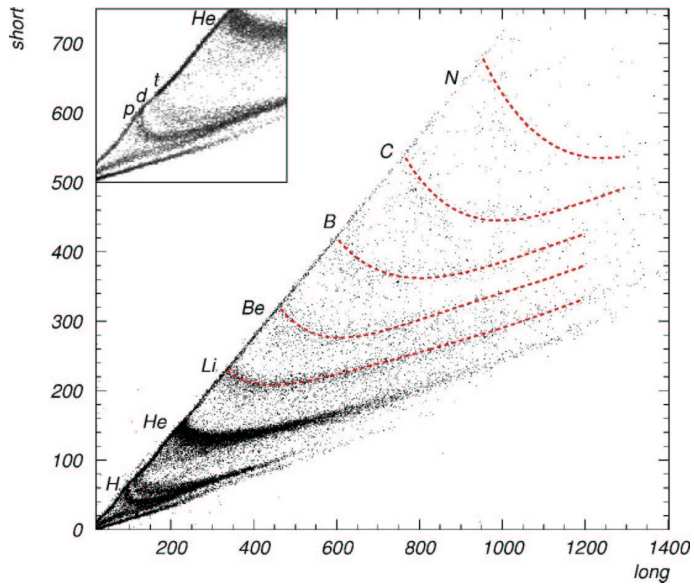

Figure 4.19: *Example of a $\Delta E - E$ array (short vs. long) used for the particle identification in the FW [Hoef00]. The inset shows the isotopic separation of hydrogen.*

4.8.4 Forward Wall electronics

In fig. 4.20 a diagram of the basic electronics scheme for one individual FW module is shown. The modules of the electronics chain (see table 4.9) were inserted in two CAMAC crates located in the experimental cave and deliver the signals to the converters in the counting room. The analog signal from the FW module photomultiplier is first split by an AAS placed next to the hodoscope, into two branches:

The time-branch: The arrival of a particle signal starts the output of a LeCroy 3420 CFD which is stopped by a cyclotron RF veto arriving at the same time for each group of 16 detectors. This output is subsequently delayed (500 ns) and sent to the counting room where it is integrated in a FERA ADC (LeCroy 4300B) to provide the time information of the detector. The later the particle arrives at the Forward Wall, the smaller the output. Since each CFD controls 16 different detectors it also provides the appropriate OR and multiplicity signals to generate the necessary triggers (FWor, FW multiplicity 1 and 2) as well as the output for the SC400 Scalers.

The energy-branch: The analog output of the energy branch is delayed 500 ns (in a cable delay box) and sent to the counting room where a passive splitter further divides it into two signals for independent 11-bit integration in two FERAs (LeCroy 4300B) within two different intervals (95 ns for the *"short"* gate and 300 ns for the *"long"* one). These 2 gates are derived from the RF signal and are generated by the TAPS main trigger.

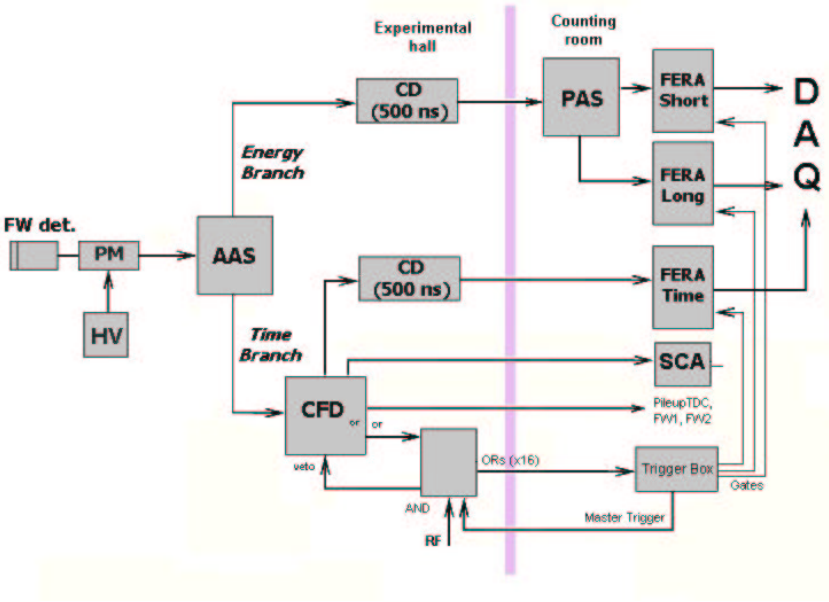

Figure 4.20: *Forward-Wall basic electronics scheme per module. The description of the different electronics modules is given in table 4.9.*

Table 4.9: *List of FW electronics modules used for each one of the 6 groups of 16 detectors.*

Acronym	Type of module	Model (# of channels)
AAS	Active Analog Splitter	Giessen ($\times$16)
CFD	Constant Fraction Discriminator	LeCroy 3420
CD	Cable delay (500 ns)	Giessen ($\times$64)
PAS	Passive Analog Splitter	($\times$16)
FERA	11-bit Fast-ADC	LeCroy 4300B ($\times$16)
SCA	Scalers	GSI SC4800 ($\times$16)

4.9 Data-acquisition system and trigger logics

The detectors used in this experiment represent a large number of measurement channels (more than 2000) and produce a large quantity of digital information. To be able to handle such a flow of data, one needs to apply event selection criteria (the *triggers logics*) and make use of a computer controlled data acquisition system. For each electric signal produced by a detector, a complex **signal amplification** $\rightarrow$ **signal digitization** $\rightarrow$ **signal selection** $\rightarrow$ **hit readout** $\rightarrow$ **hit storage** chain is activated. This intricate process makes use of different (electronics and computer) technologies. The first step of this process (amplification and primary electronics signal shaping) and, partially, the second stage (digitization) have been already discussed in the sections dedicated to the electronics associated to each detector system (sect. 4.6.5, 4.7.4, 4.8.4). I will describe the remaining steps of the data flow in the next two Sections.

4.9.1 Data acquisition system

The data acquisition system (DAQ) must perform the following four main tasks:

1. **Data stream handling:** Readout of the (analog-to-digital) converters and other electronic modules, collection of the data, and data-buffer building.

2. **On-line analysis:** Redirecting a fraction of the data buffers to the on-line analysis for event-display and control of the data quality during the experiment.

3. **Parameter control:** Adjustment of several experimental parameters of the detector system and associated electronics (such as the individual HV, discrimination thresholds, programmable delays and integration gate widths).

4. **Taping:** Storing the data buffers on magnetic tape for later off-line analysis.

The use of computer controlled data-acquisition system requires, of course, interfacing the (electronics) instruments with the computer. This has been done in the present experiment using two standard systems for DAQ [Leo92, Buen88]: CAMAC and VME[15]. We have seen in previous sections that all TAPS+DB+FW signal digitizations are performed by CAMAC modules. We will see now that TAPS data are also readout through the CAMAC dataway. The rest of the aforementioned first and fourth tasks are, however, controlled by processes running in VME modules, and, the two other tasks are managed by processes running on UNIX and VMS workstations interfacing the VMEs (table 4.10).

Three DEC stations (1 VAX/VMS and 2 UNIX) in the control room program and control the different VME processors through Ethernet. The different E6**x** (MC68030) and E7**x** (MC68040) VME boards used are produced by ELTEC and run under OS9 operating system. In table 4.10, an overview of the modules in the VME crate is given.

[15]VME (Versa Module Europa) is a flexible open-ended bus system which makes use of the modular Eurocard circuit board standard size (20 double-height slots). Its backplane interconnection bus system (VMEbus) has a 32-bit data bus. It uses TTL technology and can handle data transfers at speeds up to 40 Mbytes/s; supporting a variety of computing intensive tasks and becoming a rather popular protocol for real-time data acquisition.

Table 4.10: *Overview of the different data acquisition VME processors used. All VME cards were placed inside the slots of two different VME cages, the first slot was used as the crate manager capable of 8,16 bit transfers. (DPM stands for "Dual Port Memory" board).*

VME	Function
E6A	TAPS first-branch (6 CAMAC crates), global event builder
E7A	TAPS second-branch (7 CAMAC crates)
E6C	Acquisition server, counting room parameter control
E6B	Buffer and DLT server
E6D	Experimental hall parameter control
DPM1	DB multidetector
DPM2	FW multidetector

Data stream handling

The experimental information generated by each individual detector and treated by the electronics of the three multidetectors (TAPS, DB and FW) is finally digitized in CAMAC electronic analog-to-digital converters (either QDC and TDC modules in the TAPS case, or FERA ADC ones for the DB and FW). The DAQ is then responsible for reading all converters, building up the events (i.e. synchronizing the different *"subevents"* of the different detectors corresponding to a same reaction) and storing them in data buffers of a proper size. The data acquisition system of TAPS was used as the event builder for the whole TAPS+DB+FW combined setup. The starting point for the acquisition environment of the experiment was, thus, the standard TAPS-stand-alone DAQ [Oste95], and the additional DB and FW information was fed into the TAPS data stream.

- **TAPS data readout:**
  The basic parameters per TAPS module hit are the QDC and TDC values, as well as the bit patterns (BPUs) for the BaF_2 and veto detectors. These are read out for each accepted event. The physical information contained in these parameters is:

  1. E_n obtained by integration of the fast BaF_2 signal over 50 ns in the QDC.
  2. E_w obtained by integration of the slow BaF_2 signal over 2 μs in the QDC.
  3. TOF obtained by digitization, in the TDC, of the time period between the start-stop (master trigger signal - CFD signal) logic pulses.
  4. The number of the firing detectors (BPUs).
  5. The number of the firing veto detectors and the value of the veto-pattern (5 for charged, 2 for neutral).

  All TAPS converters (QDCs and TDCs) and bit patterns (BPUs) modules reside in 13 CAMAC crates which are individually controlled by a MC68030-processor "crate controller" (CVC-STR612). The process of digitization of the incoming detector signals takes some time. Whereas the information of the BPUs is directly available from the electronics, the QDC's have a digitization time of 1.5

μs/channel[16], and the TDC conversion time is still longer[17]. The CVC controller performs the readout of a crate autonomously and afterwards stores the result in its local memory. The readout of the modules is done through the CAMAC back-plane databus (1.5 MB/s maximum transfer speed) into the CVC with 1.7 μs/channel speed (i.e. $\approx$ 1 CAMAC cycle). The total time needed for the readout of one CAMAC crate is of the order 200 - 400 μs (therefore, taking into account the aforementioned conversion times, "reading" is for large events more time-consuming than "converting").

Once the CAMAC readout of the converters is completed, the information in each of the 13 CVC's is further read by two VME boards: E6A and E7A, via a differential VSB-bus ("VME Subsystem Bus" with a transfer rate of the order 1 - 4 Mbytes/s). The E6A processor controls a branch with 6 crates and the E7A controls a 7-crates branch.

- **DB and FW data readout:**
  For every responding DB phoswich, the DAQ reads out, through a fast FERA bus (see below), the following information delivered by the FERA ADCs:

  1. The number of the firing detector.
  2. E_f obtained by charge integration of the fast plastic BC400 signal over 70 ns time interval.
  3. E_{sl} obtained by charge integration of the slow CsI(Tl) signal over 400 ns time interval.
  4. E_{ta} obtained by charge integration of the tail of the CsI(Tl) signal over 1.5 μs.
  5. *Time* obtained by integration of the time-to-FERA-converter TFC signal.

  Similarly, for each FW hit, the DAQ collects the following parameters via a fast FERA-bus readout of the FW FERA ADCs:

  1. The number of the firing detector.
  2. E_{sh} obtained by integration of the short plastic NE102A signal over 95 ns time interval.
  3. E_l obtained by integration of the long NE115 signal over 300 ns time interval.
  4. *Time* obtained by digitization in the TDC of the time period between the start-stop logic pulses.

  At variance with the TAPS case (where the option of a fast ECL readout of the QDC and TDC is available but not exploited), the energy and time parameters of the DB and FW phoswiches, are not read out through the CAMAC backplane (TTL[18] logic technology) but via the much faster FERA data-bus (ECL logic technology). Indeed, the FERA ADC modules located in the CAMAC crates have an alternative

[16] Two per detector: a long and a short integration, however since the channels are multiplexed the maximum duration is about $16 \times 1.5 = 24$ μs

[17] They are not multiplexed; conversion time is ≈ 12 μs

[18] TTL (Transistor-Transistor Logic) is a type of digital signals.

output port at their front-side which is 8 - 10 times faster (180 ns/channel) than the (back-plane) CAMAC readout. The DB and FW data sent over their own FERA bus are transferred to 2 different "Dual Port Memory" (DPM 1190) boards. These DPM boards are further read out by the E6A VME during the time that it would otherwise be waiting for the TAPS CVC crate controllers to complete their local readout.

- **Combined TAPS+DB+FW readout:**
  The complete event building (i.e. the combination of the different "subevents" of each individual TAPS, DB or FW multidetector, corresponding to the same reaction) is performed by the E6A processor which subsequently packs them into buffers of 8-KB size (each buffer contains around 30 events since each detected event is about 0.3 KB). The E6B VME finally reads the data buffers over the VME bus and writes them to DLT tape. The whole acquisition environment is controlled by a fifth VME board, the E6C, that writes the commands into a global memory where they are recognized by the E6A and E6B boards. E6C is accessible from a DEC-VAX4000/60 station in the control room from which, e.g. start and stop requests, using Ethernet and TCP/IP protocol, can be sent.

On-line analysis

The control of the quality of the experimental data while the acquisition is running, is performed by the on-line analysis. This is accomplished by a dedicated software package *"Analysis Support Library"* (ASL) [Hejny95] exploiting the PAW, KUIP and HBOOK packages of the CERN software library [PAW90]. ASL-linked programmes, running in two DEC workstations under UNIX, offer several tools to look at raw (e.g. QDC or TDC histograms) and physical (e.g. non-calibrated photon histograms) spectra in order to monitor the individual and global operation of the experimental setup. The ASL system itself sends via Ethernet (TCP/IP protocol) a request to the E6A or E6C processors to redirect a fraction of the data buffers (normally a 1% of the total data being recorded) to its on-line analysis processes.

Parameter control

Two VME modules (E6D and E6C) are responsible of adjusting several experimental parameters of the TAPS spectrometer. The fifth VME, E6D, solely controls the TAPS CAMAC crates located in the experimental hall: individual discrimination thresholds (CFD's and LED's) and HVs. The acquisition server E6C commands also certain modules placed in the electronics and acquisition room: the programmable delays and gate-lengths of the RDVs, and the scalers.

Taping

The E6B VME module is responsible for reading the data buffers of the acquisition server E6C and, via a SCSI bus, writing them on a DLT tape. The DLT is a magnetic storage tape with 10(20) GB of (un)compressed capacity. The total data rate (kilobytes/s) that can be achieved depends on the size of the events. In the TAPS+DB+FW experiment the

Table 4.11: *Typical trigger counting rates (C.R.) and acquisition rates for the five reactions studied. The average event size is 300 bytes/event (0.3 KB/event), the maximum data taking capacity of the taping device is limited to 2000 events/s (equivalent to 600 Kbytes/s = 0.6 Mbytes/s = 50 Gbytes/day).*

Target	Au	Au	Ag	Ni	C
Ar beam intensity (nA)	3.0	12.5	8.0	8.0	1.5
TAPS LEDor C.R. (Hz)	24	1200	1000	900	300
FWor C.R. (kHz)	10	300	250	250	250
DBor C.R. (kHz)	8	-	-	-	-
Acquisition rate (evts/s)	450	1000	1200	1100	750
Taping rate (MB/s)	0.12	0.40	0.45	0.42	0.25

average event comprises 1700 signals with around 0.3 KB size (0.2 KB for the TAPS+FW high counting-rates runs). The DEC TK87 taping device has a maximum write speed of 1 Mbytes/s, but to avoid pile-up and diminish the dead time, the maximum data taking capacity (extrapolated to 100% lifetime) is reduced to $\approx$ 600 KB/s, equivalent to 2000 events per second. Table 4.11 shows the typical trigger rates, acquisition and taping rates for the five reactions studied. One experimental run[19] comprises around 100 MB of raw data (equivalent to $\approx$ 12.800 buffers, or $\approx$ 350.000 events) and is written on tape every 14 minutes approximately. During the low- (high-) counting-rates runs an average of 0.12 MB/s (0.40 MB/s), i.e. 10 GB/day (35 GB/day) were recorded.

4.9.2 Trigger logics

During our experiment, several reasons constrained the possibility of considering all produced reactions:

- The data taking system (magnetic tapes, disks ...) has a limited recording event capacity.
- Many reactions correspond to events without interest or to (background) noise of several possible origins.
- All measurement channels suffer a certain dead-time.

In our case, e.g. during the low counting-rates runs, the radio frequency of the AGOR cyclotron was 37.1 MHz and the projectile-target interaction probability $5.0 \cdot 10^{-4}$ reactions/s (see Section 4.5). These values yield around 18000 nuclear reactions per second[20]. As aforementioned, the *maximum* data taking rate of TAPS on-line acquisition system was one order of magnitude inferior (2000 events/s), although the DAQ operated at a safer $\approx$ 1000 evts/s rate. In addition, with a hard-photon multiplicity per nuclear reaction of the

[19] 1 run $\approx$ 100 MB $\approx$ 0.35 million events recorded in $\approx$ 14 min (850 s).

[20] Of which only a few 4% - 5%, $\approx$ 1000 events/s, would correspond to the most interesting central collisions associated with the largest particle multiplicities.

order of $\approx 10^{-4}$, only around 2 hard-photons events (out of the 18000 reactions) were expected per second. It is, then, clear that a reduction and a selection of the amount of produced data to be processed and stored was necessary. To achieve this goal, one imposes certain criteria which identify a certain event, such as the coincidence among two or more detectors, a condition on the number of outgoing particles, etc. This task was performed by the trigger system, i.e. the set of (electronic and computer) modules of logical choice allowing for a (fast) selection of the interesting events to be treated by the acquisition and recorded on tape.

Triggers definition

The design of the trigger system of the R2 experiment aimed at maximizing the total final hard-photon statistics in coincidence with multifragment reactions. So, it looked after a high efficiency for the hard photon ($E_\gamma > 30$ MeV) events in coincidence with charged-particles detected in the DB or FW detectors. Various trigger configurations were defined using the trigger signals delivered by the three detector systems and mixed in standard NIM logic electronics. High efficiency was achieved by a few standard trigger conditions (AND/OR conditions between TAPS, DB and/or FW) for the main known types of "γ - charged-particles" events. The various triggers defined in the present experiment are described in Table 4.12 for the low-counting-rates runs with the whole TAPS+DB+FW setup, and in Table 4.13 for the high-counting-rates runs with the TAPS+FW setup. Each trigger favored a given type of event and was down-scaled properly to balance its counting rates. A global minimum-bias trigger (e.g. DBor or FWor) was defined and recorded to be able to compute the reaction cross-section. Several other triggers were also present allowing to record more than one type of reaction at the same time. A few others were defined to control the operation of the detector system during the experiment but were not used during the off-line analysis.

Among all triggers defined in tables 4.12 and 4.13, I will mainly analyze in the next chapters those selecting the most interesting physics features for our study. These are *"photon with $E_\gamma > 15$ MeV in coincidence with particles in the DB and/or FW"* triggers (obviously, for the study of hard-photon emission in different fragment multiplicities events), *"particles in the DB and/or FW"* (a *minimum-bias trigger* since practically all nuclear reactions produce a signal in the DB or FW multidetectors), and the *neutral-pion* trigger (for calibration purposes as well as for pion background subtraction).

Trigger logics generation

Our trigger logics works in synchronous mode, i.e. the analog signals for all three multidetectors are retarded (up to 500 ns through 100 m 50-Ω cables) to wait for the decision of the coding event acceptance to be taken. Basically, there are 3 trigger modules whose outputs are combined to make the master trigger. Up to 8 different triggers arrive per trigger unit and, depending on downscaling and dead-time, build up the *master trigger* of the whole acquisition. The TAPS triggers are built from the information of the CFD and LED OR's, combined in the multiplicity module MB with the VETO information. The individual trigger rates are also read out in scaler units: the *"raw"* (the actual trigger counting rate), *"inhibited"* (the dead-time corrected trigger rate) and *"reduced"* (the

Table 4.12: *List of triggers used in the experiment during the low counting-rates runs (# 556 - 1130) with the whole TAPS+DB+FW setup: trigger number, name, event signature and DAQ reduction factor.*

#	Trigger Name	Event signature	Red. factor n ($1/2^n$)
0	TAPS NEU LOW * DB1	$E_\gamma > 15$ MeV and $M_{DB} > 3$	0
1	TAPS NEU LOW * DB2	$E_\gamma > 15$ MeV and $M_{DB} > 6$	0
2	TAPS QUASINEU HI * FW1	$E_\gamma > 40$ MeV and $M_{FW} > 3$	0
3	TAPS QUASINEU HI * FW2	$E_\gamma > 40$ MeV and $M_{FW} > 6$	0
4	TAPS QUASINEU HI * DB1	$E_\gamma > 40$ MeV and $M_{DB} > 3$	0
5	TAPS QUASINEU HI * DB2	$E_\gamma > 40$ MeV and $M_{DB} > 6$	0
6	2 TAPS NEU LOW IN 2 BLOCKS	Neutral pion event	0
7	TAPS NEU LOW * FW2 * DB2	$E_\gamma > 15$ MeV, $M_{DB} > 6$, $M_{FW} > 6$	0
16	TAPS CFD OR	$E_\gamma > 5$ MeV	9
17	TAPS LEDL OR	$E_\gamma > 15$ MeV	2
18	TAPS LEDH OR	$E_\gamma > 40$ MeV	0
19	FW OR	Particle(s) in FW	11
20	BEAM	(Beam intensity)	-
22	2 TAPS NEU LOW	2 γ above 15 MeV	-
23	DB OR	Particle(s) in DB (pre-trigger)	-
24	TAPS NEU LOW OR	$E_\gamma > 15$ MeV	2
25	TAPS NEU HI OR	$E_\gamma > 40$ MeV	1
26	FW1	$M_{FW} > 3$	11
27	FW2	$M_{FW} > 6$	8
28	DB OR AFTER S.D.	Particle(s) in DB (1/10 down-scaled)	8
29	DB2	$M_{DB} > 3$	8
30	TAPS NEU LOW * FW1	$E_\gamma > 15$ MeV and $M_{FW} > 3$	0
31	TAPS NEU LOW * FW2	$E_\gamma > 15$ MeV and $M_{FW} > 6$	0

Table 4.13: *List of valid triggers used in the experiment during the high counting-rates runs (# 1132 - 1568) with the TAPS+FW setup: trigger number, name, event signature and DAQ reduction factor.*

#	Trigger Name	Event signature	Red. factor n ($1/2^n$)
0	2 NEU LOW * FW1	2 γ with $E_\gamma > 15$ MeV, $M_{FW} > 3$	0
1	2 NEU LOW * FW2	2 γ with $E_\gamma > 15$ MeV, $M_{FW} > 6$	0
2	TAPS QUASINEU HI * FW1	$E_\gamma > 40$ MeV and $M_{FW} > 3$	1
3	TAPS QUASINEU HI * FW2	$E_\gamma > 40$ MeV and $M_{FW} > 6$	1
4	-	-	-
5	-	-	-
6	2 TAPS NEU LOW IN 2 BLOCKS	Neutral pion event	3
7	-	-	-
16	TAPS CFD OR	$E_\gamma > 5$ MeV	12
17	TAPS LEDL OR	$E_\gamma > 15$ MeV	2
18	TAPS LEDH OR	$E_\gamma > 40$ MeV	0
19	FW OR	Particle(s) in FW	15
20	BEAM	(Beam intensity)	-
22	2 TAPS NEU LOW	2 γ with $E_\gamma > 15$ MeV	5
23	-	-	-
24	TAPS NEU LOW OR	$E_\gamma > 15$ MeV	8
25	TAPS NEU HI OR	$E_\gamma > 40$ MeV	4
26	FW1	$M_{FW} > 3$	15
27	FW2	$M_{FW} > 6$	14
28	-	-	-
29	-	-	-
30	TAPS NEU LOW * FW1	$E_\gamma > 15$ MeV and $M_{FW} > 3$	4
31	TAPS NEU LOW * FW2	$E_\gamma > 15$ MeV and $M_{FW} > 6$	4

trigger rate after the downscale reduction) rates, a basic information for the calculation of each specific event cross-section (see Section 6.4.1). The beam current is also fed into the TAPS trigger module. Its inhibited rate gives the effective integrated beam through the product *(beam current)×(time)×(1-deadtime)*, needed to calculate the normalized trigger cross-sections (see Section 6.4.1).

Using the outputs of each multiplicity unit, the TAPS MLUs [21] make higher order triggers such as *"neutral low OR"*, *"two neutral low"* or *"quasi-neutral"* (defined as a neutral LEDlow or LEDhigh per block). These outputs are used to validate the output of the DB and FW trigger module.

Whenever a master trigger is validated:

- the type of trigger is conserved in a register unit;
- the logical coincidence (AND) between the master trigger signal and the RF signal, commands the *"common start"* signal of the TAPS TDC and the validation gates of the TAPS RDV;
- all analog signals of TAPS, DB and FW are digitized in the converters;
- the DAQ performs the reading of all modules and resets all the chains to zero;

Nonetheless, since it takes usually $\approx$ 500 ns to make the decision, some degree of parallelism had to be introduced (the DB pre-trigger described in Section 4.7.4) such that during the decision time, the digitization of the DB signals started (their FERA ADC conversion time being of the order of 5 μs as we have mentioned), getting aborted if a reject decision (the *"master clear"* signal of the general DAQ) arrived. If, on the contrary, the event was accepted an interrupt signal was sent to the E6A computer and the digitized detector signals were readout via FERA bus as explained also in Section 4.9.1.

Final total data volume

The total running time of the experiment (30 shifts with an average $\approx$ 50% dead time) had been, initially, proposed to collect sufficient statistics (at least 10^5 hard-photons per reaction system for off-line analysis). The final data rate collected during the whole experiment (338 running hours, equivalent to 14 days of beam-time, including experimental setup and beam commissioning) corresponded to 350 million events in 1580 runs occupying 160 GB in 20 different DLT tapes (i.e. the mean storage data rate was 11.5 GB/day). From these, only 1007 valid runs, with 183 million events, were retained for final analysis (see Table 4.14). Ultimately, for the ^{36}Ar+^{197}Au at 60*A* MeV reaction we collected more than 650.000 hard-photons (out of 170 million events), 86.000 hard-γ (out of 2 million events) for the ^{36}Ar+^{108}Ag reaction, 140.000 hard-γ (out of 3 million events) for the ^{36}Ar+^{58}Ni system, and 150.000 hard-γ (out of 3 million events) for the ^{36}Ar+^{12}C one.

[21] Memory Lookup Units.

Table 4.14: *Recorded events (all triggers summed) and hard-photons ($E_\gamma > 30$ MeV) collected (all photon triggers summed) during the finally analyzed runs for the four systems studied in this thesis.*

Target	Au (lo int.)	Au (hi int.)	Ag	Ni	C	Total
# of valid runs	574	161	66	108	98	1007
Storage (GB)	57.0	16.0	7.0	11.0	10.0	101.0
Recorded events	$170{\cdot}10^6$	$4.8{\cdot}10^6$	$2.0{\cdot}10^6$	$3.2{\cdot}10^6$	$3.0{\cdot}10^6$	$183{\cdot}10^6$
Recorded hard-γ	$655{\cdot}10^3$	$130{\cdot}10^3$	$86{\cdot}10^3$	$142{\cdot}10^3$	$151{\cdot}10^3$	$1.16{\cdot}10^6$

Chapter 5

Data analysis and detector calibration

Summary

5.1 Data analysis and simulation software packages 101
5.2 TAPS Energy calibration 102
5.3 TAPS Time calibration 104
5.3.1 Single detector time calibration 104
5.3.2 *TOF* drift correction 106
5.3.3 Walk and cross-talk correction 106
5.4 Photon reconstruction: cluster analysis 106
5.4.1 Single-detector particle identification (*PSA* vs. *TOF*) 108
5.4.2 Clustering routine 108
5.5 Dwarf-Ball analysis 114
5.5.1 DB light-charged particle isotopic identification 114
5.5.2 DB IMF identification 116
5.6 Forward Wall analysis 118
5.6.1 FW LCP/IMF separation 118

In the previous chapter we have described how the particles and fragments produced in nucleus-nucleus collisions traverse the different detectors and generate electrical signals that are subsequently shaped and digitized by the electronics system and finally stored on DLT tapes by the DAQ. The next step consists in transforming the "raw data" contained on these tapes (numerical values, channels, from the output of the digital converters) into physical quantities (MeV, ns ...). To achieve that, we need first to decode the binary information in the raw events, to separate and identify the different particles and nuclear fragments collected per event (i.e. to attribute them a given charge and mass) and, finally, to determine their energy from the detector calibration[1]. Additionally, reliable simulations of the response of the experimental setup are required to deduce physics quantities. This whole procedure is performed on an event-by-event basis with the aid of three software analysis tools, running under UNIX at the Lyon's *"Centre de Calcul de l'IN2P3"* and originally developed for the TAPS campaign at KVI in 1997 [Aphe98]: FOSTER, ROSEBUD and KANE.

In this chapter I will describe the data analysis programmes, the process of TAPS energy and time calibration, the time-of-flight drift correction, the photon identification through *PSA-TOF* techniques and the photon (momentum) reconstruction. The particle identification procedures for the DB and FW will be described as well. Fig. 5.1 shows a flowchart of the entire analysis.

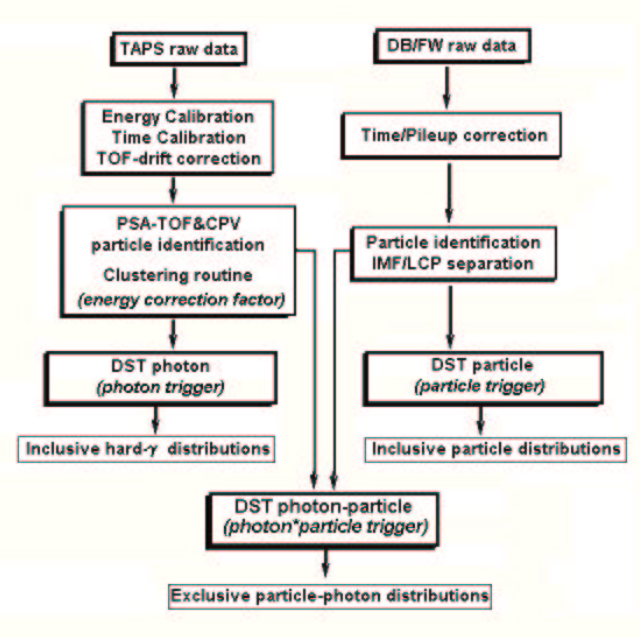

Figure 5.1: *Flowchart of the analysis. Each single analysis-step is explained in the different sections of this chapter. The final outputs (inclusive and exclusive photon/particle distributions) constitute the experimental results presented and discussed in chapters 6. and 7.*

[1]The final files containing this experimental physics-wise relevant information and ready to be analyzed are called *"Data Summary Tapes"* (DST).

5.1 Data analysis and simulation software packages

Two data-analysis packages (FOSTER and ROSEBUD) and one simulation package (KANE) have been specifically developed for the TAPS campaign at KVI in 1997 [KANE96, Aphe98]. The inclusion of the FW and DB in the experimental setup compelled me to modify those codes to include also the combined raw data decoding and particle identification procedures for those two additional particle multidetectors. These three packages were installed and developed (using CMZ, a code manager package [CMZ]) running under UNIX (HP-UX, IBM-RT and Linux platforms) at the French IN2P3 Computer Center (CC-IN2P3). The CC-IN2P3 offers an important computing power, large disk space and, in particular, a set of machines and automated tape robots allowing the user to handle the large amount of experimental data recorded ($\approx$ 150 Gbytes) via the *TMS* ("Tape Management System")[2] and *"xtage"* (tape reading/writing) services.

FOSTER: This package is basically devoted to the decoding of the raw TAPS, FW and DB data, and to the TAPS (energy and time) individual detector calibration. FOSTER is written in C/C++ and interfaces[3] the FORTRAN CERN program library CERNLIB (HBOOK and KUIP routines). It provides, thus, all interactive and graphical presentation, statistical and mathematical analysis, and objects (histograms, event files Ntuples, vectors, etc.) of the PAW [PAW90] analysis package, plus all the additional built-in TAPS-specific functions [Aphe98]. It was originally developed under VMS/Alpha, starting out from the TAPS ASL on-line package (see Section 4.9.1), and later adapted to UNIX. It is this UNIX version which was further developed and used in this thesis. FOSTER provides two sets of commands:

- Commands to dispatch the original DLT tapes (10 GB of uncompressed capacity) onto 3490 cartridges (1 GB storage capacity) handled by the *TMS* and *xtage* services. Once data have been dispatched into cartridges, FOSTER relies on a plain-text database to access the different runs (identified by an unique number).
- Commands to build useful histograms (raw/cal time and energy spectra, *PSA-TOF* spectra, scalers ...) as well as built-in functions to handle these histograms: automatic energy calibration, automatic time calibration, time-of-flight monitoring and correction, ntuple production, ...

The final output of FOSTER is one ntuple "hbook" file per run, containing all decoded (and calibrated) information for each firing TAPS module and all decoded (but still raw) data for each FW and DB firing detector. The TAPS *PSA-TOF* contour files (section 5.4.1) for subsequent photon identification are also constructed using FOSTER.

ROSEBUD: This analysis tool performs the photon shower reconstruction in TAPS and the individual particle identification in the DB and FW detectors. ROSEBUD consists on a set of fully object-oriented C++ libraries based on the ROOT framework

[2] TMS software has been conceived at the "Rutherford Appleton Laboratory" (RAL) and developed by the HEP/VM community.

[3] Via the "cfortran.h" package by B. Burow.

[ROOT] and benefiting from all its functionalities (statistical and mathematical analysis, graphical interface, "trees" event files, etc.). ROSEBUD reads the "hbook" ntuples produced by FOSTER, analyzes each firing individual detector (containing only "hits") and outputs the final physical events (containing only particles) onto a DST "tree" file per run ready to be analyzed. It can handle either real data from the FOSTER decoding system or simulated data from the GEANT3-based simulation tool KANE.

KANE: KANE is a detector simulation package designed to study the TAPS response to various kind of electromagnetic (photons, electrons, positrons and muons) and hadronic (protons, neutrons and neutral mesons) particles and for various kinds of geometries [KANE96]. It is coded in FORTRAN and interfaces GEANT3 [GEANT] for the Monte-Carlo tracking of the passage of particles through the detectors (geometry definition, tracking of particles and graphical representation of the setup and particle trajectories). In its final version it contains the whole experimental setup (i.e. the FW and DB multidetectors apart from TAPS). Different input distributions (e.g. in energy and angle) for different particles can be defined by the user to test the response of one of the detectors or of the whole setup. The output of KANE is a "hbook" ntuple with a structure fully compatible with the experimental FOSTER ntuples, which can thus be subsequently analyzed by ROSEBUD-linked programmes. A comparison of the experimental and simulated data is hence done on equal footing using exactly the same analysis procedures.

As aforementioned, the R2 experiment produced 150 Gbytes of raw data (corresponding to $\approx$ 500 million events) in 14 days. A factor 10 of data reduction was achieved, after DB/FW zero suppression, detector calibration in FOSTER and particle reconstruction within ROSEBUD. The last level *"Data Summary Tapes"* (DST) production yielded 15 Gbytes of reconstructed data containing selected information relevant to higher level physics analysis from which the final results were deduced. These data fitted onto 20 DST data volumes (3490 cartridges of 1 GB capacity) stored at Lyon's Computing Center.

5.2 TAPS Energy calibration

When a BaF_2 fires, the two time-interval integration of the analog signal delivered by the PMT gives the values of E_n and E_w. Each one of these values (in channels) is to be transformed into energies (MeV) through a linear relation:

$$E_{cal}\ (\text{MeV}) \;=\; a \;+\; gain \cdot E_{raw}(\text{channels}) \tag{5.1}$$

The ordinate at the origin of the calibration line, a, is given by the first non-zero channel of the QDC: the *"pedestal"*. It corresponds to the (adjustable) charge delivered by the QDC in the absence of any input signal. The *gain* is determined with the aid of the known energy loss of high-energy cosmic muons in a TAPS module.

Indeed, to calibrate the crystals in the wide dynamic range of TAPS (the most energetic photons produced in the present experiment, $E_\gamma \approx 200$ MeV, could deposit more than 150 MeV in a single module) we used the cosmic muons traversing the detectors since no

radioactive source produces photons with comparable energies[4]. Cosmic muons (μ^+, μ^- with $c\tau$ = 658.6 m) originate from the weak-decay of atmospheric charged pions ($c\tau$ = 7.8 m) produced in interactions of the *primary* cosmic radiation (basically, protons and α-particles) with the air in the upper atmosphere. Muons represent more than 98% of *charged* particles arriving on earth at sea level[5]. These muons have a mean energy of $\approx$ 4 GeV at ground level and, thus, they behave as minimum-ionizing particles (MIPs) depositing an average energy of roughly $\approx$ 38 MeV in the 5.9 cm vertical thickness of the TAPS crystals (the energy loss per unit length of MIP muons in BaF_2 is, applying the Bethe-Bloch formula[6], $(dE/dx)_{min}$ = 6.6 MeV/cm).

The energy calibration of the wide and narrow components of each one of the 384 TAPS BaF_2 modules was performed with the help of the FOSTER package for the different sets of runs of the experiment. This takes into account possible detectors gain's drifts due to varying experimental conditions, like temperature fluctuations or HV changes. Muons were detected and recorded during beam-on time when they vertically traversed the detectors since they mimic a high-energy photon event and can be accepted by the different hard-photon triggers[7]. They could be identified in the energy spectra of individual modules as a broad (gaussian+linear) peak centered at a channel corresponding to $\approx$ 38 MeV (see fig. 5.2). Not always, however, the muon peak could be well identified. Therefore, for a few runs and/or detectors a time-gate in a selected region of TOFs was requested to construct the energy spectra. This gate was set in a region before the prompt photon peak where no reaction products were expected. The final value for the calibrated gain per module was obtained with the expression:

$$gain(MeV/ch.) = \frac{38.0\,(MeV)}{cosmic\ peak\,(ch.) - pedestal\,(ch.)} \tag{5.2}$$

The resulting average gain per module is around 98 KeV/channel. A final monitoring of the calibration lines (E_{cal} vs. E_{raw}) for both energy components, per set of runs and per detector was also performed to check the quality and the evolution of the energy calibration files all along the experiment.

[4]The highest-energy photon radioactive sources available are a ^{244}Cm-^{13}C source producing a 6.1-MeV photon from an excited state of ^{16}O, and an ^{241}Am-^{9}Be source delivering photons with 4.43 MeV from an excited state of ^{12}C.

[5]Cosmic fluxes for different particles at sea level (Hz/cm^2) are [PDG98, Zie96]: μ: 0.021, n: 0.0142, p: $1.14\cdot10^{-4}$, π: $1.53\cdot10^{-5}$.

[6]In general, the numerical value of the minimum ionization (more precisely, of minimum energy loss) is $dE/\rho dx \approx$ 1 - 2 MeV cm^2/g for all materials [Bock98].

[7]Given the counting rate of cosmics at sea level (0.02 Hz/cm^2) and the total surface of the six TAPS blocks (6 $\times$ 25 cm $\times$ 5.9 cm = 885 cm^2), a rough estimate gives about $\approx$ 18 muons traversing TAPS per second. Among the different triggers, the sum of the photon accepted events represented $\approx$ 65% of the total acquisition rate. Considering an average $\approx$ 60% trigger lifetime, this would yield roughly 7 muons recorded per second.

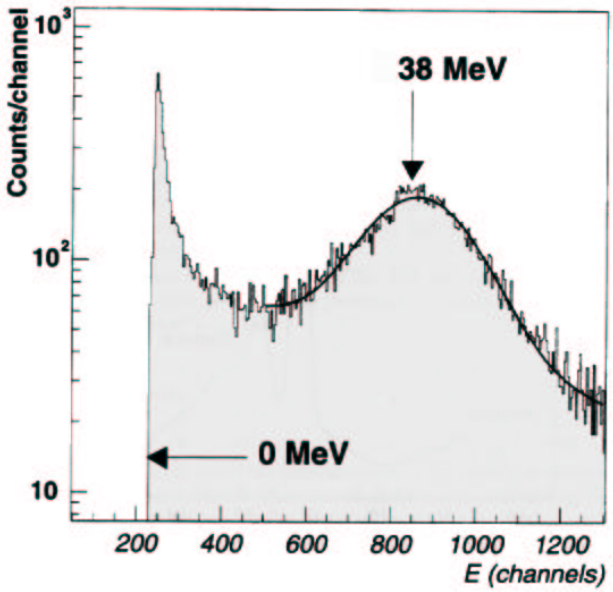

Figure 5.2: *Energy wide spectrum of a BaF_2 module during beam-time. The first arrow indicates the position of the QDC pedestal (0 MeV). The second one, indicates the position of the cosmic muon peak corresponding to a mean energy loss of 38 MeV in the BaF_2 crystal. The solid line corresponds to a fit of the signal to a gaussian+first degree polynomial function.*

5.3 TAPS Time calibration

5.3.1 Single detector time calibration

The time alignment of TAPS detectors relies on the time structure of the Ar beam. The AGOR cyclotron frequency was 37.1 MHz equivalent to a beam burst every $1/RF$ = 26.9 ns. In the occurrence of a nucleus-nucleus collision, the produced photons are the first particles to hit the TAPS modules. They need 2.2 ns to traverse the 66 cm distance separating the target position from each TAPS block.
In the former chapter I explained that the start of the TDC's is given by the logical AND between the master trigger signal and the RF signal, whereas the stop comes from a CFD signal delayed by a fixed value per module. The different triggers have a jitter in time of the order of 400 ns, which is more than one order of magnitude larger than the time between two consecutive beam pulses. Therefore, the triggers may overlap with an earlier or later RF-signal and, consequently, two prompt photon peaks appear in the accumulated TDC spectrum of each individual TAPS detector (see fig. 5.3). The observed first prompt peak, at 2.2 ns, and second photon peak, at 2.2 ns + 26.9 ns, can be used, thus, to individually align and calibrate the TDC's.

A typical calibrated *TOF* spectrum obtained during the ^{36}Ar+^{197}Au high counting-rate runs can be seen in figure 5.4. The width (FWHM) of the photon peak is 2.17 ns. This width is mainly due to the time spread of the beam burst delivered by AGOR which was around 2 ns. In the same figure, the broad structure arriving later in time, in the region

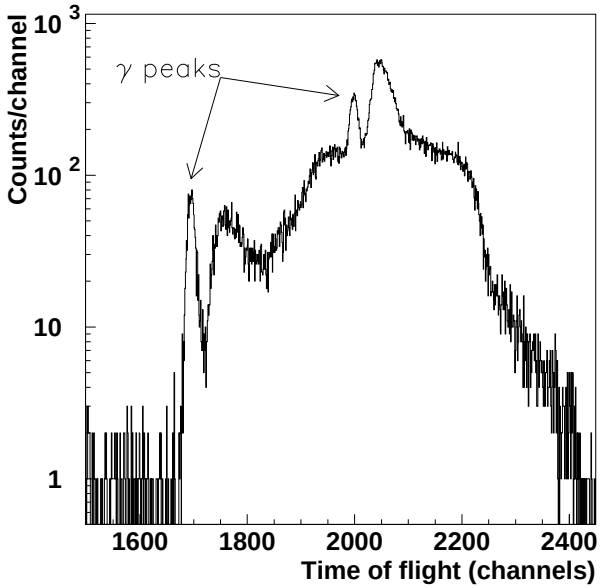

Figure 5.3: *Raw time spectrum for a BaF_2 module showing the consecutive beam pulses double-structure.*

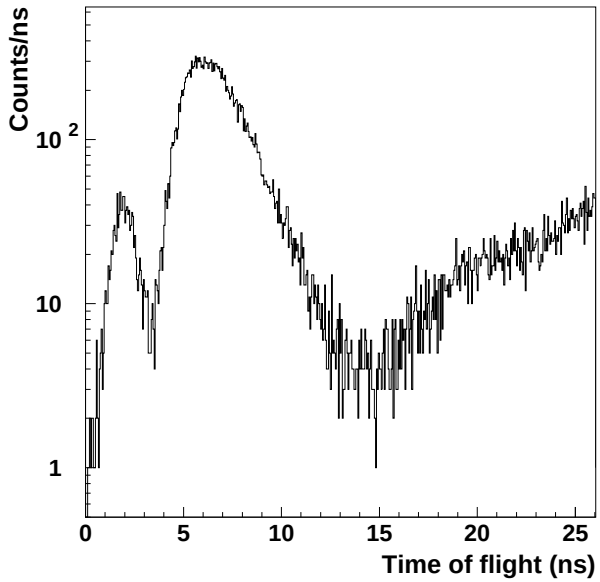

Figure 5.4: *Calibrated time-of-flight spectrum of a BaF_2-module during 20 experimental runs of the $^{36}Ar+^{197}Au$ reaction. The first (prompt) peak, centered at TOF = 2.2 ns, corresponds to the photons, the second "bump" to (slower) particles hitting TAPS.*

between 4 and 15 ns, corresponds to hadronic particles (mainly protons and neutrons) of increasingly smaller kinetic energies. The background signals before the prompt peak and beyond the particle "bump" correspond mainly to cosmic-muons events.

The final time-of-flight calibration factor for each detector is given by $TOF(ns) = 2.2 + TOF(channels) \cdot 1000 \cdot f_t$, with $f_t \approx 80$ ps/channel on the average. The range of the TDCs was 100 ns.

5.3.2 *TOF* drift correction

Drifts in the RF of the pulsed beam delivered by the AGOR cyclotron appeared all along the 14-days long beam-time due to several adjustments of the settings of the accelerator. To monitor the time stability of the beam and to correct for any drift, we accumulated every 10^5 events the aligned time spectra of the 384 TAPS modules in one single histogram, and determined the offset in the position (and the width) of the photon peak with respect to the expected position at 2.2 ns. The evolution all along the experiment of the photon peak can be seen in the upper part of fig. 5.5. The significant deviations with respect to the reference value were due mainly to an interruption of the acceleration system. The same spectrum can be seen after the correction for these RF drifts (lower part of fig. 5.5), the remaining "spikes" in the histogram correspond to events without beam that were ignored in the subsequent analysis.

5.3.3 Walk and cross-talk correction

In addition to the cyclotron-RF drifts, two more experimental effects can affect the registered *TOF* values: the cable- and TDC- induced cross-talk and the CFD walk. The "walk effect" in the CFD (the dependence of the discriminator response to the amplitude of the input signals) usually affects the position of the photon peak in the time spectra since those discriminators control the stop signals of the TDC modules [Marq95b]. This effect, of the order of 200 ps in our setup, is corrected in practice by constructing different *PSA-TOF* identification contours for 6 different photon energies domains (see Section 5.4.1). The correction of TDC cross-talk was not necessary in our experiment, at variance with former TAPS experimental campaigns, e.g. at the GANIL accelerator (see for example [Martt94, Marqt94]), mainly because the AGOR beam time resolution was anyhow of the same order as this effect, and in practice the finally obtained *TOF* spectra permitted a good particle identification.

The final resolution in the *TOF* measurements, after all time corrections, was 900 ps (FWHM), a value well appropriate for particle identification by time-of-flight.

5.4 Photon reconstruction: cluster analysis

All photons produced in this experiment (with distinctive energies in the region 10 - 200 MeV) generate an electromagnetic shower inside the BaF_2 crystals (see Appendix 1). Since the lateral dimensions of the BaF_2 modules are comparable with their Molière radius, most of the photon showers extend over more than one module[8]. The average

[8] 95% of an electromagnetic shower is laterally contained in a radius $R_{95\%} = 2\rho_M$.

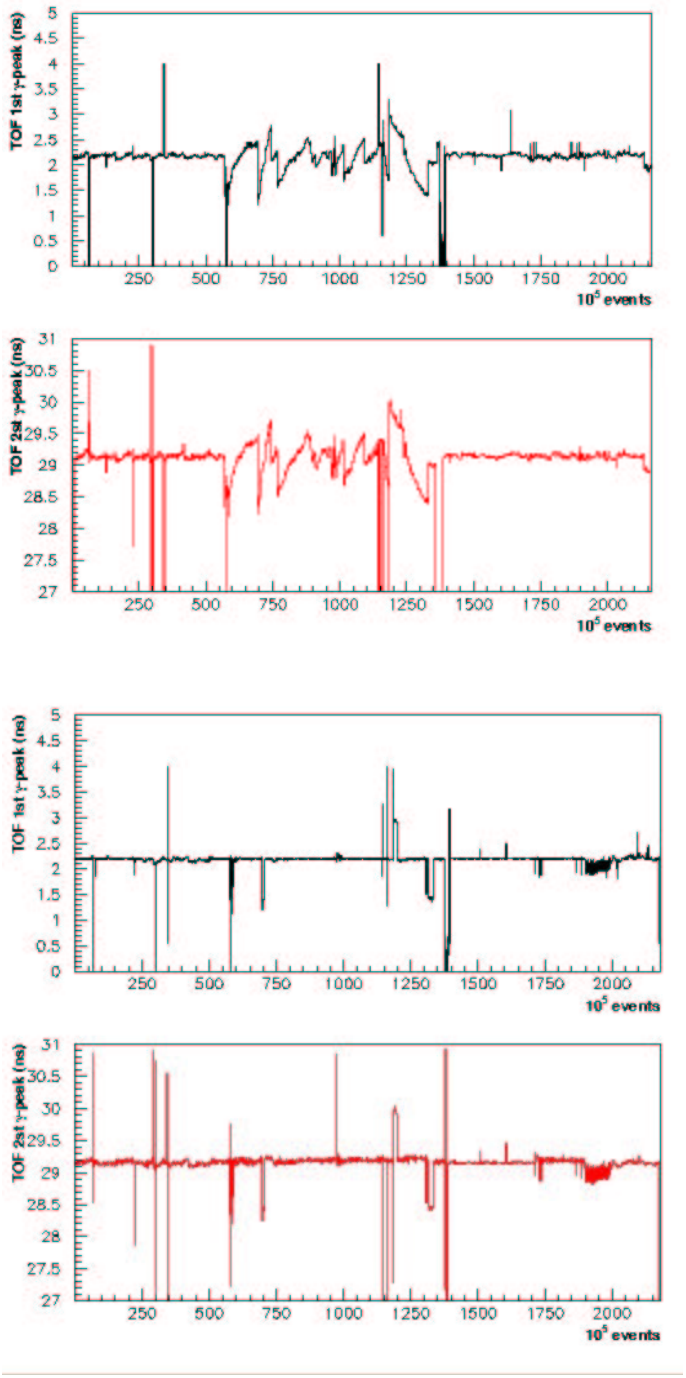

Figure 5.5: *Evolution of the position of the photon peak during the 14 days of experiment before (upper part) and after (lower part) the corrections of the RF drifts. The position of the peak is calculated every* 10^5 *accumulated events (one bin in the x-axis).*

Table 5.1: *Average number of BaF_2 modules firing with an energy deposition larger than 5 MeV for photons impinging TAPS with different experimentally measured energies. These multiplicities, obtained from experimental data, coincide very closely with the results of* GEANT *simulations.*

Incident photon energy (MeV)	30	60	120
Average cluster Multiplicity	1.2	1.6	2.2

number of BaF_2 modules (cluster multiplicity) which contain part of the electromagnetic shower with an energy deposition larger than 5 MeV (the threshold of the TAPS modules CFD) for different incident experimental photon energies are listed in table 5.1.

5.4.1 Single-detector particle identification (*PSA* vs. TOF)

The energy of a given photon incident on TAPS is obtained by summing up the information coming from the different neighbouring modules hit by the same electromagnetic shower. To reconstruct the electromagnetic shower one makes use of a clustering algorithm. The first task of this clustering routine consist in separating the desired photon signals from other non-electromagnetic signals. Indeed, since the BaF_2 crystals also respond to charged hadrons; protons, neutrons and other heavier nuclear fragments reaching TAPS will develop a hadronic shower. These hadronic showers are dominated by a succession of inelastic hadronic/nuclear interactions and, hence, show a quite different "topology" than electromagnetic ones. To be able to reconstruct a photon energy one must, first, identify the origin of the hits (electromagnetic, hadronic) through proper *PSA* vs. TOF, and CPV selections and then further disentangle the electromagnetic candidates between photons, electrons and cosmic muons.

We have seen in Section 4.6.4 that the shape of the electric pulse delivered by BaF_2 varies according to the specific ionization of the incident particle (highly-ionizing particles producing more light in delayed fluorescence decay). The *PSA*, defined as the ratio E_n/E_w, measures the proportion of prompt to delayed fluorescence light. When plotting *PSA* with respect to TOF we obtain a two-dimensional representation which exhibits different regions corresponding to the different particles (figure 5.6). From this plot constructed for different energy domains, one defines rectangular regions associated to each type of particle. The whole single-detector identification procedure is summarized in figure 5.7 and the obtained *PSA*-TOF contours used in the present experiment for the particle identification are given in table 5.2.

5.4.2 Clustering routine

The identification routine, implemented in the ROSEBUD libraries, assigns a "label" to each firing detector (*"electromagnetic"*, *"hadronic"* and *"cosmic"* candidates) and then proceeds with the clusterization algorithm to perform the shower reconstruction. A shower is defined as a continuous cluster of individual hit detectors. For each electromagnetic/cosmic cluster of neighbouring firing detectors (having at least one detector with

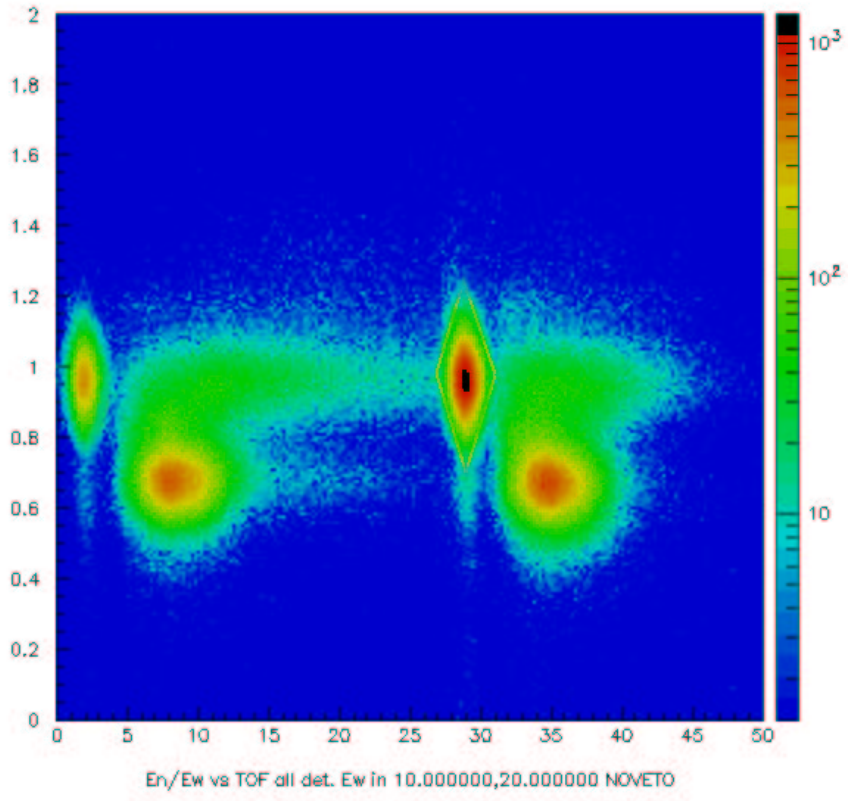

Figure 5.6: *PSA as a function of TOF for all particles detected in TAPS with energies 10 MeV $< E <$ 20 MeV. Photons events appear centered around PSA = 1 and TOF = 2.2 (+ 26.9) ns. Charged hadrons have PSA $\approx$ 0.7 and TOF = 5 - 15 (+ 26.9) ns (see table 5.2).*

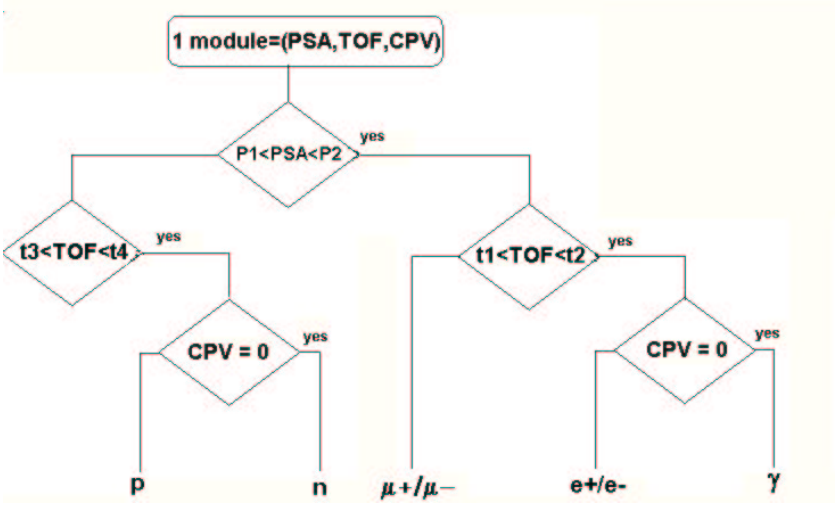

Figure 5.7: *Schema of the particle-identification procedure in TAPS as implemented into* ROSEBUD. *It makes use of the PSA $= E_n/E_w$, TOF (time-of-flight) and CPV (charged-particle-veto) information. Adapted from [Aphe98].*

Table 5.2: *List of the PSA-TOF rectangular contours used in the present experiment for particle identification in TAPS.*

	Energy range	*TOF*	*PSA*
Photons:	0 - 5 MeV	0.21 - 4.70	0.1 - 1.8
	5 - 10 MeV	0.10 - 4.30	0.1 - 1.6
	10 - 20 MeV	0.10 - 4.10	0.6 - 1.3
	20 - 60 MeV	0.32 - 3.66	0.83 - 1.15
	60 - 250 MeV	0.32 - 3.50	0.83 - 1.15
Neutrons:	0 - 250 MeV	5.0 - 15.0	0.1 - 1.8
Protons:	0 - 250 MeV	5.0 - 15.0	0.4 - 0.8
Cosmics:	0 - 5 MeV	-4.49 - 0.00	0.1 - 1.8
	5 - 10 MeV	-4.20 - 0.00	0.1 - 1.6
	10 - 20 MeV	-4.00 - 0.00	0.6 - 1.3
	20 - 60 MeV	-3.34 - 0.00	0.83 - 1.15
	60 - 250 MeV	-3.18 - 0.00	0.83 - 1.15

$E_{thresh} \geq 10$ MeV), the following four basic parameters[9] are computed:

- **Cluster multiplicity:** M_X is defined as the number of contiguous hit modules with an energy surpassing a given threshold $E_i > X$ MeV. (M_0^∞ is defined as the total number of detectors in a cluster.)

- **Cluster energy:** The energy of the cluster is:

$$E = \sum_i E_i \tag{5.3}$$

  where E_i are the individual energies of each BaF_2 belonging to the cluster. Detectors with energy below 0.4 MeV are, however, discarded from the summation in our ROSEBUD analysis.

- **Cluster direction:** The incident direction of the photon, with energy E, is obtained from the logarithmic-weighted gravity-center of the cluster according to the formula [Awe92]:

$$\vec{R} = \frac{\sum_i \omega_i \vec{r}_i}{\sum_i \omega_i} \tag{5.4}$$

$$\omega_i = \max\left(0, \omega_0 + \ln\frac{E_i}{E}\right) \tag{5.5}$$

  where $\vec{r}_i$ denote the positions of the modules and $\omega_0 = 4$ is a dimensionless parameter determined from GEANT simulations.

[9] Actually, 4 more global cluster parameters: *"Energy dispersion"*, *"Time dispersion"*, *"Surface"* and *"Linearity"* can be also computed in different experimental filters. Such parameters have been used in other experiments in order to further clean the spectrum of hard-photons from hadrons and cosmic contaminants in the very-high energy region (see [Mart97, Aphe98]).

- **Cluster time-of-flight:** The mean value of the TOF of the modules (with individual times t_i) belonging to the cluster is calculated with the formula:

$$T = \frac{1}{M_0^{\infty}} \sum_{\substack{i \\ (E_i > E_t)}} t_i \tag{5.6}$$

  where only detectors with energy above E_t = 3 MeV are taken into account.

Cluster Energy

Once the cluster energy has been computed according to relation (5.3), two additional corrections due to the TAPS experimental response to photons are still needed to achieve an absolute energy calibration:

1. **Shower leakage**: It can happen that the absorption of the electromagnetic showers by TAPS is not total. Part of the photon shower may leak out of the back side of the modules (as well as out of the front, between the detectors modules and through the sides of the detector blocks for the most outside modules). The experimental response function of TAPS blocks to photons can be seen in figure 5.8 where the "line shape" measured for a monochromatic E_γ = 55 MeV photon impinging an array of 64 BaF_2 modules is shown [Gabl94]. A reasonable good description of the shape is obtained with a parametrized Gaussian function modified by an exponential tail at the low energy side [Matu90]:

$$\begin{aligned} &y = N\ \text{Gauss} && \text{for} \quad E \geq E_{peak} \\ &y = N\ \left[\text{Gauss} + \exp\left(\frac{E-E_{peak}}{\lambda}\right)(1-\text{Gauss})\right] && \text{for} \quad E \leq E_{peak} \\ &\text{where} \quad \text{Gauss} = \exp\left(-\frac{4\ln 2 (E-E_{peak})^2}{\Gamma^2}\right) \end{aligned} \tag{5.7}$$

   The parameter N is a normalization factor, the FWHM Γ of the Gaussian describes the high-energy side of the peak, whereas λ describes the low-energy tail. Finally, the most probable energy E_{peak} is slightly smaller than the incident E_γ = 55 MeV energy. The value of E_{peak} turns out to be a simple linear function of the incident photon energy: $E_\gamma = f_{leak} \cdot E_{peak}$. The multiplicative factor f_{leak} accounts basically for the aforementioned leaking effect which leads to a systematic shift of the mean response to (slightly) lower energies. GEANT3 simulations of the TAPS response function of our setup yielded an average value f_{leak}=1.089.

2. **Muon vs photon scintillation**: Apart from the former energy loss due to the photon shower longitudinal punchthrough, there is an additional systematical shift (of comparable order) to lower values in the energy. It is due to the different response of BaF_2 to cosmic high-energy muons (used to individually calibrate the detectors) as compared to photons. Actually, whereas photons develop electromagnetic showers in matter, GeV-energy muons lose energy in matter primarily through ionization [PDG98]. This results in a difference in the efficiency to produce scintillation light in BaF_2. This effect can be also accounted for with one single factor f_{scin}.

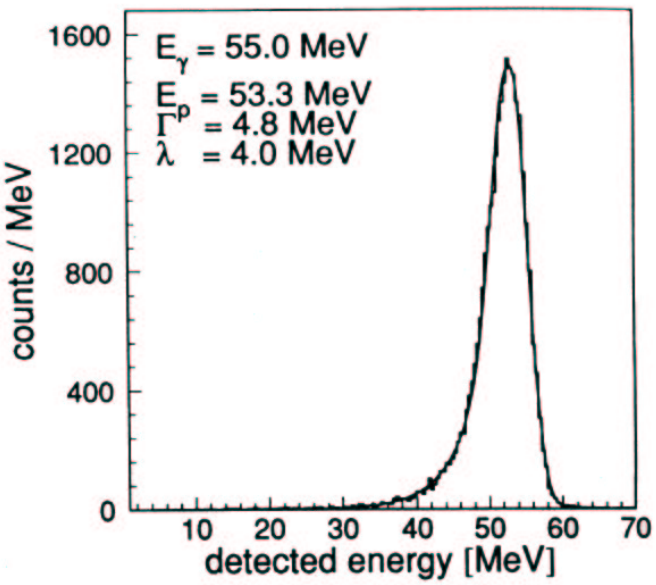

Figure 5.8: *Experimental line shape of a photon of E_γ = 55 MeV incident in a TAPS block, compared to the fitted analytical response function given by eq. (5.7). The values of the fit parameters are shown in the figure. From [Gabl94].*

The global correction factor for the energy, $f_E = f_{leak} \cdot f_{scin}$, is calculated from the ratio of the known neutral pion rest mass (m_{π^0} = 134.97 MeV) with respect to the experimental value measured in our experiment. This mass, $m_{\pi^0}^{exp}$, is obtained from the $\gamma\gamma$ invariant-mass[10] spectrum:

$$m_{inv} = \sqrt{2E_1E_2(1-\cos\theta_{12})} \tag{5.9}$$

Taking all detected γ pairs, the measured m_{inv} distribution peaks at $m_{\pi^0}^{exp}$ = 114.4 MeV (see Section 6.1.4). The global energy correction factor is, thus:

$$f_E = m_{\pi^0}/m_{\pi^0}^{exp} = 1.18 \tag{5.10}$$

and since $f_{leak} = m_{\pi^0}/m_{\pi^0}^{GEANT}$ = 1.089, we obtain also $f_{scin} = f_E/f_{leak}$ = 1.083. Therefore, the correction effects due to the leaking of the electromagnetic showers and due to the different efficiency of producing scintillation light between photons and muons, are of the same order.

The finally obtained energy correction factor f_E takes into account the average TAPS experimental response function to photons and corrects also for other minor effects affecting the energy calibration like e.g. the CFD threshold settings. The energy deposited

[10] For a general decay $X \to 1+2$, the momenta $\vec{p}_i$ and energies E_i of the two decaying products are related to the original particle mass through the invariant-mass formula:

$$m_X^2 = \left(\sum_i p_i^\mu\right)^2 = (E_1+E_2)^2 - (\vec{p}_1+\vec{p}_2)^2 = 2(E_1E_2 - p_1p_2\cos\theta_{12}) - (m_1+m_2)$$

For $\pi^0 \to \gamma\gamma$, this general expression yields ($E_i = p_i, m_i = 0$): $m_{\pi^0} = \sqrt{2\,E_1E_2(1-\cos\theta_{12})}$

Table 5.3: *Position and angular resolution for photons impinging a TAPS block with different incident energies. The angular resolution is calculated assuming the TAPS block is located 66 cm away from the target. Adapted from [Vene94].*

Incident photon energy (MeV)	50	100	200
Position resolution (cm)	2.1	1.9	1.7
Angular resolution (°)	1.8	1.6	1.5

in each detector *i* is then finally given by:

$$E_i(\mathrm{MeV}) \;=\; f_E \cdot [a_i + gain(\mathrm{MeV}/ch.) \cdot E_i(ch.)] \tag{5.11}$$

where $gain(\mathrm{MeV}/ch.)$ is obtained from expression (5.2) and a_i is the pedestal value. The reliability of such a calibration method was checked in measurements using monoenergetic tagged photons in the energy range between 45 and 790 MeV [Matu90, Gabl94]. These measurements also give a parametrization of the energy resolution for TAPS as: $\sigma/E \;=\; 0.59\%/[E_\gamma(\mathrm{GeV})]^{1/2} + 1.91\%$ (FWHM). In the photon energy range of interest for our experiment we have taken, therefore, an average energy resolution of $\pm$ 2 MeV.

Cluster position

As a photon shower spreads over more than one module we can determine its incident position with a better resolution than the detector lateral size ($\pm$ 2.9 cm equivalent to $\pm 2.5^\circ$ angular resolution at a 66 cm distance). Table 5.3 shows the mean position and angular resolution achieved with the modified gravity-center formula (5.4). An additional shower depth correction [Marq95b] has been applied in the present analysis to take into account that a photon traverses a mean distance $Z = X_0^{max} \cdot [0, \ln(E/E_c) + 1.2]$ (X_0 being the BaF_2 radiation length) inside the crystal before developing an electromagnetic shower.

The average final position resolution for the hard-photons studied in this thesis has been, therefore, taken to be $\pm$ 2.5 cm corresponding to a mean angular resolution of $\pm 2^\circ$.

5.5 Dwarf-Ball analysis

In this section I will describe the procedure for light-charged- particle (LCP) isotopic separation and intermediate-fragment (IMF) identification in the Dwarf-Ball multidetector using the pulse-shape techniques[11] (*slow* vs. *tail* and *fast* vs. *tail* plots) mentioned in Sect 4.7.3.

5.5.1 DB light-charged particle isotopic identification

As mentioned in 4.7.3, a charged particle hitting a DB module will deposit a given energy ΔE in the thin fast plastic and will usually stop in the CsI(Tl) crystal depositing the rest of its energy E. If we just consider, for the moment, the two-scintillation-component response of CsI(Tl) ($E = E_{sl} + E_{ta}$) and we plot E_{sl} versus E_{ta}, one can identify different parabolas corresponding to different particles (fig 5.9). Those parabolas do not increase uninterruptedly, there is a maximum point for which the E_{sl} and E_{ta} start decreasing both at the same time: the parabola "closes back to itself" defining a loop-like structure. This effect is due to the finite thickness of the CsI(Tl) crystals: the most energetic particles will be able to traverse them an will deposit less energy in the crystal than those that are stopped. The maximum energy a particle can deposit in the CsI(Tl) (just before punching through) corresponds to the maximum of the loop. This is the so-called *"punchthrough"* back-bend.

The position of the "punchthrough" points changes for each type of particle according to its product Z^2A (see Appendix 1). This characteristic allows to separate[12] the different isotopes of H (p, d and t) and He (^{3}He and α). The regions above the proton loop and below the α loop correspond to the neutron/photon and IMF signals respectively. The parabola separating the IMF region from the α (and the rest of LCP) signals was also determined for each individual detector:

$$E_{sl} = E_{s_0} + c_1 \cdot E_{ta} + c_2 \cdot E_{ta}^2 \tag{5.12}$$

For each DB module a linearization parameter was defined as: $P_{LCP} = E_{ta}/(E_{sl} - E_{s_0})$, allowing to project the bidimensional $E_{sl} - E_{ta}$ histograms. With this scaling, all the P_{LCP} vs. E_{ta} maps have the lines for each particle at approximately the same P_{LCP} value [Mora00]. Fig. 5.10 shows the linearized P_{LCP} histogram obtained with the different peaks corresponding to the different light-charged-particles detected.

[11] Before applying the PSA technique, however, a preliminary step consisted in properly selecting those hits recorded by the DB which effectively belong to the same reaction. Thus, for each one of the 64 detector a time gate was set around the prompt peak to discard in the subsequent analysis those pileup events not belonging to the prompt coincidence.

[12] Additionally, these punchthrough points are also used to perform the energy calibration of the (non-linear) CsI(Tl) response. Since the punchthrough points correspond to the particles being stopped at the end of the CsI(Tl) telescope, knowing the traversed plastic thickness it is easy to calculate, with the help of range-energy tables, the energy of these particles. In this experiment, however, no energy calibration for the charged particles has been undertaken since only the LCP and IMF multiplicity information was needed.

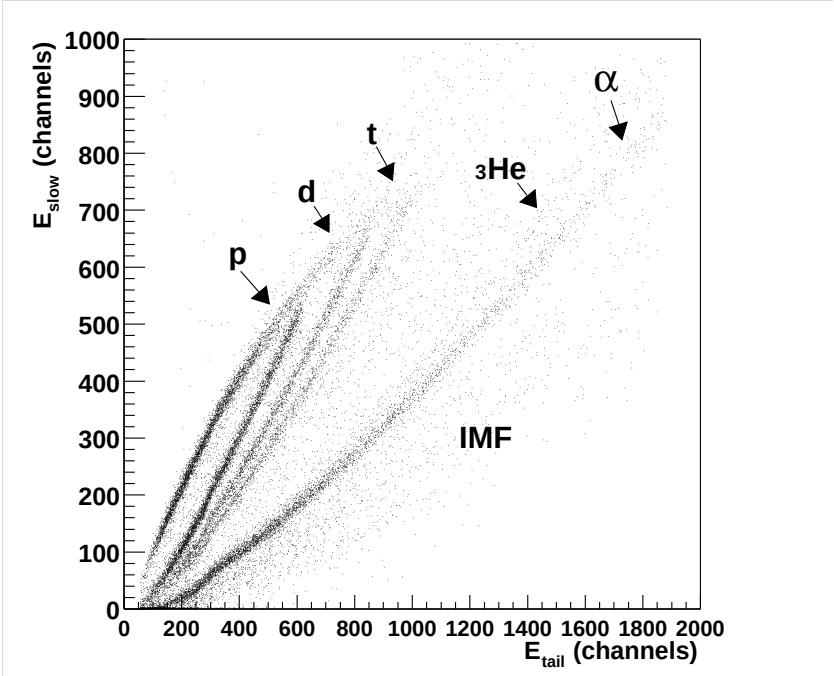

Figure 5.9: *Isotopic light-charged-particle identification with a E_{sl} vs. E_{ta} bidimensional plot for a CsI(Tl) crystal of the DB multidetector. The different "punchthrough" points for the hydrogen (p,d,t) and helium (^3He, α) can be seen. The area above the proton loop corresponds to the region of neutron and photon signals. The area below the α line is populated with IMF events.*

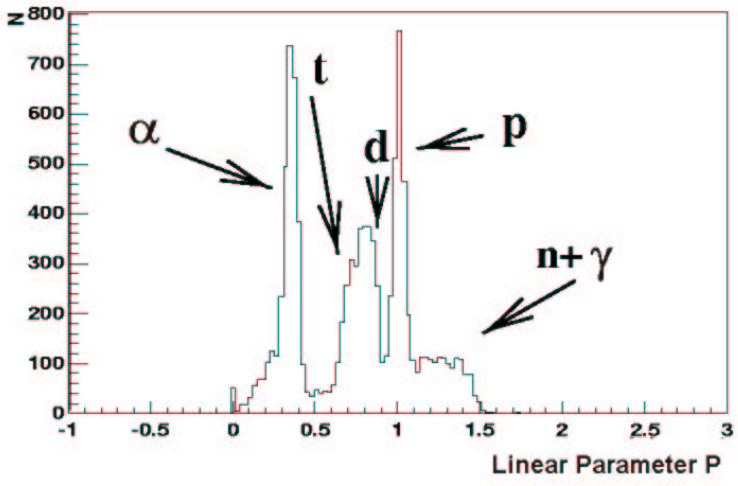

Figure 5.10: *Linear parameter P_{LCP} histogram showing the peaks of the 3 isotopes of hydrogen and the 2 isotopes of helium. From [Mora00].*

5.5.2 DB IMF identification

For each DB module, the parabola that separates the LCP region from the IMF signals (in the E_{sl} vs. E_{ta} plots) has been stored in data files to be later used by our particles- and particles-photon analysis programmes. This parabolas will allow to separate both types of reaction products and, among others, calculate the respective multiplicities M_{LCP} and M_{IMF} for our impact-parameter and multifragmentation studies respectively (see Section 7.1).

In order to individually identify the different charge of the IMF we make use of the E_f (thin DB plastic scintillation signal) vs. E_{sl} (first CsI(Tl) scintillation component) bidimensional plots (fig. 5.11). Again, by using the observed linear dependence $E_{sl} = A + B \cdot E_f$, we can perform a linearization procedure of this bidimensional array to obtain an uni-dimensional histogram from which the different IMF can be more easily separated. For each detector the following linearization function (of arbitrary units) is computed:

$$P_{IMF} = E_f - B \cdot E_{sl}/A \tag{5.13}$$

In fig. 5.12 we present the projection of fig. 5.11 through the parameter P_{IMF}. The different peaks give us the charges Z of the LCPs and IMFs up to $Z \approx 10$. Several tables with the linearization parameters used in the present experiment can be found in [Mora00].

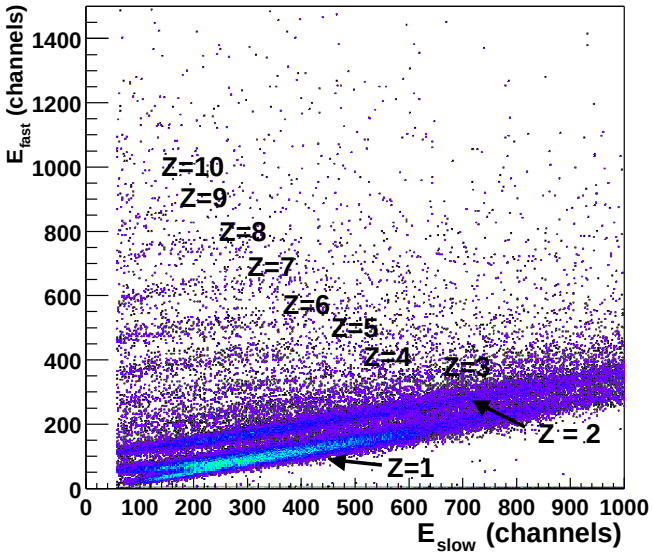

Figure 5.11: *Scatter plot of the fast vs. slow energy component from the same detector as in fig. 5.9 showing the different branches corresponding to the intermediate mass fragments for Z up to 10. The isotopes of H and He are not resolved in this type of plot.*

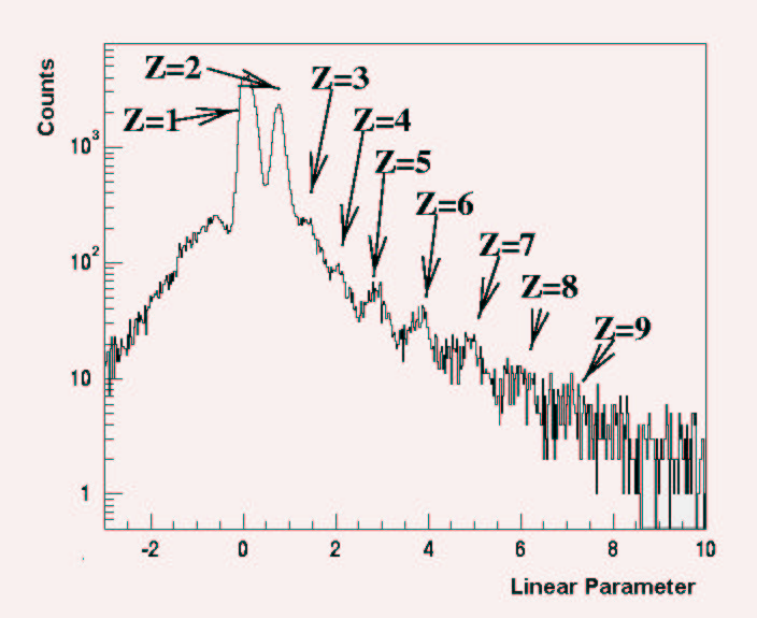

Figure 5.12: *Linearization plot of the projected E_f vs. E_{sl} bidimensional histogram shown in fig. 5.11. Each peak corresponds to the different charge Z of the particles and fragments produced in the heavy-ion reaction. Adapted from [Mora00].*

5.6 Forward Wall analysis

In this section I will outline the procedure for charged particle identification in the Forward Wall multidetector. The first step (see fig. 5.1) consists in selecting out the particles produced in the recorded reaction from the random background of uncorrelated events. The random events appear in the spectrum since the time-of-flight is measured relative to the radio frequency (RF) of the cyclotron. A gate is set on the prompt peak of each one of the 92 detectors in order to select for further analysis only those events with a prompt coincidence. The second step consists in additionally filtering the particles produced in the recorded reaction event using the "pileup" information for each FW module. Once this procedure has been applied, we can use the corrected $\Delta E - E$ spectrum to separate the LCP's from the IMF's.

5.6.1 FW LCP/IMF separation

An example of the standard $\Delta E - E$ method for charged-particle identification with a phoswich multi-detector is shown in fig. 5.13. The diagonal in such a E_{sh} vs. E_l representation corresponds to low energy particles that stop in the front (fast) NE102A layer, hence producing only the short signal: their light output is $\Delta E = C \cdot E$. Particles with higher energies punch through the NE102 layer and start traversing the second NE110 (slow) scintillator, giving rise to the different "banana-shaped" bands. From these shapes, particles can be identified. The band starting points correspond to the punchthrough backbends which differ for particles with different Z. In general, the heavier the particle the more energy it needs to traverse the first layer, so the increasing punchthrough points[13] correspond to increasingly higher Zs. The isotope identification of hydrogen can be also done (inset of fig. 4.19) but is not as direct as in Dwarf-Ball E_{sl} vs. E_{ta} plots. From this plot the IMF have been separated from the LCP on an event-by-event basis by determining for each FW detector the separation line between He and Li.

The obtention of such $\Delta E - E$ plots for each FW module is, however, not that straightforward. As explained in the FW electronics Section (4.8.4), we use 6 sets of common-gate ADCs for the "short" and "long" charge-integration of the detector signals of the 92 detectors. Thus, each ADC generates a common ("short" and "long") gate for 16 channels, i.e. all channels are integrated over the same time interval. Although this solution economizes the amount of electronics, it has the disadvantage that in multi-hit events the difference in arrival time between the analog and gating signals is not fixed due to time-of-flight differences between particles entering the various detectors and due to different delays in the electronics chain[14] [Leeg92]. Indeed, when two, or more, phoswiches fired, the start of the common gate is determined by the first arriving phoswich signal. As a result, the charge collected for the rest of firing detectors in the short and long gates will be slightly smaller as compared to single-hit events. When all events are mixed this leads to a deterioration of the particle identification (left panel of fig. 5.15). Two methods

[13] Like in the Dwarf-Ball case (see Section 5.5.1), the known position of these punchthrough points would allow for an energy calibration of the individual modules.

[14] In our setup, additionally, the 60 large detectors had PMTs with faster response times than those of the 32 smaller phoswiches. This fact, and an additional cable-length difference, resulted in a maximum $\approx$ 20 ns time difference between the outer and inner detectors, comparable to the $\approx$ 27 ns RF time.

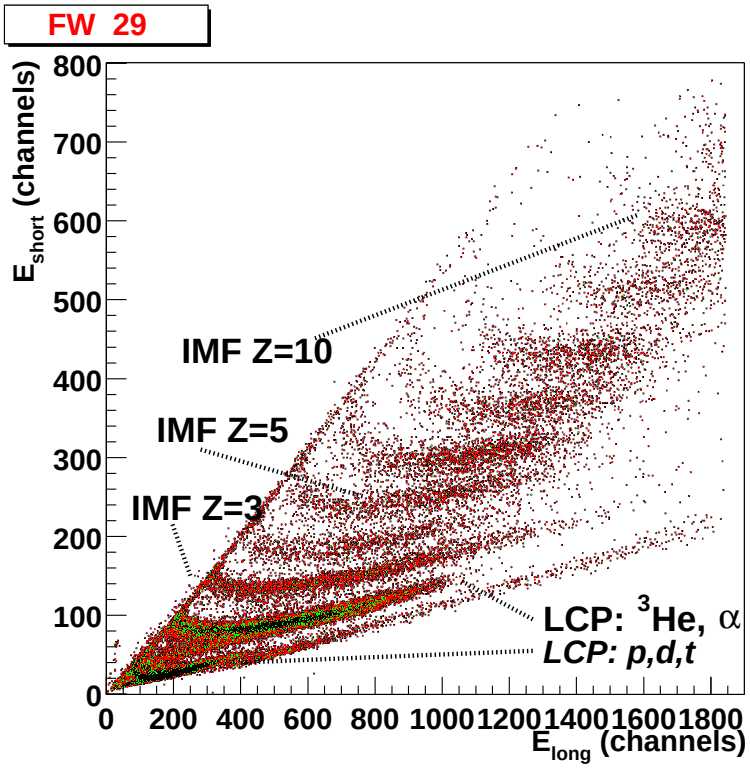

Figure 5.13: *Forward-Wall particle identification with the $\Delta E - E$ plot of a single module.*

have been applied so far to correct for this effect: either using the measured time difference between gate and phoswich signal [Leeg92] or combining a single integration over the pulse shape with a measurement of the signal-over-threshold time [Wiss97]. In the present experiment, a different correction procedure making use of the so-called *"pileup TDC"* information has been applied. The idea consists in storing the time of the common-gate generation (the CFDs "OR" of each group of 16-phoswiches) for each one of the 6 ADCs. This results in the spectra of fig. 5.14 showing several peaks corresponding to the particles produced in consecutive beam bursts. With the help of this spectrum the time of the common gate can be related to the RF signal of the accelerator. Considering only the signals with a *"PileupTDC"* belonging to the two most prominent peaks (the rest are uncorrelated background events) and selecting them separately we obtain the "clean" E_{sh} vs. E_l plot shown in the right panel of fig. 5.15.

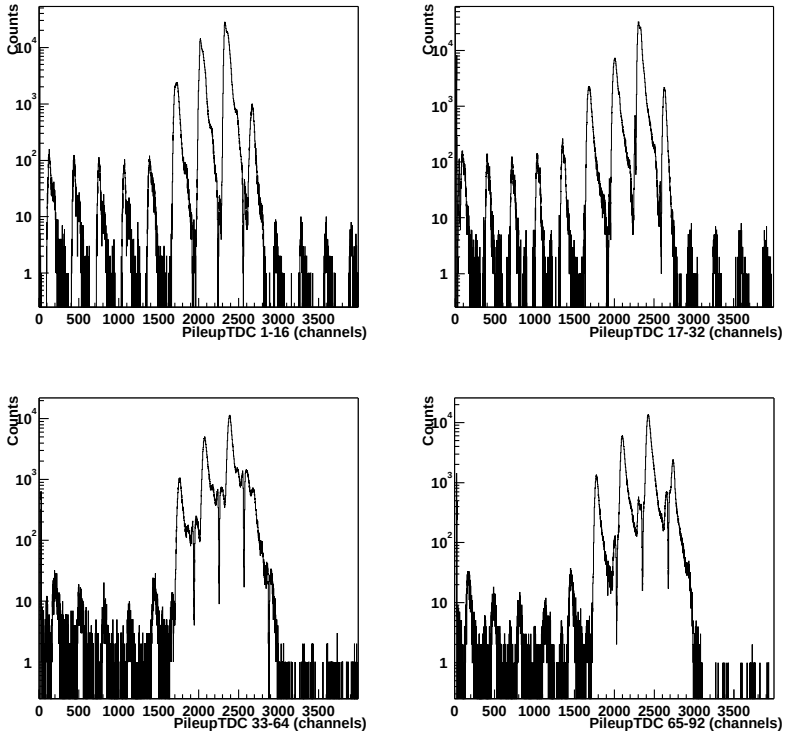

Figure 5.14: *"Pileup TDC" histogram ("OR" of the CFDs of each group of 16 or 32 common-gated phoswiches) for the four groups of 16(32) detectors of the FW. Only the events lying within the two most outstanding peaks have been retained for subsequent analysis.*

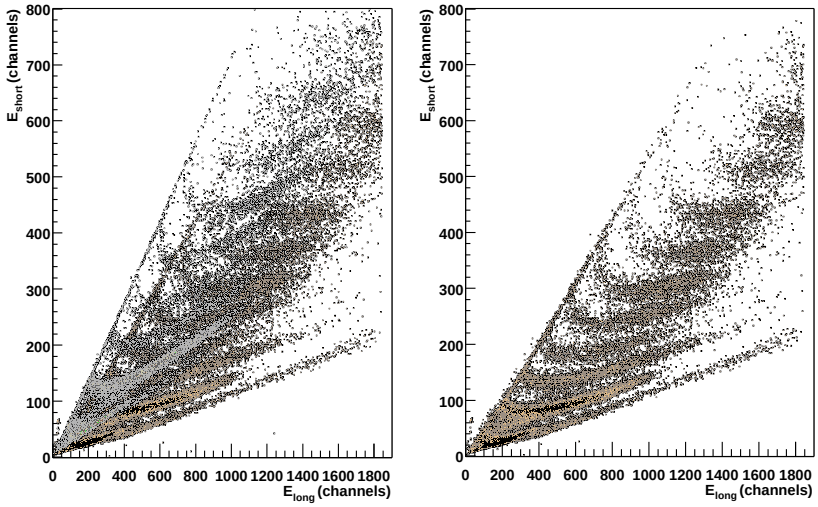

Figure 5.15: *Example of the "Pileup TDC" correction method. The left panel shows the raw E_{sh} vs. E_l plot, the right panel shows the same data after selecting a single peak in the "Pileup TDC" histogram (fig. 5.14).*

Chapter 6

Inclusive experimental results

Summary

6.1 Hard-photon energy spectra 122
6.1.1 Raw photon spectrum 122
6.1.2 Detector response function 124
6.1.3 Cosmic-rays background 125
6.1.4 Photons from neutral pion decay 125
6.1.5 Corrected inclusive photon spectra 128
6.1.6 Direct and thermal slopes and intensities 139
6.2 Hard-photon angular distributions. Source velocity analysis 142
6.2.1 “Direct” and “thermal” hard-photon angular distributions 142
6.2.2 Total hard-photon ($E_\gamma > 30$ MeV) angular distributions 147
6.3 Inclusive charged-particle and fragment distributions 153
6.3.1 Inclusive charged-particle multiplicities 153
6.3.2 Inclusive LCP and IMF multiplicities 157
6.4 Inclusive cross-sections and multiplicities 160
6.4.1 Cross-sections formulae 160
6.4.2 Charged-particle detection efficiencies 161
6.4.3 Hard-photon detection efficiency 162
6.4.4 Total reaction cross-sections 164
6.4.5 Hard-photon production cross-sections and multiplicities 166

Dealing with nucleus-nucleus reactions, a first analysis of the experimental data usually considers the inclusive measurements of the different observables. Namely, the study of $A + B \rightarrow X$ (where, e.g., X = γ, LCP, IMF) without any selection of a particular final-state of the reaction. The inclusive results for photon production in the four reactions studied are presented and discussed in Sections 6.1, 6.2 and 6.4. This discussion includes the shape of the photon spectra, the photon angular emission pattern and their absolute cross-sections and multiplicities. The particle inclusive data for total particle, LCP and IMF multiplicities are presented in Section 6.3, and the total reaction cross-sections in Section 6.4.4.

(Data from exclusive reactions aiming at the study of selected γ-particle exit-channels, to investigate the impact-parameter dependence of the hard-photon spectra and yields, will be presented in chapter 7.2. A primary interpretation of the whole inclusive and exclusive data is done in Section 7.4 of the next chapter.)

6.1 Hard-photon energy spectra

6.1.1 Raw photon spectrum

The inclusive raw photon spectra (fig. 6.1) measured for the ^{36}Ar+^{197}Au system and transformed into the NN center-of-mass ($\beta_{NN} \approx 0.18$) is constructed for the events satisfying the minimum-bias trigger "TAPS NEU LOW*DB1" accumulated during the low counting-rate runs of the experiment. The energy spectrum is obtained from $\approx 5 \cdot 10^6$ photons emitted in coincidence with some charged particle[1] and ranges from $E_\gamma \approx 15$ MeV, the threshold value of the BaF_2 leading-edge discriminators, up to more than $E_\gamma = 200$ MeV, i.e. above the kinematical limit $E_\gamma^{max} \approx 194$ MeV, given by eq. (3.2), for a heavy-ion reaction at 60A MeV bombarding energy. Before carrying out the physics analysis of this photon spectrum in order to study the characteristics of the produced photons, this raw spectrum must be corrected to take into account three experimental distortions:

- the TAPS (and Dwarf-Ball) detector response function,
- the cosmic background events (mainly muons coming from the upper part of a TAPS block in coincidence with the reaction trigger, not hitting the charged-particle veto and, thus, potentially misidentified as hard-photons), and
- the contribution coming from the two-photon decay of the neutral pions produced in the reaction.

In the next three sections we quantitatively determine the importance of these contributions in the raw energy spectrum and discuss how we have corrected their effects to retrieve the originally emitted photon spectrum.

[1] The use of a "photon*particle" trigger and not a pure photon trigger is justified in order to select those photons really coming from a nuclear reaction (and not e.g. "neutral"-like cosmic events mimicking a high-energy photon) as signaled by the detection of other reaction products of the collision (see the discussion in Section 6.4.3).

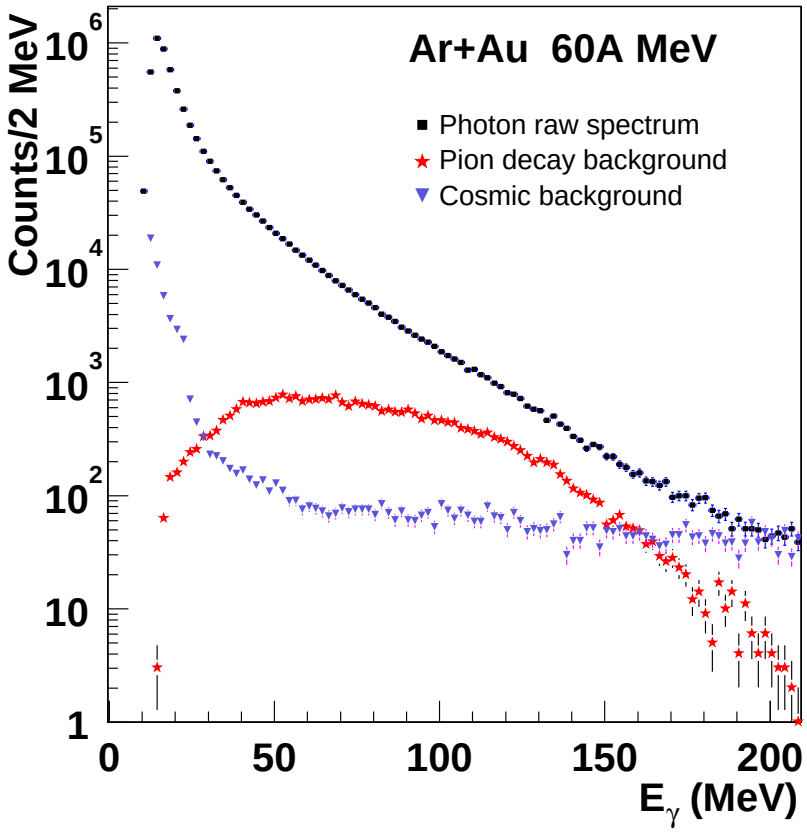

Figure 6.1: *Raw inclusive energy spectrum of photons measured with TAPS (rectangles) for the $^{36}Ar+^{197}Au$ system during the low counting-rate runs of the experiment. The triangles indicate the cosmic background and the stars the contribution of photons stemming from the decay of the π^0 produced in the reaction.*

6.1.2 Detector response function

In section 5.4.2, it was shown that the TAPS response function to photons, smears the original delta function $\delta(E - E_\gamma)$ of an incident monoenergetic photon with energy E_γ into a distribution best described by a narrow gaussian centered at a $E_{peak} = (1/1.089) \cdot E_\gamma$ with an exponential tail in the low-energy side. This finite resolution effect may modify the measured hard-photon energy spectrum. In section 3.3 it was mentioned that the energy spectrum of hard-photons emitted in heavy-ion reactions could be parameterized with two exponential functions characterized by inverse slope parameters E_0^d and E_0^t. To asses how the TAPS detector response function and our photon identification and reconstruction procedure may modify the hard-photon spectrum and, more explicitly, these slope parameters, GEANT3 Monte Carlo calculations have been performed with the KANE package. Several photon distributions with exponential shape and varying slope parameters were fed into the simulation with and without the presence of the Dwarf-Ball detector system in between the target and TAPS.

The first important conclusion of such analysis is that TAPS (and our photon reconstruction algorithms) correctly restore the initial hard-photon energy exponential distribution without significantly altering the form of the original exponential spectrum, even with the Dwarf-Ball multidetector in place. The slope parameter E_0^{meas} determined from the simulated data analysis remains close to the input slope parameter originally introduced into the KANE simulation E_0^{actual} (fig. 6.2). This procedure was performed for two different sets of simulations with and without the DB (fig. 6.2). This observation leads to two main conclusions:

- Both slopes (E_0^{actual} and E_0^{meas}) are roughly the same below $E_0 \approx 10$ MeV, although a small deviation appears towards somewhat lower measured values for higher slope values. The dependence between the measured and the original slope is linear over all the range and can be parametrized, according to the fit ($\chi^2/\nu = 0.01$) of fig. 6.2, by the conversion expression:

$$\begin{aligned} E_0^{actual} &= a \cdot E_0^{meas} + b \,, \\ \text{with } a &= 1.09 \pm 0.01 \text{ and } b = -0.60 \pm 0.03 \text{ MeV} \end{aligned} \tag{6.1}$$

- Although the simulations point out a global photon efficiency loss of 10%, due to the conversion of hard-photons in the Dwarf-Ball material (see Section 6.4.3), the Dwarf-Ball has no major influence on the exponential shape nor on the measured slope parameter. Only a minor lowering of 2% of E_0 value with respect to the case without the DB has been deduced, which can be accounted for within the fit errors of the same correction formula.

The effect of TAPS (and the DB) on the hard-photon spectra is thus small and susceptible to be quantified and corrected for with equation (6.1). Henceforth, for all slope parameters of the exponential hard-photon energy distributions quoted in this work, the correction given by formula (6.1) has been applied.

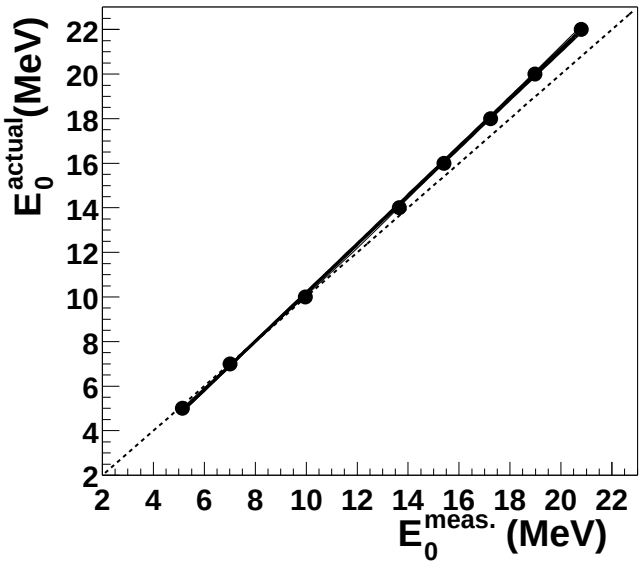

Figure 6.2: *TAPS and DB detector response influence on the inverse slope parameter of exponential hard-photon spectra simulated with the* KANE *package (E_0^{actual} versus E_0^{meas}). The wide solid line is obtained for TAPS alone as well as for the Dwarf-Ball in between the target and TAPS. The dashed line corresponds to the ideal response function.*

6.1.3 Cosmic-rays background

A first reduction of TAPS events originated by cosmics rays from those actually originated by photons produced in the reaction, is achieved by requiring in the photon trigger a coincident event in TAPS with one of the particle multidetectors (i.e. any "TAPS*FW" or "TAPS*DB" trigger). These triggers sign the simultaneous occurrence of a nuclear reaction with the detected "photon-type" hit and, hence, minimize the contamination of cosmic muons misidentified as hard-photons. In the higher-energy part of the spectrum, however, the number of photon events is low and reaches the level of the accidental rate of a muon being recorded simultaneously with a nuclear reaction. For that reason we need to further filter the photon energy spectrum by subtracting the background of electromagnetic signals (with $PSA \approx 1$) collected in the TAPS time-of-flight spectrum within a window[2] of 4.5 ns (or 3.2 ns depending on the photon energy) width well before the prompt photon peak (located at TOF = 2.2 ns), i.e. from $TOF = -4.5$ ns (or $TOF = -3.2$ ns) to TOF = 0.0 ns. These cosmic background events are indicated by stars in fig. 6.1.

6.1.4 Photons from neutral pion decay

In addition to the bremsstrahlung events, a background of photons stemming from the 2-γ electromagnetic decay of the neutral pions produced in the heavy-ion reaction contributes to the photon energy spectrum essentially in the region 50 - 160 MeV. Neutral pions can

[2]The chosen cosmic windows have the same width (4.5 ns or 3.2 ns) as the photon-peak windows corresponding to the photon-energy regions quoted in the *PSA-TOF* table 5.2.

however be identified experimentally through an invariant-mass analysis (formula (5.9)) of the two-photon events. Such events collected by the TAPS pion trigger "TWO NEU LO IN DIFF. BLOCKS" in the invariant-mass region around the π^0 mass with a FWHM resolution of 11% (fig. 6.3), originate almost exclusively from the π^0 decay[3].

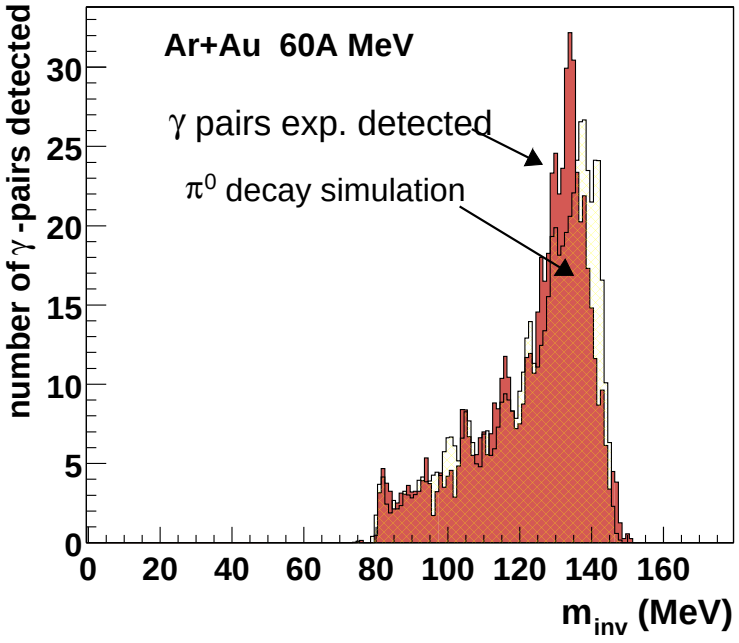

Figure 6.3: *Two-photon invariant mass distribution experimentally measured for the $^{36}Ar+^{197}Au$ system during the high counting-rate runs (solid), shown together with a* GEANT *simulation of the same number of π^0 decays (hatched histogram).*

To subtract this decay-photon component in the limited acceptance of our TAPS setup, a Monte-Carlo simulation with KANE has been performed with a π^0 event generator reproducing the experimentally measured energy and angular distributions. The pion energy distribution is described by a Maxwell-Boltzmann distribution in the *NN* center-of-mass, as proposed in [Mart97b, Mart99], with inverse slope parameter $E_0 \approx$ 15 MeV (fig. 6.4). The kinetic energy of the neutral pions, $K_{\pi^0} = E_{\pi^0} - m_{\pi^0}$, is obtained experimentally from the two decay-γ energies and relative angle through: $E_{\pi^0} = 2 \cdot \left[m_{\pi^0}^2 / (1 - \cos\theta_{12})(1 - (E_{\gamma 1} - E_{\gamma 2}/E_{\gamma 1} + E_{\gamma 2})^2) \right]$. The angular emission pattern in the nucleon-nucleon center-of-mass frame is taken of the type $(1 + b_{ani} \cos^2\theta)$, as proposed by [Mart99], with b_{ani} = 1 in agreement with former subthreshold pion measurements (^{129}Xe+^{197}Au at 44*A* MeV [Maye93], ^{40}Ar+^{197}Au system at 95*A* MeV [Schu94b, Bada96]). The double differential cross-section is therefore described by the function:

$$\frac{d^2\sigma}{dK_{\pi^0}^{cm}\, d\Omega} = K\,(1 + b_{ani}\cos^2\theta)\, p_{\pi^0}^{cm}\,(K_{\pi^0}^{cm} + m_{\pi^0})\,\exp(-K_{\pi^0}^{cm}/E_0) \qquad (6.2)$$

[3]The combinatorial background of uncorrelated 2-γ events falling within the invariant pion mass window is negligible at these incident energies.

where $p^{cm}_{\pi^0} = \sqrt{(K^{cm}_{\pi^0})^2 + 2K^{cm}_{\pi^0} m_{\pi^0}}$ is the pion momentum in the NN frame, and K a global normalization factor. The parameters (E_0, b_{ani}) were adjusted to describe the data as can be seen in fig. 6.4 for the pion kinetic energy distribution of the ^{36}Ar+^{197}Au system.

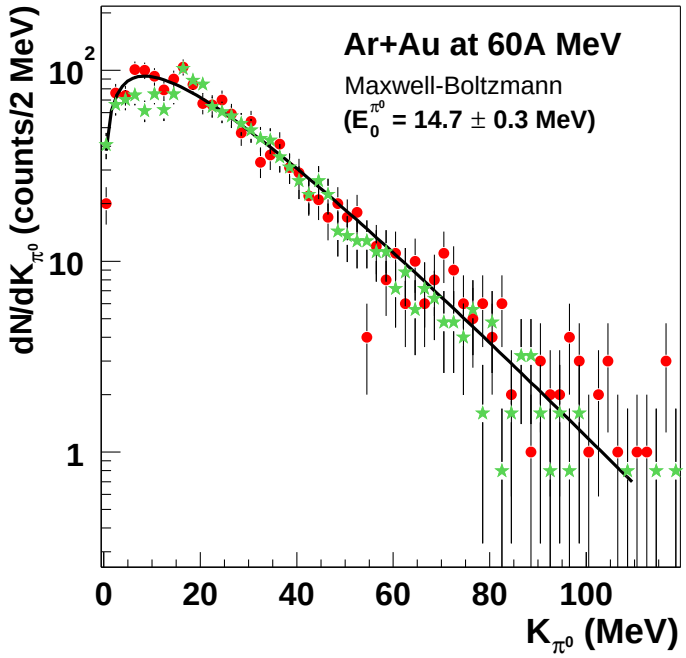

Figure 6.4: *Experimental (dots) and simulated (stars) kinetic energy distribution of the π^0 detected for the system $^{36}Ar+^{197}Au$. The experimental pion kinetic energy spectrum has been fitted to a Maxwell-Boltzmann distribution in the NN center-of-mass frame with inverse slope $E_0 \approx 15$ MeV.*

From the analysis of the simulation we find that the average neutral-pion detection efficiency of the TAPS setup is ε_{π^0} = 1.75% ± 0.1% for pions identified as such[4] in the invariant-mass range m_{inv} = 80 - 145 MeV. This total (angle- and energy- integrated) efficiency is basically governed by the geometrical acceptance of TAPS for the coincident detection of two photons ($\varepsilon_{\gamma 1} \cdot \varepsilon_{\gamma 2} = 0.14 \cdot 0.14 \approx 1.9\%$).

The energy spectrum of all *single* photons from the $\gamma\gamma$ π^0-decay (mainly consisting of events in which only one photon out of the two is detected within the acceptance of TAPS) represents the contribution of decay photons which is subtracted from the experimental hard-photon spectrum. Those π^0-photons events (stars in fig. 6.1) form a "bump" structure extending from 20 MeV up to 180 MeV with a maximum at around $E_\gamma \approx 60$ MeV. The relative contribution of this decay photons becomes specially important in the high-energy part of the photon spectrum, and at $E_\gamma \approx 130$ MeV they account roughly for

[4] Apart from the m_{inv} gate, an additional condition in the opening angle of each pair of coincident photons, $\theta_{\gamma\gamma} > 80°$, was selected for full pion identification according to GEANT simulations of our setup with the aforementioned pion input distribution.

Table 6.1: *For each considered system, raw number of hard-photons and pions experimentally detected (both figures have been corrected to take into account the respective trigger lifetimes and scaling-down factors), as well as estimated number of background photons (above 30 MeV) coming from pion decays as obtained through the simulation. This number is determined by counting the number of $\gamma\gamma$ coincidences with invariant mass lying in the range 80 MeV - 145 MeV (fig. 6.3) and having an opening angle $\theta_{\gamma\gamma} > 80^{\circ}$.*

Reaction	^{36}Ar+^{197}Au	^{36}Ar+^{197}Au	^{36}Ar+^{108}Ag	^{36}Ar+^{58}Ni	^{36}Ar+^{12}C
π^0 detected	1820	340	256	474	400
Decay-γ produced	26600	5290	3980	8060	6190
Hard-γ detected	655800	129200	86440	142130	151540
Decay-γ/Hard-γ	4.1%	4.1%	4.6%	5.6%	4.1%

a third of the net hard-photon yield.

In table 6.1 the calculated relative contribution of the pion-decay photons to the total hard-photon yield is summarized. It amounts from around 4.1% for the Gold and Carbon targets, 4.6% for the Ag target, up to at most 5.6% for the Nickel target. This mass dependence is expected since subthreshold pion production in heavy-ion reactions is a process that results from a competition between several mutually cancelling effects which depend, basically, on the size of the collision partners (number of *NN* collisions, absorption, Fermi-motion, and effect of the Coulomb barrier on the incident projectile energy) [Mart97b].

6.1.5 Corrected inclusive photon spectra

Figures 6.5 - 6.9 display the final response-function corrected and background-subtracted energy spectra $d\sigma/dE_\gamma$ calculated in the *NN* center-of-mass frame of the hard-photons produced in the five systems studied, where $d\sigma/dE_\gamma$ has been determined through:

$$\frac{d\sigma}{dE_\gamma} = \frac{1}{\varepsilon_\gamma} \cdot C \cdot \frac{dN_\gamma}{dE_\gamma} \quad \text{(mb/MeV)} \tag{6.3}$$

where C is a global normalization factor and the extrapolation to 4π of the spectra has been performed through the acceptance (ε_γ) correction described in detail in Section 6.4.3. The photon spectrum of the ^{36}Ar+^{197}Au system is shown twice: for the high counting-rate runs without the DB, and for the low counting-rate runs, with the DB. We have consciously chosen a threshold energy of $E^{thr}_{hard-\gamma}$ = 30 MeV for the definition of a hard-photon, an energy value where no significant contamination from the highest possible energy GDR photons is expected. This value corresponds, actually, to the energy for *subthreshold* hard-photon production in a heavy-ion collision at 60A MeV incident energy (see Section 3.1). We will keep this "conservative" value all throughout this work although it is clear that the contribution of bremsstrahlung photons remains still dominant in the photon spectrum down to energies of the order of $\approx$ 25 MeV [Nife90]. Above E_γ = 30 MeV, the range of hard-photon cross-section covers over 5 order of magnitude (from hundreds of mb/MeV

down to μb/MeV values). Comparison of figs. 6.5 and 6.6 demonstrates also that, as indicated by GEANT simulations, the presence of the Dwarf-Ball in between the target and TAPS does not affect significantly the shape and slope of the energy spectrum.

The most interesting feature in the spectra is the observed enhancement of the yield in the region E_γ = 30 - 60 MeV with respect to the flatter exponential fall-off describing the high-energy part of the spectra above E_γ = 60 MeV. Such a deviation is observed for the three heavier systems ^{36}Ar+^{197}Au, ^{107}Ag, ^{58}Ni (as it was also observed in the ^{86}Kr+^{58}Ni, ^{181}Ta+^{197}Au and ^{208}Pb+^{197}Au systems, see fig. 3.8) but is not present in the lightest ^{36}Ar+^{12}C reaction. In the three heavier systems, this excess of hard-photons clearly hinders the fit with a single exponential of the spectra above 30 MeV as it has been usually done in hard-photon studies [Nife90]. To properly describe the measured spectra for the heavier systems we have applied a sum of two exponential distributions corresponding, as proposed by [Mart95, Schu97], to a "direct" (coming from first-chance $pn\gamma$ collisions) and a "thermal" (secondary $pn\gamma$) hard-photon component respectively, with their corresponding weights:

$$\frac{d\sigma}{dE_\gamma} = K_d\, e^{-E_\gamma/E_0^d} + K_t\, e^{-E_\gamma/E_0^t} \tag{6.4}$$

The constants $K_{d,t}$ in formula (6.4) depend on the measured hard-photon intensities $I_{d,t}$ according to:

$$\begin{aligned} I_{d,t} &= K_{d,t} \int_{E^{thr}_{hard-\gamma}}^{\infty} e^{-E_\gamma/E_0^{d,t}}\, dE_\gamma = K_{d,t}\, E_0^{d,t}\, e^{-E^{thr}_{hard-\gamma}/E_0^{d,t}} \;\Rightarrow \\ K_{d,t} &= \frac{I_{d,t}}{E_0^{d,t}}\, e^{E^{thr}_{hard-\gamma}/E_0^{d,t}} \quad \text{, with } E^{thr}_{hard-\gamma} = 30 \text{ MeV} \end{aligned} \tag{6.5}$$

The values for the direct (E_0^d, I_d) and thermal (E_0^t, I_t) slopes and intensities extracted from the best least-square fit of the spectra with the expression (6.4) are given in table 6.2 for each system. The inverse slope parameters have been corrected with formula (6.1), their associated errors thus take into account the errors of the fit to the expression (6.4) as well as the errors of the response-function correction (eq. (6.1)). The direct slopes E_0^d remain almost constant around $E_0^d \approx 20$ MeV for the four systems in agreement with the values obtained from the systematics (eq. (3.4)). The slopes of the thermal component are softer than those of the direct component (E_0^t being between 1/3 and 1/2 times E_0^d). The contribution of thermal photons to the total hard photon yield, indicated by the relative intensities of thermal to total hard-photons I_t/I_{tot}, amounts to around 20% for the Au and Ni targets, is slightly smaller for the Ag target, and is compatible with zero for the lightest Carbon system. The characteristics of the direct and thermal slopes and relative intensities are discussed in more detail in the next two sections.

The excess of hard-photons in the region 30 - 60 MeV shows up more clearly in the energy spectrum for the ^{36}Ar+^{197}Au system plotted in a linear y-scale in the range E_γ = 30 - 70 MeV (fig. 6.10) together with the direct and thermal exponential fits. It is apparent that the thermal component already accounts for $\approx$ 40% of the total hard-photon yield at the threshold energy of 30 MeV. At lower energies, the contribution of the thermal bremsstrahlung component overcomes that of the direct component but according to the

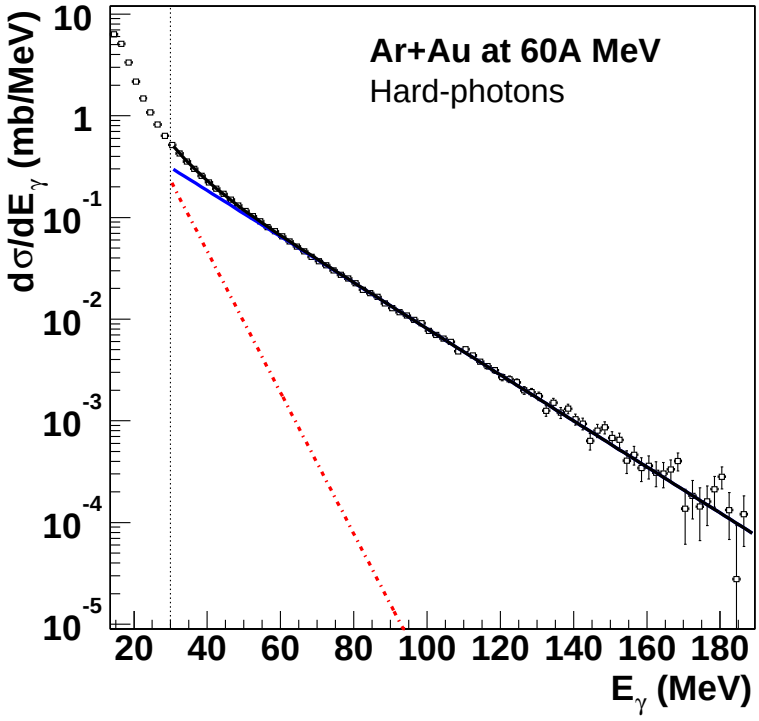

Figure 6.5: *Experimental hard photon energy spectrum measured in the NN CM for the system $^{36}Ar+^{197}Au$, during the Dwarf-Ball (low-intensity) runs. The spectrum has been fitted in the range E_γ = 30 - 180 MeV according to equation (6.4) to the sum of two exponential distributions: a direct (solid line) and a thermal one (dashed line). (The vertical dotted line indicates the low-energy threshold, $E^{thr}_{hard-\gamma}$ = 30 MeV, for hard-photons.)*

Table 6.2: *Direct and thermal hard-photon slopes and ratios of thermal to total intensities measured in the $^{36}Ar+^{197}Au$, ^{107}Ag, ^{58}Ni, ^{12}C reactions at 60A MeV. The expected values of E^d_0 according to the hard-photon systematics, eq. (3.4), are also reported.*

System	E^d_0 (MeV)	E^t_0 (MeV)	I_t/I_{tot}	$E_0^{d\,(sys)}$ (MeV)
^{36}Ar+^{197}Au	20.1 ± 1.2	6.2 ± 0.5	18.5% ± 0.5%	18.6 ± 2.0
^{36}Ar+^{197}Au	20.4 ± 1.3	6.5 ± 0.6	19.0% ± 1.0%	18.6 ± 2.0
^{36}Ar+^{107}Ag	20.1 ± 1.3	6.1 ± 0.6	14.8% ± 1.0%	19.0 ± 2.0
^{36}Ar+^{58}Ni	20.9 ± 1.3	8.8 ± 0.8	19.5% ± 1.0%	19.3 ± 2.0
^{36}Ar+^{12}C	18.1 ± 1.1	0.0 ± 0.5	0.0% ± 5.0%	19.5 ± 2.0

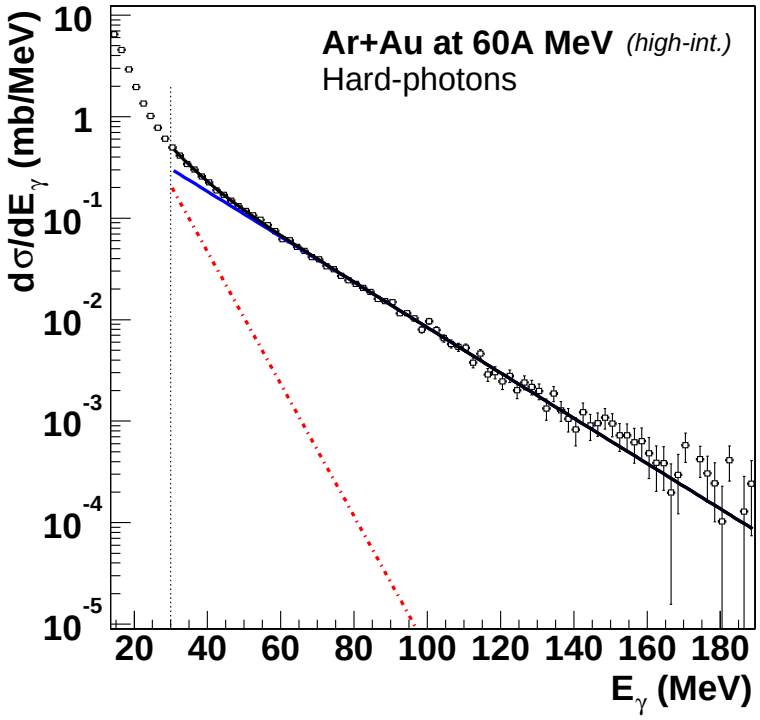

Figure 6.6: *Experimental hard photon energy spectrum measured in the NN CM for the system $^{36}Ar+^{197}Au$, during the high counting-rates runs. The spectrum has been fitted in the range E_γ = 30 - 180 MeV according to equation (6.4) to the sum of two exponential distributions: a direct (solid line) and a thermal one (dashed line).*

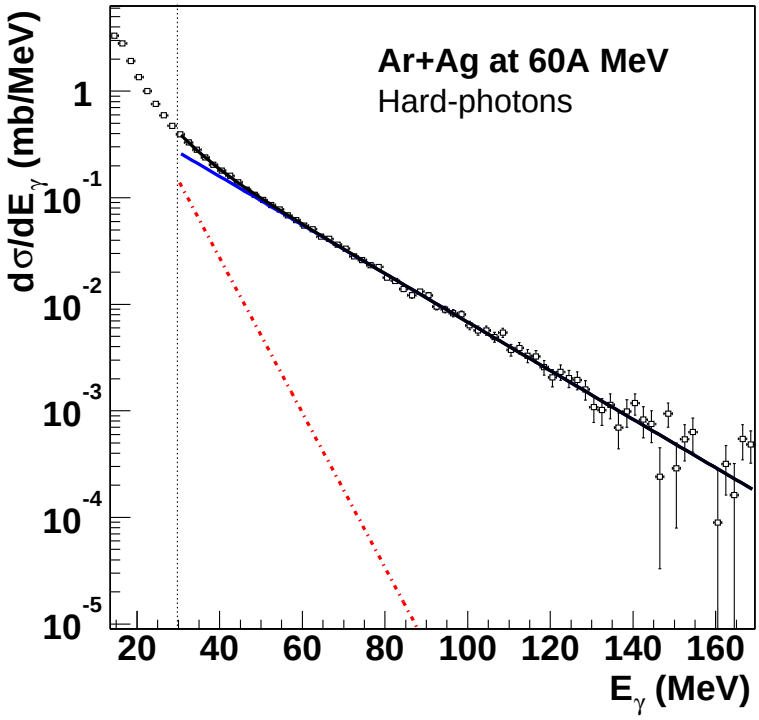

Figure 6.7: *Experimental hard photon energy spectrum measured in the NN CM for the system $^{36}Ar+^{108}Ag$ fitted in the range E_γ = 30 - 180 MeV, according to equation (6.4), to the sum of two exponential distributions: a direct (solid line) and a thermal one (dashed line).*

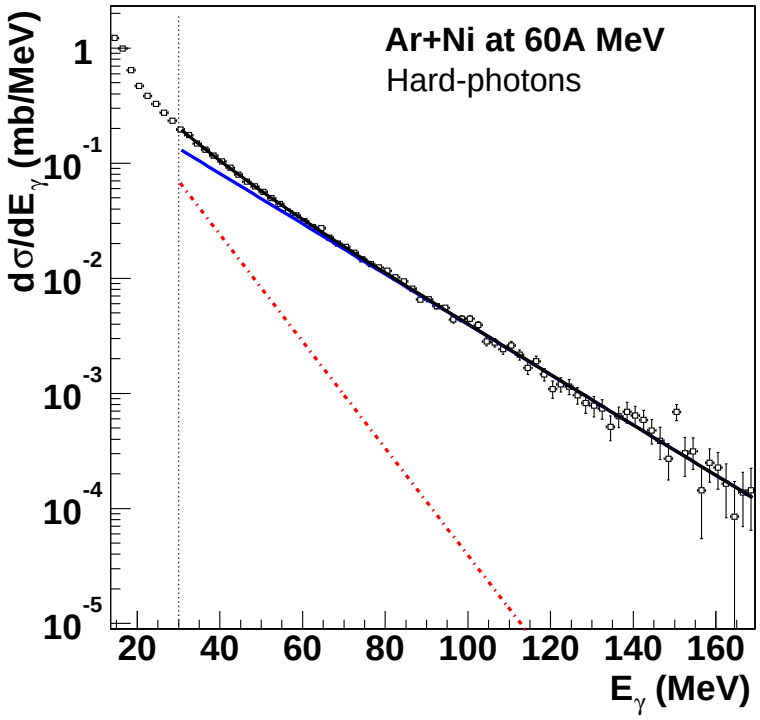

Figure 6.8: *Experimental hard photon energy spectrum measured in the NN CM for the system $^{36}Ar+^{58}Ni$ fitted in the range E_γ = 30 - 180 MeV, according to equation (6.4), to the sum of two exponential distributions: a direct (solid line) and a thermal one (dashed line).*

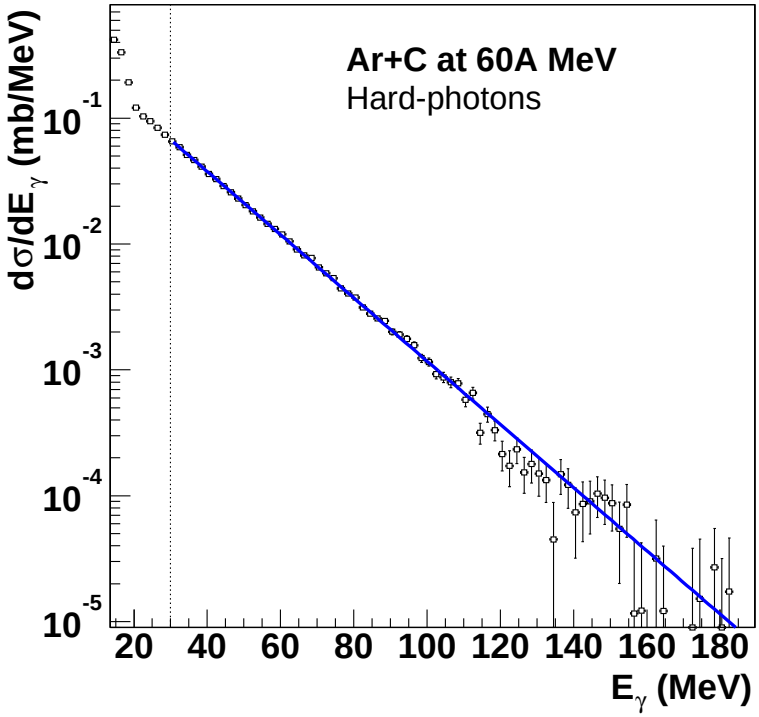

Figure 6.9: *Experimental hard photon energy spectrum measured in the NN CM for the system $^{36}Ar+^{12}C$ fitted in the range E_γ = 30 - 180 MeV just to the first direct exponential of equation (6.4) (solid line).*

aforementioned discussion on the hard-photon low-energy threshold definition, we have decided not to consider this region to completely avoid any possible contribution due to the high-energy Lorentzian tail of GDR statistical photons. The second-chance bremsstrahlung contribution can be isolated by subtracting the direct hard-photon component, corresponding to the first term of equation (6.4), from the experimentally measured energy spectrum. The resulting thermal exponential bremsstrahlung spectrum for the ^{36}Ar+^{197}Au system with slope $E_0^t \approx 6.2$ MeV is clearly seen in fig. 6.11.

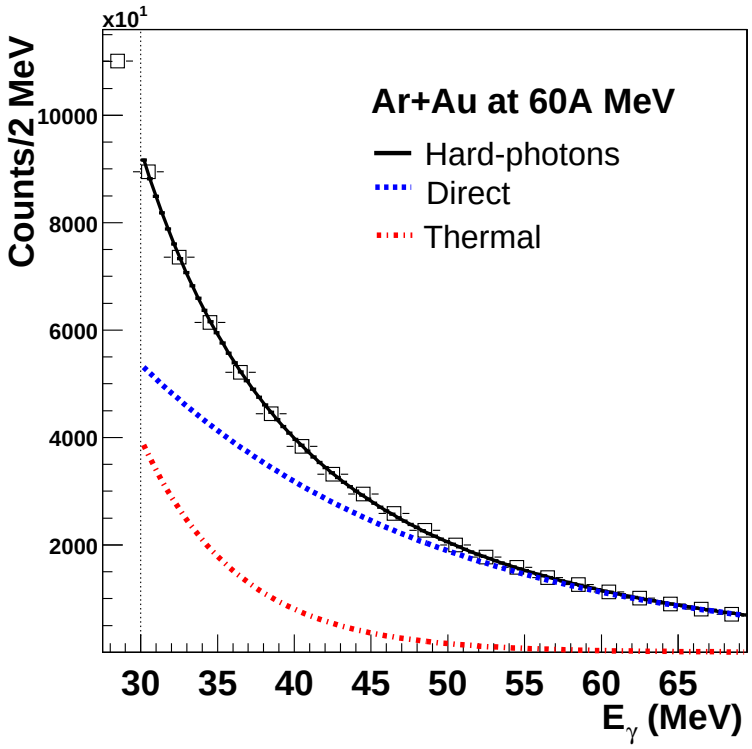

Figure 6.10: *Experimental hard-photon energy spectrum in the NN CM for the ^{36}Ar+^{197}Au reaction in the range E_γ = 30 - 70 MeV depicted in a linear-y plot to emphasize the two distinct (thermal and direct) hard-photon exponential contributions.*

The inclusive photon spectra shown so far have been calculated in the *NN* center-of-mass frame: $E_\gamma^{NN} = \gamma_{NN}(1 - \beta_{NN}\cos\theta_\gamma^{lab}) \cdot E_\gamma^{lab}$, with $\beta_{NN} \approx 0.18$ and $\gamma_{NN} = 1.017$, which assumes that hard-photons are produced from a source moving with the *NN* center-of-mass velocity. The spectra measured at $\theta_\gamma^{lab} = 90^\circ$ are not affected by the Doppler-effect ($E_\gamma^{90^\circ} = \gamma_S E_\gamma^{lab} \approx E_\gamma^{lab}$) and they are free of any assumption on the origin of the bremsstrahlung photons. Therefore, we have also analysed the photon spectra measured in the lab in the angular region θ_{lab} = 88° - 92° (fig. 6.12 for the ^{36}Ar+^{197}Au system). The deduced slopes and ratios thermal/total of the hard-photons emitted at $\theta_{lab} = 90^\circ \pm 2^\circ$ obtained through a fit to equation (6.4) for all the considered systems are reported in table 6.3. The values of the slopes agree, within the larger statistical errors, with the values obtained from the angle-integrated spectra (table 6.2). These coinciding results rule out

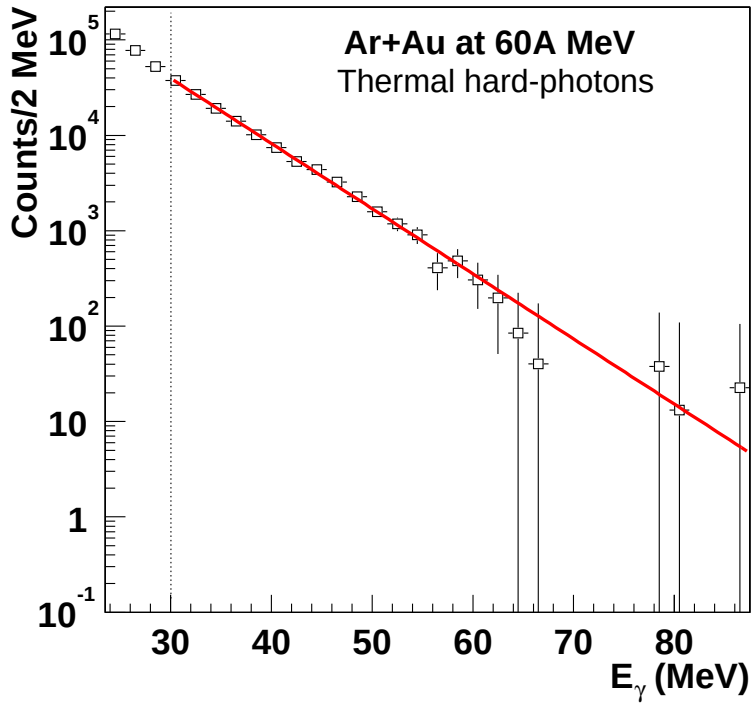

Figure 6.11: *Inclusive thermal hard-photon energy spectrum obtained from the raw photon spectrum above E_γ = 30 MeV after subtraction of the cosmic and pion-decay backgrounds, and after subtraction of the direct hard-photon component (first term of equation (6.4)). The system is $^{36}Ar+^{197}Au$ (low-intensity runs). The remaining exponential distribution above 30 MeV must correspond to hard-photon emission other than first-chance proton-neutron bremsstrahlung.*

any trivial kinematical effect as explanation for the observed enhancement of hard-photon production in the region E_γ = 30 - 60 MeV.

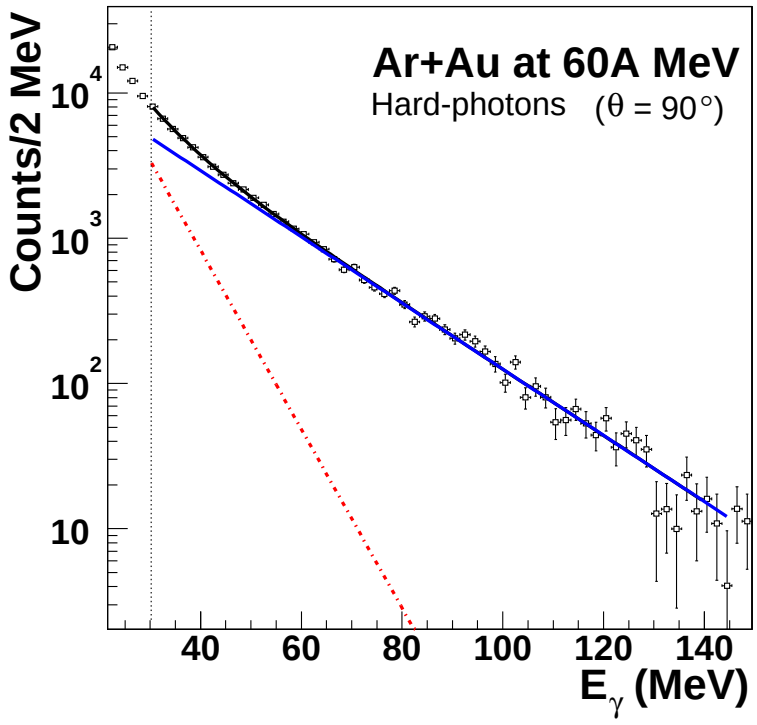

Figure 6.12: *Experimental hard-photon spectrum measured at* $\theta_{lab} = 90° \pm 2°$ *for the* $^{36}Ar+^{197}Au$ *reaction, during the low counting-rate runs. The spectrum has been fitted in the range* E_γ *= 30 - 140 MeV, according to equation (6.4), to the sum of two exponential: a direct (solid line) and a thermal one (dashed line).*

Table 6.3: *Measured ratios of thermal to total intensities, as well as direct and thermal slopes for the hard-photons measured at* $\theta^{lab} = 90° \pm 2°$ *in the* ^{36}Ar+^{197}Au, ^{107}Ag, ^{58}Ni, ^{12}C *reactions at 60A MeV.*

System	E_0^d (MeV)	E_0^t (MeV)	I_t/I_{tot}
^{36}Ar+^{197}Au	20.0 ± 1.3	6.8 ± 0.6	$18.5\% \pm 1.0\%$
^{36}Ar+^{197}Au	20.1 ± 1.5	8.5 ± 2.0	$24.0\% \pm 5.0\%$
^{36}Ar+^{107}Ag	19.3 ± 1.5	7.2 ± 1.0	$16.0\% \pm 2.0\%$
^{36}Ar+^{58}Ni	20.0 ± 1.5	10.4 ± 2.0	$25.0\% \pm 5.0\%$
^{36}Ar+^{12}C	18.2 ± 1.2	0.0 ± 0.6	$0.0\% \pm 5.0\%$

6.1.6 Direct and thermal slopes and intensities

The measured direct slopes E_0^d for the five systems (table 6.2) have basically the same value of about ≈ 20 MeV. This is expected for the prompt emission in nucleon-nucleon collisions during the first instants of the reaction before the initial kinetic energy is thermalized. In such case, the high values of the slopes just reflect the coupling of the incident energy per nucleon with the average intrinsic momentum of the colliding nucleons. The lower E_0^d value measured for the ^{36}Ar+^{12}C system ($E_0^d = 18.1 \pm 1.3$ MeV) is explained within this picture by the smaller Fermi momentum of the Carbon nucleons. This results from the lower nuclear density of ^{12}C, $p_F = \hbar(3\pi^2\rho_0/2)^{1/3} \approx 220$ MeV/c for $\rho_0(^{12}\mathrm{C}) \approx 0.10$ fm^{-3}, as compared to the saturation value, $p_F(\rho_0 = 0.16\ \mathrm{fm}^{-3}) \approx 265$ MeV/c, holding for the heavier nuclei. The measured direct slope parameters E_0^d follow, thus, the trend of their dependence with the (Coulomb-corrected) bombarding energy per nucleon, K_{Cc}^{lab}, fitting very well with the collected systematics for hard-photon production (fig. 6.13).

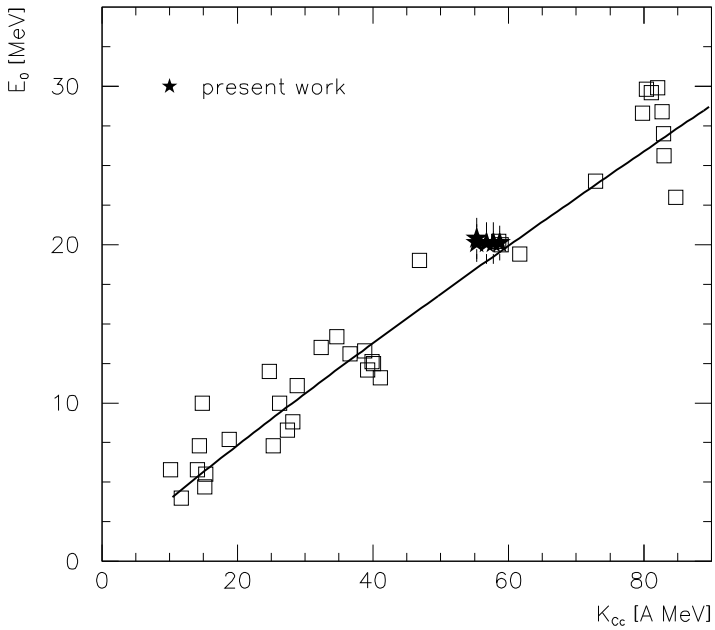

Figure 6.13: *Compilation [Schu97] of the measured (direct) hard-photon slope parameters plotted as a function of the bombarding energy per nucleon minus the Coulomb barrier energy of the reaction. Our data (inclusive E_0^d) are represented by the star symbols. The solid line represents a fit of equation (3.4) to the data.*

The thermal photon slopes E_0^t, on the contrary, do not scale with the initial available energy per nucleon in the laboratory like E_0^d but scale with the available energy in the nucleus-nucleus (AA) center-of-mass $K_{Cc}^{AA} = \mu K_{Cc}^{lab}/A_{tot}$. This can be seen in fig. 6.14 where the slopes of the thermal component for the three heavy systems studied in this

work (^{36}Ar+^{197}Au, ^{107}Ag, ^{58}Ni) are plotted together with the measured thermal slopes for the three systems studied in the TAPS campaign at GANIL in 1992 (^{86}Kr+^{58}Ni, ^{181}Ta+^{197}Au, ^{208}Pb+^{197}Au) [Schu97]. From this collected systematics we observe that the highest thermal slopes correspond to the systems with larger energy available in the AA CM. This is the case for the ^{36}Ar+^{58}Ni and ^{86}Kr+^{58}Ni reactions for which the much more symmetric projectile-target combination maximizes the total amount of energy deposited in the nucleus-nucleus center-of-mass. The linear dependence of E_0^t with K_{AA} suggest indeed that thermal photons originate in a thermal proces during later stages of the collision when the initial kinetic energy has been, at least partially, dissipated into internal degrees of freedom over the entire system.

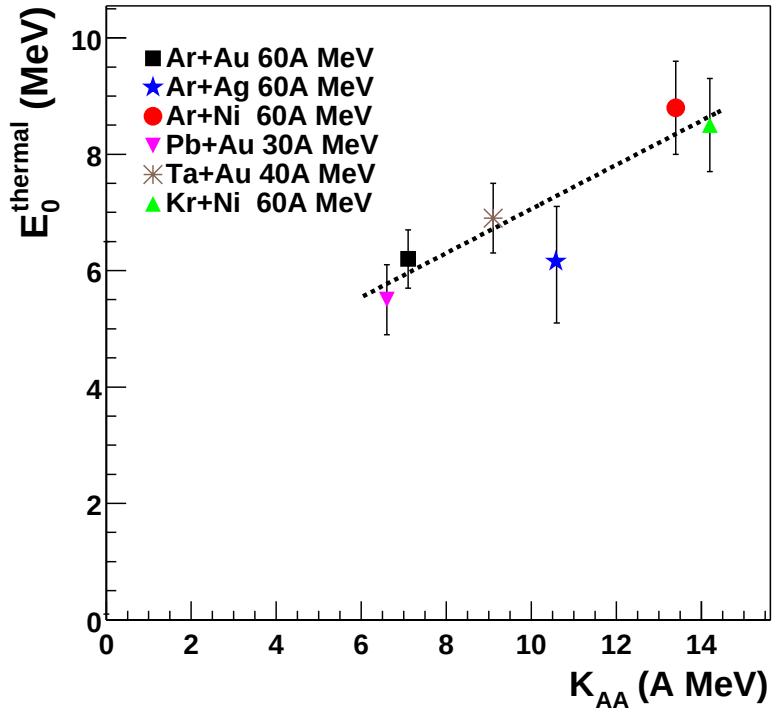

Figure 6.14: *Compilation of the measured thermal slopes E_0^t for the systems studied in the present work, ^{36}Ar+^{197}Au, ^{107}Ag, ^{58}Ni, as well as those studied in the 1992 TAPS campaign at GANIL, ^{86}Kr+^{58}Ni, ^{181}Ta+^{197}Au, ^{208}Pb+^{197}Au [Schu97], plotted as a function of the (Coulomb-corrected) total available energy in the nucleus-nucleus center-of-mass.*

Indeed, the association of the hard direct and of the softer thermal exponential slopes with first- and second- chance *NN* collisions respectively is a common ansatz in the interpretation of the kinetic energy spectra of the reaction products emitted in heavy-ion reactions. Such a double-source fit of the energy spectrum in terms of the pre-equilibrium and thermal components is a common technique analysis in the study of light-particle (proton, neutron, α) distributions measured in heavy-ion reactions (see the discussion in Section 9.3). On the one side, the harder spectral slopes of the direct component, tracking the bombarding energy per nucleon in the lab, $E_0^d(\mathrm{MeV}) \approx 1/3 K_{Cc}^{lab}(\mathrm{MeV})$ independently of

the mass of the system, must result from coupling of incident projectile nucleons' motion with target nucleons' Fermi motion in the overlap zone of the colliding nuclei. Indeed, since during the initial high-compression phase, the incident kinetic energy has not yet been dissipated, hard-photon emission results from a preequilibrium state in a process very closely related to the experimentally well-known preequilibrium emission of light particles such as high-energy protons (see e.g. [Luke93, Coni00]) and neutrons. On the other side, second-chance proton-neutron collisions that take place in a later stage of the reaction have, on average, a smaller energy available in the *pn* center-of-mass as compared to first-chance collisions, and thus lead to a softer bremsstrahlung photon energy spectrum.

The contribution of the second-chance bremsstrahlung component (table 6.2) to the total hard-photon yield I_t/I_{tot} is maximum ($\approx$ 20%) for the heaviest ^{36}Ar+^{197}Au system and for the ^{36}Ar+^{58}Ni one; is slightly lower for the ^{36}Ar+^{108}Ag reaction ($\approx$ 16%), and it has not been observed for the lightest ^{36}Ar+^{12}C one. The emission of thermal hard-photons is, therefore, a process dependent on the total size of the system and indicates the importance of volume effects for their production. On the one hand, in the small ^{36}Ar+^{12}C projectile-target combination the total amount of participant nucleons is not sufficient to achieve stopping and consequent thermalization of the nuclear system(s). Hence, only prompt $pn\gamma$ bremsstrahlung occurs, clearly dominating the photon spectrum already above E_γ = 20 MeV. For the heaviest systems, on the other hand, the larger number of nucleons present in the participant zone increases the chance of stopping and hence the probability of secondary *NN* collisions and thermalization.

Indeed, it is known that preequilibrium nucleons suffer very few collisions (in general 0 or 1) while those in a hot participant region, created during the reaction, experience on the average between 2 and 3 collisions. This is roughly the number of two-body collisions necessary to achieve thermal equilibration [Peil94, Dura92]. In light-mass systems such as ^{36}Ar+^{12}C, there is not enough matter on the way of a nucleon to experience more than one collision. Moreover, due to this higher "transparency", the system is very unlikely to develop a recompression phase (with subsequent *NN* collisions) right after the collision, as seen in BUU simulations of the reactions studied during the TAPS campaign at GANIL [Mart95, Schu97].

Whereas the absence of a thermal hard-photon component in the ^{36}Ar+^{12}C system can be explained by the absence of a stopping and thermalization process for this very-light system, the results obtained for the ^{36}Ar+^{58}Ni must include an additional consideration. Indeed, this system gives rise to the hardest spectrum ($E_0^t \approx 8.8$ MeV) and the largest I_t/I_{tot} ratio (together with the much heavier ^{36}Ar+^{197}Au reaction). This can be explained by the fact that this much more symmetric system exhibits, among the four considered systems, the largest attainable values of excitation energy $\varepsilon^\star$, which are directly correlated to the available energy in the nucleus-nucleus center-of-mass ($\varepsilon^\star \propto K_{AA}$) (table 4.4). Such larger excitation energy leads to higher temperatures which show up in harder thermal bremsstrahlung slopes.

6.2 Hard-photon angular distributions. Source velocity analysis

6.2.1 "Direct" and "thermal" hard-photon angular distributions

As discussed in Section 3.2.1, the angular distribution of bremsstrahlung photons can be interpreted as the sum of an isotropic plus an anisotropic dipolar terms in the frame of the emitting source, according to the phenomenological expression (3.6) [Berth87] inspired by the classical $d\sigma_{pn\gamma}/d\Omega$ elementary cross-section. The angular distributions measured in the laboratory frame contain an additional Lorentz-boost term, $Z = \left(1/\sqrt{1-\beta_S^2}\right)(1-\beta_S\cos\theta_{lab})$, from which the average velocity of the photon source β_S can be extracted after a two-dimensional moving-source fit of these distributions with the equation:

$$\left(\frac{d\sigma}{d\Omega}\right)_{lab} = \frac{K}{Z^2}\left[1-\alpha+\alpha\frac{\sin^2\theta_\gamma^{lab}}{Z^2}\right] E_0\, e^{-E^{thr}_{hard-\gamma}\cdot Z/E_0}, \qquad (6.6)$$

where α is the weight of the dipole component, E_0 is the energy slope parameter in the source frame and K is a normalization factor, the factor $E^{thr}_{hard-\gamma}$ = 30 (60) MeV is the low-energy threshold for E_γ and issues from the energy integration of the double-differential $d\sigma_{pn\gamma}/dE_\gamma d\Omega$ cross-section (equation (3.7)).

We have seen in the previous section that above E_γ = 60 MeV, the spectrum of hard-photons produced in ^{36}Ar+^{197}Au, ^{107}Ag, ^{58}Ni, ^{12}C is clearly dominated by "pure" direct hard-photons in all four systems. Thus, integrating these spectra above E_γ = 60 MeV for different equivalent solid-angle regions we obtain the laboratory angular distributions of the direct hard-photons emitted in each reaction (figures 6.15, 6.16, 6.17, 6.18, 6.19). To reduce statistical fluctuations, due to the acceptance and (energy-integrated) hard-photon yields, the six TAPS blocks were divided in 24 equal solid-angle $\theta-\phi$ slices. For each value of the polar angle θ, the hard-photon cross-section has been individually measured for the two associated azimuthal angles $\pm\phi$. This procedure allows also to assess quantitatively the systematical errors in the measure of $d\sigma/d\Omega$ for a certain θ, giving individual error bars for the twelve (θ, Ω) experimental points. As in the case of the energy spectra, the (isotropic) cosmic background and the photons coming from the decay of neutral pions have been subtracted from those spectra.

A least-χ^2 fit of these distributions has been performed using expression (6.6) with the parameters α and β_S left free (K can be directly related to the measured yields at $\theta = 90°$, and the *initial* fit value of the inverse slope parameter[5] E_0 is taken as the experimentally measured E_0^d reported in table 6.2). The obtained values for α and β_S are listed in table 6.4.

Before analyzing these results, we will apply the same source-velocity analysis for the laboratory angular distributions of hard-photons with energies E_γ = 30 - 45 MeV. In this region the presence of the second bremsstrahlung component shows up more intensely, accounting roughly for 30% to 40% of the total hard-photon yield. A fit of the photon

[5] Mind that now the values of E_0 in eq. (6.6) correspond to the slopes in the *laboratory* frame which are slightly lower than the inclusive E_0's computed in the NN CM frame.

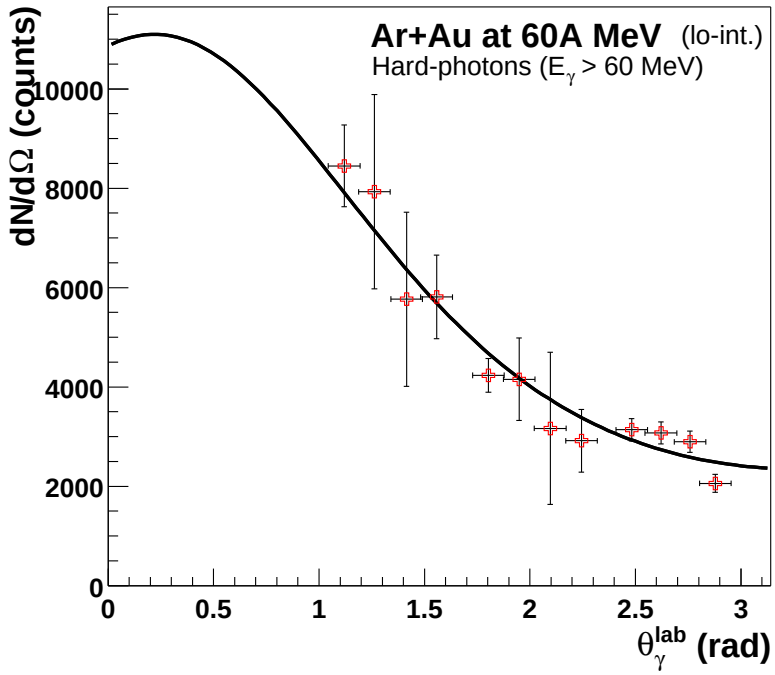

Figure 6.15: *Experimental angular distribution in the lab for hard-photons above 60 MeV measured in the system $^{36}Ar+^{197}Au$ during the low counting-rate runs and fitted (solid line) according to equation (6.6).*

Table 6.4: *Values of the "direct" hard-photon source velocities β_S, and anisotropy factors α, obtained after a Least-Squares fit with equation (6.6) of the hard-photon laboratory angular distributions above E_γ = 60 MeV for the 5 systems studied (figures 6.15, 6.16, 6.17, 6.18, 6.19). The values of the slopes E_0^d used for the fit are also reported.*

Reaction	β_S	α	E_0^d	χ^2/ν
$^{36}Ar+^{197}Au$ (lo)	0.16 ± 0.04	0.1 ± 0.2	20.2 ± 0.4	1.1
$^{36}Ar+^{197}Au$ (hi)	0.18 ± 0.04	0.0 ± 0.4	20.1 ± 0.2	0.2
$^{36}Ar+^{107}Ag$	0.18 ± 0.05	0.0 ± 0.4	19.0 ± 0.2	0.1
$^{36}Ar+^{58}Ni$	0.19 ± 0.02	0.01 ± 0.3	19.9 ± 0.3	0.3
$^{36}Ar+^{12}C$	0.21 ± 0.05	0.15 ± 0.25	18.7 ± 0.3	0.4

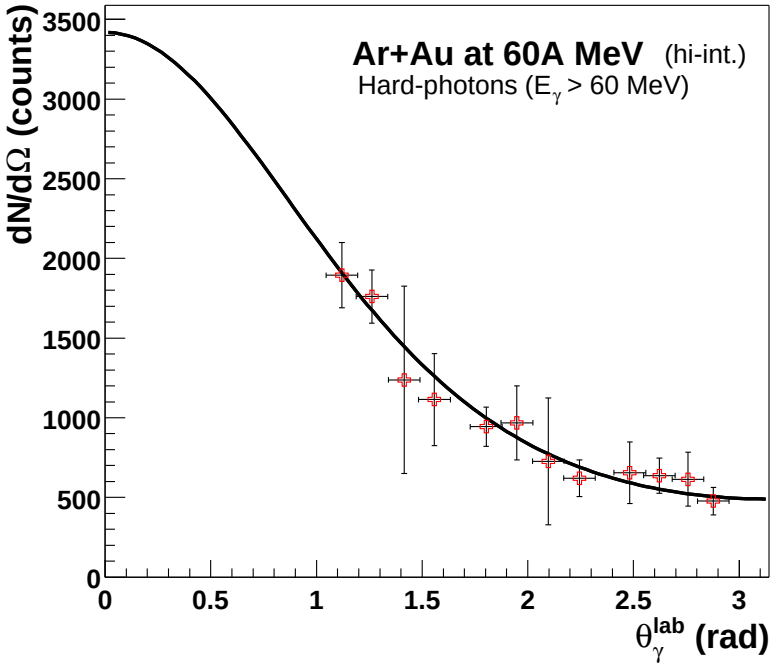

Figure 6.16: *Experimental angular distribution in the lab for hard-photons above 60 MeV measured in the system $^{36}Ar+^{197}Au$ during the high counting-rate runs and fitted (solid line) according to equation (6.6).*

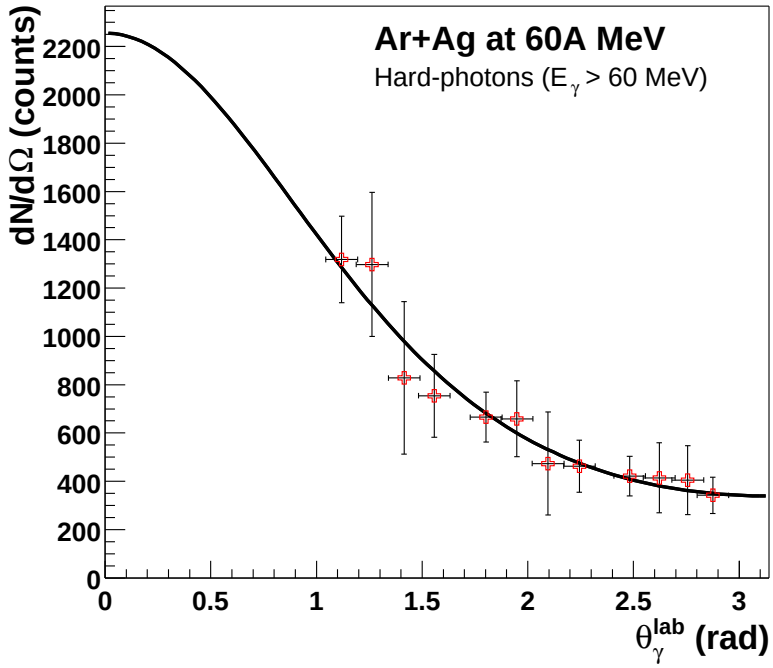

Figure 6.17: *Experimental angular distribution in the lab for hard-photons above 60 MeV measured in the system $^{36}Ar+^{108}Ag$ and fitted (solid line) according to equation (6.6).*

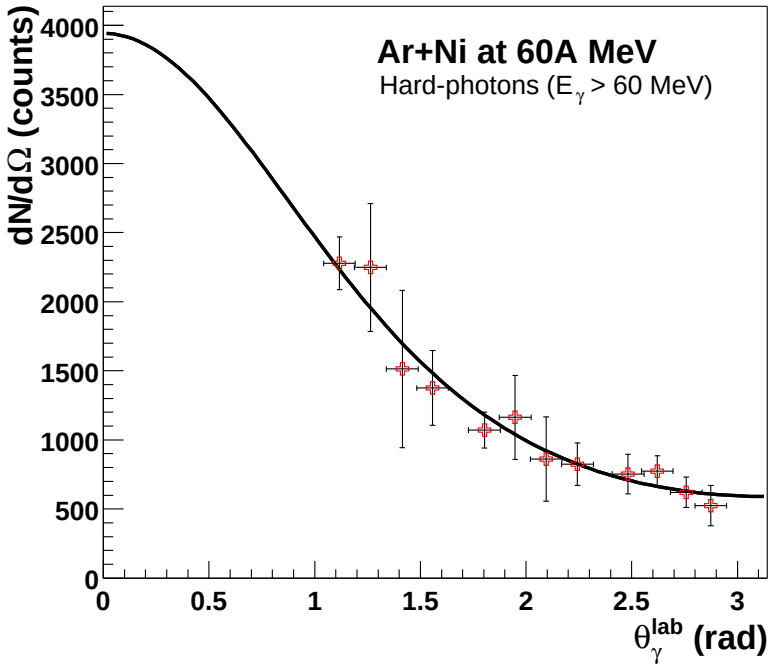

Figure 6.18: *Experimental angular distribution in the lab for hard-photons above 60 MeV measured in the system $^{36}Ar+^{58}Ni$ and fitted (solid line) according to equation (6.6).*

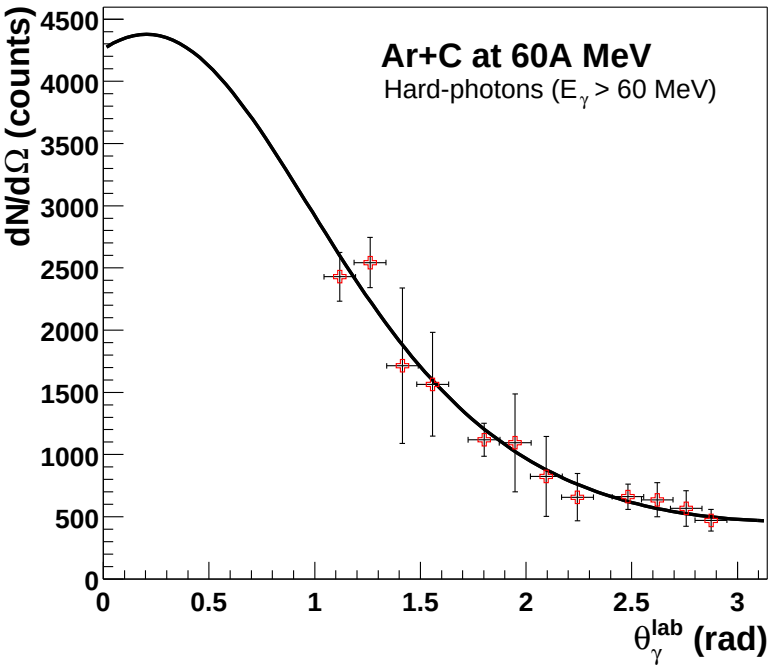

Figure 6.19: *Experimental angular distribution in the lab for hard-photons above 60 MeV measured in the system $^{36}Ar+^{12}C$ and fitted (solid line) according to equation (6.6).*

Table 6.5: *Values of the average hard-photon source velocity $\langle\beta_S\rangle$, and the anisotropy factor α, obtained after a Least-Squares fit of the laboratory angular distributions with equation (6.7) of hard-photons with energies E_γ = 30 - 45 MeV emitted in the 5 studied systems. The values of the local slope parameters E_0 in the range 30 - 45 MeV used for the fits are also reported.*

Reaction	$\langle\beta_S\rangle$	α	$E_0^{(30-45\,\mathrm{MeV})}$	χ^2/ν
^{36}Ar+^{197}Au (lo)	0.13 ± 0.01	0.0 ± 0.1	11.5 ± 0.4	1.4
^{36}Ar+^{197}Au (hi)	0.15 ± 0.01	0.0 ± 0.3	12.2 ± 0.2	0.4
^{36}Ar+^{107}Ag	0.15 ± 0.03	0.0 ± 0.3	12.7 ± 0.2	0.3
^{36}Ar+^{58}Ni	0.16 ± 0.03	0.0 ± 0.3	15.1 ± 0.2	0.8
^{36}Ar+^{12}C	0.20 ± 0.04	0.2 ± 0.15	17.2 ± 0.4	0.6

laboratory angular distributions with the following expression (using the K and E_0 experimentally measured) yields the parameters α and β_S listed in table 6.5:

$$\left(\frac{d\sigma}{d\Omega}\right)_{lab} = \frac{K}{Z^2}\left[1-\alpha+\alpha\frac{\sin^2\theta_\gamma^{lab}}{Z^2}\right] E_0\left[e^{-30\cdot Z/E_0} - e^{-45\cdot Z/E_0}\right] \qquad (6.7)$$

A direct comparison of tables 6.4 and 6.5 allows to identify the different characteristics of the direct and thermal bremsstrahlung photons. The most interesting findings are the following:

- "Direct" hard-photons: The laboratory angular distributions of the photons above 60 MeV for the four systems can be very well fitted with equation (6.6) indicating an emission from a single source moving with the nucleon-nucleon center-of-mass velocity $\beta_S = \beta_{NN} \approx 0.18$ (see table 4.4). This confirms the expected result that direct hard-photons originate from individual first-chance *NN* collisions.

- "Thermal" hard-photons: The obtained average source-velocities β_S for the systems ^{36}Ar+^{197}Au,^{107}Ag, ^{58}Ni in the energy region E_γ = 30 - 45 MeV are systematically lower than the ones measured for "pure" first-chance hard-photons (with $E_\gamma > 60$ MeV). Indeed, the presence in these reactions of a second bremsstrahlung component, which issues presumably from later nucleon-nucleon collisions when the initial velocities of the colliding nucleons have been damped, induces a lowering of the average velocity of the hard-photon moving source by a factor 10% - 25% with respect to $\beta_S \approx 0.18$ found for the higher energy hard-photons. Such a behaviour had been also observed for heavy systems in [Tam88, Tam89] and ascribed as the result of bremsstrahlung from subsequent nucleon-nucleon scatterings. This is not the case for the ^{36}Ar+^{12}C system where all photons (either above 30 MeV or above 60 MeV) are emitted from a mid-rapidity system moving with a velocity compatible with the *NN* center-of-mass velocity $\beta_S = 0.20 \pm 0.02 \approx \beta_{NN}$. This result confirms the absence of a thermal component for this system as observed in its energy spectrum.

- The strength of the dipole component in the angular distribution, i.e. the anisotropy parameter α, is found to be basically compatible with zero for the three heavier systems (^{36}Ar+^{197}Au, ^{107}Ag, ^{58}Ni), although with large (fitting) errors ($\approx \pm 0.2$), whereas $\alpha = 0.20 \pm 0.15$ for the ^{36}Ar+^{12}C reaction. On the one side, this fact seems to disagree with the usual values found in the literature for which the elementary $pn\gamma$ dipolar term with weight $\alpha \approx 0.1$ - 0.3 is found in the angular distributions [Nife90]. On the other side, it is also known that the intensity of the dipole component is a decreasing function of the total mass of the system as a consequence of the increased influence of secondary collisions in the more massive systems which smear out the preferred original beam direction of the colliding nucleons and tend to render the photon angular distributions more isotropic [Tam89]. The fact that $\alpha \approx 0$ would thus qualitatively confirm the noticeable contribution of an isotropic bremsstrahlung component issuing from second-chance proton-neutron collisions in our heavier systems. It should be noted, nonetheless, that with our TAPS setup the source-velocity fit is less sensitive to the α parameter than in other reported experiments (see e.g. [Nife90]). The reason is that, -as it can be seen from the forward peaking of the dipole component in figure 3.4-, the angular distribution is only basically sensitive to the dipolar anisotropy at small angles. In our setup, due to the position of the Forward Wall in the forward hemisphere, the minimum measured photon angle with TAPS was restricted to $\theta_\gamma \approx 57°$. Therefore no definitive conclusion can be drawn on the absence (or existence) of the dipole component for the three heavy systems with the present fit. Nonetheless, the conclusion that the strength of the dipole component is larger for the lighter ^{36}Ar+^{12}C system, as expected for pure first-chance bremsstrahlung in that system, remains still valid.

6.2.2 Total hard-photon ($E_\gamma > 30$ MeV) angular distributions

The observation that second-chance thermal hard-photons produced in the heavier systems are emitted from a source moving at a velocity lower than the velocity of the *NN* center-of-mass, at variance with the source velocity of direct hard-photons where $\beta_S \approx \beta_{NN}$, suggests that the thermal hard-photon source moves with the (lower) nucleus-nucleus center-of-mass velocity: β_{AA}(^{36}Ar+^{197}Au) = 0.05, β_{AA} (^{36}Ar+^{108}Ag) = 0.08, and β_{AA}(^{36}Ar+^{58}Ni) = 0.13. One can attempt to assess this assumption in a quantitative way by considering the relative weights of the thermal to direct hard-photon components in the region E_γ = 30 - 45 MeV: w(^{36}Ar+^{197}Au) = 0.40, w(^{36}Ar+^{108}Ag) = 0.30 and w(^{36}Ar+^{58}Ni) = 0.36. This relative yields would lead[6] to the following weighted average source velocities: $\langle\beta_S(^{36}\text{Ar}+^{197}\text{Au})\rangle$ = 0.13, $\langle\beta_S(^{36}\text{Ar}+^{108}\text{Ag})\rangle$ = 0.15, and $\langle\beta_S(^{36}\text{Ar}+^{58}\text{Ni})\rangle$ = 0.16. This result is in close agreement with the mean values extracted from the moving-source fit (table 6.5) using eq. (6.7).

This assumption is corroborated by the fact that the angular distributions of hard-photons with energy above 30 MeV measured in the lab reference frame (figs. 6.20, 6.21, 6.22, and 6.23) can actually be reasonably well reproduced (typical values of χ^2 per degree of freedom are in the range of 1.0 - 2.0) with the distribution expected for the

[6] Using the expression: $\langle\beta_S\rangle = w \cdot \beta_{AA} + (1-w) \cdot \beta_{NN}$

emission from a first-chance source with slope parameter E_0^d moving with $\beta_S^d \approx \beta_{NN}$ plus a second-chance isotropic source with slope parameter E_0^t and $\beta_S^t \approx \beta_{AA}$ (the ratios of thermal to direct intensities being fixed by those obtained from the energy spectra). Such an expression reads:

$$\left(\frac{d\sigma}{d\Omega}\right)_{lab} = \frac{K}{Z^2}\left[1-\alpha+\alpha\frac{\sin^2\theta_\gamma^{lab}}{Z^2}\right] E_0^d\, e^{-30Z/E_0^d} + \frac{K'}{Z'^2} E_0^t\, e^{-30Z'/E_0^t} \qquad (6.8)$$

where $E_0^{d,t}$ are the slope parameters of the direct and thermal components in the source frame respectively, and $Z = 1/\sqrt{1-(\beta_S^d)^2}\cdot(1-\beta_S^d\cos\theta_{lab})$ and $Z' = 1/\sqrt{1-(\beta_S^t)^2}\cdot(1-\beta_S^t\cos\theta_{lab})$ are the Lorentz-boost factors corresponding to the direct and thermal source moving frames respectively, K, K' are the normalization factors associated to the direct and thermal intensities I_d and I_t respectively, and α is the weight of the dipole component (only for the direct component). The values of the two sources velocities β_S^d and β_S^t as well as the intensity of the thermal component obtained with such a fit of the angular distributions are summarized in table 6.6.

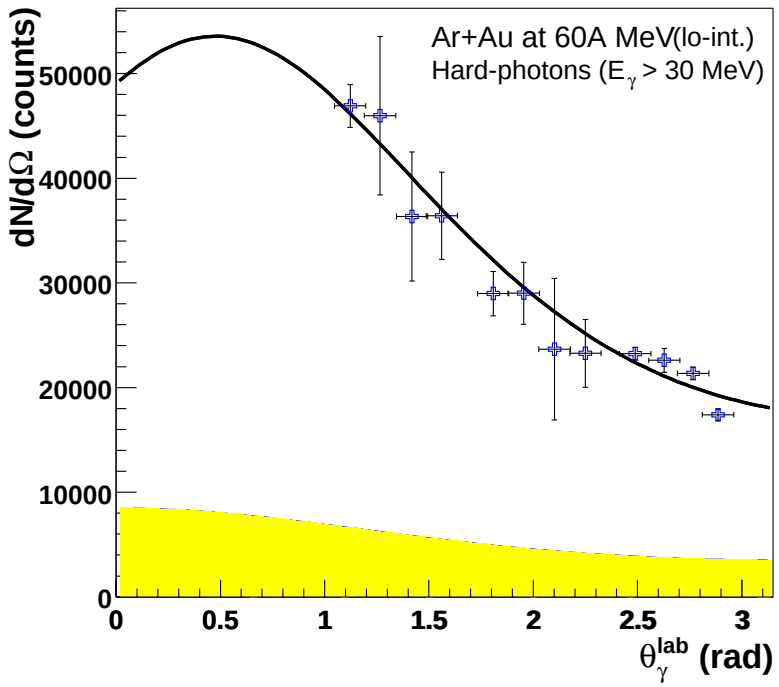

Figure 6.20: *Experimental laboratory angular distribution for hard-photons ($E_\gamma > 30$ MeV) measured in the system $^{36}Ar+^{197}Au$ during the low counting-rate runs and fitted according to equation (6.8). The hatched region indicates the estimated contribution of thermal hard-photons, emitted isotropically from a source moving with β_{AA}.*

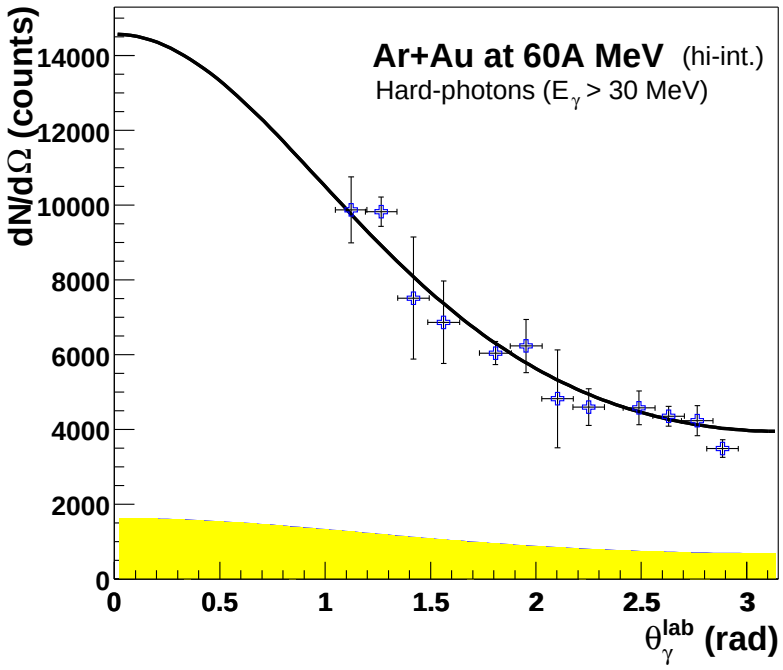

Figure 6.21: *Experimental laboratory angular distribution for hard-photons ($E_\gamma > 30$ MeV) measured in the system $^{36}Ar+^{197}Au$ during the high counting-rate runs and fitted according to equation (6.8). The hatched region indicates the estimated contribution of thermal hard-photons, emitted isotropically from a source moving with β_{AA}.*

Table 6.6: *Direct and thermal hard-photon ($E_\gamma > 30$ MeV) source velocities obtained from a double-source fit analysis, eq. (6.8), of the laboratory angular distributions.*

Reaction	β_S^d	β_S^t	α	I_t/I_{tot}	χ^2/ν
^{36}Ar+^{197}Au (lo)	0.17 ± 0.02	0.06 ± 0.01	0.13 ± 0.08	$22\% \pm 2\%$	2.0
^{36}Ar+^{197}Au (hi)	0.17 ± 0.02	0.06 ± 0.01	0.0 ± 0.0	$19\% \pm 2\%$	1.7
^{36}Ar+^{107}Ag	0.18 ± 0.01	0.09 ± 0.01	0.0 ± 0.0	$19\% \pm 2\%$	0.3
^{36}Ar+^{58}Ni	0.175 ± 0.03	0.14 ± 0.02	0.0 ± 0.0	$20\% \pm 2\%$	0.5
^{36}Ar+^{12}C	0.20 ± 0.01	0.00 ± 0.05	0.25 ± 0.05	$0\% \pm 2\%$	1.1

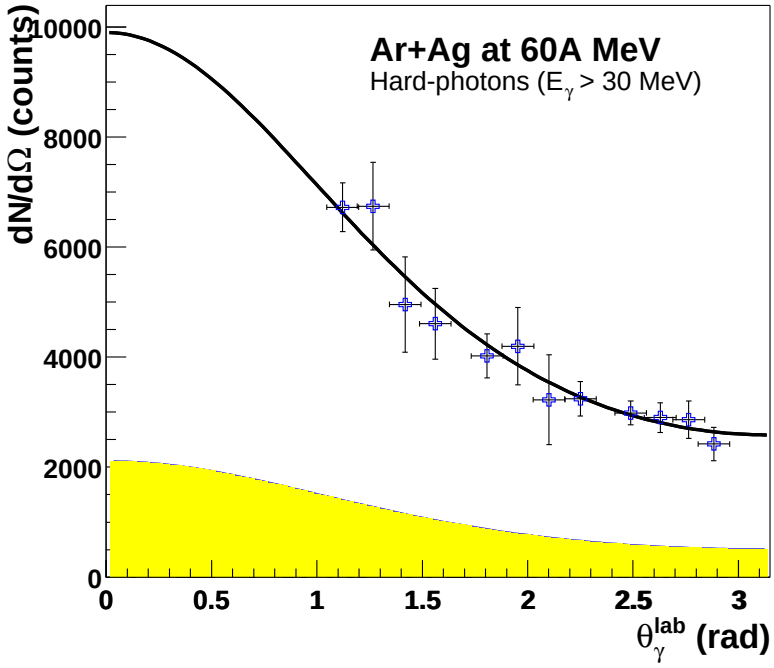

Figure 6.22: *Experimental laboratory angular distribution for hard-photons (E_γ > 30 MeV) measured in the system $^{36}Ar+^{108}Ag$ and fitted according to equation (6.8). The hatched region indicates the estimated contribution of thermal hard-photons, emitted isotropically from a source moving with β_{AA}.*

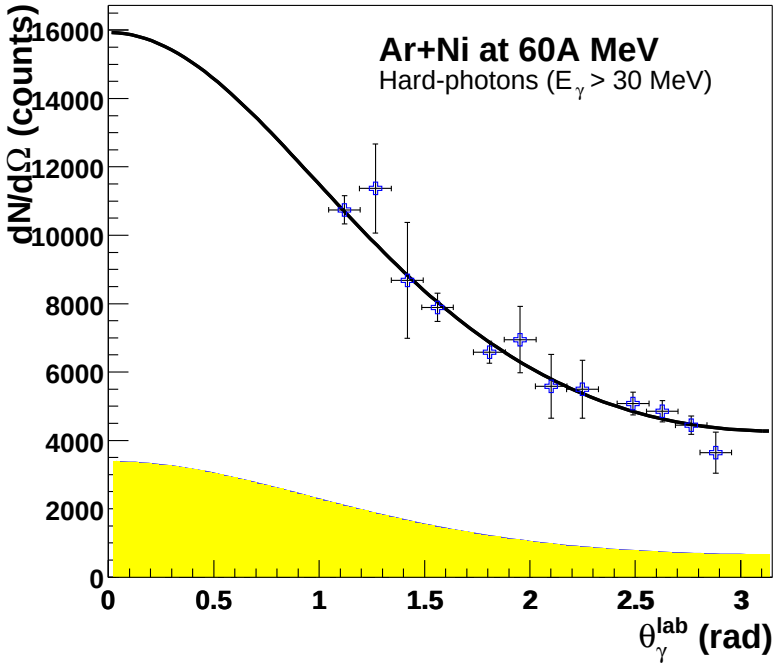

Figure 6.23: *Experimental laboratory angular distribution for hard-photons ($E_\gamma > 30$ MeV) measured in the system $^{36}Ar+^{58}Ni$ and fitted according to equation (6.8). The hatched region indicates the estimated contribution of thermal hard-photons, emitted isotropically from a source moving with β_{AA}.*

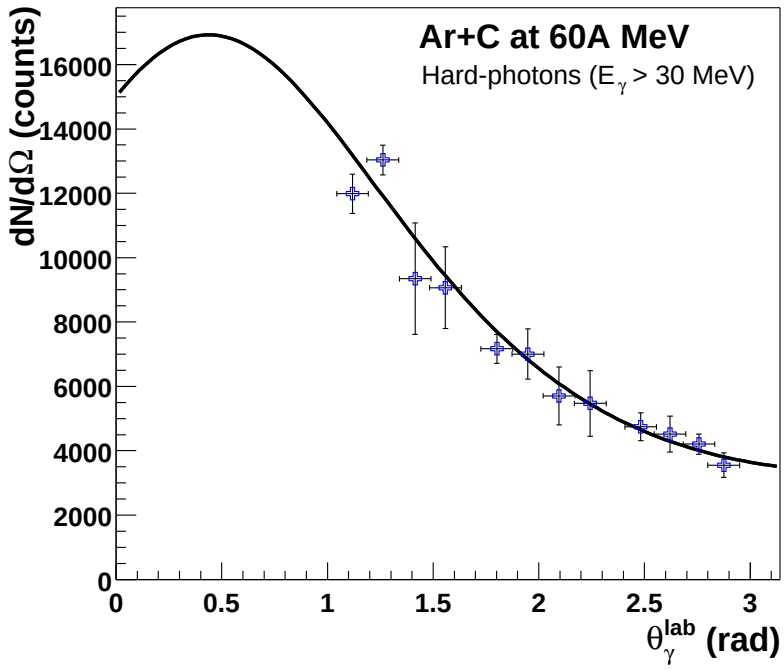

Figure 6.24: *Experimental laboratory angular distribution for hard-photons (E_γ > 30 MeV) measured in the system $^{36}Ar+^{12}C$ and fitted according to equation (6.8). No thermal hard-photon contribution (second term of eq. (6.8)) has been considered in the source-velocity fit analysis.*

6.3 Inclusive charged-particle and fragment distributions

In this Section I present the gross features of the multiplicity distributions of charged-particles, M_{CP}, detected in the Dwarf-Ball and Forward-Wall multidetector systems and produced in the ^{36}Ar+^{197}Au reaction during the low counting-rates runs, and those measured only in the Forward-Wall for the ^{36}Ar+^{108}Ag, ^{58}Ni, ^{12}C reactions. The multiplicity spectra, M_{LCP}, of the light-charged-particles with $Z < 3$, and that of the intermediate-mass-fragments, M_{IMF}, with $3 \leq Z \leq 10$ measured for the ^{36}Ar+^{197}Au system will be also discussed. These results will constitute a useful tool for the exclusive analysis of hard-photon production carried out in the following chapter.

6.3.1 Inclusive charged-particle multiplicities

The charged-particle multiplicity, M_{CP}, distribution, measured for the ^{36}Ar+^{197}Au reaction includes all charged hadrons detected but not individually identified (fig. 6.25). This spectrum has been constructed for events satisfying a minimum-bias particle trigger ("DBor" or "FWor") by adding the charged-particle multiplicities measured separately by the Dwarf-Ball, M_{CP}^{DB}, (fig. 6.26) and by the Forward-Wall, M_{CP}^{FW}, (fig. 6.27) detectors. The M_{CP} distribution has a slowly decreasing plateau which extends up to multiplicities of approximately $M_{CP} \approx 13$. The decrease is followed then by a sharply falling tail up to the largest multiplicity of detected fragments at around $M_{CP} \approx 26$. It has to be noted, however, that above $M_{CP} \approx 18$ the possible contamination due to pileup events cannot be neglected anymore (these pileup events roughly represent a factor 0.05% of the total detected events, as given by the interaction probability value for this reaction, table 4.3). This general trend, shifted of course to somewhat lower multiplicities, is also observed in the charged-particle distribution measured by the Dwarf-Ball (fig. 6.26) except that in that case the plateau in the region of intermediate multiplicities, M_{CP}^{DB} = 5 - 9, is flatter. The M_{CP}^{FW} (fig. 6.27) distribution decreases more rapidly up to $M_{CP}^{FW} \approx 13$. These features reflect the different geometrical acceptances and positions of the two particle multidetectors, and will be exploited in the exclusive analysis for the event selection criteria. In general, the lower and intermediate multiplicities correspond to peripheral and semi-peripheral reactions, and only the last bins corresponding to $\approx$ 5% of the integrated multiplicity are associated with the most central heavy-ion collisions, leading to a large number of reaction products in the exit-channel (see the discussion about the impact-parameter selection in Section 7.1).

The multiplicity distributions, M_{CP}^{FW}, measured in the Forward-Wall for the other three reactions ^{36}Ar+^{108}Ag, ^{58}Ni, ^{12}C at 60A MeV (figs. 6.28, 6.29, and 6.30) show a similar shape. However, since in those runs the DB was absent, the complete information about the reaction's global characteristics is missing, and notably the relative scale of impact-parameters associated with each multiplicity bin (see discussion in Section 7.1). Moreover, it has to be noted that due to the higher counting-rates of these reactions (see table 4.3), the contamination by accidental events where two nuclear collisions occur within the same beam burst is not negligible above the following FW multiplicity values: $M_{CP}^{FW} \approx 8$ for the two heavy systems and $M_{CP}^{FW} \approx 7$ for the ^{36}Ar+^{12}C one.

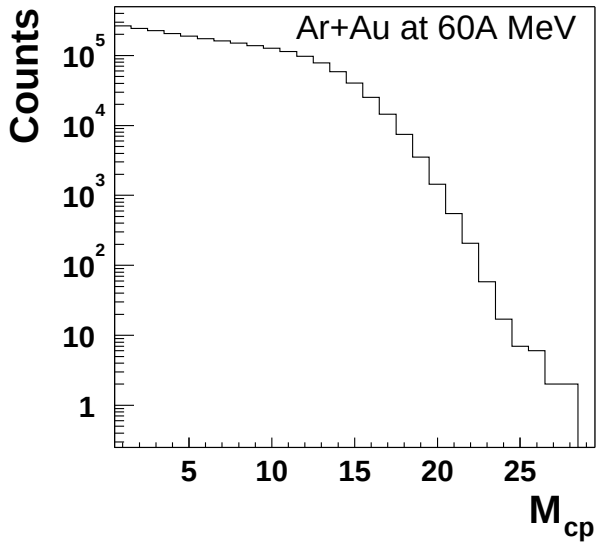

Figure 6.25: *Total inclusive charged-particle multiplicity distribution for the reaction $^{36}Ar+^{197}Au$ at 60A MeV measured with the Dwarf-Ball and Forward-Wall.*

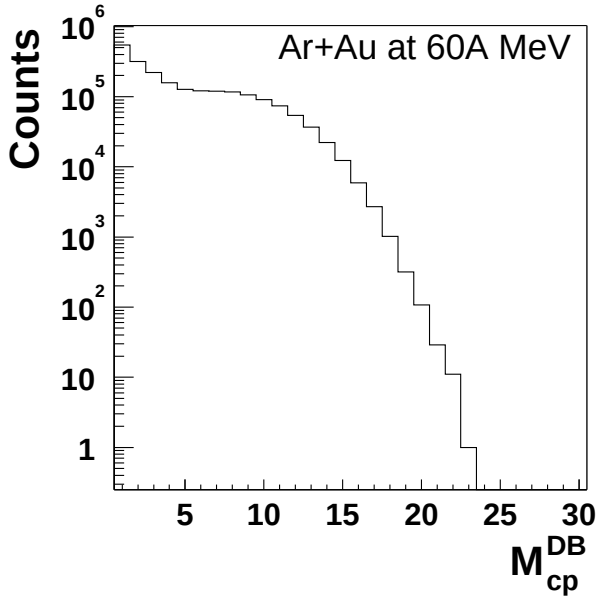

Figure 6.26: *Inclusive charged-particle multiplicity distribution detected in the Dwarf-Ball for the reaction $^{36}Ar+^{197}Au$ at 60A MeV.*

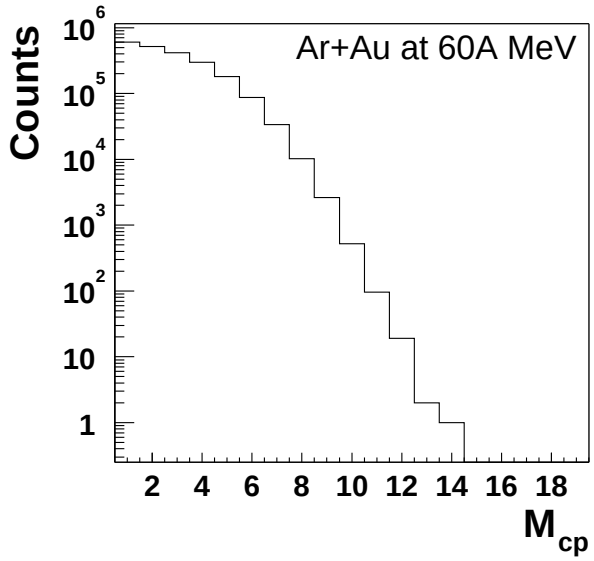

Figure 6.27: *Inclusive charged-particle multiplicity distribution detected in the Forward-Wall for the reaction $^{36}Ar+^{197}Au$ at 60A MeV.*

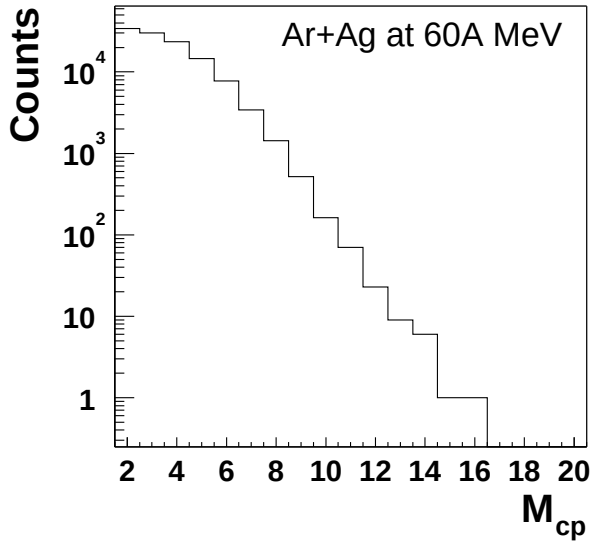

Figure 6.28: *Inclusive charged-particle multiplicity distribution detected in the Forward-Wall for the reaction $^{36}Ar+^{108}Ag$ at 60A MeV.*

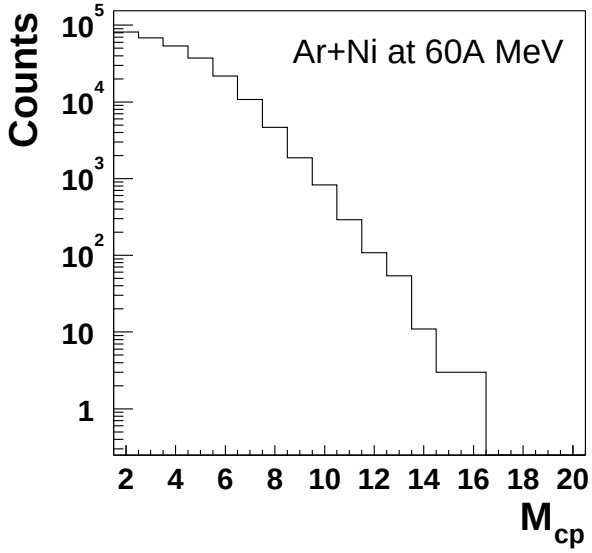

Figure 6.29: *Inclusive charged-particle multiplicity distribution detected in the Forward-Wall for the reaction $^{36}Ar+^{58}Ni$ at 60A MeV.*

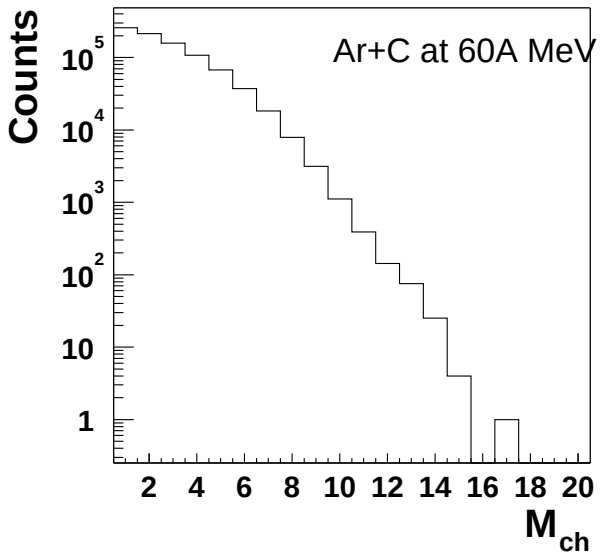

Figure 6.30: *Inclusive charged-particle multiplicity distribution detected in the Forward-Wall for the reaction $^{36}Ar+^{12}C$ at 60A MeV.*

6.3.2 Inclusive LCP and IMF multiplicities

The measured multiplicity distributions for light-charged-particles, M_{LCP}, and inter-mediate-mass-fragments, M_{IMF}, detected in the Dwarf-Ball and Forward-Wall, are shown in fig. 6.31 and in fig. 6.32 respectively. Whereas the definition of LCP as small nuclear fragments having a charge $Z < 3$ (i.e. the different isotopes of H and He) is unambiguous, this is not the case for the definition of IMFs. For the ^{36}Ar+^{197}Au reaction, since the charge of the projectile is Z_p = 18, the domain of intermediate-mass-fragments IMF will be defined as fragments detected in the DB and having a charge comprised between Z = 3 and Z = 10, this definition ensures that the detected IMF are likely to be produced in "multifragmentation"-like reactions emitted mostly in the more backwards hemisphere covered by the DB. This reduces considerably the IMF potentially coming from projectile-like fragments after evaporation (i.e. Ar-like residues) issuing from more peripheral reactions. The separation between LCPs and IMFs for each multidetector is carried out using the pulse-shape methods detailed in Sections 5.5 and 5.6.

The total distribution M_{LCP} (fig. 6.31) shows a trend and shape very close to that of the M_{CP} spectrum. This is not surprising and is just an indication that most of the charged-particles emitted in the ^{36}Ar+^{197}Au reaction are actually "light" charged particles (protons, deuterons, tritons and α's). As a matter of fact, the percentage of the total charge detected in the form of IMFs, within the DB particle acceptance, amounts to roughly $\approx$ 25%, and again only $\approx$ 25% of the nuclear reactions lead to exit channels with at least one detected IMF (fig. 6.32). The average IMF multiplicity observed in the DB for the ^{36}Ar+^{197}Au reaction is $\langle M_{IMF} \rangle \approx 1.3$. The distribution itself presents a sharp exponential-like decrease with increasing IMF multiplicity. Only 5% of the reactions producing an intermediate-mass fragment can be actually considered "true" multifragmentation reactions for which $M_{IMF} \geq 3$. The IMF distribution extends up to values above $M_{LCP} \approx 10$, but most of the reactions with $M_{IMF} \geq 7$ are due to pileup events as it can be inferred from the small change in the slope of the distribution (nonetheless, these reactions can still be considered "true" multifragmentation reactions since, even in the case of e.g. two consecutive reactions simultaneously recorded, their single M_{IMF} values are always above 3).

The relationship between the detected IMF multiplicity and the measured total charged-particle multiplicity (fig. 6.33) helps to characterize the reactions in which IMFs are emitted. Reactions with one or two IMFs are observed in the whole range of charged-particle multiplicities, M_{CP} = 1 - 20, i.e. in reactions with all possible impact-parameters, but they show a maximum for M_{CP} = 5 - 10, i.e. for semi-peripheral/semi-central reactions. As expected, multifragmentation reactions (with $M_{IMF} \geq 3$) are increasingly more probable for progressively more central reactions for which, at least, $M_{CP} \geq 10$.

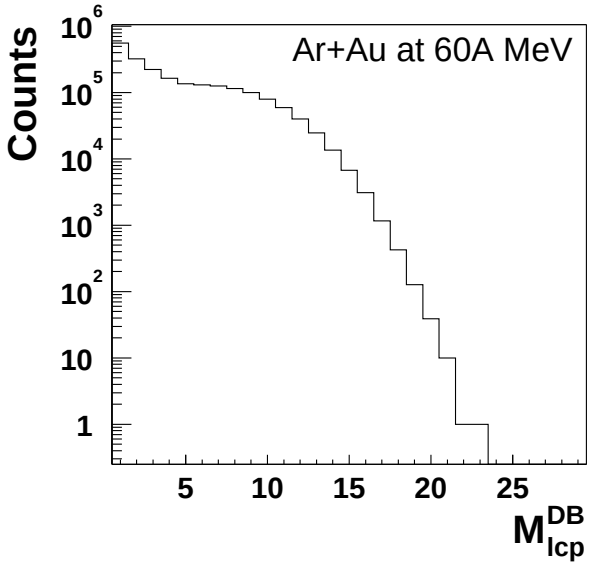

Figure 6.31: *Inclusive light-charged-particle (LCP) multiplicity distribution detected in the Dwarf-Ball for the reaction* $^{36}Ar+^{197}Au$ *at 60A MeV.*

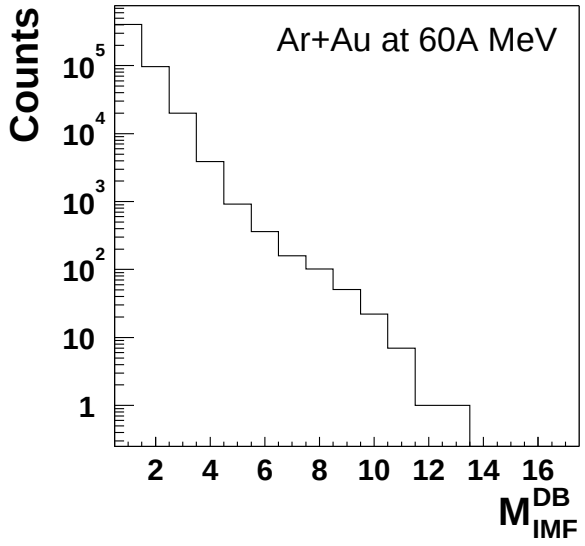

Figure 6.32: *Inclusive intermediate-mass-fragment (IMF) multiplicity detected in the Dwarf-Ball for the reaction* $^{36}Ar+^{197}Au$ *at 60A MeV.*

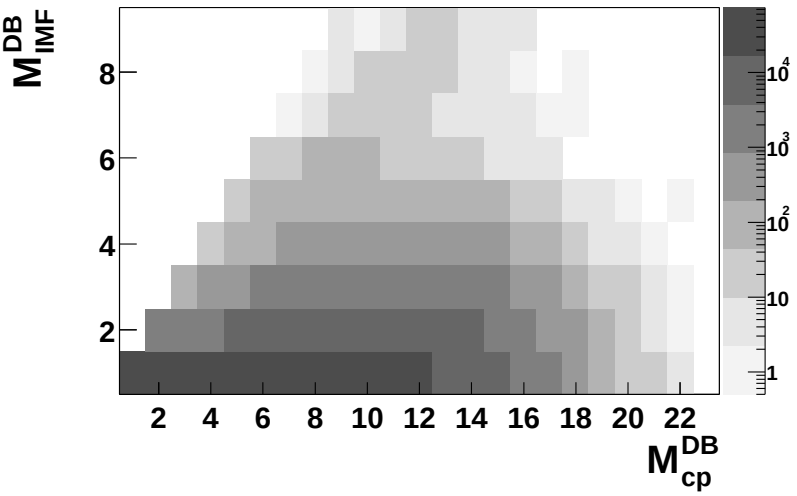

Figure 6.33: *Bidimensional plot (logz scale) of the intermediate-mass-fragment multiplicity detected in the DB (M_{IMF}) as a function of the total charged-particle multiplicity (M_{CP}) detected in the Dwarf-Ball for the reaction $^{36}Ar+^{197}Au$ at 60A MeV.*

6.4 Inclusive cross-sections and multiplicities

6.4.1 Cross-sections formulae

The inclusive cross-section of a certain reaction product X, measured with a certain trigger t, can be experimentally calculated using the following expression:

$$\sigma_X^t(\text{mb}) = \frac{1}{\varepsilon_X^t} \cdot C \cdot \frac{SD_t}{T_t} \cdot N_X^t \tag{6.9}$$

where:

- ε_X^t is the detection efficiency of the trigger for the reaction-product X. It contains the detector response (acceptance, electronics thresholds ...) and also the efficiency of the identification and reconstruction procedures of the analysis. It is obtained through proper simulations of the experimental setup with the GEANT-based KANE package.

- $C = 10^{27}/(N_{inc} N_{at/cm^2})$ is the "usual" cross-section normalization factor that takes into account the number of target nuclei per cm^2 ($N_{at/cm^2} = N_{av}(d/1000)/A$, for a target with atomic number A, and thickness d expressed in mg/cm^2), and the number of incident beam particles N_{inc} during the experiment. (N_{av} is the Avogadro's number and 10^{27} a conversion factor to express C_t in mb).

- SD_t is the DAQ scale-down factor of the trigger t, calculable dividing the inhibited trigger counting-rate by the reduced trigger counting-rate (see below).

- T_t is the life-time of the trigger t, defined as the ratio between the raw and inhibited trigger counting-rates (see below).

- N_X^t is the number of reaction-products X detected by the trigger t. Thus, e.g. for $X = \gamma$ and a photon trigger such as t="TAPS NEU LO*FOWA MUL1" or t="TAPS NEU LO*DB MUL1", N_γ^t is obtained by integrating the photon spectrum above 30 MeV after cosmic and pion subtraction. Similarly, for $X = CP$, with a particle trigger such as t="FOWA MUL1" or t="DB MUL1", N_{CP}^t is obtained integrating the measured charged-particle multiplicity distributions.

The values of N_{inc}, SD_t and T_t are obtained using the information stored on tape by the scalers electronics modules. A "scaler subevent" is written on tape roughly every 2 seconds (actually every $\approx$ 2000 recorded events) and contains four basic (accumulated) parameters per trigger:

- The integrated beam current Q_{beam} collected by the Faraday-cup 5 meters away from the reaction chamber. This value permits to calculate the actual number of Ar-beam particles, N_{inc}, incident on the target during the experiment via: $N_{inc} = Q_{beam}/(Q_{Ar}^+ Q_e)$, where $Q_{Ar}^+ = 18$ is the charge of the (fully stripped) Argon ion finally arriving at the Faraday cup and Q_e the electron charge magnitude.

- The raw number of events satisfying the trigger conditions N_{raw} ("raw scalers").

Table 6.7: *Efficiencies of TAPS for inclusive hard-photon and neutral pion detection (see Section 6.1.4), and charged particle efficiencies of the Dwarf-Ball and Forward-Wall calculated with* KANE/FREESCO *simulations for the five reactions studied.*

Reaction	ε_{γ}	ε_{cp}	$\varepsilon_{\gamma * cp}$	ε_{π^0}
^{36}Ar+^{197}Au (lo)	12.6% ± 0.3%	71.5%± 0.3% (DB)	12.4% ± 0.5% (DB)	1.75% ± 0.1%
		78.7%± 0.3% (FW)	12.4% ± 0.5% (FW)	
^{36}Ar+^{197}Au (hi)	13.8% ± 0.5%	78.7%± 0.3% (FW)	13.7% ± 0.5%	1.75% ± 0.1%
^{36}Ar+^{108}Ag	13.8% ± 0.5%	74.7%± 0.3% (FW)	13.7% ± 0.5%	1.75% ± 0.1%
^{36}Ar+^{58}Ni	13.8% ± 0.5%	71.2%± 0.3% (FW)	13.5% ± 0.5%	1.75% ± 0.1%
^{36}Ar+^{12}C	13.8% ± 0.5%	50.3%± 0.3% (FW)	12.3% ± 0.5%	1.75% ± 0.1%

- The actual number of events accepted by the trigger N_{inh} ("inhibited scalers"). (Due to the trigger dead-time, in general $N_{inh} \leq N_{raw}$).
- The actual number of trigger events recorded on tape N_{red} ("reduced scalers") after applying the selected DAQ reduction-factor of the trigger (see tables 4.12 and 4.13).

6.4.2 Charged-particle detection efficiencies

To calculate the efficiencies of the Dwarf-Ball and Forward-Wall charged-particle multidetectors, we use the FREESCO event generator implemented into the KANE package. FREESCO [Fai86] is an event-generator which simulates the production of nuclear fragments and particles issuing a nucleus-nucleus reaction assuming that they are emitted statistically from a primary hot nucleus with a given input excitation energy[7] ε^*. The efficiency of an inclusive DB and FW trigger for the observation of a given nuclear reaction is calculated by simulating 10.000 nuclear reactions with KANE/FREESCO and counting the total number of reactions finally "detected" by the two phoswich multidetectors. A reaction is said to be detected by the DB or the FW if at least one hit (corresponding to a LCP or heavier nuclear fragment) is detected by each multidetector respectively. The average thresholds of the absorbers of the DB and FW phoswiches (around 1 - 2 MeV/nucleon for the different particles) have been included in the simulations, as well as the "software" threshold values of the discriminators. With those conditions the obtained inclusive particle efficiencies of the Dwarf-Ball and Forward-Wall are listed in table 6.7 for the four systems studied.

From table 6.7 it can be seen that both the DB and the FW are capable of observing more than 70% of the total nucleus-nucleus reactions produced in the direct kinematics systems (^{36}Ar+^{197}Au, ^{108}Ag, ^{58}Ni), and ≈ 50% in the reverse kinematics ^{36}Ar+^{12}C reaction. Only the most peripheral nuclear reactions leading to the emission of particles along the beam-pipe (i.e. with $\theta < 2.4°$) are not detected by our setup. It is not surprising that the efficiency of the Forward-Wall (covering around 4% of the solid-angle) is somewhat larger than that of the Dwarf-Ball (which covers almost 80% of 4π) since, obviously,

[7] In FREESCO the initial nucleus excitation energy, ε^*, is assessed from the reaction impact parameter, the incident bombarding energy and the particular projectile-target combination.

the FW covers the most forward hemisphere of the reaction where most of the reaction products, emitted in the relatively more probable peripheral reactions, are kinematically focused in such fixed-target experiments.

6.4.3 Hard-photon detection efficiency

The efficiency for hard-photon detection of our setup is calculated with the KANE package assuming for each heavy-ion reaction that hard-photons are emitted with an exponential distribution[8] with the experimentally measured slope parameter E_0^d, from a source moving with the experimentally measured average velocities listed in table 6.5. The angular distribution is taken as the sum of an isotropic and a dipolar term with anisotropy factor $\alpha = 0.0 - 0.2$. The mean efficiency due to the detector response, is calculated simulating with KANE the emission of 10.000 hard-photons according to the former energy and angle input distribution and by dividing this number by the actual number of hard-photons finally "detected". The result of such a procedure yields $\varepsilon_\gamma^{TAPS} = 14.4\% \pm 0.5\%$ for the four targets during the high counting-rate runs (without the Dwarf-Ball), and $\varepsilon_\gamma^{TAPS} = 13.1\% \pm 0.5\%$ for the low counting-rates runs (where some e^-e^+ pair-production of the hard-photons takes place within the Dwarf-Ball material). The $\pm$ 0.5% quoted error includes the slightly different source velocities for the four systems and the uncertainty on the dipolar contribution to the total hard-photon yield (α = 0.0 - 0.2). The values of $\varepsilon_\gamma^{TAPS}$ are very close to the pure geometrical acceptance of the six TAPS blocks around the target which cover about 15% of the total solid angle. The whole identification and reconstruction photon analysis used for the real data is applied to the simulated data, the mean efficiency of this Rosebud-based analysis is $\varepsilon_\gamma^{Rosebud} \approx 96.0\% \pm 1\%$ for all systems. The final efficiency, $\varepsilon_\gamma = \varepsilon_\gamma^{TAPS} \cdot \varepsilon_\gamma^{Rosebud}$, for hard-photon detection is, thus, $\varepsilon_\gamma = 13.8\% \pm 0.5\%$ for the high counting-rates runs and $\varepsilon_\gamma = 12.6\% \pm 0.5\%$ for the low rates ones (Table 6.7).

It has to be taken into account, however, that in all our experimental results concerning photon production we have not considered a "pure" photon trigger but a combined "photon*(minimum-bias particle)" one. The reason is, as explained in Section 6.1.3, to assure the selection of photons really produced in a nuclear reaction (observed by the particle multidetectors) and thus to minimize other signals coming from, e.g., a cosmic background event. Therefore, to correctly apply formula (6.9) to compute the γ cross-section, one has to use the proper (mixed trigger) efficiency $\varepsilon_{\gamma * cp}$. In the case of hard-photons, $\varepsilon_{\gamma * cp}$ should be close to ε_γ because the production of a bremsstrahlung photons requires a rather central impact-parameter reaction which leads also to the emission of nuclear fragments and particles recorded by the FW or DB trigger. To exactly quantify the value of $\varepsilon_{\gamma * cp}$, one carries out a KANE/FREESCO particle simulation to obtain the distribution of impact-parameters (fig 6.34) "seen" by our multidetectors (i.e. the values of *b* which lead to some charged particle emitted within the acceptance windows of the DB and FW and, thus, satisfying the particle trigger conditions).

As expected from the computed absolute particle efficiencies, ε_{cp} , (Section 6.4.2), the two charged-particle detectors have a ≈100% efficiency for the central and semi-

[8] For the hard-photon efficiency calculations of our setup, the additional consideration in the simulations of the second thermal exponential does not introduce any noticeable change.

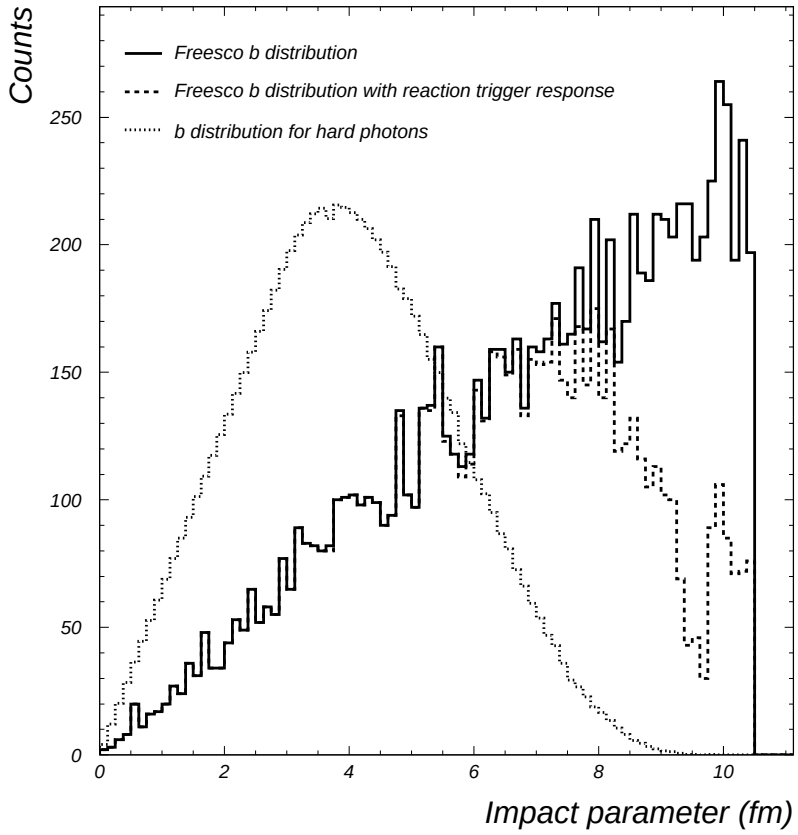

Figure 6.34: *Input distribution of impact-parameters, b, for the* $^{36}Ar+^{197}Au$ *events generated with* FREESCO *(solid line), and distribution of impact-parameters of the fraction of these simulated events which verify the "minimum-bias" particle trigger (dashed line). The distribution of impact-parameters for events leading to the emission of a hard-photon in such a heavy-ion reaction according to the "equal participant" geometrical model is also indicated (dotted line).*

central reactions in the four systems (e.g. $b < 7$ fm in fig. 6.34). For increasing impact-parameters, however, the inverse-kinematics reaction (^{36}Ar+^{12}C) leads to exit-channels whose fragments are progressively less detected. This is also the case for the three heavier systems but for much more peripheral reactions. To calculate the efficiency of the combined $\varepsilon_{\gamma * cp}$ triggers, one folds the particle efficiency as a function of impact-parameter obtained from the simulations (dashed line in fig. 6.34) with the known impact-parameter dependence of the hard-photon yield as given by the geometrical "equal-participant" model (dotted line in fig. 6.34 obtained from equations (3.12) and (3.13)). This procedure yields the final combined $\varepsilon_{\gamma * cp}$ efficiencies listed in table 6.7. For the three heaviest systems $\varepsilon_{\gamma * cp} \approx \varepsilon_{\gamma}$, and for the lightest system $\varepsilon_{\gamma * cp} \approx 0.89\varepsilon_{\gamma}$.

6.4.4 Total reaction cross-sections

To compute the reaction cross-section one applies equation (6.9) for a minimum-bias (particle) trigger, "DBor s.d."[9] for the low-counting-rates runs, and "FWor"[10], for the high-counting-rates runs. N_{react} is obtained integrating the measured charged particle multiplicity distributions (plots 6.25 and 6.28 - 6.30). The values of the total reaction cross-sections for the 5 systems studied are listed in table 6.8. The reaction cross-section for the ^{36}Ar+^{197}Au system, has been calculated with the two aforementioned "DBor s.d." and "FWor" minimum-bias triggers (the latter for the low and high counting-rates run) giving three experimental values for σ_R^{exp}. The associated errors, of the order of 10%, contain effects of statistical nature (in the number of counts, N_{react}, or in the number of incident particles, N_{inc}, determined from the Faraday cup beam charge integration) and of systematical nature (mainly due to the uncertainties in the different target thickness d (mg/cm^2)). At this point, it has to be indicated, however, that to obtain the reported cross-sections, the inhibited values of the trigger counting rates N_{inh} given by the "scalers" on tape have *not* been taken into account, but instead the raw values have been considered due to some scalers recording problem (see below). The consideration $N_{inh} \approx N_{raw}$ is true with certainty for the low counting-rate runs for which the low interaction probability allowed the whole set-up to work without any appreciable (trigger) dead-time. For the high counting-rates the trigger lifetime is not 100% and thus, in general, $N_{inh} < N_{raw}$. However, due presumably to an error in the DAQ scalers output, the recorded value of N_{raw} seems to be very close to the expected N_{inh}, and N_{inh} seems to be much too low. This effect apart (which only affects the high counting-rate values), the measured reaction cross-sections are certainly in an excellent agreement with the nucleus-nucleus (geometrical) reaction cross-section (see formula in Appendix 4).

[9] "DBor s.d." is defined as at least one hit in a Dwarf-Ball module and it is recorded on tape with a 10 "scale-down" (s.d.) pre-trigger factor (see Section 4.7.4).

[10] "FWor" is defined as at least one hit in the Forward-Wall detector.

Table 6.8: *Inclusive experimental and theoretical (geometrical) total reaction cross-sections for the five systems studied in this experiment. The cross-sections for the $^{36}Ar+^{197}Au$ reaction are given for three different considered triggers (two for the low counting-rates runs and one for the high counting-rates runs), as well as their average value.*

Reaction	σ_R^{exp} (mb)	σ_R^{theo} (mb)
^{36}Ar+^{197}Au (lo DB)	4372 ± 560	4600
^{36}Ar+^{197}Au (lo FW)	4592 ± 592	4600
^{36}Ar+^{197}Au (hi FW)	4343 ± 526	4600
^{36}Ar+^{197}Au (av.)	4426 ± 321	4600
^{36}Ar+^{108}Ag	3960 ± 481	3850
^{36}Ar+^{58}Ni	3306 ± 406	3240
^{36}Ar+^{12}C	3120 ± 700	2240

Table 6.9: *Inclusive experimental and theoretical hard-photon cross-sections for the four systems studied in this experiment. The cross-sections for the $^{36}Ar+^{197}Au$ reaction are given for three different considered triggers (two for the low counting-rates runs and one for the high counting-rates runs), as well as their average value.*

Reaction	σ_γ^{exp} (mb)	σ_γ^{sys} (mb)
^{36}Ar+^{197}Au (lo, $\gamma * DB$)	3.80 ± 0.34	3.9
^{36}Ar+^{197}Au (lo, $\gamma * FW$)	3.79 ± 0.34	3.9
^{36}Ar+^{197}Au (hi, $\gamma * FW$)	3.80 ± 0.29	3.9
^{36}Ar+^{197}Au (av.)	3.80 ± 0.18	3.9
^{36}Ar+^{108}Ag	3.09 ± 0.25	2.8
^{36}Ar+^{58}Ni	1.71 ± 0.14	1.9
^{36}Ar+^{12}C	0.60 ± 0.12	0.5

6.4.5 Hard-photon production cross-sections and multiplicities

Using equation (6.9) for a minimum-bias (photon) trigger like "TAPS NEU LOW * DB1" for the low-counting-rates runs, and "TAPS NEU LOW*FW1" for the high-counting-rates runs, and integrating the hard-photon energy spectra above E_γ = 30 MeV after cosmic and pion subtraction (i.e. integrating plots 6.5 - 6.9), we obtain the experimental hard-photon production cross-sections[11] listed in table 6.9. They are in order of the 0.5 - 5.0 milibarns depending on the target size. The associated errors are mainly due to the uncertainties in the different target thickness d (mg/cm^2). These values of σ_γ^{exp} are in a very good agreement with the expected values obtained from the systematics by applying the formula (3.8) given in Section 3.2.1.

Apart from the absolute hard-photon production cross-section, σ_γ, two other closely-related quantities are also physically relevant for the full characterization of hard-photon emission:

- the hard-photon multiplicity, M_γ, i.e. the probability of producing a hard-photon per nuclear reaction, and
- the probability, $P_{np\gamma}$, of emission of a hard-photon per individual *pn* collision.

Experimentally, M_γ^{exp} is simply derived from the ratio of the measured hard-photon to nuclear cross-sections:

$$M_\gamma^{exp} = \frac{\sigma_\gamma^{exp}}{\sigma_R^{exp}} \tag{6.10}$$

This quantity is much more free of possible experimental and/or systematical errors than σ_γ^{exp}, since the factor $C = 10^{27}/(N_{inc} N_{at/cm^2})$ is cancelled in both terms of the fraction. Therefore, any uncertainty in the value of the target thickness or in the integrated beam current does not affect the calculation of M_γ. Moreover, the aforementioned trigger

[11] The aforementioned discussion about the scalers counting-rates also holds for the hard-photon cross-sections measured for the *high* counting-rates runs.

counting-rate error in the high-intensity recorded scalers is skipped because approximatively both lifetime factors for the hard-photon and particle triggers, entering in the calculation of σ_γ^{exp} and σ_R^{exp} respectively, have a very close value in all the cases.
The hard-photon probability per *pn* collisions, $P_{np\gamma}^{exp}$, is obtained by dividing M_γ^{exp} by the impact-parameter averaged total number of individual proton-neutron collisions, $\langle N_{pn}\rangle_b$ which is computed from the "equal-participant model" parametrization given by equation (3.10):

$$P_{pn\gamma}^{exp} = \frac{M_\gamma^{exp}}{\langle N_{pn}\rangle_b} \tag{6.11}$$

The expected value of M_γ^{sys} is given by the experimental systematics of hard-photon production (via the factor P_γ^{sys}) and by the "equal participant model" prescription for incoherent *pn* bremsstrahlung (through $\langle N_{pn}\rangle_b$):

$$M_\gamma^{sys} = P_\gamma^{sys}\,\langle N_{pn}\rangle_b \tag{6.12}$$

$$P_\gamma^{sys} = (6.3 \pm 0.1)\cdot 10^{-4}\cdot e^{-30\,[\mathrm{MeV}]/E_0} \tag{6.13}$$

Employing expressions (6.10) and (6.11), together with (3.10), one obtains for the four studied systems the experimental values M_γ^{exp} and $P_{pn\gamma}^{exp}$ listed in table 6.10 and in table 6.11 respectively. These values are globally in very good agreement with the systematics of hard-photon production per *pn* collision as a function of the incident energy (fig. 6.35). Specially, in the case of the two heaviest targets (Au and Ag) the agreement is at the level of $<5\%$, and somewhat worse for the Ni ($\approx 8\%$) and C ($\approx 15\%$) targets. Even with the experimentally observed 20% contribution of thermal bremsstrahlung photons, the measured values of the hard-photon cross-sections, multiplicities and probabilities per *pn* collision are not significantly shifted from the results expected from the collected systematics for hard-photon production in incoherent *pn* collisions. This is not surprising since we know that the phenomenological formulas of the systematics (which are grossly accurate within a factor two, see fig. 6.35) have been derived from fits to experimental data of heavy systems which also contain a second-chance bremsstrahlung component (although this additional component had not been explicitly identified in the spectra so far).

The experimental *thermal* bremsstrahlung multiplicities per nuclear reaction, M_γ^t, and *thermal* probabilities per *pn* collision, $P_{pn\gamma}^t$, obtained from M_γ^{exp}, $P_{pn\gamma}^{exp}$ and the measured ratios I_t/I_{tot}, i.e. via: $(M_\gamma^t, P_{pn\gamma}^t) = I_t/I_{tot}\,(M_\gamma^{exp}, P_{pn\gamma}^{exp})$, are reported in table 6.12.

A summary of the experimental total, M_γ, and thermal, M_γ^t, bremsstrahlung multiplicities per nuclear reaction are collected in table 6.13, where we have also added the values obtained in the ^{86}Kr(60*A* MeV)+^{58}Ni reaction studied at the same bombarding energy [Mart94]. The most interesting aspect of these hard-photon multiplicities M_γ (either total or "thermal") is that they are neatly correlated with the mean number of neutron-proton collisions for each reaction (fig. 6.36). This is just a direct evidence that the probability of producing a hard-γ per nuclear reaction is proportional to the number of *pn* collisions, i.e. that they result from the incoherent summation of individual proton-neutron collisions within the participant zone. The distribution of thermal multiplicities, M_γ^t, shows (fig.

Table 6.10: *Inclusive experimental and theoretical hard-photon multiplicities per nuclear reaction, M_γ, for the four systems studied in this experiment. The experimental multiplicities for the $^{36}Ar+^{197}Au$ reaction are given for three different considered triggers (two for the low counting-rates runs and one for the high counting-rates runs), as well as their average value.*

Reaction	M_γ^{exp}	M_γ^{sys}
^{36}Ar+^{197}Au (lo $\gamma * DB$)	$(8.67 \pm 1.35)\cdot 10^{-4}$	$(8.5 \pm 0.1)\cdot 10^{-4}$
^{36}Ar+^{197}Au (lo $\gamma * FW$)	$(8.26 \pm 1.24)\cdot 10^{-4}$	$(8.5 \pm 0.1)\cdot 10^{-4}$
^{36}Ar+^{197}Au (hi $\gamma * FW$)	$(8.87 \pm 1.24)\cdot 10^{-4}$	$(8.5 \pm 0.1)\cdot 10^{-4}$
^{36}Ar+^{197}Au (av.)	$(8.62 \pm 0.74)\cdot 10^{-4}$	$(8.5 \pm 0.1)\cdot 10^{-4}$
^{36}Ar+^{108}Ag	$(7.81 \pm 1.17)\cdot 10^{-4}$	$(7.3 \pm 0.1)\cdot 10^{-4}$
^{36}Ar+^{58}Ni	$(5.48 \pm 0.82)\cdot 10^{-4}$	$(6.0 \pm 0.1)\cdot 10^{-4}$
^{36}Ar+^{12}C	$(1.91 \pm 0.57)\cdot 10^{-4}$	$(2.4 \pm 0.1)\cdot 10^{-4}$

Table 6.11: *Inclusive experimental and theoretical hard-photon probabilities per pn collision, $P_{pn\gamma}$, as well as (impact-parameter averaged) number of pn collisions, $\langle N_{pn}\rangle_b$, for the four systems studied in this experiment. The values given for the $^{36}Ar+^{197}Au$ reaction correspond for three different considered triggers (two for the low counting-rates runs and one for the high counting-rates runs), as well as their average value.*

Reaction	$P_{pn\gamma}^{exp}$	$P_{pn\gamma}^{sys}$	$\langle N_{pn}\rangle_b$
^{36}Ar+^{197}Au (lo $\gamma * DB$)	$(1.24 \pm 0.20)\cdot 10^{-4}$	$(1.24 \pm 0.02)\cdot 10^{-4}$	6.8
^{36}Ar+^{197}Au (lo $\gamma * FW$)	$(1.18 \pm 0.18)\cdot 10^{-4}$	$(1.24 \pm 0.02)\cdot 10^{-4}$	6.8
^{36}Ar+^{197}Au (hi $\gamma * FW$)	$(1.27 \pm 0.18)\cdot 10^{-4}$	$(1.24 \pm 0.02)\cdot 10^{-4}$	6.8
^{36}Ar+^{197}Au (av.)	$(1.23 \pm 0.14)\cdot 10^{-4}$	$(1.24 \pm 0.02)\cdot 10^{-4}$	6.8
^{36}Ar+^{108}Ag	$(1.37 \pm 0.21)\cdot 10^{-4}$	$(1.29 \pm 0.02)\cdot 10^{-4}$	5.7
^{36}Ar+^{58}Ni	$(1.22 \pm 0.18)\cdot 10^{-4}$	$(1.33 \pm 0.02)\cdot 10^{-4}$	4.5
^{36}Ar+^{12}C	$(1.07 \pm 0.32)\cdot 10^{-4}$	$(1.35 \pm 0.02)\cdot 10^{-4}$	1.8

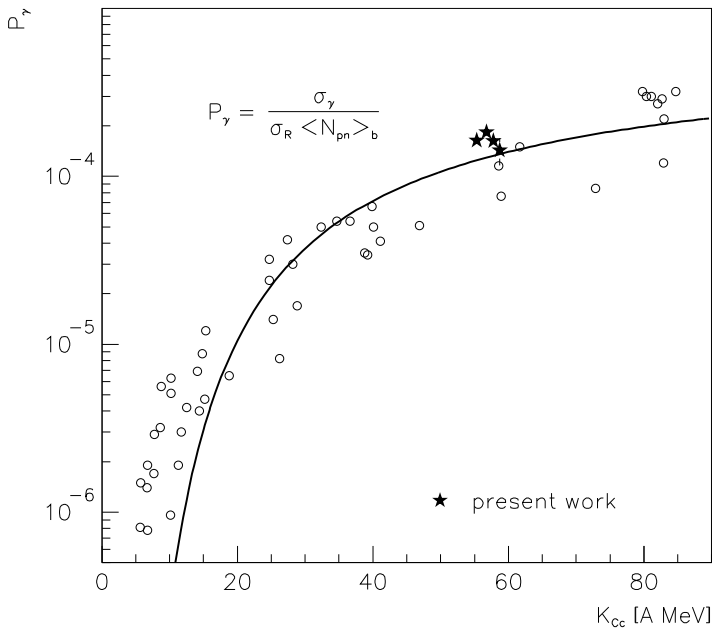

Figure 6.35: *Systematics [Schu97] of measured photon emission probabilities per pn collision, $P^{exp}_{pn\gamma}$, as a function of the (Coulomb-corrected) bombarding energy per nucleon (see also fig. 3.5). Our data are represented by stars. The solid line represents a fit to eq. (6.13).*

Table 6.12: *Inclusive experimental thermal bremsstrahlung multiplicities per nuclear reaction, M^t_γ, and thermal probabilities per pn collision, $P^t_{pn\gamma}$, for the four systems studied in this experiment. The values given for the $^{36}Ar+^{197}Au$ reaction correspond for three different considered triggers (two for the low counting-rates runs and one for the high counting-rates runs), as well as their average value.*

Reaction	M^t_γ	$P^t_{pn\gamma}$
^{36}Ar+^{197}Au (lo $\gamma * DB$)	$(1.60 \pm 0.26)\cdot 10^{-4}$	$(0.23 \pm 0.02)\cdot 10^{-4}$
^{36}Ar+^{197}Au (lo $\gamma * FW$)	$(1.53 \pm 0.25)\cdot 10^{-4}$	$(0.22 \pm 0.02)\cdot 10^{-4}$
^{36}Ar+^{197}Au (hi $\gamma * FW$)	$(1.68 \pm 0.25)\cdot 10^{-4}$	$(0.24 \pm 0.02)\cdot 10^{-4}$
^{36}Ar+^{197}Au (av.)	$(1.61 \pm 0.16)\cdot 10^{-4}$	$(0.23 \pm 0.02)\cdot 10^{-4}$
^{36}Ar+^{108}Ag	$(1.16 \pm 0.19)\cdot 10^{-4}$	$(0.20 \pm 0.02)\cdot 10^{-4}$
^{36}Ar+^{58}Ni	$(1.07 \pm 0.17)\cdot 10^{-4}$	$(0.24 \pm 0.02)\cdot 10^{-4}$
^{36}Ar+^{12}C	$(0.0 \pm 0.30)\cdot 10^{-4}$	$(0.00 \pm 0.02)\cdot 10^{-4}$

Table 6.13: *Total, M_γ, and thermal, M_γ^t, bremsstrahlung multiplicities per nuclear reaction measured in the four systems studied in this experiment and in the ^{86}Kr(60A MeV)+^{58}Ni reaction [Mart94]. The (impact-parameter averaged) number of pn collisions, $\langle N_{pn}\rangle_b$, is also indicated.*

Reaction	M_γ	M_γ^t	$\langle N_{pn}\rangle_b$
^{86}Kr+^{58}Ni	$(8.29 \pm 0.50)\cdot 10^{-4}$	$(2.05 \pm 0.14)\cdot 10^{-4}$	7.0
^{36}Ar+^{197}Au	$(8.62 \pm 0.74)\cdot 10^{-4}$	$(1.61 \pm 0.16)\cdot 10^{-4}$	6.8
^{36}Ar+^{108}Ag	$(7.81 \pm 1.17)\cdot 10^{-4}$	$(1.16 \pm 0.19)\cdot 10^{-4}$	5.7
^{36}Ar+^{58}Ni	$(5.48 \pm 0.82)\cdot 10^{-4}$	$(1.07 \pm 0.17)\cdot 10^{-4}$	4.5
^{36}Ar+^{12}C	$(1.91 \pm 0.57)\cdot 10^{-4}$	$(0.00 \pm 0.30)\cdot 10^{-4}$	1.8

6.36) two differences when compared to the total M_γ distribution: (1) a lower slope, and (2) an offset in the number of *pn* collisions, $\langle N_{pn}\rangle_b$, for which $M_\gamma = 0$. Whereas the first observation indicates that the probability of emitting a thermal hard-photon is smaller due to the lower energy available in secondary *pn* scatterings, the second one seems to point out to the existence of a threshold in the number of *pn* collisions below which no thermal bremsstrahlung emission takes place. According to this interpretation, $\langle N_{pn}\rangle_b \approx 2$ (see fig. 6.36) would be the minimal (impact-parameter averaged) value of proton-neutron collisions in a system for which secondary collisions, and therefore thermalization, can occur.

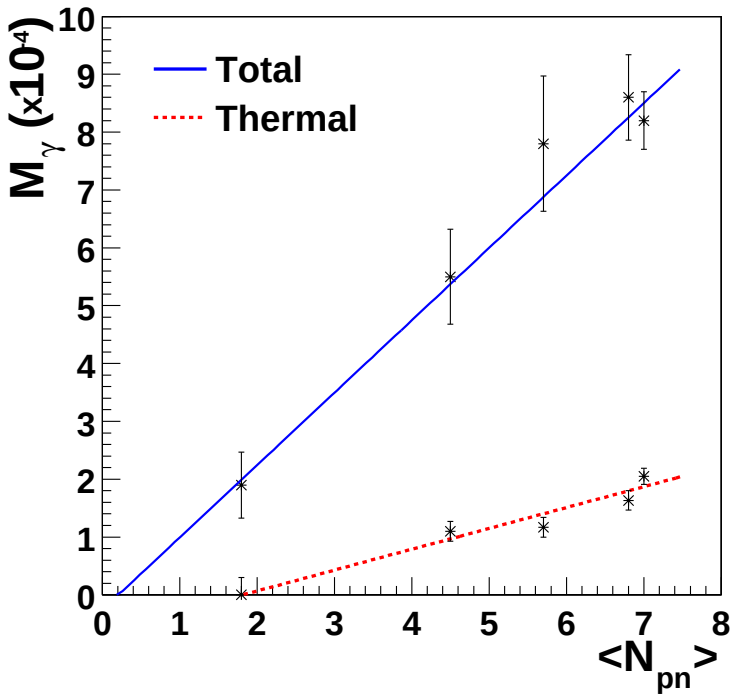

Figure 6.36: *Experimental total, M_γ, and thermal, M_γ^t, hard-photon multiplicities per nuclear reaction plotted as a function of the (impact-parameter averaged) number of pn collisions, $\langle N_{pn} \rangle_b$, in the five reactions studied by the TAPS collaboration at 60A MeV bombarding energy (the four systems of the present experiment plus the $^{86}Kr+^{58}Ni$ one studied at GANIL in 1992 [Mart94]). The solid and dashed lines are linear fits to the data points.*

Chapter 7

Exclusive experimental results

Summary

7.1 Event selection 174
7.2 Exclusive photon spectra 178
7.2.1 Central reactions 179
7.2.2 Peripheral reactions 181
7.2.3 Multifragmentation reactions 181
7.3 Impact-parameter dependence of the photon yield 184
7.4 Summary of the experimental results and preliminary interpretation 188
7.4.1 GDR photons 189
7.4.2 Coherent nucleus-nucleus bremsstrahlung 191
7.4.3 Cooperative cluster bremsstrahlung 192
7.4.4 Proton-proton ($pp\gamma$) bremsstrahlung 193
7.4.5 Bremsstrahlung from second-chance NN collisions. Preequilibrium or thermal ? 193

So far, we have only discussed purely inclusive, i.e. impact-parameter integrated, observables (hard-photon energy spectra, angular distributions and absolute cross-sections and multiplicities). Signatures of more interesting phenomena produced in compressed and hot nuclear systems undergoing e.g. a multifragmentation process, are more likely to be detected in central, i.e. small impact-parameter, collisions than in impact-parameter integrated ones. In the latter, the contributions from large centrality events are weighted very little because of $d^2b = bdbd\phi$. Whereas in the inclusive study developed in the former chapter, the final state of the produced nuclear systems is not known, in exclusive analysis, specific channels of the final-state can be selected and studied. In order to obtain more information about the mechanism of fragment and thermal hard-photon production in the considered heavy-ion reactions, one has to go, therefore, one step beyond the single-particle measurements and investigate the correlations between fragments and photons in an exclusive manner. In this Section we will investigate the dependence of the energy spectra and photon yields on the impact-parameter, mainly for the data collected for the ^{36}Ar+^{197}Au system during the low counting-rates runs for which the whole particle setup (DB+FW) was operating.

7.1 Event selection

We are interested in isolating central and peripheral collisions on an event-per-event basis by selecting one global experimental variable correlated with the impact-parameter of the reaction. Several of such observables have been proposed and used in different experiments as it has been mentioned in Section 2.1.2 (for a recent review comparing the different methods see e.g. [Fran97]). The total charged particle multiplicity M_{cp} has been used since long [Sto80] as a selector of the reaction centrality in heavy-ion experiments. The higher particle multiplicity being related with the smaller impact parameter and vice versa, an intuitive assumption supported by numerical calculations. As a matter of fact, relying on a geometrical method [Cava90] and supposing a monotonic dependence between the impact parameter b and M_{cp}, it is actually possible to quantitatively correlate a certain multiplicity to a certain value of b (within the intrinsical statistical fluctuations). In such "sharp cut-off approximation" [Cava90, Kim92], by e.g. gating on the top (bottom) $\approx$ 5% of the total charged-particle multiplicity distributions, one can determine an approximate centrality scale corresponding to a reduced impact parameter of $b/b_{max} \approx 0.2$ (0.8).

Such general approach for selecting peripheral and central collisions will be applied in our case to study the hard-photon spectra and yields as a function of impact-parameter. Nonetheless, it turns out that, since hard-photons are only produced "subthreshold", i.e. in single nucleon-nucleon collisions making use of the Fermi motion, the number of NN collisions will lower with increasing impact parameter and hence it will become less probable that two nucleons with sufficient relative momentum collide. This fact concentrates the production of hard photons at low impact parameters, as we have mentioned in the discussion of the efficiency for γ-particle triggers (Section 6.4.3). Therefore, the selection of nuclear reactions in which a hard photon is detected implies intrinsically an impact-parameter bias towards rather semi-central reactions.

This is apparent in the total particle multiplicity distribution, M_{cp}^{tot}, measured in the DB and FW when a coincident photon[1] detected in TAPS is required (fig. 7.1). This distribution peaks at M_{cp}^{tot} = 9, i.e. at the region of semi-central impact-parameters, in contrast with the inclusive particle multiplicity , M_{cp} (fig. 6.25), which shows a maximum for low particle multiplicities (i.e. for the more probable peripheral reactions). Our off-line event-type selection will be done, thus, using appropriate charged-particle multiplicity gates in this M_{cp}^{tot} distribution. More specifically, the following central, peripheral and multifragmentation reactions selection criteria have been considered for the exclusive study of the ^{36}Ar+^{197}Au system:

- Central reaction selection: M_{cp}^{tot} = 15 - 21. This condition selects the most central collisions, having large particle multiplicity detected in the DB and FW, without significant contamination of pileup events (which start to be non negligible above M_{cp} = 21 for the low counting-rate runs according to the experimental interaction probability of $\sim$0.05%). This central event selection corresponds to a cross-sections of the order of 9% of σ_{tot}.

- Peripheral reaction selection: M_{cp}^{tot} = 1 - 2. We consider as peripheral events those low-multiplicity reactions which only fire 1 or 2 detectors of the DB and FW. Such low-multiplicity criteria are the minimal conditions below which, spurious cosmic-events firing TAPS and misidentified as photons, are almost the only events recorded. This subset of peripheral events represents around 5% of the total reaction cross-section.

- Multifragmentation reaction selection: $M_{IMF}^{DB} > 3$. All reactions leading to the production of at least 3 IMF's detected in the DB, i.e. IMF's emitted at $\theta_{lab} > 32°$, are considered as multifragmentation reactions. We will not consider the IMF multiplicity measured in the FW since those events are certainly populated with intermediate-fragments coming from the projectile and we are interested in observing multifragmentation of the hot and heavy produced nuclear system(s) (see the discussion about the characteristics of the hot residue(s) produced in our reactions in Section 8.1.2). As a matter of fact, it is known, from the study of the very similar ^{36}Ar+^{197}Au at 65*A* MeV [Colin98, Sun00] and ^{56}Fe+^{197}Au 50*A* MeV [Sang95] systems, that virtually all IMFs observed at backward angles stem from the secondary decay of the highly excited heavy-target remnant. It turns out that the cross-section exhausted by such "multifragmentation" events accounts for $\sim$8% of σ_{tot}, i.e. we are selecting roughly the same number of reactions as in the case of "central" events.

The total and IMF multiplicity distributions, M_{cp}^{tot} and M_{IMF}^{DB}, with an indication of the selected gates for peripheral, central and multifragmentation reactions are shown in fig. 7.1 and 7.2 respectively.

These event selection criteria cannot be applied for the exclusive analysis of the other three reactions (^{36}Ar+^{108}Ag, ^{58}Ni, ^{12}C) studied during the high counting-rate runs without

[1] In that case, not even a hard-photon ($E_\gamma > 30$ MeV) but a photon above the LED threshold value of E_γ = 15 MeV.

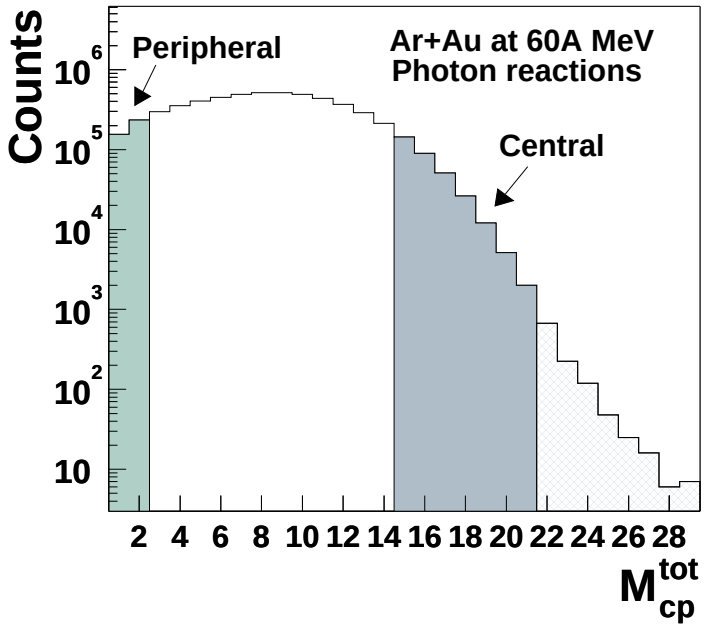

Figure 7.1: *Total charged-particle multiplicity distribution, M_{cp}^{tot}, measured with the Dwarf-Ball and Forward-Wall for $^{36}Ar+^{197}Au$ reactions in which at least one photon above 15 MeV is detected. The filled regions indicate the selected central and peripheral events, the hatched one the zone where pileup (two consecutive reactions recorded simultaneously) starts to be significant.*

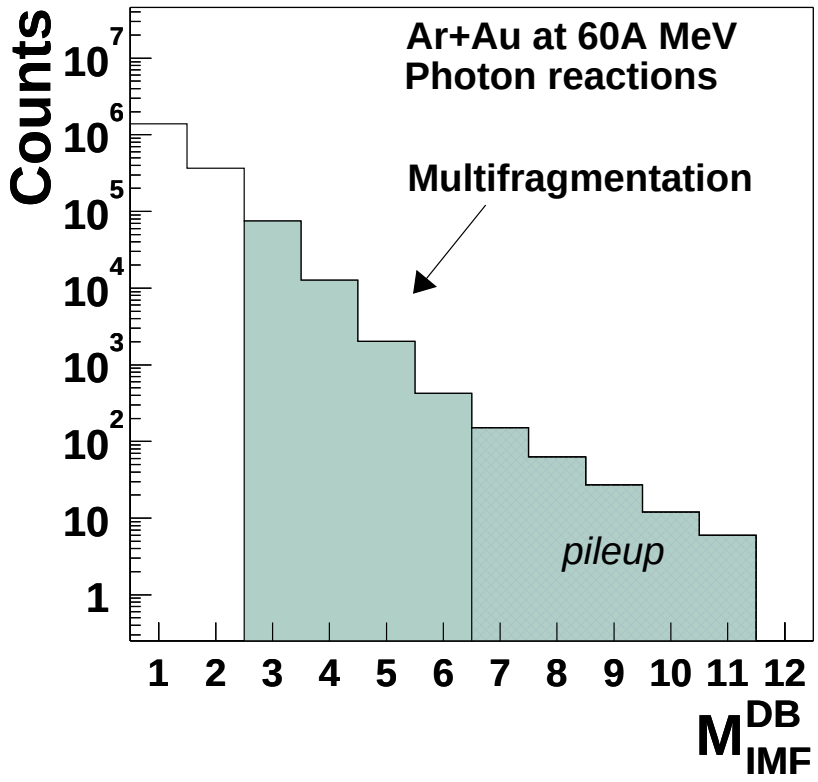

Figure 7.2: *IMF multiplicity distribution M^{DB}_{IMF} measured with the Dwarf-Ball for $^{36}Ar+^{197}Au$ at 60A MeV reactions in which at least one photon above 15 MeV is detected. The filled area corresponds to the selected region of multifragmentation events, the hatched one to the zone where pileup events are significant.*

the Dwarf-Ball (figs. 6.28, 6.29, and 6.30 display the multiplicity distributions detected in the Forward-Wall for these three heavy-ion reactions). Indeed, for these reactions one cannot associate a scale of impact parameters to each FW multiplicity bin since the assumption that more central (peripheral) collisions are related with higher (lower) values of M_{cp}^{FW} does not necessarily hold in that case because the FW is only sensitive to the fragments emitted in the forward direction. Contrarily, reaction-products emitted in central collisions usually cover the whole angular range around the target. Hence, central reactions can well lead to low values of M_{cp}^{FW} as in the case of well-defined peripheral collisions. Indeed, this effect can be shown in the bidimensional plot M_{cp}^{FW} vs M_{cp}^{tot} (fig. 7.3) obtained for the ^{36}Ar+^{197}Au reaction during the low-counting-rates runs of the experiment. A non negligible fraction of small impact-parameter reactions (e.g., with $M_{cp}^{tot} > 12$) lead to rather low Forward-Wall multiplicities ($M_{cp}^{FW} \lesssim 4$) and, conversely, most of the high-FW multiplicity reactions correspond actually to clearly peripheral reactions (for which $M_{cp}^{tot} < 5$) due to the effect of pileup reactions (we recall that for these high-counting rate reactions with interaction probabilities in the range 1.5% - 3.5%, above $M_{cp}^{FW} \approx 8$ the contamination of random coincidences can be significant).

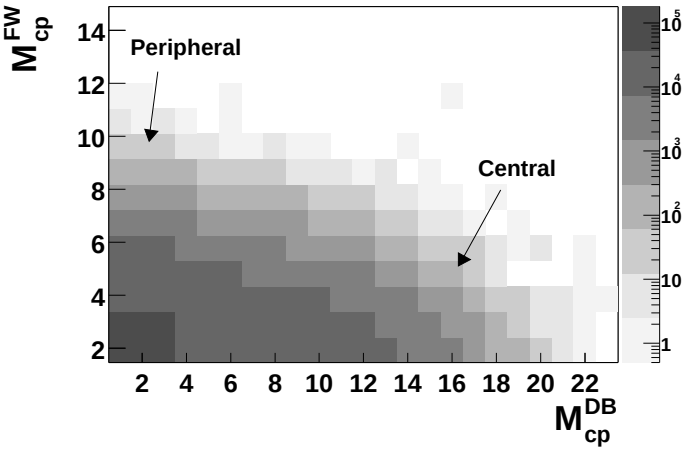

Figure 7.3: *Bidimensional plot of the Forward-Wall multiplicity (M_{cp}^{FW}) as a function of the total charged-particle multiplicity (M_{cp}) detected in the Dwarf-Ball for the reaction ^{36}Ar+^{197}Au at 60A MeV.*

7.2 Exclusive photon spectra

Making use of the event selection criteria described in the former section we will now present the resulting hard-photon spectra for central, peripheral and multifragmentation reactions for the ^{36}Ar+^{197}Au system at 60*A* MeV.

7.2.1 Central reactions

The hard-photon spectrum (after pion decay and cosmic background subtraction) for central reactions of the ^{36}Ar+^{197}Au system (fig. 7.4) presents a steeper slope in its low-energy part, as also found in the purely inclusive spectrum (fig. 6.5). We have applied, thus, the two-exponential fit with expression (6.4) used for the inclusive hard-photon energy spectra. The resulting inverse slope parameters and relative intensities of the two bremsstrahlung components are listed in table 7.1. We find values of the direct and thermal slopes fully compatible, within the errors, with those obtained in the inclusive reactions (i.e. $E_0^{d,central} \approx E_0^{d,incl}$ and $E_0^{t,central} \approx E_0^{t,incl}$), and intensities of the thermal component also comparable (18% $\pm$ 2% of the total hard-photon yield).

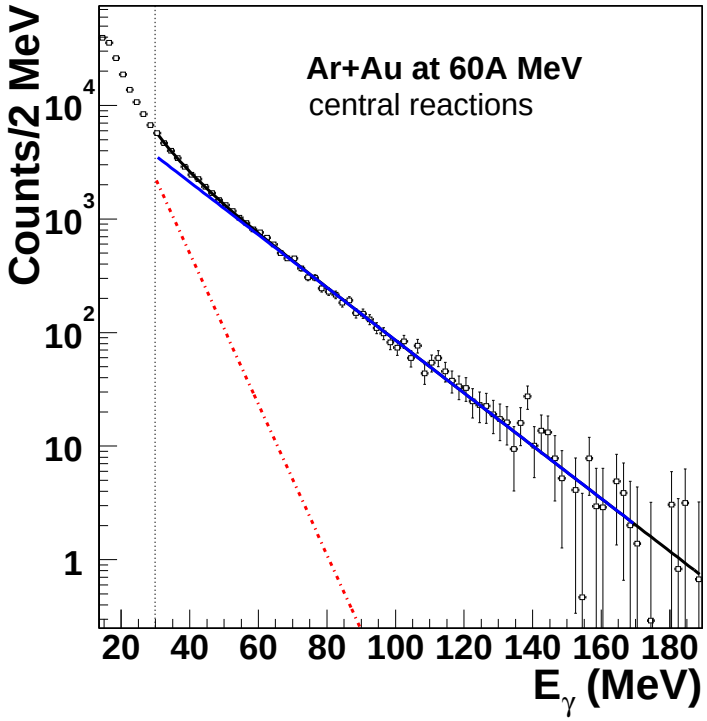

Figure 7.4: *Experimental hard photon energy spectrum measured in the NN CM for central collisions in the system $^{36}Ar+^{197}Au$. The spectrum has been fitted in the range E_γ = 30 - 150 MeV according to equation (6.4) to the sum of two exponential distributions: a direct (solid line) and a thermal one (dashed line).*

An alternative way to identify the presence of the two different slope parameters in the energy spectrum when the statistics is not high enough to perform a reliable 2-exponential fit, is provided by the so-called "local slope analysis" [Matu96d]. The local slope is deduced from an exponential fit performed over a constant energy range (e.g. ΔE_γ = 8 MeV) and by moving the centroid along the spectrum. Assuming a purely exponential spectrum, the slope parameter obtained in any local fit is equal to the global slope. In the case of two exponential components having different slopes E_1 and E_2, the local fit performed in the low energy part of the spectrum yields a value intermediate between E_1 and E_2. Moving

Table 7.1: *Measured direct and thermal slopes and ratios of thermal to total intensities in peripheral, central and multifragmentation reactions for the system $^{36}Ar+^{197}Au$ at 60A MeV.*

Reaction	E_0^d (MeV)	E_0^t (MeV)	I_t/I_{tot}
Peripheral	17.8 ± 1.3	5.0 ± 0.7	$18.0\% \pm 3.0\%$
Central	19.7 ± 1.3	6.6 ± 0.7	$18.0\% \pm 2.0\%$
Multifragmentation	20.2 ± 1.3	6.4 ± 0.7	$16.0\% \pm 2.0\%$

to higher energies results in an increase of the slope value up to a maximum value equal to E_2. We have analyzed with this method the hard-photon spectrum measured for the central ^{36}Ar+^{197}Au collisions (fig. 7.5), obtaining a clear indication of the persistence of the thermal component in the low-energy region.

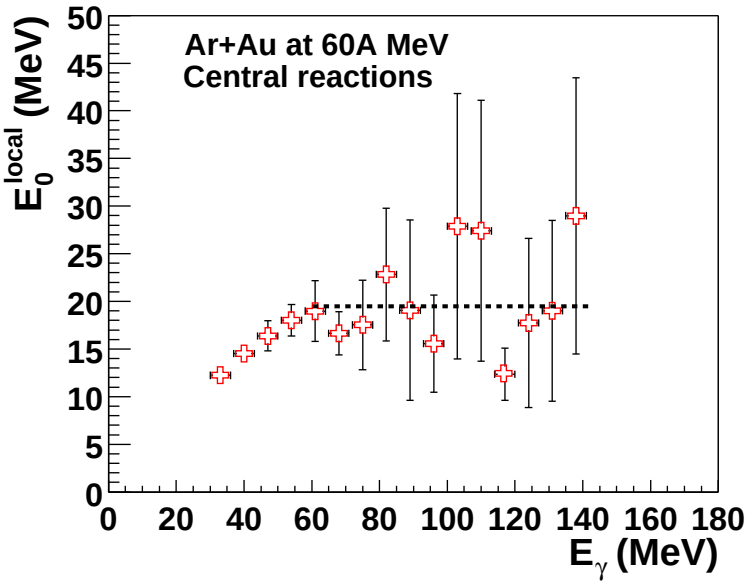

Figure 7.5: *Local slope parameters (crosses) of the experimental hard-photon spectrum measured for central $^{36}Ar+^{197}Au$ collisions at 60A MeV. The dashed line is a linear fit of the local slopes above E_γ = 60 MeV.*

The local slope parameter increases linearly from E_0 = (12 $\pm$ 2) MeV for E_γ = 30 - 60 MeV up to an almost constant value E_0 = (20 $\pm$ 2) MeV (though with high fluctuations) in the region E_γ = 60 - 130 MeV (indicated by the dashed line in fig. 7.5). This is the expected behaviour for the existence of two different exponential components in the region $E_\gamma < 60$ MeV as seen in fig. 7.4. These different local slope trends for $E_\gamma < 60$ MeV and $E_\gamma > 60$ MeV confirm unambiguously the presence of the direct and thermal components in the experimental data with different associated slopes. Therefore, thermal hard-photons are still emitted in the most dissipative central collisions of the Ar+Au

system at 60*A* MeV. This result gives support for the formation of a hot and thermalized system, even for the most violent collisions of Ar on Au at this bombarding energy.

7.2.2 Peripheral reactions

The strong low-multiplicity cut applied to select "gentle" collisions for the ^{36}Ar+^{197}Au system, which drastically limits the statistics of this type of events, and the relatively more important background of cosmic events subtracted in these peripheral collisions, lead to a hard-photon spectrum (fig. 7.6) which shows larger fluctuations in its high energy part than the preceding case. Nonetheless, we have also applied the two-exponential fit (eq. (6.4)) to the hard-photon spectrum obtaining slope parameters and relative intensities of the two bremsstrahlung components (table 7.1) which are distinct than the values found in the inclusive or central collisions. Indeed, the direct and thermal slopes are a factor $\sim$15% and $\sim$25% respectively, inferior than in those previous cases. The decreasing value of the direct hard-photon slope for large impact-parameters is a well-known observation reflecting the lower density (i.e. the smaller Fermi momenta) near the nuclear surface of the colliding ions [Mart94]. The lowering of the thermal slopes can be interpreted as a direct indication of the lower excitation energies and, correspondingly, temperatures, attained in the more peripheral reactions.

7.2.3 Multifragmentation reactions

Certainly, one of the most interesting results of this experiment is the observation that the hard-photon spectrum measured for the ^{36}Ar+^{197}Au collision in which a multiple emission of IMF is observed in the hemisphere of the reaction covered by the Dwarf-Ball presents also two distinct slopes above $E_\gamma > 30$ MeV (fig. 7.7). The two-exponential fit analysis yields direct and thermal slopes fully compatible with the inclusive values obtained without any exit-channel condition (i.e. $E_0^{d,multifrag} \approx E_0^{d,incl}$ and $E_0^{t,multifrag} \approx E_0^{t,incl}$, see table 7.1), although the percentage of thermally emitted hard-photons with respect to the total yield is perhaps slightly smaller ($[I_t/I_{tot}]_{incl} \approx (18.5 \pm 0.5)\%$ and $[I_t/I_{tot}]_{multifrag} \approx (16 \pm 2)\%$). As in the case of central collisions, the existence of such thermal bremsstrahlung component in multifragmentation processes, is an indication that the emission of intermediate-mass-fragments is done in reactions where a hot and thermalized source, which lives long enough to radiate bremsstrahlung photons, has been at some moment produced.

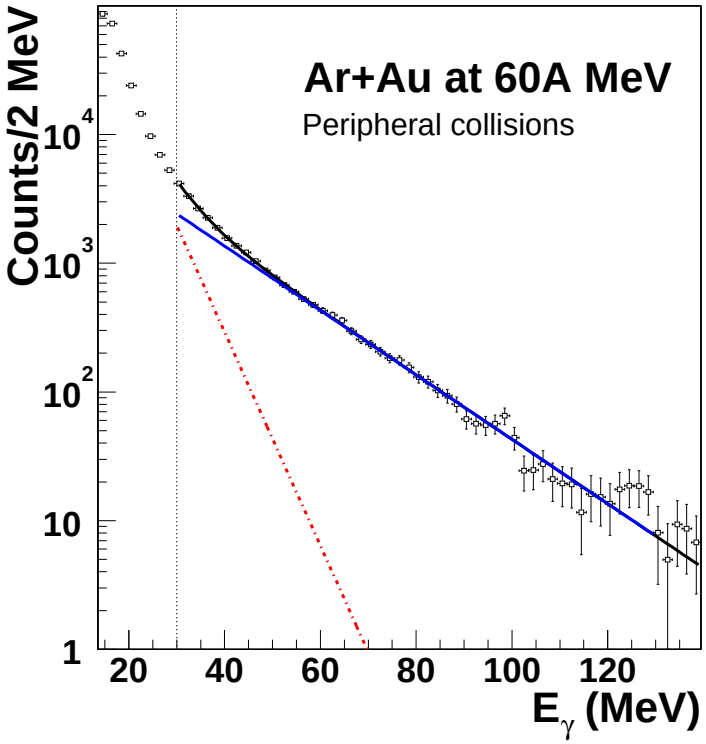

Figure 7.6: *Experimental hard photon energy spectrum measured in the NN CM for peripheral collisions in the system $^{36}Ar+^{197}Au$. The spectrum has been fitted in the range E_γ = 30 - 130 MeV according to equation (6.4) to the sum of two exponential distributions: a direct (solid line) and a thermal one (dashed line).*

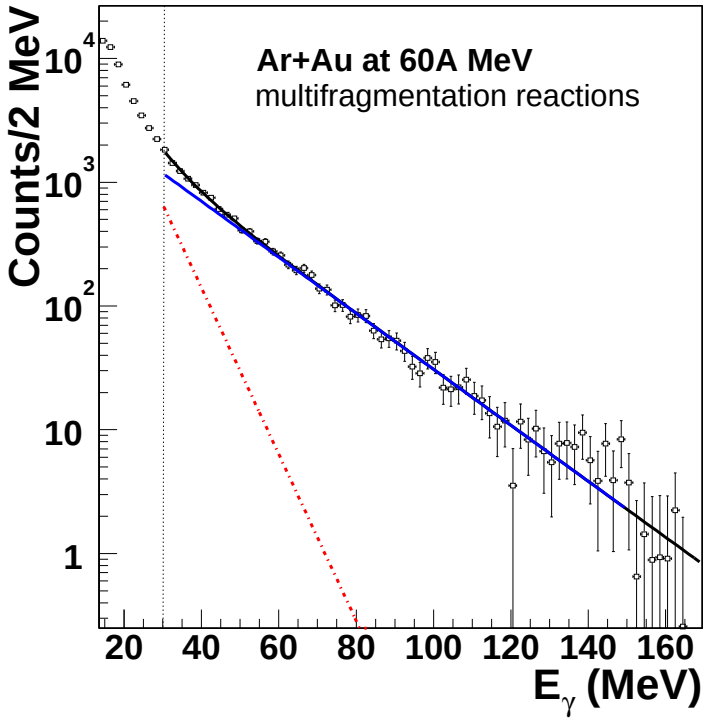

Figure 7.7: *Experimental hard photon energy spectrum measured in the NN CM for multifragmentation collisions detected in the Dwarf-Ball for the system* $^{36}Ar+^{197}Au$*. The spectrum has been fitted in the range* E_γ *= 30 - 150 MeV according to equation (6.4) to the sum of two exponential distributions: a direct (solid line) and a thermal one (dashed line).*

7.3 Impact-parameter dependence of the photon yield

We can perform a more detailed study of the dominant region of impact-parameters associated to the detected photons with $E_\gamma > 15$ MeV produced in the ^{36}Ar+^{197}Au system, by looking at the total charged-particle multiplicity measured in coincidence in the Dwarf-Ball and Forward-Wall. Above E_γ = 10 MeV three different types of photons are known to populate the experimental spectra (see Section 3.1):

1. (Mainly) GDR photons, defined as photons with energies in the range[2] 15 MeV $<$ E_γ $<$ 22 MeV,
2. "Mixed"[3] thermal+direct hard-photons in the range 30 MeV $<$ E_γ $<$ 45 MeV,
3. (Mainly) "Pure" direct hard-photons ($E_\gamma > 60$ MeV).

Since lower energy photons are produced with higher probability, we have properly scaled the particle multiplicities associated with the GDR and pure direct hard-photons to the particle-multiplicity of the thermal+direct hard-photons in order to make the comparison between the exit-channels associated to each type of photon, more apparent (fig. 7.8). Several interesting features can be remarked concerning the impact-parameter dependence of these gamma rays. Thermal and direct hard-photons are emitted in fragment multiplicity exit-channels significantly distinct than those characteristic of photons coming from the GDR decay. On the one side, GDR photons are relatively more produced than bremsstrahlung photons in the low-multiplicity ($M_{cp}^{tot} < 8$) part of the distribution, showing a maximum for $M_{cp}^{tot} \approx 8$ and then decreasing faster than the photons above 30 MeV. Hard-photons of both types, on the other side, are comparatively less produced in low-multiplicity exit-channels and they show a distinct maximum at intermediate multiplicities, M_{cp}^{tot} = 9 - 10.

Such a result is even more apparent in the distribution of the photon multiplicity (gamma yield per nuclear reaction), M_γ, versus the charged-particle multiplicity detected in the DB, M_{cp}^{DB}, for the three aforementioned types of photons emitted in the ^{36}Ar+^{197}Au reaction (fig. 7.9). This figure exhibits three interesting features:

- The photon production multiplicity shows a clear increase from peripheral (M_{cp} = 2) to semi-central ($M_{cp} \approx 7$) reactions for the three types of photons. The increase is not, however, equally steep for the GDR and hard-photons, and in the case of the bremsstrahlung component it continues to go up to more central reactions (M_{cp} = 9 - 10). The bremsstrahlung multiplicities, on the one side, grow a factor 10 between M_{cp} = 2 and M_{cp} = 10 (from $M_\gamma \approx 10^{-4}$ to $M_\gamma \approx 10^{-3}$) neatly sampling the increasing number of nucleon participants from peripheral to semi-central collisions. The GDR yield, on the other side, augments only a factor 4 from M_{cp} = 2 to M_{cp} = 7.

[2] Although GDR photons are dominant above E_γ = 10 MeV, the threshold value of our LED discriminators is at E_γ = 15 MeV.

[3] According to the ratio of intensities of the thermal component with respect to the total hard-photon yield above 30 MeV in the ^{36}Ar+^{197}Au system (table 6.2), the relative proportion of thermal to direct bremsstrahlung photons in the range 30 MeV $<$ E_γ $<$ 45 MeV is 40:60 (thus the term "mixed" for this second selected type of photons).

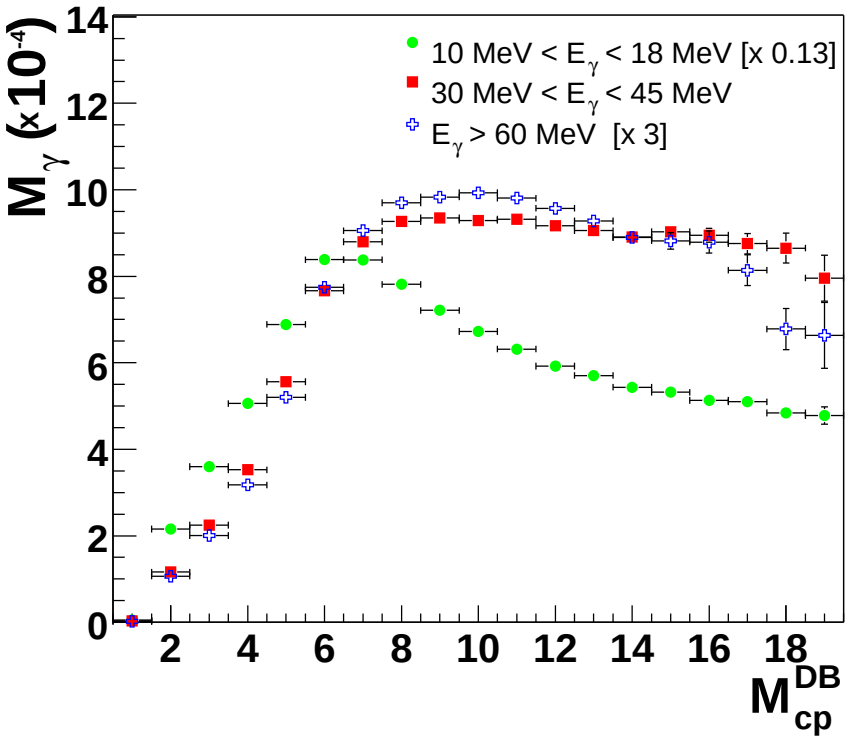

Figure 7.8: *Total charged-particle multiplicity, M_{cp}^{ot}, measured in the Dwarf Ball and Forward-Wall for the $^{36}Ar+^{197}Au$ system in coincidence with (1) "GDR photons" (defined as photons with 15 MeV < E_γ < 22 MeV), (2) "thermal+direct hard-photons" (30 MeV < E_γ < 45 MeV), and (3) "pure direct hard-photons" (E_γ > 60 MeV). The particle multiplicity distributions associated to the GDR-photons and direct hard-photons have been scaled to that of the thermal+direct hard-photons.*

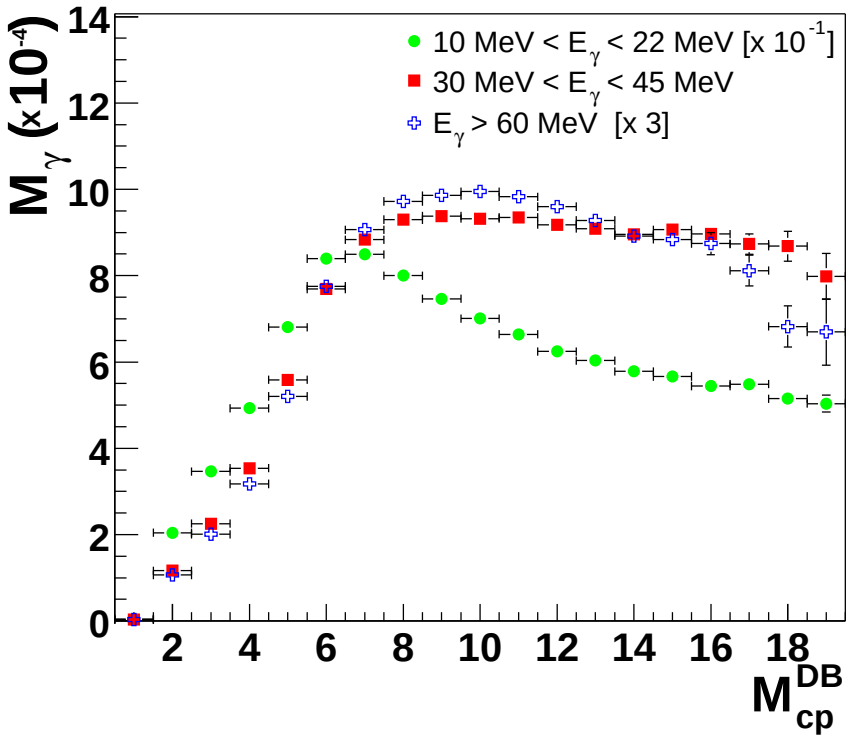

Figure 7.9: *Experimental photon yield per nuclear reaction, M_γ, as a function of the charged-particle multiplicity, M_{cp}^{DB}, measured in the Dwarf-Ball for: (1) "GDR photons", (2) thermal+direct hard-photons and (3) "pure" direct hard-photons emitted in $^{36}Ar+^{197}Au$ at 60A MeV.*

- From its maximum at M_{cp} = 7, the GDR photon multiplicity, $M_{\gamma_{GDR}}$ follows a gradual decrease for increasingly central collisions. The GDR yield is reduced roughly a factor 2 between M_{cp} = 7 and M_{cp} = 20. This result confirms the significant quench of the GDR gamma yield observed experimentally for increasingly high excitation energies ($\varepsilon^{\star} > 3A$ MeV) in several systems [Gaar87, LeFa94, Suom96, Suom98]. This quenching had been tentatively interpreted as a result of the loss of collectivity due to a change from ordered mean-field-driven motion to chaotic nucleonic motion [Gaar92]. This interpretation seems to be nicely corroborated here.

- Thermal+direct and pure direct hard-photon yields show a very similar overall dependence with the centrality of the reaction and they saturate above M_{LCP} = 9, i.e. at the region of charged-particle multiplicities corresponding to semi-central and central impact parameters where the total overlapping of the incident ^{36}Ar nucleus inside the much larger ^{197}Au target nucleus takes place. In this region of impact-parameters, the mean number of *NN* collisions saturates, i.e. $\langle N_{pn} \rangle_b = \langle N_{pn} \rangle_{max}$, and hence so does the bremsstrahlung photon production. This confirms that $M_{hard-\gamma}$ is proportional to the number of participants and ultimately to the volume of the overlap region between projectile and target at a given impact-parameter. Interestingly, for the most central collisions, above $M_{cp} \approx 16$, the emission of bremsstrahlung with E_γ = 30 - 45 MeV remains constant but the harder bremsstrahlung $E_\gamma > 60$ MeV seems to diminish (this trend is observed even if $M_{hard-\gamma}$ fluctuates due to the limited statistics).

  In summary, the very similar behaviour of the thermal and direct hard-photon yields as a function of impact parameter and, specifically, its dependence with the number of participant nucleons, confirms that the mechanism governing their production must be basically the same (incoherent *pn* bremsstrahlung) and must be different than the (collective) mechanism responsible of statistical GDR photon emission. We will discuss this aspect in more detail in the next Section.

7.4 Summary of the experimental results and preliminary interpretation

Before proceeding further, we want now to summarize the main observations collected in the inclusive and exclusive analysis of our experimental data concerning hard-photon production in four different heavy-ion reactions:

- **Inclusive spectral shapes:** Two exponential distributions with different slope parameters describe the hard-photon energy spectra above E_γ = 30 MeV. The harder ("direct") exponential accounts for at least $\approx$ 80% of the total hard-photon production. The steeper ("thermal") component shows up specially in the low-energy region of the spectra (E_γ = 30 - 60 MeV).

- **Spectral slopes:** The direct slope scales with the projectile energy per nucleon in the lab, i.e. with the initial energy per nucleon available in *first-chance NN* collisions. The thermal slope scales with the total energy available in the nucleus-nucleus center-of-mass, K_{AA}.

- **Source velocities:** Direct hard-photons are emitted from the nucleon-nucleon center-of-mass. Thermal hard-photons are emitted isotropically from a source moving with the nucleus-nucleus center-of-mass velocity.

- **Target dependence:** Thermal hard-photons are only observed in the spectra and in the angular distributions of the heavier systems (^{36}Ar+^{197}Au, ^{108}Ag, ^{58}Ni), but they are absent in the lightest (^{36}Ar+^{12}C) reaction. This last reaction presents the expected behaviour for pure first-chance bremsstrahlung (single exponential spectrum, elementary dipolar term in the angular distribution and source velocity equal to β_{NN}).

- **Inclusive multiplicities:** The total hard-photon yield per nuclear reaction is proportional to the (impact-parameter averaged) number of proton-neutron collisions occurring within the overlapping zone of the colliding ions. The thermal hard-photon multiplicities point out to the existence of a threshold of $N_{pn} \approx 2$, as the minimal number of *pn* collisions for which thermal emission takes place.

- **Exclusive spectra and slopes:** Remarkably, the thermal exponential component is also observed in central reactions and in reactions leading to multiple emission of intermediate-mass-fragments ("multifragmentation") with the same slope and (roughly) intensity as found in impact-parameter integrated spectra. The strength of the direct and thermal bremsstrahlung slopes, in contrast, diminish for peripheral reactions.

- **Exclusive multiplicities:** Thermal and direct hard-photon yields show a very similar dependence with impact-parameter, increasing a factor $\approx$ 10 when going between peripheral to semi-central reactions. They saturate in the region of semi-central and central reactions for total overlapping of the Ar nucleus inside the Au one.

Although we have already pointed out (and we have explicitly considered) that the most consistent explanation of the full experimental results relies on the existence of a thermal bremsstrahlung emission from secondary nucleon-nucleon collisions, it is the purpose of this section to assess critically this explanation together with all other possible alternative interpretations of the experimental data. Aside from the main mechanism of first-chance proton-neutron ($pn\gamma$) bremsstrahlung ("prompt" or "direct" bremsstrahlung), only the following mechanisms could *potentially* lead to the production of photons with energies above 30 MeV:

1. GDR statistical photons.
2. Coherent nucleus-nucleus bremsstrahlung.
3. Cooperative cluster bremsstrahlung.
4. $pp\gamma$ bremsstrahlung.
5. $pn\gamma$ bremsstrahlung from (preequilibrium) second-chance collisions.
6. $pn\gamma$ bremsstrahlung from (thermal) second-chance collisions.

In the rest of this chapter, I will discuss to what extent those different mechanisms could account for the deviations from the pure first-chance $pn\gamma$ scenario observed in this experiment.

7.4.1 GDR photons

As mentioned in Section 3.3 a first observation of the deviation of the hard-photon energy spectrum from the single exponential behaviour was already found in the data of Luke *et al.* [Luke93] for the system $^{14}N+^{107}Ag$ at 35*A* MeV (see fig. 3.10). The steepest shape of the low-energy part of the hard-photon spectrum is also observable in the data of Stevenson *et al.* [Stev86] for the system $^{14}N+^{208}Pb$ at 20*A*, 30*A* and 40*A* MeV but it is not apparent for the lighter $^{14}N+^{12}C$ system studied at the same bombarding energies (see fig. 3.9). Luke attributed the hard photon enhancement in the region $E_\gamma < 50$ MeV to the tail of Giant-Dipole-Resonance (GDR) photons emitted by projectile-like fragments. According to expression (3.1), the expected position of the centroid of the GDR of a Nitrogen-like nucleus, would be around $E_\gamma = 24$ MeV with a maximum width of $\Gamma_{GDR} \approx 12$ MeV (for very excited quasi-projectiles).

The first objection against this interpretation arises from the fact that the observed hard-photon enhancement in Luke and Stevenson data at $E_\gamma = 30$ MeV amounts roughly to 50% of the total bremsstrahlung yield whereas the strength of the high-energy Lorentzian tail of a GDR built on a Nitrogen-like excited fragment would represent a smaller effect at this high photon energy according to CASCADE calculations [Mart95, Schu97]. Furthermore, any enhancement due to photons issuing from the decay of GDRs of the quasiprojectile fragments in these experiments would seemingly have also shown up for the lighter $^{14}N+^{12}C$ system studied in parallel, but in that case, and significantly, *no* hard-photon excess production was observed [Stev86].

Concerning our experimental data, no pronounced structure in the usual region of the GDR photons (E_γ = 10 - 25 MeV) due to the peak of a *single* GDR is visible in the low-energy part of the photon spectra of the four studied reactions but only very steep exponential fall-offs with local slope parameters of the order $E_0^{GDR} \approx 4$ MeV (see e.g. the raw ^{36}Ar+^{197}Au photon spectrum, fig. 6.1, in the region $E_\gamma < 20$ MeV). This is due to several effects. On the one hand, our experimental energy resolution (2 MeV binning) does not allow for a fine distinction of possible isolated GDR peaks. On the other hand, and more importantly, the region E_γ = 10 - 25 MeV is expected to be likely populated with the mixed superposition of photons stemming from the decay of GDRs built, in principle, on the quasi-target, on the quasi-projectile and on any other reaction product[4]. These different GDR have different centroid positions and different degrees of excitation (leading to different GDR widths) and are modulated by a global steep exponential statistical function (see Section 3.1 and ref. [Schu97]). This results basically in the absence of any peak structure observed in the region E_γ = 10 - 25 MeV at variance with typical spectra obtained in dedicated GDR-photons experiments (see e.g. [Gaar92]). According to the GDR centroid systematics given by formula (3.1), the highest-energy GDR expected from a reaction product produced with sizeable cross-sections in our different reactions, that could constitute a source of photons close to the hard-photon threshold (E_γ = 30 MeV), corresponds to that of a quasiprojectile (Argon-like) fragment. The GDR of such a fragment would be centered at around $E_{GDR}(^{36}\mathrm{Ar}) \approx 22$ MeV with a maximum width of $\Gamma_{GDR} \approx 12$ MeV for the most excited quasiprojectiles. Any other heavier reaction-product has an increasingly lower GDR centroid, e.g. $E_{GDR}(^{197}\mathrm{Au}) \approx 13$ MeV, $E_{GDR}(^{108}\mathrm{Ag}) \approx 15$ MeV, and $E_{GDR}(^{58}\mathrm{Ni}) \approx 17$ MeV. In the case of the ^{36}Ar+^{12}C system one could argue that $E_{GDR}(^{12}\mathrm{C}) \approx 24$ MeV which is certainly close to the lowest E_γ = 30 MeV threshold for hard-photons, but in that reaction, symptomatically, there is *no* observed low-energy hard-photon enhancement (see the discussion below).

The possible interpretation of the observed hard-photon excess in the region E_γ = 30 - 60 MeV as being an evidence of the high-energy tail of such GDRs produced in the reaction is, thus, ruled out by several reasons:

1. Spectral shape: Such a long high-energy tail of the GDR Lorentzian strength distribution (up to E_γ = 60 MeV !) has never been observed before in dedicated experiments [Gaar92]. It would imply a much too large cross section in contradiction with the known characteristics of GDR production. Moreover, GDR studies have been carried out at rather moderate bombarding energies ($K_{lab} \lesssim 30A$ MeV), where the contribution of bremsstrahlung photons, being rather marginal, is nonetheless already dominant above E_γ = 25 MeV. Our reactions have projectile energies at least 2 times higher and, thus, due to the steep energy dependence of bremsstrahlung production (see fig. 6.35), lead to a much stronger production of hard-photons. Contrarily, the mechanisms that contribute to GDR formation remain the same. Therefore the ratio hard-photons/GDR photons in our experiment should be much larger than in GDR-dedicated experiments.

2. GDR yields: The GDR interpretation contradicts the observed marked suppression

[4] Additionally, some Doppler broadening of the GDR decay photons originating from the faster reaction products could also be expected.

of the GDR yield for increasing impact-parameters in our ^{36}Ar+^{197}Au system (see fig. 7.9). This GDR quenching has been already well established for high excitation energies [Suom96]. Indeed, e.g. Gaardhoje *et al.* [Gaar87] studied the GDR photon spectra from the decay of ^{110}Sn compound nucleus produced in the reaction ^{40}Ar+^{70}Ge at 15*A* and 24*A* MeV as a function of excitation energy and concluded that there existed a strong inhibition of the GDR γ decay above $\varepsilon^\star \approx 3A$ MeV. This value of $\varepsilon^\star$ corresponds to the usual range of excitation energies encountered in our 60*A* MeV bombarding energy reactions (even for the more peripheral reactions). The proposed explanations of such a damping of the GDR yield are: 1) a loss of collectivity, related to a change from ordered to chaotic behaviour; 2) a considerable enhanced particle decay at the highest $\varepsilon^\star$ that reduces the γ-emission probability and depletes the available $\varepsilon^\star$; or 3) non-equilibration of the composite system resulting again in a severe loss of collectivity until the system regains thermal equilibrium at lower temperature. The first proposed explanation is specially interesting in our case since it would confirm the fact that for large excitation energies, $\varepsilon^\star > 3A$ MeV, which are clearly attained in our four considered reactions, the intrinsic degrees of freedom (incoherent *NN* collisions) prevail over the collective ones (mean-field driven giant oscillations). In such situation thermal bremsstrahlung is presumably *the* mechanism for hard-photon emission before the global motion is damped to levels consistent with a thermal equilibrium between collective and intrinsic degrees of freedom.

3. Target dependence: An interpretation based on GDR-photons does not explain why the extra hard-photon production is only present in the heavier systems but it is absent in the lightest ^{36}Ar+^{12}C reaction (fig. 6.9). The excitation of a GDR state in a quasi-Ar or quasi-C fragment should be equally possible in this last reaction, and should also have lead to the appearance of the hard-photon enhancement in the photon spectrum of this light system.

7.4.2 Coherent nucleus-nucleus bremsstrahlung

Another mechanism which has been theoretically put forward to account for the production of hard-photons in heavy-ion reactions is that of collective nucleus-nucleus bremsstrahlung in which the two nuclei as a whole take part in the particle production process. As mentioned in Section 3.2.2, this process has indeed been observed in *few-body* nuclear systems such as $\alpha + p$ [Hoef00] or $\alpha + \alpha$ reactions. In a recent paper [Eich97], Eichmann *et al.* claimed that the bremsstrahlung due to the correlated motion of the colliding nuclei during the stopping phase of the collision could reproduce the exponential shape of the hard-photon spectrum measured in the ^{12}C(84*A* MeV)+^{12}C reaction [Gros85]. Of course, the possibility of such a process would be highly interesting for it would offer the possibility of estimating the nuclear "stopping time" of the sudden decelerated colliding ions by measuring the associated high-energy gamma-ray production [Tam89]. Several experimental observations seem, however, to be in contradiction with this assumption:

1. Coherent yield: According to [Goss90], in asymmetric heavy-ion collisions, one would expect the coherent bremsstrahlung yield to scale roughly as the square of

the $E1$ effective charge for the reaction, i.e. $\sigma_\gamma \propto \mu^2 (Z_p/A_p - Z_t/A_t)^2$, where μ is the reduced mass of the system. According to that expression, on the one hand, one would not expect any coherent emission for the ^{36}Ar+^{12}C system, in agreement with our data. On the other hand, the expected ratio of collective bremsstrahlung yields for the three heavier systems would be 0.3:3:8.8 (for ^{36}Ar+^{58}Ni, ^{108}Ag and ^{197}Au respectively), whereas experimentally (from the value of $\sigma_{\gamma E>30MeV} \times (I_t/I_{tot})$, where the second factor is the relative weight of the second hard-photon component) we obtain 0.4:0.5:0.8, i.e. roughly one order of magnitude smaller.

2. Angular distributions: The shape of the angular distributions in a pure collective approach depends upon the relative orientations of the projectile and target (from a $\sin^2\theta\cos^2\theta$ dependence for central collisions to $\sin^4\theta$ for orthogonal velocity and position vectors), and integration over impact parameters mixes the different situations leading to more complex distributions [Vasa86, Nife89]. In any case, no combination of the relative positions of the colliding nuclei leads to an additional angular component of basically isotropic character as observed experimentally.

3. Coherent spectral slopes: The shape of the coherent bremsstrahlung spectrum, following the classical theory [Jack75], corresponds to the square of the Fourier transform of the acceleration. For the observed exponential shapes of the spectra, one, therefore expects Breit-Wigner shapes of the acceleration function $\gamma(t) = [(t - t_0)^2 + \tau^2/4]^{-1}$, where $\tau = \hbar/E_0$ is the characteristic time of the deceleration of the two nuclei. The inverse slope parameter E_0 may be written in terms of a deceleration length d and the beam velocity: $d = 2\gamma v\tau = 2\gamma\beta(\hbar c/E_0)$. Using the value of the Ar-beam velocity and the inverse slope parameters of the second hard-photon component[5] listed in table 6.2 , we obtain deceleration distances (d = 12 fm for the Au and Ag targets, d = 8.2 fm for the Ni target, and d = 4.1 fm for the Carbon one) which decrease with decreasing target mass. Such result is rather surprising since intuitively one would expect the contrary behaviour, i.e. the stopping power to be superior for heavier targets.

7.4.3 Cooperative cluster bremsstrahlung

Cooperative mechanisms between (virtual) clusters of nucleons within the colliding nuclei have been also proposed as a source of hard-photons in nucleus-nucleus collisions in other theoretical works (see e.g. [Shya86]). As a matter of fact, those kind of processes between two-, three- or four-nucleon clusters which feed their energy to the photon production in a collective manner, are necessary in order to correctly describe the high-energy tail of the hard-photon spectra in the vicinity and above the kinematical limit (see the discussion and references of Section 3.1). Following this argument, deuteron-like and alpha-like bremsstrahlung processes have been for example included in DCM [Boze98, Gudi99] and BUU [Wang94] models respectively to account for hard-photon production in the *upper* region of the energy spectra. Cooperative bremsstrahlung, however, seems not to account either for our observations:

[5] In that case, the value of E_0^t corresponding to the ^{36}Ar+^{12}C system has not been taken as zero but as $E_0^t = E_0^d$ assuming that it could, presumptively, have not been observed only because it coincided with E_0^d.

1. Spectral shapes: BUU calculations including cooperative bremsstrahlung due to α clusters [Wang94], lead to an overall increase of the hard-photon cross-section (yielding, in particular, more hard photons in its high-energy part) but not to a change of the (single) exponential spectrum in the low-energy region of the spectrum.

2. Target dependence: Within such an cooperative picture, the ^{36}Ar+^{12}C reaction where no low-energy hard-photon excess is observed, is not well understood. In particular, since the ground state of the ^{12}C nucleus has been usually considered as a composite system consisting of three-α clusters[6] (see e.g. [Hira95] and references therein), if any cooperative cluster bremsstrahlung would be present at all, it certainly would have also appeared in the ^{36}Ar+^{12}C reaction, in contradiction with our observations.

7.4.4 Proton-proton ($pp\gamma$) bremsstrahlung

Bremsstrahlung from $pp\gamma$ could perfectly represent a source of hard-photons above 30 MeV. Nonetheless, as mentioned in Appendix 2, the elementary $pp\gamma$ bremsstrahlung is experimentally [Roth66, Koeh67, Edgi66, Nife89, Nife90] and theoretically [Nife89, Herr88, Scha91] known to be *at least* a factor 10 smaller than $pn\gamma$ in the range of nucleon-nucleon kinetic-energies ($K_{lab} < 300$ MeV) comparable with our heavy-ion reactions projectile energy. This is due, on the one side, to the fact that in this energy regime the *pn* (elastic) cross-section is about three times larger than the *pp* cross-section and, on the other, to the destructive interference of the radiation from the two proton lines (i.e. the *pp* system has no dipole moment in its center-of-mass) which induces a quadrupolar shape of the $pp\gamma$ process.

Therefore, even taking into account the most "optimistic" ratio $\sigma_{pn\gamma}/\sigma_{pp\gamma} \approx 10$, which would represent an overall extra contribution of 10% to the total (neutron-proton) hard-photon yield due to proton-proton bremsstrahlung, two difficulties arise in such interpretation of the experimentally observed hard-photon enhancement: 1) why $pp\gamma$ would show up more intensely in the low-energy part (E_γ = 30 - 60 MeV) of the bremsstrahlung spectra, and 2) why the proton-proton bremsstrahlung would be comparatively much larger in the heavier systems than in the lightest one.

7.4.5 Bremsstrahlung from second-chance NN collisions. Preequilibrium or thermal ?

It is by now well established that incoherent *pn* bremsstrahlung is certainly the basic (if not the only) mechanism of hard photon production above 30 MeV. In the presentation of the inclusive and exclusive results, and following the interpretation of refs. [Mart95, Marq95, Schu97], we have tacitly considered that secondary $pn\gamma$ collisions within a *thermalized* source were at the origin of the observed deviations from the expected first-chance scenario. It could be argued, however, that secondary but still preequilibrium *NN* collisions could also explain: 1) the steeper bremsstrahlung spectrum

[6] It is known that, in general, α particles are usually present as bound clusters inside the nuclei because of their high binding energy (see e.g. [Tohs96]).

in the low-energy region (less energy is available in the *NN* CM of secondary collisions than in prompt ones), 2) the target dependence of this emission (secondary *NN* collisions are more probable in heavier systems), and 3) the isotropic angular pattern (the original beam direction is lost in subsequent *NN* collisions). Two closely related but still different explanations could therefore be possible:

- Additional bremsstrahlung issues from preequilibrium secondary *pn* collisions during the first compression-expansion stage of the reaction (i.e. $NN\gamma$ collisions within the composite projectile-target transient system before t $\approx$ 100 fm/c).
- Additional bremsstrahlung issues from secondary *pn* collisions from any thermalized hot system being left after the first compression-expansion stage of the reaction (i.e. $NN\gamma$ collisions within[7] t $\approx$ 100 - 250 fm/c).

The basic question is, therefore, to ascertain whether or not this second bremsstrahlung component is being emitted from a thermalized source (and can be, therefore, really referred to as "thermal"). With the experimental results collected so-far this possibility is clearly suggested at least by two facts:

- The linear dependence of the thermal slope parameter, E_0^t, with the available energy in the nucleus-nucleus center-of-mass K_{AA}, as expected for a thermal process resulting after dissipation of the incident kinetic energy into internal degrees of freedom over the whole system.
- The fact that the ^{36}Ar+^{58}Ni system, despite being much lighter than the ^{36}Ar+^{197}Au, ^{108}Ag systems, shows a thermal component with the hardest slope ($E_0^t \approx 8.8$ MeV) and which is as intense as the Au one ($I_t/I_{tot} \approx 20\%$ in both cases). This behaviour contradicts the interpretation that the additional bremsstrahlung component is just related to the increasing number of secondary *NN* collisions in heavier systems, but it can be fully explained considering a thermal process is such a system for which the available excitation energy $\varepsilon^\star$ ($\propto K_{AA}$) is the highest among the four reactions considered.

Additionally, an increasing contribution of pre-equilibrium second-chance *pn* collisions to the total hard-photon yield has been indeed observed in heavy-ion collisions at higher bombarding energies (in the source-velocity analysis of the system ^{36}Ar+^{197}Au at 95*A* MeV [Schu94], and in the enhancement of the hard-photon multiplicity in the reaction ^{40}Ar+^{40}Ca at 180*A* MeV [Mart99]) without any apparent deviation from the single exponential behaviour. Such results point out that secondary $pn\gamma$ collisions before t $\approx$ 100 fm/c do certainly exist, but that they take place still at energies in the *NN* center-of-mass high enough to yield hard-photon slope parameters comparable to E_0^d.

To give a definitive answer to this question one needs to determine at what time our secondary (and probably higher-order) nucleon-nucleon collisions take place. Determining the emission time of hard-photons can be done via two techniques: 1) experimentally,

[7] Above t $\approx$ 300 fm/c, *NN* bremsstrahlung is unlikely to occur because the hot nuclear systems produced in the reaction have already released an important part of their excitation energy (by particle emission, oscillations ...), their temperature is lower, and Pauli-blocking within the remaining nuclei is fully restored.

via hard-photon interferometry, and 2) theoretically, comparing with transport model predictions. On the one hand, intensity interference between pairs of photons seems to confirm indeed the existence of two distinct photon sources, well separated in space and time (see [Marq95, Marq97] and fig. 3.11), and a new analysis of a much higher-statistics experiment [Oste98] is under way to verify this result. On the other hand, transport model calculations permit to follow the temporal evolution of the HI reaction and, in particular, they permit to analyse the evolution the number of *NN* collisions and of the density as a function of the reaction time. So far several studies of *NN* bremsstrahlung production have been carried out with different dynamical models:

- For heavy-systems around 50*A* MeV, QMD [Khoa91] predicts an increasing number of *NN* collisions as the system starts to compress reaching its maximum at a time (t $\approx$ 35 fm/c) slightly later than the time of maximum density (t $\approx$ 30 fm/c). Secondary (and possible higher-order) *NN* collisions are also seen to take place during the expansion stage of the system up to t $\approx$ 100 fm/c, but in principle no *NN* collisions seem to occur for longer times.

- Hard photon spectra obtained within the nuclear-exchange model including *all pn* collisions before t $\approx$ 100 fm/c give rise to a single exponential spectrum and do not seem to account for the observed enhancement in the region E_γ = 30 - 60 MeV [Vand98].

- BUU calculations [Mart95, Schu97] point out that a significant fraction of hard-photons can still be emitted in later (t $>$ 100 fm/c) *NN* collisions inside a thermalized nuclear system. If the lifetime of the thermal source is long enough, its contribution could come up to that of the first-chance collisions. Taking into account long reaction times (up to t $\approx$ 200 fm/c) where a second recompression of the emitting system occurs, the region of 30 - 60 MeV photons is "filled" with the experimentally observed "thermal" contribution.

Between the two possible second-chance mechanisms (pre-equilibrium and thermal), the thermal one would, of course, be more relevant for the study of the thermodynamical properties of hot nuclear systems, and of the origin of multifragmentation. If confirmed, thermal hard-photons would probe the intermediate dissipative stages of the reaction giving information on the temperature of the fragmenting source and hints on the possible time-scale of nuclear multifragmentation. Indeed, the presence of this component would tell us that the excited nuclear system(s) produced during the reaction zone has a longer lifetime than predicted by models based on dynamical instabilities. To analyze microscopically the possibility of such thermal mechanism, in the next chapter we have performed extensive simulations of our four reactions with two different transport models (QMD and BUU).

Chapter 8

Model comparison

Summary

8.1 Boltzmann-Uehling-Uhlenbeck (BUU) model 198
8.1.1 Description of the model 198
8.1.2 Collision dynamics in the ^{36}Ar+^{197}Au, ^{107}Ag, ^{58}Ni, ^{12}C at 60*A* MeV reactions 200
8.1.3 Bremsstrahlung production within BUU 210
8.2 Quantum Molecular Model (QMD) 218
8.2.1 Description of the model 218
8.2.2 Collision dynamics in the ^{36}Ar+^{197}Au, ^{107}Ag, ^{58}Ni, ^{12}C at 60*A* MeV reactions 219
8.2.3 Bremsstrahlung production within QMD 229

In the last 10 years the most commonly invoked theoretical framework to describe the dynamics of heavy-ion reactions at intermediate-energies and, in particular, subthreshold particle production, is founded on microscopic transport theories [Bert88] of the Boltzmann-Uehling-Uhlenbeck (BUU) [Cass90] and the Quantum-Molecular Dynamics (QMD) [Aich91] types[1]. These models describe the complex dynamics of a heavy-ion collision: a system of fermions (the nucleons) moving in a time-dependent mean-field potential and being subject to two-body collisions limited by the Pauli exclusion principle. I will review the main characteristics of BUU and QMD models in Section 8.1.1 and Section 8.2.1 following closely the discussion of ref. [Hart98]. The characteristics of the reaction dynamics of the four heavy-ion reactions considered in this thesis will be studied in Sections 8.1.2 and 8.2.2 analyzing their time evolution in coordinate and momentum space. The goal is to identify in space and time the possible sources of hard-photons and to try to microscopically ascertain their degree of thermalization at the moment of photon emission. In Sections 8.1.3 and 8.2.3 I will be mainly interested in following quantitatively the bremsstrahlung production rate as a function of time for the 4 studied reactions, as predicted by BUU and QMD simulations.

8.1 Boltzmann-Uehling-Uhlenbeck (BUU) model

8.1.1 Description of the model

We have seen in Section 2.2.3 that, to first approximation, the temporal evolution of the complex nuclear many-body system found in heavy-ion collisions can be reduced to the evolution of the *average* one-body phase space distribution $f(\vec{r},\vec{p},t) \equiv f$. This distribution represents the probability to find a nucleon with momentum $\vec{p}$ at location $\vec{r}$ and at time t, and is formally derived through the Wigner transformation of the one-body density matrix. The microscopic transport models for this one-body Wigner phase-space density distribution have been given different names and, although they all solve the Boltzmann Equation, they differ in the numerical realization: Boltzmann-Uehling-Uhlenbeck (BUU) [Bert88, Cass90, Stoe86], VUU [Krus85, Moli85], LV [Greg87], or BNV [Bona94] models. They solve the following transport equation for the one-body Wigner density $f(\vec{r},\vec{p},t)$ in the limit $\hbar \to 0$:

$$\begin{aligned}
\frac{\partial f}{\partial t} + \{f,H\} &= I_{coll}[f] \quad \Rightarrow \\
\frac{\partial f}{\partial t} + \vec{v}\cdot\nabla_r f - \nabla_r U\cdot\nabla_p f &= -\frac{4\pi^3(\hbar c)^4}{\hbar(mc^2)^2}\int \frac{\mathrm{d}^3p_1'}{(2\pi\hbar)^3}\frac{\mathrm{d}^3p_2'}{(2\pi\hbar)^3}\mathrm{d}^3p_2\,\frac{\mathrm{d}\sigma}{\mathrm{d}\Omega} \\
&\quad\times\ \left[f f_2(1-f_1')(1-f_2') - f_1' f_2'(1-f)(1-f_2)\right] \\
&\quad\times\ \delta^4(p+p_2-p_1'-p_2') \qquad (8.1)
\end{aligned}$$

The l.h.s. of this equation is the total differential of f with respect to the time assuming a momentum-independent potential U. The time-dependent mean-field potential U is

[1] Subthreshold particle production has been also commonly studied within cascade models such as the Dubna Cascade Model (DCM) [Gudi83].

calculated selfconsistently and corresponds to the real part of the Brückner G-matrix:

$$U(\vec{r},t) = \int d^3r' Re(G_a(\vec{r}-\vec{r}'))\,\rho(\vec{r}',t) \tag{8.2}$$

Usually a nuclear-density dependent Skyrme-parametrization,

$$U = \alpha\left(\frac{\rho}{\rho_0}\right) + \beta\left(\frac{\rho}{\rho_0}\right)^{\gamma} \tag{8.3}$$

of the real part of the G-matrix is employed, where ρ_0 is the saturation density of cold nuclear matter. The three parameters α, β and γ are chosen to reproduce the properties of nuclear matter at zero temperature and pressure: the binding energy per nucleon $\varepsilon = -16A$ MeV at the saturation density (ρ_0 = 0.16 fm^{-3}), and the incompressibility modulus κ_∞. A large value for κ_∞ (> 250 MeV) defines a "stiff" EoS, and a small value (< 250 MeV) a "soft" EoS. Additionally, the Coulomb interaction between protons and a finite-range Yukawa term are included.
The r.h.s. of eq. (8.1) contains a Boltzmann collision integral term, $I_{coll}[f]$. This collision term describes the influence of binary hard-core collisions between nucleon 1 and 2, where the term with $f f_2$ describes the loss of particles (in a phase space region) and the term with $f_1' f_2'$ the gain term due to collisions feeding the considered phase space region. It is supplemented with the Nordheim-Uehling-Uhlenbeck modifications [Ueh33] in order to obey the Pauli-principle in the final state of the collisions (i.e. the terms $(1-f)$ giving the probability that the nucleon state is not occupied). The δ-functions assure the conservation of the four-momentum in the *NN* collision. The in-medium *NN* cross section $d\sigma/d\Omega$ in this expression is associated to the imaginary part of the G-matrix:

$$\frac{\mathrm{d}\sigma}{\mathrm{d}\Omega}(\vec{q}) = (m^2/16\pi^2)\,G(\vec{q})\,G_a^{\dagger}(\vec{q}) \tag{8.4}$$

The cross-section σ is normally adjusted to the free nucleon-nucleon scattering. The differences from cross-sections calculated from the imaginary part of the Brückner G-matrix are minor [Boh91] and influence little the observables of a heavy ion collision. For a derivation of this equation see e.g. [Bote90, Cass90b].

The equation is solved by use of the test-particle method. Here the continuous one-body distribution function f at t = 0 is represented by an ensemble of $n \cdot (A_p + A_t)$ point-like particles. This is often viewed as an ensemble of n parallel events with $A_p + A_t$ physical particles each, where A_p and A_t denote the number of nucleons in projectile and target, respectively. The l.h.s. of eq. (8.1) can be regarded as the transport equation (Vlasov-equation) for a distribution of classical particles whose time evolution is governed by Hamilton's equations of motion

$$\dot{\vec{p}}_i = -\frac{\partial\langle H\rangle}{\partial\vec{r}_i} \quad \text{and} \quad \dot{\vec{r}}_i = \frac{\partial\langle H\rangle}{\partial\vec{p}_i} \tag{8.5}$$

The test-particles move due to their own, selfconsistently generated mean-field. The r.h.s. is taken into account by additional stochastic scattering similar to the collisions in cascade models [Yari79, Cugn80].

For a solution of equation (8.1) proper boundary conditions have to be specified. In the case of heavy ion reactions, the test particles are distributed according to the density-

and (Fermi-) momentum distribution of ground state nuclei. Initially the test particles are randomly distributed in a coordinate space sphere of radius $R = 1.12A^{1/3}$ fm (where A is the atomic number of the nucleus) and in a momentum space sphere with the radius of the corresponding Fermi momentum. The nuclei are then boosted again each other with the proper relative beam momentum.

One should keep in mind that the forces acting on the test-particles are calculated from the entire distribution including test-particles from all events, hence the n parallel events are not independent and event-by-event correlations cannot be analyzed within such one-body transport models. In the limit $n \to \infty$ the distribution of these propagated test particles at the time t represents the one-body distribution function at this time. Any one-body observable can be calculated by averaging the values weighted with the distribution function. In that way, BUU type models have succeeded in the description of one-body observables like collective flow, stopping and particle spectra, but, fluctuations and correlations, such as the formation of fragments or the description of two-particle correlations in relativistic heavy ion collisions, are beyond the scope of a transport model based on a one-body distribution function.

8.1.2 Collision dynamics in the ^{36}Ar+^{197}Au, ^{107}Ag, ^{58}Ni, ^{12}C at 60A MeV reactions

The BUU code employed in this work for the simulations of the collision dynamics of the four different heavy-ion reactions is a version [Wolf90, Wolf93] of BUU originally developed by the theory group of the University of Giessen [Cass90] and used as a sort of "standard" code by the TAPS collaboration in the last 7 years for several comparisons with experimental data [Schu97]. The advantage of a dynamical model is that it offers the possibility to follow in time the evolution of any relevant reaction quantity. In this section I will examine the density profiles in configuration and momentum space for the four reactions studied. The selected incompressibility parameter is κ_∞ = 230 MeV, corresponding to a rather soft EoS in agreement with the latest experimental results reported [Youn99], no momentum dependence is considered in the nuclear potential and the chosen number of test-particles is n = 150 for all systems (already for $n > 30$ one obtains smooth density distributions and reliable Pauli-blocking factor values [Cass90]).

Since we are interested in the reaction dynamics of collisions leading to the emission of a hard-photon, all the nucleus-nucleus collisions have been simulated at a fixed impact-parameter b corresponding to semi-central reactions for which hard-photon emission is maximal. Indeed, it has been already discussed (Section 7.1) that by selecting reactions in which hard-photons are produced, rather central collisions are favored. The average impact-parameter for reactions in which a pn bremsstrahlung photon is emitted is determined, within the "equal participant model" prescription (see Section 3.2.1), as the value of b which maximizes the product $b \times \langle N_{pn} \rangle$ given by equation (3.12). This formula[2] gives the average impact-parameters in which a hard-photon is emitted with maximum probability for the reactions ^{36}Ar+^{197}Au, ^{107}Ag, ^{58}Ni, ^{12}C at 60A MeV (table 8.1).

[2]The obtained $b \times \langle N_{pn} \rangle$ distribution for the ^{36}Ar+^{197}Au system can be seen in fig. 6.34 (dotted line).

Table 8.1: *Average impact-parameter for maximum bremsstrahlung photon emission probability in the reactions $^{36}Ar+^{197}Au$, ^{107}Ag, ^{58}Ni, ^{12}C at 60A MeV according to the "equal participant model" equation (3.12).*

Reaction	^{36}Ar+^{197}Au	^{36}Ar+^{108}Ag	^{36}Ar+^{58}Ni	^{36}Ar+^{12}C
$< b >$ (fm)	3.8	3.1	2.5	2.1

The detailed time evolution in the coordinate space (x, z) of the four considered heavy-ion reactions can be seen in figs. 8.1, 8.3, 8.5, 8.7. The plots displaying the time dependence of the same reactions in momentum space (p_x, p_z) provide a complementary information (figs. 8.2, 8.4, 8.6, 8.8). From those two plots per reaction we can extract the following information regarding their evolution in phase space:

- ^{36}Ar+^{197}Au: The Ar projectile completely penetrates the bigger gold target nucleus forming a single composite system at t $\approx$ 35 fm/c. At t $\approx$ 120 fm/c some small projectile-like remnant escapes from the back side of the remaining heavy Au-like residue together with emission of light-particles in the mid-rapidity region. In momentum space, at the beginning of the collision the two Fermi spheres, corresponding to target and projectile, are separated by the relative beam momentum. Later, at the end of the expansion stage (t $\approx$ 60 fm/c), the momentum distribution is isotropic indicating that the hot heavy residue is thermalizing[3].

- ^{36}Ar+^{108}Ag: Similarly to the former case, the argon nucleus is completely absorbed by the silver target forming a transient single composite system at t $\approx$ 30 fm/c. At t $\approx$ 90 fm/c, however, a somewhat larger projectile-like fragment than in the Au case issues from the target-like residue, and a third neck-like structure resulting from the overlapping zone between target and projectile is also visible. The total momentum distribution (originally a Fermi bi-sphere) becomes locally spherical at t $\approx$ 60 fm/c.

- ^{36}Ar+^{58}Ni: At variance with the two former cases, the Ar projectile traverses the Ni target issuing as independent fragments at t $\approx$ 80 fm/c. A smaller neck-like structure is produced in between the two primary quasitarget and quasiprojectile fragments. Equilibration seems to set in at around t $\approx$ 60 fm/c like in the former cases.

- ^{36}Ar+^{12}C: In this lightest system the reaction times are significantly lower than e.g. in the Au case. The smaller total number of nucleons makes the system much more transparent and friction either due to individual nucleon-nucleon collisions or to the

[3] In microscopical calculations the degree of equilibration can be quantified by computing the degree of anisotropy of the local momentum distribution of the colliding nucleons, which can be expressed e.g. as the ratio R = $\langle p_z^2 \rangle / 2\langle p_x^2 \rangle$. In a completely thermalized system with isotropic momentum distribution, R = 1, while in a non-equilibrium situation with large mean squared longitudinal momentum the ratio is small R = 0 [Neis90]. Other similar tests of local equilibrium in microscopical calculations are also performed by measuring the momentum relaxation time given by $(\langle p_x^2 \rangle + \langle p_y^2 \rangle / 2\langle p_z^2 \rangle)$ [Li93] or the quadrupole moment $Q_{zz}(t)$ in the rest frame of the excited residue [Bona90].

mean field is less important. At t ≈ 60 fm/c, the now heavier Ar projectile has completely traversed and disintegrated its lighter partner. At t ≈ 145 fm/c only a quasiprojectile fragment and some particles and small fragments seem to be present. In that case, the distribution of nucleon momenta is still slightly asymmetric at t > 75 fm/c, indicating that full equilibration does not occur, and that some memory of the entrance-channel is kept all throughout the reaction.

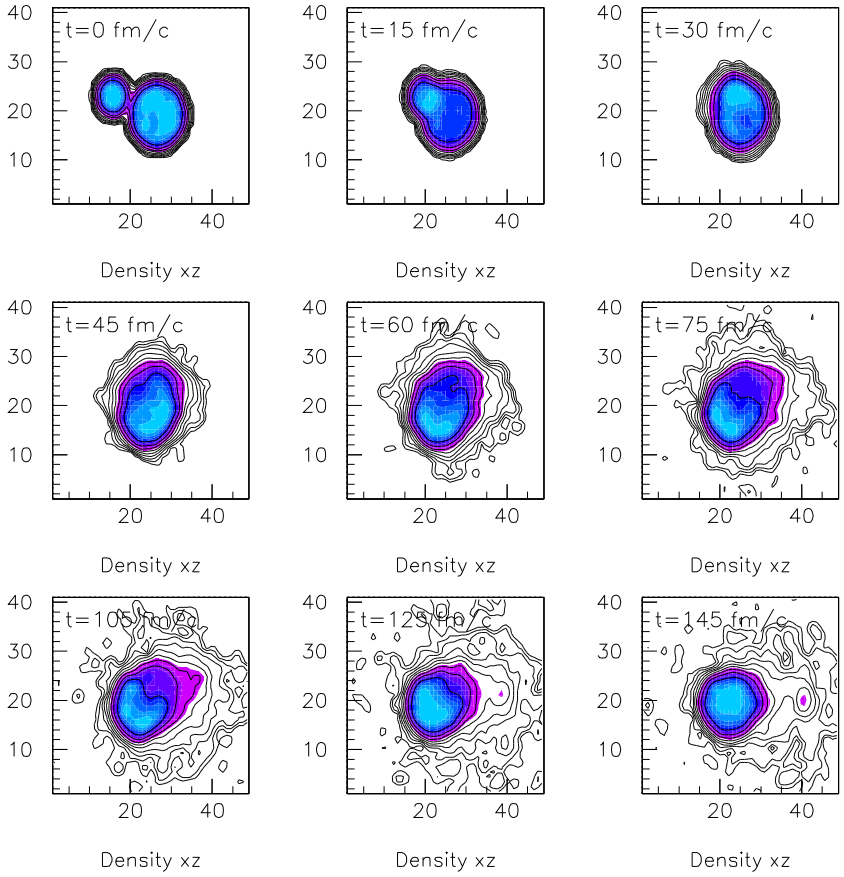

Figure 8.1: *Time evolution according to BUU of the reaction* $^{36}Ar+^{197}Au$ *at 60A MeV and b = 3.8 fm, shown as the density distribution of nucleons projected in the x,z coordinate space. The beam axis is along z, and (x,z) are measured in fm.*

The analysis of all these reactions indicates that the dominant reaction mechanism, at the (semi-central) impact-parameters for which nuclear bremsstrahlung is maximal, is incomplete fusion: a composite system is formed during the first ≈ 35 fm/c, followed by its expansion up to the separation point at t ≈ 75 - 100 fm/c. From this moment on, one heavy hot target-like residue is formed for the heaviest Au and Ag systems, whereas for the $^{36}Ar+^{58}Ni$ case the model is compatible with the experimentally well established mainly dissipative binary character of the reaction in this more symmetric projectile-target

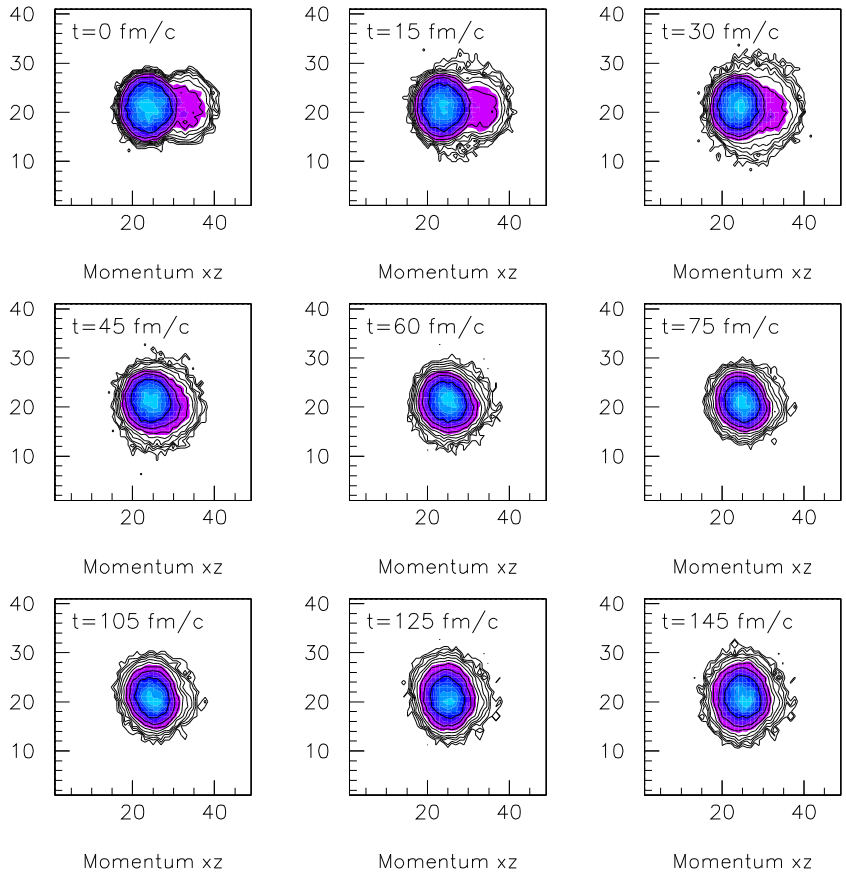

Figure 8.2: *Time evolution according to BUU of the reaction $^{36}Ar+^{197}Au$ at 60A MeV and b = 3.8 fm, shown as the density distribution of nucleons projected in the transverse-longitudinal (p_x, p_z) momentum space. (Each bin corresponds to 37.5 MeV/c).*

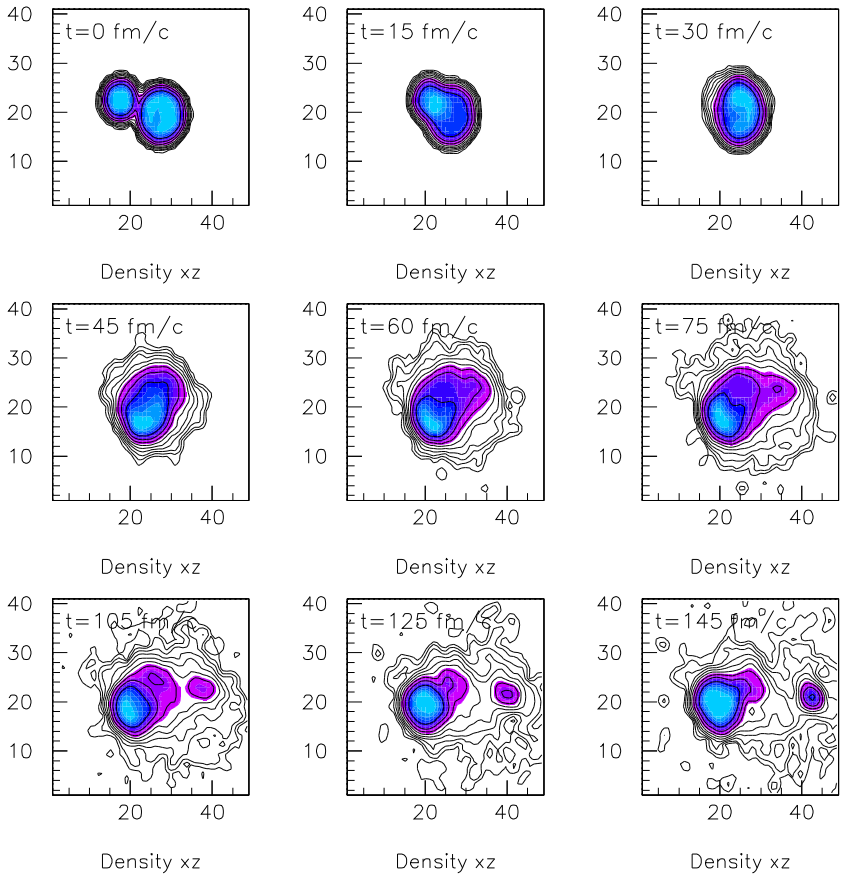

Figure 8.3: *Time evolution according to BUU of the reaction* $^{36}Ar+^{108}Ag$ *at 60A MeV and b = 3.1 fm, shown as the density distribution of nucleons projected in the* x,z *coordinate space. The beam axis is along z, and* (x,z) *are measured in fm.*

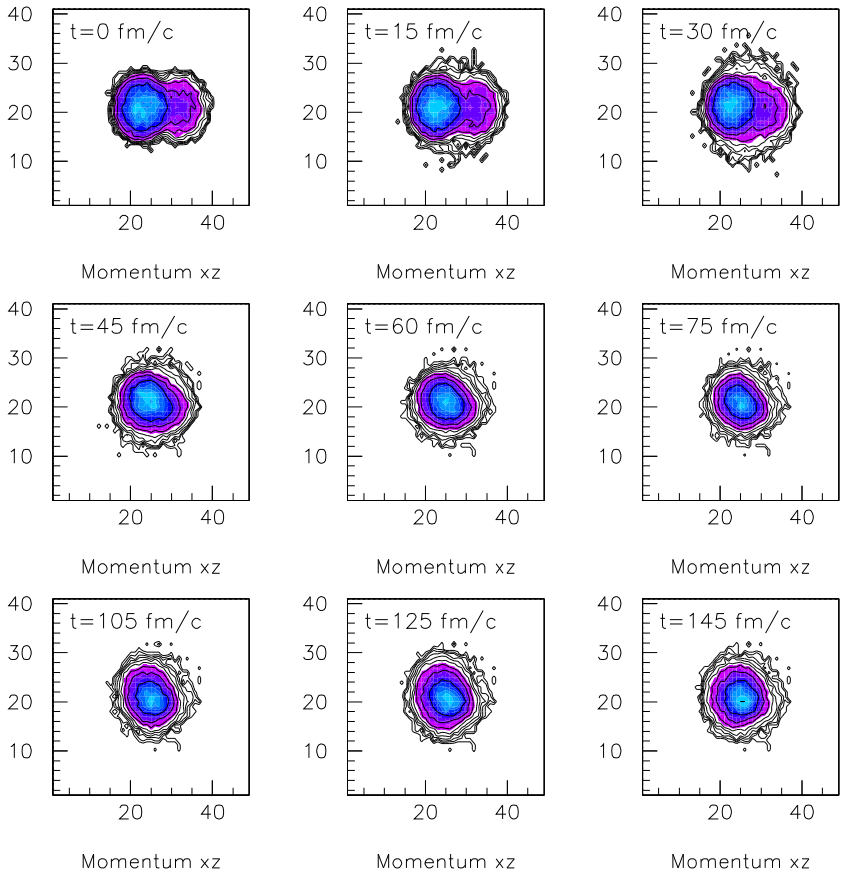

Figure 8.4: *Time evolution according to BUU of the reaction at* $^{36}Ar+^{108}Ag$ *at 60A MeV and b = 3.1 fm, shown as the density distribution of nucleons projected in the transverse-longitudinal* (p_x, p_z) *momentum space. (Each bin corresponds to 37.5 MeV/c).*

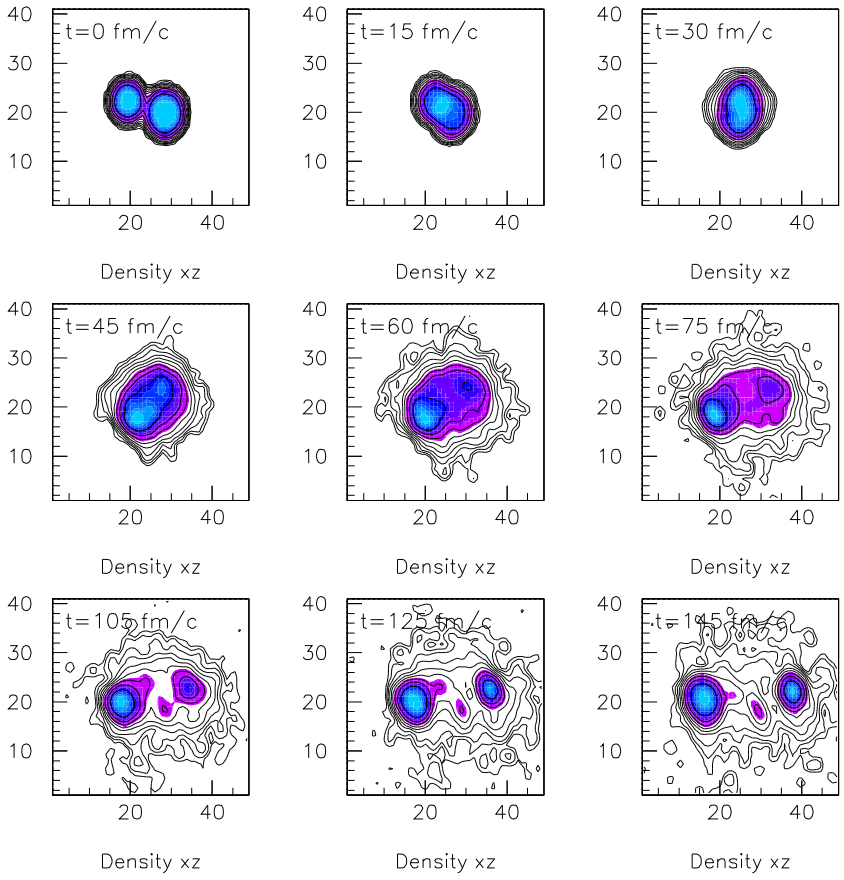

Figure 8.5: *Time evolution according to BUU of the reaction $^{36}Ar+^{58}Ni$ at 60A MeV and b = 2.5 fm, shown as the density distribution of nucleons projected in the x,z coordinate space. The beam axis is along z, and (x,z) are measured in fm.*

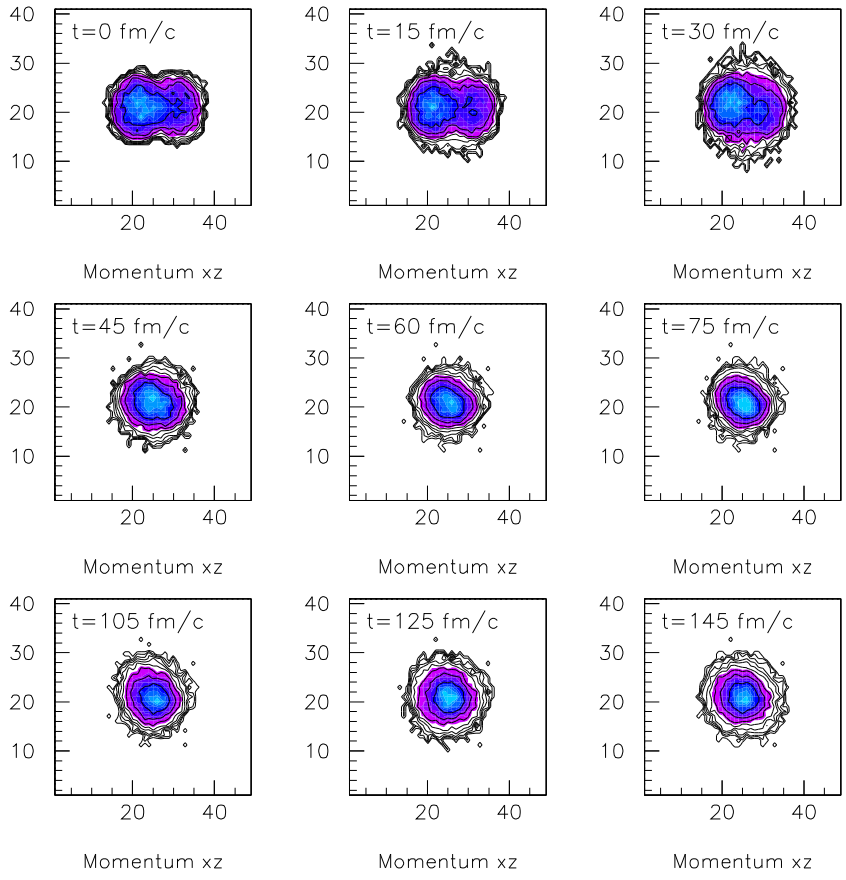

Figure 8.6: *Time evolution according to BUU of the reaction $^{36}Ar+^{58}Ni$ at 60A MeV and b = 2.5 fm, shown as the density distribution of nucleons projected in the transverse-longitudinal (p_x, p_z) momentum space. (Each bin corresponds to 37.5 MeV/c).*

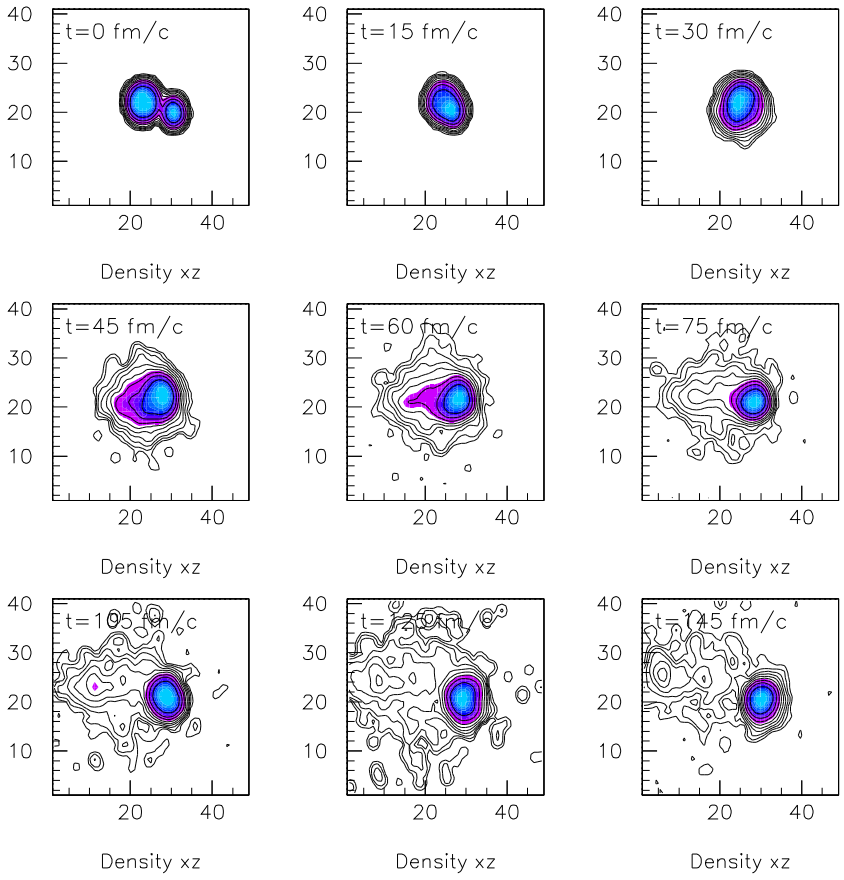

Figure 8.7: *Time evolution according to BUU of the reaction* $^{36}Ar+^{12}C$ *at 60A MeV and b = 2.1 fm, shown as the density distribution of nucleons projected in the* x,z *coordinate space. The beam axis is along z, and* (x,z) *are measured in fm.*

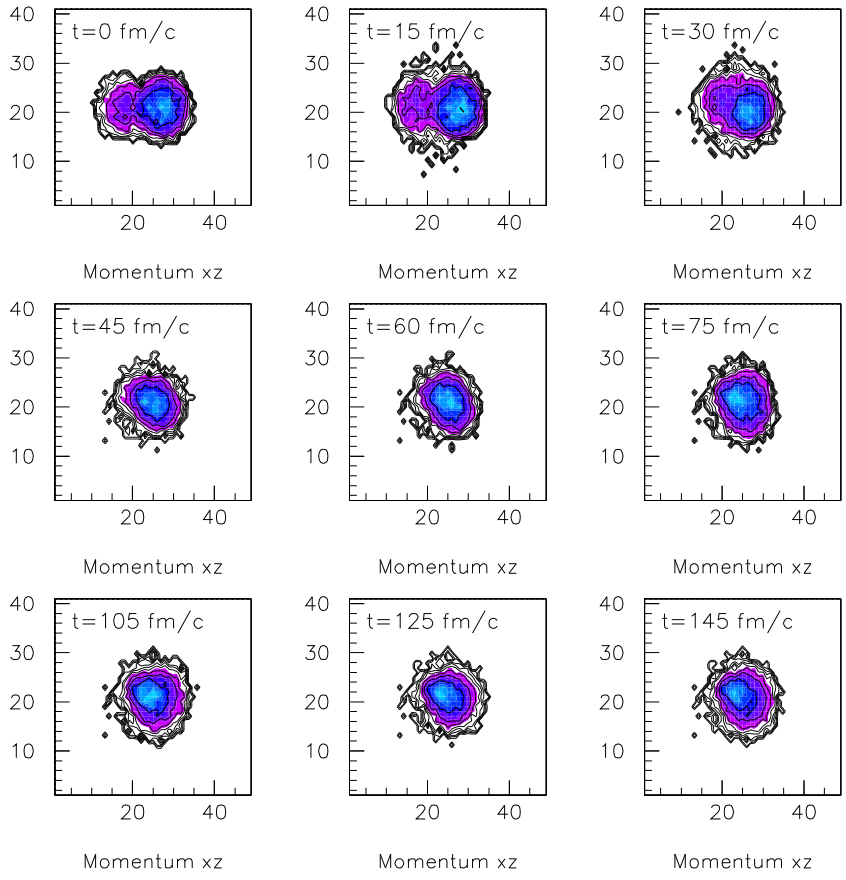

Figure 8.8: *Time evolution according to BUU of the reaction $^{36}Ar+^{12}C$ at 60A MeV and b = 2.1 fm, shown as the density distribution of nucleons projected in the transverse-longitudinal (p_x, p_z) momentum space. (Each bin corresponds to 37.5 MeV/c).*

combinations (for this system also a third structure develops in between the two biggest fragments). For the lightest ^{36}Ar+^{12}C system only one quasiprojectile survives with some individual particles and clusters emitted in the mid-rapidity region.

As a matter of fact, very recent and complete experimental results collected with the 4π MSU-array [Colin98, Colin99, Sun99a, Sun00] for ^{40}Ar-induced reactions on ^{197}Au, ^{108}Ag and ^{63}Cu at 65*A* MeV indicate that incomplete fusion with capture of most of the projectile by the heavier target or splintering collisions with capture of only a minority fraction of the projectile nucleons leading to a multi-body spray of projectile-like light fragments in the forward direction, are the dominant reaction mechanisms for central and semi-central reactions respectively. Most of the reaction products detected in this kind of collisions can be thus separated into isotropic (from the thermalized heaviest fragment) and forward-focused (pre-thermalized) emission. Additionally, the ^{36}Ar+^{58}Ni system has been thoroughly studied by the INDRA collaboration at 52*A*, 74*A* and 95*A* MeV. The dominant process of this more-symmetric system is the formation of a quasi-projectile and a quasi-target accompanied by dynamical (or preequilibrium) emission at mid-rapidity [Ma97]. Such reaction mechanisms are qualitatively predicted by our BUU calculations.

With the same BUU calculations we can follow the evolution of the maximum (local) central density[4], ρ_{max}, attained during the first compression phase (when a transient composite system is formed), its minimum value, ρ_{min}, at the end of the expansion stage (when the two original fragments are separating), and its second maximum value ρ_{max}^{2nd} reached afterwards in the remaining heavy residue (fig. 8.9 and table 8.2).

The maximum density reached during the collision is $\rho_{max} \approx 1.4\rho_0$ for the four considered systems. This feature is a result of the different impact parameters selected for each reaction which compensate somehow the different importance of the compressional effects in each projectile-target combination. The two smaller systems, however, lead at the end of the expansion phase to a minimal value, $\rho_{min} \approx 0.6\rho_0$, lower than those obtained for bigger ones ($\rho_{min} \approx 0.8\rho_0$) . According to these simulations, the subnuclear densities reached at least for the two heaviest systems (Au and Ag targets) are not low enough to drive the excited systems into the spinodal region ($\rho_{min} \lesssim 0.4\rho_0$) at the end of the expansion stage. Instead, the remaining heavy residues, driven by the nuclear force, undergo a new recompression towards the saturation density. In all cases, the value of the density reached in this second recompression is rather moderate $\rho_{max}^{2nd} \approx 1.1\rho_0$.

8.1.3 Bremsstrahlung production within BUU

We shall now present the result for the calculation of the $pn\gamma$ bremsstrahlung rate and its evolution with time. Correlating this information with the results obtained in the former section will help to identify the spatio-temporal source at the origin of the emission of thermal hard-photons. We have used the same BUU version, in which the production of bremsstrahlung photons (using the Schäfer parametrization of the $pn\gamma$ elementary

[4]The values of the density have been obtained for a (central) cube of 27 fm^3 volume. As a reference, the volumes of some of the colliding nuclei in this experiment are: $V(^{12}\mathrm{C}) = 86$ fm^3, $V(^{36}\mathrm{Ar}) = 260$ fm^3, $V(^{197}\mathrm{Au}) = 987$ fm^3.

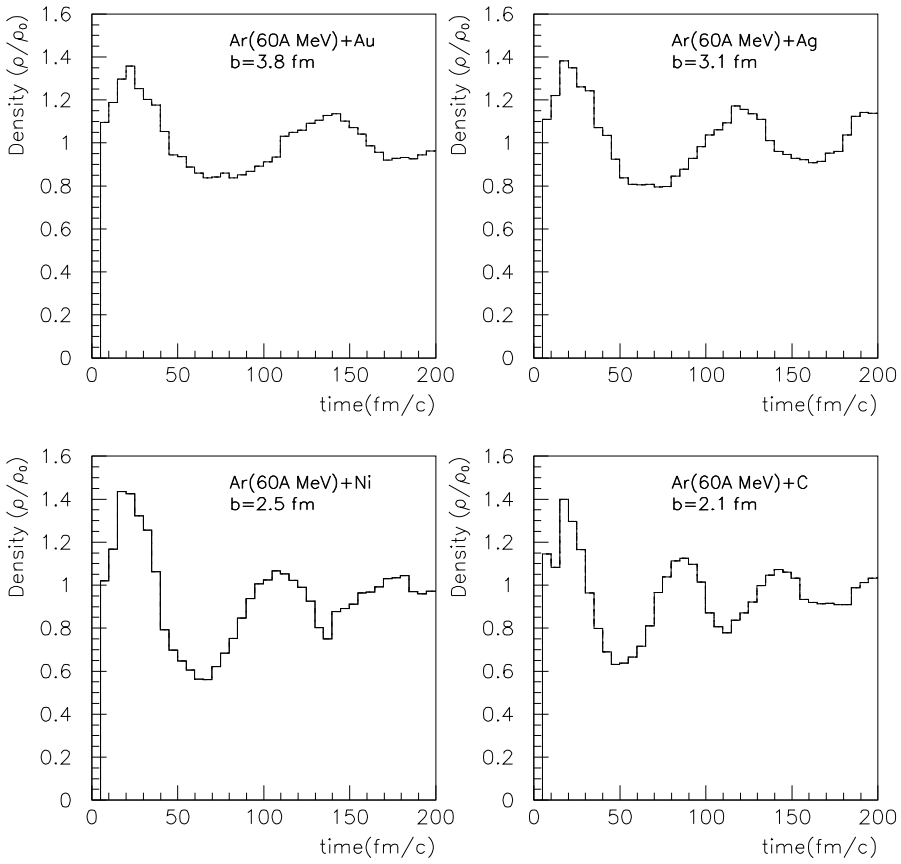

Figure 8.9: *Evolution of the (central) density in the reactions* $^{36}Ar+^{197}Au$, ^{108}Ag, ^{58}Ni, ^{12}C *at 60A MeV for the different impact-parameters, as given by BUU calculations.*

Table 8.2: *Maximum, ρ_{max}, and minimum, ρ_{min}, central densities attained respectively in the first compression stage and at the end of the first expansion stage as predicted by BUU simulations for the reactions $^{36}Ar+^{197}Au$, ^{107}Ag, ^{58}Ni, ^{12}C at 60A MeV at the impact parameters quoted in table 8.1. The density attained at the second recompression of the system ρ_{max}^{2nd} is also indicated. The value of the incompressibility modulus is κ_∞ = 230 MeV, in all cases.*

Reaction:	^{36}Ar+^{197}Au	^{36}Ar+^{108}Ag	^{36}Ar+^{58}Ni	^{36}Ar+^{12}C
1st compression:				
ρ_{max}/ρ_0	1.35	1.38	1.43	1.40
t (fm/c)	22	17	19	17
Expansion:				
ρ_{min}/ρ_0	0.84	0.80	0.56	0.63
t (fm/c)	70	70	65	50
2nd compression:				
ρ_{max}^{2nd}/ρ_0	1.14	1.16	1.06	1.12
t (fm/c)	140	120	107	87

cross-section, see Appendix 2) is implemented perturbatively [Cass90]. These simulations of the time sequence of photon production for the reactions ^{36}Ar+^{197}Au, ^{107}Ag, ^{58}Ni, ^{12}C at 60*A* MeV (figs. 8.10, 8.11, 8.12, 8.13) have been performed at the same impact-parameters used in the former section.

Two sources of hard-photons separated in time are predicted by BUU: the most intense one during the first compression stage and the second one during the recompression phase of the heavy remnant. Those two hard-photon flashes have been usually interpreted [Mart95, Schu97] as being responsible respectively for the "direct" and "thermal" hard-photon contributions observed in the experimental photon spectra. They present the following features:

- Direct hard-photons: Photons start to be emitted immediately after the beginning of the collision process ($t \approx 10$ fm/c for the four systems). The maximum of emission takes place between t $\approx$ 22 fm/c and t $\approx$ 30 fm/c, slightly after when the maximum compression of the composite system is reached (see fig. 8.9 and table 8.2). This first flash lasts up to 60 - 70 fm/c for the two heaviest systems and only 35 fm/c for the lightest C target. Those times roughly correspond to the complete geometrical passage of the two colliding ions through each other. It issues mainly from energetic first-chance *NN* collisions, when the system, far from equilibrium, as indicated by the (p_x, p_z) plots, is first compressed. A small contribution of secondary *NN* collisions during the expansion phase while the system is thermalizing (due to the effect of two-body dissipation) also accounts for some direct hard-photon production.

- Thermal hard-photons: For the three heaviest systems (^{36}Ar+^{197}Au, ^{107}Ag, ^{58}Ni), the first emission of hard-photons is followed by a second flash (with a maximum at

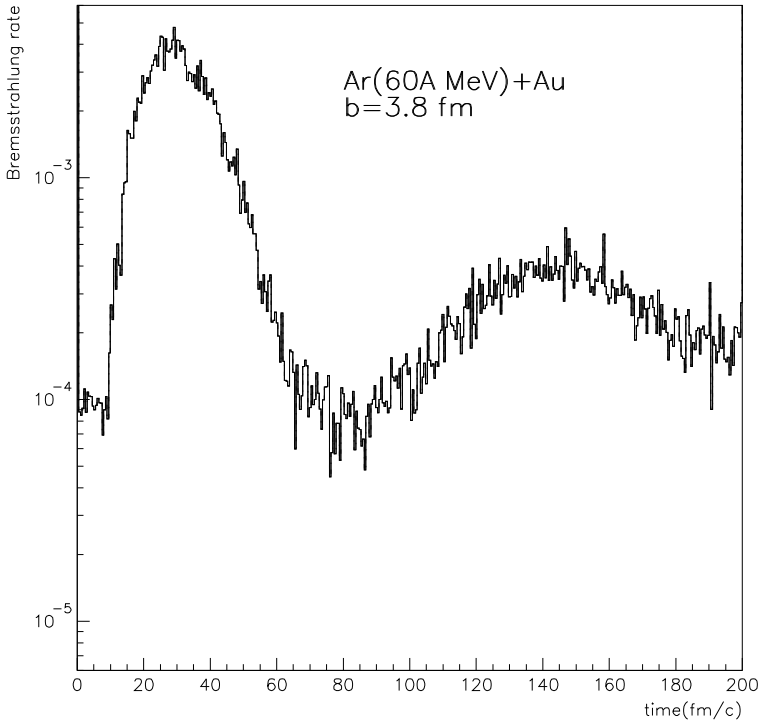

Figure 8.10: *Production rate of bremsstrahlung photons ($E_\gamma \geq 30$ MeV) as a function of time calculated with BUU assuming a rather soft EoS ($\kappa_\infty = 230$ MeV) for the system $^{36}Ar+^{197}Au$ at 60A MeV at an impact parameter b = 3.8 fm.*

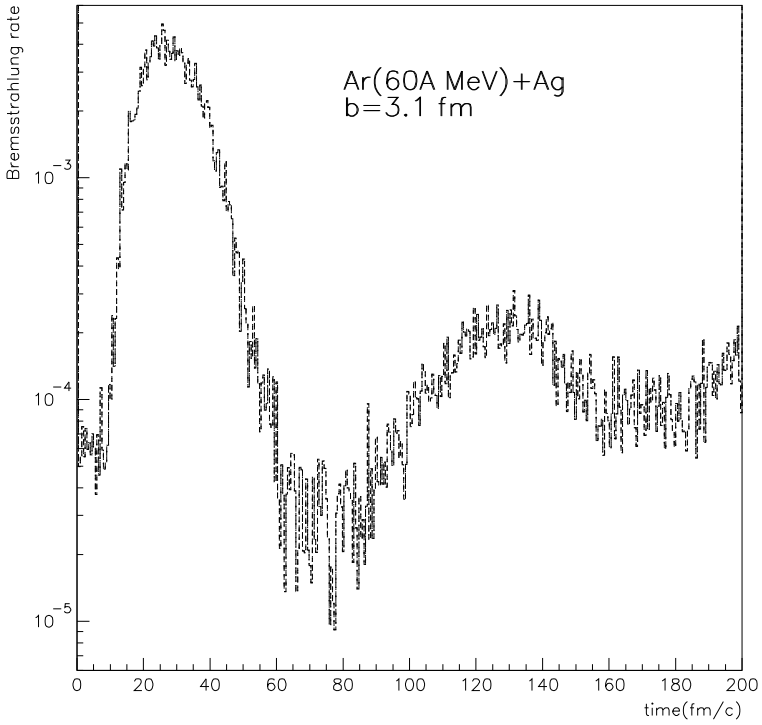

Figure 8.11: *Production rate of bremsstrahlung photons ($E_\gamma \geq 30$ MeV) as a function of time calculated with BUU assuming a rather soft EoS ($\kappa_\infty = 230$ MeV) for the system $^{36}Ar+^{108}Ag$ at 60A MeV at an impact parameter b = 3.1 fm.*

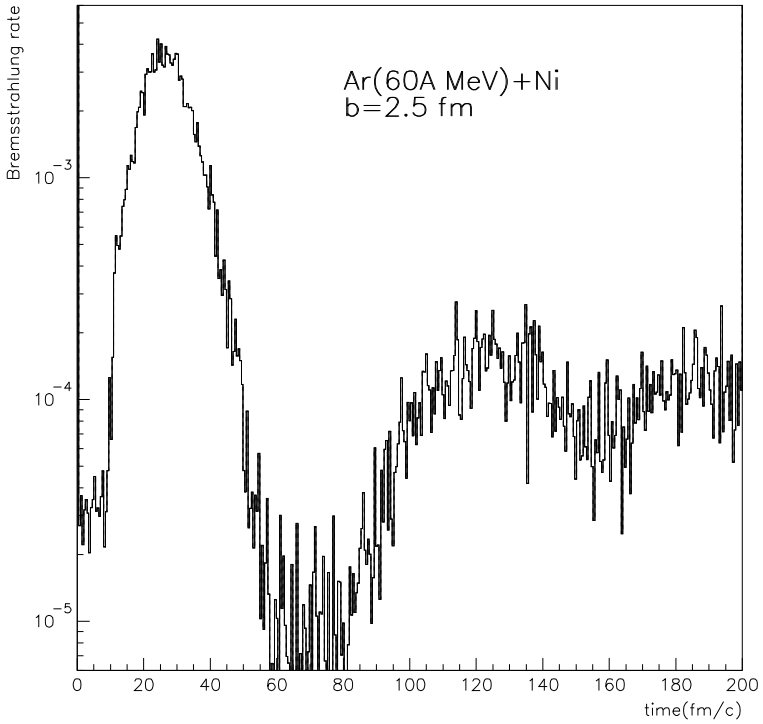

Figure 8.12: *Production rate of bremsstrahlung photons ($E_\gamma \geq 30$ MeV) as a function of time calculated with BUU assuming a rather soft EoS ($\kappa_\infty = 230$ MeV) for the system $^{36}Ar+^{58}Ni$ at 60A MeV at an impact parameter b = 2.5 fm.*

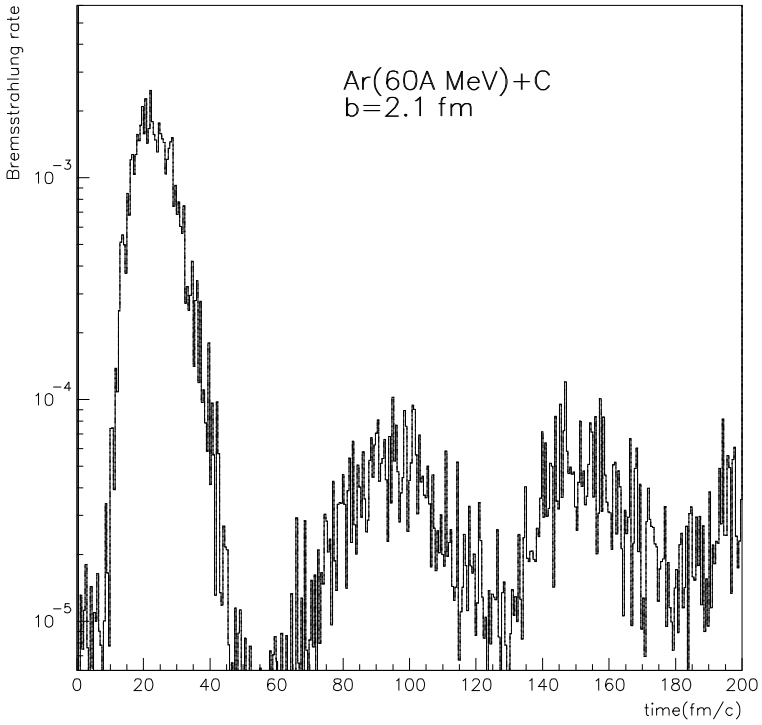

Figure 8.13: *Production rate of bremsstrahlung photons ($E_\gamma \geq 30$ MeV) as a function of time calculated with BUU assuming a rather soft EoS ($\kappa_\infty = 230$ MeV) for the system $^{36}Ar+^{12}C$ at 60A MeV at an impact parameter b = 2.1 fm.*

Table 8.3: *Relative ratio of thermal (bremsstrahlung emitted during the second compression stage of the reaction) to total hard-photons for the four studied reactions according to BUU calculations.*

Reaction	^{36}Ar+^{197}Au	^{36}Ar+^{108}Ag	^{36}Ar+^{58}Ni	^{36}Ar+^{12}C
Thermal/Total hard-γ	18%	15%	10%	5%

$t \approx$ 100 - 140 fm/c) of bremsstrahlung photons emitted from subsequent *NN* collisions inside the excited nuclear systems, during the second modest ($\rho \approx 1.1\rho_0$) compression phase. During this later phase the heavy remnant (in the Au and Ag cases) or the primary quasi-projectile and quasi-target (for the Ni case) are clearly thermalized as indicated by the isotropic nucleon momenta distributions (plots 8.2, 8.4 and 8.6). This justifies the designation of "thermal" hard-photons for this second-chance *pn*γ bremsstrahlung emission. Since the energy of the produced photon is limited by the available CM energy in the *pn* collision, this thermal hard-photon component populates more intensely the low-energy region of the hard-photon spectrum (E_γ = 30 - 60 MeV). For the ^{36}Ar+^{12}C case, this second component is not completely absent in the calculations although it is much less significant than in the other systems in agreement with our observations. The duration of this second group of *NN* collisions leading to bremsstrahlung emission depends basically on the size of the system (i.e. on the total number of participant nucleons) being maximal for the heaviest ^{36}Ar+^{197}Au one. The relative weight of the thermal component with respect to the total hard-photon yield[5] varies thus for each target as indicated in table 8.3. This result is in agreement with the experimentally observed thermal hard-photon ratios for the Au, Ag and C targets but is clearly underestimated for the Ni one (see table 6.2).

[5]It has to be noted that in BUU, as in other transport model calculations, spurious collisions do occur at the momentum-space surface due to an imperfect treatment of the Pauli blocking [Bona90]. As a consequence a low-energy bremsstrahlung photon contribution is artificially generated by the calculations. In such circumstances, the intensity of this contribution cannot be exactly calculated and introduces a relative uncertainty on the intensity of the photon sources which might be particularly significant for the second and weaker one [Barz96]. We have tried to minimize the effect of this component by subtracting from the whole bremsstrahlung rates the spurious emission collected prior to the heavy-ion contact-point. This contribution, which has been assumed constant all through the time sequence, is of the order, at most, of 10% of the total yield after integration over the reaction time.

8.2 Quantum Molecular Model (QMD)

8.2.1 Description of the model

The Quantum Molecular Dynamics (QMD) model [Aich86, Aich87b, Peil89, Aich91] provides an approach that goes beyond the one-body description of BUU simulations. QMD is a *n*-body theory which simulates heavy ion reactions on an event-by-event basis. Since it takes into account all fluctuations and correlations between the colliding nucleons, many-body processes, in particular the formation of complex fragments, are explicitly treated.

In QMD, each nucleon is represented by a coherent gaussian state characterized by 6 time-dependent parameters $\vec{r}_i$ and $\vec{p}_i$ of the form:

$$\phi_i(\vec{x}_i;t) = \left(\frac{2}{L\pi}\right)^{3/4} e^{-(\vec{x}_i-\vec{r}_i(t))^2/L}\, e^{i\vec{x}_i\vec{p}_i(t)} \tag{8.6}$$

The parameter L, which is related to the extension of the wave packet in phase space, is fixed. The total *n*-body wave function is assumed to be the direct product of coherent states like (8.6):

$$\Phi = \prod_i \phi_i(\vec{x}_i, \vec{r}_i, \vec{p}_i, t) \tag{8.7}$$

Since this expression does not use a Slater determinant (with $(A_p + A_t)!$ summation terms) it neglects antisymmetrization. First successful attempts to simulate heavy ion reactions with fully antisymmetrized states have been performed for small systems [Feld00, Ono98]. A consistent derivation of the QMD equations of motion for the wave function under the influence of both, the real and the imaginary part of the G-matrix, however, has not yet been achieved. Therefore one adds the imaginary part as a cross section and treats them as in the cascade approach.

The initial values of the parameters are chosen in a way that the ensemble of $(A_t + A_p)$ nucleons gives a smooth density distribution as well as a correct momentum distribution of the projectile and target nuclei. The time evolution of the system is calculated by means of a generalized variational principle. One starts out from the action:

$$S = \int_{t_1}^{t_2} \mathcal{L}[\Phi, \Phi^*]dt \tag{8.8}$$

with the Lagrange functional $\mathcal{L}$:

$$\mathcal{L} = \left\langle \Phi \left| i\hbar\frac{d}{dt} - H \right| \Phi \right\rangle \tag{8.9}$$

where the total time derivative includes the derivation with respect to the 6 time-dependent parameters $\vec{r}_i$ and $\vec{p}_i$. The time evolution of the parameters is obtained by the requirement that the action is stationary under the allowed variation of the wave function:

$$\delta S = \delta \int_{t_1}^{t_2} \mathcal{L}[\phi, \phi^*]dt = 0 \tag{8.10}$$

If the true solution of the Schrödinger equation is contained in the restricted set of wave functions $\phi_i(\vec{x}_i, t)$ (with parameters $\vec{r}_i, \vec{p}_i$) this variation of the action gives the exact

solution of the Schrödinger equation. If the parameter space is too restricted one obtains that wave function in the restricted parameter space which comes closest to the solution of the Schrödinger equation. Performing the variation with the test wave function, one obtains for each parameter λ an Euler-Lagrange equation:

$$\frac{d}{dt}\frac{\partial \mathcal{L}}{\partial \dot{\lambda}} - \frac{\partial \mathcal{L}}{\partial \lambda} = 0 \tag{8.11}$$

During the propagation, two nucleons suffer collisions if the distance between their centroids $|x_\alpha - x_\beta|$ is less than $\sqrt{\sigma/\pi}$. One also checks the availability of the final phase space with the so called *classical Pauli procedure*. In this procedure, a collision is blocked if the final state is already occupied.

The Hamiltonian H in equation (8.9) contains a kinetic term and mutual interactions V_{ij}, which can be interpreted as the real part of the Brückner G-matrix, complemented with the Coulomb interaction. The former can be further subdivided in a part containing the contact Skyrme-type interaction only, a contribution due to a finite range Yukawa-potential, and (optionally) a momentum dependent part:

$$\begin{aligned} V^{ij} &= G^{ij} + V^{ij}_{\text{Coul}} \\ &= V^{ij}_{\text{Skyrme}} + V^{ij}_{\text{Yuk}} + V^{ij}_{\text{mdi}} + V^{ij}_{\text{Coul}} \\ &= t_1\delta(\vec{x}_i - \vec{x}_j) + t_2\delta(\vec{x}_i - \vec{x}_j)\rho^{\gamma-1}(\vec{x}_i) + t_3\frac{\exp\{-|\vec{x}_i - \vec{x}_j|/\mu\}}{|\vec{x}_i - \vec{x}_j|/\mu} \\ &\quad + t_4\ln^2(1 + t_5(\vec{p}_i - \vec{p}_j)^2)\delta(\vec{x}_i - \vec{x}_j) + \frac{Z_i Z_j e^2}{|\vec{x}_i - \vec{x}_j|} \end{aligned} \tag{8.12}$$

Z_i, Z_j being the charges of the nucleons i and j.

The potential part of the equation of state, resulting from the interactions $V^{ij}_{\text{Skyrme}} + V^{i,j}_{\text{mdi}}$ (local interactions plus momentum dependence), then reads:

$$U = \alpha \cdot \left(\frac{\rho_{int}}{\rho_0}\right) + \beta \cdot \left(\frac{\rho_{int}}{\rho_0}\right)^\gamma + \delta \cdot \ln^2\left(\varepsilon \cdot (\Delta\vec{p})^2 + 1\right) \cdot \left(\frac{\rho_{int}}{\rho_0}\right) \tag{8.13}$$

Like in the BUU case, this generalized ansatz uses three parameters α, β, γ; two of them are fixed by the constraint that the total energy has a minimum at the saturation density $\rho = \rho_0$ with a value of $\varepsilon = -16A$ MeV which corresponds to the volume energy in the Bethe-Weizsäcker mass formula. The third parameter is fixed by the nuclear compressibility which defines, again, two different equations of state: a hard equation of state with a compressibility of $\kappa_\infty = 380$ MeV and a soft equation of state with a compressibility of $\kappa_\infty = 200$ MeV.

8.2.2 Collision dynamics in the ^{36}Ar+^{197}Au, ^{107}Ag, ^{58}Ni, ^{12}C at 60A MeV reactions

In order to study the dynamics of the heavy-ion collision we have employed in the present study the latest version of Quantum Molecular Dynamics (QMD), adapted for intermediate-

energy heavy-ion reactions [Neba99a, Neba99b]. It contains a Skyrme force without momentum dependence, yielding a rather soft equation of state (κ_∞ = 250 MeV). The 2-body collision term employs the Cugnon parametrization for the *NN* cross-section.
We have performed with QMD the same analysis carried out in Section 8.1.2 with BUU in order to study the time evolution of the four reactions in configuration and in momentum space. The simulations of the different systems at the impact parameters listed in table 8.1 indicate very similar reaction mechanisms to the BUU case (see discussion in Section 8.1.2) in the space of coordinates (x,z) (figs. 8.14, 8.16, 8.18, 8.20). Namely, the production of an excited quasi-target nuclei for the two heaviest systems (Au and Ag), the mainly binary character of the more symmetric ^{36}Ar+^{58}Ni reaction, and the existence of a single quasiprojectile fragment in the lightest ^{36}Ar+^{12}C one. Nonetheless, although both transport models show a very similar behaviour during the compression phase, the expansion and separation stages occur in a somewhat faster time-scale in the QMD case as it can be seen by comparing with figs. 8.1, 8.3, 8.5, 8.7. Even if both models share almost the same Skyrme mean-field leading to a quite similar EoS, this difference arises mainly from the different way of assessing the density entering in the nuclear potential and the strength of the Pauli blocking factor.

In momentum space (p_x, p_z), the disparity between QMD and BUU is more apparent. In the molecular model approach the original Fermi bi-sphere distribution of the colliding projectile and target nucleons remains visible until later reaction times (figs. 8.15, 8.17, 8.19, 8.21) at variance with the BUU results which indicated a rough momentum isotropy from t $\approx$ 60 fm/c. The (p_x, p_z) density profiles persist rather asymmetric until at least t $\approx$ 105 fm/c and even beyond global equilibration is not attained. This is an indication of a higher transparency of the QMD model where total thermalization is hardly attained because most of the two-body collisions are Pauli-blocked and, thus, equilibration is slower. As a matter of fact, in the framework of QMD, $b \approx$ 2 - 3 fm collisions never generate globally equilibrated nuclear matter systems [Goss97]. This will certainly have an influence in the bremsstrahlung spectra.

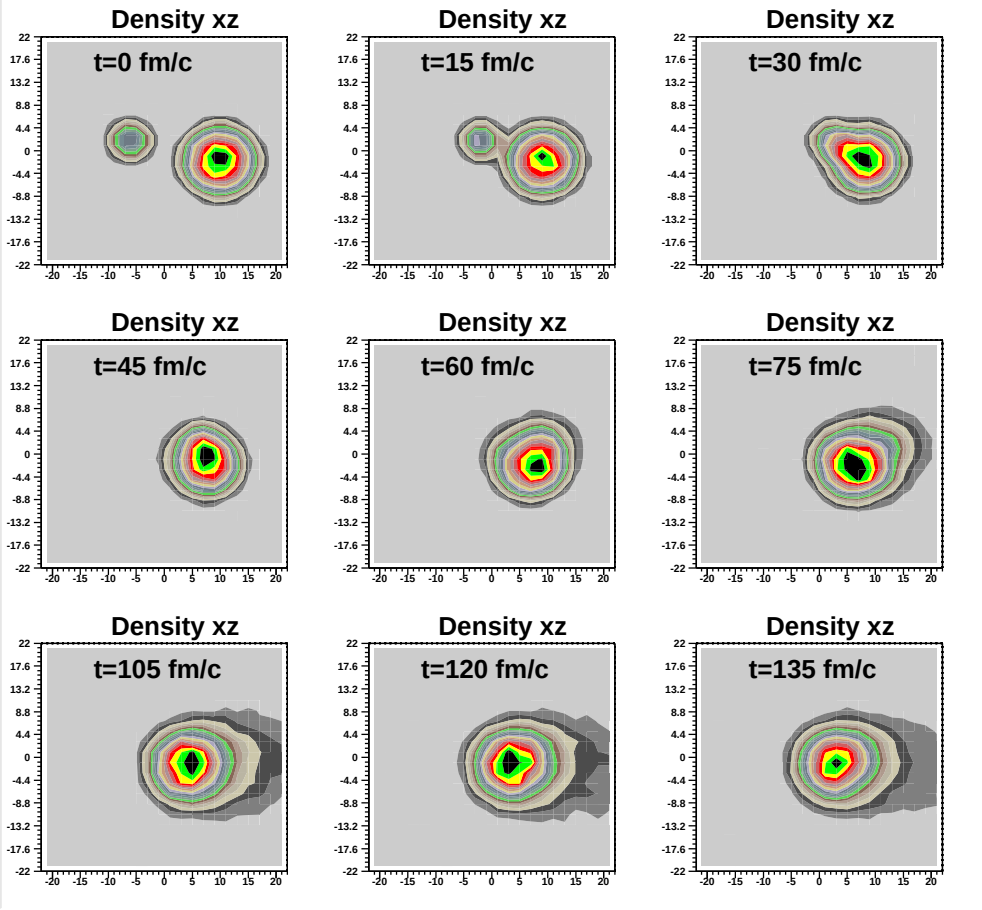

Figure 8.14: *Time evolution according to QMD of the reaction $^{36}Ar+^{197}Au$ at 60A MeV (b = 3.8 fm), shown as the density distribution of nucleons projected in the (x,z) coordinate space. The beam axis is along z, and (x,z) are measured in fm.*

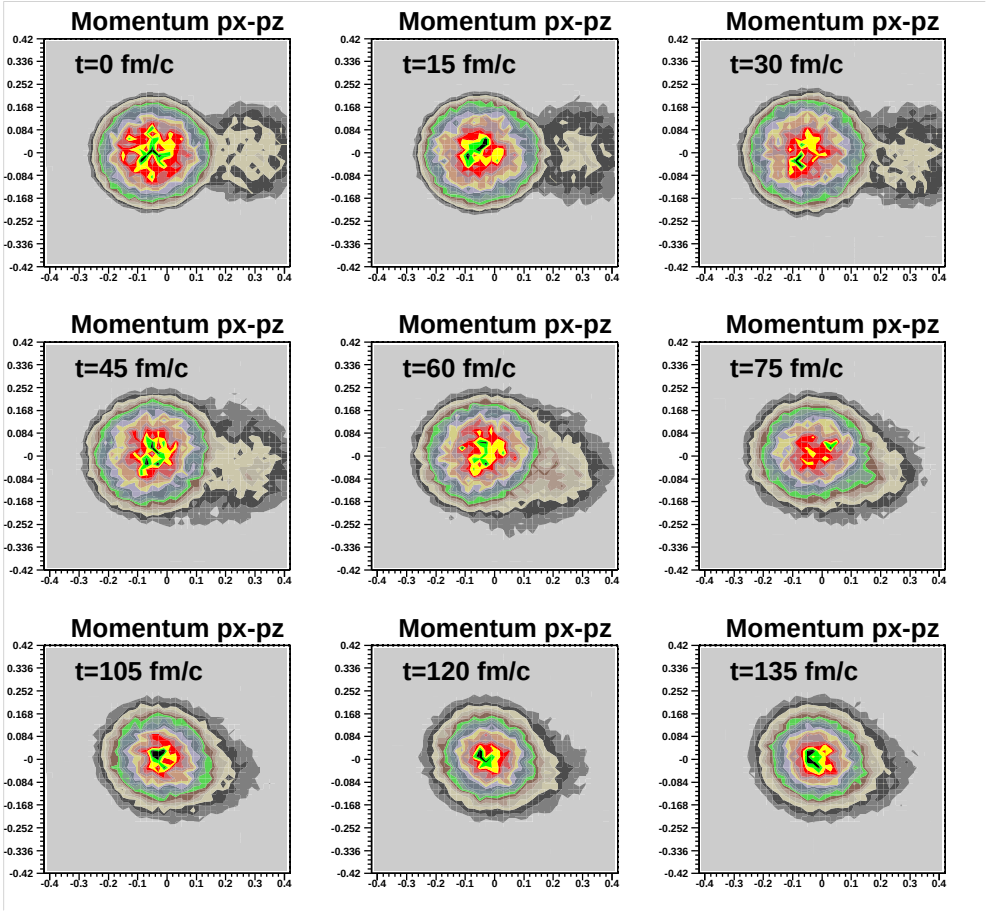

Figure 8.15: *Time evolution according to QMD of the reaction* $^{36}Ar+^{197}Au$ *at 60A MeV (b = 3.8 fm), shown as the density distribution of nucleons projected in the transverse-longitudinal* (p_x, p_z) *momentum space. (The units in both axes are GeV/c).*

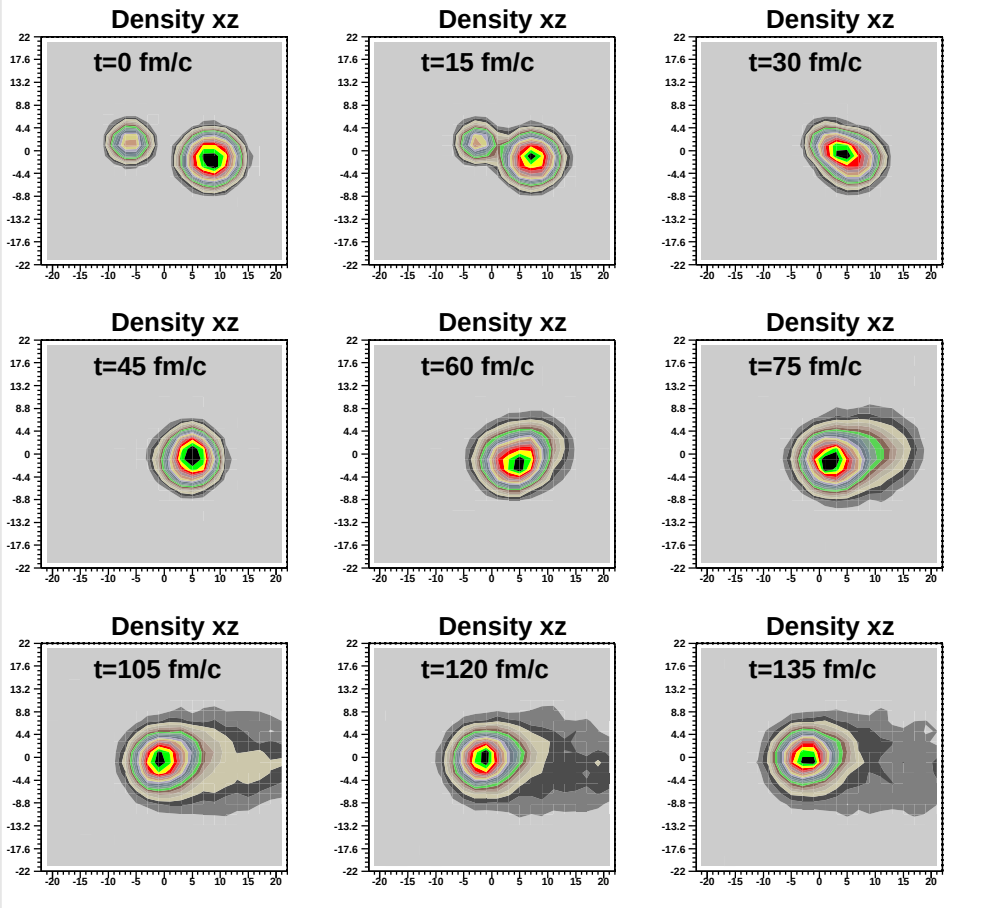

Figure 8.16: *Time evolution according to QMD of the reaction $^{36}Ar+^{108}Ag$ at 60A MeV (b = 3.1 fm), shown as the density distribution of nucleons projected in the (x,z) coordinate space. The beam axis is along z, and (x,z) are measured in fm.*

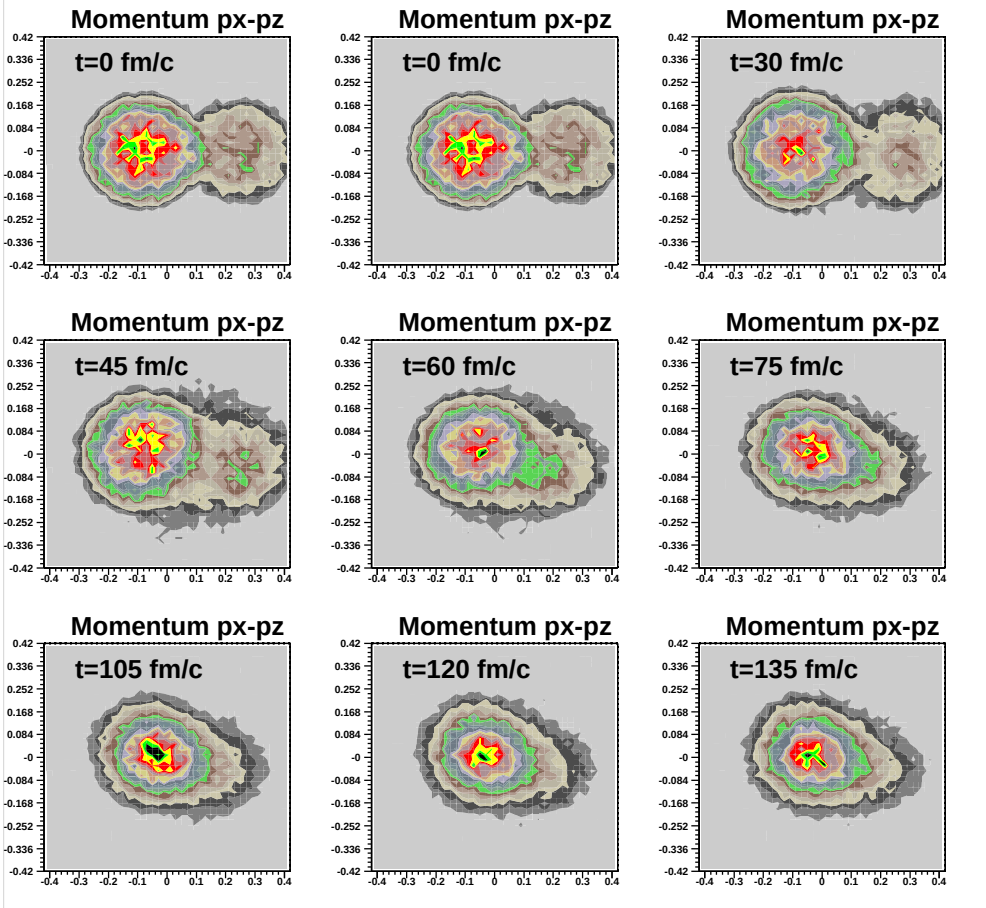

Figure 8.17: *Time evolution according to QMD of the reaction at* $^{36}Ar+^{108}Ag$ *at 60A MeV (b = 3.1 fm), shown as the density distribution of nucleons projected in the transverse-longitudinal* (p_x, p_z) *momentum space. (The units in both axes are GeV/c).*

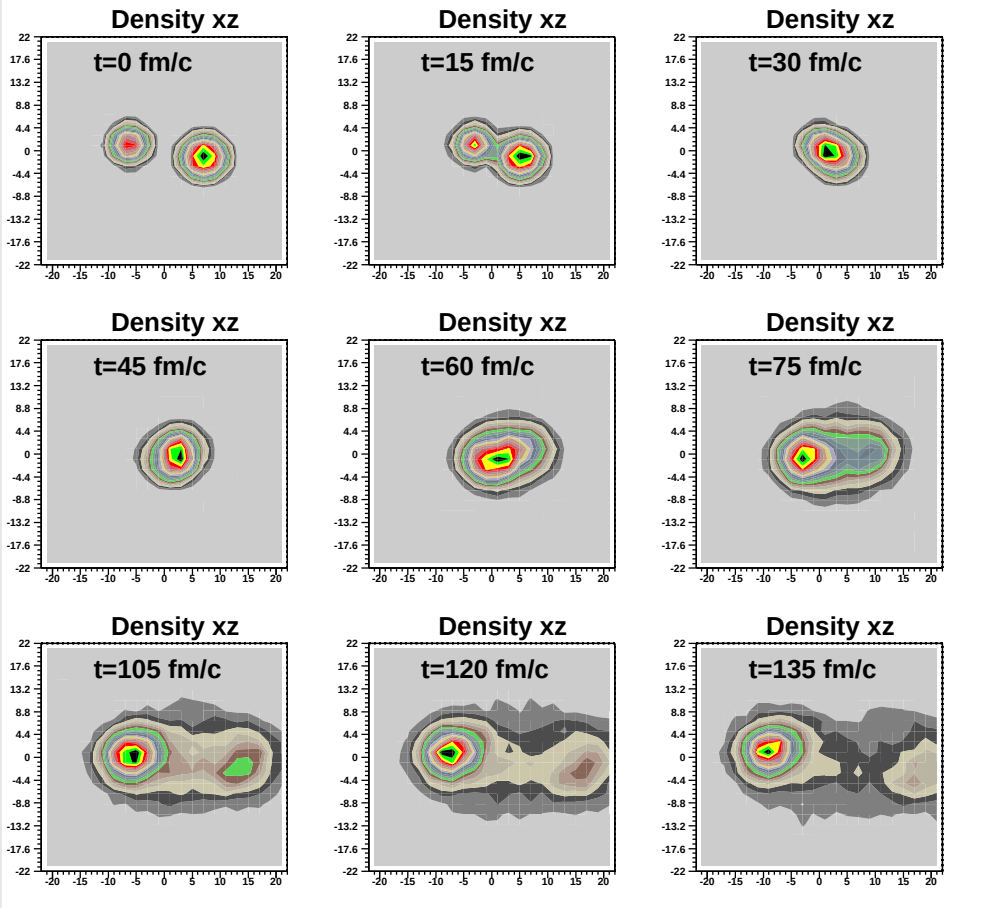

Figure 8.18: *Time evolution according to QMD of the reaction $^{36}Ar+^{58}Ni$ at 60A MeV (b = 2.5 fm), shown as the density distribution of nucleons projected in the (x,z) coordinate space. The beam axis is along z, and (x,z) are measured in fm.*

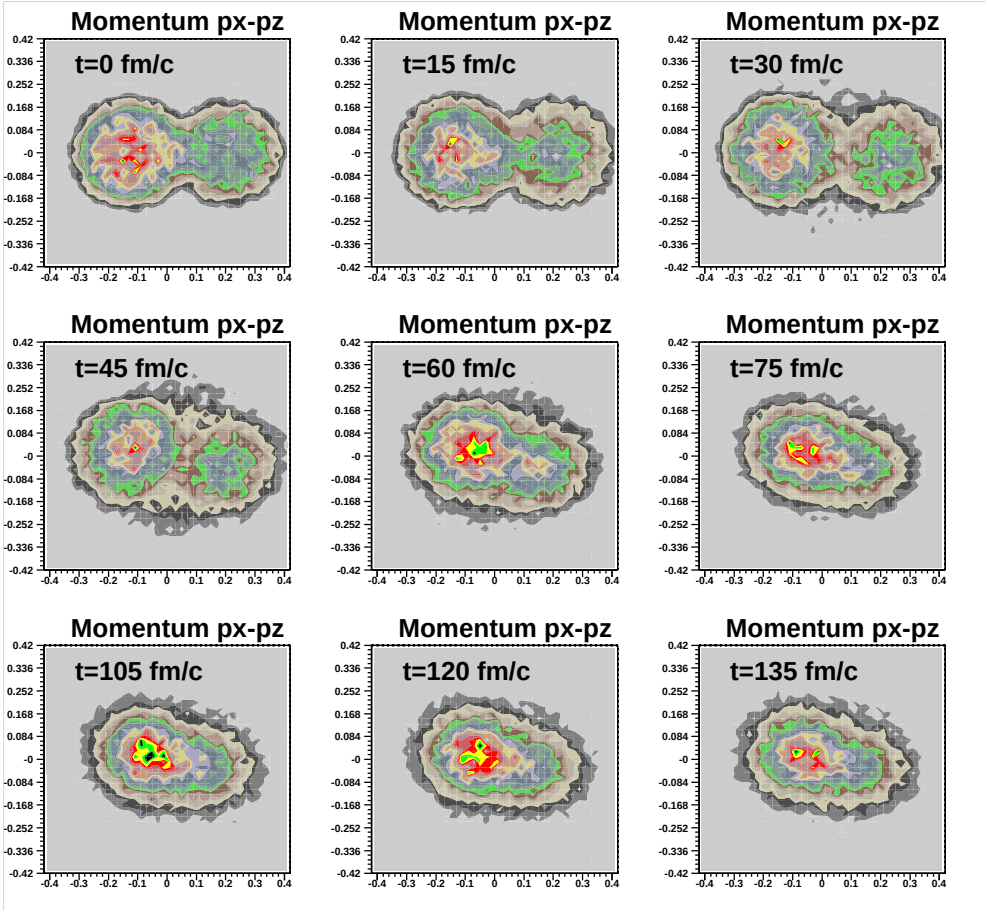

Figure 8.19: *Time evolution according to QMD of the reaction $^{36}Ar+^{58}Ni$ at 60A MeV (b = 2.5 fm), shown as the density distribution of nucleons projected in the transverse-longitudinal (p_x, p_z) momentum space. (The units in both axes are GeV/c).*

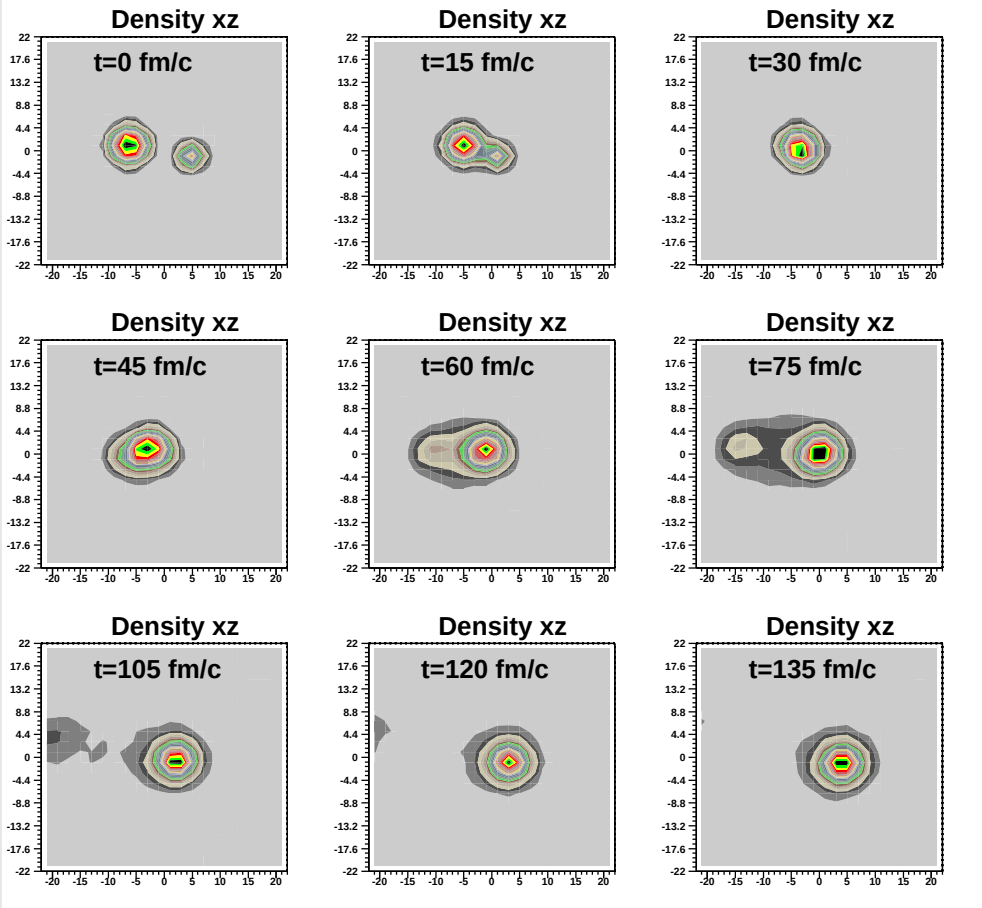

Figure 8.20: *Time evolution according to QMD of the reaction $^{36}Ar+^{12}C$ at 60A MeV (b = 2.1 fm), shown as the density distribution of nucleons projected in the (x,z) coordinate space. The beam axis is along z, and (x,z) are measured in fm.*

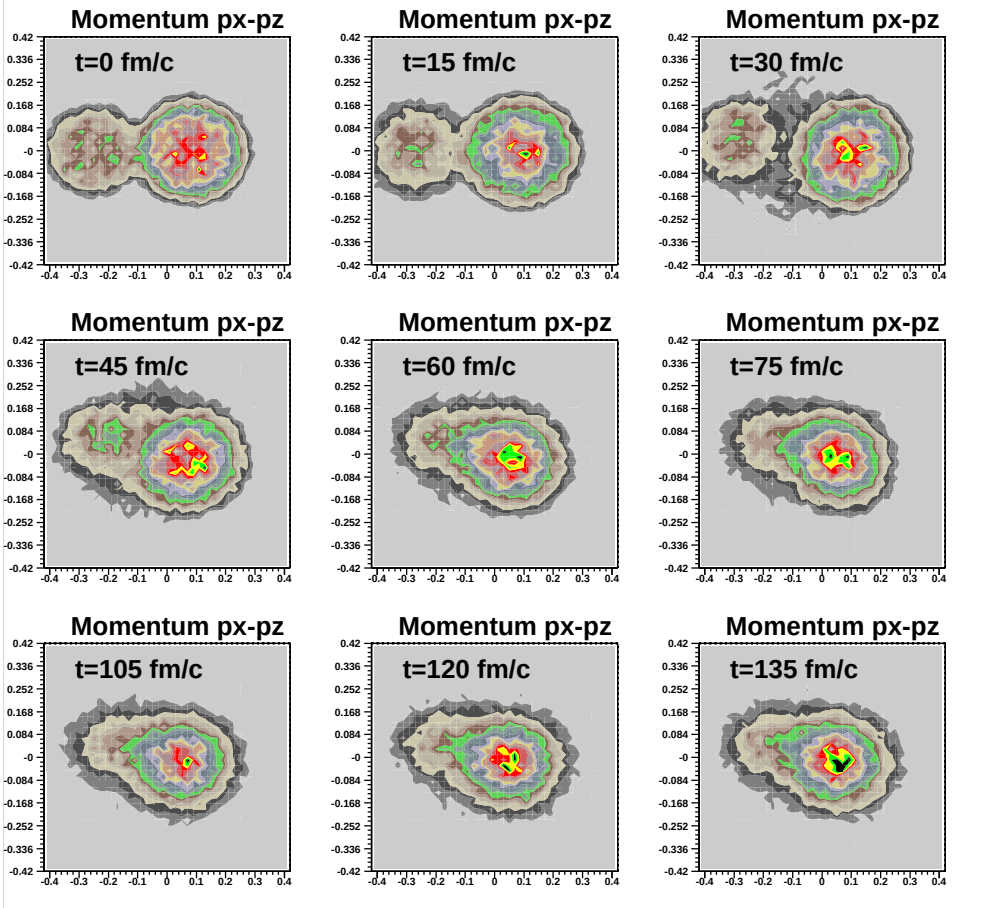

Figure 8.21: *Time evolution according to QMD of the reaction* $^{36}Ar+^{12}C$ *at 60A MeV (b = 2.1 fm), shown as the density distribution of nucleons projected in the transverse-longitudinal* (p_x, p_z) *momentum space. (The units are GeV/c).*

8.2.3 Bremsstrahlung production within QMD

The version of QMD used in the present work does not contain the production of hard-photons. As a matter of fact, although the production of other subthreshold particles such as kaons is available in different versions of QMD, only four works up to the present moment have explicitly studied hard-photon production within a "quantum" (QMD) [Ohts90, Khoa91, Li92] or pure classical (CMD) [Heue88] molecular dynamics approach. In principle, since the contribution of the $pn\gamma$ processes to the total NN cross-section is of about 10^{-3}, hard-photons induce no change in the flow of nucleons in phase space. One may then treat the photon production perturbatively and neglect the recoil momentum for final nucleons in the calculation of the time evolution of the system. In such incoherent and perturbative scenario, the appropriate convolution of the elementary bremsstrahlung cross-section with the resulting NN collision history would give relatively straightforwardly the hard-photon production rate for a given impact-parameter. This work is underway and it has not been included here. Nonetheless, although the elementary $pn \rightarrow pn\gamma$ cross-section is not yet introduced in the calculations, since the number of produced hard-photons is directly related to the number of incoherent *proton-neutron* collisions during the evolution of the heavy-ion system, one can have an insight into the mechanisms of hard-photon production by analyzing the number of NN collisions as a function of the reaction time for the four considered systems. To make a more realistic comparison with the data and with the similar BUU results presented in the former section, we have modified the QMD code to output the temporal evolution of proton-neutron (i.e. considering isospin explicitly) collisions which energetically can lead to the emission of a hard-photon, i.e. pn collisions with $K_{CM} = \sqrt{s} - (m_p + m_n) \geq 30$ MeV.

The results of such simulations for the four considered reactions (figs. 8.22, 8.23, 8.24, 8.25) indicate, as in the BUU case, that energetic proton-neutron collisions (possibly leading to a bremsstrahlung emission) take place basically in the first instants of the reaction. However, several differences appear with respect to the BUU results. On the one side, the maximum number of such collisions is shifted $\sim$20 fm/c with respect to the peak of bremsstrahlung emission found in the BUU calculations. This is due to the higher Pauli-blocking between nucleons in the molecular dynamics model which yields a "slower" increase of the first-chance NN collision rate. On the other side, no prominent second group of proton-neutron collisions is observed in QMD after the expansion of the primary system. Whereas BUU indicated clearly the existence of a second recompression yielding additional two-body collisions interpreted as the source of thermal hard photons, QMD hardly reproduces this behaviour. Nonetheless, for the three heavier systems a small augmentation of the number of pn collisions is apparent at around t $\approx$ 200 fm/c (inset of figs. 8.22, 8.23, and 8.24). Whether this is an spurious outcome or not of the numerical simulation, it is not readily answerable but such an effect seems not to be present in the lighter ^{36}Ar+^{12}C case (inset of fig. 8.25). In any case, since stopping is less important in QMD than in BUU the quasiprojectile and quasitarget fragments issue the first compression-expansion phase with higher kinetic energies and, therefore, there is less energy available for thermalization. This leads to less energetic NN collisions in the subsequent stages of the reaction. A more conclusive answer to the possible relation of the second yield of NN collisions to the observed thermal hard-photon component can

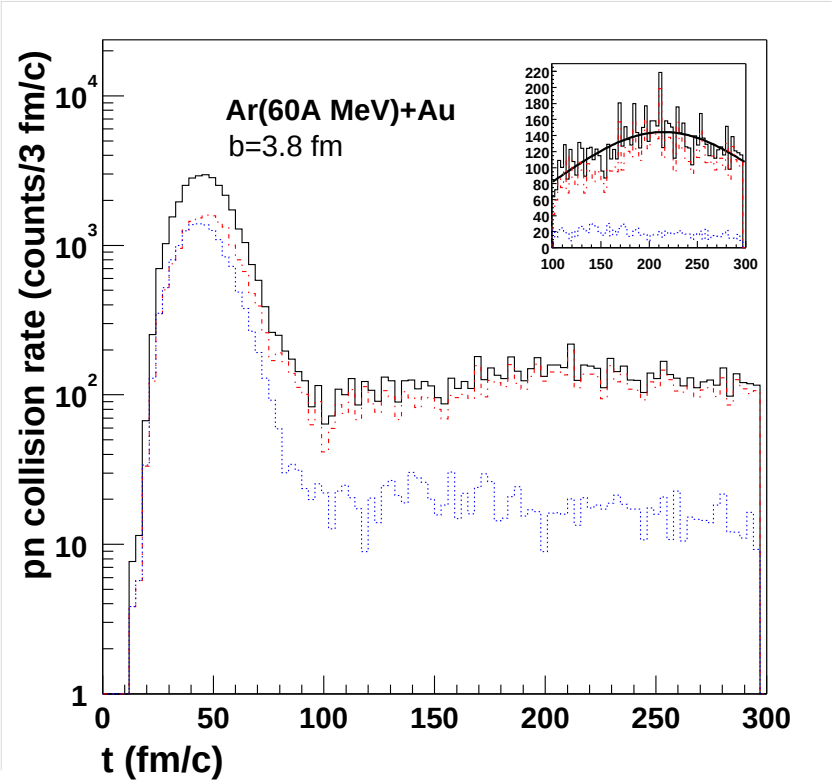

Figure 8.22: *Proton-neutron collision (with $K_{CM} \geq 30$ MeV) rate calculated with QMD as a function of time for the system $^{36}Ar+^{197}Au$ at 60A MeV and at an impact parameter b = 3.8 fm. The dashed-dotted lines correspond to pn collisions of nucleons belonging to the (quasi)target and the dotted to the (quasi)projectile. The inset shows the same figure in linear scale in the range t = 100 - 300 fm/c. (The ordinate units are arbitrary).*

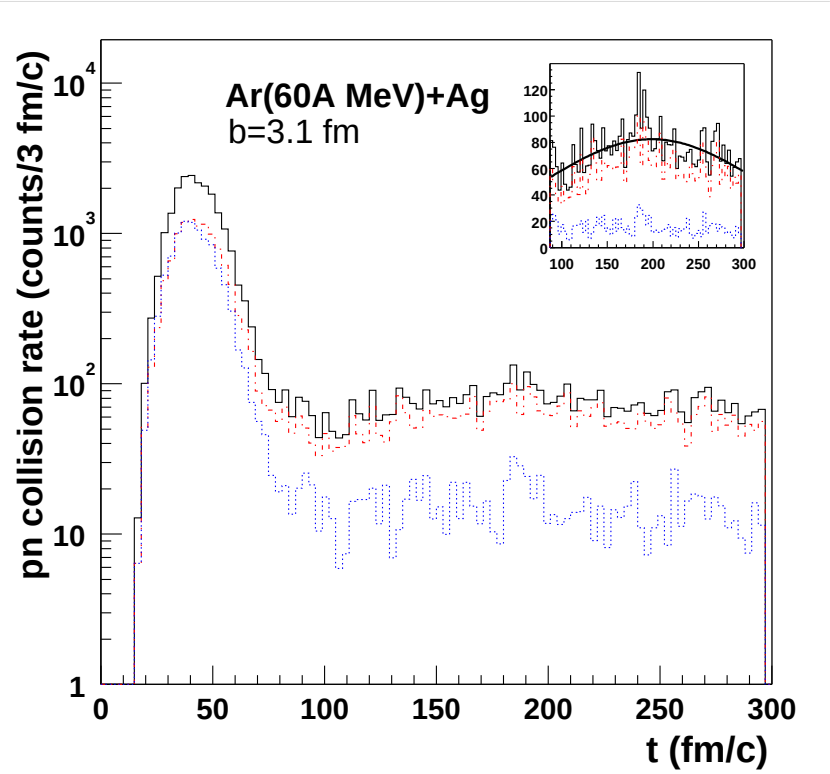

Figure 8.23: *Proton-neutron collision (with $K_{CM} \geq 30$ MeV) rate calculated with QMD as a function of time for the system $^{36}Ar+^{108}Ag$ at 60A MeV and at an impact parameter b = 3.1 fm. The dashed-dotted lines correspond to pn collisions of nucleons belonging to the (quasi)target and the dotted to the (quasi)projectile. The inset shows the same figure in linear scale in the range t = 90 - 300 fm/c. (The ordinate units are arbitrary).*

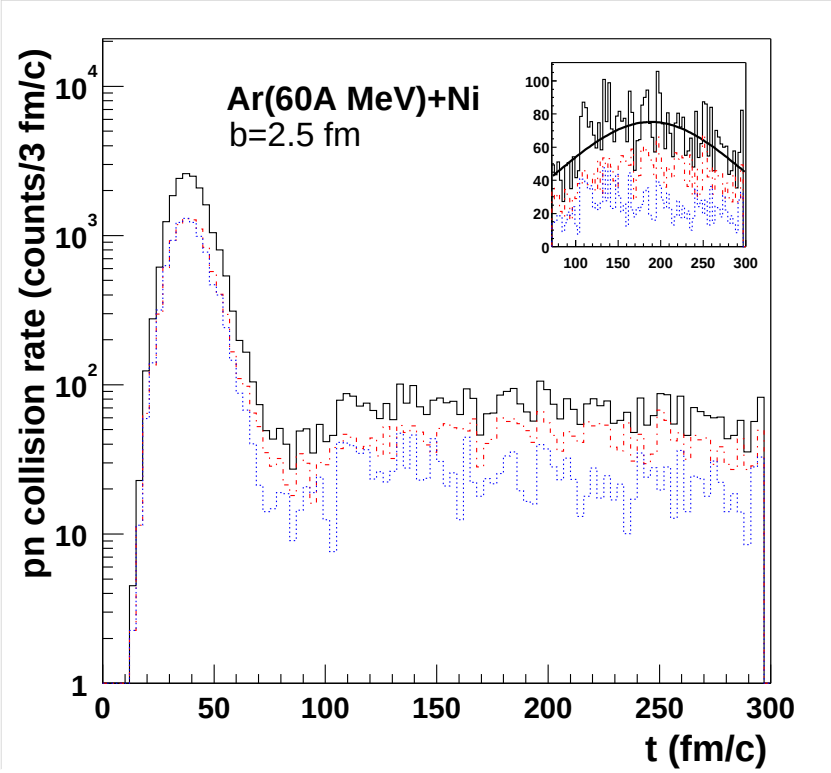

Figure 8.24: *Proton-neutron collision (with $K_{CM} \geq 30$ MeV) rate calculated with QMD as a function of time for the system $^{36}Ar+^{58}Ni$ at 60A MeV and at an impact parameter b = 2.5 fm. The dashed-dotted lines correspond to pn collisions of nucleons belonging to the (quasi)target and the dotted to the (quasi)projectile. The inset shows the same figure in linear scale in the range t = 70 - 300 fm/c. (The ordinate units are arbitrary).*

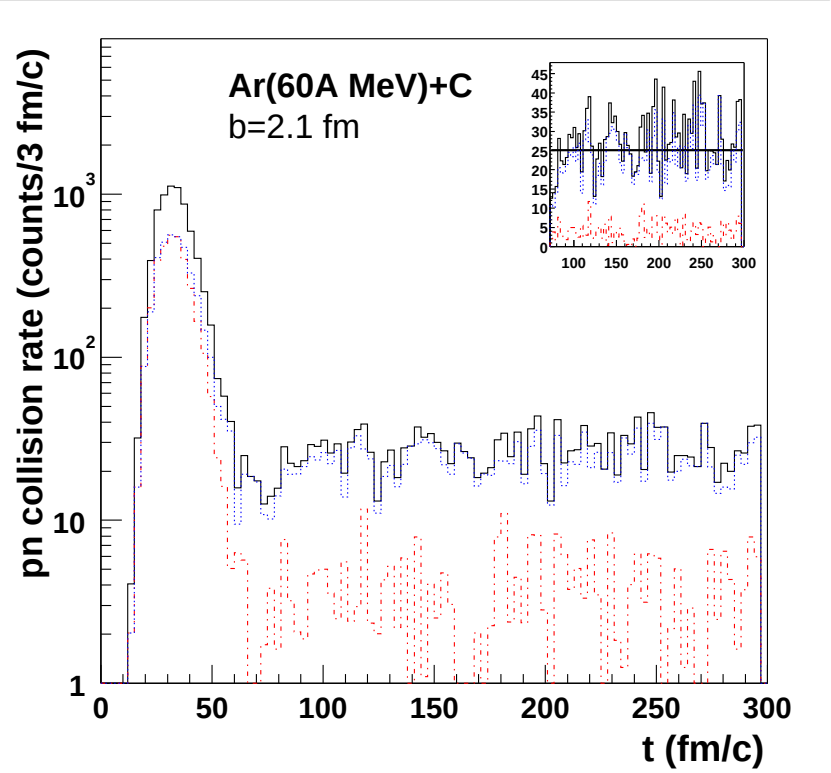

Figure 8.25: *Proton-neutron collision (with $K_{CM} \geq 30$ MeV) rate calculated with QMD as a function of time for the system $^{36}Ar+^{12}C$ at 60A MeV and at an impact parameter b = 2.1 fm. The dashed-dotted lines correspond to pn collisions of nucleons belonging to the (quasi)target and the dotted to the (quasi)projectile. The inset shows the same figure in linear scale in the range t = 70 - 300 fm/c. (The ordinate units are arbitrary).*

only be given after a complete calculation of the $pn\gamma$ bremsstrahlung rate within QMD.

Since QMD treats each nucleon as an individual wave-function, it has the advantage with respect to BUU that (in a semi-classical way) one can follow the evolution of the nucleons originally belonging to projectile or target[6]. Almost all the second-chance NN collisions taking place above t $\approx$ 100 fm/c are among nucleons belonging to the hot quasi-target residue in the case of the two heaviest target nuclei. This confirms qualitatively the existence of a (small) recompression of the excited heavy systems present at the end of the expansion phase. Although no quantitative assessment of the rate of thermal bremsstrahlung emission can be done within QMD without an actual implementation of bremsstrahlung production, these results do constitute an interesting line to follow.

In any case, and as a final comment, any microscopical model must be able to consistently explain the maximum amount of experimental observations, and hard-photons constitute a neat observable of the stopping phase of the reaction (before t $\approx$ 60 fm/c) and of the nucleon-nucleon dynamics during the first 200 fm/c, when the process of fragment formation takes place. Therefore, complex "ab initio" microscopical approaches of heavy-ion reactions, such as QMD and BUU, should be tested against the production of bremsstrahlung photons, which is an observable specially sensitive to the two-body collision term of the transport equation.

[6]Of course, such a possibility is not conceivable in a *pure* quantum description of the nucleons since, by definition, they are indistinguishable.

Chapter 9

Derivation of thermodynamical properties

Summary

9.1 Thermal bremsstrahlung model 236
9.1.1 Description of the thermal model 236
9.2 Extraction of a nuclear temperature 240
9.3 Thermal hard-photons: a new thermometer of nuclear matter . . . 243
9.4 Derivation of the nuclear “caloric curve” 246

The bulk of inclusive and exclusive experimental findings, as well as the analysis of the nucleon phase space distributions within two transport models, has permitted to interpret part of the observed hard-photon production (15% to 20% of the total yield in the ^{36}Ar+^{197}Au, ^{36}Ar+^{58}Ag, and ^{36}Ar+^{108}Ni systems) as being emitted in $NN\gamma$ collisions from a thermalized heavy target-like residue remaining after the first stages of the reaction. It seems thus rather natural to apply a thermal bremsstrahlung model to interpret these data. In this last chapter, I will use a thermal bremsstrahlung model to derive the thermodynamical properties of the hot nuclear systems produced during the reaction. In particular their temperature will be determined exploiting the radiation emission of thermal hard-photons with the experimentally observed inverse slope parameters.

9.1 Thermal bremsstrahlung model

The interpretation of the *total* hard-photon production in heavy-ion reactions within the framework of several proposed thermal models was carried out at late eighties [Nife85, Stev86, Neuh87, Prak88, Bona88]. These approaches were superseded by more dynamical models capable of reproducing, among others, the observed anisotropic component in the angular distribution, or the source velocity systematics. Moreover, some of these thermal models overestimated the hard-photon production rate by almost one order of magnitude and could hardly interpret the measured large values of the inverse slope parameters of the hard-photon spectra ($E_0 \approx 20$ MeV at e.g. 60A MeV bombarding-energies) in terms of the temperatures reached within the participant zone. All those empirical evidences were indeed more typical of a preequilibrium-like process rather than a thermal one. The possibility of a thermal bremsstrahlung component accounting for *part* of the total hard-photon yield, however, was not completely ruled out and, as matter of fact, the original model of Nifenecker and Bondorf [Nife85] already combined two different types of processes responsible for hard-photon emission: 1) first-chance collisions between projectile and target nucleons in the very first stages of the reaction, and 2) subsequent nucleon-nucleon collisions in the produced "nuclear fireball" zone. More recently, Neuhauser and Koonin [Neuh87], Bonasera [Bona88] or Alm [Alm95] also proposed such approach.

Our goal here is to apply a thermal approach, the Neuhauser and Koonin model, in order to exploit the second-chance bremsstrahlung component observed in our data to derive the thermodynamical properties of the excited nuclear systems produced in the different HI reactions considered.

9.1.1 Description of the thermal model

The description of bremsstrahlung emission within a thermal model assumes that each volume of space-time occupied by hadrons during the collision emits photons at a rate determined by its local thermodynamical conditions (temperature and density), and that the net experimental spectrum is the superposition of these many incoherent contributions. This assumption does *not* imply that photons emitted from each space-time volume are in thermal equilibrium with the hadrons (i.e. have a blackbody spectrum at the appropriate temperature) since the photon-hadron coupling is almost negligible. Instead, the number

and spectrum of photons emitted from a given volume is basically determined by the nature of the elementary nucleon-nucleon processes that occur within it.

Keeping this in mind, we will calculate the hard-photon spectra emitted from incoherent *NN* collisions within a thermalized nuclear system following the kinetic photon production prescription of Neuhauser and Koonin [Neuh87]. The emission of photons is described by a local differential rate of emission $d^6N_\gamma/d^3x\,dt\,dE_\gamma d\Omega$ calculated by approximating the emitting region as a piece of nuclear matter in thermal equilibrium characterized by local density, temperature and average momentum distribution. In such scenario, the $pn\gamma$ emission rate reads:

$$\frac{d^6N_\gamma}{d^3x\,dt\,dE_\gamma d\Omega} = \frac{8}{4\pi}\int \frac{d\vec{p}_{1i}}{(2\pi)^3}\frac{d\vec{p}_{2i}}{(2\pi)^3}\, f(\vec{p}_{1i})\, f(\vec{p}_{2i})\, \beta_{12i}\, \frac{d\sigma}{dE_\gamma} \tag{9.1}$$

Here $\vec{p}_{1,2i}$ and β_{12i} are the initial momenta and relative-velocity respectively of the colliding nucleons, $f(\vec{p})$ the single-particle momenta distribution, and $d\sigma/dE_\gamma$ the angle-integrated Pauli-blocked nucleon-nucleon bremsstrahlung cross-section which can be approximated (assuming isotropic *pn* scattering) by:

$$\frac{d\sigma}{dE_\gamma} \approx \frac{d\sigma_{free}}{dE_\gamma}\int \left[1-f(\vec{p}_{1f})\right]\left[1-f(\vec{p}_{2f})\right]\frac{d\Omega_\gamma}{4\pi}\frac{d\Omega_f}{4\pi} \tag{9.2}$$

where $d\sigma_{free}/dE_\gamma$ is the elementary nucleon-nucleon bremsstrahlung cross-section in free space, and where the following relations between the individual final momenta of the outgoing nucleons and their relative momentum have been applied:

$$\vec{p}_{1,2f} = \frac{1}{2}\vec{P}_f \pm \vec{p}_f, \quad \vec{P}_f = \vec{P}_i - \vec{p}_\gamma \tag{9.3}$$

The nucleon momentum distribution $f(\vec{r},\vec{p})$ in equations (9.1) and (9.2) is sampled according to a Fermi-Dirac equilibrium distribution at (local) temperature T with density-dependent Fermi energy $E_F(\rho)$:

$$f(\vec{r},\vec{p}) = \frac{1}{1+exp\left(\left[\sqrt{p^2+m_N^2}-E_F(\rho)\right]/T\right)} \tag{9.4}$$

Such distribution is normalized to the nucleon number density n:

$$4\int \frac{d\vec{p}}{(2\pi)^3} f(\vec{p}) = n \tag{9.5}$$

To carry out the calculations, the expression resulting of combining (9.1) and (9.2) is evaluated using relativistic kinematics and the integrals are solved by a Monte Carlo method. At this point, it is important to stress the diverse assumptions that we have considered to perform the calculations:

- The elementary $pn\gamma$ differential cross-section used in eq. (9.2) is the covariant "Schäfer parametrization" (see Appendix 2) and not the modified version of the semi-classical Jackson's formula (see Appendix 2) used originally in Neuhauser's work [Neuh87].

- Since we will be mainly interested in determining the slope of the thermal hard-photon spectrum as a function of the temperature of the emitting system, we will *not* perform the integration of the obtained (Doppler-shifted) local differential rate of emission over impact parameter and over space-time volume $d^3x\,dt$, i.e. we will *not* try to compute:

$$\frac{d\sigma_\gamma}{dE_\gamma d\Omega} = \int 2\pi b db \int \frac{d^6N_\gamma}{d^3x\,dt\,dE_\gamma^D\,d\Omega_\gamma^D}(E_\gamma^D, f)\frac{E_\gamma}{E_\gamma^D}d^3x\,dt \tag{9.6}$$

  which implies a quantitative knowledge of the spatio-temporal details of the source[1]. Indeed, the fact that the emission of thermal hard-photons occurs in a rather short flash of time compared to the total reaction time (see e.g. fig. 8.10) and that the frame of the nucleons local-average-velocity (the heavy recoiling residue remnant) is slowly moving (i.e. the Doppler-shifting is small) justifies the assumption that, apart from a global normalization factor, the shape of $d\sigma_\gamma/dE_\gamma$ will be that of $d^5N_\gamma/d^3x\,dt\,dE_\gamma$.

- The emission rates will be calculated for a nuclear system at different temperatures T and at a density equivalent to the saturation density of nuclear matter $\rho \approx \rho_0 = 0.17$ fm^{-3}, i.e. the temperature T entering in the Fermi-Dirac formula (9.4) will be the only free parameter. The choice of the density equal to ρ_0 is a reasonable assumption since we have seen in previous sections that the second flash of hard-photons takes place in nucleon-nucleon collisions at roughly the saturation density during the second compression of the system (fig. 8.9). Additionally, the rate of nucleon-nucleon collisions goes as ρ^2, which makes it very unlikely to have bremsstrahlung emission at low nuclear densities. Indeed, the model calculations indicate that the thermal bremsstrahlung yield is reduced roughly a factor 10 at densities $\sim 0.5\rho_0$ in comparison to the yield at ρ_0. In any case, we have confirmed that both the shape and slope of the $d^5N_\gamma/d^3x\,dt\,dE_\gamma$ distribution obtained from the model for a given T do not change significantly for different values of the source density ρ entering in the calculation of $E_F(\rho)$ in eq. (9.4) and in the normalization (9.5), i.e. the slope of $d^5N_\gamma/d^3x\,dt\,dE_\gamma$ turns out to be basically "controlled" by the value of T.

The thermal nucleon-nucleon bremsstrahlung photon rates for $E_\gamma > 30$ MeV, $d^5N_\gamma/d^3x\,dt\,dE_\gamma$, are shown in fig. 9.1 for three different temperatures (T = 4 MeV, T = 6 MeV and T = 8 MeV) of the same order as the typical temperatures encountered in heavy-ion reactions at intermediate-energies. The combination of the Fermi-Dirac distribution of the nucleons at these temperatures, the energy-dependent elementary $pn\gamma$ covariant cross-section, and the Pauli blocking factors results in thermal hard-photon spectra which can be reasonably well approximated by a single (Maxwell-like) exponential above E_γ = 30 MeV. Indeed, in [Stev86] it was also found that the Bremsstrahlung radiation from a hot, isotropic hadronic gas gives an essentially exponential gamma-ray energy spectrum with a slope parameter close to the temperature of the gas.

[1] Additionally, the integral over impact parameter b in eq. (9.6) "weights" σ_γ with the cross-section corresponding to the formation of the (radiating) nuclear source.

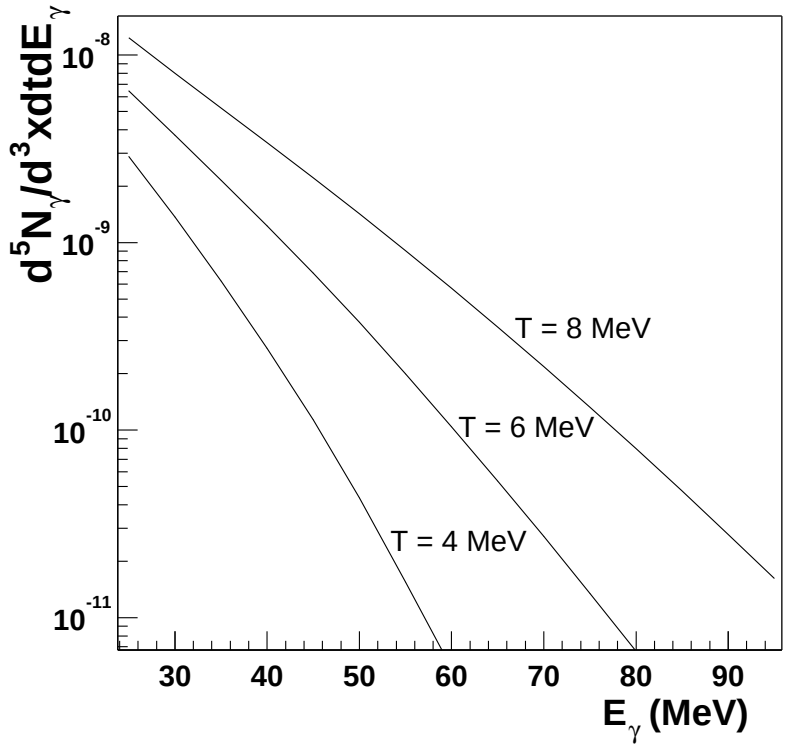

Figure 9.1: *Thermal bremsstrahlung ($pn\gamma$) emission rates, $d^5N_\gamma/d^3x\,dt\,dE_\gamma$, from a nuclear system in thermal equilibrium at the saturation density $\rho_0 = 0.17\ fm^{-3}$ for various temperatures ($T = 4$ MeV, $T = 6$ MeV and $T = 8$ MeV) as obtained with the Neuhauser and Koonin model [Neuh87].*

9.2 Extraction of a nuclear temperature

Since thermal hard-photons are emitted from a hot source, their slope parameter E_0^t should reflect the local temperature T of the nuclear system at the time of emission [Stev86, Schu97]. However, since photons are not in thermal equilibrium with the nuclear medium (photons escape the interaction region immediately after their production) E_0^t and T are not directly equivalent. We need therefore to know how to quantitatively relate E_0^t and T. The most interesting result of the calculations carried out with the thermal bremsstrahlung model of the former Section is that, indeed, the values of the inverse slope parameter E_0^t of the thermal bremsstrahlung spectra (fig. 9.1), extracted from a fit of the theoretical spectra with an exponential in the range E_γ = 30 - 70 MeV, are neatly correlated with the nuclear temperature T of the radiating nuclear system (see fig. 9.2) *independently* of the density of the emitting source. A linear fit of this dependence between E_0^t and T (in the region T = 4 - 10 MeV) gives the following quantitative relation between them:

$$\begin{aligned} T(\mathrm{MeV}) &= a \cdot E_0^t(\mathrm{MeV}) + b \\ \text{with } a &= 0.75 \pm 0.03 \text{ and } b = -0.62 \pm 0.03 \text{ MeV} \end{aligned} \tag{9.7}$$

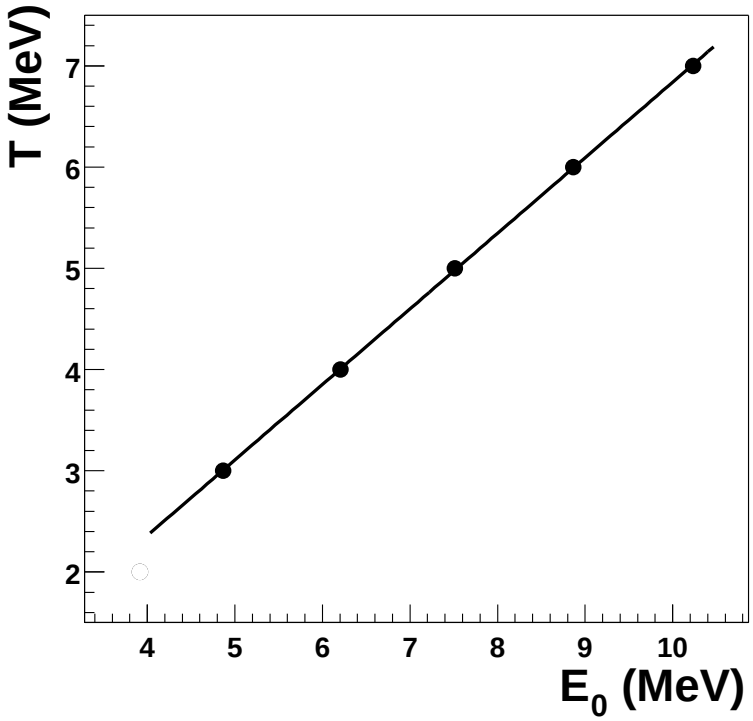

Figure 9.2: *Linear dependence between the inverse slope parameters E_0^t of bremsstrahlung photons and the temperature T of the emitting nuclear source. The different values of E_0^t are obtained from exponential fits, between E_γ = 30 MeV and E_γ = 70 MeV, of the theoretical thermal bremsstrahlung spectra (fig. 9.1) obtained for each nuclear temperature within the thermal model.*

This result is a very crucial one since it allows to directly determine the nuclear (local)

Table 9.1: *Nuclear temperatures T extracted from the experimentally measured values of the slope parameters E_0^t of the thermal component of the hard-photon spectra for the systems $^{36}Ar+^{197}Au$, $^{36}Ar+^{108}Ag$, $^{36}Ar+^{58}Ni$, $^{86}Kr+^{58}Ni$, $^{181}Ta+^{197}Au$ and $^{208}Pb+^{197}Au$ calculated by applying the formula (9.7) obtained from the thermal bremsstrahlung model.*

System	K_{lab} (MeV)	E_0^t (MeV)	T (MeV)
^{208}Pb+^{197}Au	30	5.5 ± 0.6	3.5 ± 0.4
^{36}Ar+^{107}Ag	60	6.1 ± 0.8	3.9 ± 0.5
^{36}Ar+^{197}Au	60	6.2 ± 0.5	4.0 ± 0.4
^{181}Ta+^{197}Au	40	6.9 ± 0.6	4.5 ± 0.5
^{86}Kr+^{58}Ni	60	8.5 ± 0.8	5.7 ± 0.6
^{36}Ar+^{58}Ni	60	8.8 ± 0.8	6.0 ± 0.7

temperatures attained in the excited nuclear fragments produced in the considered heavy-ion reactions at the end of the expansion stage by measuring the value of the slope of their thermal hard-photon spectra. Table 9.1 displays the temperatures obtained through application of equation (9.7) for the three heavy systems studied in the present thesis (^{36}Ar+^{197}Au, ^{36}Ar+^{108}Ag, and ^{36}Ar+^{58}Ni) as well as those of TAPS campaign at GANIL in 1992 (^{86}Kr+^{58}Ni, ^{181}Ta+^{197}Au and ^{208}Pb+^{197}Au) [Mart95, Schu97]. All the quoted values of the nuclear temperature lie in the range T = 4 - 6 MeV in coincidence with the typical values found in heavy-ion collisions at intermediate bombarding energies. As a matter of fact, the four systems with total energies in the center-of-mass below $\approx 10A$ MeV (^{36}Ar+^{197}Au, ^{36}Ar+^{108}Ag, ^{181}Ta+^{197}Au and ^{208}Pb+^{197}Au), show a temperature clustered around $T = 4.0 \pm 0.5$ MeV, whereas the two remaining ones (^{36}Ar+^{58}Ni and ^{86}Kr+^{58}Ni) with total energy above $K_{AA}^{cm} \approx 10A$ MeV, have $T \approx 6.0 \pm 0.5$ MeV. These temperatures are close to the "cracking" or "limiting" temperatures predicted by various statistical models [Bond95, Gros97].

It is interesting to compare the temperatures obtained from the thermal bremsstrahlung slope parameters with those obtained with other proposed methods. The systems ^{36,40}Ar+^{197}Au, ^{108}Ag have been experimentally studied at bombarding energies around 60A MeV by several groups. The temperatures of the excited nuclear system(s) produced in central reactions have been obtained from fits of neutron [Jian89, Leco96], proton [Eude88, Vien92, Louv93, Louv94, Sauv94] and/or α [Jian89, Soko93, Sauv94] Maxwell spectra (*kinetic* temperatures), or by the ratios of selected nuclides [Poch85, Poch87, Sain88] (*excited-state* temperatures). The obtained values are in the range of T = 4 - 7 MeV (table 9.2), in agreement with our values ($T \approx 4$ MeV), although there seems to be a small shift towards somewhat higher temperatures in the alternative methods (see discussion in next Section).

Table 9.2: *Nuclear temperatures T attained in central $^{36,40}Ar+^{197}Au$, ^{108}Ag reactions around 60A MeV bombarding energies, extracted experimentally using several proposed methods ("sl." stands for kinetic spectra slopes, and "pop." for excited-state population, see next Section). If reported in the original work, the measured values of the excitation energies $\varepsilon^\star$ are also included.*

System	Method	K_{lab} (*A*MeV)	T (MeV)	$\varepsilon^\star$ (*A*MeV)	Reference
^{40}Ar+^{197}Au	IMF* pop.	60	5.0 - 5.5	-	[Poch85, Poch87]
^{40}Ar+^{197}Au	IMF* pop.	60	5.0	-	[Sain88]
^{40}Ar+^{197}Au	*n*, α sl.	44, 77	4.9 ± 0.4	3.5	[Jian89]
^{40}Ar+^{197}Au	α sl.	44, 77	5.0	3.0 - 3.5	[Soko93]
^{40}Ar+^{197}Au	*p* sl.	60	7.5	5.5	[Louv93, Louv94]
^{40}Ar+^{197}Au	*n* sl.	60	4.0 - 6.0	3.0	[Leco96]
^{36}Ar+^{197}Au	-	60	-	5.0	[Biza93]
^{40}Ar+^{197}Au	-	65	-	5.5 ± 1.2	[Colin98, Sun00]
^{40}Ar+^{107}Ag	*p* sl.	60	5.4, 5.5, 6.9	5.5 - 7.0	[Eude88]
^{40}Ar+^{107}Ag	*p* sl.	60	4.0 - 8.0	5.5 - 7.0	[Vien92]
^{40}Ar+^{107}Ag	*p*, α sl.	58.7	4.5	-	[Sauv94]
^{40}Ar+^{107}Ag	-	65	-	6.8 ± 1.4	[Colin98, Sun00]

9.3 Thermal hard-photons: a new thermometer of nuclear matter

Three different methods have been proposed so far to determine the nuclear temperatures attained in hot systems produced in heavy-ion reactions (fig. 9.3). Following closely the discussion of reference [Siwe98], they are called here "kinetic", "isotope" (or "chemical"), and "population" temperatures. The main characteristics of these different methods are the following [Siwe98]:

1. **Slope parameters, kinetic temperatures** T_s: This most widely used method to determine a temperature of nuclei is based on measurements of the kinetic energy spectra of the emitted particles (n, p or α). A nucleus in thermal equilibrium evaporates particles with an energy distribution of Maxwell-Boltzmann type:

$$N(K) = C \cdot (K - V_C) \exp^{-(K-V_C)/T_s} \tag{9.8}$$

   where K is the kinetic energy of the emitted particle, V_C its Coulomb barrier, and T_s the temperature of the source. The main problem of this method consists in identifying experimentally the emitting source(s). This has usually been done by a "three-sources fit" of the inclusive spectra of the selected reaction product at several detection angles. This takes into account the experimentally well-known fact that particles are emitted from the two main hot sources (quasiprojectile emitting mainly in the forward hemisphere, and quasitarget, mainly in the backward one) and from the midrapidity region (direct NN emission or neck emission).

   As we will discuss, the principle of this method is the same as the one that we have employed with thermal hard-photons, although the resulting temperatures must be considered differently.

2. **Double isotopic ratio,** T_r^0: This method [Albe85] assumes that the emitters are in thermal *and* chemical equilibrium. The ratio between the yields of two isotopes (isotones) differing by one proton (neutron) depends only on the temperature and on the free proton (neutron) density. Taking the quotient of two such ratios, the proton (neutron) density cancels out and the double ratio depends only on the temperature through the simple formula [Albe85]:

$$T_r^0 = B / \ln \left[s \frac{Y_1/Y_2}{Y_3/Y_4} \right] \tag{9.9}$$

   where Y_1, Y_2, Y_3, Y_4 are the yields of the four isotopes, s depends on the spins of the populated states of each species, and B is the difference of binding energy differences $(B_2 - B_1) - (B_4 - B_3)$. At temperatures above a few MeV, however, the population of excited states should be taken into account, which means that s depends on T_r and on the number of states included. The larger the value of B the larger the sensitivity of T_r^0. Therefore, one usually studies cases where the pair of isotopes at the denominator is ^{3}He/^{4}He (or ^{6}Li/^{7}Li).

3. **Relative population of excited states,** T_{pop}: The principle of this method [Poch87] relies on the fact that a nucleus in thermal equilibrium contains clusters in ground and excited states distributed according to a probability proportional to the Boltzmann factor:

$$F_B = \exp^{-\frac{\Delta E^\star}{T_{pop}}} \tag{9.10}$$

where $\Delta E^\star = E_1^\star - E_2^\star$ is the energy difference between the two states, and T_{pop} is the temperature of the source. The ratio between the number of clusters emitted in two different states is:

$$\frac{N_{g.s.}}{N} = \frac{2J_{g.s.}+1}{2J+1} \cdot F_B \tag{9.11}$$

where $N_{g.s.}$, N are the number of fragments emitted in ground state and excited state respectively, and $J_{g.s.}$, J are their spins. From these equations, the population temperature is given by:

$$T_{pop} = \frac{\Delta E^\star}{\ln \frac{2J_{g.s.}+1}{2J+1}\frac{N_{g.s.}}{N}} \tag{9.12}$$

This method is sensitive only when the value of $\Delta E^\star$ is much larger than the temperature. The values thus obtained, in the range T_{pop} = 4 - 5 MeV independently of the type of reaction and slightly increasing with bombarding energy, are much lower than those extracted from slopes of kinetic energy spectra.

Comparing the three methods with the predictions of a sequential statistical model, Siwek *et al.* [Siwe98] concluded:

1. The slope parameters from kinetic energy spectra of LCP keep a good memory of the initial temperature. However, in real experiments they may be perturbed by the mixture of several sources, by source recoil effects after particle emission, and/or a possible contribution of collective expansion.

2. Emission time sequence and feeding from discrete state decays have large effects on the temperatures obtained from isotope thermometers. Secondary decays ("side feeding") reduce the apparent temperature values while the emission chain changes the dependence of the temperature on the excitation energy.

3. Most of the population temperatures are also very sensitive to side-feeding effects. Experimental temperatures extracted from particle unstable states remain almost constant as a function of excitation energy and do not surpass $T \approx 5$ MeV. A possible explanation could be that the source is expanding and heavy clusters are formed relatively late during this expansion, at lower temperatures.

In comparison with the usual nuclear thermometers, we have seen that thermal hard-photons provide a clear and straightforward way of calculating the nuclear temperature of the hot residues produced in a heavy-ion reaction. The advantages of the temperatures measured from the slope parameters of second-chance bremsstrahlung photons with respect to the aforementioned methods are the following:

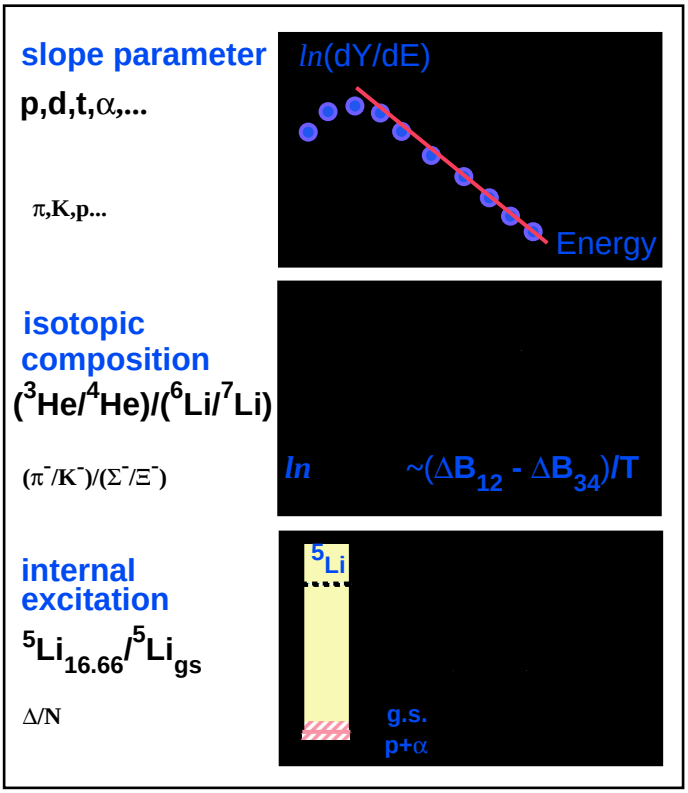

Figure 9.3: *Illustration [Poch97] of the different thermometers for nuclear systems: light-particle inverse slope parameters (upper part), double isotope ratios (middle part), and relative population of states (lower part).*

- Direct extraction of the nuclear temperature thanks to the easy identification of the thermal component in the photon spectra. Thermal hard-photons have a distinct steeper slope in the region E_γ = 30 - 60 MeV, which makes it easy to identify from the pre-equilibrium (direct hard-photon) component by means of a "double-exponential" fit analysis. The possibility of mixing different temperatures coming from different sources is then minimized.

- Thermal hard-photons are emitted just after thermal equilibrium is attained, at the moment of highest temperatures in the nuclear system. Before that moment (t $\lesssim$ 50 fm/c), prompt proton-neutron collision collisions in a pure pre-equilibrium stage dominate, and after it (t $\gtrsim$ 200 fm/c), the excitation energy is damped among more collective degrees of freedom such as GDR oscillations, the temperatures are lower, and $NN\gamma$ collisions are completely Pauli-blocked. This is clearly at variance with particles and fragments which are emitted all along the deexcitation chain of the residue from the initial T down to 0. Whereas particles measure an average T, thermal bremsstrahlung photons measure the temperature shortly after the attainment of thermal equilibrium. This makes it unnecessary to make *ad hoc* assumptions to correlate the apparent temperature with the original one.

- Thermal hard-photons suffer no distortion due to the surrounding medium. In particular they are not subject to effects difficult to control such as rescattering, side-feeding, Coulomb field or collective motion which can strongly modify the measurement of the original temperatures of the system when using thermometers based on charged-particles, neutrons or fragments.

- The production of hard-photons is favoured in semi-central and central nucleus-nucleus collision. Therefore, they intrinsically signal the thermodynamical conditions prevailing in rather excited nuclear systems, and not those of less hot systems produced in more peripheral collisions.

The fact that the nuclear temperatures obtained using the thermal bremsstrahlung slope parameters ($T \approx 4$ MeV, table 9.1) are somewhat lower than the ones obtained using the inverse slopes of the (Maxwell-Boltzmann) experimental kinetic energy distributions of different light-particles ($T \approx 5$ MeV, table 9.2) can be interpreted as due to the fact that the "kinetic" temperatures measured with p, n or α may likely contain some preequilibrium and/or collective expansion component, or that the contribution from other sources (quasiprojectile and/or mid-rapidity emission) has not been completely removed.

9.4 Derivation of the nuclear "caloric curve"

Wada *et al.* [Wada89] showed that at excitation energies per nucleon $\varepsilon^\star$ lower than $\approx 4A$ MeV, the temperatures T's deduced from the kinetic slope parameter of the Maxwell-Boltzmann spectra of particles and clusters follow the Fermi gas law (see Appendix 3): $\varepsilon^\star = aT^2$, with a value of the constant level density parameter a in the range $A/13$ to $A/8$. This relationship between the (thermal) excitation energy $\varepsilon^\star$ and the temperature T (the "caloric curve") was further studied by the ALADIN group [Poch95] over a wider

excitation energy range using "isotopic" He-Li temperatures. This curve[2] (see fig. 2.7) showed three distinctly different regions. In agreement with the previous low-energy studies, below $\varepsilon^\star \approx 3A$ MeV the rise of T_r^0 was compatible with the low-temperature approximation for a fermionic system. Within $\varepsilon^\star$ = 3*A* - 10*A* MeV an almost constant value of T, a "plateau", was found which was interpreted as indicating a phase transition, with the Fermi nuclear liquid ($\varepsilon^\star \propto T^2$) and the Boltzmann nuclear gas ($\varepsilon^\star \propto T$) regimes dominating below 3*A* MeV and above 10*A* MeV respectively. Such "plateau" was theoretically predicted by statistical models (see fig. 2.6), with a width, $\sim$7*A* MeV, measuring the "latent heat".

Indeed, one of the general expectations for a system undergoing a first-order phase transition is an enhanced heat capacity at temperatures where the phase transition occurs, reflecting the latent heat required to transform from one phase to the other[3]. Several calculations predict enhanced heat capacities for finite nuclear systems at temperatures of the order 4 - 6 MeV [Jaqa83, Bond85], due to the transformation from the Fermi liquid found in the nuclei in their ground and low excited states, to a hadron gas phase consisting of free nucleons and light clusters [Jaqa83]. The "plateau" of the ALADIN "caloric curve" was therefore consistent with the hypothesis of a mixed phase equilibrium. Furthermore, its slight rise with T was explained [Poch96] as due to the fact that the phase transition does not take place at *constant pressure* (otherwise, the "plateau" would have been fully constant [More96]). A monotonic increase of T_{He-DT} with $\varepsilon^\star$ supporting a continuous phase transition near the critical point was also found by the EOS collaboration in 1*A* GeV Au+C collisions [Haug96].

The ALADIN work has raised many discussions about the actual physical meaning of the plateau and rise observed, or about the temperature measurements reliability (for a recent discussion see e.g. [Siwe98] and references therein). Indeed, the different proposed methods of determining nuclear temperatures mentioned in the former Section give different values as can be seen in the $\varepsilon^\star$ vs. T "caloric curve" plot of fig. 9.4 [Dura99]. Whereas the "kinetic" temperatures follow approximatively the Fermi gas law in the whole range of $\varepsilon^\star$, the "double-ratio" T's saturate between 4*A* MeV - 10*A* MeV and then slowly increase with $\varepsilon^\star$ (the aforementioned "plateau" interpreted as a signal of the occurrence of the first-order liquid-gas transition), and the "excited-state" temperatures saturate over the whole range of $\varepsilon^\star$. It has been claimed [Frie90, Xi98] that this may be an indication that the different nuclear species are produced at different steps of the disassembly process. Light particles would then be emitted first (in the pre-equilibrium phase), while fragments (used for T(double-ratio) and T(excited-state) assessment) would be emitted later at lower temperatures, leading to the observed hierarchy of different temperatures.

[2]Mind that the temperature values of the "caloric curve" shown in fig. 2.7 [Poch95] are shifted a factor 1.2 with respect to the measured values [Poch97]. According to a new analysis [Xi96] of the effect of the feeding from highly lying continuum states on the first ALADIN temperatures data, this correction factor should be removed (see the ALADIN points of fig. 9.4).

[3]Indeed, in the case of the well-known liquid-gas (first-order) transition of H_20 at constant pressure, one observes that bringing more energy to the system increases the temperature of the liquid phase up to the transition point where the temperature remains constant until all the liquid is transformed into vapour. During the phase transition the energy added to the (mixed) system is used to break the bonds linking the liquid molecules. The energy cost of this transformation is the latent heat. Afterwards, the temperature rises at the typical rate of the gas.

Since we are proposing thermal hard-photons as an alternative method for estimating the nuclear temperatures reached during a heavy-ion reaction, we are interested in assessing what kind of "caloric curve" we may obtain correlating the (thermal) excitation energies attained in our systems with the temperature values extracted from the thermal bremsstrahlung spectra of the whole set of reactions considered here. However, since we have not experimentally determined the value of the excitation energies reached in our different reactions, we will use the recently reported values of $\varepsilon^\star$ measured by Colin, Sun *et al.* [Colin98, Sun00] for the very close reactions ^{36}Ar+^{197}Au, ^{107}Ag and ^{59}Cu at 65*A* MeV. According to this work, the average excitation energies per nucleon for central reactions were found to be $\varepsilon^\star$ = (5.5 $\pm$ 1.2)*A* MeV, (6.8 $\pm$ 1.4)*A* MeV, and (8.7 $\pm$ 1.8)*A* MeV, respectively for the Au, Ag and Cu targets (see the compilation in table 9.3). We have also included in this comparison the value corresponding to the ^{208}Pb+^{197}Au at 30*A* MeV system, taking the average excitation energy obtained for semi-central collisions, $\varepsilon^\star$ = (4.0 $\pm$ 1.0)*A* MeV [Leco94, Morje95]. The value of the excitation energy attained in central collisions of ^{181}Ta+^{197}Au at 40*A* MeV has been recently found[4] to be $\varepsilon^\star \approx$ 7 *A* MeV in an experiment of the INDRA collaboration [Norm00]. For the ^{86}Kr+^{58}Ni reaction at 60*A* MeV, for which we are not aware of an experimentally measured value of their excitation energy, we have estimated as an upper limit[5] for $\varepsilon^\star$ the total available center-of-mass energy, K_{AA}, subtracted of the collective (radial flow) energy, ε_{comp}, i.e.:

$$\varepsilon^\star = K_{AA} - \varepsilon_{comp} \tag{9.13}$$

To determine the average value of the compressional energy, ε_{comp}, released as ordered expansion of the system, we have made use of the parametrization proposed by ref. [Poch97] for beam energies below about 500*A* MeV:

$$\varepsilon_{comp}(\text{MeV}) = 0.09 \cdot [K_{lab}(\text{MeV}) - 25\ \text{MeV}] \tag{9.14}$$

The result of combining eqs. (9.13) and (9.14) for ^{86}Kr+^{58}Ni at 60*A* MeV, yields ε_{comp} = 2.9*A* MeV. Such a value of ε_{comp} is also in rough agreement with the value assessed alternatively making use of the conventional parametrization of the "compressional EoS" (see Appendix 3 and e.g. [Sura90]):

$$\varepsilon_{comp}(\text{MeV}) = \frac{1}{2} \cdot \frac{\kappa_\infty(\text{MeV})}{9} \left(1 - \frac{\rho_{max}}{\rho_0}\right)^2 \tag{9.15}$$

Indeed, taking $\kappa_\infty \approx$ 250 MeV and ρ_{max} = 1.4ρ_0 as given by BUU simulations for this reaction [Mart95], one obtains, $\varepsilon_{comp} \approx$ 2.1*A* MeV.

[4]This value of $\varepsilon^\star$ has been obtained indirectly by applying the formula: $\varepsilon^\star = (\mu/2A_{tot}) \cdot [v_p^2 - (2v_{qp}^2)]$, where v_p and v_{qp} are the velocity (in cm/ns) of the projectile in the lab and of the quasiprojectile in the CM respectively.

[5]In general, the energy per nucleon available in the nucleus-nucleus center-of-mass (K_{AA}) can be dissipated into several contributions: $K_{AA} + Q = \varepsilon_{th}^\star + \varepsilon_{comp} + \varepsilon_{rot} + \varepsilon_{preeq}$, where Q is the Q-value of the composite system resulting from the "incomplete fusion" of projectile and target, ε_{rot} ($\approx$ 0.5*A* MeV, see footnote on page 31) is the rotational energy of this system, and ε_{preeq} (which can be as high as 1*A* - 3 *A* MeV [Lera87, Sura89]) is the energy released prior to equilibration (either in "free streaming" projectile nucleons or in preequilibrium particle emission).

Table 9.3: *Excitation energies $\varepsilon^\star$ and nuclear temperatures T (extracted from the thermal bremsstrahlung spectra) for the systems $^{36}Ar+^{197}Au$, $^{36}Ar+^{108}Ag$, $^{36}Ar+^{58}Ni$, $^{86}Kr+^{58}Ni$, $^{181}Ta+^{197}Au$ and $^{208}Pb+^{197}Au$ at different bombarding energies. The different values of $\varepsilon^\star$ have been experimentally measured by other collaborations (stars). In the case of the $^{86}Kr+^{58}Ni$ reaction (dot), $\varepsilon^\star$ has been obtained making use of the formulas (9.13) and (9.14), and $\varepsilon^\star$ should be considered as an upper limit (mind the larger systematical errors).*

System	K_{lab} (MeV)	$\varepsilon^\star$ (AMeV)	T (MeV)
^{208}Pb+^{197}Au	30	4.0 ± 1.0 ⋆	3.5 ± 0.4
^{36}Ar+^{197}Au	60	5.5 ± 1.2 ⋆	4.0 ± 0.3
^{36}Ar+^{107}Ag	60	6.8 ± 1.4 ⋆	3.9 ± 0.5
^{181}Ta+^{197}Au	40	7.0 ± 1.5 ⋆	4.5 ± 0.4
^{86}Kr+^{58}Ni	60	$11.1\ ^{+0.5}_{-3.0}$ •	5.7 ± 0.5
^{36}Ar+^{58}Ni	60	8.7 ± 1.8 ⋆	6.0 ± 0.5

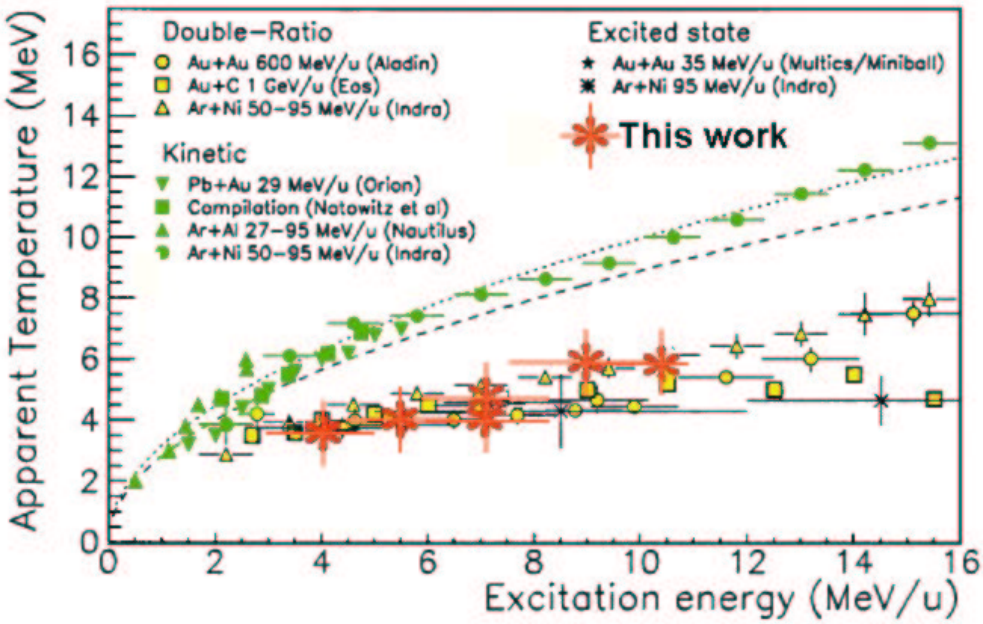

Figure 9.4: *Systematics [Dura98] of measured nuclear temperatures (obtained with the three methods described in Section 9.3) as a function of $\varepsilon^\star$ ("caloric curve"). The stars correspond to the temperatures and excitation energies obtained in the present analysis (table 9.3). The dotted and dashed lines correspond to the theoretical Fermi-liquid behaviour for two different values of the level density parameter.*

The result of the $\varepsilon^\star$ - T correlation for the 6 reactions considered in this work (table 9.3) is shown as star symbols in fig. 9.4. All the "thermal hard-photon" points seem to follow closely the (slightly increasing) "plateau" obtained using the double-ratio isotopic temperatures of the ALADIN [Poch95] and EOS [Haug96] collaborations, and *not* the Fermi-gas trend of the "kinetic" temperatures (solid and dashed lines in fig. 9.4) obtained by the INDRA collaboration [Ma97].

Although the coincidence of our data with the ALADIN "plateau" points is manifest, it is important to remind that our temperatures have been calculated using the slopes of bremsstrahlung photons emitted in nucleon-nucleon collisions. Such $NN\gamma$ collisions occur with sizeable cross-sections only around or above the saturation density $\rho \approx \rho_0$ (the Neuhauser&Koonin model predicts roughly 10 times more thermal bremsstrahlung photons at densities close to ρ_0 than at $\sim 0.5\rho_0$). Namely, in a certain way we are measuring the (maximum) temperature of the "liquid" phase[6]: the hot and heavy remaining residue. This is clearly at variance with the usual assumption in ALADIN results that the breakup (freeze-out) densities of the hot fragmenting systems produced in central collisions are below $0.5\rho_0$ (i.e. they are dilute expanding systems). As a matter of fact, it is important to remind that the so-called "caloric curve" is nothing but a projection of the more fundamental "caloric EoS" (see Appendix 3), given by the $\varepsilon = \varepsilon(T,\rho)$ "surface", onto the ε (or $\varepsilon^\star$)-T plane. Therefore, any comparison of two differently obtained sets of (T, $\varepsilon^\star$) points in the "caloric curve" is only fully meaningful, if they are "measured" at roughly the same density. Otherwise, one is comparing T - $\varepsilon^\star$ values corresponding to different isodensity lines of the nuclear equation of state.

Using the same line of reasoning, the *absence* of a thermal bremsstrahlung component in the photon spectra emitted from excited nuclear systems would be consistent with a fast spinodal breakup of the system before any second flare of $NN\gamma$ collisions could take place due to a recompression of the system. This would be a confirmation of the onset of density instabilities during the expansion phase of the reaction leading to a fast disassembly of the system rather than to the restoring of the higher densities needed for thermal $NN\gamma$ emission to take place (see Section 2.2.1). Since a thermal bremsstrahlung component has been so-far observed in all our systems (albeit for exclusive *central-reactions* only in the spectrum of the ^{36}Ar+^{197}Au system), our results seem to contradict such a dilute scenario for multifragmentation reactions and point out to a more sequential-like reaction process with a heavy residue remaining after emission of lighter fragments. Such "evaporation-like" scenario does not rule out, however, the possibility that our systems are in the liquid-gas coexistence phase around the saturation density (this metastable region lies between the spinodal and the liquid-mixture lines in the phase diagrams shown in figs. 2.1 and 2.2). To definitively determine whether in *very excited* nuclear systems ($\varepsilon^\star_{max} > 9A$ MeV) multifragmentation is due to a fast spinodal decomposition or to a slower sequential mechanism (as indicated by our results at somewhat lower excitation energies), hard-photon production in the reaction ^{129}Xe+^{112}Sn at 50A MeV was exclusively studied at GANIL in 1998 by the TAPS collaboration with a complete charged-particle detection system. The analysis of this experiment is underway in the present moment [Orte00].

[6] In that sense, since $\rho \approx \rho_0$, the slightly ascending trend of our caloric curve "plateau" is fully consistent with a liquid-gas phase transition at *constant volume*.

Conclusions and outlook

The present thesis reports on the study of nuclear matter at moderate temperatures and densities produced in nucleus-nucleus collisions at intermediate bombarding energies. An investigation of the dynamical evolution of different heavy-ion reactions, as well as of the thermodynamical state of the produced nuclear systems, excited to the vicinity of the predicted liquid-gas phase transition of nuclear matter, is carried out using hard photons ($E_\gamma > 30$ MeV) as experimental probes. These hard-photons are produced in incoherent proton-neutron bremsstrahlung collisions, $pn \rightarrow pn\gamma$, within the zone of participant nucleons. For the first time, such a study has been performed in a systematic way within a single experiment considering four different reactions (^{36}Ar+^{197}Au, ^{107}Ag, ^{58}Ni, ^{12}C at 60*A* MeV) and analyzing both exclusive as well as inclusive production modes. This approach has been made possible by exploiting the unique combination of a powerful photon spectrometer, TAPS, a nearly 4π charged-particle and intermediate-mass-fragment detector, the "Dwarf-Ball", and a charged-particle and projectile-like fragments detector, the "Forward-Wall".

We first confirm the bremsstrahlung emission in first-chance (off-equilibrium) proton-neutron collisions as the dominant origin of hard photons, as obtained by previous experiments. We then firmly establish, following the conclusions of previous TAPS measurements, the existence of a thermal radiation emission from second-chance proton-neutron collisions in semi-central and central nucleus-nucleus reactions with heavy targets. We thus exploit this observation i) to demonstrate that thermal equilibrium is reached during the reaction, ii) to establish a new thermometer based on bremsstrahlung photons, iii) to derive the thermodynamical properties of this hot matter and, in particular, to obtain a "caloric curve" (temperature versus excitation energy), and iv) to assess the time-scales of the break-up process.

The existence of a thermal component in the low-energy part of the photon bremsstrahlung spectra is founded on several conclusive experimental evidences:

- The inclusive hard-photon spectra feature two distinct exponential distributions with different slope parameters, a result which deviates from the expected behaviour of hard-photon production in first-chance nucleon-nucleon collisions. The harder (*"direct"*) component, with slope $E_0^d \approx 20$ MeV, and the steeper (*"thermal"*) $E_0^t \approx$ 6 - 9 MeV, have relative intensities 5:1.

- The *direct* slope E_0^d scales with the projectile energy per nucleon in the laboratory frame. This sets the origin of direct photons in pre-equilibrium emission in prompt nucleon-nucleon collisions. The high values of the slope reflect the coupling of the incident energy per nucleon with the average intrinsic (Fermi) momentum of the colliding nucleons.

- The *thermal* slope E_0^t shows a linear dependence with the available energy in the nucleus-nucleus center-of-mass. This observation is understood if such photons originate in processes taking place during later stages of the reaction after dissipation of the initial kinetic energy into internal degrees of freedom over the whole system. The lower thermal slope value, by a factor two to three as compared with the direct one, results from the less energy available in secondary $NN\gamma$ collisions.

- Thermal hard-photons are emitted isotropically from a source moving with the nucleus-nucleus center-of-mass velocity, according to the source-velocity analysis of the laboratory angular distributions. Direct hard-photons, on the contrary, are emitted from the nucleon-nucleon center-of-mass.

- The absence of the thermal hard-photon component in the ^{36}Ar+^{12}C reaction signals the fact that in such a light system there is not enough matter on the way of a nucleon to experience more than one collision: the resulting zone of participant nuclear matter does not have the necessary volume to achieve sufficient stopping and consequent thermalization, and pure first-chance bremsstrahlung dominates hard-photon emission. As a matter of fact, the distribution of bremsstrahlung multiplicities per nuclear reaction points out to the existence of a threshold of roughly two *pn* collisions for thermal emission to take place.

The exclusive analysis of the experimental data reveals an interesting result: the exclusive hard-photon spectra obtained for *central* and *multifragmentation* reactions in the ^{36}Ar+^{197}Au reaction present also a thermal bremsstrahlung component. Therefore, even the most violent collisions show a thermal behaviour.

We have critically analysed all possible alternative mechanisms for the production of photons with energies above 30 MeV aside from a thermal bremsstrahlung emission process: statistical photons from the Giant-Dipole-Resonances (GDR) decay, coherent bremsstrahlung, cluster bremsstrahlung, or proton-proton bremsstrahlung. Those additional interpretations can not consistently account for the full set of experimental observations. In particular, the fact that thermal and direct hard-photon yields show a very similar dependence with impact-parameter, neatly correlated with the number of participant nucleons, and that photons in the GDR region quench for increasingly central reactions, definitely rules out the attribution to GDR photons of the excess production of hard photons in the region E_γ = 30 - 60 MeV.

Detailed microscopical simulations of the four considered reactions at semi-central impact-parameters where bremsstrahlung production is maximal, have been carried out with two different transport models of Boltzmann-equation (BUU) and "Quantum" molecular-dynamics (QMD) types in order to pin down in space and time the possible sources of bremsstrahlung photons and to determine their degree of thermalization at the moment of photon emission. These calculations have confirmed the following issues:

- The reaction mechanisms for the two heaviest reactions (^{36}Ar+^{197}Au, ^{107}Ag) lead to the formation of a hot heavy quasi-target residue slowly recoiling in the laboratory frame. (This is, in turn, in agreement with recent experimental results collected with complete 4π particle multidetectors for the same systems.)

- The photon bremsstrahlung rate according to BUU, occurs in two emission flashes at t $\approx$ 30 fm/c and at t $\approx$ 130 fm/c. The first flash is more intense and takes place when the system is out of equilibrium (a minor component from a "thermalizing" stage between t $\approx$ 30 fm/c - 70 fm/c is also apparent). The second flash, accounting for roughly 20% of the total hard-photon yield, occurs when thermal equilibration,

due to two-body (nucleon-nucleon) dissipation, is attained as indicated by the rather isotropic local momentum distributions of the nucleons. This second flare is identified as the source of thermal hard-photons.

- The proton-neutron collision rates with energies in their CM above 30 MeV calculated within QMD show, for the first 100 fm/c, a similar trend as found in BUU. Although the nuclear environment in QMD is not as fully equilibrated as in the BUU case and that the transparency degree is higher, at t $\approx$ 200 fm/c, the collision rates show also a small increase in the heaviest systems (^{197}Au, ^{107}Ag). Most of these secondary *pn* collisions take place within the quasi-target remnant.

- Both transport model calculations predict a very small (or negligible) second-chance bremsstrahlung component for the lightest ^{36}Ar+^{12}C system as experimentally observed.

The formation, at the final stage of the purely dynamical evolution of the reaction, of a heavy excited remnant in thermal equilibrium which radiates bremsstrahlung photons, justifies the use of a thermal bremsstrahlung model to extract the thermodynamical properties of the system. Such a model predicts basically exponential spectra in the region E_γ = 30 - 70 MeV in agreement with our data. The slopes of such spectra are linearly correlated with the local temperature of the emitting system. This result allows to directly derive the temperature of the radiating systems from the observed thermal bremsstrahlung slopes. This hard photon thermometer shows several advantages with respect to the usual particle-based methods used so far to extract nuclear temperatures: easier identification of the thermal component (i.e. minimization of the non-equilibrium kinetic components), measurement of the maximum temperature of the system just after the attainment of thermal equilibration, intrinsic selection of semi-central and central reactions, and no final-state distortions ("side feeding", rescattering, Coulomb field and/or collective expansion).

According to the hard photon thermometer, the hot nuclear residues "prepared" in the different heavy-ion reactions with excitation energies in the range $\varepsilon^\star \approx 4A$ - $7A$ MeV, have a rather constant temperature around $T \approx 4$ MeV. The nuclear systems resulting from more symmetric colliding nuclei with excitation energies $\varepsilon^\star \approx 9A$ MeV, have a higher temperature $T \approx 6$ MeV. The correlation of the obtained temperatures with the excitation energies attained in each reaction yields, hence, "caloric curves" which are in agreement with the (slightly increasing) "plateau"-like behaviour observed by the ALADIN collaboration and interpreted as a signal of the nuclear liquid-gas phase transition, although at variance with their results our temperature is "measured" for systems which must have approximatively the saturation density of nuclear matter.

The existence of a thermal bremsstrahlung component with the observed characteristics represents a model-independent test of the attainment of thermodynamical equilibrium in semi-central and central nucleus-nucleus collisions at intermediate bombarding-energies, at least for reactions with heavy targets. The hot quasitarget systems formed at the end of the dynamical stage, with temperatures of the order of 4 MeV, seem to survive at least up to times (t $\approx$ 150 fm/c) for which a second flash of proton-neutron bremsstrahlung collisions can take place during the recompression of the hot residue. Since

nucleon-nucleon bremsstrahlung emission only takes place with sizeable cross-sections around or above the saturation density, this result is an indication that the excited hot remnant formed after the first compression-expansion stage does not multifragment rapidly due to its passage through a low-density region of the phase diagram. Since multifragment events have been indeed observed in coincidence with thermal bremsstrahlung emission, we predict therefore break-up time-scales above 150 fm/c for such system. This can be either due to the fact that the considered projectile-target combination does not produce very highly excited systems ($\varepsilon^{\star}_{max} \approx 5.0A$ MeV in ^{36}Ar+^{197}Au at 60*A* MeV) or because, in general, such a spinodal breakup mechanism is not at the origin of nuclear multifragmentation (our thermal hard-photon sources seem more to be sitting in a liquid-gas coexistence phase around the saturation density in a "evaporation-like" scenario, than undergoing a simultaneous breakup in a more dilute state).

To definitely confirm this conclusion one needs, therefore, to perform the same type of analysis of the thermal bremsstrahlung photons produced in very-heavy symmetric colliding ions at bombarding energies of the same order (i.e. around 60*A* MeV). Such entrance-channel combination leads to excitation energies in central collisions larger than the total binding energy of the system, and one may expect to reach clearly the conditions expected for a possible entrance into the low-density unstable spinodal region of the phase diagram of nuclear matter. Such an experiment (^{129}Xe+^{112}Sn at 50*A* MeV) was performed during the last TAPS campaign at GANIL in 1998 and is under analysis in the present moment.

The use of thermal hard photons as a novel powerful probe of the thermodynamical properties of hot nuclear matter, allowing for the determination of the temperature, density and time-scale of nuclear fragmentation, has been demonstrated beyond doubt. This new observable provide, thus, significant constraints for the different multifragmentation models, and valuable insights into the nuclear liquid-gas phase transition.

Conclusions (català)

Aquesta tesi reporta l'estudi de les propietats termodinàmiques de la matèria nuclear a temperatures i densitats moderades, produïda en col·lisions nucli-nucli a energies incidents intermèdies. Hem investigat l'evolució dinàmica de diferents reaccions d'ions pesants i l'estat termodinàmic dels sistemes nuclears produïts en la proximitat de la transició de fase líquid-gas de la matèria nuclear, utilitzant els "fotons durs"($E_\gamma > 30$ MeV) com a sonda experimental. Aquests fotons durs són emesos en col·lisions incoherents de *bremsstrahlung* (radiació de frenada) protó-neutró, $pn \rightarrow pn\gamma$, dins la zona de nucleons participants. Per primera vegada s'ha dut a terme un estudi d'aquestes característiques d'una manera sistemàtica en un mateix experiment, considerant quatre reaccions diferents (^{36}Ar+^{197}Au, ^{107}Ag, ^{58}Ni, ^{12}C a 60A MeV) i analitzant tant els modes de producció inclusius com els exclusius. Això ha estat experimentalment possible gràcies a l'acoblament singular d'un potent espectròmetre de fotons, TAPS, amb un multidetector de partícules carregades i de fragments de massa intermèdia cobrint el 80% de 4π, la *Dwarf-Ball*, i un multidetector de partícules carregades i de fragments quasiprojectils, el *Forward Wall*.

Hem confirmat que l'emissió principal de fotons durs té lloc en les primeres col·lisions protó-neutró (fora de l'equilibri) de *bremsstrahlung*, tal com s'havia observat en anteriors experiments. En segon lloc, i d'acord amb resultats previs de la col·laboració TAPS, hem establert de manera ferma l'existència d'una emissió de radiació tèrmica en segones col·lisions protó-neutró en reaccions semicentrals i centrals amb fitons pesants. Hem explotat, aleshores, aquest resultat per i) demostrar que l'equilibri tèrmic s'assoleix al llarg de la reacció nuclear, ii) establir un nou termomètre de la matèria nuclear basat en els fotons de *bremsstrahlung*, iii) derivar les propietats termodinàmiques dels sistemes nuclears calents i, en concret, obtenir una "corba calòrica"(temperatura en funció de l'energia d'excitació), i iv) avaluar les escales temporals del procés de fragmentació nuclear.

L'existència d'un component tèrmic en la part de baixa energia dels espectres de fotons de *bremsstrahlung* es basa en diverses evidències experimentals concloents:

- Els espectres inclusius de fotons durs resulten de la suma de dues distribucions exponencials amb pendents diferents. Aquest resultat es desvia del comportament previst per a la producció de fotons durs en primeres col·lisions nucleó-nucleó. El component més dur ("directe"), amb pendent $E_0^d \approx 20$ MeV, i el component més tou ("tèrmic"), amb $E_0^t \approx 6$ - 9 MeV, tenen una intensitat relativa 5:1.

- El pendent directe E_0^d eś proporcional a l'energia per nucleó del projectil en el sistema laboratori. Aquest resultat situa l'origen dels fotons durs "directes"en l'emissió preequilibri de primeres col·lisions nucleó-nucleó. L'elevat valor del pendent reflecteix l'acoblament entre l'energia incident per nucleó i el moment mitjà intrínsec de Fermi dels nucleons col·lisionants.

- El pendent tèrmic E_0^t mostra una dependència lineal amb l'energia disponible al centre de masses nucli-nucli. Aquesta observació constitueix una prova que aquests fotons s'originen en processos que tenen lloc durant estadis posteriors de la reacció després de la dissipació de l'energia cinètica inicial entre els graus de llibertat interns del sistema total. El valor entre dues i tres vegades inferior del pendent tèrmic

respecte del pendent directe és degut a la menor energia disponible en col·lisions $NN\gamma$ secundàries nucleó-nucleó.

- Els fotons tèrmics són emesos isotròpicament des d'una font que es mou a la velocitat del centre de masses nucli-nucli, tal com es dedueix de l'anàlisi de les distribucions angulars en el laboratori. Els fotons directes, al contrari, són emesos des del centre de masses nucleó-nucleó.

- L'absència d'un component tèrmic de fotons durs en el sistema ^{36}Ar+^{12}C s'interpreta com a deguda al fet que en aquest sistema lleuger no hi ha prou matèria nuclear com perquè els nucleons pateixin més d'una col·lisió. Atès que la zona participant resultant no té el volum necessari per arribar a frenar els nucleons incidents, no hi ha termalització i, per tant, el *bremsstrahlung* degut a col·lisions primàries domina tota l'emissió de fotons durs.

L'anàlisi exclusiva de les dades experimentals porta també a un interessant resultat: els espectres exclusius dels fotons durs mesurats en les col·lisions *centrals* i de *multifragmentació* de la reacció ^{36}Ar+^{197}Au mostren també un component tèrmic amb la mateixa intensitat i pendent que els espectres inclusius. És a dir, àdhuc les reaccions més violentes mostren un comportament tèrmic.

Hem analitzat críticament tots els possibles mecanismes alternatius, al marge de l'emissió de *bremsstrahlung* tèrmic, capaços eventualment de produir fotons amb energies per sobre dels 30 MeV: fotons estadístics del decaïment de Ressonàncies Dipolars Gegants (*GDR*), *bremsstrahlung* coherent, *bremsstrahlung* d'amàs, i *bremsstrahlung* protó-protó. Cap d'aquestes interpretacions alternatives no pot explicar de manera completa i consistent el conjunt d'observacions experimentals. En concret, el fet que la producció de fotons durs tèrmics i directes mostri una dependència molt similar amb el paràmetre d'impacte, augmentant un factor ≈ 10 entre les col·lisions perifèriques i les col·lisions semicentrals, i que la producció de fotons en la regió de la GDR disminueixi amb el paràmetre d'impacte, invalida l'atribució de l'excés de fotons durs en la regió E_γ = 30 - 60 MeV als fotons provinents de la GDR.

A nivell teòric, hem utilitzat dos models de transport diferents basats en l'equació de Boltzmann (BUU) i en una aproximació de dinàmica molecular (QMD) per realitzar detallades simulacions microscòpiques de les quatre reaccions esmentades per a paràmetres d'impacte on la producció de *bremsstrahlung* és màxima. L'objectiu d'aquests càlculs és identificar en l'espai-temps les possibles fonts de fotons de *bremsstrahlung* i determinar el seu grau de termalització en el moment d'emissió. Aquestes simulacions dibuixen el següent escenari:

- Els mecanismes de reacció de les dues reaccions més pesades (^{36}Ar+^{197}Au, ^{107}Ag) condueixen a la formació en l'estat final d'un residu calent de tipus quasifitó que recula lentament en el sistema laboratori. (Aquest resultat està d'acord amb recents observacions experimentals obtingudes amb complets multidetectors 4π de partícules.)

- L'evolució temporal del nombre de col·lisions de *bremsstrahlung* calculada amb BUU indica que l'emissió de fotons durs té lloc en dos flaixos amb màxims a t $\approx$ 30 fm/c i a t $\approx$ 130 fm/c. El primer flaix és més intens i té lloc quan el sistema és fora de l'equilibri (encara que un component menor també apareix durant la fase de termalització entre t $\approx$ 30 fm/c i 70 fm/c). El segon flaix representa al voltant del 20% de la producció total de fotons durs i té lloc en una situació d'equilibri tèrmic (deguda a la "dissipació a 2-cossos"en col·lisions nucleó-nucleó) tal com indiquen les distribucions isotròpiques dels moments dels nucleons. Aquest segon flaix és identificat com la font dels fotons durs tèrmics.

- La taxa en funció del temps del nombre de col·lisions protó-neutró (amb energies al CM per sobre dels 30 MeV) calculada amb QMD mostra, per als primers 100 fm/c, una tendència similar a la trobada amb BUU. Tot i que l'entorn nuclear no està completament equilibrat com en el cas de BUU i que el grau de transparència és superior, a t $\approx$ 200 fm/c el nombre de col·lisions augmenta lleugerament en els sistemes més pesants (^{197}Au, ^{107}Ag). La majoria d'aquestes col·lisions *pn* secundàries tenen lloc dins del residu quasifitó.

- Els dos models de transport prediuen un component de *bremsstrahlung* degut a col·lisions secundàries protó-neutró molt petita (o inexistent) per al sistema més lleuger (^{36}Ar+^{12}C) també d'acord amb les dades experimentals.

La formació al final de l'estadi purament dinàmic de la reacció d'un residu nuclear pesant i calent i que radia fotons de *bremsstrahlung* en equilibri tèrmic, justifica l'aplicació d'un model de *bremsstrahlung* tèrmic per extreure les propietats termodinàmiques del sistema. Aquest model prediu espectres gamma bàsicament exponencials en la regió E_γ = 30 - 80 MeV d'acord amb les nostres observacions. Els pendents d'aquests espectres estan linealment correlacionats amb la temperatura local del sistema emissor. Aquest resultat permet determinar de manera directa la temperatura dels sistemes nuclears a partir dels pendents de *bremsstrahlung* tèrmic. Aquest nou termòmetre "fotònic"presenta diversos avantatges respecte dels mètodes usuals basats en partícules utilitzats fins ara per mesurar les temperatures nuclears: fàcil identificació del component tèrmic (i.e., minimització dels components cinètics de no-equilibri), mesura de la temperatura màxima del sistema just després de l'assoliment de l'equilibri tèrmic, selecció intrínsica de reaccions semicentrals i centrals, i absència de distorsions degudes a interaccions en l'estat final (*side feeding*, redifusió, camp coulombià i/o expansió col·lectiva).

D'acord amb el "termòmetre fotó", els residus calents produïts en diferents reaccions d'ions pesants amb energies d'excitació de l'ordre de $\varepsilon^\star \approx 4.0A$ - $7.0A$ MeV tenen una temperatura relativament constant al voltant de $T \approx 4$ MeV. Els sistemes nuclears resultants de les col·lisions de nuclis més simètrics i, per tant, amb energies d'excitació superiors ($\varepsilon^\star \approx 9A$ MeV) mostren una temperatura més elevada ($T \approx 6$ MeV). Correlacionant les temperatures obtingudes amb el nostre mètode amb les energies d'excitació assolides en cada reacció, s'obtenen "corbes calòriques"que estan globalment d'acord amb el *plateau* (lleugerament creixent) observat per la col·laboració ALADIN i interpretat com una evidència de la transició de fase líquid-gas nuclear, encara que, contràriament

a aquests resultats, la nostra temperatura és mesurada en sistemes que es troben aproximadament a la densitat de saturació de la matèria nuclear.

L'existència d'un component de *bremsstrahlung* tèrmic amb les característiques esmentades constitueix una prova independent de models de l'assoliment de l'equilibri termodinàmic en col·lisions nucli-nucli semicentrals i centrals a energies incidents intermèdies (almenys en el cas de fitons pesants). Els sistemes calents presents al final de la fase dinàmica, amb temperatures al voltant de 4 MeV, han de sobreviure almenys fins a temps de l'ordre de t $\approx$ 150 fm/c per als quals pot tenir lloc un segon flaix de col·lisions de *bremsstrahlung* protó-neutró durant la recompressió del sistema. Atès que l'emissió de *bremsstrahlung* nucleó-nucleó només té lloc amb seccions eficaces significatives, al voltant o per sobre de la densitat de saturació, aquest resultat és una indicació clara que els residus calents formats després de la primera fase de compressió-expansió no multifragmenten a causa del seu pas per una regió de baixa densitat del diagrama de fases. Prediem, doncs, per a aquests sistemes temps de trencament per sobre dels 150 fm/c. Això pot ser bé perquè la combinació de projectil i fitó considerada no produeix sistemes molt excitats ($\varepsilon^{\star}_{max} \approx 5.0A$ MeV per ^{36}Ar+^{197}Au a 60*A* MeV) o bé perquè, en general, el mecanisme de trencament espinodal no és responsable de la multifragmentació nuclear (els nostres sistemes semblen trobar-se més en un escenari de tipus "evaporació"en una fase de coexistència líquid-gas al voltant de la densitat de saturació).

Per confirmar definitivament aquest darrer extrem cal, doncs, dur a terme el mateix tipus d'anàlisi exclusiva realitzada en aquest treball per als fotons tèrmics de *bremsstrahlung* produïts en col·lisions d'ions molt simètrics i pesants a energies incidents de l'ordre de 60*A* MeV. Aquesta combinació en el canal d'entrada de la reacció pot produir energies d'excitació en col·lisions centrals que són superiors a l'energia total de lligam dels nuclis atòmics. En aquestes circumstàncies hom espera poder arribar clarament a les condicions pròximes a un possible accés del sistema a la regió inestable espinodal del diagrama de fases de la matèria nuclear. Un experiment d'aquestes característiques (^{129}Xe+^{112}Sn a 50*A* MeV) es va realitzar durant la passada campanya de la col·laboració TAPS al laboratori GANIL el 1998, i les dades recollides estan sent analitzades en aquests moments.

L'ús dels fotons durs tèrmics com una nova i potent sonda experimental de les propietats termodinàmiques de la matèria nuclear, fet que permet la determinació de la temperatura, la densitat i l'escala temporal de la fragmentació nuclear, ha quedat demostrat més enllà de qualsevol dubte. Aquest nou observable permet establir importants constriccions als diferents models teòrics de multifragmentació existents, i aporta precioses informacions sobre la transició líquid-gas nuclear.

Conclusions (français)

Cette thèse aborde l'étude de la matière nucléaire à des températures et des densités modérées, telle qu'elle est produite dans des collisions noyau-noyau à des énergies de bombardement voisines de l'énergie de Fermi. Nous avons étudié la dynamique des collisions d'ions lourds, et l'état thermodynamique des systèmes nucléaires, chauffés et comprimés à des valeurs voisines de celles où l'on s'attend à observer la transition de la phase liquide de la matière nucléaire vers une phase gazeuse, en utilisant les photons durs ($E_\gamma >$ 30 MeV) comme sonde expérimentale. Ces photons durs sont produits par sommation incohérente du rayonnement de freinage émis lors des collisions éléméntaires entre protons et neutrons, $pn \rightarrow pn\gamma$, présents dans la zone de recouvrement des noyaux cible et projectile. Pour la première fois, une telle étude a été réalisée de façon systématique lors d'une même mesure, en considérant quatre systèmes différents (^{36}Ar+^{197}Au, ^{107}Ag, ^{58}Ni, ^{12}C à 60*A* MeV), et en analysant des modes de production inclusifs et exclusifs. Cette approche a été rendue possible en exploitant la combinaison unique d'un spectromètre de photons, TAPS, et deux multidétecteurs de particules chargées (Dwarf-Ball et Forward-Wall) offrant une couverture de l'angle solide voisine de 4π.

Les résultats obtenus permettent de confirmer l'origine dominante des photons durs comme étant le rayonnement de freinage émis dans les collisions *pn* de première chance (hors équilibre). De plus, l'existence d'une émission thermique de photons est établie de façon définitive et nous attribuons son origine au rayonnement de freinage émis dans les collisions *pn* de deuxième chance, uniquement présent de façon mesurable dans des réactions noyau-noyau semi-centrales et centrales impliquant des cibles lourdes. Nous avons pu exploiter cette observation i) pour démontrer que l'équilibre thermique est atteint lors de la réaction, ii) pour valider un nouveau thermomètre basé sur des photons du rayonnement de freinage, iii) pour déduire les propriétés thermodynamiques de la matière nucléaire chaude (en particulier, pour établir la "courbe calorique") et iv) pour évaluer les échelles de temps du processus de fragmentation.

La démonstration de l'existence d'une composante thermique dans la partie de basse énergie des spectres des photons de bremsstrahlung est fondée sur plusieurs preuves expérimentales concluantes:

- Les spectres globaux des photons durs s'avèrent être la combinaison de deux distributions exponentielles avec des paramètres de pente différents. Ce résultat contraste avec le comportement prévu pour la production de photons durs lors de collisions nucléon-nucléon de première chance. La composante dure ("directe") avec une pente $E_0^d \approx 20$ MeV, et la composante molle ("thermique"), avec $E_0^t \approx 6$ - 9 MeV, présentent des intensités relatives 5:1.

- La pente directe E_0^d est proportionnelle à l'énergie incidente par nucléon dans le repère du laboratoire. Ce résultat situe l'origine des photons durs "directs"dans l'émission de pré-équilibre lors de collisions nucléon-nucléon de première chance. Les valeurs élevées des pentes reflètent le couplage de l'énergie incidente par nucléon au moment moyen intrinsèque de Fermi des nucléons interagissants.

- Les pentes thermiques E_0^t suivent une dépendance linéaire avec l'énergie disponible dans le centre de masse noyau-noyau. Ceci constitue une preuve que ces photons

proviennent de processus thermiques qui ont lieu plus tardivement dans la réaction, après la dissipation de l'énergie incidente initiale dans tous les degrés de liberté du système total. Le fait que ces pentes soient approximativement entre deux et trois fois plus faibles que les pentes directes est dû au manque d'énergie disponible dans les collisions $NN\gamma$ secondaires.

- Les photons durs thermiques sont émis isotropiquement par une source en mouvement avec la vitesse du centre de masse noyau-noyau, comme le démontre l'analyse des distributions angulaires dans le système du laboratoire. Les photons durs directs, au contraire, sont émis à partir du centre de masse nucléon-nucléon.

- L'absence d'une composante thermique de photons durs dans le système ^{36}Ar+^{12}C est expliquée par le fait qu'il n'y a pas, dans un système aussi léger, assez de matière sur le chemin d'un nucléon pour qu'il subisse plus d'une collision. Comme la zone participant n'a pas le volume nécessaire pour arrêter suffisamment des nucléons incidents et conduire à une thermalisation du système, le bremsstrahlung de première chance domine clairement l'émission des photons durs.

L'analyse exclusive des données expérimentales amène aussi à un résultat intéressant: les spectres exclusifs des photons durs mesurés dans les collisions *centrales* et de *multi-fragmentation* de la réaction ^{36}Ar+^{197}Au, montrent aussi une composante thermique avec la même intensité et pente que les spectres inclusifs. C'est-à-dire, même les réactions les plus violentes montrent un comportement thermique.

En outre, nous avons analysé de façon critique tous les mécanismes alternatifs possibles, en plus de l'émission de bremsstrahlung thermique, capables de produire éventuelment des photons d'énergie supérieur à 30 MeV: photons statistiques résultant de la décroissance de Résonances Dipolaires Géantes (GDR), photons de rayonnement de freinage cohérent, de bremsstrahlung d'amas, ou de bremsstrahlung proton-proton. Aucune de ces interpretations alternatives ne peut rendre compte d'une façon cohérente de l'ensemble des observations expérimentales. En particulier, le fait que la production de photons durs directs et thermiques dépend similairement du paramètre d'impact, augmentant d'un facteur ≈ 10 en allant des réactions périphériques aux réactions semi-centrales, et du fait que la production des photons dans la région de la GDR diminue avec le paramètre d'impact, invalide l'attribution de l'excès de photons durs dans la région E_γ = 30 - 60 MeV comme dû aux photons statistiques provenants de la GDR.

Des simulations détaillées à l'aide de modèles microscopiques des quatre réactions considérées, pour des paramètres d'impact semi-centraux où la production de photons de bremsstrahlung est maximale, ont été effectuées avec deux modèles de transport différents, l'un basé sur l'équation de transport de Boltzmann (BUU) et l'autre sur la dynamique moléculaire (QMD), afin d'identifier dans l'espace et le temps les sources des photons de bremsstrahlung et déterminer leur degré de thermalization au moment de l'émission des photons. Ces calculs confirment que:

- Les mécanismes de réaction pour les deux systèmes les plus lourds (^{36}Ar+^{197}Au, ^{107}Ag), mènent à la formation d'un résidu lourd et chaud de quasi-cible reculant

lentement dans le repère du laboratoire (et ce en accord avec les résultats expérimentaux récents obtenus pour les mêmes systèmes avec des multidétecteurs complets de particules 4π).

- D'après BUU, l'émission des photons de bremsstrahlung se produit en deux flashes, à t $\approx$ 30 fm/c et à t $\approx$ 130 fm/c. Le premier flash est plus intense et a lieu quand le système est dans une phase de pré-équilibre. Le deuxième flash, représentant moins de 20% du taux total de photons durs, se produit quand l'équilibre thermique, dû à la dissipation à deux-corps (nucléon-nucléon), est atteint. La forme des distributions locales à peu près isotropes des impulsions des nucléons l'indique clairement.

- Les taux de collision proton-neutron (avec des énergies, dans le centre de masse, supérieures à 30 MeV) calculés avec QMD montrent, pour les 100 premiers fm/c, une tendance similaire à celle trouvée par BUU. Bien que l'environnement nucléaire ne soit pas aussi entièrement équilibré que dans le cas de BUU et que le degrée de transparence soit supérieur, à t $\approx$ 200 fm/c, les taux de collision dans les systèmes les plus lourds (^{197}Au, ^{107}Ag) présentent aussi une petite augmentation. La plupart de ces collisions $pn\gamma$ secondaires ont lieu dans le résidu quasi-cible.

- Il s'avère que ces modèles de transport ne prévoient qu'une composante très faible (ou inexistante) de bremsstrahlung de deuxième chance pour le système le plus léger (^{36}Ar+^{12}C) comme observé expérimentalement.

La formation à la fin de la phase purement dynamique de la réaction, d'un résidu nucléaire lourd et chaud et qui rayonne photons de bremsstrahlung en équilibre thermique, justifie le recours à un modèle de bremsstrahlung thermique pour extraire les proprietés thermodynamiques du système. Ce modèle prévoit des spectres exponentiels dans la région E_γ = 30 - 80 MeV, en accord avec nos données. Les inverses des paramètres de pente de tels spectres sont directement corrélés avec la température locale du système au moment de l'émission. Un tel résultat permet de déduire directement la température des systèmes rayonnants à partir des pentes thermiques. Ce nouveau thermomètre photon présente plusieurs avantages vis-à-vis des méthodes habituelles (basées en particules chargées) utilisées jusqu'à présent pour mesurer les températures nucléaires: identification facile de la composante thermique (i.e. minimisation des composantes cinétiques hors-équilibre), mesure de la température maximale du système juste après équilibration, sélection intrinsèque des réactions semi-centrales et centrales, et absence de distorsions dans l'état final ("side feeding", rediffussion, champ Coulombien et/ou expansion collective).

D'après le résultat des mesures obtenues avec le thermomètre photon, les résidus chauds produits dans differentes réactions d'ions lourds avec des énergies d'excitation dans l'intervalle $\varepsilon^\star \approx 4.0A$ - $7.0A$ MeV, ont une température constante de $T \approx 4$ MeV. Les systèmes nucléaires produits dans les collisions plus symétriques et, donc, avec des énergies d'excitation $\varepsilon^\star \approx 9A$ MeV possédent une température plus élevée, $T \approx 6$ MeV. Les températures et les énergies d'excitation obtenues sont corrélées, suivant des "courbes caloriques"qui sont globalement en accord avec le "plateau"(légèrement croissant) observé par la collaboration ALADIN, son existence étant interpreté comme une évidence

de la transition liquide-gaz nucléaire. Il faut pourtant bien préciser que notre température est “mesurée”dans des systèmes qui ont à peu près la densité de saturation de la matière nucléaire.

L’existence d’une composante thermique de bremsstrahlung possédant les caractéristiques observées représente un test indépendant du modèle de la formation de systèmes nucléaires équilibrés ayant une température de l’ordre de 4 MeV dans des collisions noyau-noyau semi-centrales et centrales avec des cibles lourdes aux énergies intermédiaires. Les systèmes chauds formés pendant la réaction semblent survivre au moins jusqu’au moment (t $\approx$ 150 fm/c) où un deuxième flash de bremsstrahlung proton-neutron peut avoir lieu, pendant la recompression du système. Puisque l’émission de bremsstrahlung nucléon-nucléon a lieu seulement autour (ou au-dessus) de la densité de saturation, ce résultat est une indication que les résidus chauds formés lors de la réaction ne (multi)fragmentent pas suite au passage par une région de basse densité du diagramme de phase. Nous prévoyons donc des échelles de temps de fragmentation supérieures à 150 fm/c pour un tel système. Ceci peut être dû au fait que la combinaison projectile-cible considérée ne produit pas de systèmes très fortement excités ($\varepsilon^{\star}_{max} \approx 5.0A$ MeV pour ^{36}Ar+^{197}Au à 60A MeV) ou parce que, en général, un mécanisme d’instabilité spinodale n’est pas à l’origine de la multifragmentation nucléaire.

Pour confirmer définitivement cette dernière conclusion, on doit réaliser le même type d’analyse exclusive realisée dans cette étude pour les photons thermiques de bremsstrahlung produits dans des collisions d’ions symétriques et lourds aux mêmes énergies de bombardement (i.e. autour de 60A MeV). Lors de collisions centrales, une telle combinaison dans le canal d’entrée peut mener à des énergies d’excitation supérieures à l’énergie de liaison du noyau atomique. On peut ainsi espérer atteindre clairement des conditions proches de celles prévues pour l’entrée du système dans la région instable spinodale du diagramme de phases de la matière nucléaire. Cette expérience (^{129}Xe+^{112}Sn à 50A MeV) a été réalisée pendant la dernière campagne de la collaboration TAPS au laboratoire GANIL en 1998 et l’analyse des données expérimentales est actuellement en cours.

L’utilisation des photons durs thermiques comme une sonde expérimentale nouvelle et performante des proprietés thermodynamiques de la matière nucléaire, en permettant la détermination de la température, de la densité et de l’échelle temporelle de la fragmentation nucléaire, a été démontré au delà de toute doute. Cette nouvelle observable établie des contraintes significatives pour les différents modèles de multifragmentation, et apporte des informations précieuses sur la transition liquide-gaz nucléaire.

Appendix 1: Scintillators

The experimental setup used in this thesis comprised 540 individual detector modules grouped into three different multidetectors: TAPS, and Dwarf-Ball and Forward Wall, for photon and charged-particle detection respectively. All the single modules of those detection systems were scintillator detectors of five different types. Two of the scintillator materials used were inorganic crystals: BaF_2 and CsI(Tl), and three of them Polyvinyltoluene-based (PVT) organic plastics: NE102A/BC-400, BC-446, and NE115. TAPS modules are made of BaF_2 crystals and TAPS charge-particle-vetoes consist of a PVT fast plastic NE102A. In the case of the Dwarf-Ball, the E detectors are CsI(Tl) crystals and the ΔE detectors are again two PVT plastics (Bicron BC-400 equivalent to NE102A, and Bicron BC-446). Finally, the Forward Wall E-ΔE phoswich telescopes are made of slow NE115 and, again, fast NE102A PVT plastics respectively. Each single scintillator was read out either with an individual PMT (in the case of TAPS) or in phoswich mode (for the DB and FW detectors).

In order to understand the performances of the used detectors, we must first consider the physical mechanism of light production by organic/inorganic scintillators and of electromagnetic shower development in large organic scintillators arrays. In this appendix, I review the working principles and characteristics of the scintillation detectors used in the present experiment.

.1 Scintillation mechanism

The principles of scintillation are described in detail e.g. in references [Leo92, Knol89, Birk64]. The detection properties of a scintillator rely on the process commonly called "luminiscence"[7]: a charged particle (either directly produced in the nuclear reaction or an electron-positron pair of the electromagnetic shower created by an original incident photon) which traverses the scintillator leaves behind it a wake of electron-hole pairs (in inorganic crystals) or excited molecules (in organic plastics) which will release a small fraction[8] of the incident ionizing energy in form of optical photons usually in the visible or near visible (UV) regions (the so-called "scintillation light"). Birk's law [Birk64] relates the light yield ΔL to the energy loss ΔE through the semi-empirical equation:

$$\Delta L = S \cdot \frac{\Delta E}{1 + k_B \cdot dE/dx} \tag{1}$$

where $k_B \approx 0.01$ g/MeV cm^2 is Birk's scintillator- and particle- dependent constant, and S the scintillation efficiency.

The performance of a scintillation device is mainly determined by its light output (i.e. the integration of equation (1) from the incoming-particle initial energy down to zero). This light-output is quoted in terms of photoelectrons per MeV of energy deposit and describes the absorption of incident energy in the material and the consecutive deexcitation via emission of scintillation radiation.

The light intensity of fluorescence has a temporal behaviour characteristic of each scintillation substance with one or more exponential decays depending on the lifetime of the

[7] One may further differentiate between (fast and temperature-independent) "fluorescence"and (slower and temperature-dependent) "phosphorescence"emissions.

[8] A maximum of 12% for crystals and ≈ 3% for plastics.

energy levels involved[9]. In the simplest case, the intensity of the scintillation light depends on the nature and energy of the particle (I_0) and on the time duration of the excited state (τ) through the relation:

$$I(t) = I_0 \cdot e^{-t/\tau} \tag{2}$$

The commonly used scintillation materials can be grouped into inorganic scintillators (like NaI(Tl), BaF_2, CsI(Tl), CsI, $PbWO_4$, BGO and CeF_3) and organic ones (polymer plastics containing aromatic rings: polystyrene, polyvinyltoluene and naphtalene; crystalline substances such as anthracene; or liquids like toluene and xylene). This classification goes in parallel with two completely different physical fluorescence mechanisms. In inorganic materials the process of fluorescence depends on energy states of the electronic band structure determined by the *lattice* of pure or doped crystals. In organic materials, fluorescence arises from (non-localized) electron transitions in the energy level structure of a *single* molecule.
From the viewpoint of experimental applications in nuclear and high-energy physics, high-energy photon (or electron) calorimetry is basically restricted to (large arrays of) inorganic scintillating crystals [Grat94], whereas organic materials are favored as fast detection (or trigger) devices for charged particles in high counting rate environments.

.2 Crystal scintillators

The luminiscence process of inorganic materials is a lattice effect intimately connected with the crystalline nature of the host material. An inorganic scintillator involves a crystalline or near-crystalline host insulator which is doped with a small concentration of impurity atoms, known as activators (e.g. CsI activated with Tl). In certain cases (such as BaF_2), the activator centers may also be caused simply by lattice imperfections in a pure crystalline material. Ionizing radiation causes electrons in the host matrix to be transferred from the valence band to the conduction band producing an electron-hole pair (the "exciton") that rapidly moves through the lattice until either it is absorbed by an activator center which subsequently decays in its characteristic time with the emission of a photon, or it recombines (within $\approx$ 10 ns at a mean distance of 1 μm from its origin).

The identification and detection of high-energy photons in crystal scintillator detectors depends on the physical mechanisms involved in the interaction of the radiation with the material. The distinctive energies of the photons produced in the experiment subject of this thesis (E_γ = 20 - 200 MeV) are well above the $E_\gamma \approx 4$ MeV energy at which the e^+e^- pair production becomes the dominant process in the interaction photon-matter, and also above the "critical energy"[PDG98], $E_c = 610/(Z + 1.24)$ = 12.7 MeV for BaF_2, where the conversion-produced e^+e^- will subsequently emit bremsstrahlung radiation when interacting with the detector material. The combination of these two effects leads to the development of an electromagnetic shower inside the BaF_2 crystals when a high-energy photon (or electron) impinges on one TAPS module. The characteristics of these showers are determined by two quantities, on the one hand, by the radiation length parameter:

$$X_0 = 716.4 \cdot A / \left[Z(Z+1) \ln(287/\sqrt{Z}) \right] \quad (\mathrm{gcm}^{-2}) \tag{3}$$

[9] Scintillation is, thus, easily distinguishable from Čerenkov emission which takes place instantaneously.

which measures the distance traversed by an e^- after which its energy is reduced by a factor 1/e by bremsstrahlung[10] and, on the other, by the Molière radius:

$$\rho_M = 21.2 \cdot X_0/E_c \quad (\text{MeV}) \tag{4}$$

which gives a measure of the average lateral spread of an electron with energy E_c.

Fig. 1 shows the development of a "classical"shower in the first few radiation lengths. The energy response of the detector system is, hence, mainly governed by the detector geometry which determines the fraction of the electromagnetic shower contained in the detector volume[11]. For BaF_2, X_0 = 2.05 cm and ρ_M = 3.4 cm, so the chosen dimensions of the TAPS crystals (25 cm $\times$ 2.95 cm) ensure a good shower recollection in the longitudinal direction and a lateral extension of the shower over more than one module as desired for good incident position reconstruction.

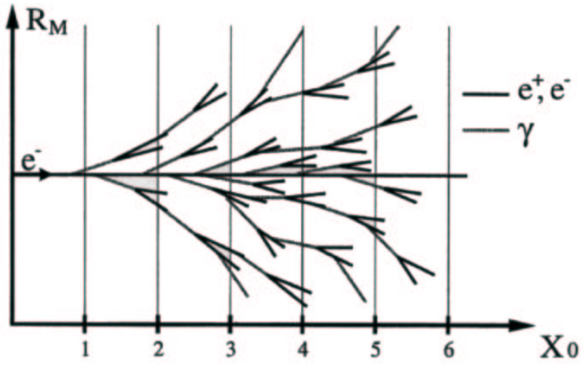

Figure 1: *Radial and longitudinal development of a "typical"electromagnetic shower. From [Schi98].*

As mentioned above, two inorganic scintillators have been used in the present experiment:

- **Barium fluoride (BaF_2)**: Such material was used as a scintillator for the first time in 1971 but the discovery of its fast component, and thus its widespread use, is from 1983 [Lava83]. BaF_2 has been chosen as the scintillator material of TAPS [Novo91] because its excellent properties investigated in various applications [Lava83, Caff86, Maje87, Novo87]: subnanosecond time resolution comparable to that of fast organic scintillators, energy resolution for lower energy gamma sources comparable to NaI(Tl), intrinsic particle identification[12] based on its two scintillation components (through the so-called "pulse-shape analysis"), good mechanical and chemical stability, high density and superior hardness against radiation damage.

[10] The mean free path of photons is closely related to the radiation length through $\lambda_{pair} = 9/7 X_0$ [Leo92].

[11] A photon-initiated cascade reaches its maximum after $t_{max} = \ln(E/E_c) - 0.5$ radiation lengths before decaying exponentially up to a 95% depth $t_{95\%} = t_{max} + 0.08Z + 9.6$ [X_0] [Bock98]. Additionally, 95% of the shower is laterally contained in a radius $R_{95\%} = 2\rho_M$.

[12] Photons and charged hadrons traversing BaF_2 have different ionization densities and produce different occupation densities of electron-hole pairs in the scintillator material. Photons mainly excite the short-lived component, while this is suppressed for protons and ions.

Table 1: *Physical, chemical and scintillation properties of BaF_2 and CsI(Tl) inorganic crystals. Collected from [Suff88, Bour94, Grat94, PDG98]. [The superindex ^{a} represents the % with respect to NaI(Tl) light output efficiency for standard PMT, and ^{f,s} refer to the fast and slow scintillation components respectively.]*

	BaF_2	CsI(Tl)
Density (g/cm^3)	4.89	4.53
Z/A	0.422	0.416
Radiation length (cm)	2.06	1.85
Molière radius (cm)	3.4	3.8
$(dE/dx)_{min}$ (MeV/cm)	6.6	5.6
Nuclear interaction length (cm)	29.9	36.5
Wavelength of peak emission (nm) ^{a}	220^f, 310^s	565
Decay time τ (ns)	0.7^f, 620^s	420 - 700, 7000 ± 500
Relative light output L(%) ^{a}	5^f, 20^s	45
Photons (N/MeV)	$\approx 10^4$	$\approx 4 \cdot 10^4$
$\Delta\tau/\Delta$T (ns/°C at 20°)	-	-2
ΔL/ΔT (%/°C at 20°)	0.0^f, -1.2^s	+0.6
Refractive index	1.49^f, 1.56^s	1.80
Radiation damage threshold (Rads)	$\approx 10^7$	$\approx 10^2$
Melting point (°C)	1280	621
Hygroscopic	No	Slightly
Solubility (g/100 g H_2O)	0.12	85
"Hardness"(Mohs)	3	2
Price (\$/cm^3)	2.5	2

- **Cesium iodide doped with thallium, CsI(Tl)**: It was used as scintillator already in 1950 [Hofs50] but also "rediscovered"recently [Grass85] due to its well adapted emission spectrum to Si-photodiodes. CsI(Tl) has several properties which make of it a suitable option for particle-detection in heavy-ion physics (see also Section .4): Good light output close to that of NaI(Tl) and a single wavelength component with *two* very different time constants (a slow one, τ_1 = 0.4 - 0.7 μs, which varies with particle type in decay, and a long one, $\tau_2 \approx 7.0$ μ, which is independent of the nature of the incident particle).

Table 1 summarizes the scintillation, physical and chemical properties of the two inorganic crystal scintillators, BaF_2 and CsI(Tl), used in our experimental setup.

.3 Plastic scintillators

Light emission in organic materials is an inherent molecular property. The vibrational levels (π electrons) of the materials can be readily excited into a high vibrational state by photons or ionizing particles and then promptly (few ns) de-excite with the emission of radiation. In order to allow light to be transmitted through appreciable distances inside

the material, a further fluorescent component is added which preferentially absorbs the scintillation light and re-emits it at longer wavelengths. Plastic scintillators consist, thus, usually in a solid solution of two luminophors (luminiscent additives) in a transparent polymer such as polyvinyltoluene[13] (PVT) or polystyrene (PST). The first solute acts as a "primary activator"and the second component, typically present in small concentrations (0.01% - 1% by weight), as "wavelength shifter"or "WLS"(i.e. it changes the wavelength of the scintillation light of the primary composite to higher values minimizing the self-absorption and matching the emitted light wavelength to the transparency window of the PMT photocatode).

The characteristics of plastic scintillation materials (light output, transparency to its own emission, decay time(s), radiation resistance) can be, thus, selected by changing the composition of the solutes and the polymer base. In our case for example, NE102A (equivalent to BC-400) consists in a polyvinyltoluene (PVT) base with 2% p-therphenyl as "primary activator", and 0.1% p-bis[2-(5-phenyloxazolyl)]benzene (POPOP) as "wavelength shifter".

The general properties of the Polyvinyltoluene-based plastic scintillators[14] are shown in table 2, whereas the individual characteristics of NE102A(BC-400), NE115, and BC-446 are summarized in table 3.

.4 Charged-particle detection with 4π arrays in nuclear physics

There are several methods employed in particle physics for the detection of charged particles, most of them usually combine central detectors (hadronic calorimeter, Čerenkov counters ...) with a powerful magnet providing an appropriate magnetic field for particle momenta measurement. In nuclear-physics, in the absence of magnetic fields, two types of (closely-related) alternative methods are employed in 4π hadronic calorimeters for the detection of charged-particles:

- two-component inorganic scintillators,
- *phoswiches*.

Both methods have been used concurrently in the experimental setup employed in this thesis.

.4.1 Two-component inorganic scintillators

We have mentioned previously that the pulse shape of scintillation light for CsI(Tl) and BaF_2 depends on the type of particle traversing the material allowing thus for its identification[15]. In the case of CsI(Tl), the light intensity has the form:

$$I = I_1 \cdot e^{-t/\tau_1} + I_2 \cdot e^{-t/\tau_2} \tag{5}$$

[13]PVT is a polymer plastic made of 2-$CH_3C_6H_4CH{=}CH_2$ monomers.

[14]The plastic scintillators used in this experiment have commercial names: NE-XXX and BC-YYY.

[15]We will not consider here the use of BaF_2 as charged-particle (or neutron) detector since we did not use this capability in our setup, however, this option has been studied in [Novo91].

Table 2: *General properties of Polyvinyltoluene (PVT) scintillators (the second and third columns correspond to the components of NE102A plastic). From [Suff88, Bicr99].*

Material	Polyvinyltoluene (PVT)	P-Therphenyl	Popop
Use	Polymer base	Primary activator	"WLS"
λ of peak emission (nm)	312	340	410
Decay Time τ (ns)	14	0.95	1.4
Quantum efficiency	7%	93%	93%
Density (g/cm^3)	1.032		
Z/A	0.541		
Radiation length (cm)	42.5		
Nuclear Int. length (cm)	79.0		
$(dE/dx)_{min}$ (MeV/cm)	2.02		
Refractive Index	1.58		
ΔL/ΔT (%/°C at 60°)	95% of that at +20°C; (independent of T from -60°C to +20°C)		
Atomic Ratio, H:C	≈ 1.1		
Coeff. linear expansion	$7.8 \cdot 10^{-5}$ (below 65°C)		
Solubility	In aromatic solvents chlorine, acetone, etc. Insoluble in water, dilute acids, lower alcohols silicone fluid, grease and alkalis.		

Table 3: *Properties of the PVT-based scintillators used in this experiment. From [Suff88, Kirk88, Bour94, Bicr99]. * BC-408 is the current commercial name for former BC-446 [Bicr99]. ** NE115 is identical to current BC-444 [Bicr99].*

	NE102A(BC-400)	BC-446*	NE115**
Light Output (% Anthracene)	65	64	41
Wavelength of Max. Emission (nm)	423	425	428
Rise time (ns)	0.9	0.9	19.5
Decay time (ns)	2.4	2.1	179.7
Pulse width (FWHM, ns)	2.7	≈ 2.5	171.9
Light attenuation Length (cm)	160	210	
# of H Atoms per cm^3 ($\times 10^{22}$)	5.23	5.23	5.25
# of C Atoms per cm^3 ($\times 10^{22}$)	4.74	4.74	4.73
Atomic Ratio H:C	1.103	1.104	1.109
# of e^- per cm^3 ($\times 10^{23}$)	3.37	3.37	3.37

with τ_1 = 0.4 - 0.7 μs and τ_2 = 7.0 $\pm$ 0.5 μs . The value of τ_1 depends on the specific ionization of the charged particle (e.g. τ_1 = 0.4 μs for 4.8 MeV α particles, and τ_1 = 0.7 μs for electrons), the value of τ_2 is independent, and the ratio I_1/I_2 depends on the type of particle (e.g. $I_1/I_2 \approx 1$ for electrons and $I_1/I_2 \approx 3$ for α's). The advantage of two-component inorganic scintillators with respect to the phoswich detectors (see next Section) is that the range of energies of application is very large since they constitute a homogeneous detector.

The usual method of identification consist thus in plotting the value I_1, integrated e.g. within 0.3 to 0.8 μs, as a function of I_2 (integrated in a charge integrator e.g. within the interval 1.6 μs to 2.6 μs). Fig. 5.9 of Section 5.5.1, shows such a plot for the isotopic identification of H and He in the Dwarf-Ball modules.

.4.2 Phoswiches

The name "phoswich", standing for "phosphor sandwich", appears in 1952 [Wilk52] to refer to an association of two scintillators 1 and 2 with different constant times but readout by the same photomultiplier (being, thus, necessary that scintillator 2 be transparent to the scintillation light of 1). In the last 10 years, the design and construction of 4π detectors for charged particles produced in high multiplicity heavy-ion reactions at intermediate-energies has boosted the use of large arrays of such phoswich detectors [Suff88]. By measuring (integrating) the intensity of the light output within two appropriately chosen time intervals, one can determine the energies deposited in the two scintillators. Fig. 2 shows a view of the two components of a typical pulse. The thin "fast"component (1-mm thick NE102A scintillator) emits almost all its light within the interval [t0,t1]($<$ 95 ns), whereas the large "slow"component (5-cm thick NE115 scintillator) needs the interval [t0,t2]($\approx$ 300 ns) to emit most of its light. Usually, the first detector is thin enough to allow (most of) the incident particles punch through (acting as a "ΔE detector"). The second scintillator, glued to the back side of the first one, measures the rest of the energy E = $E_{tot} - \Delta E$.

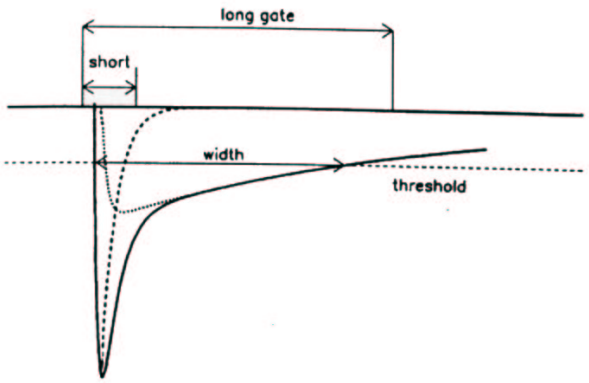

Figure 2: *Schematic view of the fast (dashed line) and slow (dotted line) pulses of a phoswich detector. The drawn line is the sum of the two signals. The duration of the two integration ("short"and "long") gates and the signal over threshold time are indicated. From [Wiss97].*

In general, the ΔE-E telescope identification technique exploits the different energy deposit (depending on the particle's nature and energy) of an incident particle when it traverses the two different materials of the combined module. This is quantitatively expressed by the Bethe-Bloch formula which can be approximated by:

$$dE/dx \approx \alpha \cdot Z^2 A/E_{tot} \tag{6}$$

Hence, measuring the energy ΔE deposited by a particle inside a first detector, thin enough not to stop the particle, and the remaining energy E left in the subsequent detector, we are capable of knowing the initial energy of the particle ($E_{tot} = \Delta E + E$) and, thus, determine the product ($Z^2 A$). Indeed, the different particles populate different lines in bidimensional ΔE-E plots ("ΔE-E arrays") according to their own $Z^2 A$, allowing to determine the value of this product. If the resolution of the detector is good enough to separate adjacent lines, one can measure the charge and mass of the particle. Several types of ΔE-E arrays for the Dwarf-Ball and Forward Wall detectors have been shown in figures 5.11 and 5.13 respectively.

Appendix 2: Nuclear Bremsstrahlung

Bremsstrahlung, from the classical point of view, is the electromagnetic radiation emitted whenever a charge is accelerated or decelerated. Since nuclei contain protons, photon emission due to bremsstrahlung may in principle occur in any nuclear reaction. In a more general way, nucleon-nucleon bremsstrahlung, $NN \rightarrow NN\gamma$, is the lowest energy elastic process by which a photon is produced in the scattering of two decelerated (pre-scattering) or accelerated (post-scattering) nucleons undergoing the strong interaction[16].

The first photon emission attributed to nucleon-nucleon bremsstrahlung processes, $pp \rightarrow pp\gamma$ and $pn \rightarrow pn\gamma$, was observed in $p+d$ reactions in the 60's [Gott65, Warn65, Koeh67], although high-energy ($E_\gamma \gtrsim 30$ MeV) photon production in proton-nucleus collisions had been already reported somewhat earlier [Wils52, Cohe63, Edgi66]. Since the bremsstrahlung process is sensitive to meson exchange currents as well as to off-shell effects in the nucleon-nucleon interaction, the motivation for such experiments was to constraint the various potential models of the fundamental NN interaction in the low-energy region. However, it appeared that these data could be described by soft-photon calculations that did not include off-shell effects. More recent studies (see e.g. [Shkl97] and references therein) showed that the characteristics patterns of bremsstrahlung are not very sensitive to the different parametrizations of the NN potential and the quality of the experimental data available up to the 90's did not point out to a preferable NN potential. Since the early 90's high-precision few-body bremsstrahlung experiments are being carried out at various laboratories. The present accuracy of the data [Huis99, Mess99] has been improved and allows to identify the higher order effects of the process.

Nuclear bremsstrahlung in collisions between nuclei was observed for the first time around 1984 [Gros84, Gros84b, Bear85, Gros85]. As described in Section 3.2.1, the measurements of the photon spectra and angular distributions, the photon source velocity as well as the impact-parameter dependence of the photon multiplicity, indeed suggested that hard-photons, conventionally defined as photons with $E_\gamma > 30$ MeV, originate from bremsstrahlung in independent proton-neutron collisions $pn \rightarrow pn\gamma$ [Nife89, Nife90].

All theoretical (microscopical or statistical) approaches willing to describe hard-photon production in heavy-ion collisions, require the microscopic nucleon-nucleon-γ cross-section as a basic ingredient. Unfortunately, as mentioned above, experimental $NN\gamma$ data are scarce due to several intrinsic difficulties of the process[17] and, thus, a parametrization of the cross-section based exclusively on experimental data and covering the complete range of γ energies and angles for all initial and final nucleon momenta is not (yet) available. Therefore, the models rely on a theoretical prediction of the elementary $NN\gamma$ bremsstrahlung process. In the last years several parametrizations of this fundamental cross-section have been proposed within different approaches:

[16] Usually one just considers elastic NN collisions in which (at least) one of the colliding nucleons is a proton, i.e. processes $pp \rightarrow pp\gamma$ and $pn \rightarrow pn\gamma$, the process $nn \rightarrow nn\gamma$ (proceeding, in a field-theoretical framework, through charged currents) has a vanishingly small cross-section.

[17] The measurement of the double differential cross-section of the three-particle final state needs the coincident measurement of angles and energies of the two outgoing nucleons and of the photon in a wide range of values. Such measurements need large acceptance detectors which have not been available until very recently (e.g. COSY, TAPS+SALAD).

- **Classical electrodynamics**: The $pn\gamma$ cross-section is derived from the dipole approximation for the radiation emitted in the collision of a non-relativistic particle with a fixed hard sphere [Jack75]. This double differential cross-section reads (see next Section):

$$\frac{d^2\sigma_{pn\to pn\gamma}}{dE_\gamma d\Omega_\gamma} = \frac{e^2}{4\pi}\frac{\sigma_{pn}}{4\pi^2}\frac{\beta^2}{E_\gamma}\left(\frac{2}{3}+\sin^2\theta_\gamma\right) \tag{1}$$

  where β denotes the velocity of the nucleons in the nucleon-nucleon CM frame and σ_{pn} the angle-integrated elastic *pn* cross-section. Such classical expression has been used for many years as e.g. in the works of [Baue86, Khoa91, Wang94].

- **Detailed balance** from the reverse process $\gamma d \to pn$: Detailed balance has been used [Bona88, Praka88, Herr88, Oblo89] to invert the measured cross-sections for the absorption of photons of E_γ = 30 - 150 MeV by nuclei. This process is well described by the quasideuteron model [Lev79] which assumes that photoabsorption proceeds via disintegration of proton-neutron pairs in the nucleus. The phenomenological angle-integrated quasideuteron cross-section reads:

$$\frac{d\sigma_{pn\to d\gamma}}{dE_\gamma} = \frac{K\,(E_\gamma - 2.226)^{2/3}}{E_\gamma^3}\,e^{-60[\mathrm{MeV}]/E_\gamma} \tag{2}$$

- **Potential** or **Covariant** (meson-exchange) models: Equation (1) neglects meson exchange effects which substantially modify the $pn\gamma$ cross-section [Brow73, Neuh87]. Taking into account the contributions of internal (meson-exchange) diagrams, several angle-integrated (assuming isotropic emission in the *NN* center-of-mass frame) energy differential cross-section for $pn\gamma$ bremsstrahlung have been proposed and used in the literature: Nakayama [Naka89, Pins89, Fabr90], Schäfer [Scha91, Cass90], Danielewicz [Gan94], or classical-modified [Russo94] parametrizations.

In the next two sections we derive respectively the classical and the covariant expressions for the elementary $NN\gamma$ bremsstrahlung cross-sections commonly used in the studies of hard-photon production in heavy-ion reactions.

.1 Classical $NN\gamma$ Bremsstrahlung cross-section

Bremsstrahlung emission in nucleon-nucleon collisions ($pp \to pp\gamma$ and $pn \to pn\gamma$) can be described within classical electrodynamics [Jack75] in terms of the deceleration or acceleration of one (two) proton(s). The energy radiated by the accelerated proton(s) per unit frequency and unit solid angle is expressed in terms of the vector potential $\vec{A}_k(\omega,\theta)$ [Nife89]:

$$\frac{d^2I}{d\omega d\Omega_\gamma} = \frac{e^2}{4\pi^2 c}\left(\sum_{k=1,2}\vec{A}_k(\omega,\theta)\right)^2 \tag{3}$$

$$\text{where}\quad \vec{A}_k(\omega,\theta) = Z_k\int_\infty^\infty \frac{d}{dt}\left[Z\cdot\frac{\vec{n}\times(\vec{n}\times\vec{\beta})}{1-\vec{n}\cdot\vec{\beta}}\right]\cdot e^{i\omega(t-\vec{n}\cdot\vec{r}(t)/c)}dt \tag{4}$$

Here $Z_k = 1$, $\vec{\beta}_k$ and $\vec{r}_k(t)$ are the charge, and the (time-dependent) velocity and position of the proton(s), and $\vec{n}$ the direction of the emitted photon. Thus each proton contributes to the cross section of the process with the following amplitude[18]:

$$\int \frac{d}{dt}\left[Z \cdot \frac{\vec{n}\times(\vec{n}\times\vec{\beta})}{1-\vec{n}\cdot\vec{\beta}}\right] \cdot e^{i\omega(t-\vec{n}\cdot\vec{r}(t)/c)}dt \approx \tag{5}$$

$$Z \cdot \frac{\vec{n}\times(\vec{n}\times\vec{\beta}(t))}{1-\vec{n}\cdot\vec{\beta}(t)} \tag{6}$$

In the "sudden approximation"or "low-energy approach", the change in $\vec{\beta}$ is considered to be instantaneous, therefore the phase term of (5) is ignored, resulting in equation (6). In the general case when two protons collide, both contribute with amplitude (6) before and after the scattering process, resulting in four amplitudes. The intensity per frequency and solid angle is then given by:

$$\frac{d^2I}{d\omega d\Omega_\gamma} = \frac{e^2}{4\pi^2 c}\left|\sum_{k=1,2}\left[\frac{\vec{n}\times(\vec{n}\times\vec{\beta}_f^k)}{1-\vec{n}\cdot\vec{\beta}_f^k} - \frac{\vec{n}\times(\vec{n}\times\vec{\beta}_i^k)}{1-\vec{n}\cdot\vec{\beta}_i^k}\right]\right|^2 \tag{7}$$

where $\vec{\beta}_i^k$ and $\vec{\beta}_f^k$ are the velocity of proton k before and after the collision respectively.

The probability P to observe a photon of energy E_γ per interaction is related to the intensity per frequency ($dI = E_\gamma dP$ and $\hbar\omega = E_\gamma$) according to:

$$\frac{d^2I}{d\omega d\Omega_\gamma} = \hbar E_\gamma \frac{d^2P}{dE_\gamma d\Omega_\gamma} \tag{8}$$

From eqs. (7) and (8) and assuming that, since the scattering is nearly isotropic, the interference between both ingoing and outgoing amplitudes of (7) averages out in an inclusive measurement, a general formula can be derived for the photon-production probability per unit energy and solid angle in a nucleon-nucleon collision:

$$\frac{d^2P}{dE_\gamma d\Omega_\gamma} = \frac{\alpha}{4\pi^2 E_\gamma}\left(< F(\beta_f, \theta_\gamma^{'}) > + F(\beta_i, \theta_\gamma)\right), \tag{9}$$

with

$$F(\beta, \theta_\gamma) = \left(\sum_{k=1,2}\left[\frac{\vec{n}\times(\vec{n}\times\vec{\beta}^k)}{1-\vec{n}\cdot\vec{\beta}^k}\right]\right)^2 \tag{10}$$

where $\alpha = e^2/\hbar c$ and where, since the direction of $\vec{\beta}_f$ is random with respect to $\vec{\beta}_i$, the outgoing term $F(\beta_f, \theta_\gamma^{'})$ in (7) has been averaged over the angle of the photon $\theta_\gamma^{'}$ with respect to the outgoing proton.

In the center-of-mass frame, $A_1\beta_i^1 = -A_2\beta_i^2$ and $A_1\beta_f^1 \approx -A_2\beta_f^2$ (β^1 is the velocity of the beam particle). With $\beta_i = \beta_i^1$ and $\beta_f = \beta_f^1$, the following photon production probabilities have been obtained for proton-neutron and proton-proton bremsstrahlung

[18] In this section, the discussion follows closely that of [Wils95, Hoef99].

[Wils95, Hoef99]:

$p+n \rightarrow p+n+\gamma$:

$$\begin{aligned} F_{pn\gamma}(\beta,\theta) &= \frac{\beta^2 \sin^2\theta}{(1-\beta\cos\theta)^2} \\ \frac{d^2P_{pn\gamma}}{dE_\gamma d\Omega_\gamma} &\approx \frac{\alpha}{4\pi^2 E_\gamma}\left(\frac{2}{3}\beta_f^2+\beta_i^2\sin^2\theta\right) \end{aligned} \tag{11}$$

$p+p \rightarrow p+p+\gamma$:

$$\begin{aligned} F_{pp\gamma}(\beta,\theta) &= \frac{4\beta^4 \sin^2\theta\cos^2\theta}{(1-\beta^2\cos^2\theta)^2} \\ \frac{d^2P_{pp\gamma}}{dE_\gamma d\Omega_\gamma} &\approx \frac{\alpha}{4\pi^2 E_\gamma}\left(\frac{2}{15}\beta_f^4+\beta_i^4\sin^2\theta\cos^2\theta\right) \end{aligned} \tag{12}$$

In both cases the classical $NN\gamma$ bremsstrahlung production has a $1/E_\gamma$ energy dependence (however, it has to be noted that β_f is also dependent on E_γ). Although expressions (11) and (12) contain an isotropic component associated with the velocity β_f of the outgoing proton, the photon emission from proton-proton collisions is of quadrupole character ($\sin^2\theta\cos^2\theta$) and therefore more suppressed as compared with the ($\sin^2\theta$) dipolar radiation from proton-neutron collisions. Moreover, the probability for $pp\gamma$ bremsstrahlung is, to first approximation, a factor β^2 smaller than that of the $pn\gamma$ process. The contribution from proton-proton bremsstrahlung can be, therefore, basically neglected in nucleus-nucleus collisions at intermediate-energies.

Finally, the classical double-differential bremsstrahlung $pn\gamma$ cross-section is obtained from the photon-production probability (11) by:

$$d\sigma_\gamma = \sigma_{el}\, dP \Longrightarrow \frac{d^2\sigma_{pn\gamma}}{dE_\gamma d\Omega_\gamma} \approx \frac{\alpha}{4\pi^2 E_\gamma}\sigma_{el}\left(\frac{2}{3}\beta_f^2+\beta_i^2\sin^2\theta\right) \tag{13}$$

with σ_{el} being the angle integrated elastic pn cross-section.

The classical angle-integrated energy spectrum of bremsstrahlung photons issuing from a $pn\gamma$ collision at E_p = 200 MeV bombarding energy is shown as a dashed line in fig. 1.

.2 Covariant $NN\gamma$ Bremsstrahlung cross-section

The classical equation (13) is a non-relativistic approximation of the "true"$pn\gamma$ cross-section and hence only valid, at best, in the photon long-wavelength limit. Jackson's formula particularly neglects several quantal effects which can be important such as, e.g., the contribution of internal radiation from virtual (charged) pion exchange between the colliding nucleons. This contribution allows neutrons and protons to exchange their identity during the collision leading to an increase of the pn scattering angular distribution

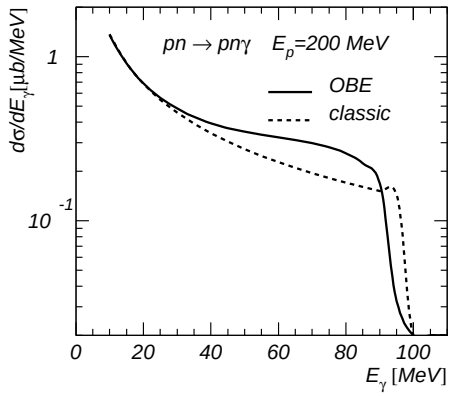

Figure 1: *Bremsstrahlung photon spectrum for a pnγ collision at K_{beam} = 200 MeV according to the classical soft-photon formula (13) (dashed line) and to the covariant expression (15) (solid line). From [Schu97].*

at backwards angles and to an enhancement of the highest energy hard-photon production [Russo94] (see fig. 1, solid line). A consistent calculation that takes relativity, quantum mechanics and exchange currents into account can be performed using Feynman's diagrammatical method. The relevant Feynman graphs for photon bremsstrahlung in *pn* scattering are shown in figure 2. Such calculation requires the determination of the nucleon-nucleon scattering amplitude (T-matrix or G-matrix) in terms of a proper relativistic and gauge-invariant effective meson-exchange (OBE) model for the nucleon-nucleon interaction (see Section 1.4). In a quantal description of the photon production, the cross-section is calculated from [Itzy85]:

$$\frac{d\sigma_\gamma}{dE_\gamma d\Omega_\gamma d\Omega_q} = \frac{m_N^4}{4|\vec{p}_p|(2\pi)^5 E_p} \cdot \frac{E_\gamma |\vec{q}|^2 |T_\gamma|^2}{2\,|E_n'(q - E_\gamma \cos\theta) + E_p'(q + E_\gamma \cos\theta)|} \qquad (14)$$

where E_p, E_p', and E_n' are the initial and final energies of the proton and the final energy of the neutron respectively, $\vec{q}$ is the relative momentum between the proton and the neutron, and $|T_\gamma|^2$ is the transition amplitude of the $pn\gamma$ process.

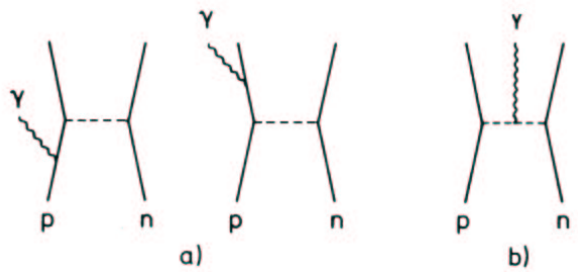

Figure 2: *Feynman diagrams of the pnγ bremsstrahlung process showing the radiation originating from the exchanged charged mesons, internal lines in b), which interferes constructively with the external radiation, diagrams a), accounting for the "classical" bremsstrahlung.*

Schäfer *et al.* [Scha91] have obtained this differential photon cross-section after calculating the matrix elements resulting from a parametrization of the nucleon-nucleon T-matrix in terms of OBE amplitudes which includes over 10 mesons [Horo87] and provides a good fit to elastic nucleon-nucleon scattering data for 100 - 400 MeV laboratory energies. This expression agrees with the measurements of the differential gamma spectrum produced in neutron-proton bremsstrahlung with a neutron beam of 170 MeV average energy [Male91]. This so-called "Schäfer parametrization"has been thus very often used as the elementary photon production cross-section in BUU transport calculations for particle production in nucleus-nucleus reactions [Cass90]. In this thesis we have employed the following useful analytical representation of the differential cross-section $d\sigma/dE_\gamma$ as a function of the invariant energy $\sqrt{s}$ of the nucleon-nucleon system [Cass90]:

$$\frac{d\sigma}{dE_\gamma} = \frac{1}{E_\gamma}\sqrt{1-E_\gamma/E_\gamma^{max}}\, f(E_\gamma, K_{cm}) \quad (\mu b)\,, \tag{15}$$

with

$$\begin{aligned} f(E_\gamma, K_{cm}) &= a + b\,E_\gamma e^{-c(E_\gamma - d)^2}, \\ a &= 9.74 + 0.037\,K_{cm}, \\ b &= 0.91 - 0.14\arctan(0.045\,K_{cm} - 7.66), \\ c &= 12.365/(18.27 + K_{cm})^{2.38}, \\ d &= 1.5\,K_{cm}, \end{aligned}$$

where K_{cm}(MeV) is the total kinetic energy of the colliding nucleons in their CM system. Figure 1 (solid line) shows the differential bremsstrahlung cross-section obtained with equation (15). From this plot one can grossly outline the main features of this elementary $d\sigma_{pn\gamma}/dE_\gamma$ cross-section:

- It shows the typical $1/E_\gamma$ behaviour of the semiclassical limit (13) only for fairly low γ-energies, $E_\gamma \leq 0.2\,E_\gamma^{max}$.
- The cross-section remains rather constant for a wide range of photon energies, $E_\gamma \approx (0.2 - 0.9)\,E_\gamma^{max}$.
- It sharply drops near $E_\gamma^{max} = (E_p + E_n)^2 - 2\,m_N^2/[2\,(E_p + E_n)]$ (the maximum energy available in the NN center-of-mass system) and does not show the stronger enhancement obtained for photon energies near E_γ^{max} typical of other covariant models[19] (see e.g. [Naka89]).

Finally, integrating the differential yield over energies above E_γ = 30 MeV in the laboratory-system one obtains the hard-photon emission probability (dotted-dashed curve) displayed in fig. 3 as a function of the bombarding energy of the proton-neutron system.

[19] Although this effect is due to an improper description of very low energy resonances in the *pn*-channel, it is claimed [Scha91] that such resonances do not survive in the nuclear medium encountered in heavy-ion reactions.

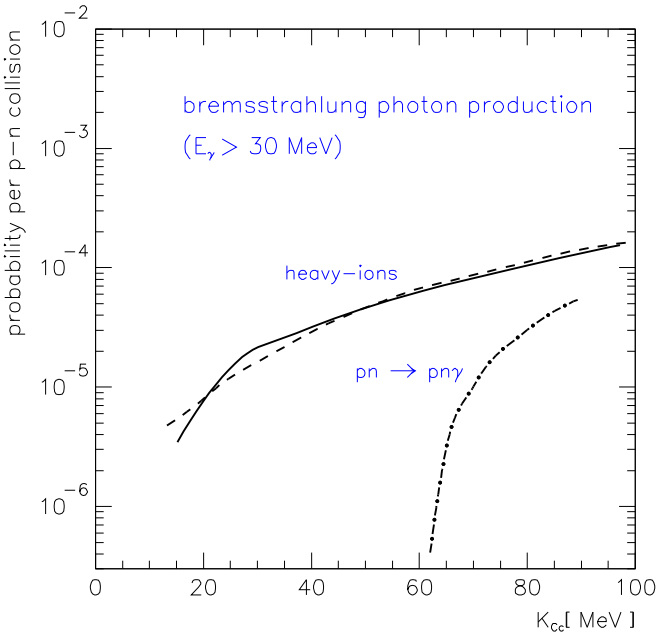

Figure 3: *Hard-photon emission probability per proton-neutron collision versus the (Coulomb-corrected) bombarding energy per nucleon in: 1) nucleus-nucleus collisions (solid and dashed lines, obtained within BUU and DCM calculations respectively), and in 2) free proton-neutron collisions (dotted-dashed line). Both curves have been obtained using the Schäfer parametrization of the elementary pnγ cross-section, eq. (15). Adapted from [Schu97].*

Appendix 3: The nuclear Equation-of-State

The notion of equation of state (EoS) is central in statistical physics since it allows to establish a relation linking the state variables characterizing a certain system at thermodynamical equilibrium. If the microscopic properties of a system are known along with the statistics of the particles, one can calculate the partition function of the system. From one of the "state functions"or "thermodynamical potentials"of the system written in terms of its proper variables like ε(S,N), F(T,V,N) or μ(T,P), all other standard thermodynamical variables can be straightforwardly obtained by simple differentiation. The so-called "thermodynamical"equation of state (EoS) is the relation between the pressure, the density and temperature, P = P(ρ,T), and it is essentially given by the derivative of the internal energy per nucleon of the system, ε = E/A, with respect to the density at constant entropy S:

$$P(V,T) = -\left(\frac{\partial E}{\partial V}\right)_S = +\frac{N}{V^2}\left(\frac{\partial E}{\partial \rho}\right)_S \Longrightarrow \quad (1)$$

$$P(\rho,T) = \rho^2\left(\frac{\partial \varepsilon}{\partial \rho}\right)_S \quad (2)$$

When dealing with nuclear matter properties, the states are usually characterized by two (macro)canonical variables: the density ρ and the temperature T. So starting with the definition of the internal energy per nucleon ε as a function of ρ and T, the nuclear EoS is simply defined as the functional dependence $\varepsilon = \varepsilon(\rho,T)$ which is usually called the "caloric"equation of state. We shall now turn our attention to this "caloric EOS" in a schematic way (within a Fermi-Dirac approach for the kinetic energy term, and a Skyrme interaction for the nuclear mean-field potential).

.1 EoS of cold nuclear matter

At T = 0 nuclear matter can be treated as a degenerate Fermi gas, and one can divide its total *internal* energy per nucleon, ε, as a sum of a (Fermi) kinetic energy ε_k and a potential nuclear mean field U which, in a simple ansatz, both depend only on the nuclear density ρ:

$$\varepsilon(\rho, T=0) = \varepsilon_k(\rho) + U(\rho) \quad (3)$$

The first term, the *average* Fermi kinetic energy per nucleon, reads[20]:

$$\varepsilon_k(\rho) = \frac{3}{5}\varepsilon_F(\rho) = \frac{3}{5}\frac{p_F(\rho)^2}{2m_N} \quad \text{with } p_F(\rho) = \hbar\left(\frac{3\pi^2}{2}\rho\right)^{1/3} \quad (4)$$

In the ground-state: $p_F \approx 265$ MeV/c, $\varepsilon_F \approx 38A$ MeV and $\varepsilon_k \approx 23A$ MeV.

The second term of eq. (3), the nuclear mean field potential $U(\rho)$, can be written effectively (neglecting any momentum dependence of the nuclear force) as a local density-dependent force of the Skyrme type:

[20] At normal density, $\rho_0 = 0.16$ fm^{-3}, nucleons are non-relativistic, and the Fermi energy and momentum can be related by $\varepsilon_F \approx p_F^2/2m_N$.

$$U(\rho) = \alpha \left(\frac{\rho}{\rho_0}\right) + \beta \left(\frac{\rho}{\rho_0}\right)^{\gamma} \tag{5}$$

The constants α and β are adjusted to reproduce the ground state properties of nuclear matter[21], $\varepsilon(\rho_0 = 0.16\ \mathrm{fm}^{-3}, T = 0\ \mathrm{MeV}) = -16A$ MeV, and γ is related to the nuclear incompressibility modulus κ_∞ which measures the resistance of nuclear matter against compression around the saturation point[22]. In thermodynamics the (adiabatic) compressibility K is defined as the derivative of the density with respect to the pressure at constant entropy:

$$K = \frac{1}{\rho}\left(\frac{\partial \rho}{\partial P}\right)_S \tag{6}$$

The incompressibility modulus κ is the inverse of the compressibility K and in nuclear physics is customarily defined as: $\kappa_\infty \equiv 9/(\rho K) = 9\,(\partial P/\partial \rho)_S$. Equivalently, κ can be also defined by the change in energy of a nucleus as a reply to a change in its radius R [Peil94]:

$$\kappa = R^2 \left(\frac{\partial^2 \varepsilon}{\partial R^2}\right) = 9\left[\frac{P}{\rho} + \rho^2 \left(\frac{\partial^2 \varepsilon}{\partial^2 \rho}\right)\right]_{T,N} \tag{7}$$

At $\rho = \rho_0$, the pressure vanishes by definition and the incompressibility constant reads:

$$\kappa_\infty = 9\rho_0^2 \left(\frac{\partial^2 \varepsilon}{\partial \rho^2}\right)_{\rho=\rho_0} \tag{8}$$

Usually, it is said that the EoS is "soft"[23] if $\kappa_\infty \approx 200$ MeV (i.e. the fundamental *NN* scattering is more attractive-like) and "hard"if $\kappa_\infty \approx 400$ MeV (i.e. the elementary *NN* scattering is more repulsive-like). For κ_∞ = 200 MeV ("soft"EoS), α = -178, β = 139 and γ = 1.17 in eq. (5). Alternatively, for κ_∞ = 400 MeV ("hard"EoS), α = -62, β = 23 and γ = 2.

Considering eqs. (3), (4) and (5), one can therefore express the EoS of cold nuclear matter as:

$$\varepsilon(\rho, T=0) = \frac{3}{5}\frac{\hbar^2}{2m_N}\left(\frac{3\pi^2}{2}\rho\right)^{2/3} + \alpha\left(\frac{\rho}{\rho_0}\right) + \beta\left(\frac{\rho}{\rho_0}\right)^{\gamma} \tag{9}$$

.2 EoS of moderately hot and compressed nuclear matter

So far we have dealt with the EoS of cold nuclear matter. The temperature of the system is the second thermodynamical variable of importance for the equation of state. In a general

[21] The density dependent repulsive term in eq. (5) must appear with a higher power of ρ than the attractive part, i.e. $\gamma > 0$, so that the nuclear system does not collapse.

[22] It is important to stress that κ_∞ gives information on the EoS dependence of ρ at the neighborhood of the saturation point (largest curvatures implying that more energy is necessary for compression) but does not give any information about nuclear matter at higher densities.

[23] As a matter of fact, there seems to be strong evidence in favour of a "soft"but *momentum-dependent* EoS for nuclear matter, but we will not consider this complication here.

way, moving away from the saturation point in the density-temperature plane, we can decompose the internal energy of a nuclear system, $\varepsilon(\rho,T)$, in its ground-state energy ε_0 (the *bulk* or *volume* term in the binding energy per nucleon at zero temperature):

$$\varepsilon_0 \equiv \varepsilon(\rho=\rho_0,T=0) = \varepsilon_k(\rho_0)+U(\rho_0) = 23A \text{ MeV} - 39A \text{ MeV} = -16A \text{ MeV},$$

and in an excitation energy $\varepsilon^\star$. Namely, one can write:

$$\varepsilon(\rho,T) = \varepsilon_0 + \varepsilon^\star(\rho,T) \tag{11}$$

The excitation energy $\varepsilon^\star$ (whose maximum theoretical value in a heavy-ion collision corresponds to the total energy available in the nucleus-nucleus center-of-mass) can be furhter simplified as the sum of a pure "compressional"part $\varepsilon^\star_{comp}$ (due to a variation of the density at zero temperature) and a "thermal"one $\varepsilon^\star_{th}$ (only depending on the temperature), i.e.:

$$\varepsilon^\star(\rho,T) = \varepsilon^\star_{comp}(\rho) + \varepsilon^\star_{th}(T) \tag{12}$$

Let's study separately the two terms of equation (12):

- The compressional energy $\varepsilon^\star_{comp}$ corresponds to the coherent movement of the nucleons in the system. It consists of a kinetic energy term stemming from the (density-dependent) Fermi motion, $\varepsilon_F \sim \rho^{2/3}$, and the "actual"compressional energy, $\Delta U = U(\rho) - U(\rho_0)$, which is the difference of the nuclear mean field potential energy at the densities ρ and ρ_0 respectively. It can be written explicitly as: $\varepsilon^\star_{comp}(\rho) = \Delta U(\rho) + \varepsilon_k[(\rho/\rho_0)^{2/3} - 1]$, where U denotes the nuclear mean field potential energy and $\varepsilon_k \approx 23A$ MeV is the average Fermi energy per nucleon in the ground state. One commonly uses a simple functional form for $\varepsilon^\star_{comp}$ which is quadratic on the density and contains the incompressibility modulus [Stoe86]:

$$\varepsilon^\star_{comp}(\rho) = \frac{\kappa_\infty}{18}\left(1-\frac{\rho}{\rho_0}\right)^2 \tag{13}$$

  Thus, the equation of state for T = 0 and $\rho \neq \rho_0$ (i.e. no thermal effects) can be written:

$$\varepsilon(\rho,T=0) = \varepsilon_0 + \frac{\kappa_\infty}{18}\left(1-\frac{\rho}{\rho_0}\right)^2 \tag{14}$$

- The thermal energy $\varepsilon^\star_{th}$(T) corresponds to the random movement of the nucleons inside the system and consists of the kinetic energy above the degenerate Fermi gas. For moderately excitations energies ($\varepsilon^\star_{th} < 3A$ MeV), the thermal excitation energy is related to the temperature by the Fermi-gas relation (setting the Boltzmann constant $k_B \equiv 1$):

$$\varepsilon^\star_{th}(T) = aT^2 \quad \text{with } a = 1/8 - 1/12 \tag{15}$$

  The formal derivation of (15) as well as the thermodynamical properties of a general Fermi gas can be found e.g. in [Path77]. In the nuclear case, relation (15) can be

simply derived for a nucleus of mass A at the temperature T within a Fermi model description [Sura90]. In this independent-particle model, the (discrete) energy level density of a particle inside a nucleus (i.e. the number of states with energy between E and $E + dE$) is defined as:

$$d(E) = \sum_{\nu} \delta(E - E_{\nu}) \tag{16}$$

The total kinetic energy of the system is then given by the integral:

$$E = \int_0^{\infty} E' \frac{1}{1 + e^{[E' - E'_F(T)]/T}} d(E') \, dE' \tag{17}$$

where $E_F(T)$ is the Fermi energy of the system. Expression (17) is an example of the typical Fermi-Dirac integrals commonly found in the statistical theory of Fermi-Dirac systems and not readily calculable [Path77]. In the limit of low temperatures, however, the Fermi-Dirac factor can be written as:

$$\frac{1}{1 + e^{[E - E_F(T)]/T}} \approx \theta(E - E_F(T)) - \frac{\pi^2}{6} T^2 \delta'(E - E_F(T)) + \ldots \tag{18}$$

where θ is the Heaviside step function and δ' the derivative of the Dirac delta function. Bringing expression (18) into eq. (17) (and replacing $d(E)$ by an equivalent "smooth"function), one obtains a development of the kinetic energy of the system for low temperatures which reads, to order T^2 [Sura90]:

$$E = \int_0^{E_F(T=0)} E' \, dE' + \frac{\pi^2}{6} d(E_F(T=0)) \, T^2 + \ldots \tag{19}$$

Since $E = E(T=0) + E^{\star}_{th}$, we can easily identify the second term of eq. (19) as the thermal excitation energy of the nucleus, written in the well-known form:

$$E^{\star}_{th} \approx a T^2 \approx \frac{\pi^2}{6} d(E_F(T=0)) \, T^2 \tag{20}$$

This equation defines the so called "level density parameter"a characterizing the single particle model used to describe the nucleus, and indicates that as T increases, the Fermi nuclear liquid is excited into low lying excited states whose level density[24] grows as $\rho(\varepsilon) \sim \exp(2\sqrt{aE})$ [Beth37]. In a Fermi gas degenerated in spin and isospin, a amounts to:

$$a = \frac{\pi^2}{4} \frac{A}{E_F(T=0)} \approx A/15 \ \text{MeV}^{-1} \tag{21}$$

[24]The level density $d(E)$ defined by eq. (16) counts the number of levels per unity of energy for a one-body theory, whereas the density of states $\rho(E)$ gives the number of states accessible as a function of the total energy of the nucleus.

to be compared with the experimentally measured values a = A/8 - A/12 MeV^{-1}. Microscopic calculations [Sura85] have shown that the value of $E^{\star}_{th}$ given by equation (20) is very close to the self-consistent Hartree-Fock thermal excitation energy and hence can be compared to experimental energies. The same calculations have shown that the range of validity of this set of equations can be extended with confidence up to $\varepsilon^{\star} \approx 3A$ MeV with a = A/8 - A/12. This allows to relate experimentally the measured values of $\varepsilon^{\star}$ to the actual temperature of an (slightly) excited nucleus via $T \approx \sqrt{10\varepsilon^{\star}_{th}}$.

The EoS for $\rho = \rho_0$ (i.e. no compression effects) and T < 4 MeV reads finally:

$$\varepsilon(\rho_0, T < 4 \text{ MeV}) \;=\; \varepsilon_0 + aT^2 \tag{22}$$

In summary, the general form of the EoS of nuclear matter at *low* temperatures and densities can be written (see e.g. [Chas97]):

$$\begin{aligned} \varepsilon(\rho,T) &= \frac{3}{5}\varepsilon_F(\rho) + \frac{\pi^2}{4}\frac{T^2}{\varepsilon_F(\rho)} + U(\rho) \\ &= \frac{3}{5}\varepsilon_F(\rho)\left[1 + \frac{5\pi^2}{12}\left(\frac{T}{\varepsilon_F(\rho)}\right)^2\right] + \alpha\left(\frac{\rho}{\rho_0}\right) + \beta\left(\frac{\rho}{\rho_0}\right)^{\gamma} \end{aligned} \tag{23}$$

with $\varepsilon_F(\rho) = \frac{\hbar^2}{2m_N}\left(\frac{3\pi^2}{2}\rho\right)^{2/3}$. Having specified the internal energy, one can now determine any other thermodynamic function. The specific heat $c_V = (\partial\varepsilon/\partial T)_V$ and entropy $s = \int^T c_V/T' dT'$ per nucleon coincide in the approximation to order T^2 of the EoS given by (23):

$$c_V(\rho,T) = s(\rho,T) = \frac{\pi^2}{2}\left[\frac{T}{\varepsilon_F(\rho)}\right] \tag{24}$$

The partition function can be determined from the (Helmholtz) free energy ($F = E - ST$):

$$Z = e^{-F/T} = e^{(sT-\varepsilon)/T} = e^{\left\{-\frac{3}{5}\varepsilon_F(\rho) - U(\rho) + \frac{\pi^2}{4}\left[\frac{T^2}{\varepsilon_F(\rho)}\right]\right\}} \tag{25}$$

From this partition function, Z, it is easy to determine the pressure and compressibility[25] of nuclear matter described by the equation-of-state (23):

[25]Of course P and κ_∞ can be also straightforwardly obtained from eqs. (2) and (8) respectively.

$$
\begin{aligned}
P(V,T) &= T\left[\left(\frac{\partial}{\partial V}\right)\ln Z\right]_V = -\rho^2 T\left[\left(\frac{\partial}{\partial \rho}\right)\ln Z\right]_\rho \Longrightarrow \\
P(\rho,T) &= \frac{2}{5}\rho\varepsilon_F(\rho)+\frac{\pi^2}{6}\rho\frac{T^2}{\varepsilon_F(\rho)}+\frac{\alpha}{\rho_0}\rho^2+\gamma\beta\rho_0\left(\frac{\rho}{\rho_0}\right)^{\gamma+1} \\
&= \frac{2}{5}\rho\varepsilon_F(\rho)\left[1+\frac{5\pi^2}{12}\left(\frac{T}{\varepsilon_F(\rho)}\right)^2\right]+\frac{\alpha}{\rho_0}\rho^2+\gamma\beta\rho_0\left(\frac{\rho}{\rho_0}\right)^{\gamma+1} \qquad (26) \\
\kappa_\infty(\rho,T) &= 9\left(\frac{\partial P}{\partial \rho}\right)_S \\
&= 6\varepsilon_F(\rho)+\frac{5\pi^2}{2}\frac{T^2}{\varepsilon_F(\rho)}+18\frac{\alpha}{\rho_0}\rho+9(\gamma+1)\gamma\beta\left(\frac{\rho}{\rho_0}\right)^{\gamma} \qquad (27)
\end{aligned}
$$

.3 EoS of hot nuclear matter

At high temperatures (higher than the chemical potential value, i.e. than the Fermi energy at a given density, but still below the meson and particle-antiparticle production thresholds) and/or at low densities, the hadronic properties of nuclear matter can be considered that of an ideal Maxwell-Boltzmann gas (i.e. we expect that nuclei vaporize into individuals nucleons at $\varepsilon^\star >> \varepsilon_0$, where $\varepsilon_0 = 8A$ MeV is the empirical binding energy per nucleon). The simplest ansatz for the internal energy is given, therefore, by the classical *ideal* (i.e. *non-interacting*: $\varepsilon = \varepsilon_k$) gas limit[26]:

$$\varepsilon(T) = \frac{3}{2}T \qquad (28)$$

The rest of thermodynamical properties of high-temperature nuclear matter are, then, those of the well-known Maxwell-Boltzmann gas:

$$
\begin{aligned}
c_V &= \frac{3}{2} && (29)\\
P &= \rho T && (30)\\
\kappa_\infty &= 9\rho T && (31)\\
s &= \ln\left\{e^{5/2}\frac{\rho}{\lambda_T^3}g_{s,i}\right\} && (32)
\end{aligned}
$$

In expression (32) the entropy per nucleon is given by the Sackur-Tetrode law with $\lambda_T = h/\sqrt{2\pi m T}$, and $g_{s,i}$ is the spin-isospin degeneracy factor.

[26]Formula (28) is actually the asymptotic value for the full non-interacting non-relativistic Fermi gas, i.e. it neglects the influence of the interactions on the thermal energy, but it contains the Fermi degeneracy energy [Stoe86].

Appendix 4: Heavy-ion kinematics formulae

Assuming a projectile nucleus (with charge Z_p, mass A_p and incident kinetic energy K_{lab} below 1A GeV) colliding against a target nucleus (with charge Z_t and mass A_t) at rest in the laboratory system, the following (classical) formulas have been used in this work:

- Interaction radius of the reaction:

$$R_{int}(\text{fm}) \quad = \quad 1.16 \cdot (A_t^{1/3} + A_p^{1/3}) + 2.0$$

- Coulomb "barrier":

$$V_C(\text{MeV}) \quad = \quad e^2 \cdot \frac{Z_t \cdot Z_p}{R_{int}(\text{fm})} \qquad \text{with } e^2 = 1.439976 \text{ MeV fm}$$

- Total reaction cross-section:

$$\sigma_R(\text{mb}) \quad = \quad 10 \cdot \pi \cdot R_{int}^2(\text{fm}) \cdot \left(1 - \frac{V_C(\text{MeV})}{K_{lab}(\text{MeV})}\right)$$

- (Coulomb-corrected) kinetic energy in the laboratory system:

$$K_{Cc}^{lab}(A \text{ MeV}) \quad = \quad \frac{K_{lab}(\text{MeV}) - V_C(\text{MeV})}{A_p}$$

- (Coulomb-corrected) kinetic energy in the nucleus-nucleus system:

$$K_{Cc}^{AA}(A \text{ MeV}) \quad = \quad \mu \cdot \frac{K_{Cc}^{lab}(A \text{ MeV})}{A_{tot}}$$

- Velocity of the beam:

$$\beta_{lab} \quad = \quad \sqrt{\frac{2K_{Cc}^{lab}(A \text{ MeV})}{m_N} + \left(\frac{K_{Cc}^{lab}(A \text{ MeV})}{m_N}\right)^2} \qquad \text{with } m_N = 931.502 \text{ MeV}$$

- Velocity of the nucleus-nucleus center-of-mass:

$$\begin{aligned} \beta_{AA} \quad &= \quad \frac{p_{lab}(\text{MeV})}{E_{Cc}^{lab}(\text{MeV}) + A_t(\text{MeV})} \\ \text{with } p_{lab}(\text{MeV}) \quad &= \quad \sqrt{2K_{Cc}^{lab}(\text{MeV})A_p(\text{MeV}) + K_{Cc}^{lab}(\text{MeV})^2} \\ \text{and } E_{Cc}^{lab}(\text{MeV}) \quad &= \quad K_{Cc}^{lab}(\text{MeV}) + A_p(\text{MeV}) \end{aligned}$$

- Velocity of the nucleon-nucleon center-of-mass:

$$\beta_{NN} \quad = \quad \frac{p_{lab}(A \text{ MeV})}{K_{Cc}^{lab}(A \text{ MeV}) + 2m_N(\text{MeV})}$$

- Grazing angle in the CM and LAB frames:

$$\theta_{gr}^{cm} = 2 \cdot \arctan\left(0.72 \cdot \frac{Z_p Z_t}{R_{int}\sqrt{\mu K_{Cc}^{lab}(\mathrm{MeV}) \cdot (2 - \mu K_{Cc}^{lab}(\mathrm{MeV}))}}\right)$$

$$\theta_{gr}^{lab} = \arctan\left(\frac{\sin\theta_{gr}^{cm}}{\cos\theta_{gr}^{cm} + A_p/A_t}\right)$$

Appendix 5: Dwarf-Ball electronics and pre-trigger logics

Figure 1: *Detailed DB electronics and pre-trigger logics.*

Bibliography

[Abe96] Y. Abe, S. Ayik, P.-G. Reinhard, and E. Suraud. *Phys. Rep.* **275**, 49 (1996).

[Agak98] G. Agakichiev and the CERES-TAPS collaboration. *Eur. Phys. J.* **C4**, 431 (1998).

[Aich86] J. Aichelin and H. Stöcker. *Phys. Lett.* **B176**, 14 (1986).

[Aich87b] J. Aichelin, A. Rosenhauer, G. Peilert, H. Stöcker, and W. Greiner. *Phys. Rev. Lett.* **58**, 1926 (1987).

[Aich91] J. Aichelin. *Phys. Rep.* **202**, 233 (1991).

[Aich94] J. Aichelin and D. Ardouin. *Int. Workshop on Multiparticle Correlations and nuclear reactions*. World Scientific, Nantes, 1994.

[Alar85] Alarja *et al. Nucl. Inst. and Meth.* **A242**, 352 (1985).

[Albe85] S. Albergo *et al. Nuov. Cim.* **A89**, 1 (1985).

[Alm95] T. Alm, E. L. Bratkovskaya, G. Röpke, A. D. Sedrakian, and V. D. Toneev. *Phys. Rev.* **C52**, 1972 (1995).

[Aphe98] L. Aphecetche. PhD thesis, Thèse Université de Caen, 1998.

[Aver94] R. Averbeck, R. Holzmann, A. Schubert, *et al. GSI Sci. Rep.* **80** (1994).

[Aver98] R. Averbeck. In Y. Schutz and H. Löhner, editors, *IV TAPS Workshop Sept. '97*, Ed. Frontières, Paris, Mont Sainte-Odile, 1998.

[Awe92] T. Awes *et al. Nucl. Inst. and Meth.* **A311**, 130 (1992).

[Ayik90] S. Ayik and C. Grégoire. *Nucl. Phys.* **A513**, 187 (1990).

[Bacr95] C. Bacri *et al. Phys. Lett.* **B353**, 27 (1995).

[Bada96] A. Badala *et al. INFN Report* (1996). INFN-BE-96-03.

[Barz96] H. Barz, B. Kämpfer, G. Wolf, and W. Bauer. *Phys. Rev.* **C53**, R553 (1996).

[Bass98] S. Bass, M. Belkacem, M. Bleicher, *et al. Prog. Part. Nucl. Phys.* **41**, 255 (1998).

[Baue86] W. Bauer *et al. Phys. Rev.* **C34**, 2127 (1986).

[Baue95] W. Bauer. *Phys. Rev.* **C51**, 803 (1995).

[Baye85] D. Baye and P. Descouvemont. *Nucl. Phys.* **A443**, 302 (1985).

[Baye92] D. Baye *et al. Nucl. Phys.* **A550**, 250 (1992).

[Bear85] K. Beard *et al. Phys. Rev.* **C32**, 1111 (1985).

[Beau96] L. Beaulieu *et al. Phys. Rev. Lett.* **77**, 462 (1996).

[Beau99] L. Beaulieu *et al. Preprint IUCF 2000* (1999).

[Bene94] D. J. Morrissey, W. Benenson, and W. A. Friedman. *Ann. Rev. Nucl. Part. Sci.* **44**, 27–64 (1994).

[Bert83] G. Bertsch and P. Siemens. *Phys. Lett.* **B126**, 9 (1983).

[Bert83b] G. Bertsch. *Nucl. Phys.* **A400**, 221 (1983).

[Bert88] G. Bertsch and S. D. Gupta. *Phys. Rep.* **160**, 189 (1988).

[Bert96] G. Bertsch and P. Danielewicz. *Phys. Lett.* **B367**, 55 (1996).

[Berth87] R. Bertholet *et al. Nucl. Phys.* **A474**, 541 (1987).

[Beth37] H. Bethe. *Rev. Mod. Phys.* **9**, 69 (1937).

[Beth71] H. Bethe. *Ann. Rev. Nucl. Sci.* **21**, 93 (1971).

[Bicr99] Bicron. *Scintillators Catalog* (1999).

[Bida98] H. Bidar and D. Jou. *Phys. Rev.* **C57**, 2068 (1998).

[Birk64] J. Birks. *The Theory and Practice of Scintillation Counting*. Pergamon Press, Oxford, 1964.

[Biro87] T. Biro *et al. Nucl. Phys.* **A475**, 541 (1987).

[Biza93] G. Bizard *et al. Phys. Lett.* **B302**, 162 (1993).

[Blai80] J. Blaizot. *Phys. Rep.* **64**, 171 (1980).

[Blai95] J. Blaizot. *Nucl. Phys.* **A591**, 435 (1995).

[Bobel95] I. Bobeldijk *et al. Phys. Lett.* **B353**, 32 (1995).

[Bock98] R. Bock and A. Vasilescu. *The Particle Detector Briefbook*. Springer Verlag, 1998.

[Boh91] A. Bohnet *et al. Phys. Rev.* **C44**, 2111 (1991).

[Bona88] A. Bonasera, M. D. Toro, and C. Gregoire. *Nucl. Phys.* **A483**, 738 (1988).

[Bona90] A. Bonasera *et al. Nuovo Cimento* **A103**, 309 (1990).

[Bona94] A. Bonasera, F. Gulminelli, and J. Molitoris. *Phys. Rep.* **243**, 1 (1994).

[Bond85] J. Bondorf. *Nucl. Phys.* **A444**, 460 (1985).

[Bond95] J. P. Bondorf, A. S. Botvina, A. S. Ilinov, I. N. Mishustin, and K. Sneppen. *Phys. Rep.* **257**, 133 (1995).

[Bord99] B. Borderie *et al. Eur. Phys. J.* **A6**, 197 (1999).

[Borg00] N. Borghini *et al. hep-ph/0001284.*

[Borg99] J. Borg, I. Mishustin, and J. Bondorf. *Phys. Lett.* **B470**, 13 (1999).

[Bote90] W. Botermans and R. Malfliet. *Phys. Rep.* **198**, 115–194 (1990).

[Botv95] A. Botvina *et al. Nucl. Phys.* **A584**, 737 (1995).

[Boug97] R. Bougault *et al.* In I. Iori, editor, *XXXV International Winter Meeting on Nucl. Physics*, Università Degli Studi di Milano, Bormio Italy, January 1997.

[Boug99] R. Bougault *et al.* In H. Feldmeier *et al.*, editors, *"Multifragmentation" XXVII Int. Work. on Gross Properties of Nuclei and Nuclear Excitations*, GSI, Hirschegg Austria, January 1999.

[Bour94] C. Bourgeois. In *Ecole Joliot-Curie de Physique Nucléaire 1994*, IN2P3-CNRS, Maubuisson, Sep 1994. IPNO-DRE 95-02.

[Boze98] P. Bozek, P. Danielewicz, K. Gudima, and M. Ploszajczak. *Phys. Lett.* **B421**, 31 (1998).

[Brac89] A. Bracco *et al. Phys. Rev. Lett.* **62**, 2080 (1989).

[Brow73] G. Brown. *Phys. Rev.* **C8**, 1706 (1973).

[Buen88] M. Buenerd. *Comptes Rendus Ecole Joliot-Curie, Sep. 1988*. les Eds. de Physique, 1988.

[Burg91] G. F. Burgio and P. Chomaz. *Nucl. Phys.* **A529**, 157 (1991).

[CMZ] CodeME. *CMZ: A Source Code Management System*. CERN Program Library and CodeME, version 1.49 edition, 1996.

[Caff86] Caffrey. *TNS NS-33 1* page 230 (1986).

[Camp97] X. Campi and H. Krivine. *Nucl. Phys.* **A620**, 46 (1997).

[Cass90] W. Cassing, V. Metag, U. Mosel, and K. Niita. *Phys. Rep.* **188**, 363 (1990).

[Cass90b] W. Cassing and U. Mosel. *Prog. Nucl. Part, Phys.* **25**, 1 (1990).

[Cass99] W. Cassing and E. L. Bratkovskaya. *Phys. Rep.* **308**, 65 (1999).

[Cava90] C. Cavata *et al. Phys. Rev.* **C42**, 1760 (1990).

[Char88] R. Charity *et al. Nucl. Phys.* **A483**, 371 (1988).

[Chas97] K. C. Chase, A. Z. Mekjian, and P. Bhattacharyya. *Phys. Rev.* **C55**, 1410 (1997).

[Chom00] P. Chomaz, V. Duflot, and F. Gulminelli. In I. Iori, editor, *XXXVIII International Winter Meeting on Nucl. Physics*, Università Degli Studi di Milano, Bormio Italy, January 2000.

[Chom94] P. Chomaz. *Phys. Rev. Lett.* **73**, 3512 (1994).

[Chri90] P. Christrillin. *Phys. Rep.* **190**, 63 (1990).

[Cohe63] D. Cohen, B. Moyer, H. Shaw, and C. Waddell. *Phys. Rev.* **130**, 1505 (1963).

[Colin98] E. Colin *et al. Phys. Rev.* **C57**, R1032 (1998).

[Colin99] E. Colin *et al. Pre-print, Nuclear Group SUNY* (1999).

[Coni00] R. Coniglione *et al. Phys. Lett.* **B471**, 339 (2000).

[Cser86] L. P. Csernai and J. Kapusta. *Phys. Rep.* **131**, 223 (1986).

[Cser95] L. Csernai. *Introduction to relativistic heavy ion collisions*. John Wiley & Sons, 1995.

[Cugn80] J. Cugnon. *Phys. Rev.* **C22**, 1885 (1980).

[Cugn83] J. Cugnon and D. L'Hote. *Nucl. Phys.* **A397**, 519 (1983).

[Cugn87] J. Cugnon. *Nucl. Phys.* **A462**, 751 (1987).

[Cuss93] D. Cussol. *Nucl. Phys.* **A561**, 298 (1993).

[DAgo99] M. D'Agostino *et al. Nucl. Phys.* **A650**, 329 (1999).

[DEnte93] D. d'Enterria. *Reaction mechanisms in heavy-ion collisions at Fermi energies: Study of the reaction* $^{238}U+^{197}Au$ *at 15 MeV/nucleon*. Master's thesis, Dept. Física UAB, 1993.

[DEnte95] D. d'Enterria. *Phys. Rev.* **C52**, 3179 (1995).

[Dani96] P. Danielewicz and S. Pratt. *Phys. Rev.* **C53**, 249 (1996).

[DeTa95] C. DeTar. Quark-gluon plasma from numerical simulations of lattice qcd. In R. C. Hwa, editor, *Quark - Gluon plasma. Vol. 2*, World Scientific, Singapore, April 1995.

[Dors99] C. O. Dorso, V. C. Latora, and A. Bonasera. *Phys. Rev.* **C60**, 034606 (1999).

[Dura92] D. Durand. *Nucl. Phys.* **A541**, 266 (1992).

[Dura95] D. Durand. *Phys. Lett.* **B345**, 397 (1995).

[Dura97] D. Durand. In Y. Schutz and H. Löhner, editors, *IV TAPS Workshop Sept. '97*, Ed. Frontières, Paris, Mont Sainte-Odile, 1998.

[Dura98] D. Durand. *Nucl. Phys.* **A630**, 52c (1998).

[Dura99] D. Durand. *Nucl. Phys.* **A654**, 273c (1999).

[Edgi66] J. Edgington and B. Rose. *Nucl. Phys.* **89**, 523 (1966).

[Egel81] C. Egelhaaf, G. Bohlen, H. Fuchs, A. Gamp, H. Hohmeyer, and H. Kluge. *Phys. Rev. Lett.* **46**, 813 (1981).

[Eich97] U. Eichmann and W. Greiner. *J. Phys.* **G23**, L65–L76 (1997).

[Eude88] P. Eudes. *LPCC T 88 01*. PhD thesis, Thèse Université de Caen, 1988.

[Eude98] P. Eudes *et al.* In I. Iori, editor, *XXXVI Int. Winter Meeting on Nucl. Physics*, Università Degli Studi di Milano, Bormio Italy, January 1998.

[Fabr90] E. Fabrici *et al. Phys. Rev.* **C42**, 2163 (1990).

[Fai86] G. Fai and J. Randrup. *Comput. Phys. Commun.* **42**, 385 (1986).

[Feld00] H. Feldmeier and J. Schnack. *cond-mat/0001207* (2000).

[Fish67] M. Fisher. *Rep. Prog. Part. Phys* **30**, 615 (1967).

[Fox78] G. Fox and S. Wolfram. *Phys. Rev. Lett.* **41**, 1581 (1978).

[Fran97] F. Frankland *et al.* In I. Iori, editor, *XXXX International Winter Meeting on Nucl. Physics*, Università Degli Studi di Milano, Bormio Italy, January 1997.

[Frie54] G. Friedlaender. *Phys. Rep.* **94**, 727 (1954).

[Frie88] W. Friedman. *Phys. Rev. Lett.* **60**, 2125 (1988).

[Frie90] W. Friedman. *Phys. Rev.* **C42**, 667 (1990).

[GEANT] C. A. Group. *GEANT Detector Description and Simulation Tool*. CERN, Geneva, w5013 edition, 1993.

[Gaar87] J. J. Gaardhoje, A. M. Bruce, J. D. Garrett, B. Herskind, D. Barnéoud, M. Maurel, H. Nifenecker, J. A. Pinston, P. Perrin, C. Ristori, F. Schussler, A. Bracco, and M. Pignanelli. *Phys. Rev. Lett.* **59**, 1409 (1987).

[Gaar92] J. Gaardhoje. *Ann. Rev. Nucl. Part. Sci.* **42**, 483 (1992).

[Gabl94] A. Gabler, W. Doering, M. Fuchs, B. Krusche, V. Metag, R. Novotny, M. Roebig-Landau, H. Stroeher, V. Tries, C. Molenaar, H. Loehner, J. van Pol, A. Raschke, M. Ŝumbera, L. Venema, H. Wilschut, R. Averbeck, W. Niebur, A. Schubert, R. Simon, R. Beck, J. Peise, G. Miller, R. Owens, and G. Anton. *Nucl. Inst. and Meth.* **A346**, 168 (1994).

[Gali94] J. Galin. *Jour. Phys.* **G20**, 1105 (1994).

[Gan94] N. Gan, K.-T. Brinkmann, A. L. Caraley, B. J. Fineman, W. J. Kernan, R. L. McGrath, and P. Danielewicz. *Phys. Rev.* **C49**, 298 (1994).

[Geno99] E. Genouin-Duhamel. *LPCC T99-01*. PhD thesis, Thèse Université de Caen, 1999.

[Gilk94] M. Gilkes *et al. Phys. Rev. Lett.* **73**, 1590 (1994).

[Glas94] T. Glasmacher *et al. Phys. Rev.* **C50**, 952 (1994).

[Glend88] N. Glendenning. *Phys. Rev.* **C37**, 2733 (1988).

[Glend92] N. Glendenning. *Phys. Rev.* **D46**, 1274 (1992).

[Gogn75] D. Gogny. In G. Ripka and M. Porneuf, editors, *Trieste Int. Conf. on Nuclear Self-Consistent Fields*. North-Holland, Amstermdam, 1975.

[Gold96] F. Goldenbaum *et al. Phys. Rev. Lett.* **77**, 1230 (1996).

[Gong91] W. Gong, W. Bauer, C. K. Gelbke, and S. Pratt. *Phys. Rev.* **C43**, 781 (1991).

[Goss90] C. Gosset *et al. Phys. Rev.* **C42**, R1800 (1990).

[Goss95] J. Gossiaux *et al. Phys. Rev.* **C51**, 3357 (1995).

[Goss97] P. B. Gossiaux and J. Aichelin. *Phys. Rev.* **C57**, 2109 (1997).

[Gott65] B. Gottschalk and W. Shlaer. *Phys. Lett.* **16**, 294 (1965).

[Grass85] Grassman *et al. Nucl. Inst. and Meth.* **228**, 323 (1985).

[Grat94] G. Gratta, H. Newman, and R. Y. Zhu. *Ann. Rev. Nucl. Part. Sci.* **44**, 453–500 (1994).

[Greg87] C. Gregoire, B. Remaud, F. Sebille, L. Vinet, and Y. Raffray. *Nucl. Phys.* **A465**, 317 (1987).

[Gros84] E. Grosse. Pions and high-energy photons from nucleus-nucleus collisions. In *Bad Honnef 1984, Proceedings Coincident Particle Emission From Continuum States In Nuclei*, pages 574–581, 1984.

[Gros84b] E. Grosse. In N. Cindro, W. Greiner, and R. Caplar, editors, *Fundamental problems in heavy-ion collisions*, page 347. World Scientific, Singapore, 1984.

[Gros85] P. Grimm and E. Grosse. *Prog. Part. Nucl. Phys.* **15**, 339 (1985).

[Gros97] D. Gross. *Phys. Rep.* **279**, 119 (1997).

[Gudi83] K. Gudima and V. Toneev. *Nuc. Phys.* **A400**, 173c (1983).

[Gudi96] K. Gudima, T. Matulewicz, H. Delagrange, F. Marqués, G. Martínez, R. Ostendorf, M. Ploszajczak, Y. Schutz, V. Toneev, P. Bozek, S. Hlavàĉ, R. Holzmann, A. Schubert, R. Simon, V. Wagner, H. Löner, J. van Pol, R. Siemssen, H. Wilschut, J.Díaz, and A. Marín. *Phys. Rev. Lett.* **76**, 2412 (1996).

[Gudi99] K. Gudima and M. Ploszajczak. *Acta Phys. Polon.* **B29**, 2277 (1998).

[Gutb89] H. H. Gutbrod, A. M. Poskanzer, and H. G. Ritter. *Rep. Prog. Phys.* **52**, 1267 (1989).

[Hadd96] F. Haddad *et al. Z. Phys.* **A354**, 321 (1996).

[Hage64] R. Hagedorn. *Relativistic kinematics*. W.A. Benjamin, NY, 1964.

[Hart98] C. Hartnack *et al. Eur. Phys. J.* **A1**, 151 (1998).

[Haug96] J. A. Hauger *et al. Phys. Rev. Lett.* **77**, 235 (1996).

[Haus52] Hauser and Feshback. *Phys. Rep.* **87**, 366 (1952).

[Hein00] U. Heinz and M. Jacob. *nucl-th/0002042*.

[Heis88] H. Heiselberg, C. Pethick, and D. Ravenhall. *Phys. Rev.* **C61**, 818 (1988).

[Heis99] H. Heiselberg. *nucl-th/991202*.

[Hejny95] W. Hejny. *TAPS Analysis Support Library*, 1995.

[Herr88] N. Herrmann, R. Bock, H. Emling, R. Freifelder, A. Gobbi, E. Grosse, K. D. Hildenbrand, R. Kulessa, T. Matulewicz, F. Rami, R. S. Simon, H. Stelzer, J. Wessels, P. R. Maurenzig, A. Olmi, A. A. Stefanini, *et al. Phys. Rev. Lett.* **60**, 1630 (1988).

[Heue88] R. Heuer *et al. Z. Phys.* **A330**, 315 (1988).

[Hing87] R. Hingmann, W. Kühn, V. Metag, R. Mühlhans, R. Novotny, and A. Ruckelshausen. *Phys. Rev. Lett.* **759**, 58 (1987).

[Hira95] Y. Hirabayashi, Y. Sakuragi, and Y. Abe. *Phys. Rev. Lett.* **74**, 4141 (1995).

[Ho93] Y.-K. Ho *et al. J. Phys.* **G19**, 1045 (1993).

[Hoef00] M. Hoefman *et al. in preparation* (2000).

[Hoef94] M. Hoefman *et al. KVI Annual Report* page 53 (1994).

[Hoef99] M. Hoefman. PhD thesis, Rijksuniversiteit Groningen, 1999.

[Hofm94] H. Hofmann, J. Bacelar, M. Harakeh, T. Poelhekken, and A. van der Woude. *Nucl. Phys.* **A571**, 301 (1994).

[Hofs50] J. Hofstadter. *Nucleonics* **6 5**, 70 (1950).

[Horo83] C. Horowitz. *Nucl. Phys.* **A399** (1983).

[Horo87] C. Horowitz. *Phys. Rev.* **C35**, 1442 (1987).

[Hub90] F. Hubert. *Atomic Data and Nuclear Data Tables* **46** (1990).

[Hube92] J. Hubele *et al. Phys. Rev.* **C46**, 1577 (1992).

[Huis99] H. Huisman *et al. Phys. Rev. Lett.* **83**, 40 (1999).

[Iori93] I. Iori *et al. Nucl. Inst. and Meth.* **A325**, 458 (1993).

[Itzy85] C. Itzykson and J. Zuber. *Quantum Field Theory*. McGraw Hill, NY, 1985.

[Jack75] J. Jackson. *Classical Electrodynamics*. John Wiley & Sons, NY, 1975.

[Jahn99] U. Jahnke *et al. Phys. Rev. Lett. 83* page 4959 (1999).

[Jako82] B. Jakobsson, G. Jonsson, B. Lindkvist, and A. Oskarsson. *Z. Phys.* **A307**, 293 (1982).

[Jaqa83] H. Jaqaman, A. Z. Mekjian, and L. Zamick. *Phys. Rev.* **C27**, 2782 (1983).

[Jeon94] S. Jeong *et al. Phys. Rev. Lett.* **72**, 3468 (1994).

[Jian89] D. X. Jiang *et al. Nucl. Phys.* **A503**, 560 (1989).

[Jou98] D. Jou, J. Casas-Vazquez, and G. Lebon. *Extended Irreversible Thermodynamics*. Springer Verlag, Germany, 2nd edition, 1998.

[KANE96] L. Aphecetche, Y. Charbonnier, Y. Schutz, T. Matulewicz, and G. Martínez. *GANIL Report* **R9702**, 1 (1997).

[KVI95b] A. Drentje, H. Kiewert, and J. Schippers. *KVI Annual Report* page 45 (1995).

[Khoa91] D. Khoa, N. Ohtsuka, S. Huang, M. Ismail, A. Faessler, M. E. Shabshiry, and J. Aichelin. *Nucl. Phys.* **A529**, 363 (1991).

[Kim92] Y. D. Kim *et al. Phys. Rev.* **C45**, 338–352 (1992).

[Kirk88] J. Kirkby. (1986). Invited talk given at the *INFN Eloisation Project - Workshop on Vertex Detectors: State of the Art and Perspectives*, Erice, Italy, Sep. 21-26, 1986.

[Knol89] G. Knoll. *Radiation Detection and Measurement*. John Wiley & Sons, NY, 1989.

[Knol93] J. Knoll and R. Lenk. *Nucl. Phys* **A561**, 501 (1993).

[Koch90] V. Koch *et al. Phys. Lett.* **B236**, 135 (1990).

[Koeh67] P. Koehler *et al. Phys. Rev. Lett.* **18**, 933 (1967).

[Kol86] Kol. *KVI Annual Report* page 132 (1986).

[Krus85] H. Kruse, B. Jacak, and H. Stöcker. *Phys. Rev. Lett.* **54**, 289 (1985).

[Kwat88] M. Kwato-Njock, M. Maurel, E. Monnand, H. Nifenecker, P. Perrin, J. Pinston, F. Schussler, and Y. Schutz. *Nucl. Phys.* **A489**, 368 (1988).

[Kwia95] K. Kwiatkowski *et al. Nucl. Inst. and Meth.* **A360**, 571 (1995).

[Kwia98] K. Kwiatkowski *et al. Phys. Lett.* **B423**, 21 (1998).

[Laco80] M. Lacombe. *Phys. Rev.* **C21**, 861 (1980).

[Lamb78] D. Lamb. *Phys. Rev. Lett.* **41**, 1623 (1978).

[Lamp88] A. R. Lampis *et al. Phys. Rev.* **C38**, 1961 (1988).

[Latt00] J. Lattimer and M. Prakash. *astro-ph/0002203*.

[Lava83] Laval. *Nucl. Inst. and Meth.* **206**, 169 (1983).

[LeFa94] J. L. Faou, T. Suomijärvi, Y. Blumenfeld, P. Piattelli, C. Agodi, N. Alamanos, R. Alba, F. Auger, G. Bellia, P. Chomaz, R. Coniglione, A. D. Zoppo, P. Finocchiaro, N. Frascaria, J. Gaardhoje, J. P. Garron, A. Gillibert, M. Lamehi-Rachti, R. Liguori-Neto, C. Maiolino, E. Migneco, G. Russo, J. C. Roynette, D. Santonocito, P. Sapienza, J. Scarpaci, and A. Smerzi. *Phys. Rev. Lett.* **72**, 3321 (1994).

[Leco94] J. Lecolley *et al. Phys. Lett.* **B325**, 317 (1994).

[Leco96] F.-R. Lecolley. *LPCC T96-01*. PhD thesis, Thèse Université de Caen, 1996.

[Lee97] S. J. Lee and A. Z. Mekjian. *Phys. Rev.* **C56**, 2621 (1997).

[Leeg92] H. Leegte, E. Koldenhof, A. Boonstra, H. Wilschut, I, and I. *Nucl. Inst. and Meth.* **A313**, 26 (1992).

[Lefo99] T. Lefort *et al. nucl-ex/9910017*.

[Leo92] W. Leo. *Techniques for Nuclear and Particle Physics Experiments*. Springer Verlag, Germany, 1992.

[Lera87] S. Leray *et al. J. Phys.* **47**, C4–275 (1987).

[Lev79] J. Levinger. *Phys. Lett.* **B82**, 181 (1979).

[Li92] G. Li, Y. Lofty, S. Huang, and A. Faessler. *J. Phys. G: Nucl. Part. Phys.* **18**, 291–302 (1992).

[Li93] G. Li. *Prog. Part. Nucl. Phys.* **31**, 159 (1993).

[Li99] X. D. Li, I. Bombaci, M. Dey, J. Dey, and E. P. J. van den Heuvel. *Phys. Rev. Lett.* **83**, 3776 (1999).

[Lid87] Liden. *Nucl. Inst. and Meth.* **A253**, 305 (1987).

[Llope95] W. Llope *et al. Phys. Rev.* **C51**, 1325 (1995).

[Lope84] J. Lopez and P. Siemens. *Nucl. Phys.* **A431**, 728 (1984).

[Louv93] M. Louvel *et al. Nucl. Phys.* **A559**, 137 (1993).

[Louv94] M. Louvel *et al. Phys. Lett.* **B320**, 221 (1994).

[Luka97] J. Lukasik *et al. Phys. Rev.* **C55**, 1906 (1997).

[Luke93] S. Luke, R. Vandenbosh, W. Beneson, J. Clayton, K. Joh, D. Krofeheck, and T. Murakami. *Phys. Rev. C* **47**, 1211 (1993).

[Lyn83] W. Lynch and W. Friedman. *Phys. Rev.* **C28**, 16 (1983).

[Ma97] N. Ma *et al. Phys. Rev.* **C49**, 298 (1994).

[Mach87] R. Machleidt. *Phys. Rep.* **149**, 1 (1987).

[Mach94] R. Machleidt. *Phys. Rep.* **242**, 5 (1994).

[Maje87] Majewski. *Nucl. Inst. and Meth.* **A260**, 373 (1987).

[Male91] F. Malek *et al. Phys. Lett.* **B266**, 255 (1991).

[Malf88] R. Malfliet. *Prog. Part. Nucl. Phys.* **21** (1988).

[Malf92] R. Malfliet. *Nucl. Phys.* **A545**, 3 (1992).

[Mari95] N. Marie. PhD thesis, Thèse Université de Caen, 1995.

[Mari97] N. Maire *et al. Phys. Lett.* **B391**, 15 (1997).

[Marq95] F. Marqués, G. Martínez, Y. Schutz, J. Díaz, M. Franke, S. Hlávač, R. Holzmann, P. Lautridou, F. Lefèvre, H. Löhner, A. Marín, T. Matulewicz, W. Mittig, R. Ostendorf, J. van Pol, J. Québert, P. Roussel-Chomaz, A. Schubert, R. Siemssen, R. Simon, Z. Sujkowski, V. Wagner, H. Wilschut, and G. Wolf. *Phys. Lett.* **B349**, 30 (1995).

[Marq95b] F. Marqués, F. Lefèvre, G. Martínez, T. Matulewicz, R. Ostendorf, and Y. Schutz. *Nucl. Inst. and Meth.* **A365**, 392 (1995).

[Marq97] F. Marqués, G. Martínez, T. Matulewicz, R. Ostendorf, and Y. Schutz. *Phys. Rep.* **284**, 91 (1997).

[Marqt94] M. Marqués. PhD thesis, Universitat de València, 1994.

[Mart94] G. Martínez, J. Díaz, M. Franke, S. Hlaváč, R. Holzmann, P. Lautridou, F. Lefèvre, H. Löhner, A. Marín, F. Marqués, T. Matulewicz, W. Mittig, R. Ostendorf, J. van Pol, J. Québert, P. Roussel-Chomaz, Y. Schutz, A. Schubert, R. Siemssen, R. Simon, Z. Sujkowski, V. Wagner, and H. Wilschut. *Phys. Lett.* **B334**, 23 (1994).

[Mart95] G. Martínez, F. Marqués, Y. Schutz, G. Wolf, J. Díaz, M. Franke, S. Hlaváč, R. Holzmann, P. Lautridou, F. Lefèvre, H. Löhner, A. Marín, T. Matulewicz, W. Mittig, R. Ostendorf, J. van Pol, J. Québert, P. Roussel-Chomaz, A. Schubert, R. Siemssen, R. Simon, Z. Sujkowski, V. Wagner, and H. Wilschut. *Phys. Lett.* **B349**, 23 (1995).

[Mart97] G. Martínez, L. Aphecetche, Y. Charbonnier, H. Delagrange, T. Matulewicz, and Y. Schutz. *Nucl. Inst. and Meth.* **A391**, 435 (1997).

[Mart97b] G. Martínez. In Y. Schutz and H. Löhner, editors, *IV TAPS Workshop Sept. '97*, Ed. Frontières, Paris, Mont Sainte-Odile, 1998.

[Mart99] G. Martínez *et al. Phys. Lett.* **B461**, 28 (1999).

[Martt94] G. Martínez. *Dependance de la production de photon durs avec le paramètre d'impact dans les collisions entre ions lourds aux énergies intermédiaires*. PhD thesis, Universitat de València, 1994.

[Maru94] T. Maruyana *et al. Nucl. Phys.* **A573**, 653 (1994).

[Matu89] T. Matulewicz, E. Grosse, H. Emling, H. Grein, R. Kulessa, F. Baumann, G. Domogala, and H. Freiesleben. *Nucl. Inst. and Meth.* **A274**, 501 (1989).

[Matu90] T. Matulewicz, E. Grosse, H. Emling, R. Freifelder, H. Grein, W. Henning, N. Herrmann, R. Kulessa, R. Simon, H. Wollersheim, B. Schoch, J. Vogt, M. Wilhelm, J. Kratz, R. Schmidt, and R. Janssen. *Nucl. Inst. and Meth.* **A289**, 194 (1990).

[Matu96d] T. Matulewicz, H. Delagrange, F. M. Marques, G. Martínez, and Y. Schutz. *GANIL Report* (1996). GANIL-P-96-26.

[Maye93] R. Mayer, W. Henning, R. Holzmann, R. Simon, H. Delagrange, F. Lefèvre, T. Matulewicz, R. Merrouch, W. Mittig, R. Ostendorf, Y. Schutz, F. Berg, W. Kühn, V. Metag, R. Novotny, M. Pfeiffer, A. Boonstra, H. Löhner, L. Venema, H. Wilschut, D. Ardouin, H. Dąbrowski, B. Erazmus, D. Lebrun, L. Sezac, F. Ballester, E. Casal, J. Díaz, J. Ferrero, M. Marqués, G. Martínez, H. Nifenecker, B. Fornal, L. Freindl, and Z. Sujkowski. *Phys. Rev. Lett.* **70**, 904 (1993).

[Mcle86] L. McLerran. *Rev. Mod. Phys.* **58**, 1021 (1986).

[Mess99] J. Messchendorp *et al. Phys. Rev. Lett.* **82**, 2649 (1999).

[Meta93] V. Metag. *Prog. Part. Nucl. Phys.* **30**, 75 (1993).

[Mign92] E. Migneco *et al. Nucl. Inst. and Meth.* **A314**, 31 (1992).

[Migne99] E. Migneco *et al. Phys. Lett.* **B**, in press (1999).

[Ming99] Y.-M. Zheng, C. M. Ko, B.-A. Li, and B. Zhang. *Phys. Rev. Lett.* **83**, 2534 (1999).

[Moli85] J. Molitoris and H. Stöcker. *Phys. Rev.* **C32**, R346 (1985).

[Mora00] M. Mora. Master's thesis, Universidad de Salamanca, 2000.

[Mora99] K. Morawetz, V. Špička, P. Lipavsky, G. Kortemeyer, C. Kuhrts, and R. Nebauer. *Phys. Rev. Lett.* **82**, 3767–3770 (1999).

[More93] L. G. Moretto and G. J. Wozniak. *Ann. Rev. Nucl. Part. Sci.* **43**, 379–456 (1993).

[More96] L. Moretto *et al. Phys. Rev. Lett.* **76**, 2822 (1996).

[More97] L. Moretto. *Phys. Rep.* **287**, 287 (1997).

[Morje95] M. Morjean *et al. Nucl. Phys.* **A591**, 371 (1995).

[Mose91] U. Mosel. *Ann. Rev. Nucl. Partic. Sci.* **41**, 29 (1991).

[Mose93] U. Mosel and V. Metag. *Nucl. Phys. News* **3**, 25 (1993).

[Muel99] W. Mueller *et al.* In H. Feldmeier *et al.*, editors, *"Multifragmentation"XXVII Int. Work. on Gross Properties of Nuclei and Nuclear Excitations,* GSI, Hirschegg, Austria, January 1999.

[Mull99] H. Mueller *et al. nucl-th/9910038*.

[Myer76] W. Myers. *Atomic Data Nucl. Data Tables* **17**, 411 (1976).

[Myhr88] F. Myhrer and J. Wroldsen. *Rev. Mod. Phys.* **60**, 629 (1988).

[Naka89] K. Nakayama. *Phys. Rev.* **C39**, 1475 (1989).

[Neba98] R. Nebauer, J. Aichelin, N. LeNeindre, and R. Bougault. *nucl-th/9807064* (1998).

[Neba99a] R. Nebauer *et al. Nucl. Phys.* **A658**, 67 (1999).

[Neba99b] R. Nebauer and J. Aichelin. *Nucl. Phys.* **A650**, 65 (1999).

[Nege82] J. Negele. *Rev. Mod. Phys.* **54**, 913 (1982).

[Neis90] L. Neise *et al. Nucl. Phys.* **A519**, 375c (1990).

[Neuh87] D. Neuhauser and S. Koonin. *Nucl. Phys.* **A462**, 163 (1987).

[Nife85] H. Nifenecker and J. Bondorf. *Nucl. Phys.* **A442**, 478 (1985).

[Nife89] H. Nifenecker and J. Pinston. *Prog. Part. Nucl. Phys.* **23**, 271 (1989).

[Nife90] H. Nifenecker and J. Pinston. *Annu. Rev. Nucl. Part. Sci.* **40**, 113 (1990).

[Niit88] K. Niita *et al. Nucl. Phys.* **A482**, 525c (1988).

[Norm00] J. Normand. *private communication* (2000).

[Novo87] R. Novotny. *Nucl. Inst. and Meth.* **A262**, 340 (1987).

[Novo91] R. Novotny. *IEEE Trans. Nucl. Sci.* **NS-38**, 379 (1991).

[Oblo89] P. Oblozinsky. *Phys. Rev.* **C40**, 1591 (1989).

[Oesc99] H. Oeschler *et al.* In H. Feldmeier *et al.*, editors, *"Multifragmentation" XXVII Int. Work. on Gross Properties of Nuclei and Nuclear Excitations*, GSI, Hirschegg, Austria, January 1999.

[Ohts90] N. Ohtsuka, M. Shabshiry, M. Ismail, A. Faessler, and J. Aichelin. *J. Phys. G: Nucl. Part. Phys.* **16**, L155–L161 (1990).

[Ono98] A. Ono. *Phys. Rev.* **C59**, 853 (1999).

[Orte00] R. Ortega. In *V TAPS Workshop*, Czechoslovak Journal of Physics, Řež near Prague, September 1999.

[Oste95] R. Ostendorf. In R. Simon, editor, *III TAPS Workshop*, GSI, Bosen, Germany, September 1995.

[Oste98] R. Ostendorf and the TAPS Collaboration. *GANIL E154c Experiment Proposal* (1998).

[PAW90] R. Brun *et al.* In *New Computing techniques in physics research*. Editions du CNRS, CERN, 1990.

[PDG98] C. Caso *et al. Eur. Phys. J.* **C3**, 1–794 (1998).

[Pan98] J. Pan, S. D. Gupta, and M. Grant. *Phys. Rev. Lett.* **80**, 1182 (1998).

[Pan98b] J. Pan and S. D. Gupta. *Phys. Rev.* **C57**, 1839 (1998).

[Path77] R. Pathria. *Statistical Mechanics*. Pergamon Press, Oxford, 1977.

[Peil89] G. Peilert, H. Stöcker, A. Rosenhauer, A. Bohnet, J. Aichelin, and W. Greiner. *Phys. Rev.* **C39**, 1402 (1989).

[Peil94] G. Peilert, H. Stöcker, and W. Greiner. *Rep. Prog. Phys.* **57**, 533 (1994).

[Pien00] L. Pienkowski *et al. to appear in Phys. Lett. B.*

[Pins89] J. Pinston *et al. Phys. Lett.* **B218**, 128 (1989).

[Poch85] J. Pochodzalla *et al. Phys. Rev. Lett.* **55**, 177 (1985).

[Poch87] J. Pochodzalla *et al. Phys. Rev.* **C35**, 1695 (1987).

[Poch95] J. Pochodzalla, T. Möhlenkamp, T. Rubehn, A. Schütauf, A. Wörner, E. Zude, M. Begemann, T. Blaich, H. Emling, and A. Ferrero. *Phys. Rev. Lett.* **75**, 1040 (1995).

[Poch96] J. Pochodzalla *et al. Phys. Rev. Lett.* **76**, 2823 (1996).

[Poch97] J. Pochodzalla. *Prog. Part. Nucl. Phys.* **39**, 443 (1997).

[Pol96] J. van Pol, H. Wilschut, H. Löhner, R. Siemssen, P. Lautridou, F. Lefèvre, T. Matulewicz, M. Marqués, W. Mittig, R. Ostendorf, P. Roussel-Chomaz, Y. Schutz, S. H. c, R. Holzmann, A. Schubert, R. Simon, V. Wagner, M. Franke, W. Kühn, M. Notheisen, R. Novotny, F. Ballester, J. Díaz, A. Marín, G. Martínez, and A. Kugler. *Phys. Rev. Lett.* **76**, 1425 (1996).

[Polt95] J. van Pol. *Dissipation Mechanisms studied with Nuclear Bremsstrahlung*. PhD thesis, Rijksuniversiteit Groningen, 1995.

[Pout95] J. Pouthas *et al. Nucl. Inst. and Meth.* **A357**, 418 (1995).

[Povh95] B. Povh, K. Rith, C. Scholz, and F. Zetsche. *Particles and Nuclei*. Springer Verlag, 1995.

[Prak88] M. Prakash, P. Braun-Munzinger, J. Stachel, and N. Alamanos. *Phys. Rev.* **C37**, 1959 (1988).

[Praka88] M. Prakash *et al. Phys. Rev.* **C37**, 1959 (1988).

[Puel77] F. Puelhofer. *Nucl. Phys.* **A280**, 267 (1977).

[Puri96] R. K. Puri, C. Hartnack, and J. Aichelin. *Phys. Rev.* **C54**, 28–31 (1996).

[ROOT] R. Brun and F. Rademakers. *Nucl. Inst. and Meth.* **A389**, 81 (1997). see http://root.cern.ch.

[Raja99] K. Rajagopal. *hep-ph/9908360*.

[Rand88] J. Randrup and R. Vandenbosch. *Nucl. Phys.* **A490**, 418 (1988).

[Rand90] J. Randrup and B. Remaud. *Nucl. Phys.* **A514**, 339 (1990).

[Rasc92] A. Raschke. Master's thesis, Univ. Münster, Germany, 1992.

[Rasch97] A. Raschke. PhD thesis, Rijksuniversiteit Groningen, 1997.

[Reev91] H. Reeves. *Phys. Rep.* **201**, 335–356 (1991).

[Reid68] R. Reid. *Ann. Phys.* **50**, 411 (1968).

[Rem86] B. Remington, M. Blann, and G. F. Bertsch. *Phys. Rev. Lett.* **57**, 2909 (1986).

[Repo92] T. Reposeur, J. Clayton, W. Benenson, M. Cronqvist, S. Hannuschke, S. Howden, J. Karn, D. Krofcheck, A. Nadasen, C. Ogilvie, R. Pfaff, J. Stevenson, A. V. Molen, , G. Westfall, K. Wilson, J. Winfeld, and B. Young. *Phys. Lett.* **B276**, 418 (1992).

[Ries92] S. Riess, G. Enders, A. Hofmann, W. Kühn, V. Metag, R. Novotny, W. Mittig, Y. Schutz, A. Villari, H. Emling, H. Grein, E. Grosse, W. Henning, R. Holzmann, R. Kulessa, T. Matulewicz, and H. Wollersheim. *Phys. Rev. Lett.* **69**, 1504 (1992).

[Rive96] M. Rivet *et al. Phys. Lett.* **B388**, 219 (1996).

[Roth66] K. Rothe *et al. Phys. Rev.* **157**, 1247 (1966).

[Russo94] G. Russo *et al. Nucl. Phys.* **A575**, 449 (1994).

[Sain88] F. Saint-Laurent *et al. Phys. Lett.* **B202**, 190 (1988).

[Salo97] S. Salou. PhD thesis, Thèse Université de Caen, 1997.

[Sang95] T. C. Sangster. *Phys. Rev.* **C51**, 1280 (1995).

[Sauv94] J. Sauvestre *et al. Phys. Lett.* **B335**, 300 (1994).

[Scha91] M. Schäfer, T. Biró, W. Cassing, U. Mosel, H. Nifenecker, and J. Pinston. *Z. Phys.* **A339**, 391 (1991).

[Schi98] D. Schinzel. *Nucl. Inst. and Meth.* **A419**, 217 (1998).

[Schr84] W. Schroeder and J. Huizenga. *Treatise on Heavy Ion Science Vol. 2*. A. Bromley, Plenum Press, NY, 1984.

[Schr92] W. Schroeder. *Nucl. Phys.* **A538**, 439 (1992).

[Schreu98] H. Schreuder. In *XV Int. Conf. on cyclotrons and their applications*, IOP Publishing, Caen, 1998.

[Schu94] A. Schubert, R. Holzmann, S. Hlavác, R. Kulessa, W. Niebur, R. Simon, P. Lautridou, F. Lefèvre, F. Marqués, T. Matulewicz, W. Mittig, R. Ostendorf, P. Roussel-Chomaz, Y. Schutz, H. Löhner, J. van Pol, R. Siemssen, H. Wilschut, F. Ballester, J. Díaz, A. Marín, G. Martínez, V. Metag, R. Novotny, V. Wagner, and J. Québert. *Phys. Rev. Lett.* **72**, 1608 (1994).

[Schu94b] A. Schubert, R. Holzmann, S. Hlavác, R. Kulessa, W. Niebur, R. Simon, P. Lautridou, F. Lefèvre, F. Marqués, T. Matulewicz, W. Mittig, R. Ostendorf, P. Roussel-Chomaz, Y. Schutz, H. Löhner, J. van Pol, R. Siemssen, H. Wilschut, F. Ballester, J. Díaz, A. Marín, G. Martínez, V. Metag, R. Novotny, V. Wagner, and J. Québert. *Phys. Lett.* **B328**, 10 (1994).

[Schu96] Y. Schutz. *Acta Phys. Polon.* **B27**, 263 (1996).

[Schu97] Y. Schutz, G. Martínez, F. Marqués, A. Marín, T. Matulewicz, R. Ostendorf, P.Bozek, H. Delagrange, J. Díaz, M. Franke, K. Gudima, S. Hlaváč, R. Holzmann, P. Lautridou, F. Lefèvre, H. Löhner, W. Mittig, M. Ploszajczak, J. van Pol, J. Québert, P. Roussel-Chomaz, A. Schubert, R. Siemssen, R. Simon, Z. Sujkowski, V. Toneev, V. Wagner, H. Wilschut, and G. Wolf. *Nucl. Phys.* **A622**, 405 (1997).

[Schw99] C. Schwarz *et al.* In H. Feldmeier *et al.*, editors, *"Multifragmentation"XXVII Int. Work. on Gross Properties of Nuclei and Nuclear Excitations*, GSI, Hirschegg, Austria, January 1999.

[Serb47] R. Serber. *Phys. Rep.* **72**, 1114 (1947).

[Sero86] B. D. Serot and J. D. Walecka. *Adv. Nucl. Phys.* **16**, 1–327 (1986).

[Shap94] O. Shapiro. *Nucl. Phys.* **A573**, 143 (1994).

[Shar88] M. Sharma, W. Borghols, S. Brandenburg, S. Crona, A. van der Woude, and M. Harakeh. *Phys. Rev.* **C38**, 2562 (1988).

[Shkl97] V. Shklyar, B. Kampfer, B. Reznik, and A. Titov. *Nucl. Phys.* **A628**, 255 (1998).

[Shya86] R. Shyam and J. Knoll. *Nucl. Phys* **A448**, 322 (1986).

[Siem83] G. Siemens. *Nature* **305**, 2782 (1983).

[Siwe98] A. Siwek, D. D. F. Gulminelli, and J. Peter. *Phys. Rev.* **C57**, 2507 (1998).

[Skyr59] T. Skyrme. *Nucl. Phys.* **9**, 615 (1959).

[Snov86] K. Snover. *Ann. Rev. Nucl. Part. Sci.* **36**, 545 (1986).

[Sobo91] L. Sobotka, L. Gallamore, A. Chbihi, D. Sarantites, D. Stracener, W. Bauer, D. Bowman, N. Carlin, R. DeSouza, C. Gelbke, W. Gong, S. Hannuschke, Y. Kim, W. Lynch, R. Ronningen, M. T. andF. Zhu, J. Beene, M. Halbert, and M. Thoennessen. *Phys. Rev.* **C46**, 819 (1992).

[Soko93] A. Sokolov *et al. Nucl. Phys.* **A562**, 273 (1993).

[Sorg89] H. Sorge, H. Stöcker, and W. Greiner. *Ann. Phys.* **192**, 266 (1989).

[Souz90] R. de Souza *et al. Nucl. Inst. and Meth.* **A295**, 109 (1990).

[Souz91] R. de Souza *et al. Phys. Lett.* **B268**, 6 (1991).

[Stah87] T. Stahl *et al. Z. Phys.* **A327**, 311 (1987).

[Stev86] J. Stevenson, K. Beard, W. Benenson, J. Clayton, E. Kashy, A. Lampis, D. Morrissey, M. Samuel, R. Smith, C. Tam, and J. Winfeld. *Phys. Rev. Lett.* **57**, 555 (1986).

[Sto80] R. Stock. *Phys. Rev. Lett.* **44**, 1243 (1980).

[Sto86] R. Stock. *Phys. Rep.* **135**, 261 (1986).

[Stoe86] H. Stöcker and W. Greiner. *Phys. Rep.* **137**, 277 (1986).

[Stra90] D. Stracener, D. Sarantites, L. Sobotka, J. Elson, J. Hood, Z. Majka, V. Abenante, and A. Chbihi. *Nucl. Inst. and Meth.* **A294**, 485 (1990).

[Stro96] H. Ströher. *Nucl. Phys. News* **6**, 7 (1996).

[Suff88] M. Suffert. *Comptes Rendus Ecole Joliot-Curie Sep. 1988*. ed. M. Buenerd, Eds. de Physique, Paris, 1988.

[Sun00] R. Sun *et al. Phys. Rev. Lett.* **84**, 43 (2000).

[Sun99a] R. Sun *et al. Pre-print, Nuclear Group SUNY* (1999).

[Suom96] T. Suomijärvi, Y. Blumenfeld, P. Piattelli, J. H. L. Faou, C. Agodi, N. Alamanos, R. Alba, F. Auger, G. Bellia, P. Chomaz, R. Coniglione, A. D. Zoppo, P. Finocchiaro, N. Frascaria, J. J. Gaardhoje, J. P. Garron, *et al. Phys. Rev.* **C53**, 2258 (1996).

[Suom98] T. Suomijärvi, P. Piattelli, D. Santonocito, Y. Blumenfeld, C. Agodi, N. Alamanos, R. Alba, F. Auger, G. Bellia, P. Chomaz, M. Colonna, R. Coniglione, A. D. Zoppo, P. Finocchiaro, N. Frascaria, A. Gillibert, J. H. L. Faou, K. Loukachine, C. Maiolino, E. Migneco, J. Roynette, P. Sapienza, and J. Scarpaci. *RIKEN Symposium on Dynamics in Hot Nuclei, March 13-14* (1998). IPNO DRE 98-09.

[Sura85] E. Suraud *et al. Phys. Lett.* **B164**, 212 (1985).

[Sura89] E. Suraud *et al. Phys. Lett.* **B229**, 362 (1989).

[Sura90] E. Suraud. In *Ecole Joliot-Curie de Physique Nucléaire 1990*, page 160, IN2P3-CNRS, Maubuisson, Sep. 1990.

[Sura92] E. Suraud, S. Ayik, M. Belkacem, and J. Stryjewski. *Nucl. Phys.* **A542**, 141 (1992).

[Sura93] E. Suraud. In J. Díaz, G. Martínez, and Y. Schutz, editors, *II TAPS Workshop*, World Scientific, Guardamar, P. Valencià, June 1993.

[TAPS97] *The first 10 years with TAPS.* Universität Gießen, Gießen, 1997.

[Tam88] C. Tam *et al. Phys. Rev.* **C38**, 2526 (1988).

[Tam89] C. Tam, J. Stevenson, W. Benenson, Y. Chen, J. Clayton, E. Kashy, A. Lampis, D. Morrissey, M. S. T. Murakami, and J. Winfield. *Phys. Rev.* **C39**, 1371 (1989).

[Tama97] B. Tamain and D. Durand. In *Int. Summ. School Les Houches*, Les Houches France, 1996.

[TerH87] B. ter Haar and R. Malfliet. *Phys. Rep.* **149**, 207 (1987).

[Tire98] O. Tirel. PhD thesis, Thèse Université de Caen, 1998.

[Tohs96] A. Tohsaki. *Phys. Rev. Lett.* **76**, 3518 (1996).

[Traut99] W. Trautmann *et al.* In H. Feldmeier *et al.*, editors, *"Multifragmentation"XXVII Int. Work. on Gross Properties of Nuclei and Nuclear Excitations*, GSI, Hirschegg, Austria, January 1999.

[Ueh33] E. Uehling and G. Uhlenbeck. *Phys. Rev.* **43**, 552 (1933).

[Vand98] R. Vandenbosch. *private communication* (1998).

[Vasa85] D. Vasak *et al. J. Phys.* **G11**, 1309 (1985).

[Vasa86] D. Vasak. *Phys. Lett.* **B176**, 276 (1986).

[Vene94] L. Venema. PhD thesis, Rijksuniversiteit Groningen, 1994.

[Vien92] E. Vient *et al. Nucl. Phys.* **A571**, 588 (1994).

[Viol99] V. Viola *et al.* In H. Feldmeier *et al.*, editors, *"Multifragmentation"XXVII Int. Work. on Gross Properties of Nuclei and Nuclear Excitations,* GSI, Hirschegg, Austria, January 1999.

[Viyo79] Y. Viyogi *et al. Phys. Rev. Lett.* **42**, 33 (1979).

[Wada89] R. Wada *et al. Phys. Rev.* **C39**, 497 (1989).

[Wale74] J. Walecka. *Ann. Phys* **83**, 491 (1974).

[Wang94] Z. Wang, Y. Ho, and Z. Pan. *Phys. Rev.* **C49**, 2104 (1994).

[Warn65] R. Warner. *Phys. Lett.* **18**, 289 (1965).

[Warw83] A. I. Warwick *et al. Phys. Rev.* **C27**, 1083 (1983).

[Weis37] V. Weisskopf. *Phys. Rep.* **52**, 295 (1937).

[Wilk52] D. Wilkinson. *Rev. Sci. Instr.* **23**, 414 (1952).

[Wils52] R. Wilson. *Phys. Rep.* **85**, 563 (1952).

[Wils95] H. Wilschut. In R. Simon, editor, *III TAPS Workshop*, GSI, Bosen, Germany, September 1995.

[Wiss97] L. Wissing *et al. Nucl. Inst. and Meth.* **A397**, 472 (1997).

[Wolf90] G. Wolf, G. Batko, W. Cassing, U. Mosel, K. Niita, and M. Schäfer. *Nucl. Phys.* **A517**, 615 (1990).

[Wolf93] G. Wolf, W. Cassing, and U. Mosel. *Nucl. Phys.* **A552**, 549 (1993).

[Wong96] C. Wong. *Introduction to high energy heavy-ion collisions*. World Scientific, Singapore, 1996.

[Xi96] H. Xi *et al. Phys. Rev.* **C54**, R2163 (1996).

[Xi98] H. Xi *et al. Phys. Rev.* **C58**, R2636 (1998).

[Yane96] R. Yanez *et al. Phys. Lett.* **B376**, 29 (1996).

[Yari79] Y. Yariv and Z. Frankel. *Phys. Rev.* **C20**, 2227 (1979).

[Youn99] D. Youngblood, Y.-W. Lui, and H. L. Clark. *Phys. Rev. Lett.* **82**, 691 (1999).

[Yuka35] H. Yukawa. *Proc. Phys. Math. Soc. Jpn.* **17** (48).

[Zami73] L. Zamick. *Phys. Lett.* **B45**, 313 (1973).

[Zie96] J. F. Ziegler. *IBM Journal Res. Develop.* **40**, No. 1 (1996).

List of Figures

1.1 *Nuclear equation-of-state around the ground-state (or saturation) point [Lee97]. "Thermodynamical"EoS* $P = P(T,\rho)$ *(upper figure) and "caloric"EoS* $\varepsilon = \varepsilon(T,\rho)$ *(lower figure) of nuclear matter for different isothermal curves (from bottom to top):* T_i *(MeV) = 0, 3, 5, 7, 10, 15.16 (=* T_z *at which the minimum pressure is zero), and 20.95 (=* T_c*, the critical temperature); obtained with a nuclear mean-field interaction of the form* $U = U(\rho)$*. The saturation point* 0 *corresponds to P = 0 (otherwise the system would expand or contract) or* ε *= -16 MeV, T = 0 MeV and* ρ_0 *= 0.16 fm*$^{-3}$*. The critical point c in this model is at* T_c *= 20.95 MeV,* $\rho_c = 0.39\rho_0$ *= 0.062 fm*$^{-3}$ *and P = 0.4 MeV fm*$^{-3}$*. The dotted points delimit the mechanically unstable low-density "spinodal"region where* $dP/d\rho \mid_T < 0$ *(i.e. the region where the incompressibility* κ_∞ *becomes negative). In the lower figure, the dashed line corresponds to the zero pressure, and the solid circles to the points of minimum energy for each temperature T. (See Section 2.2.1 for the details of this plot.)* 3

1.2 *Basic central nucleon-nucleon potential (for spin S = 0 and isospin T = 1). From [Mach94].* 4

1.3 *Comparison between the EoS,* $P = P(T,V)$*, of a Van der Waals gas and the EoS of nuclear matter (described by a density-dependent Skyrme mean-field potential) [Jaqa83, Bert88].* 5

1.4 *Phase diagram of nuclear matter in the temperature versus baryochemical potential (*T*,* μ_B*) plane [Aver98], where* μ_B *has been derived from yield ratios of particles produced in nucleus-nucleus collisions at different incident energies. The solid (dashed) curve through the data points represents the predicted curve of chemical (thermal) freeze-out.* 6

2.1 *The low density part of the phase diagram of nuclear matter and the critical region of the liquid-gas phase transition. The trajectories depicted in the figure correspond to the possible paths followed by a nuclear system produced in a central heavy-ion reaction.* 17

2.2 *Isentropes in the (ε, ρ) plane corresponding to the critical point (open circle, $s = 2.7$) and the end point of the spinodal (full circle, $s = 2.4$). Also shown inside the mixture zone (shadow) are the spinodal (dashed line), and the Maxwell construction of the final entropy per nucleon curve s, as well as the unstable isentropes s_i and s_f (dotted lines). [According to this model, in the small gap between $s = 2.4$ and $s = 2.7$ the system experiences neither fragmentation nor instantaneous vaporization but goes from one phase to another in a continuous manner]. Adapted from [Lope84].* . 19

2.3 *Landau-Vlasov simulations [Hadd96]: Density profile in coordinate space for the Ar(44A MeV)+Ag reaction at different impact parameters (upper part). Time evolution of the normalized mean density for the same reaction (lower part).* 24

2.4 *Photography of a multifragmentation reaction as seen by nuclear emulsion experiments with heavy-ion beams at intermediate energies [Jako82].* 28

2.5 *Schematic view [Geno99] of the different decay-modes of an excited nuclear system produced in a heavy-ion collision for increasing excitation energies.* 29

2.6 *Correlation excitation energy - temperature for a nucleus of mass A = 100 according to the Copenhagen statistical multifragmentation model [Bond85]. The dashed (solid) line illustrates the temperature of a free nucleon gas (of a Fermi liquid).* 30

2.7 *Caloric curve of nuclei determined by the dependence of the so-called "isotope temperature" T_{HeLi} (see Section 9.3) on the excitation energy per nucleon $\varepsilon^\star$ [Poch95]. The solid curve corresponds to the Fermi liquid curve $\varepsilon^\star = T^2/10$, and the dotted one to the classical Boltzmann gas relation $\varepsilon^\star \propto 3/2\,T$.* 30

3.1 *Typical photon spectra, in the NN center-of-mass, emitted in a heavy-ion reaction at intermediate energies and measured with the TAPS photon spectrometer: in the low-energy ($E_\gamma < 50$ MeV) region (upper figure, [Schu97]), and in the region 20 MeV $< E_\gamma <$ 200 MeV (lower figure, [Gudi99]). The different elementary contributions according to a "Dubna Cascade Model" calculation are identified on the bottom figure (the closed circles represent the experimental photon spectrum after cosmic-ray background subtraction).* 37

3.2 *Schematic representation of total photoabsorption cross-section on nuclei. Adapted from [Chri90].* 40

3.3 *Systematics of the experimentally measured hard-photon inverse slope parameter E_0 as a function of the Coulomb corrected bombarding energy per nucleon K_{Cc}. From [Polt95].* 42

3.4 *Measured angular distribution of hard photons ($E_\gamma > 25$ MeV) in comparison to isotropic (dot-dashed) and dipole (dotted) radiation from the nucleus-nucleus system and to isotropic emission (dashed) from the nucleon-nucleon system. The solid line shows the best fit to the data with a source velocity of $\beta = 0.094 \pm 0.020$. From [Cass90].* 44

3.5 *Dependence of the bremsstrahlung photon production with respect to the (Coulomb-corrected) beam energy per nucleon measured for various systems. From [Polt95].* 44
3.6 *Definitions of the geometrical parameters used in the "equal participant model". From [Schu97].* 46
3.7 *Variation of the number of proton-neutron collisions, N_{pn}, with the impact parameter, b, calculated using eq. (3.12) for the system $^{86}Kr+^{58}Ni$. Dots represent the number of first chance pn collisions calculated with a BUU model. From [Schu97].* 46
3.8 *Hard photon spectra for the systems a) $^{86}Kr+^{58}Ni$ at 60A MeV, b) $^{181}Ta+^{197}Au$ at 39.5A MeV, and c) $^{208}Pb+^{197}Au$ at 29.5A MeV measured in the TAPS campaign at GANIL in 1992. The deviation from the pure single exponential behaviour is apparent for all systems in the region of hard-photon energies $E_\gamma \approx$ 30 - 60 MeV. From [Schu97].* 50
3.9 *Inclusive hard photon spectrum measured at $\theta = 90^\circ$ for the systems $^{14}N+^{208}Pb$ and $^{14}N+^{12}C$ at beam energies of 40A (squares), 30A (circle), and 20A (diamond) MeV [Stev86]. Theoretical curves are those of a thermal bremsstrahlung model.* 51
3.10 *Inclusive hard photon spectrum measured at $\theta = 90^\circ$ for the system $^{14}N+^{108}Ag$ [Luke93]. The solid line is the result of a fit to two exponentials. The dashed and the dotted lines are the components of the fit.* 51
3.11 *Experimental γ-γ correlation function, $C_{12}(Q_{inv})$, for $^{86}Kr+^{58}Ni$ at 60A MeV (right side) and for $^{181}Ta+^{197}Au$ at 39.5A MeV (left side) compared to calculations based on Monte Carlo sampling for one source (dotted line), two sources (dashed line) and two sources of which one is fragmented (solid line). From [Schu97].* 52
3.12 *Inclusive photon spectrum for the system $^{86}Kr+^{58}Ni$ at 60A MeV showing the direct and thermal bremsstrahlung regions as well as the low-energy statistical (GDR and discrete-state gamma decay) one. The approximative times of emission of these different types of photons are also indicated.* 54

4.1 *Layout of TAPS, Dwarf-Ball and Forward Wall multidetectors as pictured by* GEANT. *The Ar beam enters the setup diagonally from the upper right part of the figure. The Carbon-fiber scattering chamber, in which the Dwarf-Ball is located and which matches the front part of the Forward Wall, is not shown.* 59
4.2 *Photography of the experimental setup. The beam pipe enters the setup from the right, and the backsides of 3 out of the 6 TAPS blocks are seen.* . 60
4.3 *Floor plan of the KVI facility at Groningen, The Netherlands.* 61
4.4 *Picture of AGOR cyclotron.* 62
4.5 *Photography of AGOR spiral "Dees".* 62
4.6 *Operating diagram (energy versus charge-to-mass ratio) for AGOR, indicated by the (red) solid lines. The (yellow) circles represent the beams which have been accelerated so far. Adapted from [KVI95b].* 63
4.7 *Photographs of the Carbon-fiber scattering chamber used for TAPS experiments at KVI [Hoef99].* 64

4.8 *Drawing of the basic detection element in TAPS: A hexagonal BaF_2 module with its associated CPV-detector.* 68

4.9 GEANT *representation of one TAPS block comprising 8×8 BaF_2 crystals with their respective NE102A veto detector.* 70

4.10 *Typical dimensions of a single NE102A CPV module. The lightguide lengths vary from 18 to 35 cm depending on the position of the CPV module in the block. From [Rasch97].* 71

4.11 *E_n vs. E_w for a single BaF_2 crystal [Schu97]. The upper branch corresponds to the detection of photons and electrons (or high-energy neutrons) and the lower one to (low-energy) neutrons and LCP. The intrinsic properties of the two different scintillation components of the BaF_2 material allow to differentiate between electromagnetic-like (mainly photons) and hadronic-like (mainly protons) hits in the so-called "Pulse-Shape Analysis"(PSA) technique.* 72

4.12 *Simplified TAPS electronics diagram per BaF_2-CPV module. The description of the different electronics modules is given in table 4.6.* 73

4.13 *Photographs of the Dwarf-Ball: a) The DB placed on the top lid of the carbon scattering chamber. b) Open view of the DB. Most of the detectors of one hemisphere, and all signal cables and PMT voltage dividers, have been removed to allow for a view of the device. The white Teflon tape wraps each phoswich and lightguide.* 76

4.14 *Photograph (upper part) and cross-sectional view (left module in the lower part) of a hexagonal element of the Dwarf-Ball. The white Teflon tape covers the plastic-CsI(Tl) phoswiches and the Lucite light guide. The Ta/Au foils cover the front side of each detector.* 80

4.15 *Example of a typical array used for light-charged-particle identification in the DB: Isotopic identification of LCP using the CsI(Tl) "tail"(also called "long") versus "slow"energies 2D-plots [Stra90].* 81

4.16 *Schematic diagram of the Dwarf-Ball electronics. The description of the different electronics modules is given in table 4.8. A more detailed scheme of the whole DB electronics and pre-trigger logics can be found in Appendix 5.* 81

4.17 *Photograph of the backside of the Forward Wall multidetector. The two groups of small and large individual phoswiches can be seen surrounded by the aluminum box. The beam passes through the central hole.* 84

4.18 *Photograph (upper part) and cross-sectional view (lower part) of a small (and large) FW phoswich module.* 86

4.19 *Example of a $\Delta E - E$ array (short vs. long) used for the particle identification in the FW [Hoef00]. The inset shows the isotopic separation of hydrogen.* 87

4.20 *Forward-Wall basic electronics scheme per module. The description of the different electronics modules is given in table 4.9.* 88

5.1 *Flowchart of the analysis. Each single analysis-step is explained in the different sections of this chapter. The final outputs (inclusive and exclusive photon/particle distributions) constitute the experimental results presented and discussed in chapters 6. and 7.* 100
5.2 *Energy wide spectrum of a BaF_2 module during beam-time. The first arrow indicates the position of the QDC pedestal (0 MeV). The second one, indicates the position of the cosmic muon peak corresponding to a mean energy loss of 38 MeV in the BaF_2 crystal. The solid line corresponds to a fit of the signal to a gaussian+first degree polynomial function.* 104
5.3 *Raw time spectrum for a BaF_2 module showing the consecutive beam pulses double-structure.* 105
5.4 *Calibrated time-of-flight spectrum of a BaF_2-module during 20 experimental runs of the ^{36}Ar+^{197}Au reaction. The first (prompt) peak, centered at TOF = 2.2 ns, corresponds to the photons, the second "bump"to (slower) particles hitting TAPS.* 105
5.5 *Evolution of the position of the photon peak during the 14 days of experiment before (upper part) and after (lower part) the corrections of the RF drifts. The position of the peak is calculated every 10^5 accumulated events (one bin in the x-axis).* 107
5.6 *PSA as a function of TOF for all particles detected in TAPS with energies 10 MeV $< E <$ 20 MeV. Photons events appear centered around PSA = 1 and TOF = 2.2 (+ 26.9) ns. Charged hadrons have PSA $\approx$ 0.7 and TOF = 5 - 15 (+ 26.9) ns (see table 5.2).* 109
5.7 *Schema of the particle-identification procedure in TAPS as implemented into* ROSEBUD. *It makes use of the PSA $= E_n/E_w$, TOF (time-of-flight) and CPV (charged-particle-veto) information. Adapted from [Aphe98].* . 109
5.8 *Experimental line shape of a photon of E_γ = 55 MeV incident in a TAPS block, compared to the fitted analytical response function given by eq. (5.7). The values of the fit parameters are shown in the figure. From [Gabl94].* 112
5.9 *Isotopic light-charged-particle identification with a E_{sl} vs. E_{ta} bidimensional plot for a CsI(Tl) crystal of the DB multidetector. The different "punchthrough"points for the hydrogen (p,d,t) and helium (^3He, α) can be seen. The area above the proton loop corresponds to the region of neutron and photon signals. The area below the α line is populated with IMF events.* 115
5.10 *Linear parameter P_{LCP} histogram showing the peaks of the 3 isotopes of hydrogen and the 2 isotopes of helium. From [Mora00].* 115
5.11 *Scatter plot of the fast vs. slow energy component from the same detector as in fig. 5.9 showing the different branches corresponding to the intermediate mass fragments for Z up to 10. The isotopes of H and He are not resolved in this type of plot.* 116
5.12 *Linearization plot of the projected E_f vs. E_{sl} bidimensional histogram shown in fig. 5.11. Each peak corresponds to the different charge Z of the particles and fragments produced in the heavy-ion reaction. Adapted from [Mora00].* 117

5.13 *Forward-Wall particle identification with the $\Delta E - E$ plot of a single module.* 119
5.14 *"Pileup TDC"histogram ("OR"of the CFDs of each group of 16 or 32 common-gated phoswiches) for the four groups of 16(32) detectors of the FW. Only the events lying within the two most outstanding peaks have been retained for subsequent analysis.* 120
5.15 *Example of the "Pileup TDC"correction method. The left panel shows the raw E_{sh} vs. E_l plot, the right panel shows the same data after selecting a single peak in the "Pileup TDC"histogram (fig. 5.14).* 120

6.1 *Raw inclusive energy spectrum of photons measured with TAPS (rectangles) for the $^{36}Ar+^{197}Au$ system during the low counting-rate runs of the experiment. The triangles indicate the cosmic background and the stars the contribution of photons stemming from the decay of the π^0 produced in the reaction.* 123
6.2 *TAPS and DB detector response influence on the inverse slope parameter of exponential hard-photon spectra simulated with the* KANE *package (E_0^{actual} versus E_0^{meas}). The wide solid line is obtained for TAPS alone as well as for the Dwarf-Ball in between the target and TAPS. The dashed line corresponds to the ideal response function.* 125
6.3 *Two-photon invariant mass distribution experimentally measured for the $^{36}Ar+^{197}Au$ system during the high counting-rate runs (solid), shown together with a* GEANT *simulation of the same number of π^0 decays (hatched histogram).* 126
6.4 *Experimental (dots) and simulated (stars) kinetic energy distribution of the π^0 detected for the system $^{36}Ar+^{197}Au$. The experimental pion kinetic energy spectrum has been fitted to a Maxwell-Boltzmann distribution in the NN center-of-mass frame with inverse slope $E_0 \approx 15$ MeV.* 127
6.5 *Experimental hard photon energy spectrum measured in the NN CM for the system $^{36}Ar+^{197}Au$, during the Dwarf-Ball (low-intensity) runs. The spectrum has been fitted in the range E_γ = 30 - 180 MeV according to equation (6.4) to the sum of two exponential distributions: a direct (solid line) and a thermal one (dashed line). (The vertical dotted line indicates the low-energy threshold, $E^{thr}_{hard-\gamma}$ = 30 MeV, for hard-photons.)* 130
6.6 *Experimental hard photon energy spectrum measured in the NN CM for the system $^{36}Ar+^{197}Au$, during the high counting-rates runs. The spectrum has been fitted in the range E_γ = 30 - 180 MeV according to equation (6.4) to the sum of two exponential distributions: a direct (solid line) and a thermal one (dashed line).* 131
6.7 *Experimental hard photon energy spectrum measured in the NN CM for the system $^{36}Ar+^{108}Ag$ fitted in the range E_γ = 30 - 180 MeV, according to equation (6.4), to the sum of two exponential distributions: a direct (solid line) and a thermal one (dashed line).* 132
6.8 *Experimental hard photon energy spectrum measured in the NN CM for the system $^{36}Ar+^{58}Ni$ fitted in the range E_γ = 30 - 180 MeV, according to equation (6.4), to the sum of two exponential distributions: a direct (solid line) and a thermal one (dashed line).* 133

6.9 *Experimental hard photon energy spectrum measured in the NN CM for the system $^{36}Ar+^{12}C$ fitted in the range E_γ = 30 - 180 MeV just to the first direct exponential of equation (6.4) (solid line).* 134

6.10 *Experimental hard-photon energy spectrum in the NN CM for the $^{36}Ar+^{197}Au$ reaction in the range E_γ = 30 - 70 MeV depicted in a linear-y plot to emphasize the two distinct (thermal and direct) hard-photon exponential contributions.* 135

6.11 *Inclusive thermal hard-photon energy spectrum obtained from the raw photon spectrum above E_γ = 30 MeV after subtraction of the cosmic and pion-decay backgrounds, and after subtraction of the direct hard-photon component (first term of equation (6.4)). The system is $^{36}Ar+^{197}Au$ (low-intensity runs). The remaining exponential distribution above 30 MeV must correspond to hard-photon emission other than first-chance proton-neutron bremsstrahlung.* 136

6.12 *Experimental hard-photon spectrum measured at $\theta_{lab} = 90^\circ \pm 2^\circ$ for the $^{36}Ar+^{197}Au$ reaction, during the low counting-rate runs. The spectrum has been fitted in the range E_γ = 30 - 140 MeV, according to equation (6.4), to the sum of two exponential: a direct (solid line) and a thermal one (dashed line).* 137

6.13 *Compilation [Schu97] of the measured (direct) hard-photon slope parameters plotted as a function of the bombarding energy per nucleon minus the Coulomb barrier energy of the reaction. Our data (inclusive E_0^d) are represented by the star symbols. The solid line represents a fit of equation (3.4) to the data.* 139

6.14 *Compilation of the measured thermal slopes E_0^t for the systems studied in the present work, $^{36}Ar+^{197}Au$, ^{107}Ag, ^{58}Ni, as well as those studied in the 1992 TAPS campaign at GANIL, $^{86}Kr+^{58}Ni$, $^{181}Ta+^{197}Au$, $^{208}Pb+^{197}Au$ [Schu97], plotted as a function of the (Coulomb-corrected) total available energy in the nucleus-nucleus center-of-mass.* 140

6.15 *Experimental angular distribution in the lab for hard-photons above 60 MeV measured in the system $^{36}Ar+^{197}Au$ during the low counting-rate runs and fitted (solid line) according to equation (6.6).* 143

6.16 *Experimental angular distribution in the lab for hard-photons above 60 MeV measured in the system $^{36}Ar+^{197}Au$ during the high counting-rate runs and fitted (solid line) according to equation (6.6).* 144

6.17 *Experimental angular distribution in the lab for hard-photons above 60 MeV measured in the system $^{36}Ar+^{108}Ag$ and fitted (solid line) according to equation (6.6).* 144

6.18 *Experimental angular distribution in the lab for hard-photons above 60 MeV measured in the system $^{36}Ar+^{58}Ni$ and fitted (solid line) according to equation (6.6).* 145

6.19 *Experimental angular distribution in the lab for hard-photons above 60 MeV measured in the system $^{36}Ar+^{12}C$ and fitted (solid line) according to equation (6.6).* 145

6.20 *Experimental laboratory angular distribution for hard-photons ($E_\gamma > 30$ MeV) measured in the system $^{36}Ar+^{197}Au$ during the low counting-rate runs and fitted according to equation (6.8). The hatched region indicates the estimated contribution of thermal hard-photons, emitted isotropically from a source moving with β_{AA}.* 148

6.21 *Experimental laboratory angular distribution for hard-photons ($E_\gamma > 30$ MeV) measured in the system $^{36}Ar+^{197}Au$ during the high counting-rate runs and fitted according to equation (6.8). The hatched region indicates the estimated contribution of thermal hard-photons, emitted isotropically from a source moving with β_{AA}.* 149

6.22 *Experimental laboratory angular distribution for hard-photons ($E_\gamma > 30$ MeV) measured in the system $^{36}Ar+^{108}Ag$ and fitted according to equation (6.8). The hatched region indicates the estimated contribution of thermal hard-photons, emitted isotropically from a source moving with β_{AA}.* 150

6.23 *Experimental laboratory angular distribution for hard-photons ($E_\gamma > 30$ MeV) measured in the system $^{36}Ar+^{58}Ni$ and fitted according to equation (6.8). The hatched region indicates the estimated contribution of thermal hard-photons, emitted isotropically from a source moving with β_{AA}.* 151

6.24 *Experimental laboratory angular distribution for hard-photons ($E_\gamma > 30$ MeV) measured in the system $^{36}Ar+^{12}C$ and fitted according to equation (6.8). No thermal hard-photon contribution (second term of eq. (6.8)) has been considered in the source-velocity fit analysis.* 152

6.25 *Total inclusive charged-particle multiplicity distribution for the reaction $^{36}Ar+^{197}Au$ at 60A MeV measured with the Dwarf-Ball and Forward-Wall.* 154

6.26 *Inclusive charged-particle multiplicity distribution detected in the Dwarf-Ball for the reaction $^{36}Ar+^{197}Au$ at 60A MeV.* 154

6.27 *Inclusive charged-particle multiplicity distribution detected in the Forward-Wall for the reaction $^{36}Ar+^{197}Au$ at 60A MeV.* 155

6.28 *Inclusive charged-particle multiplicity distribution detected in the Forward-Wall for the reaction $^{36}Ar+^{108}Ag$ at 60A MeV.* 155

6.29 *Inclusive charged-particle multiplicity distribution detected in the Forward-Wall for the reaction $^{36}Ar+^{58}Ni$ at 60A MeV.* 156

6.30 *Inclusive charged-particle multiplicity distribution detected in the Forward-Wall for the reaction $^{36}Ar+^{12}C$ at 60A MeV.* 156

6.31 *Inclusive light-charged-particle (LCP) multiplicity distribution detected in the Dwarf-Ball for the reaction $^{36}Ar+^{197}Au$ at 60A MeV.* 158

6.32 *Inclusive intermediate-mass-fragment (IMF) multiplicity detected in the Dwarf-Ball for the reaction $^{36}Ar+^{197}Au$ at 60A MeV.* 158

6.33 *Bidimensional plot (logz scale) of the intermediate-mass-fragment multiplicity detected in the DB (M_{IMF}) as a function of the total charged-particle multiplicity (M_{CP}) detected in the Dwarf-Ball for the reaction $^{36}Ar+^{197}Au$ at 60A MeV.* 159

6.34 *Input distribution of impact-parameters, b, for the $^{36}Ar+^{197}Au$ events generated with* FREESCO *(solid line), and distribution of impact-parameters of the fraction of these simulated events which verify the "minimum-bias"particle trigger (dashed line). The distribution of impact-parameters for events leading to the emission of a hard-photon in such a heavy-ion reaction according to the "equal participant"geometrical model is also indicated (dotted line).* 163

6.35 *Systematics [Schu97] of measured photon emission probabilities per pn collision, $P^{exp}_{pn\gamma}$, as a function of the (Coulomb-corrected) bombarding energy per nucleon (see also fig. 3.5). Our data are represented by stars. The solid line represents a fit to eq. (6.13).* 169

6.36 *Experimental total, M_γ, and thermal, M^t_γ, hard-photon multiplicities per nuclear reaction plotted as a function of the (impact-parameter averaged) number of pn collisions, $\langle N_{pn}\rangle_b$, in the five reactions studied by the TAPS collaboration at 60A MeV bombarding energy (the four systems of the present experiment plus the $^{86}Kr+^{58}Ni$ one studied at GANIL in 1992 [Mart94]). The solid and dashed lines are linear fits to the data points.* . . . 171

7.1 *Total charged-particle multiplicity distribution, M^{tot}_{cp}, measured with the Dwarf-Ball and Forward-Wall for $^{36}Ar+^{197}Au$ reactions in which at least one photon above 15 MeV is detected. The filled regions indicate the selected central and peripheral events, the hatched one the zone where pileup (two consecutive reactions recorded simultaneously) starts to be significant.* 176

7.2 *IMF multiplicity distribution M^{DB}_{IMF} measured with the Dwarf-Ball for $^{36}Ar+^{197}Au$ at 60A MeV reactions in which at least one photon above 15 MeV is detected. The filled area corresponds to the selected region of multifragmentation events, the hatched one to the zone where pileup events are significant.* 177

7.3 *Bidimensional plot of the Forward-Wall multiplicity (M^{FW}_{cp}) as a function of the total charged-particle multiplicity (M_{cp}) detected in the Dwarf-Ball for the reaction $^{36}Ar+^{197}Au$ at 60A MeV.* 178

7.4 *Experimental hard photon energy spectrum measured in the NN CM for central collisions in the system $^{36}Ar+^{197}Au$. The spectrum has been fitted in the range E_γ = 30 - 150 MeV according to equation (6.4) to the sum of two exponential distributions: a direct (solid line) and a thermal one (dashed line).* 179

7.5 *Local slope parameters (crosses) of the experimental hard-photon spectrum measured for central $^{36}Ar+^{197}Au$ collisions at 60A MeV. The dashed line is a linear fit of the local slopes above E_γ = 60 MeV.* 180

7.6 *Experimental hard photon energy spectrum measured in the NN CM for peripheral collisions in the system $^{36}Ar+^{197}Au$. The spectrum has been fitted in the range E_γ = 30 - 130 MeV according to equation (6.4) to the sum of two exponential distributions: a direct (solid line) and a thermal one (dashed line).* 182

7.7 *Experimental hard photon energy spectrum measured in the NN CM for multifragmentation collisions detected in the Dwarf-Ball for the system $^{36}Ar+^{197}Au$. The spectrum has been fitted in the range E_γ = 30 - 150 MeV according to equation (6.4) to the sum of two exponential distributions: a direct (solid line) and a thermal one (dashed line).* 183

7.8 *Total charged-particle multiplicity, M_{cp}^{tot}, measured in the Dwarf Ball and Forward-Wall for the $^{36}Ar+^{197}Au$ system in coincidence with (1) "GDR photons"(defined as photons with 15 MeV $< E_\gamma <$ 22 MeV), (2) "thermal+direct hard-photons"(30 MeV $< E_\gamma <$ 45 MeV), and (3) "pure direct hard-photons"($E_\gamma >$ 60 MeV). The particle multiplicity distributions associated to the GDR-photons and direct hard-photons have been scaled to that of the thermal+direct hard-photons.* 185

7.9 *Experimental photon yield per nuclear reaction, M_γ, as a function of the charged-particle multiplicity, M_{cp}^{DB}, measured in the Dwarf-Ball for: (1) "GDR photons", (2) thermal+direct hard-photons and (3) "pure"direct hard-photons emitted in $^{36}Ar+^{197}Au$ at 60A MeV.* 186

8.1 *Time evolution according to BUU of the reaction $^{36}Ar+^{197}Au$ at 60A MeV and b = 3.8 fm, shown as the density distribution of nucleons projected in the x,z coordinate space. The beam axis is along z, and (x,z) are measured in fm.* 202

8.2 *Time evolution according to BUU of the reaction $^{36}Ar+^{197}Au$ at 60A MeV and b = 3.8 fm, shown as the density distribution of nucleons projected in the transverse-longitudinal (p_x, p_z) momentum space. (Each bin corresponds to 37.5 MeV/c).* 203

8.3 *Time evolution according to BUU of the reaction $^{36}Ar+^{108}Ag$ at 60A MeV and b = 3.1 fm, shown as the density distribution of nucleons projected in the x,z coordinate space. The beam axis is along z, and (x,z) are measured in fm.* 204

8.4 *Time evolution according to BUU of the reaction at $^{36}Ar+^{108}Ag$ at 60A MeV and b = 3.1 fm, shown as the density distribution of nucleons projected in the transverse-longitudinal (p_x, p_z) momentum space. (Each bin corresponds to 37.5 MeV/c).* 205

8.5 *Time evolution according to BUU of the reaction $^{36}Ar+^{58}Ni$ at 60A MeV and b = 2.5 fm, shown as the density distribution of nucleons projected in the x,z coordinate space. The beam axis is along z, and (x,z) are measured in fm.* 206

8.6 *Time evolution according to BUU of the reaction $^{36}Ar+^{58}Ni$ at 60A MeV and b = 2.5 fm, shown as the density distribution of nucleons projected in the transverse-longitudinal (p_x, p_z) momentum space. (Each bin corresponds to 37.5 MeV/c).* 207

8.7 *Time evolution according to BUU of the reaction $^{36}Ar+^{12}C$ at 60A MeV and b = 2.1 fm, shown as the density distribution of nucleons projected in the x,z coordinate space. The beam axis is along z, and (x,z) are measured in fm.* 208

8.8 *Time evolution according to BUU of the reaction $^{36}Ar+^{12}C$ at 60A MeV and b = 2.1 fm, shown as the density distribution of nucleons projected in the transverse-longitudinal (p_x, p_z) momentum space. (Each bin corresponds to 37.5 MeV/c).* 209

8.9 *Evolution of the (central) density in the reactions $^{36}Ar+^{197}Au$, ^{108}Ag, ^{58}Ni, ^{12}C at 60A MeV for the different impact-parameters, as given by BUU calculations.* 211

8.10 *Production rate of bremsstrahlung photons ($E_\gamma \geq 30$ MeV) as a function of time calculated with BUU assuming a rather soft EoS (κ_∞ = 230 MeV) for the system $^{36}Ar+^{197}Au$ at 60A MeV at an impact parameter b = 3.8 fm.* 213

8.11 *Production rate of bremsstrahlung photons ($E_\gamma \geq 30$ MeV) as a function of time calculated with BUU assuming a rather soft EoS (κ_∞ = 230 MeV) for the system $^{36}Ar+^{108}Ag$ at 60A MeV at an impact parameter b = 3.1 fm.* 214

8.12 *Production rate of bremsstrahlung photons ($E_\gamma \geq 30$ MeV) as a function of time calculated with BUU assuming a rather soft EoS (κ_∞ = 230 MeV) for the system $^{36}Ar+^{58}Ni$ at 60A MeV at an impact parameter b = 2.5 fm.* 215

8.13 *Production rate of bremsstrahlung photons ($E_\gamma \geq 30$ MeV) as a function of time calculated with BUU assuming a rather soft EoS (κ_∞ = 230 MeV) for the system $^{36}Ar+^{12}C$ at 60A MeV at an impact parameter b = 2.1 fm.* . 216

8.14 *Time evolution according to QMD of the reaction $^{36}Ar+^{197}Au$ at 60A MeV (b = 3.8 fm), shown as the density distribution of nucleons projected in the (x,z) coordinate space. The beam axis is along z, and (x,z) are measured in fm.* 221

8.15 *Time evolution according to QMD of the reaction $^{36}Ar+^{197}Au$ at 60A MeV (b = 3.8 fm), shown as the density distribution of nucleons projected in the transverse-longitudinal (p_x, p_z) momentum space. (The units in both axes are GeV/c).* 222

8.16 *Time evolution according to QMD of the reaction $^{36}Ar+^{108}Ag$ at 60A MeV (b = 3.1 fm), shown as the density distribution of nucleons projected in the (x,z) coordinate space. The beam axis is along z, and (x,z) are measured in fm.* 223

8.17 *Time evolution according to QMD of the reaction at $^{36}Ar+^{108}Ag$ at 60A MeV (b = 3.1 fm), shown as the density distribution of nucleons projected in the transverse-longitudinal (p_x, p_z) momentum space. (The units in both axes are GeV/c).* 224

8.18 *Time evolution according to QMD of the reaction $^{36}Ar+^{58}Ni$ at 60A MeV (b = 2.5 fm), shown as the density distribution of nucleons projected in the (x,z) coordinate space. The beam axis is along z, and (x,z) are measured in fm.* 225

8.19 *Time evolution according to QMD of the reaction $^{36}Ar+^{58}Ni$ at 60A MeV (b = 2.5 fm), shown as the density distribution of nucleons projected in the transverse-longitudinal (p_x, p_z) momentum space. (The units in both axes are GeV/c).* 226

8.20 *Time evolution according to QMD of the reaction $^{36}Ar+^{12}C$ at 60A MeV (b = 2.1 fm), shown as the density distribution of nucleons projected in the (x,z) coordinate space. The beam axis is along z, and (x,z) are measured in fm.* 227

8.21 *Time evolution according to QMD of the reaction $^{36}Ar+^{12}C$ at 60A MeV (b = 2.1 fm), shown as the density distribution of nucleons projected in the transverse-longitudinal (p_x, p_z) momentum space. (The units are GeV/c).* . . 228

8.22 *Proton-neutron collision (with $K_{CM} \geq 30$ MeV) rate calculated with QMD as a function of time for the system $^{36}Ar+^{197}Au$ at 60A MeV and at an impact parameter b = 3.8 fm. The dashed-dotted lines correspond to pn collisions of nucleons belonging to the (quasi)target and the dotted to the (quasi)projectile. The inset shows the same figure in linear scale in the range t = 100 - 300 fm/c. (The ordinate units are arbitrary).* 230

8.23 *Proton-neutron collision (with $K_{CM} \geq 30$ MeV) rate calculated with QMD as a function of time for the system $^{36}Ar+^{108}Ag$ at 60A MeV and at an impact parameter b = 3.1 fm. The dashed-dotted lines correspond to pn collisions of nucleons belonging to the (quasi)target and the dotted to the (quasi)projectile. The inset shows the same figure in linear scale in the range t = 90 - 300 fm/c. (The ordinate units are arbitrary).* 231

8.24 *Proton-neutron collision (with $K_{CM} \geq 30$ MeV) rate calculated with QMD as a function of time for the system $^{36}Ar+^{58}Ni$ at 60A MeV and at an impact parameter b = 2.5 fm. The dashed-dotted lines correspond to pn collisions of nucleons belonging to the (quasi)target and the dotted to the (quasi)projectile. The inset shows the same figure in linear scale in the range t = 70 - 300 fm/c. (The ordinate units are arbitrary).* 232

8.25 *Proton-neutron collision (with $K_{CM} \geq 30$ MeV) rate calculated with QMD as a function of time for the system $^{36}Ar+^{12}C$ at 60A MeV and at an impact parameter b = 2.1 fm. The dashed-dotted lines correspond to pn collisions of nucleons belonging to the (quasi)target and the dotted to the (quasi)projectile. The inset shows the same figure in linear scale in the range t = 70 - 300 fm/c. (The ordinate units are arbitrary).* 233

9.1 *Thermal bremsstrahlung (pnγ) emission rates, $d^5N_\gamma/d^3x\,dt\,dE_\gamma$, from a nuclear system in thermal equilibrium at the saturation density $\rho_0 = 0.17$ fm^{-3} for various temperatures (T = 4 MeV, T = 6 MeV and T = 8 MeV) as obtained with the Neuhauser and Koonin model [Neuh87].* 239

9.2 *Linear dependence between the inverse slope parameters E_0^t of bremsstrahlung photons and the temperature T of the emitting nuclear source. The different values of E_0^t are obtained from exponential fits, between E_γ = 30 MeV and E_γ = 70 MeV, of the theoretical thermal bremsstrahlung spectra (fig. 9.1) obtained for each nuclear temperature within the thermal model.* 240

9.3 *Illustration [Poch97] of the different thermometers for nuclear systems: light-particle inverse slope parameters (upper part), double isotope ratios (middle part), and relative population of states (lower part).* 245

9.4 *Systematics [Dura98] of measured nuclear temperatures (obtained with the three methods described in Section 9.3) as a function of ε^* ("caloric curve"). The stars correspond to the temperatures and excitation energies obtained in the present analysis (table 9.3). The dotted and dashed lines correspond to the theoretical Fermi-liquid behaviour for two different values of the level density parameter.* 249

1 *Radial and longitudinal development of a "typical"electromagnetic shower. From [Schi98].* 272

2 *Schematic view of the fast (dashed line) and slow (dotted line) pulses of a phoswich detector. The drawn line is the sum of the two signals. The duration of the two integration ("short"and "long") gates and the signal over threshold time are indicated. From [Wiss97].* 276

1 *Bremsstrahlung photon spectrum for a pnγ collision at K_{beam} = 200 MeV according to the classical soft-photon formula (13) (dashed line) and to the covariant expression (15) (solid line). From [Schu97].* 284

2 *Feynman diagrams of the pnγ bremsstrahlung process showing the radiation originating from the exchanged charged mesons, internal lines in b), which interferes constructively with the external radiation, diagrams a), accounting for the "classical"bremsstrahlung.* 284

3 *Hard-photon emission probability per proton-neutron collision versus the (Coulomb-corrected) bombarding energy per nucleon in: 1) nucleus-nucleus collisions (solid and dashed lines, obtained within BUU and DCM calculations respectively), and in 2) free proton-neutron collisions (dotted-dashed line). Both curves have been obtained using the Schäfer parametrization of the elementary pnγ cross-section, eq. (15). Adapted from [Schu97].* 286

1 *Detailed DB electronics and pre-trigger logics.* 300

List of Tables

2.1 *Characteristics of the three experimentally observed dominant decay modes of excited nuclear systems produced in heavy-ion reactions. n are neutrons, LCPs light charged-particles (Z = 1, 2), IMF the fragments with Z = 3 - 20, and HFs heavy fragments with Z > 20.* 29

4.1 *AGOR cyclotron specifications.* 63
4.2 *Characteristics of the Argon beam used in the experiment.* 64
4.3 *Characteristics of the different targets and total estimated counting rates for the different reactions for the selected target thickness - beam intensity combinations.* 66
4.4 *Properties of the reactions Ar+X (X = ^{197}Au, ^{107}Ag, ^{58}Ni, ^{12}C) at K_{lab}= 60A MeV, computed with the formulas listed in Appendix 4.* 67
4.5 *Positions of the 6 TAPS blocks for the KVI experiment. The distances and angles correspond to the center of the frontal side of each block.* 71
4.6 *List of TAPS electronics modules used per BaF_2-CPV detector.* 74
4.7 *Dwarf-Ball telescope positions and thicknesses of their CsI(Tl) and plastic scintillators.* 77
4.8 *List of the basic Dwarf-Ball electronics modules used in the experiment (W.U. stands for "Washington University"custom-made modules).* 83
4.9 *List of FW electronics modules used for each one of the 6 groups of 16 detectors.* 88
4.10 *Overview of the different data acquisition VME processors used. All VME cards were placed inside the slots of two different VME cages, the first slot was used as the crate manager capable of 8,16 bit transfers. (DPM stands for "Dual Port Memory"board).* 90
4.11 *Typical trigger counting rates (C.R.) and acquisition rates for the five reactions studied. The average event size is 300 bytes/event (0.3 KB/event), the maximum data taking capacity of the taping device is limited to 2000 events/s (equivalent to 600 Kbytes/s = 0.6 Mbytes/s = 50 Gbytes/day).* . . 93
4.12 *List of triggers used in the experiment during the low counting-rates runs (# 556 - 1130) with the whole TAPS+DB+FW setup: trigger number, name, event signature and DAQ reduction factor.* 95
4.13 *List of valid triggers used in the experiment during the high counting-rates runs (# 1132 - 1568) with the TAPS+FW setup: trigger number, name, event signature and DAQ reduction factor.* 96

4.14 *Recorded events (all triggers summed) and hard-photons ($E_\gamma > 30$ MeV) collected (all photon triggers summed) during the finally analyzed runs for the four systems studied in this thesis.* 98

5.1 *Average number of BaF_2 modules firing with an energy deposition larger than 5 MeV for photons impinging TAPS with different experimentally measured energies. These multiplicities, obtained from experimental data, coincide very closely with the results of* GEANT *simulations.* 108

5.2 *List of the PSA-TOF rectangular contours used in the present experiment for particle identification in TAPS.* 110

5.3 *Position and angular resolution for photons impinging a TAPS block with different incident energies. The angular resolution is calculated assuming the TAPS block is located 66 cm away from the target. Adapted from [Vene94].* 113

6.1 *For each considered system, raw number of hard-photons and pions experimentally detected (both figures have been corrected to take into account the respective trigger lifetimes and scaling-down factors), as well as estimated number of background photons (above 30 MeV) coming from pion decays as obtained through the simulation. This number is determined by counting the number of $\gamma\gamma$ coincidences with invariant mass lying in the range 80 MeV - 145 MeV (fig. 6.3) and having an opening angle $\theta_{\gamma\gamma} > 80°$.* 128

6.2 *Direct and thermal hard-photon slopes and ratios of thermal to total intensities measured in the ^{36}Ar+^{197}Au, ^{107}Ag, ^{58}Ni, ^{12}C reactions at 60A MeV. The expected values of E_0^d according to the hard-photon systematics, eq. (3.4), are also reported.* 130

6.3 *Measured ratios of thermal to total intensities, as well as direct and thermal slopes for the hard-photons measured at $\theta^{lab} = 90° \pm 2°$ in the ^{36}Ar+^{197}Au, ^{107}Ag, ^{58}Ni, ^{12}C reactions at 60A MeV.* 138

6.4 *Values of the "direct"hard-photon source velocities β_S, and anisotropy factors α, obtained after a Least-Squares fit with equation (6.6) of the hard-photon laboratory angular distributions above E_γ = 60 MeV for the 5 systems studied (figures 6.15, 6.16, 6.17, 6.18, 6.19). The values of the slopes E_0^d used for the fit are also reported.* 143

6.5 *Values of the average hard-photon source velocity $\langle\beta_S\rangle$, and the anisotropy factor α, obtained after a Least-Squares fit of the laboratory angular distributions with equation (6.7) of hard-photons with energies E_γ = 30 - 45 MeV emitted in the 5 studied systems. The values of the local slope parameters E_0 in the range 30 - 45 MeV used for the fits are also reported.* 146

6.6 *Direct and thermal hard-photon ($E_\gamma > 30$ MeV) source velocities obtained from a double-source fit analysis, eq. (6.8), of the laboratory angular distributions.* 149

6.7 *Efficiencies of TAPS for inclusive hard-photon and neutral pion detection (see Section 6.1.4), and charged particle efficiencies of the Dwarf-Ball and Forward-Wall calculated with* KANE/FREESCO *simulations for the five reactions studied.* 161

6.8 *Inclusive experimental and theoretical (geometrical) total reaction cross-sections for the five systems studied in this experiment. The cross-sections for the $^{36}Ar+^{197}Au$ reaction are given for three different considered triggers (two for the low counting-rates runs and one for the high counting-rates runs), as well as their average value.* 165

6.9 *Inclusive experimental and theoretical hard-photon cross-sections for the four systems studied in this experiment. The cross-sections for the $^{36}Ar+^{197}Au$ reaction are given for three different considered triggers (two for the low counting-rates runs and one for the high counting-rates runs), as well as their average value.* 166

6.10 *Inclusive experimental and theoretical hard-photon multiplicities per nuclear reaction, M_γ, for the four systems studied in this experiment. The experimental multiplicities for the $^{36}Ar+^{197}Au$ reaction are given for three different considered triggers (two for the low counting-rates runs and one for the high counting-rates runs), as well as their average value.* 168

6.11 *Inclusive experimental and theoretical hard-photon probabilities per pn collision, $P_{pn\gamma}$, as well as (impact-parameter averaged) number of pn collisions, $\langle N_{pn}\rangle_b$, for the four systems studied in this experiment. The values given for the $^{36}Ar+^{197}Au$ reaction correspond for three different considered triggers (two for the low counting-rates runs and one for the high counting-rates runs), as well as their average value.* 168

6.12 *Inclusive experimental thermal bremsstrahlung multiplicities per nuclear reaction, M_γ^t, and thermal probabilities per pn collision, $P_{pn\gamma}^t$, for the four systems studied in this experiment. The values given for the $^{36}Ar+^{197}Au$ reaction correspond for three different considered triggers (two for the low counting-rates runs and one for the high counting-rates runs), as well as their average value.* 169

6.13 *Total, M_γ, and thermal, M_γ^t, bremsstrahlung multiplicities per nuclear reaction measured in the four systems studied in this experiment and in the ^{86}Kr(60A MeV)$+^{58}Ni$ reaction [Mart94]. The (impact-parameter averaged) number of pn collisions, $\langle N_{pn}\rangle_b$, is also indicated.* 170

7.1 *Measured direct and thermal slopes and ratios of thermal to total intensities in peripheral, central and multifragmentation reactions for the system $^{36}Ar+^{197}Au$ at 60A MeV.* 180

8.1 *Average impact-parameter for maximum bremsstrahlung photon emission probability in the reactions $^{36}Ar+^{197}Au$, ^{107}Ag, ^{58}Ni, ^{12}C at 60A MeV according to the "equal participant model" equation (3.12).* 201

8.2 *Maximum, ρ_{max}, and minimum, ρ_{min}, central densities attained respectively in the first compression stage and at the end of the first expansion stage as predicted by BUU simulations for the reactions $^{36}Ar+^{197}Au$, ^{107}Ag, ^{58}Ni, ^{12}C at 60A MeV at the impact parameters quoted in table 8.1. The density attained at the second recompression of the system ρ_{max}^{2nd} is also indicated. The value of the incompressibility modulus is κ_∞ = 230 MeV, in all cases.* 212

8.3 *Relative ratio of thermal (bremsstrahlung emitted during the second compression stage of the reaction) to total hard-photons for the four studied reactions according to BUU calculations.* 217

9.1 *Nuclear temperatures T extracted from the experimentally measured values of the slope parameters E_0^t of the thermal component of the hard-photon spectra for the systems $^{36}Ar+^{197}Au$, $^{36}Ar+^{108}Ag$, $^{36}Ar+^{58}Ni$, $^{86}Kr+^{58}Ni$, $^{181}Ta+^{197}Au$ and $^{208}Pb+^{197}Au$ calculated by applying the formula (9.7) obtained from the thermal bremsstrahlung model.* 241

9.2 *Nuclear temperatures T attained in central $^{36,40}Ar+^{197}Au$, ^{108}Ag reactions around 60A MeV bombarding energies, extracted experimentally using several proposed methods ("sl."stands for kinetic spectra slopes, and "pop."for excited-state population, see next Section). If reported in the original work, the measured values of the excitation energies $\varepsilon^\star$ are also included.* 242

9.3 *Excitation energies $\varepsilon^\star$ and nuclear temperatures T (extracted from the thermal bremsstrahlung spectra) for the systems $^{36}Ar+^{197}Au$, $^{36}Ar+^{108}Ag$, $^{36}Ar+^{58}Ni$, $^{86}Kr+^{58}Ni$, $^{181}Ta+^{197}Au$ and $^{208}Pb+^{197}Au$ at different bombarding energies. The different values of $\varepsilon^\star$ have been experimentally measured by other collaborations (stars). In the case of the $^{86}Kr+^{58}Ni$ reaction (dot), $\varepsilon^\star$ has been obtained making use of the formulas (9.13) and (9.14), and $\varepsilon^\star$ should be considered as an upper limit (mind the larger systematical errors).* 249

1 *Physical, chemical and scintillation properties of BaF_2 and CsI(Tl) inorganic crystals. Collected from [Suff88, Bour94, Grat94, PDG98]. [The superindex ^{a} represents the % with respect to NaI(Tl) light output efficiency for standard PMT, and ^{f,s} refer to the fast and slow scintillation components respectively.]* 273

2 *General properties of Polyvinyltoluene (PVT) scintillators (the second and third columns correspond to the components of NE102A plastic). From [Suff88, Bicr99].* 275

3 *Properties of the PVT-based scintillators used in this experiment. From [Suff88, Kirk88, Bour94, Bicr99]. * BC-408 is the current commercial name for former BC-446 [Bicr99]. ** NE115 is identical to current BC-444 [Bicr99].* 275